

Small animal imaging: Technological and methodological advances to improve the translational power

Edited by

Monique R. Bernsen, Terry Jones, Wendy McDougald, Laura Mezzanotte,
Carmel Mary Moran, Adriana Tavares and Louise Van Der Weerd

Published in

Frontiers in Medicine



FRONTIERS EBOOK COPYRIGHT STATEMENT

The copyright in the text of individual articles in this ebook is the property of their respective authors or their respective institutions or funders. The copyright in graphics and images within each article may be subject to copyright of other parties. In both cases this is subject to a license granted to Frontiers.

The compilation of articles constituting this ebook is the property of Frontiers.

Each article within this ebook, and the ebook itself, are published under the most recent version of the Creative Commons CC-BY licence. The version current at the date of publication of this ebook is CC-BY 4.0. If the CC-BY licence is updated, the licence granted by Frontiers is automatically updated to the new version.

When exercising any right under the CC-BY licence, Frontiers must be attributed as the original publisher of the article or ebook, as applicable.

Authors have the responsibility of ensuring that any graphics or other materials which are the property of others may be included in the CC-BY licence, but this should be checked before relying on the CC-BY licence to reproduce those materials. Any copyright notices relating to those materials must be complied with.

Copyright and source acknowledgement notices may not be removed and must be displayed in any copy, derivative work or partial copy which includes the elements in question.

All copyright, and all rights therein, are protected by national and international copyright laws. The above represents a summary only. For further information please read Frontiers' Conditions for Website Use and Copyright Statement, and the applicable CC-BY licence.

ISSN 1664-8714
ISBN 978-2-83251-138-1
DOI 10.3389/978-2-83251-138-1

About Frontiers

Frontiers is more than just an open access publisher of scholarly articles: it is a pioneering approach to the world of academia, radically improving the way scholarly research is managed. The grand vision of Frontiers is a world where all people have an equal opportunity to seek, share and generate knowledge. Frontiers provides immediate and permanent online open access to all its publications, but this alone is not enough to realize our grand goals.

Frontiers journal series

The Frontiers journal series is a multi-tier and interdisciplinary set of open-access, online journals, promising a paradigm shift from the current review, selection and dissemination processes in academic publishing. All Frontiers journals are driven by researchers for researchers; therefore, they constitute a service to the scholarly community. At the same time, the *Frontiers journal series* operates on a revolutionary invention, the tiered publishing system, initially addressing specific communities of scholars, and gradually climbing up to broader public understanding, thus serving the interests of the lay society, too.

Dedication to quality

Each Frontiers article is a landmark of the highest quality, thanks to genuinely collaborative interactions between authors and review editors, who include some of the world's best academicians. Research must be certified by peers before entering a stream of knowledge that may eventually reach the public - and shape society; therefore, Frontiers only applies the most rigorous and unbiased reviews. Frontiers revolutionizes research publishing by freely delivering the most outstanding research, evaluated with no bias from both the academic and social point of view. By applying the most advanced information technologies, Frontiers is catapulting scholarly publishing into a new generation.

What are Frontiers Research Topics?

Frontiers Research Topics are very popular trademarks of the *Frontiers journals series*: they are collections of at least ten articles, all centered on a particular subject. With their unique mix of varied contributions from Original Research to Review Articles, Frontiers Research Topics unify the most influential researchers, the latest key findings and historical advances in a hot research area.

Find out more on how to host your own Frontiers Research Topic or contribute to one as an author by contacting the Frontiers editorial office: frontiersin.org/about/contact

Small animal imaging: Technological and methodological advances to improve the translational power

Topic editors

Monique R. Bernsen — Erasmus Medical Center, Netherlands
Terry Jones — University of California, Davis, United States
Wendy McDougald — University of Edinburgh, United Kingdom
Laura Mezzanotte — Erasmus Medical Center, Netherlands
Carmel Mary Moran — University of Edinburgh, United Kingdom
Adriana Tavares — University of Edinburgh, United Kingdom
Louise Van Der Weerd — Leiden University Medical Center (LUMC), Netherlands

Citation

Bernsen, M. R., Jones, T., McDougald, W., Mezzanotte, L., Moran, C. M.,
Tavares, A., Van Der Weerd, L., eds. (2022). *Small animal imaging: Technological and
methodological advances to improve the translational power*.
Lausanne: Frontiers Media SA. doi: 10.3389/978-2-83251-138-1

Table of contents

- 05 **Editorial: Small animal imaging: Technological and methodological advances to improve the translational power**
Monique R. Bernsen, Wendy McDougald, Laura Mezzanotte, Carmel M. Moran, Adriana Tavares and Louise van der Weerd
- 08 **A Purification Method of ^{18}F -FP-(+)-DTBZ via Solid-Phase Extraction With Combined Cartridges**
Yuyin Dai, Ri Sa, Feng Guan, Qi Wang, Yinghua Li and Hongguang Zhao
- 16 **Prediction of Ovarian Follicular Dominance by MRI Phenotyping of Hormonally Induced Vascular Remodeling**
Liat Fellus-Alyagor, Inbal E. Biton, Hagit Dafni, Filip Bochner, Ron Rotkopf, Nava Dekel and Michal Neeman
- 28 **Fluorinated PLGA-PEG-Mannose Nanoparticles for Tumor-Associated Macrophage Detection by Optical Imaging and MRI**
Giorgia Zambito, Siyuan Deng, Joost Haeck, Natasa Gaspar, Uwe Himmelreich, Roberta Censi, Clemens Löwik, Piera Di Martino and Laura Mezzanotte
- 40 **A Systems-Level Analysis of Total-Body PET Data Reveals Complex Skeletal Metabolism Networks *in vivo***
Karla J. Suchacki, Carlos J. Alcaide-Corral, Samah Nimale, Mark G. Macaskill, Roland H. Stimson, Colin Farquharson, Tom C. Freeman and Adriana A. S. Tavares
- 47 **PET/CT Technology in Adult Zebrafish: A Pilot Study Toward Live Longitudinal Imaging**
Carl Tucker, Richard Collins, Martin A. Denvir and Wendy A. McDougald
- 54 **Voxel-Based Analysis of $[^{18}\text{F}]$ -FDG Brain PET in Rats Using Data-Driven Normalization**
Silke Proesmans, Robrecht Raedt, Charlotte Germonpré, Emma Christiaen, Benedicte Descamps, Paul Boon, Veerle De Herdt and Christian Vanhove
- 62 **Translation of Preclinical PET Imaging Findings: Challenges and Motion Correction to Overcome the Confounding Effect of Anesthetics**
Alan Miranda, Daniele Bertoglio, Sigrid Stroobants, Steven Staelens and Jeroen Verhaeghe
- 75 **Multi-Scale Imaging of Vascular Pathologies in Cardiovascular Disease**
Ashish Tiwari, Betsalel Elgrably, Galit Saar and Katrien Vandoorne

- 95 **[¹⁸F] Sodium Fluoride Dose Reduction Enabled by Digital Photon Counting PET/CT for Evaluation of Osteoblastic Activity**
Maria I. Menendez, Richard R. Moore, Mahmoud Abdel-Rasoul, Chadwick L. Wright, Soledad Fernandez, Rebecca D. Jackson and Michael V. Knopp
- 103 **Multimodal *in vivo* Imaging of the Integrated Postnatal Development of Brain and Skull and Its Co-modulation With Neurodevelopment in a Down Syndrome Mouse Model**
Sergi Llambrich, Rubèn González, Julia Albaigès, Jens Wouters, Fopke Marain, Uwe Himmelreich, James Sharpe, Mara Dierssen, Willy Gsell, Neus Martínez-Abadías and Greetje Vande Velde
- 119 **Recent Technical Advances in Accelerating the Clinical Translation of Small Animal Brain Imaging: Hybrid Imaging, Deep Learning, and Transcriptomics**
Wuwei Ren, Bin Ji, Yihui Guan, Lei Cao and Ruiqing Ni
- 132 **Molecular Imaging of Aortic Aneurysm and Its Translational Power for Clinical Risk Assessment**
Vinamr Rastogi, Sanne J. M. Stefens, Judith Houwaart, Hence J. M. Verhagen, Jorg L. de Bruin, Ingrid van der Pluijm and Jeroen Essers



OPEN ACCESS

EDITED AND REVIEWED BY
Giorgio Treglia,
Ente Ospedaliero Cantonale
(EOC), Switzerland

*CORRESPONDENCE

Monique R. Bernsen
m.bernsen@erasmusmc.nl
Carmel M. Moran
carmel.moran@ed.ac.uk

SPECIALTY SECTION

This article was submitted to
Nuclear Medicine,
a section of the journal
Frontiers in Medicine

RECEIVED 15 November 2022

ACCEPTED 23 November 2022

PUBLISHED 12 December 2022

CITATION

Bernsen MR, McDougald W,
Mezzanotte L, Moran CM, Tavares A
and van der Weerd L (2022) Editorial:
Small animal imaging: Technological
and methodological advances to
improve the translational power.
Front. Med. 9:1099233.
doi: 10.3389/fmed.2022.1099233

COPYRIGHT

© 2022 Bernsen, McDougald,
Mezzanotte, Moran, Tavares and van
der Weerd. This is an open-access
article distributed under the terms of
the [Creative Commons Attribution
License \(CC BY\)](#). The use, distribution
or reproduction in other forums is
permitted, provided the original
author(s) and the copyright owner(s)
are credited and that the original
publication in this journal is cited, in
accordance with accepted academic
practice. No use, distribution or
reproduction is permitted which does
not comply with these terms.

Editorial: Small animal imaging: Technological and methodological advances to improve the translational power

Monique R. Bernsen^{1*}, Wendy McDougald^{2,3},
Laura Mezzanotte⁴, Carmel M. Moran^{3*}, Adriana Tavares³ and
Louise van der Weerd^{5,6}

¹AMIE Core Facility, Erasmus MC, University Medical Center Rotterdam, Rotterdam, Netherlands, ²Siemens, Molecular Imaging, Hoffman Estates, IL, United States, ³BHF-University Centre for Cardiovascular Science, University of Edinburgh, Edinburgh, United Kingdom, ⁴Department of Radiology and Nuclear Medicine, Erasmus MC, University Medical Center Rotterdam, Rotterdam, Netherlands, ⁵Department of Human Genetics, Leiden University Medical Center (LUMC), Leiden, Netherlands, ⁶Department of Radiology, Leiden University Medical Center (LUMC), Leiden, Netherlands

KEYWORDS

small animal imaging, standardization, technological advances, methodological advances, translational power, harmonization

Editorial on the Research Topic

Small animal imaging: Technological and methodological advances to improve the translational power

Small-animal imaging is a dynamic research field with continuing technological and methodological advances. It plays an important role in biomedical research by helping us to increase our understanding of biological and disease processes, to evaluate new drugs and treatments, and to identify and evaluate imaging biomarkers. In this respect it is important to consider the many aspects involved in the planning, design, and execution of small animal imaging studies. This includes, amongst others, the choice of animal model, the imaging technique to be used, aspects regarding animal handling and monitoring, data processing and analysis methods and method quantification and calibration. All these aspects are important with regards to adhering to the 3R principles for ethical use of laboratory animals in scientific research, and in strengthening the scientific value and translational power of the obtained results.

This Special Topic aims at generating a widespread understanding of the importance of robust and standardized methods in small animal imaging. This Special Topic contains 12 papers, eight original research manuscripts and four (mini-)reviews, describing various aspects of animal handling, tracer development and imaging techniques.

In the papers by [Miranda et al.](#), [Proesmans et al.](#), and [Ren et al.](#) some specific challenges encountered in small animal brain imaging are identified and methodological advances to overcome the challenges and to improve robustness of research methods are discussed. [Proesmans et al.](#) highlight the challenges of inter- and intra-subject variability with the most used quantification methods for glucose metabolism in the brain, and issues with the use of different PET acquisition methods across studies. In their paper

they then present a framework for statistical voxel-based analysis of glucose uptake in the rat brain using histogram-based intensity normalization that enables more standardized and harmonized quantification of brain glucose metabolism. A broader approach to the challenges and opportunities in small animal imaging in brain research is presented in the paper by [Ren et al.](#). In their mini-review they discuss recent technological developments in this field including hybrid and multiscale imaging, data processing methods, awake animal imaging, transcriptomics, and on-chip pharmacokinetics. [Miranda et al.](#) further zoom in on the confounding effect of anesthesia of laboratory animals during brain imaging and discuss the pros and cons of awake, but restrained, animal imaging and argue for an approach for non-restrained, awake imaging using advanced motion correction methodology. Also in the area of brain imaging, [Llambich et al.](#) report on the added value of a longitudinal, multi-modal imaging approach for multi-system analysis of complex genetic disorders. In a Down syndrome mouse model, they were able to show that such a research approach could reveal the alterations in the coordinated morphogenesis of brain and skull during disease development and response to treatment.

The importance and added value of multi-modal, multiscale and longitudinal imaging approaches are also highlighted in four other papers in this Special Topic. In recent years, the use of zebrafish for disease models has been increasing. Zebrafish have several advantages compared to other vertebrate models used in modeling human diseases, particularly for large-scale genetic mutant and therapeutic compound screenings. Most researchers use the embryonic or larval stage where the zebrafish is fully transparent and can be readily imaged using standard light microscope techniques. To fully utilize the potential of zebrafish for disease models imaging, techniques not limited by the need for transparent subject are needed. In the study by [Tucker et al.](#), a new PET/CT imaging platform for adult zebrafish imaging that can maintain normal aquatic physiology during scanning is presented, thereby enabling longitudinal assessment of molecular interactions within the adult zebrafish. [Suchacki et al.](#) report on the use of a total-body positron emission tomography (PET) network analysis of murine ^{18}F -FDG scans, as a biomarker of glucose metabolism in bones. The reported approach is suitable for studying dynamic multi-bone metabolic interactions *in vivo* and due to the diversity of PET radiotracers alongside the advent of clinical total-body PET systems the technique could be used to reveal new physiological and pathological tissue interactions beyond skeletal metabolism. With regards to bone imaging, [Menendez et al.](#), demonstrate the feasibility of dose reduction during ^{18}F -Sodium fluoride imaging of osteoblastic activity *via* the use of digital photon counting PET/CT. The need for multi-scale imaging in elucidating complex disease processes is also

discussed by [Tiwari et al.](#) In their review paper they describe complex mechanisms in cardiovascular disease focusing on changes in endothelial cells lining the blood vessels, and how developments in preclinical multi-scale imaging can aid in enhancing the biological understanding of the interactions between endothelial cells and the immune system. In addition, they argue how this could lead to earlier diagnoses and ways for improved patient management. [Rastogi et al.](#) also discuss the importance of multi-modal molecular imaging in cardiovascular disease research. In their paper they focus on aortic aneurysms and highlight the need for better imaging biomarkers for risk-assessment in patients with an aortic aneurysm. They discuss recent developments in molecular imaging techniques and stress that despite the identification of very promising markers and imaging targets, clinical translation is still limited and that in-patient testing and clinical trials of these techniques are needed.

Identification and evaluation of imaging biomarkers and imaging agents are, as mentioned, an important aspect in the field of small animal imaging. In this Research Topic two papers report on improved methods for the production of specific imaging agents. [Dai et al.](#) tested a method for more efficient purification of the Vesicular monoamine transporter type 2-targeting tracer, ^{18}F -FP-(+)-DTBZ. Change into a commonly used HPLC-based method they propose a modified solid-phase extraction method that significantly simplifies tracer purification and reduces processing time without loss of radiochemical purity or *in vivo* performance. In the field of nanoparticle-based, imaging agents, [Zambito et al.](#) describe an approach for *in vivo* visualization of tumor-associated macrophages to study their role during cancer growth and metastasis. Their imaging agent consists of perfluoro-15-crown-5-ether encapsulated in PLGA-based nanoparticles functionalized *via* PEG chains with mannose and FITC making it suitable as an MRI contrast agent and for *in vitro* optical imaging. Through the functionalization with mannose, the particles have specific targeting properties for mannose-receptor overexpressing cells like tumor-associated macrophages.

The collection of papers in this Research Topic demonstrates the diversity of aspects in imaging technology, and the important role of small animal imaging in developing new imaging techniques and methods. They also highlight challenges still faced in standardization and harmonization of procedures, some specific for the preclinical setting but also still encountered during clinical implementation. To further the tremendous potential of imaging techniques in biomedical research and their use for personalized patient care, standardization and harmonization of methods and protocols are crucial. Hopefully, this Research Topic contributes to an increase in awareness for this need within the research community.

Author contributions

All authors listed have made a substantial, direct, and intellectual contribution to the work and approved it for publication.

Conflict of interest

The authors declare that the research was conducted in the absence of any commercial or financial relationships

that could be construed as a potential conflict of interest.

Publisher's note

All claims expressed in this article are solely those of the authors and do not necessarily represent those of their affiliated organizations, or those of the publisher, the editors and the reviewers. Any product that may be evaluated in this article, or claim that may be made by its manufacturer, is not guaranteed or endorsed by the publisher.



A Purification Method of ^{18}F -FP-(+)-DTBZ via Solid-Phase Extraction With Combined Cartridges

Yuyin Dai[†], Ri Sa[†], Feng Guan, Qi Wang, Yinghua Li* and Hongguang Zhao*

Department of Nuclear Medicine, The First Hospital of Jilin University, Changchun, China

OPEN ACCESS

Edited by:

Laura Mezzanotte,
Erasmus Medical Center, Netherlands

Reviewed by:

Kun Zheng,
Peking Union Medical College
Hospital (CAMS), China
Kritika Subramanian,
Weill Cornell Medicine, United States

*Correspondence:

Yinghua Li
liyinh@jlu.edu.cn
Hongguang Zhao
zhaohg@jlu.edu.cn

[†]These authors share first authorship

Specialty section:

This article was submitted to
Nuclear Medicine,
a section of the journal
Frontiers in Medicine

Received: 11 April 2021

Accepted: 17 June 2021

Published: 09 July 2021

Citation:

Dai Y, Sa R, Guan F, Wang Q, Li Y and
Zhao H (2021) A Purification Method
of ^{18}F -FP-(+)-DTBZ via Solid-Phase
Extraction With Combined Cartridges.
Front. Med. 8:693632.
doi: 10.3389/fmed.2021.693632

Background: To optimize [^{18}F] 9-fluoropropyl-(+)-dihydrotetrabenazine (^{18}F -FP-(+)-DTBZ) purification via solid-phase extraction (SPE) with combined cartridges to facilitate its widespread clinical application.

Methods: A modified SPE purification method, employing Sep-Pak PS-2 and Sep-Pak C18 cartridges, was used for the preparation of ^{18}F -FP-(+)-DTBZ. This method was compared to the purification method of high-pressure liquid chromatography (HPLC) and SPE with one cartridge, following quality control test and positron emission tomography (PET) imaging in healthy volunteers and patients with parkinson's disease (PD).

Results: A SPE purification method integrating Sep-Pak PS-2 and Sep-Pak C18 cartridges was implemented successfully. The retention time of ^{18}F -FP-(+)-DTBZ purified by HPLC, SPE with Sep-Pak PS-2, SPE with Sep-Pak C18, and SPE with combined use of Sep-Pak PS-2 and Sep-Pak C18 cartridges was 8.7, 8.8, 8.7, and 8.9 min, respectively. Fewest impurity peak was detected in ^{18}F -FP-(+)-DTBZ purified by the SPE with combined use of Sep-Pak PS-2 and Sep-Pak C18 cartridges. This modified SPE purification method provided a satisfactory radiochemical yield of $29 \pm 1.8\%$ with radiochemical purity $>99\%$ and shortened synthesis time to 27 min. The brain uptake of ^{18}F -FP-(+)-DTBZ purified by the modified SPE was comparable to that purified by HPLC in both healthy volunteers and PD patients.

Conclusions: A SPE method integrating Sep-Pak PS-2 and Sep-Pak C18 cartridges for purification of ^{18}F -FP-(+)-DTBZ may be highly suited to automatic synthesis for routine clinical applications, as it provides excellent radiochemical purity, high yield as well as operational simplicity.

Keywords: ^{18}F -FP-(+)-DTBZ, ^{18}F -FDG, PET/CT, solid phase extraction, Parkinson disease

INTRODUCTION

Vesicular monoamine transporter type 2 (VMAT2) plays critical role in the mechanism of packaging and transporting neurotransmitters from the cytosol into synaptic vesicle, verifying its status as an objective marker of nigrostriatal terminal integrity (1, 2). VMAT2 located on vesicle membranes in neurons and its activity largely affects the scale of dopamine release (3). The activity of the presynaptic monoaminergic binding site is less likely influenced by the medication or compensatory mechanisms, as it is active only when VMAT2-containing neurons are active (4). Therefore, it is a reliable and objective biomarker for exploring neurological and psychiatric

disorders such as Parkinson disease (PD) (5), Alzheimer's disease and dementia with Lewy bodies (6), as well as endocrine system disease such as diabetes (7–9).

The imaging of VMAT2 has potential advantages such as better image quality and quantification, shorter time between tracer administration and scanning, shorter scan duration, and no requirement for prior blockade of the thyroid to prevent radioactive iodine uptake (10–15). To date, different kinds of agents for VMAT2 have been investigated to map VMAT2 distribution, and some of them have been tested in humans and achieved favorable results (16–18). For example, as early as in 1996, Frey et al. (19) found that PD patients had reduction in specific [^{11}C]dihydrotetrabenazine (DTBZ) distribution volume in the putamen (–61%) and in the caudate nucleus (–43%). Similarly, regional specific uptake ratio of [^{18}F] 9-fluoropropyl-(+)-DTBZ (^{18}F -FP-(+)-DTBZ) of caudate, putamen, substantia nigra, and globus pallidus in the moderate and advanced PD patients were significantly lower than those in the healthy human subjects (16). More encouragingly, Li et al. (8) provided evidence that dysfunction of streptozotocin-diabetic retinas was detected by ^{18}F -FP-(+)-DTBZ imaging at least 4 weeks earlier than other examinations such as electroretinogram, color fundus photography, and angiography. Generally, widespread use of this agent could facilitate the disease diagnosis and monitoring treatment response.

However, the published methods of purification of this agent cost a long preparation time, which limits its routine application for VMAT2 tracing. High-pressure liquid chromatography (HPLC) is a conventional method used for purification of ^{11}C -labeled or ^{18}F -labeled DTBZ to eliminate the pseudo-carrier. The procedure of this purification method was relatively complex, and the preparation of clinically useful radiotracer using HPLC lasted over 1 h. Subsequently, solid phase extraction (SPE) were adopted and the shortest synthesis time for ^{18}F -FP-(+)-DTBZ using SPE was 40 min in the published studies (20, 21). Therefore, purification of ^{18}F -FP-(+)-DTBZ is in need to improve in order to increase the application of this tracer. In the present study, we employed a SPE method with combined use of Sep-Pak PS-2 and Sep-Pak C18 cartridges to purify ^{18}F -FP-(+)-DTBZ to maximize the final yield and simplify the purification process. With this method, ^{18}F -FP-(+)-DTBZ can be expanded into the clinical setting to test the usefulness of ^{18}F -FP-(+)-DTBZ in the diagnosis and monitoring of diseases.

MATERIALS AND METHODS

Chemicals and Reagents

All reagents were commercially acquired and utilized without further purification unless otherwise stated. 4,7,13,16,21,24-Hexaoxa-1,10-diazabicyclo [8.8.8] hexacosane (K222, 98.0 %) was purchased from ABX (Germany). Anhydrous acetonitrile and potassium carbonate (K_2CO_3) were purchased from Sigma (America). All SPE cartridges were purchased from Waters Corporation (USA). To activate Sep-Pak QMA, Sep-Pak C18, and Sep-Pak PS-2, we flushed them with 5 mL absolute ethanol followed by 10 mL water.

Radiosynthesis of ^{18}F -FP-(+)-DTBZ

Precursor of ^{18}F -FP-(+)-DTBZ was synthesized in the College of Chemistry, Jilin University (Figure 1). ^{18}F was produced in a cyclotron by ^{18}O (p, n) ^{18}F nuclear reaction. ^{18}F was passed into the CFN-MPS200 multi-functional synthesis module through the target transmission system and captured by the Sep-Pak QMA anion exchange column. The residual liquid was put into the oxygen water recovery unit. QMA was eluted with a 0.9 mL $\text{K}_2.2.2 / \text{K}_2\text{CO}_3$ mixture. Then, ^{18}F was rinsed into the reaction bottle. The eluent was dried through successive evaporation with nitrogen (N_2) flow (30 mL/min) at 100°C for 3 min to remove water and acetonitrile. Next, the residue was redried under the same N_2 flow at 110°C for 2 min. A total of 1.0 mg TsOP-(+)-DTBZ precursor solution in anhydrous was introduced into the reaction tube. Then, radiofluorination was performed in the reaction bottle at 120°C for 12 min and cooled to 40°C . We transferred the mixture from the reaction bottle to the transfer bottle. The reaction bottle was cleaned using 5 mL 5% ethanol solution, which was then poured into the transfer bottle. The crude product solution purification by HPLC or SPE and the final solution in the collection bottle was passed through a Millex GV for sterilization and diluted to 10 mL with saline in a sterile bottle. The synthesis route and diagram of the automated system of ^{18}F -FP-(+)-DTBZ are outlined in Figure 2.

HPLC Purification of ^{18}F -FP-(+)-DTBZ

After radiofluorination, we transferred the crude product to preparative HPLC (mobile phase of acetonitrile: 50 mM ammonium acetate = 57:43; flow 4 mL/min, velocity; 280 nm, ultraviolet absorption wavelength; ultraviolet absorption peak in 12 + 2 min, plus or minus 2 min 14 radiation peak, collect radiation peak), and then absorbed on C18 column after dilution with saline solution. Exactly 1.5 mL of ethanol was to elute the C18 column. Ethanol was diluted to 10% concentration using 0.9% sodium chloride. The final products of ^{18}F -FP-(+)-DTBZ were obtained following aseptic filtration.

SPE Purification of ^{18}F -FP-(+)-DTBZ

The crude product solution was passed through the small column of Sep-Pak PS-2 and/or Sep-Pak C18 to eliminate unreacted [^{18}F] fluoride and water-soluble impurities, which finally was channeled to the waste liquid bottle. To determine the optimum concentration of elution ethanol, we used 10 mL ethanol with different concentrations from 5 to 70% to wash out the impurities, and found that the lost rate was in acceptable range when the ethanol concentration was below 30% (Figure 3A). Similarly, to determine the optimum volume of elution ethanol, we used 30% ethanol with different volumes from 4 to 20 mL of ethanol to wash out impurities, and found the loss rate was in acceptable range when using 10 mL ethanol or below 10 mL. The best final condition for elution ethanol was as follows: for the first time, 7 mL 5% ethanol solution was used to wash out impurities to the waste vial; for the second time, 8 mL 5% ethanol solution was used to wash out excess impurities to the waste vial; for the third time, 8 mL 30% ethanol solution was used for further removal of impurities to the waste vial. Then, the final product

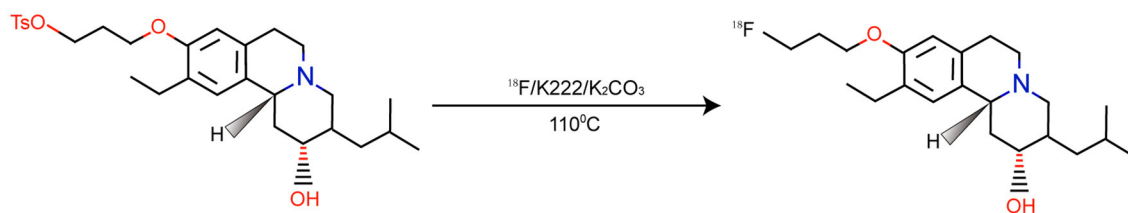


FIGURE 1 | Synthesis route of ^{18}F -FP-(+)-DTBZ.

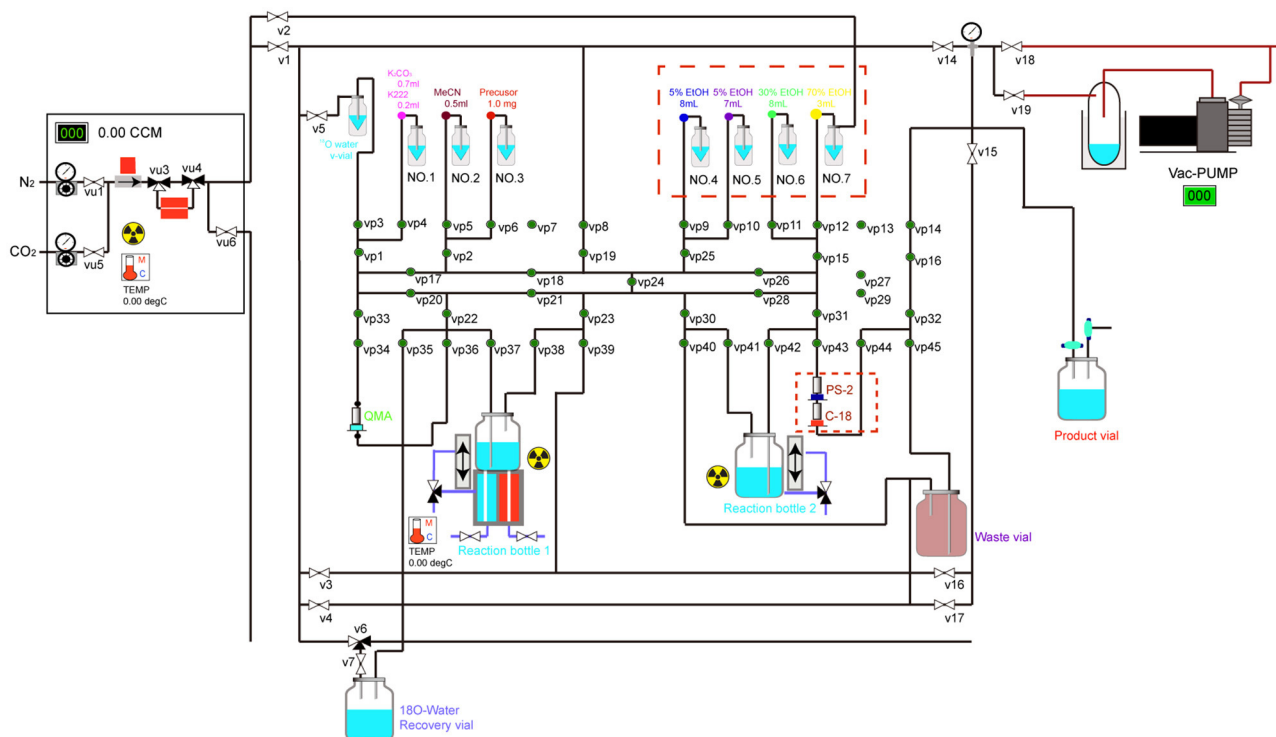


FIGURE 2 | Diagram of the automated system of radiosynthesis of ^{18}F -FP-(+)-DTBZ.

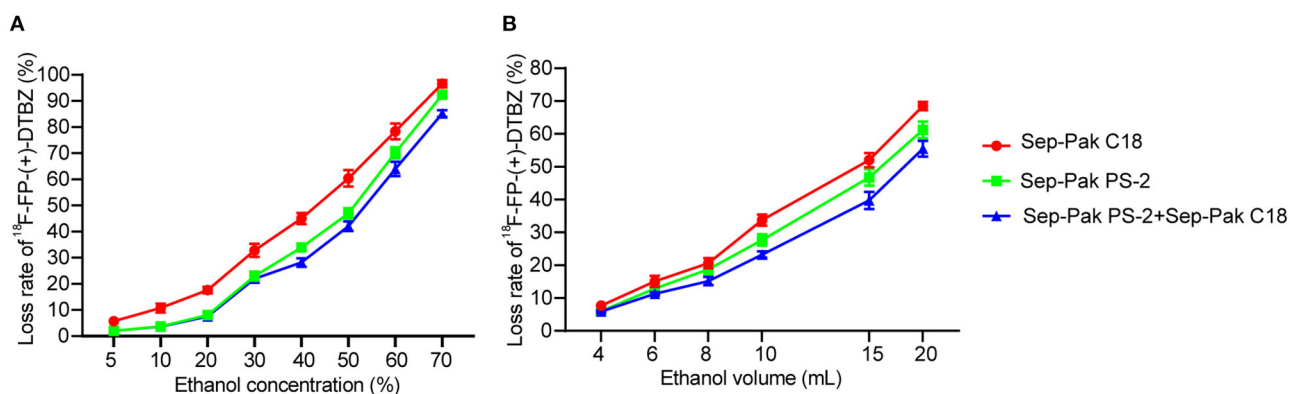


FIGURE 3 | Loss rate of ^{18}F -FP-(+)-DTBZ using Sep-Pak PS-2 cartridge and/or Sep-Pak C18 cartridges under different concentration of 10 mL ethanol elution (A) and different volume of 30% ethanol elution (B).

was eluted with 3 mL 70% ethanol solution to the product vial as 70% ethanol was enough to elute the all product (**Figure 3B**).

Quality Control of ^{18}F -FP-(+)-DTBZ

Visual Inspection

The ^{18}F -FP-(+)-DTBZ product solution was visually examined in the labeling hot cell through the leading glass window under bright light.

pH

We employed the pH indicator paper (pH 2–9) referring to the attached indicator chart to estimate the pH value of the purified ^{18}F -FP-(+)-DTBZ product.

Radiochemical Purity

Before purity analysis, a reference substance solution (non-radioactive FP-(+)-DTBZ; 20 μL , 2.7 mmol/L) was injected into the analytical HPLC system. The chemical purity of ^{18}F -FP-(+)-DTBZ after purification was determined by HPLC with UV detection at 280 nm and radiation purity of the product was monitored by HPLC with radiation detector. Simultaneously, thin layer chromatography (TLC) was also applied to the determine the radiation purity.

Bacterial Endotoxin Test

Limulus Amebocyte Lysate (LAL) assay was applied to test for bacterial endotoxins.

Imaging Quality

Two healthy volunteers and two PD patients underwent PET/CT scan to test the imaging quality of ^{18}F -FP-(+)-DTBZ from HPLC and SPE with combined use of Sep-Pak PS-2 and Sep-Pak C18 cartridges. This study was approved by the Ethics Committee of the First Hospital of Jilin University (20K070-001) and conducted in accordance with the 1964 Declaration of Helsinki and its later amendments or comparable ethical standards. Patients were recruited for enrollment in this study from December 2020 through January 2021 at our institute, with agreement from the oncologists and on determination of the patients' eligibility.

RESULTS

The loss rate of SPE with combined use of Sep-Pak PS-2 and Sep-Pak C18 cartridges was lower than that of SPE with one cartridge at the same concentration of ethanol and same volume of ethanol elution (**Figure 3**).

The identity of ^{18}F -FP-(+)-DTBZ was confirmed by comparing the retention time of the radioactive product with that of FP-(+)-DTB. The retention time of ^{18}F -FP-(+)-DTBZ purified by HPLC, SPE with Sep-Pak PS-2, SPE with Sep-Pak C18, and SPE with combined use of Sep-Pak PS-2 and Sep-Pak C18 cartridges was 8.7, 8.8, 8.7, and 8.9 min, respectively. Either ^{18}F -FP-(+)-DTBZ purified by HPLC or SPE matched well with that of FP-(+)-DTBZ within an admissible error. Fewest impurity peak was detected in ^{18}F -FP-(+)-DTBZ purified by SPE with

combined use of Sep-Pak PS-2 and Sep-Pak C18 cartridges in all purification methods (**Figure 4**).

Comparison of HPLC and SPE purification method of ^{18}F -FP-(+)-DTBZ is presented in **Table 1**. The radiochemical purity exceeded 99%, and the product was radiochemically stable for at least 3 h for the tracers purified by HPLC and SPE with combined use of Sep-Pak PS-2 and Sep-Pak C18 cartridges. The synthesis time of ^{18}F -FP-(+)-DTBZ with SPE purification was significantly shorter than that with HPLC purification. Brain uptake of ^{18}F -FP-(+)-DTBZ purified by SPE with combined use of Sep-Pak PS-2 and Sep-Pak C18 cartridges was comparable to that purified by HPLC in both healthy volunteers and PD patients (**Figure 5**). In healthy volunteers, a symmetric distribution pattern of ^{18}F -FP-(+)-DTBZ was shown in caudate, putamen, globus pallidus, substantia nigra. In PD patients, ^{18}F -FP-(+)-DTBZ avidity in nigrostriatal regions reduced obviously (**Figure 5**).

DISCUSSION

In this study, we optimized SPE purification of ^{18}F -FP-(+)-DTBZ via combining Sep-Pak PS-2 and Sep-Pak C18 cartridges. The radiochemical purity from this modified SPE purification method was much more ideal for clinical use than those purified by HPLC or SPE with one cartridge. By testing the imaging quality of ^{18}F -FP-(+)-DTBZ in healthy volunteers and PD patients, we further elucidated that the imaging quality of ^{18}F -FP-(+)-DTBZ from the modified SPE was comparable to that from HPLC. Additionally, the preparation time of ^{18}F -FP-(+)-DTBZ synthesis was shortened to 27 minutes via use of the modified SPE purification.

In the early 1990s, ^{11}C labeled tetrabenazine (TBZ), dihydrotetrabenazine (DTBZ), and methoxytetrabenazine (MTBZ) were continuously investigated as tracers for imaging of VMAT2 (22, 23). At that time, silica gel semi-preparative HPLC was mainly adopted in the purification of different kinds of tracers. ^{11}C -TBZOMe was purified using a silica gel semi-preparative HPLC column, by passing the HPLC solvent (CH_2Cl_2 : hexane: (isopropanol: diethylamine 24:1) 37:62:1; 6 mL/min) through the extraction column and onto the HPLC column (24). Similarly, in the preparation of ^{11}C -TBZ and ^{11}C -DTBZ, the radiotracer was also purified using semipreparative silica gel chromatography and prepared for injection by evaporation of the HPLC solvent (23, 25). Considering the half time of radionuclide, ^{18}F -labeled DTBZ analogs ($T_{1/2} = 110$ min) will be more practical to increase the application in clinics equipped with PET scanners but not with sufficient resources to make ^{11}C ($T_{1/2} = 20$ min) (26, 27). Radiosynthesis of ^{18}F -FP-(+)-DTBZ was firstly reported in 2006 (26). It is prepared with ^{18}F fluoride as a substitute for the O-tosylate leaving group of precursors, catalyzed by K222/ K_2CO_3 following the purification of the reaction mixture via semipreparative HPLC column. The preparation of ^{18}F labeled compound took about 50–55 min at the end of synthesis.

Since HPLC is a long and laborious process, accompanied by considerable loss of radioactive product, multiple sequential solid-phase cartridges were, therefore, adopted to optimize

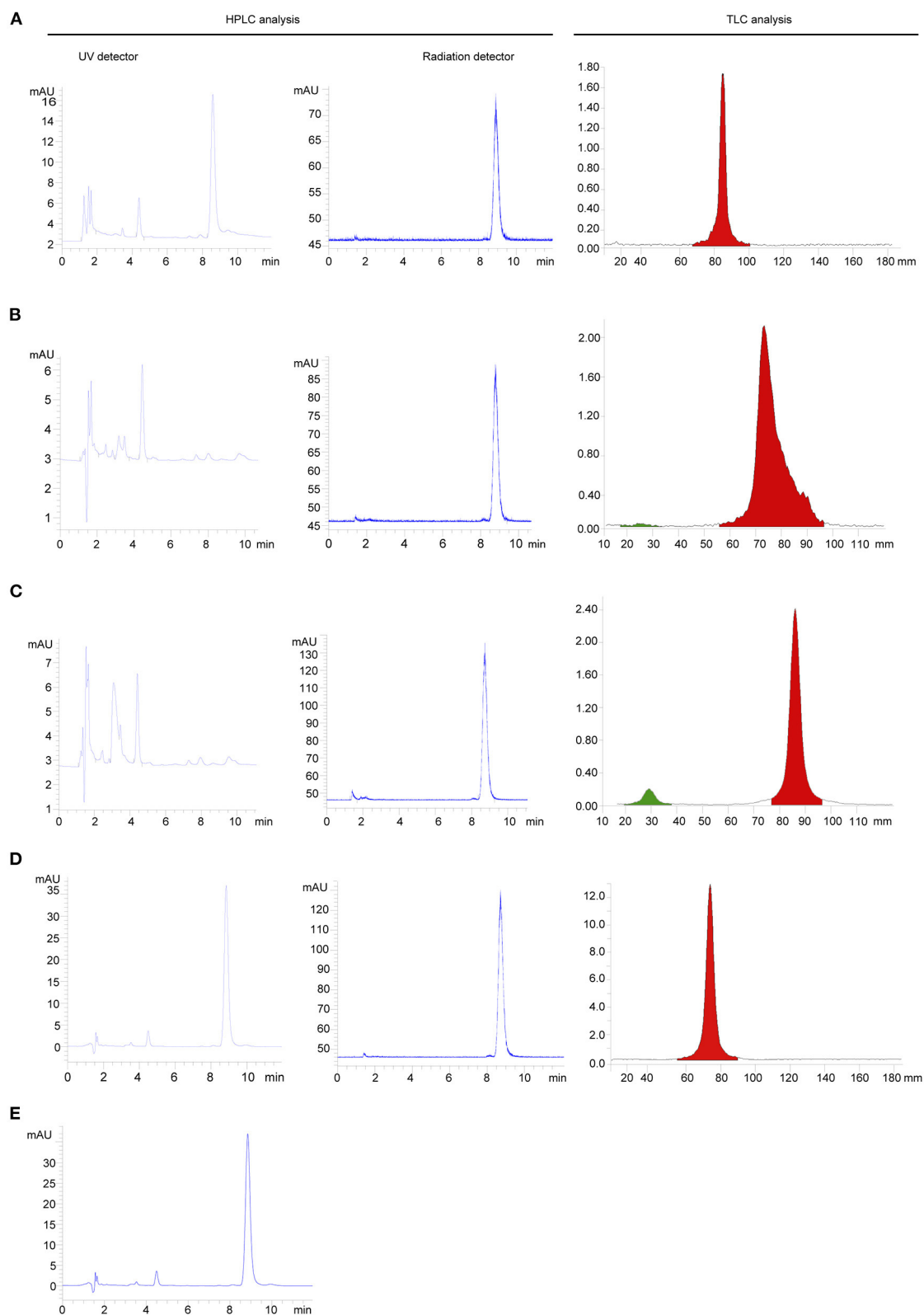
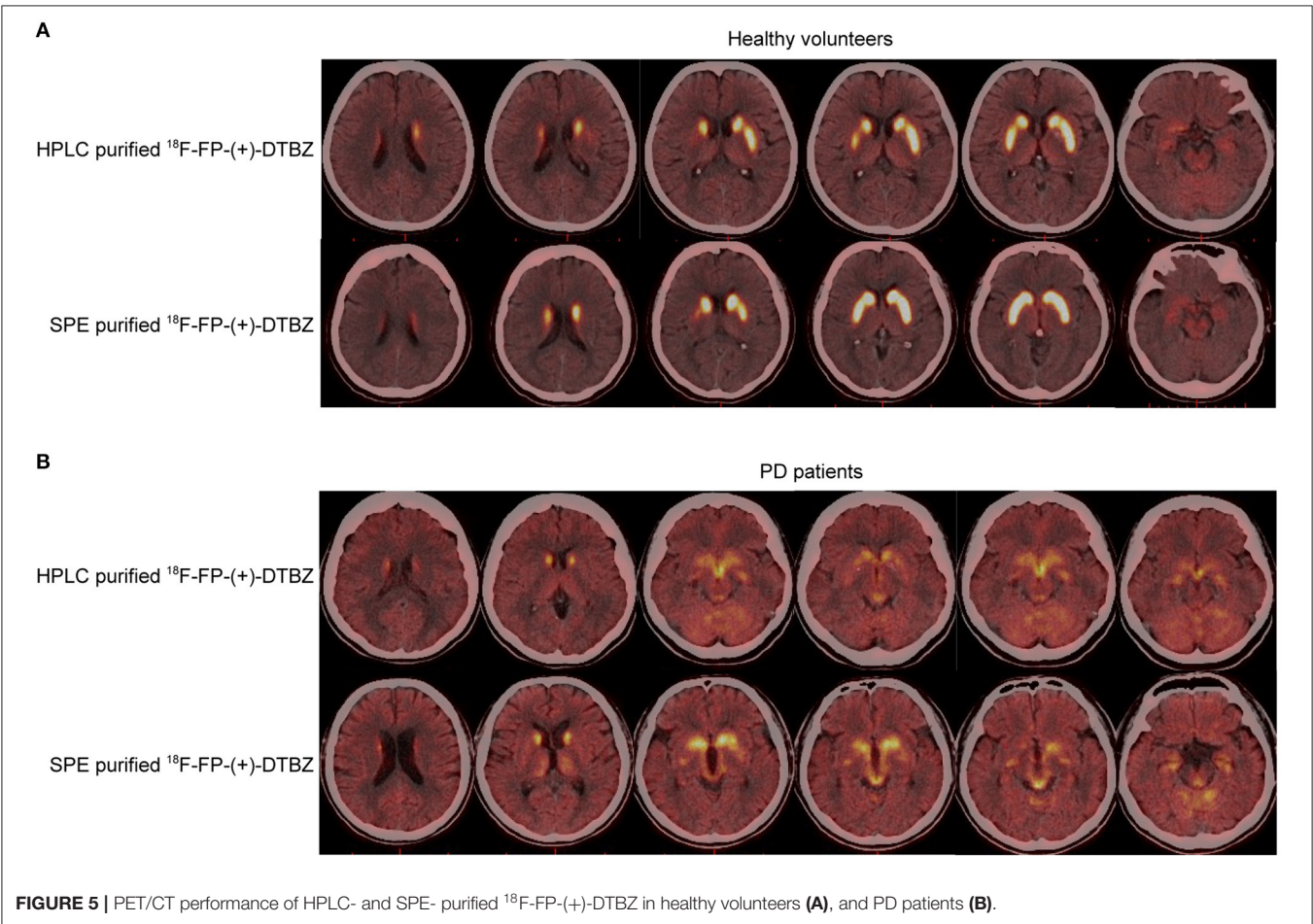


FIGURE 4 | HPLC and TLC analysis of radiochemical purity of ^{18}F -FP-(+)-DTBZ purified by HPLC (A), SPE with Sep-Pak PS-2 (B), SPE with Sep-Pak C18 (C) SPE with combined use of Sep-Pak PS-2 and Sep-Pak C18 (D), and radiochemical purity of FP-(+)-DTBZ (E).

TABLE 1 | Comparison between HPLC and SPE purification of ¹⁸F-FP-(+)-DTBZ.

Column	HPLC	SPE		
	YMC-Pack ODS-AM	Sep-Pak C18	Sep-Pak PS-2	Sep-Pak C18, Sep-Pak PS-2
Precursor (mg)	1	1	1	1
Procedure synthesis time (min)	65	27	26	27
Synthesis times	3	3	3	5
Yield (GBq)	4.6 ± 5.7%	4.8 ± 8.3%	5.0 ± 10.2%	5.1 ± 7.9%
Yield rate	11 ± 2.3%	25 ± 2.3	27 ± 2.1	29 ± 1.8 %
Activity concentration at the end of synthesis (MBq/mL)	2.3 × 10 ³	1.5 × 10 ³	1.7 × 10 ³	1.7 × 10 ³
Appearance (visual inspection)	Clear, transparent, free of impurities	Clear, transparent, free of impurities	Clear, transparent, free of impurities	Clear, transparent, free of impurities
PH	6–7	6–7	6–7	6–7
Radiochemical purity (radio-HPLC)	99.2%	98.5%	98.0%	99.0%
Radiochemical purity (radio-HPLC) after 3 half time	96.3%	95.6%	95.1%	96.0%
Bacterial endotoxin test (EU/ml)	<15	<15	<15	<15
K2.2.2 comparing to standard reference	less than standard K2.2.2 spots	less than standard K2.2.2 spots	less than standard K2.2.2 spots	less than standard K2.2.2 spots
Retention time (min)	8.7	8.8	8.7	8.9

HPLC, high pressure liquid chromatography; SPE, solid-phase extraction.


FIGURE 5 | PET/CT performance of HPLC- and SPE- purified ¹⁸F-FP-(+)-DTBZ in healthy volunteers (A), and PD patients (B).

the preparation of different radiotracers in the early 2010s (20, 21, 28). It is worth noting that the preparation time distinguishes HPLC- from SPE-purified ¹⁸F-FP-(+)-DTBZ. For instance, in 2010, Zhu et al. employed different precursors (-OTs or -Br as the leaving group at the 9-propoxy position), reagents [K₂222/K(2)CO(3) vs. tributylammonium bicarbonate] and solvents (acetonitrile vs. DMSO), reaction temperature, reaction time, and purification method with SPE (Oasis HLB) to improve ¹⁸F-FP-(+)-DTBZ radiosynthesis. This method generated a satisfactory radiochemical yield of 21–41% ($n = 10$) with radiochemical purity > 95% and shortened the synthesis time to 40 min (20). In 2014, a new ¹¹C-labeled radiotracer, 10-(11) C-dihydrotetrabenazine (10-¹¹C-DTBZ) was successfully synthesized and purified by SPE using an alumina Sep-Pak cartridge, the final 10-¹¹C-DTBZ product was obtained. The overall synthesis time was only 20 min from bombardment to release of the product for quality control (29). In 2019, SPE with Sep-Pak C18 cartridge was implemented into the purification of the ¹⁸F-FP-(+)-DTBZ (30). In this study, they have tested purification effect of SPE equipped with different cartridges including Sep-Pak Oasis, tC2, C8, tC18, CN, Chromafix C18 Hydrox, Chromafix C18, and Chromfix C4, and finally focused on the Sep-Pak tC18 with suitable ethanol-water elution as this system showed the smallest loss in activity. The desired product was obtained in 35 min. In 2020, Zhao et al. (31) successfully obtained a radiolabeling method of ¹⁸F-FP-(+)-DTBZ under the optimized conditions (P/K₂CO₃ = 1:8, heating at 120°C for 3 min in dimethyl sulfoxide). The automated synthesis gave a high activity yield of 30–55% in about 40 min with a >99.0% radiochemical purity. Taken together, using SPE instead of HPLC for purification is the trend for different kinds of radiotracers.

Herein, we modified the SPE purification equipped with two different cartridges to obtain four goals: eliminate the residual chemical impurities, achieve excellent radiochemical purity, maximize the final product, and simplified purification method. In the previous studies, SPE with one cartridge was used for the purification of ¹⁸F-FP-(+)-DTBZ. However, SPE with two cartridges have not been reported. In our study, we have compared the loss rate and radiochemical purity of ¹⁸F-FP-(+)-DTBZ from SPE with two cartridges to those from SPE with one cartridge. Of note, SPE with two cartridges showed lower loss rate than SPE with one cartridge under the same concentration or same volume of ethanol elution. Whereas, under the same elution condition, although radiation purity of product from SPE with one cartridge was comparable to that from SPE with combined cartridges in the analysis of analytic HPLC with radiation detector, both HPLC analysis with UV detector and TLC analysis showed fewer impurity peaks in ¹⁸F-FP-(+)-DTBZ from SPE with two cartridges comparing to that from SPE with

one cartridge. Therefore, considering the loss rate, radiochemical purity and final yield, ¹⁸F-FP-(+)-DTBZ from SPE with two cartridges was more likely to obtain favorable products than SPE with one cartridge. In addition, we have compared radiochemical purity, final yield, imaging quality and synthesis time of products purified from SPE with two cartridges to those from HPLC. Radiochemical purity, final yield and imaging quality of SPE with two cartridges were comparable to those from HPLC, while synthesis time of radiotracer from SPE with two cartridges was much shorter than that from HPLC, which indicated that the modified SPE purification was suitable for the clinic use.

In conclusion, the present study demonstrated an improved purification approach for ¹⁸F-FP-(+)-DTBZ, using SPE with two different cartridges (Sep-Pak PS-2 and Sep-Pak C18). The desired product was prepared in 27 min with a $29 \pm 1.8\%$ yield rate. This SPE purification method is highly suited to automatic synthesis for routine clinical applications.

DATA AVAILABILITY STATEMENT

The raw data supporting the conclusions of this article will be made available by the authors, without undue reservation.

ETHICS STATEMENT

The studies involving human participants were reviewed and approved by the Ethics Committee of The First Hospital of Jilin University. The patients/participants provided their written informed consent to participate in this study. Written informed consent was obtained from the individual(s) for the publication of any potentially identifiable images or data included in this article.

AUTHOR CONTRIBUTIONS

YL and HZ designed the study. YD, RS, FG, and YL participated radiosynthesis of tracer. QW and HZ analyzed scans and data. YD and RS wrote and revised the draft. All authors contributed to the article and approved the submitted version.

FUNDING

This study was funded by the Jilin Scientific and Technological Development Program (No. 20200201334JC).

ACKNOWLEDGMENTS

We thank the College of Chemistry, Jilin University for their excellent technical assistance.

REFERENCES

- Kong Y, Zhou H, Feng H, Zhuang J, Wen T, Zhang C, et al. Elucidating the relationship between diabetes mellitus and Parkinson's Disease using (18)F-FP-(+)-DTBZ, a positron-emission tomography probe for vesicular monoamine transporter 2. *Front Neurosci.* (2020) 14:682. doi: 10.3389/fnins.2020.00682
- Shi X, Zhang Y, Xu S, Kung HF, Qiao H, Jiang L, et al. Decreased striatal vesicular monoamine transporter type 2 correlates with the nonmotor symptoms in Parkinson disease. *Clin Nucl Med.* (2019) 44:707–13. doi: 10.1097/RLU.0000000000002664
- Eiden LE, Weihe E. VMAT2: a dynamic regulator of brain monoaminergic neuronal function interacting with drugs of abuse. *Ann N Y Acad Sci.* (2011) 1216:86–98. doi: 10.1111/j.1749-6632.2010.05906.x

4. Wilson JM, Kish SJ. The vesicular monoamine transporter, in contrast to the dopamine transporter, is not altered by chronic cocaine self-administration in the rat. *J Neurosci.* (1996) 16:3507–10. doi: 10.1523/JNEUROSCI.16-10-03507.1996
5. Sanchez-Catasa CA, Bohnen NI, Yeh FC, D'Cruz N, Kanel P, Müller M. Dopaminergic nigrostriatal connectivity in early Parkinson disease: *in vivo* neuroimaging study of (11)C-DTBZ PET combined with correlational tractography. *J Nucl Med.* (2021) 62:545–52. doi: 10.2967/jnumed.120.248500
6. Villemagne VL, Okamura N, Pejoska S, Drago J, Mulligan RS, Chételat G, et al. Differential diagnosis in Alzheimer's disease and dementia with Lewy bodies via VMAT2 and amyloid imaging. *Neurodegener Dis.* (2012) 10:161–5. doi: 10.1159/000334535
7. Naganawa M, Lim K, Nabulsi NB, Lin SF, Labaree D, Ropchan J, et al. Evaluation of pancreatic VMAT2 binding with active and inactive enantiomers of [(18)F]FP-DTBZ in healthy subjects and patients with type 1 diabetes. *Mol Imaging Biol.* (2018) 20:835–45. doi: 10.1007/s11307-018-1170-6
8. Li J, Chen P, Bao Y, Sun Y, He J, Liu X. PET imaging of vesicular monoamine transporter 2 in early diabetic retinopathy using [(18)F]FP-(+)-DTBZ. *Mol Imaging Biol.* (2020) 22:1161–9. doi: 10.1007/s11307-019-01443-1
9. Normandin MD, Petersen KF, Ding YS, Lin SF, Naik S, Fowles K, et al. *In vivo* imaging of endogenous pancreatic β -cell mass in healthy and type 1 diabetic subjects using 18F-fluoropropyl-dihydrotetrabenazine and PET. *J Nucl Med.* (2012) 53:908–16. doi: 10.2967/jnumed.111.100545
10. Okamura N, Villemagne VL, Drago J, Pejoska S, Dhamija RK, Mulligan RS, et al. *In vivo* measurement of vesicular monoamine transporter type 2 density in Parkinson disease with (18)F-AV-133. *J Nucl Med.* (2010) 51:223–8. doi: 10.2967/jnumed.109.070094
11. Lin KJ, Lin WY, Hsieh CJ, Weng YH, Wey SP, Lu CS, et al. Optimal scanning time window for 18F-FP-(+)-DTBZ (18F-AV-133) summed uptake measurements. *Nucl Med Biol.* (2011) 38:1149–55. doi: 10.1016/j.nucmedbio.2011.05.010
12. Chang CC, Hsiao IT, Huang SH, Lui CC, Yen TC, Chang WN, et al. 8F-FP-(+)-DTBZ positron emission tomography detection of monoaminergic deficient network in patients with carbon monoxide related parkinsonism. *Eur J Neurol.* (2015) 22:845–52. e59–60. doi: 10.1111/ene.12672
13. Lin KJ, Weng YH, Wey SP, Hsiao IT, Lu CS, Skovronsky D, et al. Whole-body biodistribution and radiation dosimetry of 18F-FP-(+)-DTBZ (18F-AV-133): a novel vesicular monoamine transporter 2 imaging agent. *J Nucl Med.* (2010) 51:1480–5. doi: 10.2967/jnumed.110.078196
14. Alexander PK, Lie Y, Jones G, Sivaratnam C, Bozinovski S, Mulligan RS, et al. Management impact of imaging brain vesicular monoamine transporter type 2 in clinically uncertain Parkinsonian Syndrome with (18)F-AV133 and PET. *J Nucl Med.* (2017) 58:1815–20. doi: 10.2967/jnumed.116.189019
15. Boileau I, Rusjan P, Houle S, Wilkins D, Tong J, Selby P, et al. Increased vesicular monoamine transporter binding during early abstinence in human methamphetamine users: Is VMAT2 a stable dopamine neuron biomarker? *J Neurosci.* (2008) 28:9850–6. doi: 10.1523/JNEUROSCI.3008-08.2008
16. Hsiao IT, Weng YH, Hsieh CJ, Lin WY, Wey SP, Kung MP, et al. Correlation of Parkinson disease severity and 18F-DTBZ positron emission tomography. *JAMA Neurol.* (2014) 71:758–66. doi: 10.1001/jamaneurol.2014.290
17. Bohnen NI, Koeppe RA, Meyer P, Ficarò E, Wernette K, Kilbourn MR, et al. Decreased striatal monoaminergic terminals in Huntington disease. *Neurology.* (2000) 54:1753–9. doi: 10.1212/WNL.54.9.1753
18. Bohnen NI, Albin RL, Koeppe RA, Wernette KA, Kilbourn MR, Minoshima S, et al. Positron emission tomography of monoaminergic vesicular binding in aging and Parkinson disease. *J Cereb Blood Flow Metab.* (2006) 26:1198–212. doi: 10.1038/sj.jcbfm.9600276
19. Frey KA, Koeppe RA, Kilbourn MR, Vander Borgh T, Albin RL, Gilman S, et al. Presynaptic monoaminergic vesicles in Parkinson's disease and normal aging. *Ann Neurol.* (1996) 40:873–84. doi: 10.1002/ana.410400609
20. Zhu L, Liu Y, Plössl K, Lieberman B, Liu J, Kung HF. An improved radiosynthesis of [18F]AV-133: a PET imaging agent for vesicular monoamine transporter 2. *Nucl Med Biol.* (2010) 37:133–41. doi: 10.1016/j.nucmedbio.2009.10.005
21. Wu X, Zhou X, Zhang S, Zhang Y, Deng A, Han J, et al. Brain uptake of a non-radioactive pseudo-carrier and its effect on the biodistribution of [(18)F]AV-133 in mouse brain. *Nucl Med Biol.* (2015) 42:630–6. doi: 10.1016/j.nucmedbio.2015.03.009
22. Vander Borgh T, Kilbourn MR, Koeppe RA, DaSilva JN, Carey JE, Kuhl DE, et al. *In vivo* imaging of the brain vesicular monoamine transporter. *J Nucl Med.* (1995) 36:2252–60.
23. DaSilva JN, Kilbourn MR, Domino EF. *In vivo* imaging of monoaminergic nerve terminals in normal and MPTP-lesioned primate brain using positron emission tomography (PET) and [11C]tetrabenazine. *Synapse.* (1993) 14:128–31. doi: 10.1002/syn.890140205
24. DaSilva JN, Kilbourn MR, Mangner TJ. Synthesis of a [11C]methoxy derivative of alpha-dihydrotetrabenazine: a radioligand for studying the vesicular monoamine transporter. *Appl Radiat Isot.* (1993) 44:1487–9. doi: 10.1016/0969-8043(93)90103-H
25. Kilbourn M, Lee L, Vander Borgh T, Jewett D, Frey K. Binding of alpha-dihydrotetrabenazine to the vesicular monoamine transporter is stereospecific. *Eur J Pharmacol.* (1995) 278:249–52. doi: 10.1016/0014-2999(95)00162-E
26. Goswami R, Ponde DE, Kung MP, Hou C, Kilbourn MR, Kung HF. Fluoroalkyl derivatives of dihydrotetrabenazine as positron emission tomography imaging agents targeting vesicular monoamine transporters. *Nucl Med Biol.* (2006) 33:685–94. doi: 10.1016/j.nucmedbio.2006.05.006
27. Kung MP, Hou C, Goswami R, Ponde DE, Kilbourn MR, Kung HF. Characterization of optically resolved 9-fluoropropyl-dihydrotetrabenazine as a potential PET imaging agent targeting vesicular monoamine transporters. *Nucl Med Biol.* (2007) 34:239–46. doi: 10.1016/j.nucmedbio.2006.12.005
28. Zhu L, Qiao H, Lieberman BP, Wu J, Liu Y, Pan Z, et al. Imaging of VMAT2 binding sites in the brain by (18)F-AV-133: the effect of a pseudo-carrier. *Nucl Med Biol.* (2012) 39:897–904. doi: 10.1016/j.nucmedbio.2012.05.002
29. Li X, Chen Z, Tang J, Liu C, Zou P, Huang H, et al. Synthesis and biological evaluation of 10-(11) C-dihydrotetrabenazine as a vesicular monoamine transporter 2 radioligand. *Arch Pharm.* (2014) 347:313–9. doi: 10.1002/ardp.2013.00307
30. Zhao R, Zha Z, Yao X, Ploessl K, Choi SR, Liu F, et al. VMAT2 imaging agent, D6-[(18)F]FP-(+)-DTBZ: improved radiosynthesis, purification by solid-phase extraction and characterization. *Nucl Med Biol.* (2019) 72–3:26–35. doi: 10.1016/j.nucmedbio.2019.07.002
31. Zhao C, Liu C, Tang J, Xu Y, Xie M, Chen Z. An efficient automated radiosynthesis and bioactivity confirmation of VMAT2 tracer [(18)F]FP-(+)-DTBZ. *Mol Imaging Biol.* (2020) 22:265–73. doi: 10.1007/s11307-019-01379-6

Conflict of Interest: The authors declare that the research was conducted in the absence of any commercial or financial relationships that could be construed as a potential conflict of interest.

Copyright © 2021 Dai, Sa, Guan, Wang, Li and Zhao. This is an open-access article distributed under the terms of the Creative Commons Attribution License (CC BY). The use, distribution or reproduction in other forums is permitted, provided the original author(s) and the copyright owner(s) are credited and that the original publication in this journal is cited, in accordance with accepted academic practice. No use, distribution or reproduction is permitted which does not comply with these terms.



Prediction of Ovarian Follicular Dominance by MRI Phenotyping of Hormonally Induced Vascular Remodeling

Liat Fellus-Alyagor¹, Inbal E. Biton², Hagit Dafni², Filip Bochner¹, Ron Rotkopf³, Nava Dekel¹ and Michal Neeman^{1*}

¹ Department of Biological Regulation, Weizmann Institute of Science, Rehovot, Israel, ² Department of Veterinary Resources, Weizmann Institute of Science, Rehovot, Israel, ³ Department of Life Science Core Facilities, Weizmann Institute of Science, Rehovot, Israel

OPEN ACCESS

Edited by:

Monique Bernsen,
Erasmus Medical Center, Netherlands

Reviewed by:

Maurits A. Jansen,
University of Edinburgh,
United Kingdom
Yu Qian,
University of Texas MD Anderson
Cancer Center, United States

*Correspondence:

Michal Neeman
michal.neeman@weizmann.ac.il

Specialty section:

This article was submitted to
Translational Medicine,
a section of the journal
Frontiers in Medicine

Received: 19 May 2021

Accepted: 26 July 2021

Published: 20 August 2021

Citation:

Fellus-Alyagor L, Biton IE, Dafni H,
Bochner F, Rotkopf R, Dekel N and
Neeman M (2021) Prediction of
Ovarian Follicular Dominance by MRI
Phenotyping of Hormonally Induced
Vascular Remodeling.
Front. Med. 8:711810.
doi: 10.3389/fmed.2021.711810

In the mammalian female, only a small subset of ovarian follicles, known as the dominant follicles (DFs), are selected for ovulation in each reproductive cycle, while the majority of the follicles and their resident oocytes are destined for elimination. This study aimed at characterizing early changes in blood vessel properties upon the establishment of dominance in the mouse ovary and application of this vascular phenotype for prediction of the follicles destined to ovulate. Sexually immature mice, hormonally treated for induction of ovulation, were imaged at three different stages by dynamic contrast-enhanced (DCE) MRI: prior to hormonal administration, at the time of DF selection, and upon formation of the corpus luteum (CL). Macromolecular biotin-bovine serum albumin conjugated with gadolinium-diethylenetriaminepentaacetic acid (b-BSA-GdDTPA) was intravenously injected, and the dynamics of its extravasation from permeable vessels as well as its accumulation in the antral cavity of the ovarian follicles was followed by consecutive T₁-weighted MRI. Permeability surface area product (permeability) and fractional blood volume (blood volume) were calculated from b-BSA-GdDTPA accumulation. We found that the neo-vasculature during the time of DF selection was characterized by low blood volume and low permeability values as compared to unstimulated animals. Interestingly, while the vasculature of the CL showed higher blood volume compared to the DF, it exhibited a similar permeability. Taking advantage of immobilized ovarian imaging, we combined DCE-MRI and intravital light microscopy, to reveal the vascular properties of follicles destined for dominance from the non-ovulating subordinate follicles (SFs). Immediately after their selection, permeability of the vasculature of DF was attenuated compared to SF while the blood volume remained similar. Furthermore, DFs were characterized by delayed contrast enhancement in the avascular follicular antrum, reflecting interstitial convection, whereas SFs were not. In this study, we showed that although DF selection is accompanied by blood vessel growth, the new vasculature

remained relatively impermeable compared to the vasculature in control animal and compared to SF. Additionally, DFs show late signal enhancement in their antrum. These two properties may aid in clinical prediction of follicular dominance at an early stage of development and help in their diagnosis for possible treatment of infertility.

Keywords: MRI, ovary, dominant follicle, corpus luteum, angiogenesis, permeability, blood volume, bi-modal imaging

INTRODUCTION

The oocytes, which are the female gametes, reside in the ovary while encapsulated by multi-cellular structures comprising together the ovarian follicles. In a sexually mature female, at any given time point, the ovary is populated by multiple follicles at different developmental stages (1–3). In the early primordial follicle, the oocyte is surrounded by a single layer of flattened granulosa cells. The development of primordial follicle into primary and secondary follicles at early folliculogenesis is characterized by proliferation of granulosa cells alongside the formation of an additional layer of theca cells, at the outer part of the follicle. Further development of the follicles from the preantral to the antral stages, is associated with the formation of a plasma exudate-filled cavity, known as the follicle antrum.

The majority of the female gametes, at all developmental stages, degenerate through a process known as atresia, while a small fraction continues their growth. During sexual maturation, the so far hormonally independent folliculogenic process acquires dependency on the cyclic secretion of the pituitary-derived gonadotropins. The gonadotropin follicle-stimulating hormone (FSH) induces growth of a subset of antral follicles up to the stage of the Graafian, also known as preovulatory, follicles. This event consists of upregulation of the receptors for another pituitary gonadotropin, luteinizing hormone (LH), as well as the production of estrogen, inhibin, and activin. The mid-cycle peak of LH released from the pituitary, known as the LH surge, will affect only these follicles expressing the LH receptor (LHR) to undergo the ovulatory changes. After follicle rupture and the subsequent release of the oocyte, collectively known as ovulation, the ovulating follicle will go through further differentiation to become the corpus luteum (CL) and will secrete progesterone, which supports the uterine endometrium preparation required for the establishment of pregnancy (2, 4). At each reproductive cycle, two populations of antral follicles develop, the follicles destined to ovulate, known as the dominant follicles (DFs) and the subordinate follicles (SFs), that will not ovulate and will undergo atresia. In the mouse, selection of DFs occurs 36 h after the exposure to FSH. At this stage, a sub-population of follicles, which expresses LHR, and thus is sensitive to this gonadotropin, had emerged (5).

Angiogenesis, defined as the sprouting of new blood vessels from pre-existing ones, plays a fundamental role in ovarian physiology and is essential for folliculogenesis, DF selection, and ovulation [reviewed in (6–9)]. The highly intensive dynamics of the angiogenic events that accompanies folliculogenesis is

governed by vascular endothelial growth factor (VEGF) (10–15). Angiogenesis induced by VEGF is often characterized by increased vascular permeability, which allows vessel growth, followed by their re-stabilization upon pericyte recruitment. The rate of vessel permeability and their following re-stabilization vary between vessels, tissues, and physiological processes (16, 17).

During their development, follicles comprise a peripheral vascular network that is restricted to the theca cell layer. After ovulation, formation of the CL involves a massive angiogenic process, in which blood vessels penetrate into the so-far avascular inner parts of the follicle (18–22).

A leading hypothesis regarding the mechanism of DF selection and subsequent ovulation/CL formation suggests that DF advantage over the SF is facilitated by the development of a richer peripheral vasculature that amplifies the local exposure to gonadotropins. Along this line, increased vascularization of individual follicles in rhesus monkeys that resulted in preferential accumulation of gonadotropins has been demonstrated (23). Moreover, *in vivo* studies in cattle showed that maintenance of follicular vasculature and appropriate blood supply to follicles are essential for establishment of follicular dominance (24). In mares, differential blood flow and blood flow velocity are early parameters for identification of DF (25). One of the few studies that used rodents showed that larger follicles exhibit wider capillaries and higher capillary blood perfusion, supporting this hypothesis (26).

Most of the *in vivo* imaging studies on the ovarian vasculature were performed by color Doppler ultrasonography. Parameters, such as blood flow velocity in arterial and venous vessels, were characterized extensively in the ovaries of large animals such as cows (27, 28), ewes (29–31) and mares (25), and found to be associated with DF selection and CL formation; ultrasound imaging of the vasculature is also very common in women. However, the resolution provided by ultrasound methods in rodents is not sufficient for the visualization of small follicles. Moreover, small vessels are not properly represented by this method and the extracted parameters are limited mainly to blood flow-related ones.

Magnetic resonance imaging (MRI) offers higher resolution and provides multiple functional vessel parameters. The diffusion rate of fluids crossing from the vascularized theca layer to the antrum measured by MRI in rat follicles was found to decrease in preovulatory follicles (32). Changes in the perfusion of the ovary during the ovulatory response were also studied through pulsed arterial spin labeling MRI (33, 34). This method was also applicable for arterial blood velocity measurements. Vessel permeability and fractional blood volume were studied by

dynamic contrast enhanced (DCE) MRI, using high-molecular-weight b-BSA-GdDTPA, in ovarian grafts for evaluation of the success of graft implantation and revascularization in the transplanted tissue (35–39). However, no such studies reported the dynamics of the angiogenic process that accompanies DF selection. Generating such information may assist in improving outcome for infertility treatments, particularly for patients that respond poorly to the hormonal treatment.

In this study, we investigated the dynamic changes in tissue concentration of b-BSA-GdDTPA during the angiogenic processes that accompany major events in ovarian physiology. We additionally compared blood volume and permeability of DF and SF shortly after dominance establishment, using multi-modality imaging acquired through an ovarian imaging window that allowed integration of high-resolution MRI with intravital microscopy (40, 41).

MATERIALS AND METHODS

Animals

All experiments were carried out according to Israel regulations on animal experimentation and Weizmann Institute guidelines. All experimental protocols were reviewed and approved by Weizmann Institutional Animal Care and Use Committee (IACUC). Sexually immature C57BL/6J female mice (22–28 days old) were used for all experiments.

Induction of Ovulation

Mice (C57BL/6J; Invigo, Jerusalem, Israel) were subcutaneously injected with 5 IU of the FSH analog, pregnant mare's serum gonadotropin (PMSG, National Hormone & Peptide Program, Harbor-UCLA Medical Center, California, U.S.A.; or Syncopart PMSG, Ceva, France) dissolved in 100 μ l of Dulbecco's phosphate buffered saline (PBS). A dose of 5 IU of the LH analog, human chorionic gonadotropin (hCG, Sigma Aldrich, Rehovot, Israel) dissolved in 100 μ l of PBS, was intraperitoneally administered to the animals 48 h after PMSG. Ovulation occurred \sim 12 h later.

MRI of Ovaries Before and During DF Selection Process

Mice were studied at the sexually immature stage (non-injected, $n = 6$) and during DF selection, at 36–48 h after injection of PMSG ($n = 5$). Anesthesia was achieved by Isoflurane (5% for induction, 1–2% for maintenance) mixed with oxygen (1 L/min), delivered through a nasal mask. Respiration rate was monitored during MRI and kept throughout the experimental period at 60–80 breaths per minute. Body temperature was maintained at 37°C throughout the experiment using a circulating water blanket. Once anesthetized, a silicone catheter was inserted into the tail vein and the mice were placed at a head-supine position in a 9.4-T BioSpec Magnet 94/20 USR system (Bruker, Karlsruhe, Germany), equipped with gradient coil system capable of producing pulse gradient of up to 40 gauss/cm in each of the three dimensions. A linear volume coil was used for excitation and a 2-cm surface coil for detection (Bruker, Karlsruhe Germany). For the calculation of pre-contrast R_1 , a set of T_1 -weighted 3D-gradient echo (MDEFT) images (TR: 10 ms, TE = 3.25 ms, two

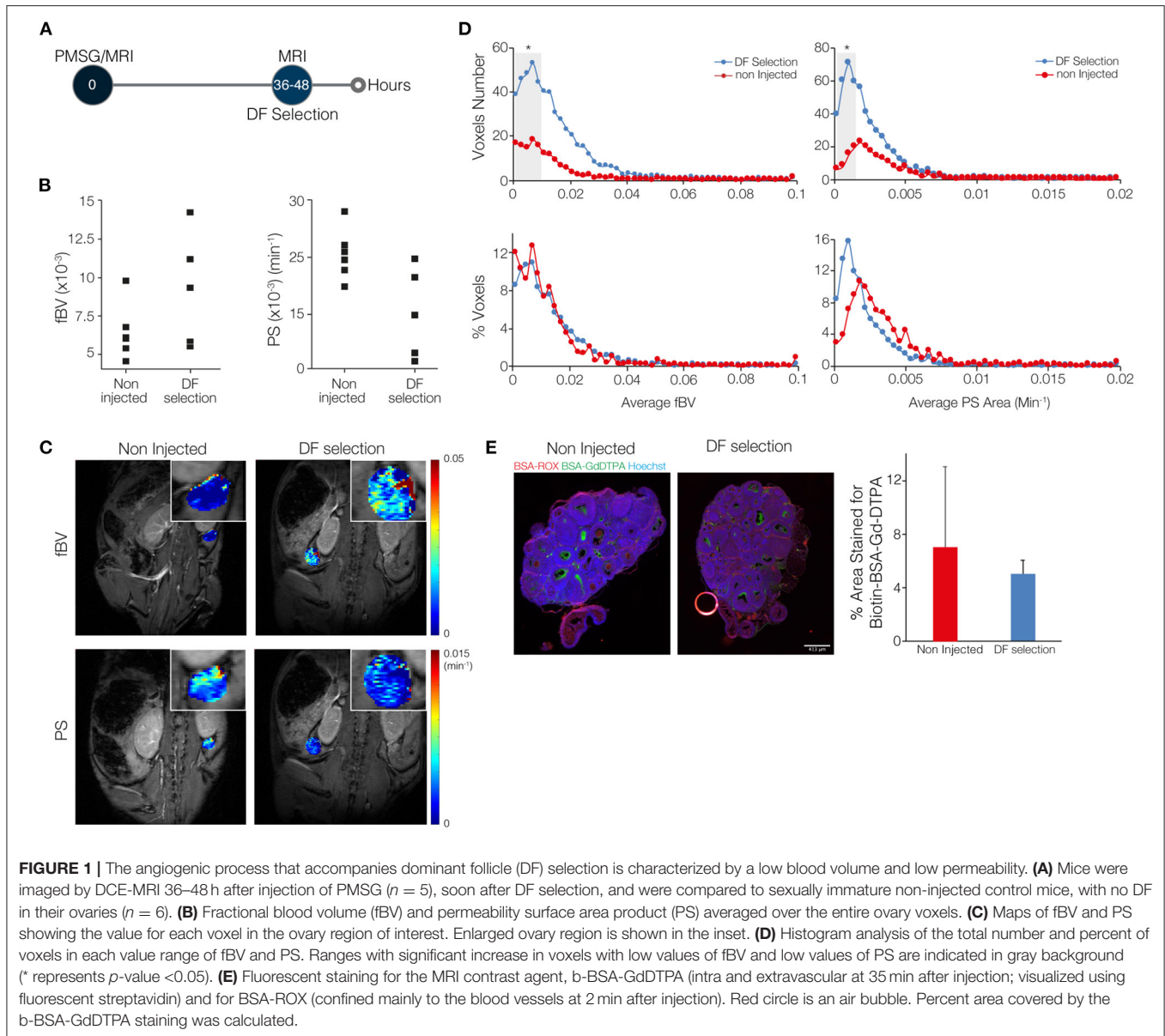
averages, matrix: $256 \times 256 \times 64$, FOV: $30 \times 30 \times 32$ mm, voxel size: $117 \times 117 \times 500$ μ m, scan time: 133 s) were acquired with varying flip angles (FA; 5°, 15°, 30°, 50°, and 70°). Then, b-BSA-GdDTPA [approximate MW is 82 kDa, final concentration in the blood = 100 mg/ml, \sim 0.8 g per kg; Symo Chem, Germany (42)] was injected intravenously through the pre-placed tail vein catheter (bolus injection over 1 min) and dynamic contrast enhancement was acquired using 3D T_1 -weighted images with a FA of 15° for a period of 35 min post injection (all other parameters are as stated above). The fluorescent tag carboxy-X-rhodamine (ROX, Molecular Probes, Oregon, USA) conjugated to bovine serum Albumin (BSA-ROX) was injected to the tail vein upon imaging completion. Mice were sacrificed 2 min later, before noticeable extravasation of BSA-ROX from the vessels, and their ovaries were collected for immunohistochemistry.

MRI of Ovaries During DF Selection and After Ovulation

Mice were imaged by MRI during DF selection (36–48 h after PMSG injection, $n = 8$ mice, 12 ovaries). Mice were allowed to recover from anesthesia upon completion of imaging. Subsequently, ovulation was induced by hCG, and the same mice were anesthetized and imaged again 4–12 h after ovulation, at the time of corpora lutea (CL) formation. MRI was performed as mentioned above.

Combined MRI and Microscopy Through Ovarian Imaging Window

High-resolution MRI was performed after mounting an MRI-compatible ovarian imaging window (40, 43) on sexually immature mice ($n = 5$). The ovary was carefully pulled out through a small incision in the peritoneum and placed inside the window by attaching the ovarian fat pad to the window with minimal amount of surgical glue (Vetbond, 3M, Maplewood, Minnesota, USA). After PMSG injection, at the time of DF selection, mice were anesthetized by a mix of Domitor (Medetomidine, 1 mg/kg, Vetoquinol, Lure Cedex, France) and Ketamine (75 mg/kg, Vetoquinol, Lure Cedex, France). Ovaries were imaged in the 9.4-T BioSpec MRI with a 10-mm 1H receive-only planar loop surface coil used in combination with a local preamplifier (Bruker, Germany) and 1H linear resonator for excitation. DCE-MRI was performed using T_1 -weighted 3D-gradient echo (FLASH) images (TR: 10 ms, TE: 3.25 ms, two averages, matrix: $512 \times 512 \times 48$, FOV: $20 \times 20 \times 16$ mm, pixel size: $39 \times 39 \times 330$ μ m, scan time: 123 s) with varying flip angles (FA, 5°, 15°, 30°, 50°, and 70°) pre-contrast and FA of 15° post-contrast for a period of 25–35 min (all other parameters are as stated above). At the same day, while still anesthetized ovaries were also imaged using the MVX10 stereomicroscope (Olympus, Tokyo, Japan). Mice were injected with hCG and then allowed to recover from anesthesia by injection of Antisedan (atipamezole hydrochloride, 1 mg/kg, Zoetis, New Jersey, USA). On the next day, upon ovulation, mice were anesthetized by Isoflurane, injected with the fluorescent marker FITC-Dextran (500,000 KD, Sigma-Aldrich, Rehovot, Israel) and imaged again in the stereomicroscope (Figure 1C). Based on the microscopy



images, follicles that transformed into CL were identified, and regions of interest were selected for further MRI image analysis.

Data Analysis

Voxel-by-voxel data analysis was performed using purpose-written MATLAB (Math Works Inc. Massachusetts, USA) scripts to generate R_1 maps and subsequently concentration maps of b-BSA-GdDTPA in the ovary region of interest as described (41). Briefly, pre-contrast R_1 maps were derived from the variable FA data by a non-linear fit to the following equation:

$$I(a) = \frac{M_0 \sin a (1 - e^{-TR \bullet R_{1pre}})}{1 - \cos a \bullet e^{-TR \bullet R_{1pre}}} \quad (1)$$

Where I is the signal intensity as a function of the pulse FA α , and the pre-exponent term, M_0 , includes contributions from both the spin density and the T_2 relaxation.

Post-contrast R_1 values (R_{1post}) were calculated from pre- and post-contrast 3D-GE signal intensities:

$$\frac{I_{(pre)}}{I_{(post)}} = \frac{M_0 \sin a \left(\frac{1 - e^{-TR \bullet R_{1(pre)}}}{1 - \cos a \bullet e^{-TR \bullet R_{1(pre)}}} \right)}{M_0 \sin a \left(\frac{1 - e^{-TR \bullet R_{1(post)}}}{1 - \cos a \bullet e^{-TR \bullet R_{1(post)}}} \right)} \quad (2)$$

Concentrations were calculated based on the relaxivity (r_1) of biotin-BSA-GdDTPA (that was measured for each batch separately) with the following equation:

$$c(t) = r_1^{-1} (R_{1post} - R_{1pre}) \quad (3)$$

Two vascular properties were derived by linear regression from the dynamic change in concentration during the first 15 min post-contrast: fractional blood volume (fBV, also referred to as

blood volume), calculated as the ratio between the extrapolated concentration of contrast agent at the time of administration and the initial concentration in the blood, and permeability surface area product (PS, also referred to as permeability; units: min^{-1}), calculated as the initial rate of contrast accumulation normalized to initial blood concentration (**Supplementary Figure 1**) (41). After fBV and PS maps were calculated for the ovary ROI, histograms were generated for fBV (range: 0–0.1 or 0.5) and PS (range: 0–0.02 min^{-1}) values and plotted in 50 bins. Histograms are presented in voxel numbers per bin and in percentage of voxels per bin formats.

For the calculation of late enhancement and late clearance, the rate of changes in concentration of b-BSA-GdDTPA over the 25–35 min post-contrast was derived by linear regression. To remove spikes of overestimated contrast concentration, a maximum threshold of 10 mM was set (<5% of the ROI voxels, distribution of these voxels is described in **Supplementary Figure 2**). This threshold was set for observation purposes, i.e., to facilitate identification of follicles.

Immunofluorescence and Immunohistochemistry

After MRI ovaries were collected, fixed in 4% paraformaldehyde, and embedded in paraffin blocks, 4- μm sections were made. Ovaries that were imaged through the MRI-compatible imaging window were taken at the same orientation as they were placed in the window, and 4- μm sections were made from the part of the ovary that was imaged by the stereomicroscope, to match the fluorescent intravital images. Hematoxylin and eosin (H&E) staining was done for one slide from each ovary.

Immunofluorescence was used for validation of blood volume and permeability. Intravascular and extravasated b-BSA-GdDTPA was visualized using Streptavidin Cy2 (Jackson ImmunoResearch, PA, USA), whereas intravascular BSA-ROX could be observed directly in paraffin sections.

Statistical Analysis

For the experiments of 36–48 h post PMSG vs. control mice, a linear mixed effects model with treatment as a fixed factor, and mouse and ovary as random factors, was used to calculate the statistical significance difference in averaged fBV and PS between the groups. The statistical significance of histograms was calculated for each bin separately with unpaired Student's *t*-test ($p < 0.05$). In cases where two ovaries from the same animal were imaged, they were averaged.

For the DF selection vs. CL formation experiments, a linear mixed effects model with treatment as a fixed factor, and mouse and ovary as random factors, was used to calculate the statistical significance difference in averaged fBV and PS between the two time points for the same subjects. Again, the statistical significance of histograms was calculated for each bin separately with a paired Student's *t*-test.

For DF vs. SF experiments, a paired Student's *t*-test was used to test the difference in averaged fBV and PS between the two sub-populations.

RESULTS

The angiogenic process that accompanies DF selection was studied against three relative processes: ovarian angiogenesis in non-injected mice, angiogenesis of CL formation, and angiogenesis of SF (**Supplementary Figure 2**).

DF Angiogenesis Shows Low Blood Volume and Low Permeability

Blood volume and permeability were derived from the dynamic changes in tissue concentration of b-BSA-GdDTPA, while marking a region of interest around the ovary. Ovarian average blood volume and average permeability were calculated according to the average signal intensity in the ovary. These values were then compared between ovaries of sexually immature mice that were imaged at 36–48 h after PMSG injection, the time of DF selection, and ovaries of same-age non-injected mice, in which DF selection does not take place (**Figure 1A**; a representative time lapse movie of post-contrast injection T_1 -weighted images, describing signal enhancement over time is shown in **Supplemental Digital Content 1**). The average blood volume and permeability at the time of DF selection were not statistically different (**Figure 1B**). Voxel-by-voxel maps of blood volume and permeability showed that ovaries that contained DF showed more voxels with high blood volume values and less voxels with high permeability values (**Figure 1C**). Histogram representation of the voxel-by-voxel maps showed an increase in the number of voxels at the low levels of blood volume and permeability after DF selection. However, no changes were detected upon normalization of the histograms to the size of the tissue (**Figure 1D**). The visualization of b-BSA-GdDTPA in histological sections of ovaries that were previously imaged by the MRI, using a fluorescently conjugated streptavidin, showed an accumulation of the contrast agent in the antrum of large follicles in PMSG-injected mice as well as in large follicles of non-injected controls. This was evident in the percent area of the ovary that was stained for b-BSA-GdDTPA, which was similar in the two groups (**Figure 1E**; separate channels of this staining and higher-magnification images are shown in **Supplementary Figure 3**).

CL Demonstrate Increased Blood Volume but Similar Permeability Compared to DF

To compare blood volume and permeability in the transition from DF to CL, we imaged the same mouse at two time points, first at the time of DF selection (36–48 h after PMSG injection) and later at the time of CL formation (about 5–13 h after ovulation, which is 17–25 h after hCG administration; **Figure 2A**). A significant elevation in ovarian average blood volume was seen in the CL, which matches the massive angiogenic process taking place during its formation (**Figure 2B**). However, no significant change in average permeability was observed. Maps of the vascular parameters also showed an increase in blood volume in several areas in the ovary but no change in permeability (**Figure 2C**). The histograms showed an increase in the number of voxels in low values of blood volume, and no change in permeability (**Figure 2D**). Immunofluorescent staining of the same ovaries validated these results, showing

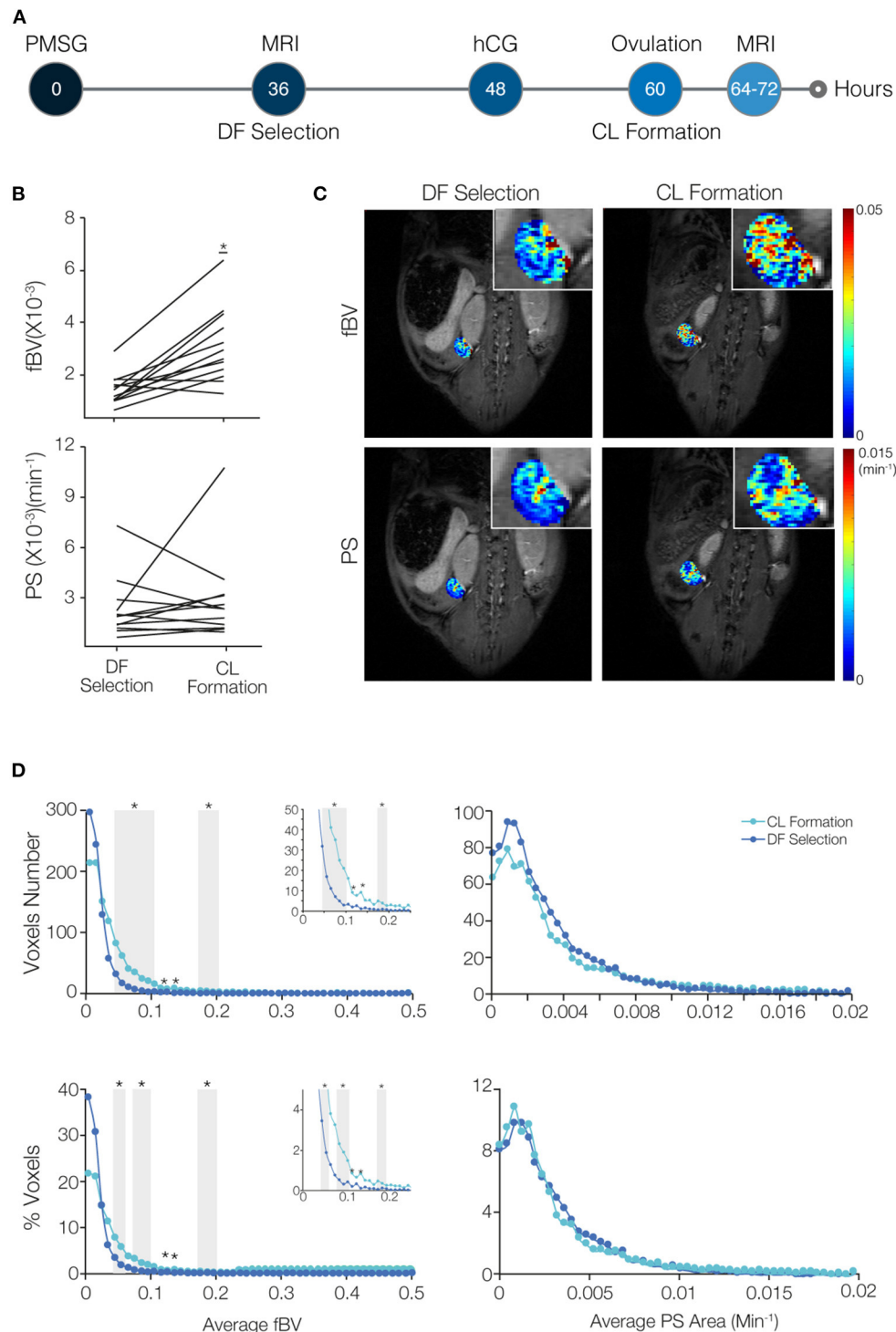
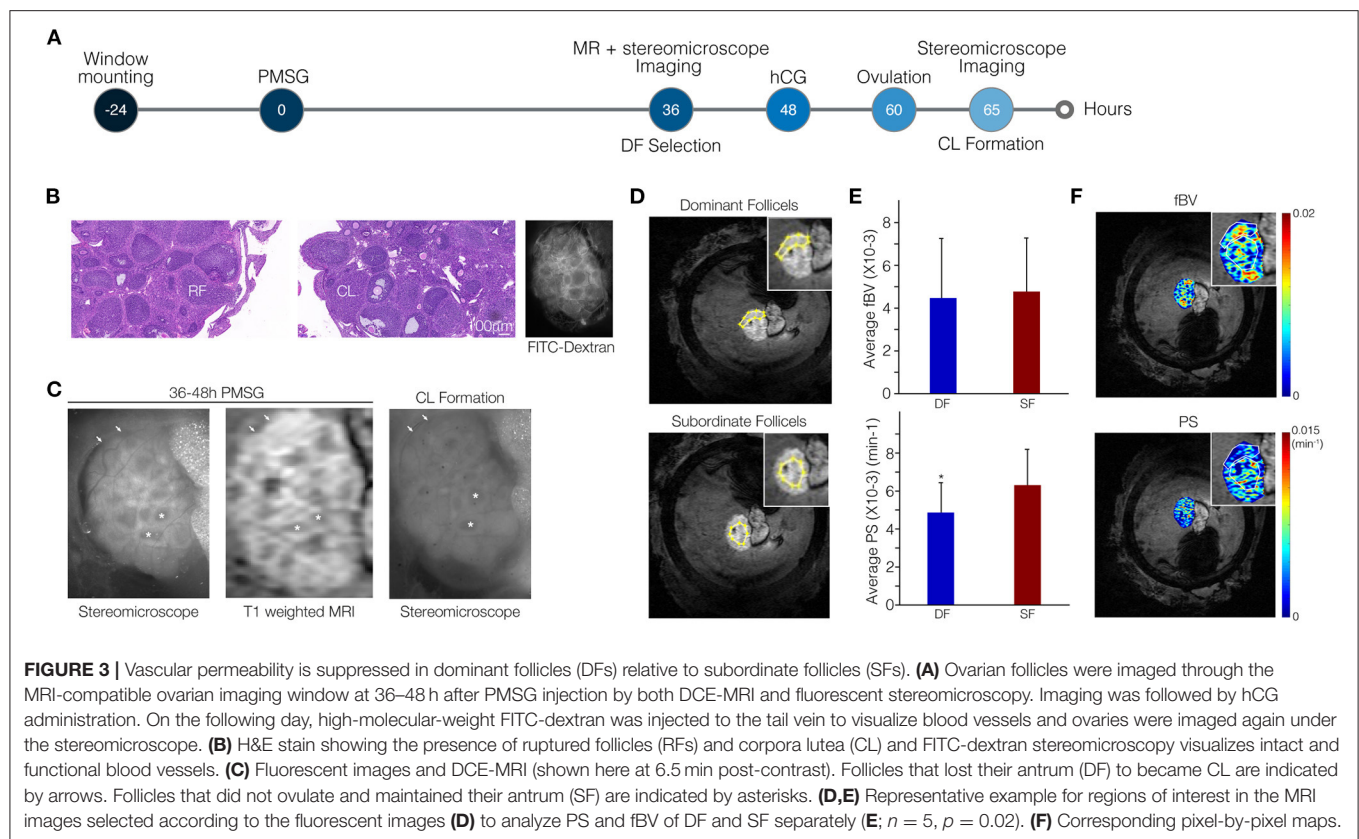


FIGURE 2 | Blood volume increases while permeability surface area remains restrained in the transition of the dominant follicle (DF) to form the corpus luteum (CL). **(A)** Mice were imaged by DCE-MRI soon after DF selection (36–48 h after PMSG injection) and then injected with hCG. On the next day, after ovulation occurred and at the time of CL formation, mice were imaged again ($n = 8$ mice, 12 ovaries). **(B)** Fractional blood volume (fBV) and permeability surface area product (PS) averaged over the entire ovary voxels. Significant change is indicated (* indicates p -value = 0.0006). **(C)** Maps of fBV and PS with enlarged ovary region in the inset. **(D)** Histogram analysis of the total number and percent of voxels in each value range of fBV and PS. Ranges with significant increase in voxels with low values of fBV are indicated by gray background (* indicates p -value < 0.05). Inserts show the enlargement of the histogram at the fBV range of 0–0.25.



that blood vessels penetrating the forming CL had minimal permeability, while, in the same animal, the antrum of an antral follicles that did not ovulate had high accumulation of b-BSA-GdDTPA (Supplementary Figure 5).

DF Present Low permeability and Late Enhancement Compared to SF

To increase resolution and enable distinction between blood vessel parameters of the DF and of SF, we made use of an MRI-compatible ovarian imaging window for both DCE-MRI and intra-vital fluorescent imaging (Figure 3A; a representative time lapse movie of post-injection T_1 weighted images, describing signal enhancement over time is shown in Supplementary Digital Content 2).

We imaged the mice at the time of DF selection through the ovarian imaging window by high-resolution MRI. A stereomicroscope was employed to image these same ovaries again, at the following day, upon hCG-induced ovulation (Figure 3A). Viability of the ovary was confirmed by the presence of ruptured follicles and CL indicating that ovulation did take place in the imaged ovaries. Additionally, functionality of blood vessels in the window-mounted ovary was maintained as evident by spreading of the intravenously injected fluorophore in the FITC-dextran images (Figure 3B). Fluorescent and MRI images were comparable, allowing identification of follicles that transformed into CL and lost their antrum upon ovulation. These follicles were defined retrospectively as DF; follicles that

did not lose their antrum were defined as SF (Figure 3C). The MRI resolution was improved dramatically from a voxel size of $117 \times 117 \times 500 \mu\text{m}$ to $39 \times 39 \times 330 \mu\text{m}$, allowing the clear identification and analysis of single follicles. Regions including clusters of DF or SF were marked in the MRI images and blood volume and permeability were calculated (Figure 3D). We found that DF vessels exhibited significantly lower permeability as compared to SF. However, no significant change in blood volume was detected (Figure 3E). Lower permeability in the region of SF relative to DF region was also depicted in the vascular parameter maps (Figure 3F). Moreover, DF and SF, discriminated by their high or low LH receptor staining, respectively, showed similar CD34 but also similar alpha smooth muscle actin staining (Supplementary Figure 6).

The vascular parameters, blood volume (fBV) and permeability (PS), were derived from the early dynamics (15 min) of b-BSA-GdDTPA. Further analysis of the later dynamics revealed that b-BSA-GdDTPA continued its accumulation in DF throughout the time of the experiment (up to 33 min post-contrast), while the concentration of b-BSA-GdDTPA in SF reached a steady state 6–16 min after injection and then showed a slow clearance (Figure 4A). Color-coded maps of early (PS) and late contrast accumulation were compared to fluorescent images taken before and after ovulation (Figures 4B–D). This comparison depicted late enhancing ovarian foci with low permeability that correlated with DF. Other areas showed a

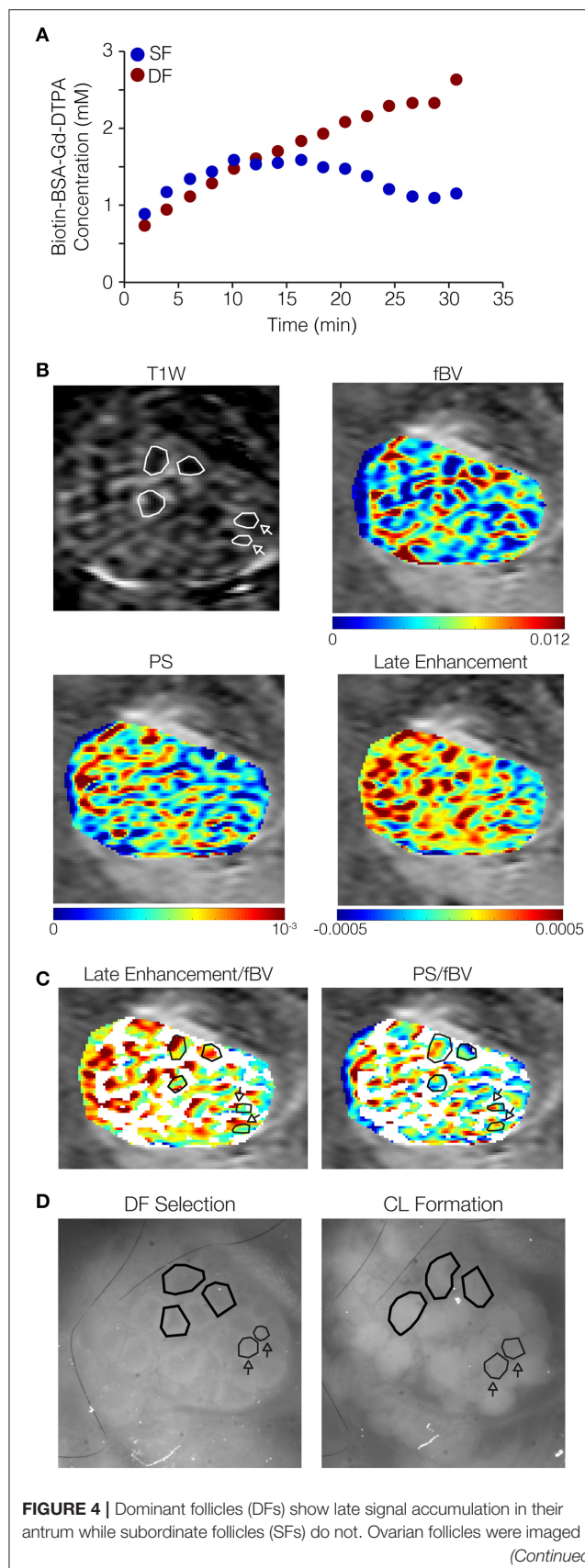


FIGURE 4 | through the ovarian imaging window after DF selection (36–48 h after PMSG injection), by MRI and fluorescent stereomicroscope, and again by stereomicroscope after formation of corpora lutea (CL; ~16 h after hCG administration). **(A)** Representative curves derived from a single mouse (out of five mice analyzed), of concentrations of b-BSA-GdDTPA over time for DF (red, continuous accumulation) and SF (blue, reaching a steady state followed by clearance). **(B)** Representative ovary imaged by DCE-MRI (3 min post-contrast image is shown); DF in polygons, SF in polygons indicated by arrows. Contrast accumulation follow-up for 35 min was used for the derivation of vascular parameters maps: fBV (initial contrast concentration), PS (accumulation rate at the first 15 min), and late enhancement (accumulation rate over that 25–35 min post-contrast). Color-coded late enhancement map shows positive enhancement (yellow through red) and zero to negative enhancement (stasis or clearance of contrast agent; green through blue). **(C)** PS and late enhancement maps overlayed with binary fBV map representing the highly vascularized layer around big follicles (white; selectively showing fBV values of 0.006 and above). Follicles indicated by polygons: positive late enhancement and low PS, identified by corresponding stereomicroscope images as follicles that lost their antrum and became CL. Follicles indicated by polygons indicated by arrows: zero or negative late enhancement and high PS, identified as follicles that did not lose their antrum upon ovulation. **(D)** Stereomicroscope images (without a fluorescent marker) of the same ovary at DF selection and CL formation.

decrease or no change in contrast agent concentration and correlated to SF (Figure 4C).

A summary of the findings in this study can be found in Table 1.

DISCUSSION

In this study, we focused on functional vascular changes that characterize early stages of DF selection. We utilized DCE-MRI for the three-dimensional non-invasive visualization of the mouse ovarian vasculature combined with high-resolution imaging performed using an MRI-compatible ovarian window reported by us previously recently (40, 43, 44). The window spatially holds the ovary to reduce motion and allows a smaller field of view. Combined with a matched surface coil for detection, it improves the signal-to-noise ratio. This multi-imaging modality enabled evaluation of blood vessel properties and observation of dynamic patterns of contrast agent distribution at the follicle level, allowing comparison between different populations of follicles in a way that was not possible in previously published MRI experiments in murine ovaries (33, 35–39).

Increase in blood volume is a hallmark of the DF (25, 45). In concordance, the increase in blood volume was clearly visible when looking at the voxel-by-voxel vascular parameter maps of ovaries of PMSG vs. non-injected animals. The histogram analysis revealed that the angiogenic process at this stage was characterized by elevated low values of blood volume, suggesting an increase in small vessels or a minor increase in vessels width. However, normalization of the histograms to the tissue size showed that the growth in vessels was proportional to the growth in tissue volume. This could be explained by the restriction of the vasculature to the surface of the follicles at this stage and is

TABLE 1 | Results summary of fBV and PS in different experiments.

	fBV	PS	Delayed Enhancement	Figure Presenting Results
Ovaries of non-injected mice compared to ovaries of PMSG-injected mice	↑	↑		1
Ovaries of PMSG-injected mice compared to ovaries of PMSG +hCG mouse	↓	=		2
DF vs. SF	=	↓	↑	3, 4

A change in a value is indicated by an arrow (increase or decrease). All changes are in respect to the ovary of the PMSG injected mouse. No change is indicated by (=).

in concordance with the lack of statistical significance in average ovarian blood volume.

Upon CL formation, we detected a substantial increase in blood volume, as expected. In contrast to the vessels of the DF, the vessels of the forming CL were characterized by higher values of blood volume, indicating the formation of either more vessels or larger vessels in this process. In this case, their growth was not proportional but higher than the growth in tissue size. In previous studies done in our lab, arterial spin labeling MRI was used to assess ovarian perfusion at a time window of up to 10 h after hCG administration (33, 34). Perfusion was shown to be decreased at 2 h after hCG injection, followed by a transient rise that was proportional to the growth in tissue weight. However, these experiments were done at an earlier time point prior to ovulation.

The moderate permeability seen in the angiogenesis associated with DF selection and CL formation might point at a quick stabilization of the forming vessels. This could not be explained by a change in α SMA, but could be attributed to other molecular factors. Fast stabilization of the DF and the CL vasculature could have a functional advantage in allowing higher efficiency of hormone transmission. Small molecules and proteins up to 100 kDa are transported in and out the follicle by osmosis (46, 47). Our MRI contrast agent, b-BSA-GdDTPA, being about 82 kDa in size, represents such proteins. One example for a small protein produced by the follicle in association to dominance establishment is inhibin. Inhibin (31 kDa) is a gonadal origin hormone that negatively feeds back the synthesis and secretion of the pituitary FSH (48). Since one of the major characteristic properties of the DF is its ability to shift its dependence from FSH to LH while the SFs are still dependent on FSH for their survival, inhibin is a key factor in DF selection. The low permeability of the DF may contribute to the efficient transmission of inhibin from the follicle to the peripheral blood system, thus contributing to the declining levels of FSH.

It was previously shown that in the CL, LH-induced VEGFA upregulation directly influences an increase in permeability by downregulating VE-cadherin, occluding, and claudin5 (49), allegedly in contrast to our findings. However, these experiments were done at a later stage of CL developments (after oocyte fertilization, at the early stages of pregnancy) whereas our experiments were conducted as soon as 5 h after ovulation. It was also shown that blood vessels of the CL have increased permeability as soon as 2–10 h after hCG injection (50–52). CL permeability was also shown to facilitate the infiltration of immune cells, which have a role in ovulation, CL function, and angiogenesis (53–55). Therefore, our results may suggest a permeability switch occurring in the CL, starting with

high permeability, which allows the infiltration of immune cells, followed by low permeability. An additional increase in permeability may be induced in early stages of pregnancy. It is also important to note that the results of our study do not suggest that vessels are not permeable during the early stage of CL formation, but that the permeability that accompanies CL formation is similar to permeability during DF selection, which, in both cases, is kept moderate.

We further detected a differential pattern of contrast agent accumulation between DF and SF during DCE-MRI. Accumulation of b-BSA-GdDTPA in DF was continuous (up to 33 min after injection of b-BSA-GdDTPA), while in SF, clearance was observed at around 25 min. In addition to the decrease in permeability that was detected in DF, this result could point at a difference in extracellular matrix (ECM) components of the DF, leading to a slower passage from the blood vessels to the antrum. An ECM component that is known to be expressed differentially between DF and SF is fibronectin, which increases in the theca cell layer and stroma with follicular development while its level in the granulosa cells decreases, making the follicle more rigid and less permissive for large solutes to travel from the blood vessels to the antrum (56). Nevertheless, the involvement of fibronectin or any other ECM component in the late enhancement phenomena and low permeability of the DF is to be elucidated.

Our results suggest measurable vasculature functional parameters that discriminate DF from SF soon after their selection. This discrimination may be clinically relevant in cases of poor responders to hormonal stimulation during assisted reproductive technologies. It was reported that a number of 15 retrieved oocytes during *in vitro* fertilization procedures is optimal for live birth outcome (57). However, in some cases, patients do not reach this number and are defined as poor ovarian responders with a low prognosis (58, 59). The method described in this study can assist in unveiling the molecular mechanisms and physiological processes that occur in low prognosis patients with the intention to resolve them. In the clinics, DFs are usually identified by size deviation from the SF using ultrasound. The functional vascular parameters evaluated here by MRI may offer DF detection prior to size deviation. Furthermore, discrimination between DF and SF and the ability to detect DF at an early developmental stage in the mouse ovary opens the possibility for investigation of dominance establishment following different intervention as well as in transgenic mouse models.

To conclude, in this study, we used *in vivo* multi-modality imaging of the vasculature to track the dynamics of blood flow identifying moderate permeability and late enhancement as

hallmarks of the DF. We further suggested the employment of these properties as predictive markers for DF as early as at the initial stage of their selection.

DATA AVAILABILITY STATEMENT

The raw data supporting the conclusions of this article will be made available by the authors, without undue reservation.

ETHICS STATEMENT

The animal study was reviewed and approved by Weizmann Institute IACUC.

AUTHOR CONTRIBUTIONS

LF-A conducted all experiments and data analysis. IB guided and assisted in MRI experiments. HD wrote MATLAB codes for data analysis and assisted with data analysis. FB designed the ovarian imaging window and assisted in surgery of animals. RR performed statistical analysis. MN and ND supervised the

work. All authors contributed to the article and approved the submitted version.

FUNDING

This work was supported by the Seventh Framework European Research Council Advanced Grant 232640-IMAGO. MN is incumbent of the Helen and Morris Mauerberger Chair in Biological Sciences.

ACKNOWLEDGMENTS

The authors would like to thank and acknowledge the following for their contribution to this manuscript: Ishai Sher for the graphic design of figures, Beni Siani for animal tendance, and Yinon Cohen for editing assistance.

SUPPLEMENTARY MATERIAL

The Supplementary Material for this article can be found online at: <https://www.frontiersin.org/articles/10.3389/fmed.2021.711810/full#supplementary-material>

REFERENCES

- McGee EA, Hsueh AJ. Initial and cyclic recruitment of ovarian follicles. *Endocr Rev.* (2000) 21:200–14. doi: 10.1210/edrv.21.2.0394
- Richards JS, Pangas SA. The ovary: basic biology and clinical implications. *J Clin Invest.* (2010) 120:963–72. doi: 10.1172/JCI41350
- Rimon-Dahari N, Yerushalmi-Heinemann L, Alyagor L, Dekel N. Ovarian folliculogenesis. *Results Probl Cell Differ.* (2016) 58:167–90. doi: 10.1007/978-3-319-31973-5_7
- Knobil E. William Harvey and the physiology of reproduction. *Physiologist.* (1981) 24:3–7.
- Salomon Y, Yanovsky A, Mintz Y, Amir Y, Lindner HR. Synchronous generation of ovarian hCG binding sites and LH-sensitive adenylate cyclase in immature rats following treatment with pregnant mare serum gonadotropin. *J Cyclic Nucleotide Res.* (1977) 3:163–76.
- Plendl J. Angiogenesis and vascular regression in the ovary. *Anat Histol Embryol.* (2000) 29:257–66. doi: 10.1046/j.1439-0264.2000.00265.x
- Ramakrishnan S, Subramanian IV, Yokoyama Y, Geller M. Angiogenesis in normal and neoplastic ovaries. *Angiogenesis.* (2005) 8:169–82. doi: 10.1007/s10456-005-9001-1
- Robinson RS, Woad KJ, Hammond AJ, Laird M, Hunter MG, Mann GE. Angiogenesis and vascular function in the ovary. *Reproduction.* (2009) 138:869–81. doi: 10.1530/REP-09-0283
- Brown HM, Russell DL. Blood and lymphatic vasculature in the ovary: development, function and disease. *Hum Reprod Update.* (2014) 20:29–39. doi: 10.1093/humupd/dmt049
- Danforth DR, Arbogast LK, Ghosh S, Dickerman A, Rofagha R, Friedman CI. Vascular endothelial growth factor stimulates preantral follicle growth in the rat ovary. *Biol Reprod.* (2003) 68:1736–41. doi: 10.1095/biolreprod.101.000679
- Zimmermann RC, Hartman T, Kavic S, Pauli SA, Bohlen P, Sauer MV, et al. Vascular endothelial growth factor receptor 2-mediated angiogenesis is essential for gonadotropin-dependent follicle development. *J Clin Invest.* (2003) 112:659–69. doi: 10.1172/JCI200318740
- Fraser HM, Wilson H, Rudge JS, Wiegand SJ. Single injections of vascular endothelial growth factor trap block ovulation in the macaque and produce a prolonged, dose-related suppression of ovarian function. *J Clin Endocrinol Metab.* (2005) 90:1114–22. doi: 10.1210/jc.2004-1572
- Iijima K, Jiang JY, Shimizu T, Sasada H, Sato E. Acceleration of follicular development by administration of vascular endothelial growth factor in cycling female rats. *J Reprod Dev.* (2005) 51:161–8. doi: 10.1262/jrd.51.161
- Taylor PD, Wilson H, Hillier SG, Wiegand SJ, Fraser HM. Effects of inhibition of vascular endothelial growth factor at time of selection on follicular angiogenesis, expansion, development and atresia in the marmoset. *Mol Hum Reprod.* (2007) 13:729–36. doi: 10.1093/molehr/gam056
- McFee RM, Artac RA, McFee RM, Clopton DT, Smith RA, Rozell TG, et al. Inhibition of vascular endothelial growth factor receptor signal transduction blocks follicle progression but does not necessarily disrupt vascular development in perinatal rat ovaries. *Biol Reprod.* (2009) 81:966–77. doi: 10.1095/biolreprod.109.078071
- Nagy JA, Benjamin L, Zeng H, Dvorak AM, Dvorak HF. Vascular permeability, vascular hyperpermeability and angiogenesis. *Angiogenesis.* (2008) 11:109–19. doi: 10.1007/s10456-008-9099-z
- Bates DO. Vascular endothelial growth factors and vascular permeability. *Cardiovasc Res.* (2010) 87:262–71. doi: 10.1093/cvr/cvq105
- Ferrara N, Chen H, Davis-Smyth T, Gerber HP, Nguyen TN, Peers D, et al. Vascular endothelial growth factor is essential for corpus luteum angiogenesis. *Nat Med.* (1998) 4:336–40. doi: 10.1038/nm0398-336
- Wulff C, Wilson H, Rudge JS, Wiegand SJ, Lunn SF, Fraser HM. Luteal angiogenesis: prevention and intervention by treatment with vascular endothelial growth factor trap (A40). *J Clin Endocrinol Metab.* (2001) 86:3377–86. doi: 10.1210/jcem.86.7.7662
- Zimmermann RC, Hartman T, Bohlen P, Sauer MV, Kitajewski J. Preovulatory treatment of mice with anti-VEGF receptor 2 antibody inhibits angiogenesis in corpora lutea. *Microvasc Res.* (2001) 62:15–25. doi: 10.1006/mvre.2001.2312
- Hazzard TM, Xu F, Stouffer RL. Injection of soluble vascular endothelial growth factor receptor 1 into the preovulatory follicle disrupts ovulation and subsequent luteal function in rhesus monkeys. *Biol Reprod.* (2002) 67:1305–12. doi: 10.1095/biolreprod67.4.1305
- Kuhnert F, Tam BY, Sennino B, Gray JT, Yuan J, Jocson A, et al. Soluble receptor-mediated selective inhibition of VEGFR and PDGFRbeta signaling during physiologic and tumor angiogenesis. *Proc Natl Acad Sci USA.* (2008) 105:10185–90. doi: 10.1073/pnas.0803194105
- Zeleznik AJ, Schuler HM, Reichert LE Jr. Gonadotropin-binding sites in the rhesus monkey ovary: role of the vasculature in the selective distribution of human chorionic gonadotropin to the preovulatory follicle. *Endocrinology.* (1981) 109:356–62. doi: 10.1210/endo-109-2-356

24. Acosta TJ. Studies of follicular vascularity associated with follicle selection and ovulation in cattle. *J Reprod Dev.* (2007) 53:39–44. doi: 10.1262/jrd.18153
25. Acosta TJ, Gastal EL, Gastal MO, Beg MA, Ginther OJ. Differential blood flow changes between the future dominant and subordinate follicles precede diameter changes during follicle selection in mares. *Biol Reprod.* (2004) 71:502–7. doi: 10.1095/biolreprod.104.027896
26. Vollmar B, Laschke MW, Rohan R, Koenig J, Menger MD. *In vivo* imaging of physiological angiogenesis from immature to preovulatory ovarian follicles. *Am J Pathol.* (2001) 159:1661–70. doi: 10.1016/S0002-9440(10)63013-1
27. Matsui M, Miyamoto A. Evaluation of ovarian blood flow by colour Doppler ultrasound: practical use for reproductive management in the cow. *Vet J.* (2009) 181:232–40. doi: 10.1016/j.tvjl.2008.02.027
28. Luttgenau J, Bollwein H. Evaluation of bovine luteal blood flow by using color Doppler ultrasonography. *Reprod Biol.* (2014) 14:103–9. doi: 10.1016/j.repbio.2014.03.003
29. Brown BW, Emery MJ, Mattner PE. Ovarian arterial blood velocity measured with Doppler ultrasonic transducers in conscious ewes. *J Reprod Fertil.* (1980) 58:295–300. doi: 10.1530/jrf.0.0580295
30. El-Sherry TM, Derar R, Bakry R. Changes in blood flow in ovine follicles and serum concentration of estradiol 17 beta (E2) and nitric oxide (NO) around the time of ovulation in Ossimi ewes. *Anim Reprod Sci.* (2013) 138:188–93. doi: 10.1016/j.anireprosci.2013.02.019
31. Oliveira ME, Feliciano MA, D'Amato CC, Oliveira LG, Bicudo SD, Fonseca JF, et al. Correlations between ovarian follicular blood flow and superovulatory responses in ewes. *Anim Reprod Sci.* (2014) 144:30–7. doi: 10.1016/j.anireprosci.2013.10.012
32. Tempel C, Schiffenbauer YS, Meir G, Neeman M. Modulation of water diffusion during gonadotropin-induced ovulation: NMR microscopy of the ovarian follicle. *Magn Reson Med.* (1995) 34:213–8. doi: 10.1002/mrm.1910340212
33. Tempel C, Neeman M. Perfusion of the rat ovary: application of pulsed arterial spin labeling MRI. *Magn Reson Med.* (1999) 41:113–23. doi: 10.1002/(SICI)1522-2594(199901)41:1<113::AID-MRM16>3.0.CO;2-G
34. Tempel C, Neeman M. Spatial and temporal modulation of perfusion in the rat ovary measured by arterial spin labeling MRI. *J Magn Reson Imaging.* (1999) 9:794–803. doi: 10.1002/(SICI)1522-2586(199906)9:6<794::AID-JMRI6>3.0.CO;2-P
35. Israely T, Dafni H, Granot D, Nevo N, Tsafiriri A, Neeman M. Vascular remodeling and angiogenesis in ectopic ovarian transplants: a crucial role of pericytes and vascular smooth muscle cells in maintenance of ovarian grafts. *Biol Reprod.* (2003) 68:2055–64. doi: 10.1095/biolreprod.102.011734
36. Israely T, Dafni H, Nevo N, Tsafiriri A, Neeman M. Angiogenesis in ectopic ovarian xenotransplantation: multiparameter characterization of the neovasculature by dynamic contrast-enhanced MRI. *Magn Reson Med.* (2004) 52:741–50. doi: 10.1002/mrm.20203
37. Israely T, Nevo N, Harmelin A, Neeman M, Tsafiriri A. Reducing ischaemic damage in rodent ovarian xenografts transplanted into granulation tissue. *Hum Reprod.* (2006) 21:1368–79. doi: 10.1093/humrep/del010
38. Cohen Y, Dafni H, Avni R, Raz T, Biton I, Hemmings B, et al. In search of signaling pathways critical for ovarian graft reception: Akt1 is essential for long-term survival of ovarian grafts. *Fertil Steril.* (2014) 101:536–44. doi: 10.1016/j.fertnstert.2013.10.007
39. Cohen Y, Dafni H, Avni R, Fellus L, Bochner F, Rotkopf R, et al. Genetic and pharmacological modulation of Akt1 for improving ovarian graft revascularization in a mouse model. *Biol Reprod.* (2016) 94:14. doi: 10.1095/biolreprod.115.131987
40. Martins AF, Clavijo Jordan V, Bochner F, Chirayil S, Paranawithana N, Zhang S, et al. Imaging insulin secretion from mouse pancreas by MRI is improved by use of a zinc-responsive MRI sensor with lower affinity for Zn(2+) ions. *J Am Chem Soc.* (2018) 140:17456–7464. doi: 10.1021/jacs.8b07607
41. Dafni H, Cohen B, Ziv K, Israely T, Goldshmidt O, Nevo N, et al. The role of heparanase in lymph node metastatic dissemination: dynamic contrast-enhanced MRI of Eb lymphoma in mice. *Neoplasia.* (2005) 7:224–33. doi: 10.1593/neo.04433
42. Dafni H, Landsman L, Schechter B, Kohen F, Neeman M. MRI and fluorescence microscopy of the acute vascular response to VEGF165: vasodilation, hyper-permeability and lymphatic uptake, followed by rapid inactivation of the growth factor. *NMR Biomed.* (2002) 15:120–31. doi: 10.1002/nbm.724
43. Bochner F, Fellus-Alyagor L, Kalchenko V, Shinar S, Neeman M. A novel intravital imaging window for longitudinal microscopy of the mouse ovary. *Sci Rep.* (2015) 5:12446. doi: 10.1038/srep12446
44. Bochner F, Fellus-Alyagor L, Ketter D, Golani O, Biton I, Neeman M. Bimodal magnetic resonance and optical imaging of extracellular matrix remodelling by orthotopic ovarian tumours. *Br J Cancer.* (2020) 123:216–25. doi: 10.1038/s41416-020-0878-7
45. Fraser HM. Regulation of the ovarian follicular vasculature. *Reprod Biol Endocrinol.* (2006) 4:18. doi: 10.1186/1477-7827-4-18
46. Shalgi R, Kraicer P, Rimon A, Pinto M, Soferman N. Proteins of human follicular fluid: the blood-follicle barrier. *Fertil Steril.* (1973) 24:429–34. doi: 10.1016/S0015-0282(16)39730-8
47. Andersen MM, Kroll J, Byskov AG, Faber M. Protein composition in the fluid of individual bovine follicles. *J Reprod Fertil.* (1976) 48:109–18. doi: 10.1530/jrf.0.0480109
48. Makanji Y, Zhu J, Mishra R, Holmquist C, Wong WP, Schwartz NB, et al. Inhibin at 90: from discovery to clinical application, a historical review. *Endocr Rev.* (2014) 35:747–94. doi: 10.1210/er.2014-1003
49. Groten T, Fraser HM, Duncan WC, Konrad R, Kreienberg R, Wulff C. Cell junctional proteins in the human corpus luteum: changes during the normal cycle and after HCG treatment. *Hum Reprod.* (2006) 21:3096–102. doi: 10.1093/humrep/del286
50. Gerdes U, Gafvels M, Bergh A, Cajander S. Localized increases in ovarian vascular permeability and leucocyte accumulation after induced ovulation in rabbits. *J Reprod Fertil.* (1992) 95:539–50. doi: 10.1530/jrf.0.0950539
51. Koos RD. Increased expression of vascular endothelial growth/permeability factor in the rat ovary following an ovulatory gonadotropin stimulus: potential roles in follicle rupture. *Biol Reprod.* (1995) 52:1426–35. doi: 10.1095/biolreprod52.6.1426
52. Mitsube K, Brannstrom M, Haraldsson B. Modulation of microvascular permeability in the preovulatory rat ovary by an ovulatory gonadotropin stimulus. *Fertil Steril.* (2013) 99:903–9. doi: 10.1016/j.fertnstert.2012.11.017
53. Turner EC, Hughes J, Wilson H, Clay M, Mylonas KJ, Kipari T, et al. Conditional ablation of macrophages disrupts ovarian vasculature. *Reproduction.* (2011) 141:821–31. doi: 10.1530/REP-10-0327
54. Care AS, Diener KR, Jasper MJ, Brown HM, Ingman WV, Robertson SA. Macrophages regulate corpus luteum development during embryo implantation in mice. *J Clin Invest.* (2013) 123:3472–87. doi: 10.1172/JCI60561
55. Cohen-Fredarow A, Tadmor A, Raz T, Meterani N, Addadi Y, Nevo N, et al. Ovarian dendritic cells act as a double-edged pro-ovulatory and anti-inflammatory sword. *Mol Endocrinol.* (2014) 28:1039–54. doi: 10.1210/me.2013-1400
56. Berkholtz CB, Lai BE, Woodruff TK, Shea LD. Distribution of extracellular matrix proteins type I collagen, type IV collagen, fibronectin, and laminin in mouse folliculogenesis. *Histochem Cell Biol.* (2006) 126:583–92. doi: 10.1007/s00418-006-0194-1
57. Sunkara SK, Rittenberg V, Raine-Fenning N, Bhattacharya S, Zamora J, Coomarasamy A. Association between the number of eggs and live birth in IVF treatment: an analysis of 400 135 treatment cycles. *Hum Reprod.* (2011) 26:1768–74. doi: 10.1093/humrep/der106

58. Ferraretti AP, La Marca A, Fauser BC, Tarlatzis B, Nargund G, Gianaroli L, et al. ESHRE consensus on the definition of 'poor response' to ovarian stimulation for in vitro fertilization: the Bologna criteria. *Hum Reprod.* (2011) 26:1616–24. doi: 10.1093/humrep/der092
59. Poseidon G, Alviggi C, Andersen CY, Buehler K, Conforti A, De Placido G, et al. A new more detailed stratification of low responders to ovarian stimulation: from a poor ovarian response to a low prognosis concept. *Fertil Steril.* (2016) 105:1452–3. doi: 10.1016/j.fertnstert.2016.02.005

Conflict of Interest: The authors declare that the research was conducted in the absence of any commercial or financial relationships that could be construed as a potential conflict of interest.

Publisher's Note: All claims expressed in this article are solely those of the authors and do not necessarily represent those of their affiliated organizations, or those of the publisher, the editors and the reviewers. Any product that may be evaluated in this article, or claim that may be made by its manufacturer, is not guaranteed or endorsed by the publisher.

Copyright © 2021 Fellus-Alyagor, Biton, Dafni, Bochner, Rotkopf, Dekel and Neeman. This is an open-access article distributed under the terms of the Creative Commons Attribution License (CC BY). The use, distribution or reproduction in other forums is permitted, provided the original author(s) and the copyright owner(s) are credited and that the original publication in this journal is cited, in accordance with accepted academic practice. No use, distribution or reproduction is permitted which does not comply with these terms.



Fluorinated PLGA-PEG-Mannose Nanoparticles for Tumor-Associated Macrophage Detection by Optical Imaging and MRI

Giorgia Zambito^{1,2,3†}, Siyuan Deng^{4†}, Joost Haeck⁵, Natasa Gaspar^{1,2,6}, Uwe Himmelreich⁷, Roberta Censi⁴, Clemens Löwik^{1,2}, Piera Di Martino^{4*} and Laura Mezzanotte^{1,2*}

OPEN ACCESS

Edited by:

Wu Yuan,
The Chinese University of Hong
Kong, China

Reviewed by:

Sridhar Goud,
National Institutes of Health (NIH),
United States
Ankit Saneja,
Institute of Himalayan Bioresource
Technology (CSIR), India

*Correspondence:

Piera Di Martino
piera.dimartino@unicam.it
Laura Mezzanotte
l.mezzanotte@erasmusmc.nl

[†]These authors have contributed
equally to this work and share first
authorship

Specialty section:

This article was submitted to
Translational Medicine,
a section of the journal
Frontiers in Medicine

Received: 20 May 2021

Accepted: 27 July 2021

Published: 27 August 2021

Citation:

Zambito G, Deng S, Haeck J,
Gaspar N, Himmelreich U, Censi R,
Löwik C, Di Martino P and
Mezzanotte L (2021) Fluorinated
PLGA-PEG-Mannose Nanoparticles
for Tumor-Associated Macrophage
Detection by Optical Imaging and
MRI. *Front. Med.* 8:712367.
doi: 10.3389/fmed.2021.712367

¹ Department of Radiology and Nuclear Medicine, Erasmus Medical Center, Rotterdam, Netherlands, ² Department of Molecular Genetics, Erasmus Medical Center, Rotterdam, Netherlands, ³ Medres Medical Research GmbH, Cologne, Germany, ⁴ School of Pharmacy, University of Camerino, Camerino, Italy, ⁵ Applied Molecular Imaging Facility of Erasmus MC (AMIE) Core Facility, Erasmus Medical Center, Rotterdam, Netherlands, ⁶ Percuros B.V., Enschede, Netherlands, ⁷ Biomedical MR Unit, Molecular Small Animal Imaging Center (MoSAIC), University of Leuven (KU Leuven), Leuven, Belgium

Tumor-associated macrophages (TAMs) promote cancer growth and metastasis, but their role in tumor development needs to be fully understood due to the dynamic changes of tumor microenvironment (TME). Here, we report an approach to visualize TAMs by optical imaging and by Fluorine-19 (¹⁹F) magnetic resonance imaging (MRI) that is largely applied to track immune cells *in vivo*. TAMs are targeted with PLGA-PEG-mannose nanoparticles (NPs) encapsulating perfluoro-15-crown-5-ether (PFCE) as MRI contrast agent. These particles are preferentially recognized and phagocytized by TAMs that overexpress the mannose receptor (MRC1/CD206). The PLGA-PEG-mannose NPs are not toxic and they were up-taken by macrophages as confirmed by *in vitro* confocal microscopy. At 48 h after intravenous injection of PLGA-PEG-mannose NPs, 4T1 xenograft mice were imaged and fluorine-19 nuclear magnetic resonance confirmed nanoparticle retention at the tumor site. Because of the lack of ¹⁹F background in the body, observed ¹⁹F signals are robust and exhibit an excellent degree of specificity. *In vivo* imaging of TAMs in the TME by ¹⁹F MRI opens the possibility for detection of cancer at earlier stage and for prompt therapeutic interventions in solid tumors.

Keywords: cell tracking, perfluorocarbon, tumor-associated macrophage, contrast agent, ¹⁹F, magnetic resonance imaging, breast cancer

INTRODUCTION

Inflammation is one the major effect of cancer and it plays a pivotal role in cancer progression and metastasis (1). In healthy conditions, macrophages (M ϕ) exert pro-inflammatory and cytotoxic effect leading the immune response against tumor development (2). In solid tumors, tumor associated-macrophages (TAMs) are generally skewed away from the classical activation toward an alternative tumor promoting phenotype and becoming the major constituent of tumor malignancy (3, 4). Thus, presence of TAMs in the tumor microenvironment (TME) is correlated with increased tumor metastasis, angiogenesis, and tumor aggressiveness (5). In recent studies, histological sample of necrotic breast cancers have shown high

tumor-associated macrophage infiltration correlating with unfortunate prognosis (6). Indeed, TAMs can efficiently enter the necrotic core of the breast cancer and still functioning in hypoxic-necrotic areas. In this regard, the ability to label and observe TAMs non-invasively and over the time can tremendously help to understand the temporal and spatial localization of this population in the TME (7).

Recently, the magnetic resonance imaging (MRI) technique has been used to image inflammation and to track immune cells *in vivo* with no need of radiation (8). In particular, perfluorocarbons (PFCs) are emerging as promising contrast agents for MRI cell tracking (9, 10). This is because, fluorine-based contrast agents are found only in traces in biological tissue meaning that the fluorine background is minimal and that the signal from exogenous fluorine is highly specific *in vivo* (10). Amongst PFCs, perfluoro-15-crown-5-ether (PFCE) is one of the most attractive MRI contrast agents because it is FDA approved in a form of emulsion and therefore it is not toxic (11). However, most of PFCs are not miscible with hydrophilic or hydrophobic solvents due to the strong carbon-fluorine covalent bond and strong electron withdrawing effects of fluorine. Thus, PFCs are typically prepared as lipid-based nano-emulsions with low toxicity and longer circulation time (12). However, nano-drops of PFCs show limited stability *in vivo* due to the low affinity amongst the PFCs, the continuous phase and the surfactant (7). In general, the physical structure of nano-emulsion may also restrict the combination with other functional molecules such as drugs, fluorescent tracker or surface ligand for specific targeting. To this purpose, biodegradable organic-based nanocarriers like liposomes, dendrimers, micelles, and polymeric NPs act as protector and provide a good stability of the payload (13). In this context, different strategies can be used for tumor targeting and tumor imaging (14). For instance, “Passively targeted” nanoparticles (NPs) exploit solely the enhanced permeability and retention (EPR) effect and allow to target cancer systemically. However, the circulation of passively targeted NPs is often prevented by main physiological barriers: the extravasation of the tumor vasculature especially for high-EPR tumors that reduces nanocarrier accumulation; the NPs clearance by mononuclear phagocytic system (MPS), sinusoidal cells of the liver and Kupffer cells (15). On the contrary, “actively targeted” nanoparticles can help to overcome such barriers and to deliver greater amount of payload to the desired compartment thanks to the functionalization of the polymeric surface. Amongst nanocarriers, poly-lactic-co-glycolic acid (PLGA) an FDA approved copolymer, is one of the most exploited system in pre-clinical research owed to its biodegradability, biosafety, biocompatibility, versatility in formulation and functionalization and long shelf-life (16, 17).

Herein, we have focused on ^{19}F -based PLGA nanoparticles (NPs) to detect TAMs accumulation in humanized mice bearing breast cancer as tumor model (4T1 cells). To this purpose, PLGA NPs have been designed to encapsulate PFCE contrast agent and preserving its magnetic properties (18, 19). In addition, the polymeric shell of PLGA has been functionalized with polyethylene glycol (PEG) chains that enhance the plasmatic half-life of PLGA NPs and prevents the rapid opsonization

by the mononuclear phagocyte system (MPS) for *in vivo* purposes. To actively target tumor-associated macrophages, the surface of PLGA-PEG nanoparticles has been also decorated with mannosamine ligand that is preferentially recognized and internalized by TAMs overexpressing mannose receptors (CD206) (20). In addition, fluorescein isothiocyanate (FITC) has been linked to the polymeric shell of the PLGA-PEG NPs allowing further *in vitro* and *ex vivo* validations. All in all, intravenously injected mannose- decorated ^{19}F based-PLGA-PEG NPs aim to enhance targeting of recruited tumor-associated macrophages in a humanized mouse model of breast cancer by ^{19}F -MRI.

MATERIALS AND METHODS

Materials

Unless stated, chemicals were purchased from Sigma Aldrich (Stenheim, Germany) and used as received. Poly (D,L-lactide-co-glycolide) (PLGA) copolymer (50/50, Resomer RG502H Mw 24,000-38,000) was purchased from Boehringer Ingelheim (Ingelheim am Rhein, Germany). Perfluoro-15-crown ether (PFCE) was provided by Exfluor Research Corporation (Texas, USA). Agilent Polystyrene calibration kit for GPC characterization was obtained from Agilent Technologies (Santa Clara, U.S.A.). Ultrapure water was produced in the laboratory according to a Milli-Q[®] system (Merck Millipore, Darmstadt, Germany).

Proton Nuclear Magnetic Resonance Spectroscopy (^1H -NMR)

Chemical structures and number-average molecular weight (M_n) of synthesized polymers were characterized by proton nuclear magnetic resonance spectroscopy (^1H NMR, Varian Mercury plus 400, Crawley, UK) using CDCl_3 or D_2O as solvents. Chemical shifts were referred to the solvent peak ($\delta = 7.26$ ppm for CDCl_3 , $\delta = 4.79$ ppm for D_2O).

Gel Permeation Chromatography

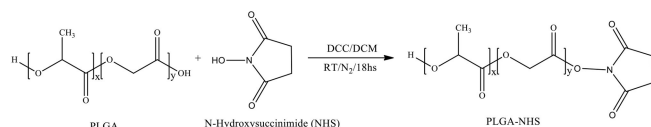
Gel permeation chromatography (GPC) was employed to determine the weight average molecular weight (M_w), number average molecular weight (M_n) and the polydispersity index (PDI) of copolymers. GPC measurements were carried out by using a TSK gel G4000HHR column (Tosoh Bioscience, Tokyo, Japan), 7.8 mm ID \times 30.0 cm L, pore size 5 μm . Polystyrenes of defined molecular weights ranging from 580 to 377,400 Da were used as calibration standards. The eluent was tetrahydrofuran (THF), the elution rate was 1.0 ml/min and the column temperature was 35°C. The samples were dissolved in THF at a concentration of 5 mg/ml.

Fourier Transform Infrared Spectroscopy

Infrared spectra of the synthesized polymer were recorded by a Fourier transform infrared spectrophotometer (FT-IR, PerkinElmer, USA) at the wavelength range of 4,000-500 cm^{-1} . All the spectra were recorded against a background of an air spectrum.

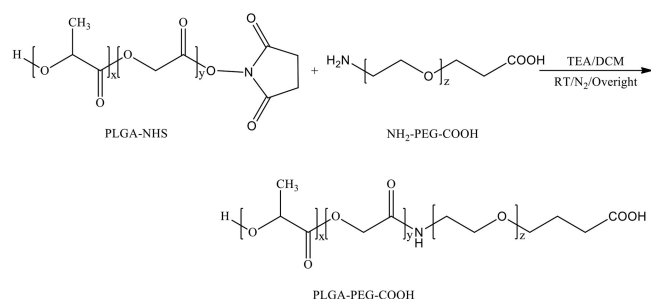
Synthesis and Characterization of Polymers: PLGA-PEG-COOH, PLGA-PEG-FITC, and PLGA-PEG-Mannosamine

Carboxyl terminal groups of PLGA were activated and converted to PLGA-NHS for the subsequent conjugation with polyethylene glycol (PEG). Briefly, 2 g PLGA 503H polymer was dissolved in 10 ml anhydrous dichloromethane (DCM) followed by adding an excess of N-hydroxy succinimide (NHS, 46.0 mg, 0.4 mmol) and N,N'-dicyclohexylcarbodiimide (DCC, 82.5 mg, 0.4 mmol). The reaction was stirred at room temperature overnight, under the N₂ atmosphere. To purify, PLGA-NHS was precipitated in diethyl ether and washed by cold mixture of diethyl ether and methanol three times to remove the residual NHS.

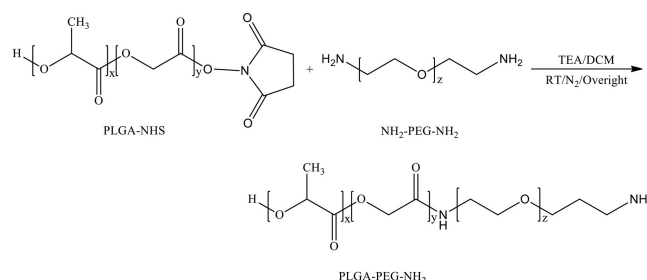


Chemical Synthesis Scheme of PLGA-NHS

PLGA-PEG copolymers with carboxyl terminal groups and amino terminal groups were synthesized by conjugated amino groups of NH₂-PEG-COOH and NH₂-PEG-NH₂ correspondingly to the N-hydroxysuccinimide esters of resulting PLGA-NHS. In details, PLGA-NHS (500 mg, 0.015 mmol) was dissolved in 5 ml anhydrous DCM. Then NH₂-PEG-COOH or NH₂-PEG-NH₂ (44.1 mg, 0.015 mmol) was added in the DCM solution with trimethylamine (TEA, 13.3 μ l, 0.09 mmol) as catalyst. The reaction was processed at room temperature overnight, under N₂ atmosphere. PLGA-PEG copolymer was precipitated with a cold mixture of diethyl ether and methanol and washed three times by the same solvents, then dried by desiccator under vacuum. number-average molecular weight (M_n), the molecular weights (M_w) and the polydispersity index (PDI) were characterized by gel permeation chromatography (GPC, TSK gel G4000HHR column (Tosoh Bioscience, Tokyo, Japan). M_n and chemical structures were determined by proton nuclear magnetic resonance spectroscopy (¹H-NMR, arian Mercury plus 400, Crawley, UK).

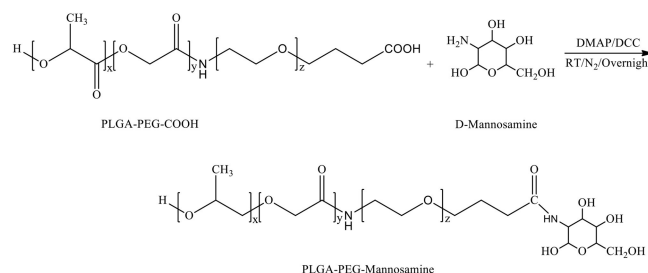


Chemical synthesis scheme of PLGA-PEG-COOH



Chemical Synthesis Scheme of PLGA-PEG-NH₂

D-mannosamine was covalently conjugated to the acid terminal groups of PLGA-PEG-COOH copolymer to yield PLGA-PEG-mannosamine copolymer. Briefly, the synthesized PLGA-PEG-COOH copolymers (200 mg, 0.006 mmol) were dissolved in 2.5 ml D-mannosamine solution in Dimethyl formamide (DMF) at a concentration of 0.025M. Then, 4-dimethylaminopyridine (DMAP, 7.3 mg, 0.06 mmol) and DCC (123.8 mg, 0.6 mmol) were added stepwise. The reaction mixture was stirred at room temperature overnight under nitrogen atmosphere. PLGA-PEG-mannosamine was precipitated in a cold mixture of diethyl ether and methanol, dried by desiccator under vacuum. M_n , M_w , and PDI were characterized by GPC, and chemical structures were determined by ¹H-NMR spectroscopy.



Chemical Synthesis Scheme of PLGA-PEG-Mannosamine

Fluorescein isothiocyanate (FITC) was conjugated to PLGA-PEG-NH₂ to yield fluorescently labeled PLGA-PEG nanoparticles. FITC (4.21 mg, 0.011 mmol) and PLGA-PEG-NH₂ (100 mg, 0.0027 mmol) were dissolved in 2.5 ml anhydrous dimethylsulfoxide (DMSO) at room temperature overnight. To purify, the reaction mixture was dialyzed against DMSO and water sequentially (M_w cutoff = 12-24 kDa), then isolated by lyophilization as a yellow powder. The FITC conjugation was characterized by measurement of fluorescence absorption at an excitation wavelength of 490 nm and an emission wavelength of 530 nm using Spectramax (iD3, Molecular Devices, USA). The FITC conjugation yield was calculated according to Formula 1.

Nanoparticle Formulation

PFCE encapsulated PLGA-PEG NPs were formulated by PFCE/O/W double emulsion solvent evaporation method using PLGA-PEG, PLGA-PEG-mannosamine, or PLGA-PEG-FITC to obtain NPs with different surface ligands (7). PFCE loaded PLGA or PLGA-PEG NPs formulation was described in **Figure 1B**. Briefly, the first emulsion was prepared by dropwise adding PFCE (890 μ l) into 3 ml DCM containing 90 mg polymer along with homogenization (Ultra-Turrax T25, IKA-WERKE, Germany) at 3,000 rpm for 20 min at RT. Subsequently, the first emulsion was dropped into 18 ml of 1% w/v PVA water solution and homogenized (Ultra-Turrax® T25 digital, IKA, Staufen, Germany) in an ice bath at a speed of 13,500 rpm for 20 min. Then the emulsion was gently stirred at RT overnight for solvent evaporation and NPs solidification. NPs were isolated by centrifugation (High speed micro-centrifuge, D3024R, Scilogex, Rocky Hill, CT, USA) at 10,000 g for 30 min at 4°C, and washed three times by water to remove PVA. Afterwards, NPs were lyophilized (Freeze dryer, FreeZone, Labconco, Kansas City, MO, USA) by using 7% w/v sucrose as lyoprotectant and stored at -20°C . Empty NPs were prepared by suspended the first PFCE/O emulsion step, with only the second O/W emulsion evaporation in the same conditions as described.

Size and Zeta Potential

Zeta potential, polydispersity index (PDI) and size of the nanoparticles were characterized by dynamic light scattering (DLS) at fixed at fixed 90° scattering angle at 25°C by Malvern Zetasizer 2000 (Malvern, UK). Suspensions were diluted in distilled water. Measurements were performed in triplicate at room temperature.

Scanning Electron Microscopy

Nanoparticle morphology was determined by a field emission-scanning electron microscope (FE -SEM Zeiss Sigma 300, Zeiss, Germany). SEM sample stage was prepared by placing a double-sided adhesive carbon tape on an aluminum stub. One small drop of 1 mg/ml nanoparticle sample suspended in ultrapure water was placed on the sample stage and then dried at 37°C overnight. Subsequently, the dried sample was sputtered under vacuum with a chromium layer of approximately 100 Å thickness (Quorum Q150T ES, Quorum Technologies, UK) prior to analysis.

Determination of PFCE Encapsulation Efficacy by ^{19}F NMR

PFCE load content and encapsulation efficiency of PLGA-PEG, and PLGA-PEG-MN nanoparticles was determined by Fluorine-19 nuclear magnetic resonance spectroscopy (^{19}F -NMR). Lyophilized nanoparticles were dissolved in CDCl_3 containing 0.1 M trifluoroacetic acid (TFA) as internal standard. The amount of PFCE was calculated by the integration ratio between PFCE peak to TFA peak. Fluorine contents were calculated according to the **Formula 1** and **Formula 2**.

$$\text{PFCE load content} = \frac{\text{PFCE volume loaded in nanoparticles}}{\text{Weight of nanoparticles}} \quad (1)$$

$$\text{PFCE encapsulation efficiency \%} = \frac{\text{PFCE encapsulated volume}}{\text{PFCE total volume}} \times 100\%. \quad (2)$$

Cell Culture

Murine macrophage Raw 264.7 cell line and 4T1 cells (murine mammary carcinoma cells) purchased from (ATCC® TIB-71™) were cultured in complete DMEM medium (Sigma, St. Louis, Mo, USA) supplemented with 10% fetal bovine serum (FBS) and 1% of penicillin and streptomycin and incubated at 37°C with 5% CO_2 . When cell confluence reached around 80%, dead cells were washed away with PBS (Lonza) and live cells were detached by cell scraper. Cells were centrifuged and re-suspended with 8 ml of fresh DMEM medium. Cell counting was performed using BioRad TC20 cell counter.

Cell Cytotoxicity and Uptake Assay of Polarized Macrophages

Cytotoxicity of targeted or untargeted PLGA or PLGA-PEG nanoparticles was tested for Raw 264.7 cells by Pierce LDH assay kit (Thermo Scientific) and following manufacturer's instructions. Cells were treated with nanoparticles at different concentrations ranging from 0 to 2.5 mg/ml and incubated for 24 h. For uptake assay, Raw 264.7 cells were first polarized for anti-tumorigenic (M1) or pro-tumorigenic (M2) phenotypes. M1 phenotype was made by incubating cells for 24 h with lipopolysaccharide (LPS) (100 ng/ml) and Interferon-gamma ($\text{IFN-}\gamma$) (50 ng/ml), both purchased from Sigma-Aldrich. M2 phenotype was made by incubating cells with Interleukin-4 (IL-4, Sigma-Aldrich) (20 ng/ml) for 24 h to obtain M2 highly expressing CD206 receptor. After polarization, cells were seeded in 24-well plates (8×10^4 cells per well) and incubated with targeted or un-targeted PLGA-PEG nanoparticles (1 mg/ml). Incubation was performed for 1, 6, and 24 h at 37°C . After the incubation time, wells were gently washed with PBS to discard particles not up taken and green fluorescence of FITC was measured by selecting excitation wavelength at 490 nm an emission wavelength of 530 nm by Spectramax (iD3 series, Molecular Devices). Raw 264.7 cells not polarized (M0 phenotype) were used as control and all the tests were performed multiple times in triplicate.

Fluorescence Microscopy

Internalization of PLGA nanoparticles targeted (PLGA-FITC-PEG-Mannose loaded with PFCE) or untargeted (PLGA-FITC-PEG loaded with PFCE) nanoparticles was confirmed by confocal microscopy. Raw 264.7 cells were seeded in a six well plate (80,000 cells per well). After cell attachment, cells were treated with targeted or untargeted nanoparticles (1 mg/ml) for 1 h. Wells were then washed three times and lysosomes were stained by deep red LysoTracker™ dye (Thermo Fisher Scientific) incubated for 20 min before cell fixation. Cells were then washed gently with PBS three times and fixated with 4% paraformaldehyde (PFA) for 20 min. After PBS wash, cell membrane was stained by PKH26 red fluorescent cell membrane label kit (Sigma-Aldrich, City, state) and nuclei were stained with Vectashield mounting-DAPI blue

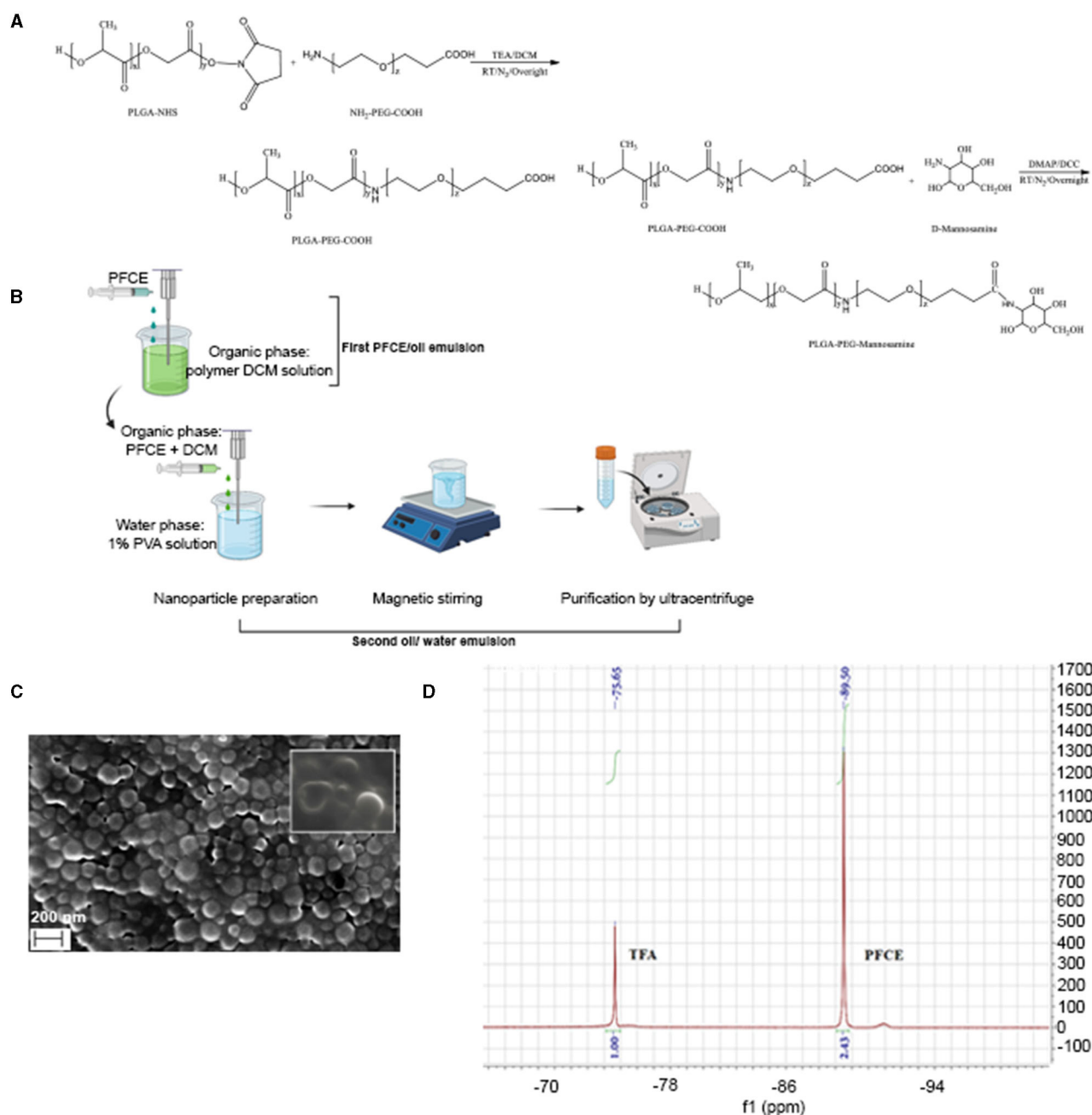


FIGURE 1 | Chemical synthesis and characterization of PLGA-PEG nanoparticles. **(A)** Illustrative chemical synthesis of PLGA-PEG-COOH and PLGA-PEG-mannose copolymers. **(B)** Schematic illustration for PFCE/Oil/Water double-emulsion and solvent-evaporation method used to produce PLGA-PEG, PLGA-PEG-mannosamine, or PLGA-PEG-FITC nanoparticles. Scanning Electron Microscopy (SEM) of PLGA-PFCE nanoparticles. **(C)** Scanning electron microscopy (SEM) image of PFCE encapsulating PLGA NPs. **(D)** ¹⁹F-NMR spectrum of PFCE encapsulated PLGA-PEG-FITC-mannose NPs in CDCl₃ d in ppm: -75.65 (3F, CF₃COOH); -89.50 (20F, C₁₀F₂₀O₆).

fluorescent dye (LSBio). Fluorescent NPs uptaken by Raw 264.7 cells were imaged by Leica SP5 confocal microscope equipped with Ar-He/Ne lasers (Leica Microsystems, Wetzlar, Germany). A 63x magnification with oil immersion objective

(Carl Zeiss, Oberkochen, Germany) was used for cell imaging. Nanoparticles, cell membranes and lysosomes were visualized with respective channels at 488 nm (green), 561 nm (red), and 633 nm (deep-red).

In vitro Fluorine-19 Magnetic Resonance Spectroscopy

Eppendorf tubes loaded with different concentrations of PFCE ranging from 5 to 100 μl were used to create a calibration curve. An MR 901 Discovery 7T magnet (Agilent Technologies, Santa Clara, CA, USA) with a preclinical front-end (GE Healthcare, Little Chalfont, UK) was used for MRS acquisition. The system is equipped with a gradient set with a maximum gradient strength of 300 mT m^{-1} , a rise-time of 600 $\text{T m}^{-1} \text{s}^{-1}$ and an inner diameter of 310 mm. For transmission and reception, an in-house-built dual tuned $^1\text{H}/^{19}\text{F}$ single channel surface coil with a diameter of 2 cm was used. The ^{19}F MRS spectrum was recorded using a EchoSCI sequence (TR/TE = 1,250/15 ms, NEX = 128, FOV = 6 cm, slice thickness = 2.5 cm). MRS processing was performed in SAGE 7.6.2 (GE Healthcare, Little Chalfont, UK) on the MR 901 Discovery system. For processing of the data, time domain signals were apodized with a 10 Hz line broadening function, after which the signal was zero-filled to 4,096 points. Subsequently the time domain signal was Fourier transformed and the resulting spectrum was properly phased to show an absorption mode resonance line. ^{19}F in the sample was quantified by reference to a standard curve, which was obtained by measuring a dilution series of PFCE with known ^{19}F content.

Mouse Model

BALB/c mice (6–8-week years old) were provided access to food and water *ad libitum* and were hosted in the animal facility at the Erasmus MC (Rotterdam, The Netherlands). All experiments were performed according to the guidelines for animal care of the Erasmus MC Animal Experiments Committee. For tumor mouse model, 8×10^4 of LUC2 luciferase-expressing 4T1 breast cancer cells were injected subcutaneously in the left flank of the mice ($n = 4$ mice for each group). This cell line has been chosen because is a late state of breast cancer and exhibits necrosis. Tumor growth was measured by calipers and by bioluminescence imaging by IVIS spectrum imager (model, Perkin Elmer, city, state).

In vivo Fluorine-19 Magnetic Resonance Spectroscopy

^1H and ^{19}F images were acquired 48 h after injection of 1 mg/ml of targeted (PLGA-PEG-FITC-Mannose loaded with PFCE) or untargeted (PLGA-PEG-FITC loaded with PFCE) nanoparticles by 7T MRI system (Bruker Biospin, city, Germany). All the subcutaneous breast tumors have a diameter ranging between ~ 0.6 and $\sim 0.8 \text{ mm}^3$ of diameter. *In vivo* imaging was done using a custom built dual $^1\text{H}/^{19}\text{F}$ coil for *in vivo* imaging. Mice ($n = 4$ for each group) were anesthetized using 1.5% isoflurane (Isoflutek, Laboratorios Karizoo). Body temperature was monitored and regulated during imaging. Reference tube of known ^{19}F concentration ($7.01\text{E} + 19 \text{ }^{19}\text{F}$ for PLGA-PEG-Mannose concentrated 1 mg/ml; and $4.95\text{E} + 19 \text{ }^{19}\text{F}$ for PLGA-PEG nanoparticles) was placed alongside the mouse to optimize quantification of fluorine detected at the tumor site.

Magnetic resonance spectrometry was used to measure the ^{19}F content per cell. The ^{19}F MRS spectrum was recorded using a EchoSCI sequence (TR/TE = 1,250/15 ms, NEX = 128, FOV =

6 cm, slice thickness = 2.5 cm). MRS processing was performed in SAGE 7.6.2 (GE Healthcare, Little Chalfont, UK) on the MR 901 Discovery system. For processing of the data, time domain signals were apodized with a 10 Hz line broadening function, after which the signal was zero-filled to 4,096 points. Subsequently the time domain signal was Fourier transformed and the resulting spectrum was properly phased to show an absorption mode resonance line. ^{19}F in the sample was quantified by reference to a standard curve, which was obtained by measuring a dilution series of PFCE with known ^{19}F content.

Ex vivo Determination of PFCE Encapsulation Efficacy by ^{19}F NMR Spectroscopy

A 400 MHz Bruker Avance II NMR spectrometer (Bruker Biospin, Rheinstetten, Germany) was used to perform ^{19}F NMR with a 5 mm broadband probe, which can operate at 376.5 MHz for *ex vivo* experiments. Excised organs (liver, lungs, and spleens and 4T1 subcutaneous tumors) were harvested and flash frozen by liquid nitrogen. The prepared sample (0.4 ml, mixed with D_2O) was transferred to a 5 mm NMR tube (Wilmad, Vineland, NJ, USA). As a reference compound, 5-fluorocytosine (0.1 ml, 5 mM ^{19}F concentration) was added to determine the chemical shift and ^{19}F concentration for each sample. The pH value of the sample was confirmed to be around 7 when preparing the sample using Bromothymol blue indicator and the temperature was maintained at 37°C during the experiment. The acquisition parameters were as follows: frequency = 376.5 MHz, spectral width = 350 ppm, relaxation delay = 5 s, data points = 64k. After phase and baseline correction of the acquired ^{19}F NMR spectra using the Topspin software (Bruker Biospin, Rheinstetten, Germany), the ^{19}F NMR signals were quantified relative to the 5-fluorocytosine signals (reference) by peak integration. The total ^{19}F content of the excised organs (4T1 tumor, liver, spleen and lungs) was determined and the results were normalized to the tissue weight generating a signal expressed as a number of fluorine atoms per gram of tissue.

Statistical Analysis

The data are presented as mean \pm standard deviation (SD). *In vitro* and *in vivo* tests were performed using Graphpad 7 software and One-way ANOVA and *t*-test analysis of variance were used to analyze the differences between the groups. Significance was attributed when $P < 0.001$ (*) for *in vitro* tests and $P < 0.05$ (*) for *in vivo* tests.

RESULTS

Synthesis and Characterization of Polymers

PLGA-PEG-NH₂, PLGA-PEG-COOH, PLGA-PEG-FITC and PLGA-PEG-mannose copolymers were successfully synthesized with a yield of ~ 60 –85%. The synthesis of PLGA-PEG-mannose copolymer is shown in **Figure 1A**. Details of the polymer characteristics such as number-average molecular weight (M_n), the molecular weights (M_w) and the polydispersity index (PDI)

are provided in **Table 1**. All the resulting copolymers presented PDI approximately of 1.4–1.7 with unimodal and symmetric peak in the GPC. This result confirmed the synthesized copolymer possessed narrow distribution of molecular weight.

The conjugation of mannosamine to PLGA-PEG copolymer was confirmed by comparing $^1\text{H-NMR}$ spectra of PLGA-PEG-mannose to those of PLGA-PEG-COOH (**Supplementary Figure 1A**) and D-mannosamine (**Supplementary Figure 1B**). The peaks at 1.58 and 5.22 ppm were characteristics of methyl groups and methine groups of glycolic acid (GA) segments, while the peak at 4.82 ppm was attributed to methylene group of lactic acid (LA) segments, which were both contributed by PLGA chains (**Supplementary Figure 1C**). The peak observed at 3.64 ppm corresponded to methylene groups of PEG segment. The integration ratio between the characteristic peaks of PEG and PLGA chains reveals that PEG was chemically conjugated on PLGA with mole ratio around 1:1. The peaks of mannosamine overlapped with the peak of PEG (3.62 ppm), therefore only one small peak at 4.11 ppm was detected and attributed to mannosamine (21).

FT-IR analysis was carried out to further confirm the amide bond formed between PLGA and PEG segments, and also the chemical conjugation of mannosamine onto PLGA-PEG-COOH copolymer. FT-IR spectra of PLGA-PEG-COOH and PLGA-PEG-Mannosamine copolymers were displayed in **Supplementary Figure 2**. The absorption peaks at 1,630 and 1,510 cm^{-1} were assigned to the C=O and N-H bonds, respectively, which reveals the successful conjugation via amide

linkage between PLGA and PEG segment of the PLGA-PEG copolymer (22). Compared with the spectrum of PLGA-PEG-COOH copolymer, the one corresponding to PLGA-PEG-mannosamine presents new peaks at 3,264, 2,917, 2,851 cm^{-1} attributed to the stretching vibrations of the O-H and the C-H bonds of methylene and methyne groups, respectively, which were contributed by mannosamine. This result demonstrated that the mannosamine was efficiently conjugated onto the PLGA-PEG-COOH copolymer. The FITC conjugation molar ratio of PLGA-PEG-FITC copolymer was 85% measured by the fluorescence absorption according to standard curve build by pure FITC solution.

Formulation and Characterization of PLGA-PEG Nanoparticles

Formulation of PFCE loaded PLGA-PEG nanoparticles (NPs) is illustrated in **Figure 1B**. NPs showed a mean diameter in the range of ~ 239 and ~ 345 nm depending on nanoparticle formulation. PFCE encapsulated nanoparticles showed a slightly higher diameter of ~ 50 nm compared with the empty ones. All the particles were also monodispersed presenting a low polydispersity index (PDI). Additionally, all the nanoparticles displayed negative zeta potentials due to the existence of terminal carboxyl groups in the PLGA polymer that is in the deprotonated form at physiological pH (23). Indeed, zeta potential values were between -31 and -17 mV (**Table 2**). Mannosamine decorated PLGA-PEG NPs presented a less negative zeta potential compared with the other NPs without

TABLE 1 | Mn, Mw, and PDI of PLGA-PEG and PLGA-PEG-mannose copolymers.

Name	Mw ^a (kDa)	Mn ^a (kDa)	LA:GA ^b	PLGA:PEG ^b	PDI ^a
PLGA-PEG-COOH	14	10	1:1	1:0.93	1.4
PLGA-PEG-mannose	9.2	7.3	1:0.95	1:0.82	1.3
PLGA-PEG-NH ₂	18.7	12.7	1:1	1:0.98	1.5
PLGA-PEG-FITC	–	–	1:1	1:0.92	–

^aDetermined by GPC; ^bDetermined by $^1\text{H-NMR}$.

TABLE 2 | Particle Size, PDI, and Zeta potential of PLGA-PEG nanoparticles.

Nanoparticles	Load	Particle size (nm)	PDI ^[iii]	Zeta potential (mV)
PLGA ^[i] -PEG	–	258 ± 10	0.28 ± 0.01	–22.3 ± 0.6
PLGA ^[i] -PEG	+PFCE ^[ii]	371 ± 8	0.23 ± 0.03	–26.3 ± 0.4
PLGA ^[i] -PEG-FITC	–	299 ± 12	0.36 ± 0.05	–26.8 ± 0.4
PLGA ^[i] -PEG-FITC	+PFCE ^[ii]	345 ± 8	0.20 ± 0.01	–24.2 ± 0.2
PLGA ^[i] -PEG-mannose	–	199 ± 3	0.10 ± 0.03	–12.9 ± 0.6
PLGA ^[i] -PEG-mannose	+PFCE ^[ii]	386 ± 3	0.23 ± 0.00	–17.9 ± 0.1
PLGA ^[i] -PEG-mannose-FITC	–	222 ± 4	0.22 ± 0.09	–24.2 ± 2.0
PLGA ^[i] -PEG-mannose-FITC	+PFCE ^[ii]	318 ± 4	0.10 ± 0.02	–19.6 ± 0.4

^[i] PLGA, poly(lactide-co-glycolide).

^[ii] Perfluoro-15-crown-5-ether.

^[iii] Polydispersity index.

mannosamine due to the partial neutralization of the negative charges by mannosamine.

Nanoparticles (NPs) were observed by scanning electron microscopy (SEM) where images confirmed that the PLGA-PFCE nanoparticles had a relatively uniform diameter of ~ 200 nm with a spherical shape and smooth surface (**Figure 1C**).

In some cases, nanoparticles showed dented appearance supposedly due to the phase separation of PFCE from nanoparticles during the analysis (24). This finding is therefore an indirect effect of the presence of PFCE within nanoparticles.

As depicted in **Figure 1D**, two peaks were highlighted in the spectrum at $\delta = -75.65$ ppm for fluorine atoms of TFA and at $\delta = -89.50$ ppm for fluorine atoms of PFCE. The amount of PFCE encapsulated was calculated from the integration ratio between PFCE peak and TFA peak. PLGA-PEG and PLGA-PEG-mannose nanoparticles had a comparable fluorine encapsulation efficiency: 65.2% for PLGA-PEG, 67.1% for PLGA-PEG-mannose, and similar load content (6.45 $\mu\text{l}/\text{mg}$ for PLGA-PEG and 6.64 $\mu\text{l}/\text{mg}$ for PLGA-PEG-mannose). Quantification and encapsulation efficiency are outlined in **Table 3**.

Cell Cytotoxicity and NPs Uptake Assay of Polarized Macrophages

Initial studies were performed to assess cell viability when M2-like Raw264.7 macrophages were treated with targeted or untargeted PLGA nanoparticles. Cytotoxicity assay was performed incubating macrophages with different concentration of nanoparticles ranged between 0 and 2.5 mg/ml and incubated for 24 h at 37°C. Around 100% of cells were not affected by the treatment and all type of nanoparticles were well-tolerated (**Figure 2A**).

To test if fluorescent targeted or untargeted nanoparticles were preferentially up-taken by macrophages with M2-like phenotype, we first polarized Raw264.7 macrophages into M1-like macrophages, M2-like macrophages, and unpolarized macrophages (M0-like phenotype). Later, cells were incubated with targeted and untargeted PEGylation or not, FITC-PLGA nanoparticles (1 mg/ml) for 6 h. **Figure 2B** shows that targeted and PEGylated PLGA nanoparticles were preferentially up-taken by M2-like polarized macrophages. Particularly for the M0-like phenotype, not significant differences were highlighted by the uptake of the different nanoparticles. For the M1-like phenotype group, targeted-PEG-PLGA NPs particles had greater uptake (~ 1.20 -fold) than un-PEGylated-mannose NPs and also higher uptake than untargeted PEGylated particles (~ 1.7 -fold). For M2-like phenotype group, targeted-PEG-PLGA NPs have roughly a 2.5-fold higher uptake compared to untargeted-pegylated

nanoparticles and \sim eight-fold higher than un-PEGylated-mannose NPs. Statistical analysis was performed with one-way ANOVA, for triplicate samples and significance attributed when $P < 0.001$. Taken together, PLGA-PEG-mannose nanoparticles resulted in the highest uptake by M2-like macrophages compared to M0-like and M1-like macrophages, suggesting that both PEGylation and mannose ligand stimulate the cellular uptake.

To confirm cellular internalization of NPs, M0, M1 and M2-like Raw 264.7 macrophages were treated with targeted and untargeted nanoparticles conjugated or not with PEG (1 mg/ml). Confocal images of labeled polarized macrophages are shown in **Figure 2C**, where PLGA-PEG nanoparticles conjugated with FITC were stained in green, cell membrane in magenta, and lysosomes in red.

In vivo Fluorine-19 Nuclear Magnetic Resonance

In order to calculate the amount of ^{19}F encapsulated in targeted and untargeted PLGA-PEG NPs, a curve of reference was built using different dilutions of pure ^{19}F ranged between 5 and 100 μl (**Figure 3A**). *In vitro* quantification of ^{19}F spins encapsulated in 1 mg/ml of targeted and untargeted PLGA-PEG NPs revealed an adequate number of ^{19}F -atoms for further *in vivo* evaluations. In particular $7.01\text{E} + 19$ ^{19}F were detected for PLGA-PEG nanoparticles and $4.95\text{E} + 19$ ^{19}F were detected for PLGA-PEG-mannose nanoparticles.

4T1-breast xenograft mice ($n = 4$ per group) received 1 mg/ml of targeted or untargeted-PLGA-PEG nanoparticles intravenously (200 μl of suspension in PBS). ^{19}F signals from the tumor site were quantified 48 h after NPs injection by MRS. A spectrum of ^{19}F signal was successfully measured from the tumor area of mice injected with targeted PLGA nanoparticle by 7T MRI as shown in **Figure 3B** (top). As for untargeted-PLGA-PEG nanoparticles, the signal-to-noise ratio measured from the tumor site was low and fluorine quantification was not possible. This suggests that the targeted-PLGA-PEG nanoparticles have a more efficient accumulation at the tumor site compared to the untargeted-PLGA-PEG nanoparticles. Notably, preliminary data from *ex vivo* ^{19}F NMR suggests that ^{19}F signal detected in the tumors after treatment with targeted-PLGA-PEG NPs was four-fold greater compared to untargeted-PLGA-PEG NPs (**Supplementary Figure 3**).

DISCUSSION

In this study, we have assessed PLGA-PEG NPs decorated with mannose ligand for TAMs detection by ^{19}F -MRI. This approach

TABLE 3 | PFCE load content and PFCE encapsulation efficiency PLGA-PEG nanoparticles characterized by *in vitro* ^{19}F -NMR.

	Name	Number of F-atoms	Load content ($\mu\text{l}/\text{mg}$)	Encapsulation efficiency (%)
^{19}F -NMR ⁽¹⁾	PLGA-PEG-FITC- PFCE-	3.14 E + 20	6.45	65.2
	PLGA-PEG-mannose -FITC-PFCE	2.82 E + 20	6.64	67.1

⁽¹⁾Values are calculated for 1 mg of NPs dissolved in CDCl_3 solvent before the analysis at ^{19}F -NMR.

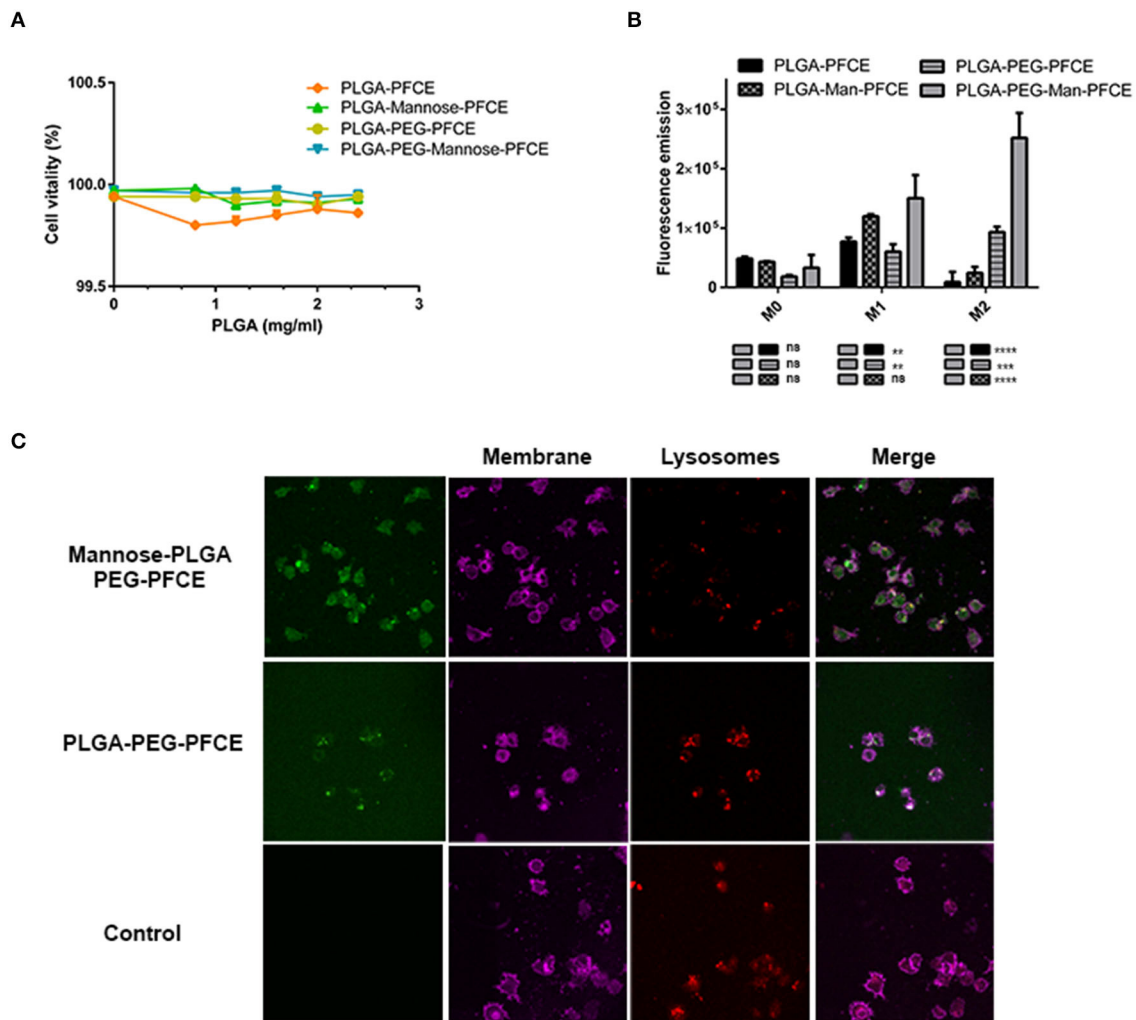


FIGURE 2 | Characterization of nanoparticles *in vitro*. **(A)** Cytotoxicity tests for Raw264.7 macrophage cells treated for 24 h with PLGA-PFCE, PLGA-PFCE-Mannose, PLGA-PEG-PFCE, and PLGA-PEG-mannose-PFCE nanoparticles (final concentration 1 mg/ml). **(B)** Uptake efficiency of Raw264.7 macrophage cells polarized in M0 (negative control), M1 (pro-inflammatory), M2 (anti-inflammatory) phenotype and treated for 1 h with PLGA-PFCE, PLGA-PFCE-mannose, PLGA-PEG-PFCE and PLGA-PEG-mannose-PFCE nanoparticles (final concentration 1 mg/ml). **(C)** Confocal images of polarized M2-polarized Raw264.7 macrophages treated for 1 h with mannose (top) and untargeted (middle) PLGA-PEG NPs. Negative control for PLGA-PEG nanoparticles is shown in the bottom panels. Nanoparticles are shown in green color (FITC labeled); cell membrane is shown in magenta color; lysosomes are shown in deep-red color.

has exploited the use of different types of PLGA nanoparticles that are not toxic, stable and by definition more resistant to mechanical stress. In addition, polymeric nanoparticles of PLGA offer the advantage to be further functionalized with target ligands. PEGylation and mannosylation show an influence in circulation and cellular uptake of nanoparticles. Actually, first of all, PEGylation of PLGA nanoparticles protects them from complement activation (i.e., opsonization) with longer circulation in the blood stream, with the consequence of an improved opportunity for the drug to be released to the target site.

Secondly, mannosylation can act as cellular membrane-docking ligand allowing for nanoparticle internalization in mannose-expressing macrophages especially the M2 macrophages due to overexpression of mannose receptor.

Thus, mannose can be used for intracellular delivery of relevant payloads (20, 25, 26).

Here, we decided to encapsulate the PFCE perfluorocarbon as contrast agent for ^{19}F -MRI. PLGA nanoparticles used as carrier ensure PFCE stability for long storage, allowing for lyophilize, solubilize in suspensions and freeze the particles. In our study, we could produce PLGA nanoparticles of narrow size the distribution and a size approximately between 330 and 390 nm irrespective to the nanoparticle formulation (**Table 2**). SEM images for PLGA-PFCE NPs confirmed rounded and smoothed surface of nanoparticles. However, PLGA-PEG NPs did not provide resolved photos due to the interference of PVA surfactant with the analysis. Thus, images of NPs obtained by TEM would provide more accurate analysis for size and shape of PLGA-PEG NPs. NPs showed minimal toxicity *in vitro* when

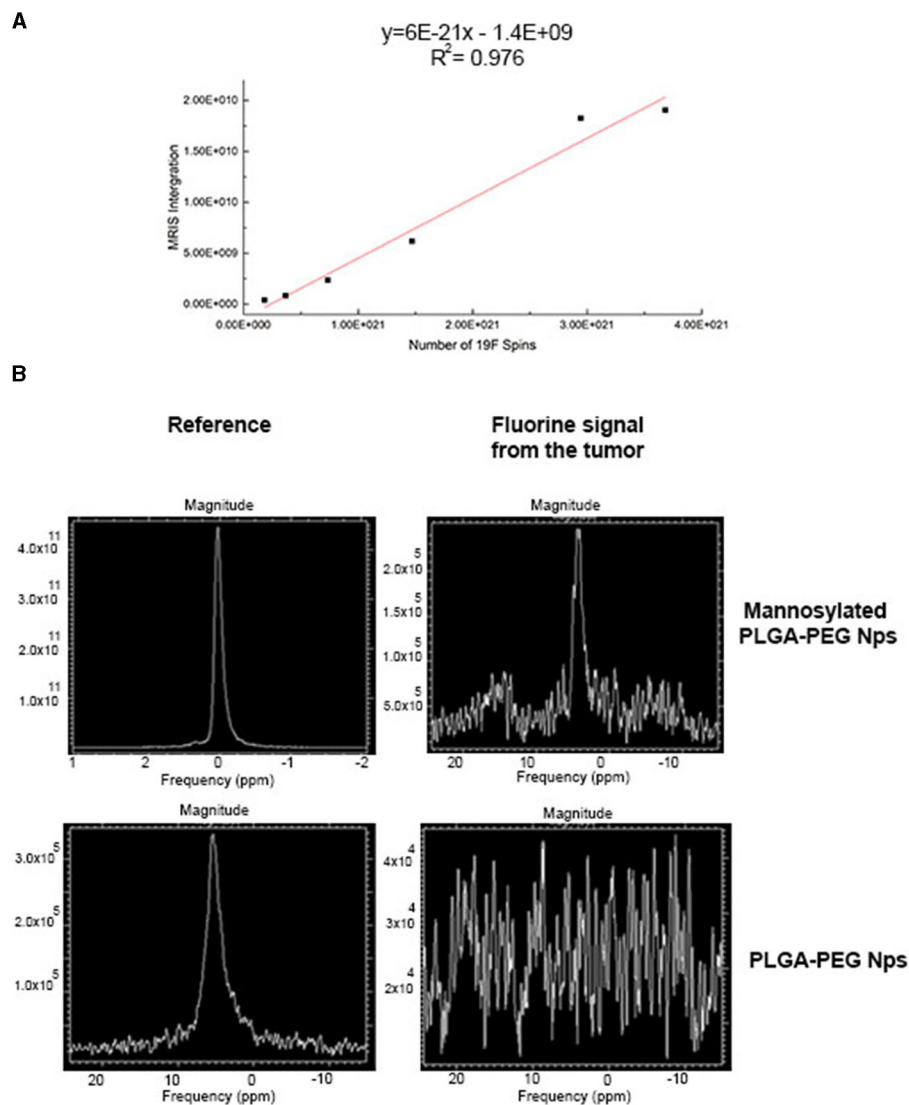


FIGURE 3 | PFCE magnetic resonance measurement by ^{19}F -MRI spectroscopy (MRS). **(A)** Standard curve of pure PFCE contrast agents measured at different dilution volumes ranging from 5 and 100 μl . **(B)** ^{19}F -MRI spectrum of PFCE detected from 4T1 tumor-bearing mice and treated with PLGA-PEG-mannose nanoparticles (top graph) and with PLGA-PEG nanoparticles (bottom graph). Respective external reference tubes (left) were used to set up image acquisition methods and for PFCE measurements at the tumor site.

incubated with macrophages also for higher concentration like 2.5 mg (**Figure 1A**). However, it has been shown that vitality of cells is not affected if treated with 20 mg/million cells of PLGA nanoparticles (27). The ^{19}F -payload of particles is similar amongst the different groups as demonstrated by ^{19}F -MRS and ^{19}F -NMR analyses. All the PFCE-nanoparticles were also able to target TAMs and be internalized by them especially if they were PEGylated and mannosylated (**Figures 2B,C**).

Finally, PFCE used for *in vivo* studies is known to be non-toxic in biological systems. Finally, PFCE used for *in vivo* studies is known to be non-toxic in biological systems. However, ^{19}F -based cell tracking suffers from detection sensitivity and in general thousands of cells per voxel are required for detection of labeled cells (28). When injection of targeted-PEG-PLGA

nanoparticles, fluorine signals were detected 48 h after injections. We observed higher liver retention of nanoparticles *in vivo* most probably due to the continuous uptake by liver like Kupffer cells, liver sinusoidal endothelial cells (LSECs), and hepatic stellate cells (HSCs) (29). This might be overcome by treating mice with clodronate liposomes before NPs injection and blocking non-specific uptake by Kupffer macrophages in the liver and increasing ^{19}F -signal due to the greater retention of targeted-PLGA NPs in the tumor site (30). Recently, it has also been demonstrated that an antifouling-polymer coatings may block non-specific uptake of nanoparticles by liver (31). For untargeted PLGA-nanoparticles, the ^{19}F signals in the tumor did not exceed the background noise arising from the surrounding organs. For targeted PLGA-nanoparticles in the

tumor site, the ^{19}F signals in the tumor had a weak intensity when measured by MRI *in vivo*, but the concentration of the PFCE could be successfully quantified by ^{19}F MRS. Furthermore, *ex vivo* ^{19}F NMR data confirmed higher retention of ^{19}F signals at the tumor site after injection of targeted-PLGA-PEG NPs compared to injected untargeted-PLGA-PEG NPs (**Supplementary Figure 3**). We believe that higher magnetic field strengths or more sophisticated detectors might compensate with the sensitivity of the detection allowing to measure fewer amount of fluorine in the tumor. Altogether the results presented in the study prove the efficacy of delivering PLGA-PEG-mannose nanoparticles by TAMs reaching the tumor site *in vivo*. Future studies will focus on accumulation of functionalized PEGylated-nanoparticles delivered by TAMs as a function of tumor growth stage and as a function of the trafficking and timing of TAMs *in vivo*.

DATA AVAILABILITY STATEMENT

The original contributions presented in the study are included in the article/**Supplementary Material**, further inquiries can be directed to the corresponding author/s.

ETHICS STATEMENT

The animal study was reviewed and approved by Erasmus MC Animal Experiments Committee (Animal work protocol number 17-867-53).

REFERENCES

- Noy R, Pollard JW. Tumor-associated macrophages: from mechanisms to therapy. *Immunity*. (2014) 41:49–61. doi: 10.1016/j.immuni.2014.06.010
- Yang M, McKay D, Pollard JW, Lewis CE. Diverse functions of macrophages in different tumor microenvironments. *Cancer Res*. (2018) 78:5492–503. doi: 10.1158/0008-5472.CAN-18-1367
- Mantovani A, Marchesi F, Malesci A, Laghi L, Allavena P. Tumour-associated macrophages as treatment targets in oncology. *Nat Rev Clin Oncol*. (2017) 14:399–416. doi: 10.1038/nrclinonc.2016.217
- Choi J, Gyamfi J, Jang H, Koo JS. The role of tumor-associated macrophage in breast cancer biology. *Histol Histopathol*. (2018) 33:133–45. doi: 10.14670/HH-11-916
- Yang L, Zhang Y. Tumor-associated macrophages: from basic research to clinical application. *J Hematol Oncol*. (2017) 10:58. doi: 10.1186/s13045-017-0430-2
- Yang M, Li Z, Ren M, Li S, Zhang L, Zhang X, et al. Stromal Infiltration of Tumor-Associated Macrophages Conferring Poor Prognosis of Patients with Basal-Like Breast Carcinoma. *J Cancer*. (2018) 9:2308–16. doi: 10.7150/jca.25155
- Srinivas M, Boehm-Sturm P, Figdor CG, de Vries IJ, Hoehn M. Labeling cells for *in vivo* tracking using ^{19}F MRI. *Biomaterials*. (2012) 33:8830–40. doi: 10.1016/j.biomaterials.2012.08.048
- Ahrens ET, Bulte JWM. Tracking immune cells in vivo using magnetic resonance imaging. *Nat Rev Immunol*. (2013) 13:755–63. doi: 10.1038/nri3531
- Temme S, Bönner F, Schrader J, Flögel U. ^{19}F magnetic resonance imaging of endogenous macrophages in inflammation. *Wiley Interdiscip Rev Nanomed Nanobiotechnol*. (2012) 4:329–43. doi: 10.1002/wnan.1163
- Srinivas M, Heerschap A, Ahrens ET, Figdor CG, de Vries IJM. (^{19}F) MRI for quantitative *in vivo* cell tracking. *Trends Biotechnol*. (2010) 28:363–70. doi: 10.1016/j.tibtech.2010.04.002
- Ahrens ET, Zhong J. *In vivo* MRI cell tracking using perfluorocarbon probes and fluorine-19 detection. *NMR Biomed*. (2013) 26:860–71. doi: 10.1002/nbm.2948
- Rho J, Stares E, Adams SR, Lister D, Keach B, Ahrens ET. Paramagnetic fluorinated nanoemulsions for *in vivo* F-19 MRI. *Mol Imaging Biol*. (2020) 22:665–74. doi: 10.1007/s11307-019-01415-5
- Diou O, Tsapis N, Giraudeau C, Valette J, Gueutin C, Bourasset F, et al. Long-circulating perfluorooctyl bromide nanocapsules for tumor imaging by ^{19}F MRI. *Biomaterials*. (2012) 33:5593–602. doi: 10.1016/j.biomaterials.2012.04.037
- Schleich N, Po C, Jacobs D, Ucakar B, Gallez B, Danhier F, et al. Comparison of active, passive and magnetic targeting to tumors of multifunctional paclitaxel/SPIO-loaded nanoparticles for tumor imaging and therapy. *J Control Release*. (2014) 194:82–91. doi: 10.1016/j.jconrel.2014.07.059
- Blanco E, Shen H, Ferrari M. Principles of nanoparticle design for overcoming biological barriers to drug delivery. *Nat Biotechnol*. (2015) 33:941–51. doi: 10.1038/nbt.3330
- Mir M, Ahmed N, Rehman AU. Recent applications of PLGA based nanostructures in drug delivery. *Colloids Surf B Biointerfaces*. (2017) 159:217–31. doi: 10.1016/j.colsurfb.2017.07.038
- Attia ME, Anton N, Wallyn J, Omran Z, Vandamme TF. An overview of active and passive targeting strategies to improve the nanocarriers efficiency to tumour sites. *J Pharm Pharmacol*. (2019) 71:1185–98. doi: 10.1111/jphp.13098
- Zhou Y, Que K-T, Tang H-M, Zhang P, Fu Q-M, Liu Z-J, et al. Anti-CD206 antibody-conjugated Fe₃O₄-based PLGA nanoparticles selectively promote tumor-associated macrophages to polarize to the pro-inflammatory subtype. *Oncol Lett*. (2020) 20:298. doi: 10.3892/ol.2020.12161

AUTHOR CONTRIBUTIONS

GZ, SD, LM, and PD designed the experiments. GZ, SD, and UH performed the experiments and analysed the data. GZ, SD, and LM wrote the manuscript. JH provided expertise on MRI measurements. GZ, SD, NG, RC, PD, CL, UH, and LM critically revised the manuscript for important intellectual content. All authors have read and agreed to the published version of the manuscript.

FUNDING

This work was supported by the Applied Molecular Imaging facility of Erasmus MC (AMIE) and by the Nanomedicine Innovation Center Erasmus (NICE) of Erasmus MC of Rotterdam (The Netherlands). We acknowledge the funding for this work provided by the European Commission under the H2020 MSCA-RISE award grant number 777682 (CANCER) and under the H2020-MSCA-ITN award, grant number 675743 (ISPIC).

SUPPLEMENTARY MATERIAL

The Supplementary Material for this article can be found online at: <https://www.frontiersin.org/articles/10.3389/fmed.2021.712367/full#supplementary-material>

19. Anani T, Rahmati S, Sultana N, David AE. MRI-traceable theranostic nanoparticles for targeted cancer treatment. *Theranostics*. (2021) 11:579–601. doi: 10.7150/thno.48811
20. Scodeller P, Simón-Gracia L, Kopanchuk S, Tobi A, Kilk K, Säälik P, et al. Precision targeting of tumor macrophages with a CD206 binding peptide. *Sci Rep*. (2017) 7:14655. doi: 10.1038/s41598-017-14709-x
21. Alonso-Sande M, des Rieux A, Fievez V, Sarmiento B, Delgado A, Evora C, et al. Development of PLGA-mannosamine nanoparticles as oral protein carriers. *Biomacromolecules*. (2013) 14:4046–52. doi: 10.1021/bm401141u
22. Boddu SH, Vaishya R, Jwala J, Vadlapudi A, Pal D, Mitra A. Preparation and characterization of folate conjugated nanoparticles of doxorubicin using PLGA-PEG-FOL polymer. *Med Chem*. (2011) 2:068–075. doi: 10.4172/2161-0444.1000117
23. Govender T, Stolnik S, Garnett MC, Illum L, Davis SS. PLGA nanoparticles prepared by nanoprecipitation: drug loading and release studies of a water soluble drug. *J Control Release*. (1999) 57:171–85. doi: 10.1016/S0168-3659(98)00116-3
24. Srinivas M, Tel J, Schreibelt F, Cruz L-J, Amiri H, Heerschap A, et al. PLGA-encapsulated perfluorocarbon nanoparticles for simultaneous visualization of distinct cell populations by (2015) 19F MRI. *Nanomedicine (Lond)*. 10:2339–48. doi: 10.2217/nnm.15.76
25. Yang R, Xu J, Xu L, Sun X, Chen Q, Zhao Y, et al. Cancer cell membrane-coated adjuvant nanoparticles with mannose modification for effective anticancer vaccination. *ACS Nano*. (2018) 12:5121–9. doi: 10.1021/acsnano.7b09041
26. Li Y, Wu H, Ji B, Qian W-P, Xia S, Wang L, et al. Targeted imaging of CD206 expressing tumor-associated M2-like macrophages using mannose-conjugated antibiofouling magnetic iron oxide nanoparticles. *ACS Appl Bio Mater*. (2020) 3:4335–47. doi: 10.1021/acsbm.0c00368
27. Swider E, Koshkina O, Tel J, Cruz LJ, de Vries JM, Srinivas M. Customizing poly(lactic-co-glycolic acid) particles for biomedical applications. *Acta Biomater*. (2018) 73:38–51. doi: 10.1016/j.actbio.2018.04.006
28. Makela A. V, Gaudet JM, and Foster PJ. Quantifying tumor associated macrophages in breast cancer: a comparison of iron and fluorine-based MRI cell tracking. *Sci Rep*. (2017) 7:42109. doi: 10.1038/srep42109
29. Park J-K, Utsumi T, Seo Y-E, Deng Y, Satoh A, Saltzman WM, et al. Cellular distribution of injected PLGA-nanoparticles in the liver. *Nanomedicine*. (2016) 12:1365–74. doi: 10.1016/j.nano.2016.01.013
30. Schiedner G, Hertel S, Johnston M, Dries V, van Rooijen N, Kochanek S. Selective depletion or blockade of Kupffer cells leads to enhanced and prolonged hepatic transgene expression using high-capacity adenoviral vectors. *Mol Ther*. (2003) 7:35–43. doi: 10.1016/S1525-0016(02)00017-5
31. Nabil G, Bhise K, Sau S, Atef M, El-Banna HA, Iyer Ak. Nano-engineered delivery systems for cancer imaging and therapy: Recent advances, future direction and patent evaluation. *Drug Discov Today*. (2019) 24:462–91. doi: 10.1016/j.drudis.2018.08.009

Conflict of Interest: GZ was employed by Medres Medical Research GmbH (Cologne, Germany). NG is employed by Percuros B.V. (Enschede, The Netherlands).

The remaining authors declare that the research was conducted in the absence of any commercial or financial relationships that could be construed as a potential conflict of interest.

Publisher's Note: All claims expressed in this article are solely those of the authors and do not necessarily represent those of their affiliated organizations, or those of the publisher, the editors and the reviewers. Any product that may be evaluated in this article, or claim that may be made by its manufacturer, is not guaranteed or endorsed by the publisher.

Copyright © 2021 Zambito, Deng, Haack, Gaspar, Himmelreich, Censi, Löwik, Di Martino and Mezzanotte. This is an open-access article distributed under the terms of the Creative Commons Attribution License (CC BY). The use, distribution or reproduction in other forums is permitted, provided the original author(s) and the copyright owner(s) are credited and that the original publication in this journal is cited, in accordance with accepted academic practice. No use, distribution or reproduction is permitted which does not comply with these terms.



A Systems-Level Analysis of Total-Body PET Data Reveals Complex Skeletal Metabolism Networks *in vivo*

Karla J. Suchacki¹, Carlos J. Alcaide-Corral^{1,2}, Samah Nimale¹, Mark G. Macaskill^{1,2}, Roland H. Stimson¹, Colin Farquharson³, Tom C. Freeman³ and Adriana A. S. Tavares^{1,2*}

¹ University/British Heart Foundation (BHF) Centre for Cardiovascular Science, The Queen's Medical Research Institute, University of Edinburgh, Edinburgh, United Kingdom, ² Edinburgh Imaging, University of Edinburgh, Edinburgh, United Kingdom, ³ The Roslin Institute, The Royal (Dick) School of Veterinary Studies (RDSVS), Easter Bush Campus, University of Edinburgh, Edinburgh, United Kingdom

OPEN ACCESS

Edited by:

Manoj Kumar,
National Institute of Mental Health and
Neurosciences (NIMHANS), India

Reviewed by:

Sridhar Goud,
National Institutes of Health (NIH),
United States
Chandana Nagaraj,
National Institute of Mental Health and
Neurosciences (NIMHANS), India

*Correspondence:

Adriana A. S. Tavares
adriana.tavares@ed.ac.uk

Specialty section:

This article was submitted to
Translational Medicine,
a section of the journal
Frontiers in Medicine

Received: 13 July 2021

Accepted: 23 August 2021

Published: 20 September 2021

Citation:

Suchacki KJ, Alcaide-Corral CJ,
Nimale S, Macaskill MG, Stimson RH,
Farquharson C, Freeman TC and
Tavares AAS (2021) A Systems-Level
Analysis of Total-Body PET Data
Reveals Complex Skeletal Metabolism
Networks *in vivo*.
Front. Med. 8:740615.
doi: 10.3389/fmed.2021.740615

Bone is now regarded to be a key regulator of a number of metabolic processes, in addition to the regulation of mineral metabolism. However, our understanding of complex bone metabolic interactions at a systems level remains rudimentary. *in vitro* molecular biology and bioinformatics approaches have frequently been used to understand the mechanistic changes underlying disease at the cell level, however, these approaches lack the capability to interrogate dynamic multi-bone metabolic interactions *in vivo*. Here we present a novel and integrative approach to understand complex bone metabolic interactions *in vivo* using total-body positron emission tomography (PET) network analysis of murine ¹⁸F-FDG scans, as a biomarker of glucose metabolism in bones. In this report we show that different bones within the skeleton have a unique glucose metabolism and form a complex metabolic network, which could not be identified using single tissue simplistic PET standard uptake values analysis. The application of our approach could reveal new physiological and pathological tissue interactions beyond skeletal metabolism, due to PET radiotracers diversity and the advent of clinical total-body PET systems.

Keywords: bone, positron emission tomography, metabolism, system biology, network analysis

INTRODUCTION

The availability of large *in vitro* cell and tissue omic datasets and bioinformatic tools have equipped researchers to understand molecular processes that cause disease, and identify and develop new therapeutics (1). However, novel systems approaches are needed to understand complex *in vivo* physiological and pathological interactions at multi-tissue level. Positron emission tomography (PET) imaging allows for the non-invasive *in vivo* investigation of signalling pathways owing to the radiotracer principle and total-body dynamic PET lends itself to deciphering complex biological processes and interactions (2–6), such as those found associated with the skeletal system. Here we present an integrative approach to understand complex tissue interactions *in vivo* using total-body PET network analysis that is directly applicable to emerging clinical total-body dynamic imaging. We initially focused on the skeletal system as it provides an ideal model for analysing complex interactions. The skeleton serves multiple functions *in vivo* such as organ protection, allowing for

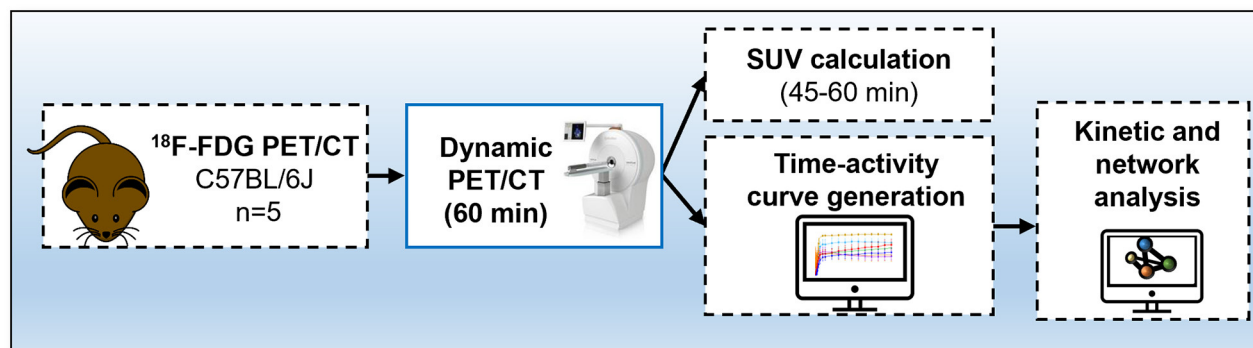


FIGURE 1 | Protocol for ^{18}F -fluorodeoxyglucose (FDG) PET/CT. Mice received an intravenous bolus injection *via* tail-vein of ^{18}F -FDG and immediately underwent a 60-min total-body emission scan. A CT scan was conducted at the end of each PET scan. Time activity-curves and standard uptake values were calculated and network analysis was performed to visualise interactions between bones using the Pearson correlation values.

weight-bearing motion, providing a niche for haematopoiesis and has recently emerged to have major endocrine functions, for example by the bone-specific protein, osteocalcin (7–10). Bone and cartilage are significant sites of glucose uptake in mice and humans (9, 11, 12). However, it remains unclear if different bones within the skeleton have specialised roles in glucose metabolism. Here, we aim to explore whether glucose metabolism in different bones are associated with one another *in vivo* using ^{18}F -fluorodeoxyglucose (^{18}F -FDG) dynamic total-body PET.

METHODS

Animals and Study Design

Studies were done in compliance with all relevant ethical regulations under project licences granted by the UK Home Office, and were approved by the University of Edinburgh Animal Welfare and Ethical Review Board. Male 13-week-old C57BL/6JCr1 ($n = 5$) mice were housed at 22–23°C on a 12h light/dark cycle with free access to water and food. Animals were fasted for 4h prior to start of dynamic PET/CT acquisition. The experimental design is outlined in Figure 1.

Imaging Data Acquisition and Reconstruction

Prior to PET/CT imaging, mice were weighed, anaesthetised with a pre-set with a mixture of 0.5/0.5 L/min of oxygen/nitrous oxide and 3% isoflurane and transferred to the microPET/CT scanner (nanoPET/CT, Mediso, Hungary). General anaesthesia was maintained throughout the duration of the PET/CT study (0.5/0.5 L/min of oxygen/nitrous oxide and 2% isoflurane), and vital signs, including temperature and respiration rate, were monitored during the experiments. Animals received a tail vein intravenous bolus injection of ^{18}F -fluorodeoxyglucose (^{18}F -FDG, 15.08 ± 5.87 MBq, mean \pm SD; Group 2). ^{18}F -FDG was produced in-house (Edinburgh Imaging) using standard methods of radiolabelling (13).

Immediately following radiotracer administration, animals underwent a total-body emission scan followed by a CT scan (semi-circular full trajectory, maximum field of view, 360 projections, 50 kVp, 300 ms and 1:4 binning). Collected PET images underwent attenuation correction using the CT data. PET images were reconstructed between 0 and 60 min into 6 x 30, 3 x 60, 2 x 120, and 10 x 300 s frames using Mediso's iterative Tetra-tomo 3D reconstruction algorithm and the following settings: four iterations, six subsets, full detector model, low regularisation, spike filter on, voxel size 0.4 mm and 400–600 keV energy window. PET data were corrected for random coincidences, scatter, and attenuation.

Image Processing and Standard Uptake Value Calculation

Reconstructed images were analysed using PMOD 3.7 software (PMOD Technologies, Switzerland). Volumes of interest (VOI) were drawn around the tibiae, femurs, humeria, radius and ulnas (forearm), spine, sternum and skull. To distinguish bone tissue from bone marrow and surrounding tissues, the VOIs were segmented using previously defined Hounsfield Units, HU, (332–50000) generated using HU obtained from the acquisition of a CT tissue equivalent material (TEM) phantom (CIRS, model 091) and mouse CT scans, as we have previously reported (9). All dynamic PET data were then corrected for time delays between start of the scan and injection of radiotracer. Time activity-curves were generated and standard uptake values (SUVs) were calculated by normalising radioactive concentration in VOI for the injected dose and the animal weight. To estimate the bone uptake at equilibrium, SUV averages were taken from three PET frames between 45 and 60 min post-radiotracer administration. The CT HU were extracted from the VOI of the tibiae, femurs, humeria, forearm spine, sternum, and skull.

Network Analysis of Total-Body PET Data

Non-decay corrected dynamic total-body PET data was summarised into a table with rows representing average ^{18}F -FDG signal from individual bones for all mice and columns the

time of the recording. The file was saved as a comma separated variable (.csv) file. This was loaded in the network analysis tool Graphia (<https://graphia.app/>) (14). Pearson correlations were calculated and a relationship matrix graph was constructed by performing an all versus all comparison of the ^{18}F -FDG signal profiles from each bone (correlation cut off value of $R > 0.7$ and k-nearest neighbours, kNN, of 3). By minimising the number of edges the structure of the relationship between tissue-accumulation profiles are revealed, as reflected by graph's structure and edge weights, where the nodes represent each bone and edges represent correlations above the selected threshold, where the threshold value was set to maintain the number of nodes in the network hence all available data.

Statistical Analysis, Data Presentation, and Reproducibility

^{18}F -FDG SUV averages were analysed for normal distribution using the Shapiro-Wilk normality test. Simple multiple linear regression was conducted to assess CT and SUV correlations. Data are represented as the average \pm SEM, unless otherwise stated in the results section. All statistical analysis was performed using Prism 8 (GraphPad v8, USA). Mouse cartoon networks were created with BioRender.com.

RESULTS

Murine Bone Density to Energy Metabolism Quotient Diversity Identified by Whole-Body PET/CT Analysis

^{18}F -FDG PET imaging has been extensively used for quantification of glucose metabolism *in vivo*. Using whole-body ^{18}F -FDG PET/CT data (Figure 2A) we extracted the standardised uptake values (SUV) and Hounsfield Units (HU) from the appendicular [tibia, femur, humerus, ulna, and radius (forearm)] and the axial (spine, sternum, and skull) skeleton (Figures 2B–E).

Our PET results showed that overall ^{18}F -FDG uptake in the skeleton was bone specific and un-related to bone density measured by quantitative computed tomography (qCT). Measured SUVs in the axial skeleton were higher than in the appendicular skeleton while measured HU from qCT showed higher mineral density in the appendicular skeleton than in the axial skeleton. These findings were congruent throughout the analysis at individual subject-level (heat maps, Figure 2B), group averages statistical analysis (Box-and-whisker plots, Figures 2C,D) and relative fraction analysis (pie-charts, Figure 2E).

Murine Bone Energy Metabolism Network Identified by Dynamic Total-Body PET/CT Analysis Shows Spine Density Has Strongest Dependence on Glucose Metabolism

Having identified murine bone density to energy metabolism quotient diversity (Figure 2), we tested if individual bones' distinct metabolism formed functional interconnected networks

at a system level. A network clustering analysis was performed on the extracted time-activity curves of ^{18}F -FDG obtained using dynamic 1-h total-body PET scanning (Figure 3A) to investigate interactions between individual bones and identify if glucose skeletal metabolism networks were present.

We found a unique functional network (Figures 3B,C) whereby there was a high connectivity between long bones (femur, tibia). Meanwhile, the spine showed very little connectivity to any other bony tissue in the glucose metabolism (^{18}F -FDG) network. Furthermore, the spine, which had the weakest connectivity in the ^{18}F -FDG skeletal network, was the only bone to show a strong positive correlation ($r^2 = 0.9965$) between ^{18}F -FDG uptake and bone density (by CT HU, Figure 3D).

DISCUSSION

Our study demonstrates that in mice, different bones within the skeleton have unique molecular signatures and form a distinct metabolic network. Of importance, the metabolic dissimilarity observed between the spine and the rest of the skeleton, identified only by the ^{18}F -FDG total-body network and not standard whole-body SUV analysis, may be of significant clinical importance and could impact on the development of new treatments for metabolic and bone diseases.

The bones of the skeleton are classically divided into two anatomical classifications: the axial skeleton (bones along the body's long axis) and the appendicular skeleton (appendages of the axial skeleton). In addition to bone location, bones can form *via* two fundamentally different processes. Flat bones (e.g., the skull and scapula) are formed by intramembranous ossification, whereas long bones (e.g., tibia and humerus) are formed by endochondral ossification (15). Traditionally, dual energy x-ray absorptiometry (DEXA) or qCT have been used for quantification of bone density (16, 17). Our data shows that the classification of bones based on anatomical location, formation or density do not recapitulate complex bone metabolic functions as determined by total-body dynamic ^{18}F -FDG PET both at individual bone level and system connectivity level. Therefore, highlighting the importance of bone-specific endocrine functions in addition to classic functions in organ protection and locomotion.

Previously, in murine models of ageing, ^{18}F -FDG PET/CT analysis has shown that the spine had reduced ^{18}F -FDG uptake compared to other skeletal sites and this uptake was reduced with increasing age (12). In humans, osteoporosis, a systemic skeletal disease characterised by low bone mass and microarchitectural deterioration is estimated to be responsible for 80–95% of hip and spine fractures in humans (18, 19). Our total-body PET network finding that the spine has a distinct energy metabolism/bone density dynamics than other bones suggests spine fragility during the ageing process might be underpinned by a stronger dependence on glucose metabolism. This would be supported by evidence showing that altered glucose metabolism commonly occur with ageing (20). It follows from these data that future treatments for bone diseases such as osteoporosis may

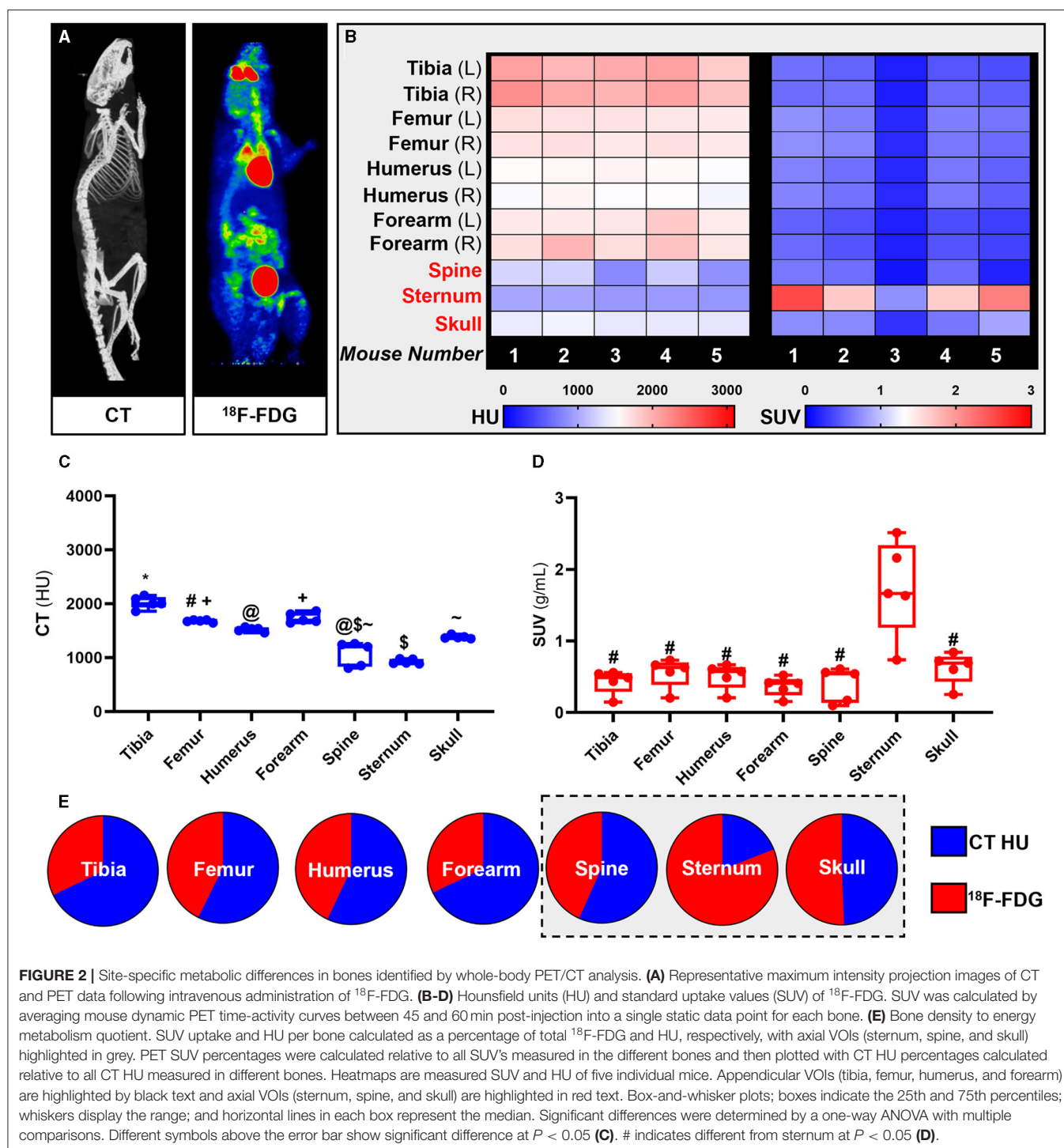
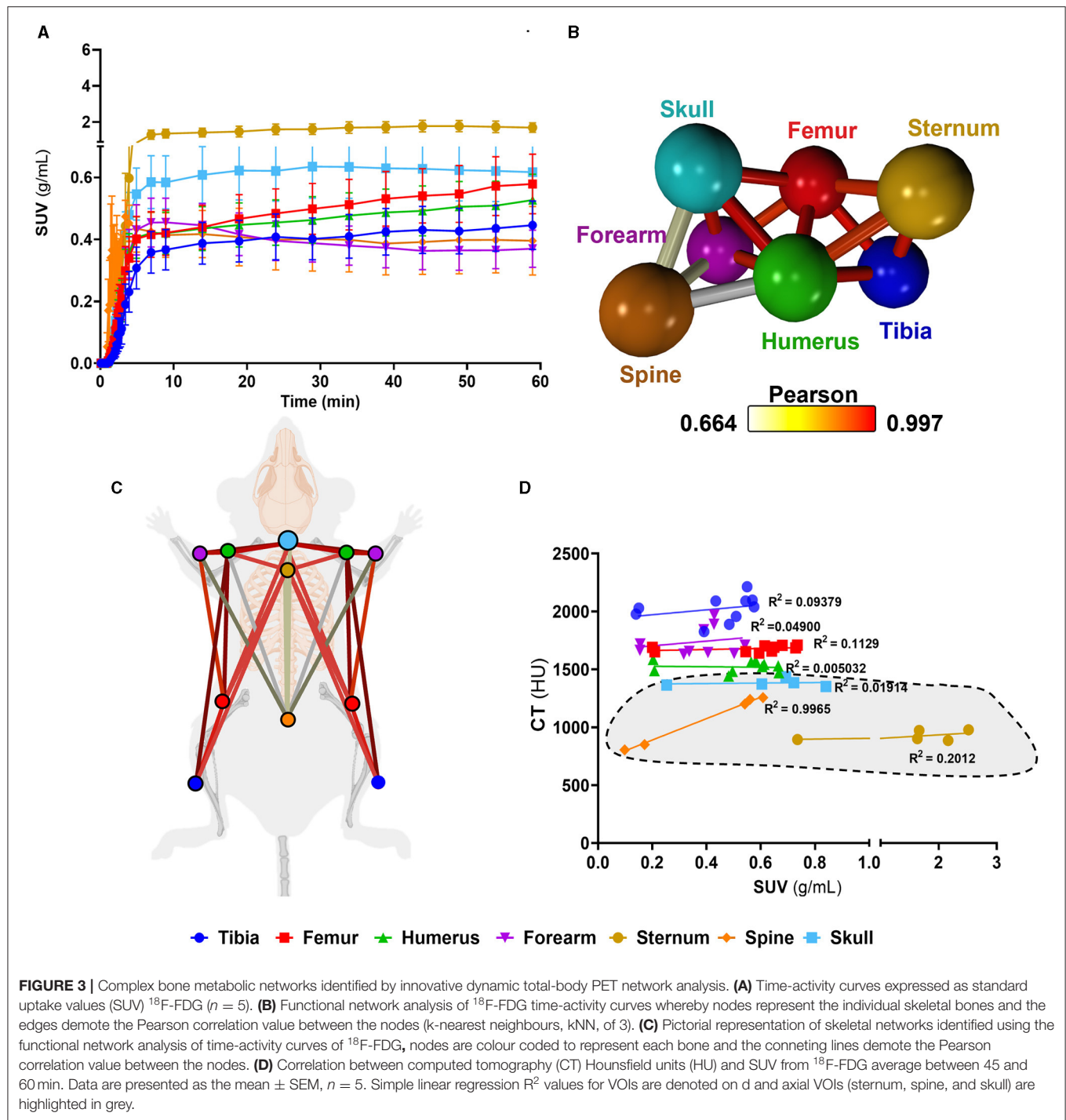


FIGURE 2 | Site-specific metabolic differences in bones identified by whole-body PET/CT analysis. **(A)** Representative maximum intensity projection images of CT and PET data following intravenous administration of ^{18}F -FDG. **(B–D)** Hounsfield units (HU) and standard uptake values (SUV) of ^{18}F -FDG. SUV was calculated by averaging mouse dynamic PET time-activity curves between 45 and 60 min post-injection into a single static data point for each bone. **(E)** Bone density to energy metabolism quotient. SUV uptake and HU per bone calculated as a percentage of total ^{18}F -FDG and HU, respectively, with axial VOIs (sternum, spine, and skull) highlighted in grey. PET SUV percentages were calculated relative to all SUV's measured in the different bones and then plotted with CT HU percentages calculated relative to all CT HU measured in different bones. Heatmaps are measured SUV and HU of five individual mice. Appendicular VOIs (tibia, femur, humerus, and forearm) are highlighted by black text and axial VOIs (sternum, spine, and skull) are highlighted in red text. Box-and-whisker plots; boxes indicate the 25th and 75th percentiles; whiskers display the range; and horizontal lines in each box represent the median. Significant differences were determined by a one-way ANOVA with multiple comparisons. Different symbols above the error bar show significant difference at $P < 0.05$ **(C)**. # indicates different from sternum at $P < 0.05$ **(D)**.

beneficiate from tailoring of the treatment strategies based on skeletal site-specific metabolic differences while keeping in mind systems level interactions beyond bone mineralisation. The new network approach could help unleash further knowledge on bone function. For example, it could also be interesting to investigate skeletal networks using ^{18}F -NaF, a radiotracer previously used as marker of active mineralisation, as metabolic bone disease may be more osteoblastic than osteolytic.

General anaesthesia, typically required for dynamic PET/CT imaging of live rodents, could be a limitation of the current work. Previous studies have shown that isoflurane can affect the uptake of ^{18}F -FDG (21, 22), thus it is important to consider this caveat when interpreting *in vivo* small animal PET/CT data.

In conclusion, we have shown that simplistic CT HU and PET SUV analysis fail to interrogate functional system-level networks that are present *in vivo*. Our novel network-based analyses of



PET data have highlighted that the spine has a unique glucose metabolic function where bone density is strongly dependent on glucose metabolism. Applying our new PET network analysis approach to other preclinical studies and clinical studies holds great promise in not only revealing further physiological and pathological intricacies of the skeleton, but can also be used to understand physiological and pathological tissue interactions between organ systems. Our data are directly relevant to human

health due to the recent development of the first clinical total-body PET systems, which will provide an opportunity to investigate if our findings in mice translate to humans. One can easily envision the application of the innovative total-body PET network analysis technique reported in this paper in a variety of diseases and the characterisation of network changes or losses during pathology, for example, were there is metabolic disruption at system-levels.

DATA AVAILABILITY STATEMENT

The datasets generated and analyzed for this study will be deposited upon manuscript acceptance in the “PET is Wonderful” data repository hosted by Edinburgh Datashare (<https://datashare.ed.ac.uk/handle/10283/3219>).

ETHICS STATEMENT

Studies were done in compliance with all relevant ethical regulations under project licences granted by the UK Home Office, and were approved by the University of Edinburgh Animal Welfare and Ethical Review Board.

AUTHOR CONTRIBUTIONS

AT and KS: conceptualisation and writing—original draft preparation. KS, CJAC, SN, MGM, RS, CF, TE, and AT: writing—review and editing. AT: funding acquisition. All authors contributed to the article and approved the submitted version.

REFERENCES

- Hacker M, Hicks RJ, Beyer T. Applied systems biology—embracing molecular imaging for systemic medicine. *Eur J Nucl Med Mol Imaging*. (2020) 47:2721–5. doi: 10.1007/s00259-020-04798-8
- Cherry SR, Badawi RD, Karp JS, Moses WW, Price P, Jones T. Total-body imaging: transforming the role of positron emission tomography. *Sci Transl Med*. (2017) 9:eaaf6169. doi: 10.1126/scitranslmed.aa6169
- Cherry SR, Jones T, Karp JS, Qi J, Moses WW, Badawi RD. Total-body PET: maximizing sensitivity to create new opportunities for clinical research and patient care. *J Nucl Med*. (2018) 59:3–12. doi: 10.2967/jnumed.116.184028
- Jones T. Total body PET imaging from mice to humans. (2020) 8:77. doi: 10.3389/fphy.2020.00077
- Saboury B, Morris MA, Farhadi F, Nikpanah M, Werner TJ, Jones EC, et al. Reinventing molecular imaging with total-body PET, part i: technical revolution in evolution. *PET Clin*. (2020) 15:427–38. doi: 10.1016/j.cpet.2020.06.012
- Saboury B, Morris MA, Nikpanah M, Werner TJ, Jones EC, Alavi A. Reinventing molecular imaging with total-body PET, part ii: clinical applications. *PET Clin*. (2020) 15:463–75. doi: 10.1016/j.cpet.2020.06.013
- Liu JM, Rosen CJ, Ducey P, Kousteni S, Karsenty G. Regulation of glucose handling by the skeleton: insights from mouse and human studies. *Diabetes*. (2016) 65:3225–32. doi: 10.2337/db16-0053
- Suchacki KJ, Roberts F, Lovdel A, Farquharson C, Morton NM, MacRae VE, et al. Skeletal energy homeostasis: a paradigm of endocrine discovery. *J Endocrinol*. (2017) 234:R67–79. doi: 10.1530/JOE-17-0147
- Suchacki KJ, Tavares AAS, Mattiucci D, Scheller EL, Papanastasiou G, Gray C, et al. Bone marrow adipose tissue is a unique adipose subtype with distinct roles in glucose homeostasis. *Nat Commun*. (2020) 11:3097. doi: 10.1038/s41467-020-16878-2

FUNDING

AT is funded by the British Heart Foundation (FS/19/34/34354); and is a recipient of a Wellcome Trust Technology Development Award (221295/Z/20/Z) and a Chan Zuckerberg Initiative DAF grant number 2020-225273, an advised fund of Silicon Valley Community Foundation. KS and RS are funded by the Medical Research Council (MR/S035761/1) and RS is funded by the Chief Scientist Office (SCAF/17/02). MGM is funded by the British Heart Foundation (RG/16/10/32375). CF is supported by the Biotechnology and Biological Sciences Research Council (BBSRC) through an Institute Strategic Programme Grant Funding (BB/J004316/1). The British Heart Foundation is greatly acknowledged for providing funding toward establishment of the preclinical PET/CT laboratory (RE/13/3/30183). We thank Mr. William Mungal for invaluable technical assistance with the animal experiments; CJAC is supported by the Edinburgh Preclinical Imaging core facility.

ACKNOWLEDGMENTS

We are grateful to Dr. Tashfeen Walton and Dr. Christophe Lucatelli (Edinburgh Imaging, University of Edinburgh) for radiotracer production.

- Guntur AR, Rosen CJ. Bone as an endocrine organ. *Endocr Pract*. (2012) 18:758–62. doi: 10.4158/EP12141.RA
- Mobasheri A, Vannucci SJ, Bondy CA, Carter SD, Innes JF, Arteaga MF, et al. Glucose transport and metabolism in chondrocytes: a key to understanding chondrogenesis, skeletal development and cartilage degradation in osteoarthritis. *Histol Histopathol*. (2002) 17:1239–67. doi: 10.14670/HH-17.1239
- Zoch ML, Abou DS, Clemens TL, Thorek DL, Riddle RC. *In vivo* radiometric analysis of glucose uptake and distribution in mouse bone. *Bone Res*. (2016) 4:16004. doi: 10.1038/boneres.2016.4
- Jacobson O, Kiesewetter DO, Chen X. Fluorine-18 radiochemistry, labeling strategies and synthetic routes. *Bioconjug Chem*. (2015) 26:1–18. doi: 10.1021/bc500475e
- Freeman TC, Horsewell S, Patir A, Harling-Lee J, Regan T, Shih BB, et al. Graphia: a platform for the graph-based visualisation and analysis of complex data. *bioRxiv*. (2020) doi: 10.1101/2020.09.02.279349
- Berendsen AD, Olsen BR. Bone development. *Bone*. (2015) 80:14–8. doi: 10.1016/j.bone.2015.04.035
- Blake GM, Fogelman I. The role of DXA bone density scans in the diagnosis and treatment of osteoporosis. *Postgrad Med J*. (2007) 83:509–17. doi: 10.1136/pgmj.2007.057505
- Jain RK, Vokes T. Dual-energy x-ray absorptiometry. *J Clin Densit*. (2017) 20:291–303. doi: 10.1016/j.jocd.2017.06.014
- Melton LJ, 3rd, Thamer M, Ray NF, Chan JK, Chesnut CH, 3rd, Einhorn TA, et al. Fractures attributable to osteoporosis: report from the National Osteoporosis Foundation. *J Bone Miner Res*. (1997) 12:16–23. doi: 10.1359/jbmr.1997.12.1.16
- Kanis JA, Cooper C, Rizzoli R, Reginster JY, Scientific Advisory Board of the European Society for C, Economic Aspects of O, et al. European guidance for the diagnosis and management of osteoporosis in postmenopausal women. *Osteoporos Int*. (2019) 30:3–44. doi: 10.1007/s00198-018-4704-5

20. Kalyani RR, Egan JM. Diabetes and altered glucose metabolism with aging. *Endocrinol Metab Clin North Am.* (2013) 42:333-47. doi: 10.1016/j.ecl.2013.02.010
21. Hildebrandt IJ, Su H, Weber WA. Anesthesia and other considerations for *in vivo* imaging of small animals. *ILAR J.* (2008) 49:17-26. doi: 10.1093/ilar.49.1.17
22. Fueger BJ, Czernin J, Hildebrandt I, Tran C, Halpern BS, Stout D, et al. Impact of animal handling on the results of 18F-FDG PET studies in mice. *J Nucl Med.* (2006) 47: 999-1006.

Conflict of Interest: The authors declare that the research was conducted in the absence of any commercial or financial relationships that could be construed as a potential conflict of interest.

Publisher's Note: All claims expressed in this article are solely those of the authors and do not necessarily represent those of their affiliated organizations, or those of the publisher, the editors and the reviewers. Any product that may be evaluated in this article, or claim that may be made by its manufacturer, is not guaranteed or endorsed by the publisher.

Copyright © 2021 Suchacki, Alcaide-Corral, Nimale, Macaskill, Stimson, Farquharson, Freeman and Tavares. This is an open-access article distributed under the terms of the Creative Commons Attribution License (CC BY). The use, distribution or reproduction in other forums is permitted, provided the original author(s) and the copyright owner(s) are credited and that the original publication in this journal is cited, in accordance with accepted academic practice. No use, distribution or reproduction is permitted which does not comply with these terms.



PET/CT Technology in Adult Zebrafish: A Pilot Study Toward Live Longitudinal Imaging

Carl Tucker¹, Richard Collins², Martin A. Denvir³ and Wendy A. McDougald^{3,4*}

¹ Bioresearch & Veterinary Services (BVS) Aquatics Facility, College of Medicine and Veterinary Medicine, University of Edinburgh, Edinburgh, United Kingdom, ² Edinburgh College of Arts, University of Edinburgh, Edinburgh, United Kingdom, ³ British Heart Foundation (BHF)-Centre for Cardiovascular Science, College of Medicine and Veterinary Medicine, University of Edinburgh, Edinburgh, United Kingdom, ⁴ Edinburgh Preclinical Imaging, Edinburgh Imaging, University of Edinburgh, Edinburgh, United Kingdom

OPEN ACCESS

Edited by:

Francesco Ciccone,
University of Catanzaro, Italy

Reviewed by:

Maurizio Conti,
Siemens Healthcare, United States
Cesar Molinos Solsona,
Bruker, Germany

*Correspondence:

Wendy A. McDougald
wmcdoug2@ed.ac.uk

Specialty section:

This article was submitted to
Nuclear Medicine,
a section of the journal
Frontiers in Medicine

Received: 15 June 2021

Accepted: 07 September 2021

Published: 11 October 2021

Citation:

Tucker C, Collins R, Denvir MA and
McDougald WA (2021) PET/CT
Technology in Adult Zebrafish: A Pilot
Study Toward Live Longitudinal
Imaging. *Front. Med.* 8:725548.
doi: 10.3389/fmed.2021.725548

Decades of research have confirmed the beneficial and advantageous use of zebrafish (*Danio rerio*) as a model of human disease in biomedical studies. Not only are 71% of human genes shared with the zebrafish many of these genes are linked to human diseases. Currently, numerous transgenic and mutant genetic zebrafish lines are now widely available for use in research. Furthermore, zebrafish are relatively inexpensive to maintain compared to rodents. However, a limiting factor to fully utilising adult zebrafish in research is not the fish but the technological imaging tools available. In order to increase the utilisation of adult zebrafish, which are not naturally transparent, requires new imaging approaches. Therefore, this feasibility study: (1) presents an innovative designed PET/CT adult zebrafish imaging platform, capable of maintaining normal aquatic physiology during scanning; (2) assesses the practical aspects of adult zebrafish imaging; and (3) set basic procedural guidelines for zebrafish imaging during a PET/CT acquisition.

Methods: With computer aided design (CAD) software an imaging platform was developed for 3D printing. A 3D printed zebrafish model was created from a CT acquisition of a zebrafish using the CAD software. This model and subsequently euthanised zebrafish were imaged post-injection using different concentrations of the radiotracer [¹⁸F]FDG with CT contrast.

Results: PET/CT imaging was successful, revealing levels as low as 0.01 MBq could be detected in the fish. In the zebrafish imaging post-injection distribution of the radiotracer was observed away from the injection site as well as tissue uptake. Potential preliminary husbandry and welfare guidelines for the fish during and after PET/CT imaging were determined.

Conclusion: Using PET/CT for adult zebrafish imaging as a viable non-invasive technological tool is feasible. Adult zebrafish PET/CT imaging has the potential to be a key imaging technique offering the possibilities of enhanced biomedical understanding and new translational data sets.

Keywords: 3D printing, zebrafish, radiotracer [¹⁸F]FDG, pre-clinical PET CT, longitudinal imaging

INTRODUCTION

With zebrafish (*Danio rerio*) as a well-established valuable model to investigate human diseases, continued growth in this field research is expected. In fact, 71% of human genes are associated with one zebrafish orthologue, and of 3,176 human genes with morbidity identification, 82% (2,601) are related to at least one zebrafish orthologue (1). Furthermore, with advancements in targeted genomic mutation tools, such as CRISPR/Cas9, the zebrafish is increasingly utilised for high throughput genotype-phenotyping modelling of human disease has increased (2–5). For example, various zebrafish transgenic lines expressing cell-specific fluorophore markers are available for human neurodegenerative and cardiovascular diseases research, amongst others (6–9). However, most researchers use the embryonic or larval stage where the zebrafish is fully transparent and can be readily imaged using standard light microscope techniques. The challenge arises in the adult where the skin is no longer transparent and where more complex imaging techniques are needed to study organ development or to assess impact of surgical or genetic interventions. *In vivo* imaging of the adult zebrafish is therefore a key topic for further research and development (10, 11).

An important part of this challenge is the need for suitable platforms capable of maintaining fish under physiological conditions during image acquisition over time periods of several hours. Such a platform may also facilitate sequential imaging of the same fish thus allowing longer term assessment of developmental or disease-repair mechanisms over months or even years. Increasing use of the adult zebrafish means that new imaging approaches need to be developed to help support novel translatable research and bridge the imaging gap between existing imaging techniques in the embryo across to the adult.

Positron emission tomography coupled with computed tomography (PET/CT) could provide that bridge by overcoming the hurdles of extending imaging beyond the embryonic stages. Pre-clinical PET/CT is a powerful non-invasive imaging tool already extensively used in rodent pre-clinical research. It supports the investigations and evaluations of underlying biological mechanisms, the physiological processes in a healthy or diseased model. Pre-clinical research areas such as cardiovascular or neurodegenerative diseases, oncology and drug discovery regularly take advantage of PET/CT's fully quantitative functionality (12–20).

This feasibility study addresses an unmet need for advanced imaging in the adult zebrafish using PET/CT. Here, we describe the development and early testing of an aquatic imaging platform to maintain a stable physiological state in adult zebrafish during PET/CT image acquisitions designed to accommodate different commercial scanners with the capability of screening drugs and radiotracers with a modestly high-throughput. The development of non-invasive molecular imaging of adult zebrafish has the potential to substantially improve our understanding of biological pathways and ultimately support the development of novel therapeutic strategies for human disease.

MATERIALS AND METHODS

3D Printed Imaging Platform

Using the McNeel Rhinoceros version 5.3.2 (Seattle, WA USA) 3D computer aided design (CAD) modelling software an aquatic zebrafish imaging platform, composed of a water chamber with monitoring equipment and two separate holding tanks for dosing and recovery has been designed. Designed concept includes monitoring to ensure correct water flow levels, pressure, salinity, oxygen, pH level, automatic dosing (chemical monitoring: anaesthesia, CT contrast, radiotracers or therapeutics) and temperature for zebrafish sustainability throughout imaging. Multiple water chambers as well as inserts were designed. A prototype of the water chamber was printed on a Stratasys Objet 260 Connex 3D printer (Los Angeles, CA USA), using the acrylic based photopolymer material Vero Clear. Imaging chamber has dimensions of 50.0 mm (length) and a 20.0 mm outer diameter, with internal and external sectioned designs. Printed prototype contains a single outer sectioned for the zebrafish placement. The imaging chamber system is an enclosed flow compartment with environmental monitoring to ensure stable physiology during scanning and a flow pump to circulate water continuously through the system. Dosing and recovery tanks are similarly constructed and environmentally monitored. The dosing chamber is also designed to permit delivery of anaesthetic, CT contrast, radiotracers or other therapeutics within the circulating water. The imaging system includes a designed “bed” holder allowing the platform to sit just beyond the forefront of the scanner bed.

Zebrafish 3D Printed Model

A CT acquisition of an adult Zebrafish was exported into OsiriX v.7.0 (Bernex, Switzerland). OsiriX's 3D volume and surface rendering tools were used on the FBP reconstructed images, converted from DICOM to standard tessellation language (STL) files and exported into Rhinoceros CAD software. The STL files were then edited to include a simplistic vascular circulatory system (hollow cylinder, radius 0.50 mm), cleaning of unwanted surfaces and artefacts. The prepared CAD files were 3D printed using the Stratasys Objet 260 Connex 3D printer using material Vero Clear. This phantom is dimensionally, geometrically an adult zebrafish with a main simplistic representative circular vascular system. The phantom replaces the use of animals used in determining imaging methods/feasibility, compliant with the National Centre for the Replacement, Refinement and Reduction of Animals in Research (NC3Rs).

PET/CT Imaging

All images were acquired with the zebrafish imaging platform placed just beyond the frontend of the scanner bed, positioned inside the bore at the isocenter, aligning sagittal, axial and coronal planes. Zebrafish and/or the 3D printed zebrafish models were placed directly inside the water filled imaging platform. CT acquisitions were acquired with the standard protocol (tube voltage 50 kVp, 300 ms, 360 projections) and reconstructed using the filtered back projection (FBP) method with a Cosine filter. Twenty-minute PET acquisitions were acquired in which

images were reconstructed using ordered subsets expectation maximisation (OSEM) method with 4 iterations and 6 subsets, with scatter, normalisation and randoms corrections. All PET and CT imaging was done on the Mediso nanoPET/CT (Budapest, Hungary).

Preparation of Zebrafish 3D Printed Model

A concentration of 2 ml of water with 0.75 ml of CT contrast agent Ominpaque was prepared for use. Prior to imaging, measured radiotracer ^{18}F -deoxyglucose, [^{18}F]FDG (0.01–1 MBq) with the CT contrast concentration was injected directly into the designed general simplistic vascular circulatory system using a Hamilton 35-gauge needle under a binocular microscope. The phantom was imaged at different times for $n = 4$.

Preparation of Zebrafish (Adult Wild Type Wik)

In a series of pilot experiments, adult wild-type zebrafish were first euthanised using Tricaine [Sigma Aldrich, Cat.# A-5040, 4.2%w/v (21)] and the brain destroyed by a modified pithing method using a 15-gauge needle in compliance with the schedule 1 *UK Animals (Scientific Procedures) Act 1986 (ASPA)* prior to placing the animal in the scanner. In this scenario the heart continues to beat for 30–60 min after brain death thus maintaining circulation and the integrity of the fish tissue during the imaging period (22, 23).

An initial activity concentration of 2 mL of water, 65 MBq of radiotracer [^{18}F]FDG with 0.75 mL of CT contrast agent Ominpaque was prepared for use. Measured various amounts (0.01–2 MBq) of the activity concentration was injected into the hearts or pectoral cavity of the adult zebrafish using a Hamilton 35-gauge needle under binocular microscope guidance prior to imaging. PET/CT imaging started 30 or 40-min post-injections. Overall $n = 12$ euthanised zebrafish were imaged.

RESULTS

3D Printed Imaging Platform

Figure 1 displays the first digital design for the printed prototype chamber used in testing the feasibility of PET/CT imaging of adult zebrafish in a sustainable aquatic imaging platform. This prototype was used in the image acquisition testing of the 3D model zebrafish and for subsequent PET/CT imaging of zebrafish.

Zebrafish 3D Printed Model

CT images of two euthanised adult zebrafish were acquired for the designed 3D print a zebrafish model. **Figure 2** shows the results of developing the 3D printed zebrafish model; CT acquisition, STL files, CAD preparation, including creating the 1 mm diameter hollow elongated cylinder inside for the injection of CT contrast and radiotracer and (4) the final Vero Clear 3D printed zebrafish model.

PET/CT Imaging

The fundamental and vital principle of PET/CT imaging lies in the scanner's ability to detect the injected radiotracer. Therefore, various levels of radiotracer were injected to determine the lowest levels suitable for detection in zebrafish

imaging. Additionally, a crucial consideration when acquiring pre-clinical PET/CT images is the well-being and welfare of the animals. Establishing the foundations for standard procedures in accordance with the National Centre for the Replacement, Refinement and Reduction (NC3Rs) principles and the Animals (Scientific Procedures) Act 1986 is a critical aspect of studying the feasibility of adult zebrafish PET/CT imaging. At this stage and in conjunction with radiotracer levels, imaging time as well as required radioactive zebrafish recovery times were considered, thus, allowing for the eventual proper fish transportation to the aquatic facility.

Zebrafish 3D Printed Model

A 20-min PET/CT was acquired immediately after the zebrafish 3D model was injected with the CT contrast agent and 0.01 MBq of [^{18}F]FDG using the water filled zebrafish imaging platform. Imaging data sets from the 3D printed model indicate that the injected concentration of [^{18}F]FDG can be detected within the 0.5 mm radius elongated cylindrical cavity. **Figure 3** displays the detection of [^{18}F]FDG in the 3D model PET image, though the majority is seen at the injection sites. In **Figure 4A** the CT contrast is clearly seen in the 3D model's simplistic vascular system. Additionally, in **Figure 4B** [^{18}F]FDG is also detected within the model's vascular system. **Figure 4** is a clear indication that a mixture of CT contrast agent and the low level 0.05 MBq of [^{18}F]FDG is detectable.

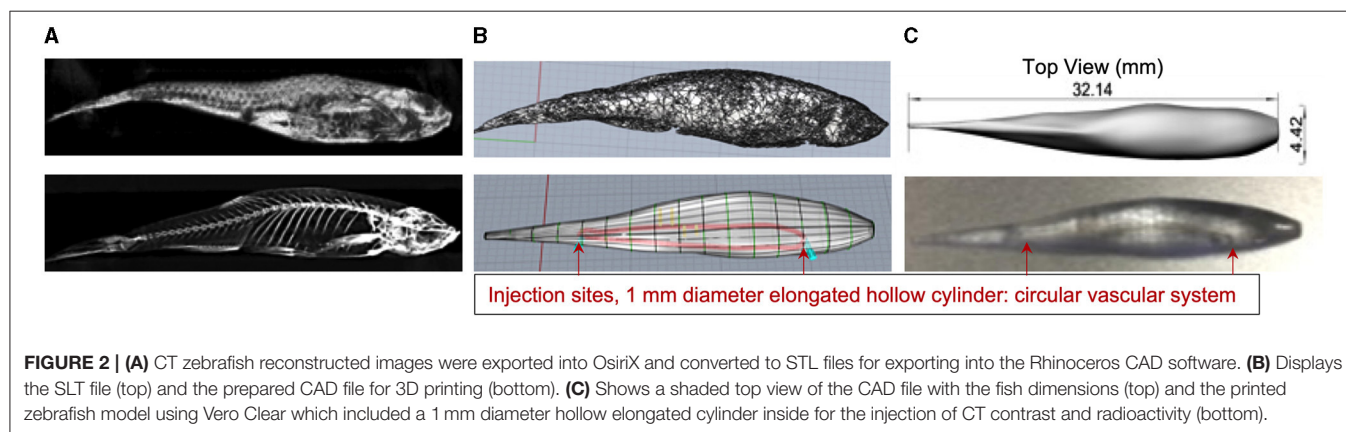
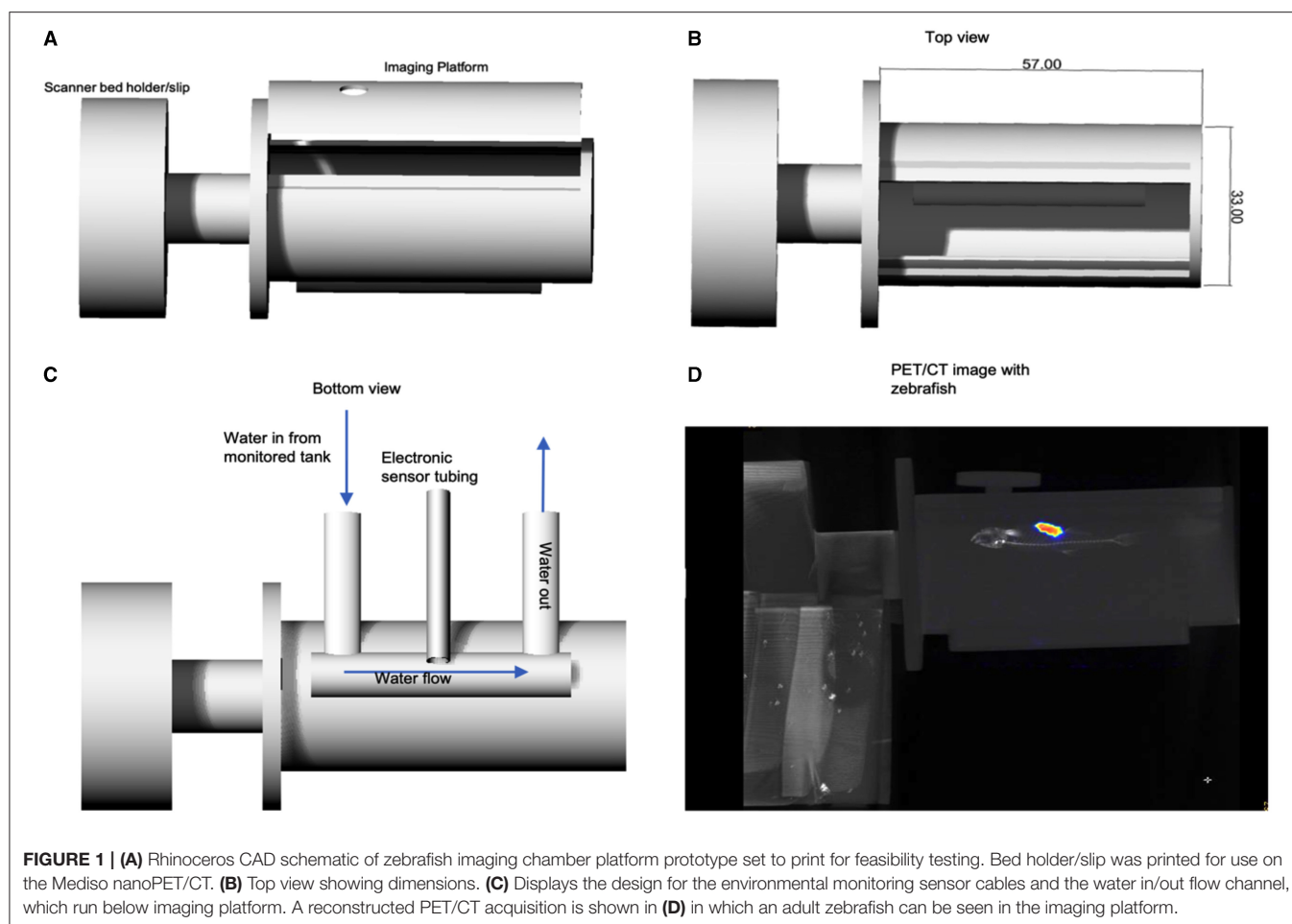
Zebrafish (Adult Wild Type Wik)

PET/CT acquisitions of the adult zebrafish were imaged with various amounts of [^{18}F]FDG with CT contrast agent, which ranged from 0.01 to 2 MBq. As noted, this was done to assess the viability of the low levels of radiotracer detection as well as determining recovery times for the radioactive zebrafish after imaging for proper husbandry and transportation of the fish (i.e., radioactivity less than background).

A euthanised adult zebrafish, pectoral cavity post-injection with CT contrast agent and 0.43 MBq of [^{18}F]FDG, is shown in **Figure 5**. As noted, all images were acquired as a 20-min PET, a standard CT with the zebrafish placed inside the water filled imaging platform. PET/CT image, shown in **Figure 5A**, clearly reveals distribution and uptake of the [^{18}F]FDG within the zebrafish, with possible uptake in the liver. A full histological analysis has yet to be performed. However, organs demonstrating [^{18}F]FDG uptake would be areas representing metabolically active organs including the liver, gut, and heart. For a visual comparison, **Figure 5B** shows a pectoral cavity post-injection with CT contrast agent and 0.03 MBq of [^{18}F]FDG which did not circulate around the zebrafish in the same manner as the other.

DISCUSSION

We demonstrated that a commercial pre-clinical PET/CT is capable of detecting the common PET radiotracer [^{18}F]FDG at low enough dose levels plausible for safe zebrafish imaging and recovery. The lowest dose level detected was 0.01 MBq, albeit within the 1 mm diameter 3D printed zebrafish model hollow cylinder, "vascular system," **Figures 3, 4**. In the pithed-zebrafish



the lowest detectable [^{18}F]FDG dose was 0.05 MBq (Figure 5) which confirms that high doses of tracer are not required. A cursory check of [^{18}F]FDG uptake, shown in Figure 5, using the maximum standard uptake value (SUV) revealed activity in those selected areas. Extracting a SUV max from the zebrafish images indicates PET quantitative analysis can be accomplished.

This study used the method of direct injection of radiotracer by a Hamilton 35-gauge needle directly into the heart or

the pectoral cavity. Therefore, we have not yet tested the method of introducing or treating zebrafish with anaesthesia, CT contrast, radiotracers or therapeutics *via* the circulating water in our physiological chamber. However, potential guidelines for the welfare and recovery of live fish, especially critical for longitudinal studies can be extrapolated from our results. For example, this study would indicate that a dose of 0.5 MBq for a 20-min PET/CT would be sufficient for

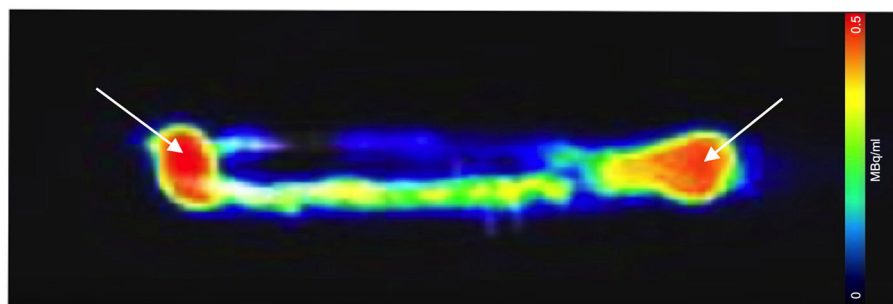


FIGURE 3 | Sagittal PET/CT image acquisition of the 3D printed zebrafish model post-injection of 0.01 MBq of [^{18}F]FDG. [^{18}F]FDG is seen within the 1 mm simplistic vascular system, though substantial amounts remained at the injection site (white arrows). Adjustments to the injection procedure were made allowing for improve follow in the hollow plastic cavity.

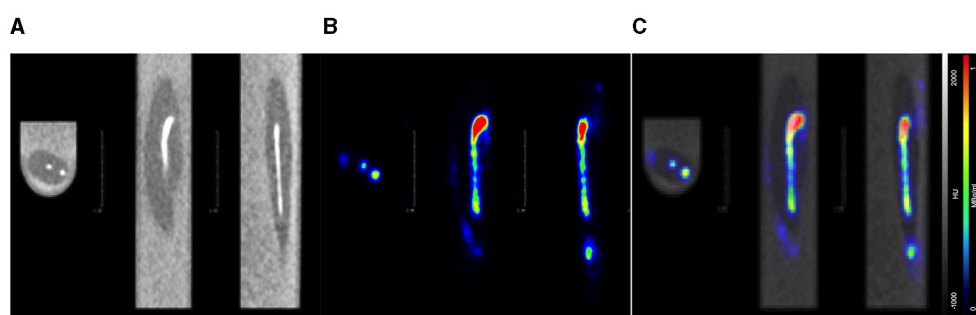


FIGURE 4 | Axial, coronal, and sagittal PET/CT image acquisition of the 3D printed zebrafish model post-injection of 0.05 MBq of [^{18}F]FDG. **(A)** CT image displays the CT contrast (white line) within the model's vascular system. **(B)** PET image reveals [^{18}F]FDG (coloured line) within the model's vascular system. **(C)** Fused PET/CT confirms CT contrast and [^{18}F]FDG are within the model's vascular system.

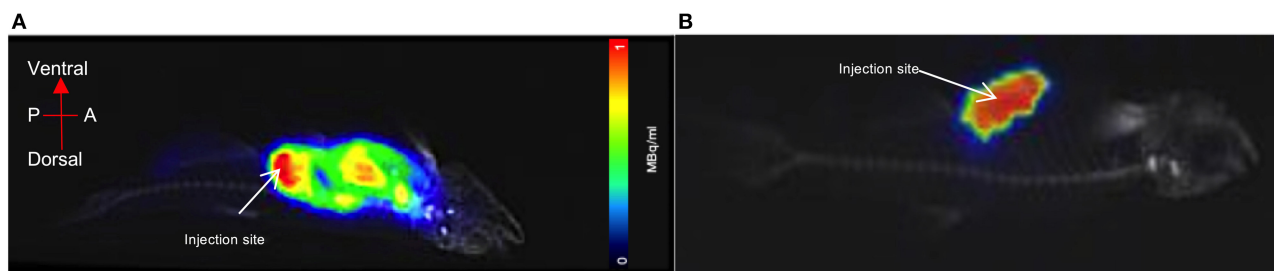


FIGURE 5 | PET acquisition of a euthanized zebrafish inside the imaging platform. **(A)** The mixture of CT contrast and [^{18}F]FDG (0.5MBq) was injected into the pectoral cavity immediately following confirmed death and allowed to circulate for 30 min prior to imaging. Distribution and uptake of the activity can be seen away from the injection site. The tracer distribution away from the injection site (red) areas will represent metabolically active organs such as the liver, gut or heart. **(B)** For visual comparison of [^{18}F]FDG uptake and distribution, radiotracer has remained at the injection site (pectoral cavity).

detection, thus requiring $\sim 4\text{h}$ of recovery to reach a safe level for transport back to the aquatic facility. It should be noted, (1) radioactivity at background levels or below is considered safe for transportation, based off the International Atomic Energy Agency (IAEA) regulations, (2) the time frame estimated is subject to change based on future work observing the recovery of live zebrafish, adhering to ASPA and the NC3Rs observational guidelines. The current time frame is

to establish an initial guideline, which was determined using the decay time of ^{18}F and post-measurements of the deceased imaged fish.

In 2013 Koba et al. published proof of concept studies using PET/CT for larger goldfish (40 g) research, thus supporting the feasibility of this research avenue (17). More recently, in 2017 Merrifield et al. developed an aquatic flow cell system capable of monitoring zebrafish during pre-clinical MRI acquisitions (24).

In a similar fashion, the PET/CT imaging platform is designed to contain future in/out water flow tubing with electronic sensors for monitoring temperature, pressure, salinity, oxygen, and pH level of the water. Unfortunately, though, routine *in vivo* imaging of adult zebrafish has yet to be established. Now, with greater insight as to the requirements, practicalities of maintaining a suitable dosing, imaging and recovery systems the probability of successfully imaging adult zebrafish increases. Furthermore, our imaging platform design provides the ability for different scanner bed holders/slips to be 3D printed, thus, adopting to different scanners, **Figure 1**. This approach also allows for the zebrafish to be imaged in the forefront of the scanner bed in order to reduce potential scatter and void attenuation through a scanner bed.

Literature spanning three decades has validated the zebrafish as an excellent model for researching human diseases and drug development. For instance, atherosclerotic disease in zebrafish using [^{18}F]FDG, which is the mainstay radioligand in PET imaging and consequently has been the most common radioligand used in imaging studies of atherosclerosis (25, 26). As noted, PET/CT plays a pivotal role in therapeutics and radiotracer development, discovery or repurposing. Results in this capacity have direct translational applications to clinical research and patients. However, from start of research to regulatory approval, a new therapeutic drug typically takes 10–15 years before it reaches the pharmacist. The ability to incorporate live zebrafish PET/CT imaging has the potential to immediately reduce that timescale, by a minimum of 2 years (27). Pre-clinical PET/CT imaging of live zebrafish will assist expeditiously by statistical power/high throughput (large n number). This will be achieved by enhancing our understanding of the molecular pathogenesis of disease, increase confidence and success rate when identifying the drug lead compound for future development, and streamlining the validation of the effectiveness of the compound (large n numbers for reduced cost compared with alternative pre-clinical species). Therefore, reducing attrition rate for drug candidate selection and characterisation prior to expensive and lengthy human studies, reducing the R&D timescale.

This imaging platform provides the zebrafish research community access to a translatable molecular imaging modality. Thus, shortening research translation time and increasing the relevance of research findings to humans. Additionally, in a cardiovascular context, this adult zebrafish imaging potentially provides newer insights into vascular heart repair mechanisms. Thus, allowing for new approaches to assess novel therapeutic options that could improve recovery of heart function following cardiac injury, such as myocardial infarction.

Researching models of hyperglycaemia in zebrafish, after injecting 20 MBq of [^{18}F]FDG in the pectoral cavity Dorsemans et al. (28) successfully acquired a PET/CT noting a wide distribution of [^{18}F]FDG. Likewise, in 2017 for proof of concept Snay et al. successfully imaged zebrafish with 0.74–1.29 MBq of [^{18}F]FDG, with 10 min PET followed by a 10 min CT acquisition (29). Albeit, in both cases the zebrafish imaging was done with the fish out of water, either in agar or wrapped in a tissue. More recently, for proof of concept Nazario et al. (30) intraperitoneally injected zebrafish with [^{18}F]FDG, or ^{18}F -NaF, (2–3 MBq) for

5 min PET/CT imaging (30). Here they were able successfully image with the fish placed in a water/tricaine solution filled 15 mL tube. Though not imaged under favourable physiological conditions these recent proof of concepts studies show promise as well as the interest in zebrafish PET/CT imaging.

Nevertheless, continued small fish PET/CT protocol and methodology imaging strategic research is needed in order to fully develop imaging guidelines and best practise procedures. For example, future work will include the use of live zebrafish receiving a concentration of CT contrast, [^{18}F]FDG and anaesthetic *via* immersion (inhalation) and tail vein injections. Additionally, recovery procedures will be expanded to include zebrafish physical observations during recovery.

CONCLUSION

This pre-clinical PET/CT feasibility study successfully demonstrates the possibility of adult zebrafish imaging using [^{18}F]FDG. The development of PET/CT imaging technology to image adult zebrafish has the potential to enhance and expand research in this highly versatile animal model system by extending structural and functional imaging capabilities beyond the embryo.

DATA AVAILABILITY STATEMENT

The raw data supporting the conclusions of this article will be made available by the authors, without undue reservation.

ETHICS STATEMENT

The animal study was reviewed and approved by the University of Edinburgh Animal Welfare and Ethical Review Board. All experiments were carried out in accordance with the accepted standards of humane animal care under the regulation of the UK Animal (Scientific Procedures) Act 1986 and EU Directive 2010/63/EU. All adult WIK zebrafish were end of life euthanized in accordance with ASPA schedule 1 procedure.

AUTHOR CONTRIBUTIONS

WM developed and designed the zebrafish imaging platform, created image acquisition protocols, acquired the 3D model and zebrafish images, carried out the data collection, analysis, and drafted the manuscript. CT assisted in the handling of the zebrafish, interpretation of the data, and the revising of the manuscript. RC assisted in the designing of the zebrafish imaging platform and 3D fish model, 3D printed the platform, and model as well as assisted in the revision of the manuscript. MD assisted in the interpretation of the data and the revising of the manuscript. All authors participated in the conception of the study and design, read, and approved the final manuscript.

ACKNOWLEDGMENTS

The authors would like to thank all the team members at the Bioresearch and Veterinary Services, Aquatics Facility, College of Medicine and Veterinary Medicine, University of Edinburgh and Edinburgh Pre-clinical Imaging, University of Edinburgh for their support and assistance throughout the

different stages of this study. The authors would also like to thank Anne Grant, with the Clinical Imaging Facilities, Edinburgh Imaging for her support. The authors thank the National Centre for the Replacement, Refinement and Reduction of Animals in Research (NC3Rs), funding WM. The authors also thank the Medical Research Council (MRC) and the British Heart Foundation (BHF).

REFERENCES

- Howe K, Clark MD, Torroja CF, Torrance J, Berthelot C, Muffato M, et al. The zebrafish reference genome sequence and its relationship to the human genome. *Nature*. (2013) 496:498–503. doi: 10.1038/nature12111
- Fuentes R, Letelier J, Tajer B, Valdivia L, Mullins M. Fishing forward and reverse: advances in zebrafish phenomics. *Mech Dev*. (2018) 154:296–308. doi: 10.1016/j.mod.2018.08.007
- Auer TO, Duroure K, Cian A De, Concordet J. Highly efficient CRISPR/Cas9-mediated knock-in in zebrafish by homology-independent DNA repair. *Genome Res*. (2014) 24:142–53. doi: 10.1101/gr.161638.113
- Lieschke GJ, Currie PD. Animal models of human disease: zebrafish swim into view. *Nat Rev Genet*. (2010). 8:353–67. doi: 10.1038/nrg2091
- Shin JT, Fishman MC. From zebrafish to human: modular medical models. *Annu Rev Genomics Hum Genet*. (2002) 3:311–40. doi: 10.1146/annurev.genom.3.031402.131506
- Bandmann O, Burton EA. Neurobiology of disease genetic zebra fish models of neurodegenerative diseases. *Neurobiol Dis*. (2010) 40:58–65. doi: 10.1016/j.nbd.2010.05.017
- González-rosa JM, Burns CGE. Zebrafish heart regeneration: 15 years of discoveries. *Wiley Regen*. (2017) 4:105–23. doi: 10.1002/reg2.83
- Wyatt C, Bartoszek EM, Yakse E. Methods for studying the zebrafish brain: past, present and future. *Eur J Neurosci*. (2015) 42:1746–63. doi: 10.1111/ejn.12932
- Huttner IG, Trivedi G, Jacoby A, Mann SA, Vandenberg JJ, Fatkin D, et al. Transgenic zebrafish model of a human cardiac sodium channel mutation exhibits bradycardia, conduction-system abnormalities and early death. *J Mol Cell Cardiol*. (2013) 61:123–32. doi: 10.1016/j.yjmcc.2013.06.005
- Merrifield G, Mullin J, Gallagher L, Tucker C, Jansen M, Denvir M, et al. Developing cardiac magnetic resonance imaging in the live zebrafish. *Heart*. (2015) 101(Suppl. 6):A6.1–A6. doi: 10.1136/heartjnl-2015-308734.16
- van den Thillart G, Körner F, van Waarde A, Erkelens C, Lugtenburg J. A flow-through probe for in Vivo³¹P NMR spectroscopy of unanesthetized aquatic vertebrates at 94 tesla. *J Magn Reson*. (1989) 84:573–9. doi: 10.1016/0022-2364(89)90121-2
- McGirr R, Hu S, Yee SP, Kovacs MS, Lee TY, Dhanvantari S. Towards PET imaging of intact pancreatic beta cell mass: a transgenic strategy. *Mol Imaging Biol*. (2011) 13:962–72. doi: 10.1007/s11307-010-0435-5
- Fushiki H, Miyoshi S NA. Pre-clinical validation of orthotopically-implanted pulmonary tumor by imaging with 18FF-fluorothymidine-positron emission tomography/computed tomography. *Anticancer Res*. (2013) 33:4741–9.
- Palmer M, Shen B, Jeon J, Lin J, Chin FT, Rao J. Preclinical kinetic analysis of the Caspase-3/7 PET tracer 18FF-C-SNAT: quantifying the changes in blood flow and tumor retention after chemotherapy. *J Nucl Med*. (2015) 56:1415–21. doi: 10.2967/jnumed.115.155259
- Massoud TF, Gambhir SS. Molecular imaging in living subjects: seeing fundamental biological processes in a new light. *Genes Dev*. (2003) 17:545–80. doi: 10.1101/gad.1047403
- Boschi S, Lee JT, Beykan S, Slavik R, Wei L, Spick C, et al. Synthesis and preclinical evaluation of an Al18FF radiofluorinated GLU-UREA-LYS(AHX)-HBED-CC PSMA ligand. *Eur J Nucl Med Mol Imaging*. (2016) 43:2122–30. doi: 10.1007/s00259-016-3437-y
- Koba W, Jelicks LA, Fine EJ. MicroPET/SPECT/CT imaging of small animal models of disease. *Am J Pathol*. (2013) 18F2:319–24. doi: 10.1016/j.ajpath.2012.09.025
- Haylock AKF, Spiegelberg D, Mortensen AC, Selvaraju RK, Nilvebrant J, Eriksson O, et al. Evaluation of a novel type of imaging probe based on a recombinant bivalent mini-antibody construct for detection of CD44v6-expressing squamous cell carcinoma. *Int J Oncol*. (2016) 48:461–70. doi: 10.3892/ijo.2015.3290
- Zhang C, Pan J, Lin K-S, Dude I, Lau J, Zeisler J, et al. Improved 68Ga-labelled truncated peptides targeting the neuropeptide Y1 receptor for cancer imaging by positron emission tomography. *J Nucl Med*. (2016) 57(Suppl. 2):1160.
- Appelbe OK, Zhang Q, Pelizzari CA, Weichselbaum RR, Kron SJ. Image-guided radiotherapy targets macromolecules through altering the tumor microenvironment. *Mol Pharm*. (2016) 13:3457–67. doi: 10.1021/acs.molpharmaceut.6b00465
- Westerfield M. *The Zebrafish Book. A Guide for the Laboratory Use of Zebrafish (Danio Rerio)*. 5th ed. Eugene: Univ. of Press (2007).
- Hecker L, Khait L, Sessions SK, Birla RK. Functional evaluation of isolated zebrafish hearts. *Zebrafish*. (2008) 5:319–22. doi: 10.1089/zeb.2008.0550
- Pieperhoff S, Wilson KS, Baily J, de Mora K, Maqsood S, Vass S, et al. Heart on a plate: histological and functional assessment of isolated adult zebrafish hearts maintained in culture. *PLoS ONE*. (2014) 9:e96771. doi: 10.1371/journal.pone.0096771
- Merrifield GD, Mullin J, Gallagher L, Tucker C, Jansen MA, Denvir M, et al. Rapid and recoverable in vivo magnetic resonance imaging of the adult zebrafish at 7T. *Magn Reson Imaging*. (2017) 37:9–15. doi: 10.1016/j.mri.2016.10.013
- Evans NR, Tarkin JM, Chowdhury MM, Warburton EA, Rudd JHF. PET imaging of atherosclerotic disease: advancing plaque assessment from anatomy to pathophysiology. *Curr Atheroscler Rep*. (2016) 18F:30. doi: 10.1007/s11883-016-0584-3
- Tang D, Geng F, Yu C, Zhang R. Recent application of zebrafish models in atherosclerosis research. *Front Cell Dev Biol*. (2021) 9:643697. doi: 10.3389/fcell.2021.643697
- Agdeppa ED, Spilker ME. A review of imaging agent development. *AAPS J*. (2009) 11:286–99. doi: 10.1208/s12248-009-9104-5
- Dorsemans A, Lefebvre C, Ait-arsa I, Jestin E, Meilhac O, Diotel N. Acute and chronic models of hyperglycemia in zebrafish: a method to assess the impact of hyperglycemia on neurogenesis and the biodistribution of radiolabeled molecules. *J Vis Exp*. (2017) 124:55203. doi: 10.3791/55203
- Snay E, Dang M, Fahey F, Zon L. Developing a practical approach to imaging PET/CT of zebrafish. *J Nucl Med*. (2017) (Suppl. 58):1127.
- Nazario L, Vierstraete J, Bek J, et al. In vivo PET/CT imaging in zebrafish using 18FF-FDG and 18FF-NaF. *EMIM*. (2019).

Conflict of Interest: The authors declare that the research was conducted in the absence of any commercial or financial relationships that could be construed as a potential conflict of interest.

Publisher's Note: All claims expressed in this article are solely those of the authors and do not necessarily represent those of their affiliated organizations, or those of the publisher, the editors and the reviewers. Any product that may be evaluated in this article, or claim that may be made by its manufacturer, is not guaranteed or endorsed by the publisher.

Copyright © 2021 Tucker, Collins, Denvir and McDougald. This is an open-access article distributed under the terms of the Creative Commons Attribution License (CC BY). The use, distribution or reproduction in other forums is permitted, provided the original author(s) and the copyright owner(s) are credited and that the original publication in this journal is cited, in accordance with accepted academic practice. No use, distribution or reproduction is permitted which does not comply with these terms.



Voxel-Based Analysis of [18F]-FDG Brain PET in Rats Using Data-Driven Normalization

Silke Proesmans¹, Robrecht Raedt¹, Charlotte Germonpré¹, Emma Christiaen², Benedicte Descamps², Paul Boon¹, Veerle De Herdt¹ and Christian Vanhove^{2*}

¹ 4Brain Lab, Department of Head and Skin, Ghent University, Ghent, Belgium, ² IbiTech-MEDISIP-Infinity Lab, Department of Electronics and Information Systems, Ghent University, Ghent, Belgium

OPEN ACCESS

Edited by:

Wendy McDougald,
University of Edinburgh,
United Kingdom

Reviewed by:

Zhenjian Zhuo,
Guangzhou Medical University, China
Thomas Nickl-Jockschat,
The University of Iowa, United States

*Correspondence:

Christian Vanhove
christian.vanhove@UGent.be

Specialty section:

This article was submitted to
Translational Medicine,
a section of the journal
Frontiers in Medicine

Received: 19 July 2021

Accepted: 24 September 2021

Published: 20 October 2021

Citation:

Proesmans S, Raedt R, Germonpré C,
Christiaen E, Descamps B, Boon P,
De Herdt V and Vanhove C (2021)
Voxel-Based Analysis of [18F]-FDG
Brain PET in Rats Using Data-Driven
Normalization. *Front. Med.* 8:744157.
doi: 10.3389/fmed.2021.744157

Introduction: [18F]-FDG PET is a widely used imaging modality that visualizes cellular glucose uptake and provides functional information on the metabolic state of different tissues *in vivo*. Various quantification methods can be used to evaluate glucose metabolism in the brain, including the cerebral metabolic rate of glucose (CMR_{glc}) and standard uptake values (SUVs). Especially in the brain, these (semi-)quantitative measures can be affected by several physiological factors, such as blood glucose level, age, gender, and stress. Next to this inter- and intra-subject variability, the use of different PET acquisition protocols across studies has created a need for the standardization and harmonization of brain PET evaluation. In this study we present a framework for statistical voxel-based analysis of glucose uptake in the rat brain using histogram-based intensity normalization.

Methods: [18F]-FDG PET images of 28 normal rat brains were coregistered and voxel-wisely averaged. Ratio images were generated by voxel-wisely dividing each of these images with the group average. The most prevalent value in the ratio image was used as normalization factor. The normalized PET images were voxel-wisely averaged to generate a normal rat brain atlas. The variability of voxel intensities across the normalized PET images was compared to images that were either normalized by whole brain normalization, or not normalized.

To illustrate the added value of this normal rat brain atlas, 9 animals with a striatal hemorrhagic lesion and 9 control animals were intravenously injected with [18F]-FDG and the PET images of these animals were voxel-wisely compared to the normal atlas by group- and individual analyses.

Results: The average coefficient of variation of the voxel intensities in the brain across normal [18F]-FDG PET images was 6.7% for the histogram-based normalized images, 11.6% for whole brain normalized images, and 31.2% when no normalization was applied. Statistical voxel-based analysis, using the normal template, indicated regions of significantly decreased glucose uptake at the site of the ICH lesion in the ICH animals, but not in control animals.

Conclusion: In summary, histogram-based intensity normalization of [18F]-FDG uptake in the brain is a suitable data-driven approach for standardized voxel-based comparison of brain PET images.

Keywords: [18F]-FDG, PET, intensity normalization, voxel-based analysis, rat brain

INTRODUCTION

[18F]-fluorodeoxyglucose positron emission tomography ([18F]-FDG PET) is increasingly used for the diagnosis, staging, prognosis, and response evaluation of a variety of diseases (1, 2). Especially in the brain, evaluation of the global and regional cerebral glucose consumption provides essential information on brain function and metabolism in neurological disorders. PET image interpretation in clinical practice is mainly performed by visual inspection, but an increasingly important role has been established for (semi-)quantitative image analysis, for example by standard uptake values (SUVs) or the cerebral metabolic rate of glucose (CMR_{glc}) (3).

In general, PET (semi-)quantification methods commonly rely on region of interest (ROI)-based or voxel-wise statistical comparison between PET scans of patients and healthy subjects (4). Both methods have their limitations and difficulties. ROI-based analysis can be biased by the choice of the ROI, while voxel-based analysis is less biased but requires a large pool of healthy subjects. Another challenging issue related to (semi-)quantitative brain PET analysis is that uptake of [18F]-FDG in the brain poses a large degree of variability due to physical or biological factors, and inconsistent image acquisition, processing and analysis (5). Especially in the brain, [18F]-FDG uptake, and thus measures such as SUVs, are affected by several physiological factors, including blood glucose level, age, gender, circadian rhythm, and stress (6, 7). Therefore, intensity normalization of the PET signal is recommended for comparing [18F]-FDG uptake in ROIs or voxel values in the brain (8).

Intensity normalization is usually performed by scaling voxel intensities based on the average uptake in a previously defined reference region where tracer uptake is not affected by the studied disease, or based on a data-driven approach where the average uptake in the whole brain is the simplest and most used method. However, these methods might introduce bias depending on the choice of reference region or the presence of regional uptake changes, respectively (8, 9). The lack of standardization of intensity normalization procedures has been recognized as a major weakness for the harmonization of (semi-)quantitative [18F]-FDG PET analysis (10).

The effect of different normalization procedures on lesion visualization was investigated in a recent paper by López-González et al. (8) using simulated data. Data-driven methods, and the histogram-based intensity normalization method in particular, seemed to introduce the least bias when performing voxel-wise statistical analysis on PET data. In this paper, a workflow will be presented to create a normal [18F]-FDG rat brain atlas using histogram-based intensity normalization.

Additionally, the same intensity normalization approach will be used to detect changes in glucose metabolism in a rat model for intracerebral hemorrhage (ICH). The nature and mechanisms of glucose uptake changes post-ICH are outside the scope of this article. However, the use of a normal brain PET atlas has been proven useful for the analysis of extensive as well as subtle metabolic changes in the brain in pathological circumstances (11–13). Therefore, the feasibility of using the histogram-based intensity normalization procedure in subsequent voxel-wise

statistical comparison of post-ICH [18F]-FDG PET images with the normal rat brain atlas will be demonstrated in this paper.

METHODS

Animals

Twenty-eight healthy adult male Sprague-Dawley rats (Envigo, The Netherlands) of 11 weeks old and with an average weight of 317.4 ± 25.7 g were included in this study for the generation of the normal rat brain atlas. Later, 18 of these 28 animals were used in further experimental procedures. In 9 of these animals an ICH was induced, and the 9 other animals were used as a saline control for subsequent voxel-wise comparison of ICH or control PET scans with the normal brain atlas. Animals were individually housed under controlled conditions (12/12 h light/dark cycle, temperature 20–24°C and relative humidity 40–60%) and handled over a period of 6 days for 10 min per day to reduce stress during the experimental procedures. Animals received food and water *ad libitum* and were fasted during the nights before [18F]-FDG PET scanning. The animals were treated according to the European guidelines (directive 2010/63/EU) and the protocol was approved by the local Ethical Committee on Animal Experiments of Ghent University (ECD 19/80).

Scanning Procedures

Animals were food deprived for at least 12 h before tracer injection to lower their blood glucose level (6), so that [18F]-FDG would not compete with endogenous glucose uptake via GLUT-transporters in the brain. 32.5 ± 7.8 MBq [18F]-FDG was administered intravenously into one of the lateral saphenous tail veins under short anesthesia (2% isoflurane and oxygen mixture). Immediately afterwards, animals were awakened and placed in a heated cage, to reduce tracer uptake in brown fat. The cage was placed inside a dark room, to minimize uptake into the Harderian glands, reducing spill-over effects from these glands to the brain.

After 60 min of tracer uptake, a 15 min static PET scan was acquired (β -cube, Molecubes NV, Ghent, Belgium) under general anesthesia (2% isoflurane and oxygen mixture) and using a heated animal bed. PET data were iteratively reconstructed with Molecubes β -Cube software (Version 1.5.7) by an Ordered Subset Expectation Maximization (OSEM) algorithm using 30 iterations and 1 subset into a $196 \times 196 \times 384$ matrix with a voxel size of 400 μ m. An energy window of 30% centered on the 511 keV photopeak was used. The voxel values in these reconstructed images were expressed as kBq/cc and were converted to SUVs. SUVs were voxel-wise calculated as follows: $\frac{C_i}{D/W}$, where C_i represents the radioactivity concentration (kBq/cc) measured by the PET scanner in voxel i , D is the decay-corrected injected [18F]-FDG activity (kBq) and W is the weight of the animal (g).

Afterwards, TurboRARE T2-weighted magnetic resonance imaging (MRI) was performed on a 7T system (PharmaScan 70/16, Bruker, Germany) under general anesthesia using a transmit/receive volume coil with 40 mm inner diameter (Bruker, Germany). A circulating-water heating pad and a pressure sensor were used to maintain the animals' body temperature and monitor their respiratory rhythm, respectively. After optimizing

the magnetic field homogeneity the following acquisition parameters were used: repetition time 3,700 ms, echo time 37 ms, in-plane slice resolution $109 \times 109 \mu\text{m}^2$, 30 contiguous slices of $600 \mu\text{m}$ thickness, matrix size 320×320 , 4 averages, resulting in a total acquisition time of 9 min.

Normal Rat Brain Atlas

Pre-processing

The reconstructed PET images were preprocessed using a four-step procedure: converting, cropping, filtering and coregistration. First, the reconstructed PET DICOM images were converted to NIfTI format using the MRtrix3 (14) command *mrconvert*. In the second preprocessing step, images were cropped into a $80 \times 80 \times 80$ matrix ($32 \times 32 \times 32$ mm field-of-view) to only visualize the brain using the MRtrix3 command *mrccrop*. The cropped images were then smoothed by a Gaussian filter with a full width at half maximum (FWHM) of 1 mm using the MRtrix3 command *mrfilter*. Finally, all converted, cropped and filtered PET images were geometrically aligned by non-linear coregistration using the *population_template* command in MRtrix3, which generated an initial brain atlas template by voxel-wisely averaging all coregistered images ($n = 28$).

Normalization Procedures

The acquired, reconstructed, converted, cropped, filtered, and coregistered images were normalized via different procedures in order to compare the variability of voxel intensities in the brain across the normalized PET images. After each normalization method, voxel-wise calculations of the mean and standard deviation across the images were performed by *mrmath* in MRtrix3. Next, coefficient-of-variation (CoV) maps were generated by voxel-wise calculation of: $\sigma_i/\mu * 100\%$, with μ_μ and

σ_σ being the mean and standard deviation across all normalized PET images in voxel i .

Data-Driven Histogram-Based Normalization

Each individually converted, cropped, filtered, and coregistered PET image was voxel-wisely divided by the initial brain atlas template using the MRtrix3 command *mrcalc*. The resulting ratio image was used to generate a histogram of the voxel-wisely calculated ratios, only including ratios within the normal brain region. The normal brain region was defined as all voxels with voxel intensities larger than 50% of the maximum [18F]-FDG brain uptake on the initial brain template.

The maximum of the histogram, which represents the most prevalent ratio in the brain, was used as normalization factor. Each individually converted, cropped, filtered, and coregistered PET image was divided by this normalization factor using *mrcalc*. Subsequently, the final normal [18F]-FDG rat brain atlas was generated by voxel-wisely calculating the average and standard deviation of all histogram-based normalized PET images using *mrmath*.

Global Mean Scaling

Global mean scaling, or whole-brain normalization, was performed by scaling the images to the average [18F]-FDG uptake value in the whole brain. The whole brain region was defined as all voxels with voxel intensities larger than 50% of the maximum [18F]-FDG brain uptake on the initial brain template. The mean SUV value inside this brain region was calculated for each PET image individually and used as normalization factor.

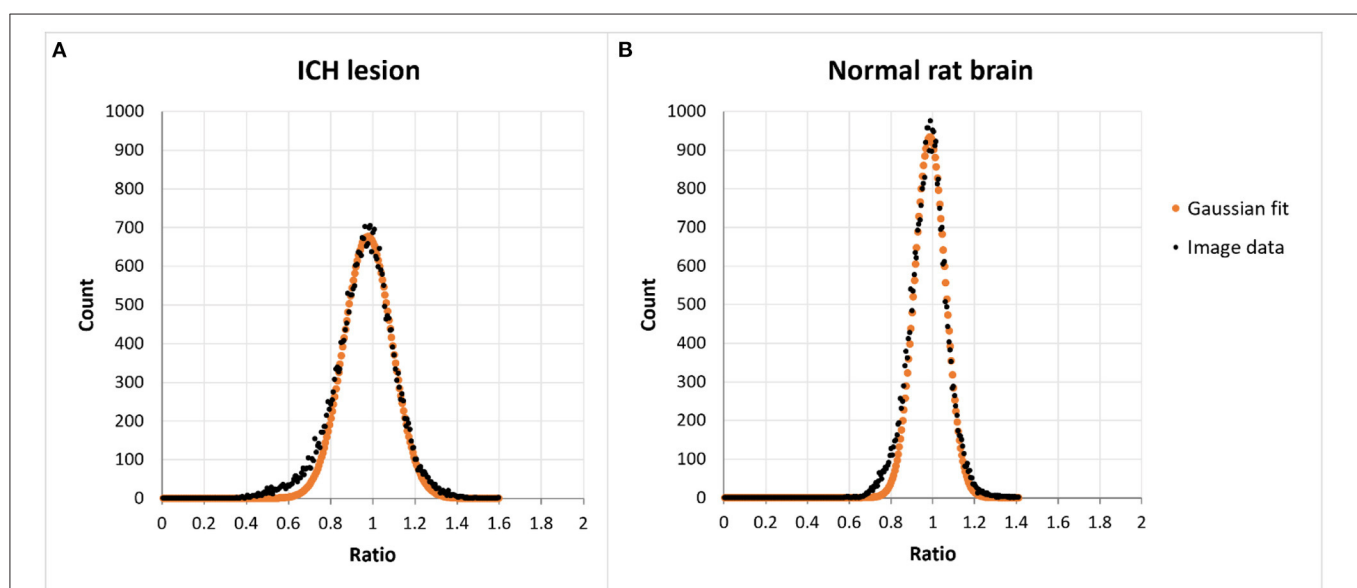


FIGURE 1 | Histograms of the voxel values present in ratio-images obtained by voxel-wise dividing a PET image with the normal rat brain atlas template obtained from (A) an animal with an ICH lesion and (B) a normal [18F]-FDG rat brain scan. In animals with a lesion there is a higher prevalence of lower ratios without affecting the peak position.

No Normalization

Lastly, the converted, cropped, filtered, and coregistered images were further analyzed without performing any normalization and with voxel values expressed as SUVs.

ICH Animal Model

ICH Induction

In nine animals, an ICH was induced by striatal injection of 0.6U collagenase (type VII-S, C2399, Sigma-Aldrich) dissolved in 0.7 μ l saline (AP 0.5, ML 3.5, DV 6.0 mm relative to Bregma). Nine other animals were injected with 0.7 μ l saline as a control. The injections were performed under general anesthesia (2% isoflurane and oxygen mixture) using a Neuro-Syringe (model 7001, point style 4, Hamilton) and a Quintessential Stereotaxic Injection system (Stoelting, IL, USA), at a flowrate of 0.14 μ l/min. After injection, the syringe was left in place for an additional 5 min to prevent backflow.

Preprocessing and Histogram-Based Normalization

One day after inducing ICH, [18F]-FDG PET scans were acquired using the same imaging procedure as described above. The acquired PET scans were also preprocessed as described above. After reconstruction, conversion to NIFTI format, cropping, 1 mm Gaussian filtering and coregistration on the generated normal rat brain atlas, ratio images were calculated by voxel-wisely dividing the individual post-ICH or post-saline [18F]-FDG PET images by the normal rat brain atlas template. The post-ICH or post-saline images were then normalized using the most prevalent ratio within the normal brain region obtained from the normal rat brain atlas.

Voxel-Wise Analysis

Group Analysis

After preprocessing and normalization, post-ICH ($n = 9$) or post-saline injection ($n = 9$) images were voxel-wisely compared to the normal [18F]-FDG rat brain images ($n = 28$) using group-level analysis. Voxel-wise t -test statistics with False Discovery Rate (FDR) based correction for multiple comparisons ($p < 0.05$) were calculated in the Statistical Parametric Mapping software tool (SPM12 version 7771). The results of this group analysis were overlaid on T2-weighted average templates of the ICH or control animals, which were generated by the *popultion_template* command in MRtrix3. Overlays were made with PMOD software (PMOD Technologies version 3.405, Zürich, Switzerland).

Individual Analysis

Individual histogram-based normalized images of ICH and control animals were transformed into Z-score maps by voxel-wise calculation of Z-score statistics: $z = \frac{x_i - \mu_i}{\sigma_i}$, where μ and σ represent the mean and standard deviation of voxel i in the normal database and x is the voxel value of voxel i in the coregistered and normalized PET scan of an ICH or control animal. A 95% confidence interval was calculated for all Z-scores in the brain and Z-score maps were subsequently thresholded to only show Z-scores outside of this confidence interval, representing the 2.5% lowest and 2.5% highest values in

the images. The final thresholded Z-score images were overlaid on T2-weighted average templates in PMOD.

RESULTS

Histogram-Based Normalization

As described above, histograms of ratios, obtained by voxel-wisely dividing [18F]-FDG PET images by the normal rat brain atlas template, were generated for the calculation of a normalization factor. **Figure 1** shows the histograms obtained from a post-ICH (A) and of a normal (B) [18F]-FDG PET image. Black dots represent the prevalence of a particular ratio, whereas the orange dots represent a Gaussian curve that fits through these histogram data.

The image of the ICH animal shows somewhat higher prevalence of lower ratios (0.4–0.8) and lower counts around the maximum of the histogram as compared to the normal image. The peak of the histogram, representing the most prevalent ratio, is centered around the value of one in both images.

[18F]-FDG Normal Rat Brain Atlas

The generation of a histogram-based normalized normal brain atlas was feasible and straightforward using MRtrix3 software. **Figure 2** shows the normal rat brain atlas after histogram-based intensity normalization. Voxel-wise coefficients of variation in this atlas, representing the relative variability between voxel values across all images in the normal rat brain atlas, are shown in **Figure 3**.

As shown in **Table 1**, the mean CoV in the brain after histogram-based normalization was $6.71 \pm 2.05\%$, which is 78% lower than when the images were not normalized. In the latter case, when non-normalized SUV images were used to generate a normal rat brain atlas, the mean CoV in the brain was $31.17 \pm 1.54\%$. The mean CoV after histogram-based normalization was 42% lower compared to the whole brain normalization method (mean CoV: $11.61 \pm 1.41\%$).

Voxel-Wise Statistical Analysis

The PET images of nine ICH animals and nine control animals were preprocessed and normalized in the same way as the images of the normal brain atlas. Statistical voxel-wise comparisons of [18F]-FDG images post-ICH with the normal rat brain atlas were performed on a group level to visualize regions of significantly increased or decreased glucose uptake after correction for multiple comparisons. **Figure 4** shows the resulting images of this group analysis after histogram-based normalization. The analysis clearly shows a region of significantly decreased glucose uptake at the site of the ICH lesion (**Figure 4A**). No significant regions were observed when comparing [18F]-FDG images of control animals to the normal rat brain atlas (**Figure 4B**).

The generation of Z-score maps and subsequent thresholding by a 95% confidence interval, resulted in the visualization of regions with significantly increased or decreased glucose metabolism compared to the normal rat brain template on an individual level. **Figure 5** shows the thresholded Z-map of an ICH animal (A) and of a control animal (B) overlaid on the corresponding T2 templates. In the ICH animal, a clear

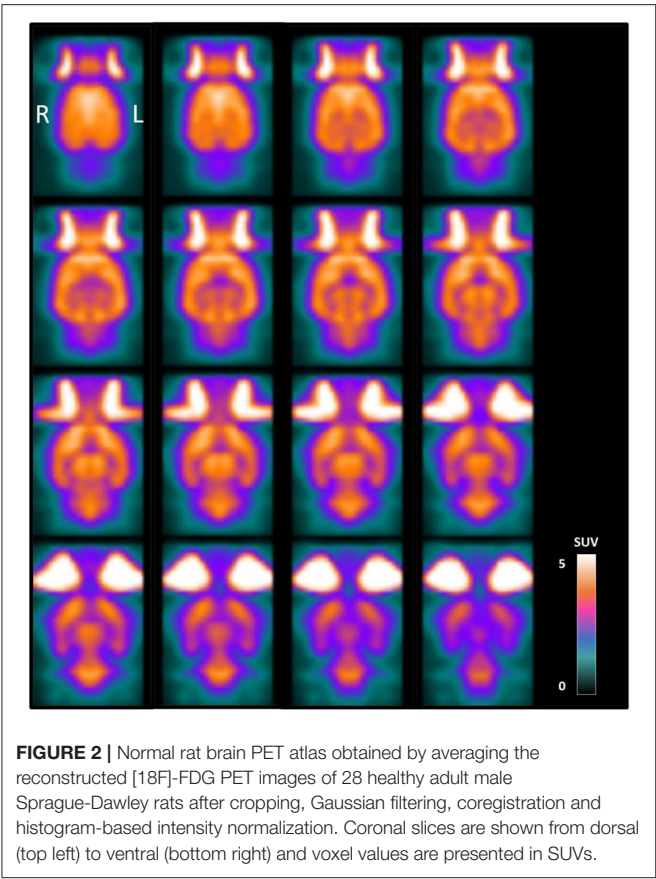


FIGURE 2 | Normal rat brain PET atlas obtained by averaging the reconstructed [18F]-FDG PET images of 28 healthy adult male Sprague-Dawley rats after cropping, Gaussian filtering, coregistration and histogram-based intensity normalization. Coronal slices are shown from dorsal (top left) to ventral (bottom right) and voxel values are presented in SUVs.

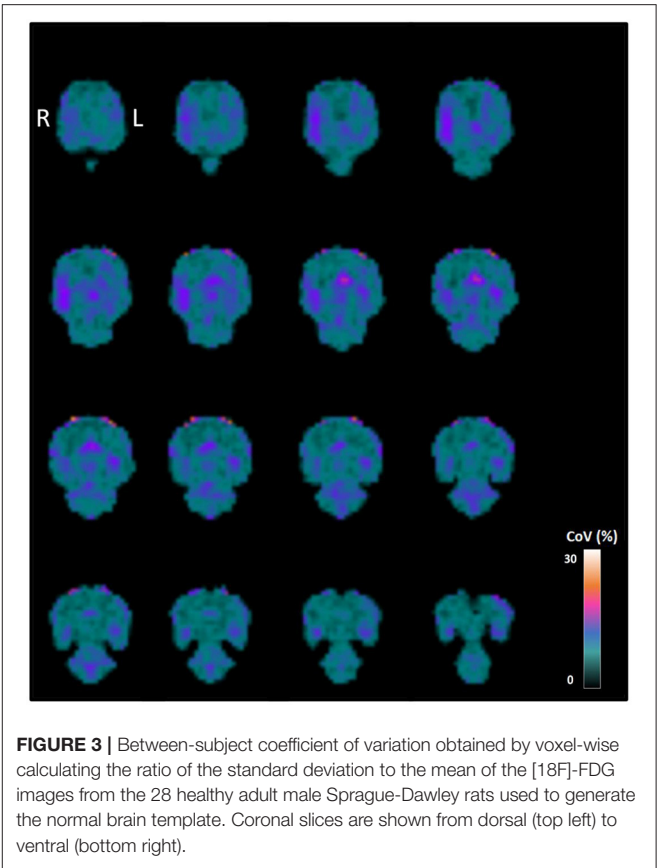


FIGURE 3 | Between-subject coefficient of variation obtained by voxel-wise calculating the ratio of the standard deviation to the mean of the [18F]-FDG images from the 28 healthy adult male Sprague-Dawley rats used to generate the normal brain template. Coronal slices are shown from dorsal (top left) to ventral (bottom right).

TABLE 1 | Mean CoV values in the brain for the different PET templates.

Normalization method	CoV (%)
Histogram-based	6.71 ± 2.05
Global mean scaling	11.61 ± 1.41
No normalization	31.17 ± 1.54

region of decreased glucose uptake is visible at the site of the lesion. In the control animal, no such regions of significantly increased or decreased glucose uptake are visible. Instead, the voxels representing the lowest 2.5% and highest 2.5% of voxel values in the brain, are sparsely distributed across the brain, as would be expected.

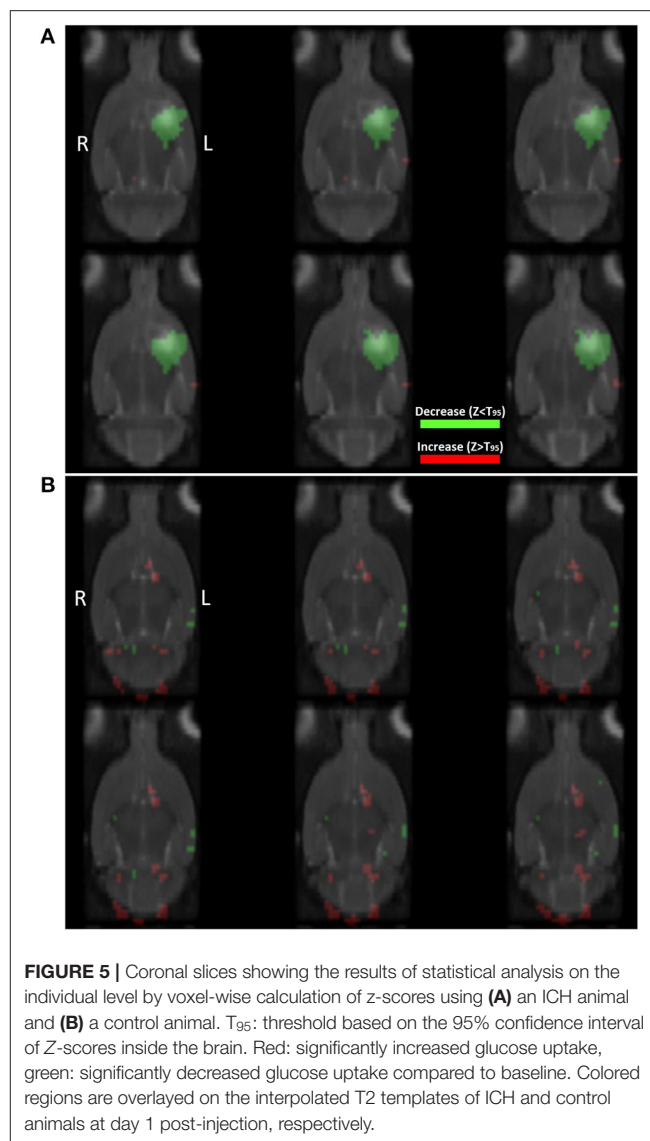
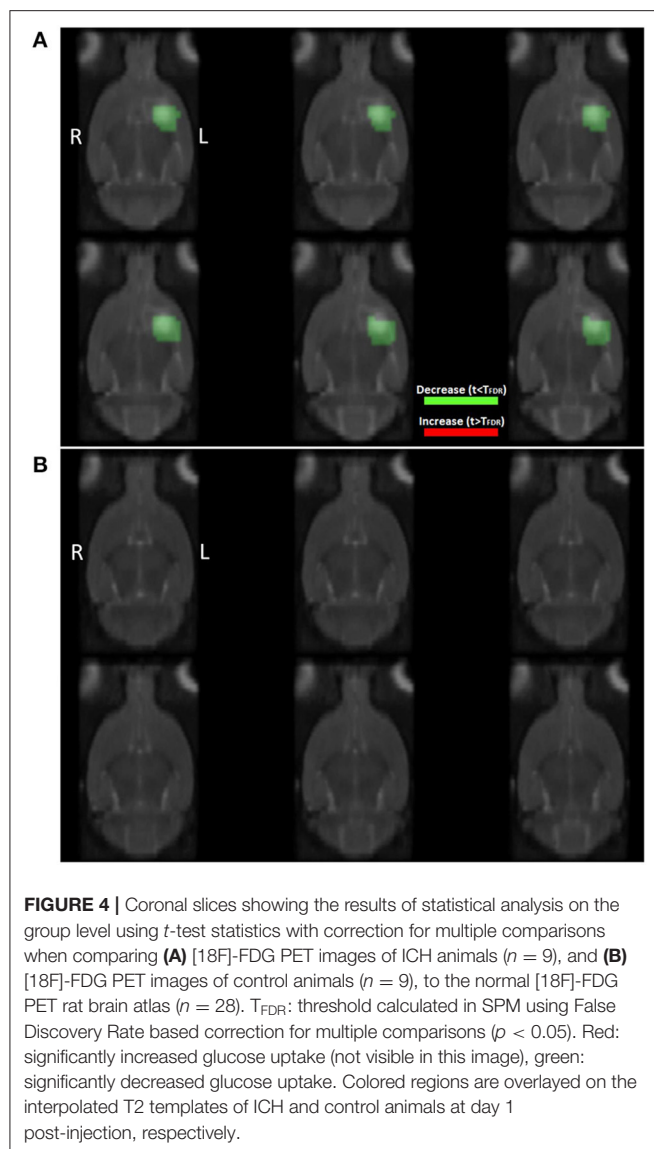
DISCUSSION

The goals of this study were 2-fold: (1) to present a workflow for the creation of a normal [18F]-FDG PET rat brain atlas based on a data-driven histogram-based approach for intensity normalization, and (2) to use these data-driven normalized data in a voxel-wise statistical analysis to detect significant changes in glucose uptake in a rat model for ICH when compared to the normal rat brain template. As our data shows, histogram-based intensity normalization seems to be an accurate approach

to detect changes in glucose metabolism in the rat brain using a normal database.

Recent ground truth-based research by López-González et al. (8) investigated the effect of different PET normalization methods on the detection of simulated hypometabolic patterns. As the authors of this study have shown, under- or overestimation of the normalization factor can lead to significant differences in PET interpretation, demonstrating the importance of accurate and appropriate use of intensity normalization methods. Indeed, normalization is essential for accurate PET analysis, which was clearly demonstrated by the high CoV ($31.17 \pm 1.54\%$) in our analysis when no normalization was performed on the imaging data.

The high CoV across non-normalized SUV images might lie in the fact that the SUV measure is highly influenced by inter- and intra-variable factors. SUVs are calculated as the measured radioactivity concentration in a voxel multiplied with the subject's weight and divided by the decay-corrected injected tracer dose (5). However, [18F]-FDG uptake in the brain is affected by many other factors, besides the injected dose and subject's weight. For example, biological factors such as blood glucose level, gender and age, and methodological issues such as scanner calibration and tracer spill or backflow while injecting, may severely influence SUV-based quantification (15–17). Several SUV correction methods have been used to decrease inter- and intra-animal variability, such as correction



for pre- or post-scan blood glucose level or serum corticosterone concentration (6). Still, inter-animal CoV varies between 9.57 and 69.11% depending on the SUV correction factor that is used (6), again indicating the influence of different PET normalization or quantification methods on result interpretation.

Common intensity normalization methods include the use of a reference region or data-driven approaches. Regions such as the cerebellum, pons, white matter and primary sensorimotor cortex have been used as reference region in different types of diseases (9, 18, 19). However, normalization based on a reference could be biased by the choice of the reference area, which should not be affected by the disease that is studied (8, 9). Thus, the size and location of a reference region should be very carefully chosen depending on the disease state. One of the most widely employed methods of data-driven normalization is global mean scaling, where the average brain uptake value is used as reference. Depending on the brain region, the mean CoV

is expected to be around 7.7–9.9% for whole-brain normalized images (20). In our study, the CoV across all PET global mean-normalized images was similar ($11.61 \pm 1.41\%$). However, as seen in our histogram data, glucose uptake alterations in pathological situations might induce bias when using this normalization method. This might lead to underestimation of the normalization factor and visualization of unspecific regions of altered glucose uptake (8).

The disadvantages of the abovementioned methods have led to the development of new data-driven methods of intensity normalization, which are thought to induce less bias during PET analysis (8, 21–23). In the histogram-based intensity normalization method, ratio images are generated by voxel-wisely dividing coregistered PET images by a normal database template. When histograms of these ratios are generated, the maximum of the histogram that represent the most prevalent ratio is chosen as normalization factor. In our study, histograms

of [18F]-FDG images post-ICH showed a higher prevalence of lower ratios (0.4–0.8) than the histograms of normal [18F]-FDG rat brain scans. As mentioned above, these lower values in the image might have an effect on the global whole brain uptake and could thus induce bias when using normalization methods based on global mean scaling. The most prevalent values in the histograms, which were centered around 1, were unaffected by these lower ratio values, demonstrating that the histogram-based procedure might be a more robust method of intensity normalization. The much lower CoV ($6.71 \pm 2.05\%$) found after histogram-based normalization across normal [18F]-FDG rat brain scans as compared to global mean scaling or no normalization, also indicates that our results are influenced to a much lesser extent by intersubject variability when using this intensity normalization method.

Voxel-wise statistical comparisons between [18F]-FDG PET scans of ICH animals and the normal rat brain atlas clearly showed a region of decreased PET signal at the site of the lesion. Both the group-level and individual-level analysis methods proved to be feasible after histogram-based intensity normalization, since no clear regions of significantly altered glucose uptake were found when comparing [18F]-FDG PET scans of control animals to the normal database.

Although this study is situated in the preclinical field, the methodology and analysis procedures are translatable to clinical research. In this study, a workflow of PET atlas generation was proposed using a recent intensity normalization technique, yielding good results. In the future, it might be advantageous to construct gender- and age-specific atlases as a way to ameliorate diagnosis, prognosis, and response evaluation in the clinic. Similarly, gender-, age-, and strain-specific atlases for different animal models could be developed in a preclinical setting. In this way, individual as well as group analyses of pathological PET alterations compared to normal [18F]-FDG uptake, could be tailored to the biological characteristics of the subjects in question.

There are some limitations to this study. First, only male rats were used in the experimental procedures. Thus, the results of this study cannot be generalized to female rats. This choice was made because of the potential effects of the estrous cycle on PET changes in female rats (24, 25). As stated above, experimental as

well as clinical research could benefit from sex-specific normal PET atlases for subsequent analysis. Second, there was some variability in injected [18F]-FDG dose (32.5 ± 7.8 MBq) due to variations in daily [18F]-FDG availability in our facility. However, before any normalization method was performed, PET voxel-values in kBq/cc were converted to SUVs as a correction for injected dose and animal weight.

In conclusion, histogram-based intensity normalization is a useful data-driven technique for PET normalization and reduces the inter-subject variability compared to the commonly used global mean scaling method and no normalization. This approach is suitable for voxel-wise statistical analysis of glucose uptake changes compared to a normal brain atlas, on an individual as well as on a group level. This work highlights the importance of the harmonization of intensity normalization of [18F]-FDG PET images for subsequent voxel-wise analysis.

DATA AVAILABILITY STATEMENT

The raw data supporting the conclusions of this article will be made available by the authors, without undue reservation.

ETHICS STATEMENT

The animal study was reviewed and approved by the Ethical Committee on Animal Experiments of Ghent University.

AUTHOR CONTRIBUTIONS

SP, RR, BD, PB, VD, and CV: study design. SP: experimental work and data collection. CG: development of animal model. SP, RR, EC, VD, and CV: data analysis. SP, RR, VD, and CV: manuscript preparation. All authors manuscript review.

FUNDING

SP was supported by the Ghent University Special Research Fund (BOF, 01D27418). RR was supported by the BOF, CG, and EC were supported by the Research Foundation Flanders (FWO, 1181719N and 1S90218N). PB was supported by the FWO, BOF and Ghent University. VD was supported by Ghent University.

REFERENCES

- Schöll M, Damián A, Engler H. Fluorodeoxyglucose PET in neurology and psychiatry. *PET Clin.* (2014) 9:371–90. doi: 10.1016/j.cpet.2014.07.005
- Boellaard R. Need for standardization of 18F-FDG PET/CT for treatment response assessments. *J Nucl Med.* (2011) 52:93–100. doi: 10.2967/jnumed.110.085662
- Varrone A, Asenbaum S, Vander Borght T, Booij J, Nobili F, Någren K, et al. EANM procedure guidelines for PET brain imaging using [18F]FDG, version 2. *Eur J Nucl Med Mol Imaging.* (2009) 36:2103–10. doi: 10.1007/s00259-009-1264-0
- Ohta Y, Nariai T, Ishii K, Ishiwata K, Mishina M, Senda M, et al. Voxel- and ROI-based statistical analyses of PET parameters for guidance in the surgical treatment of intractable mesial temporal lobe epilepsy. *Ann Nucl Med.* (2008) 22:495–503. doi: 10.1007/s12149-008-0140-5
- Kinahan PE, Fletcher JW. Positron emission tomography-computed tomography standardized uptake values in clinical practice and assessing response to therapy. *Semin Ultrasound, CT MRI.* (2010) 31:496–505. doi: 10.1053/j.sult.2010.10.001
- Deleye S, Verhaeghe J, wyffels L, Dedeurwaerdere S, Stroobants S, Staelens S. Towards a reproducible protocol for repetitive and semi-quantitative rat brain imaging with 18 F-FDG: Exemplified in a memantine pharmacological challenge. *Neuroimage.* (2014) 96:276–87. doi: 10.1016/j.neuroimage.2014.04.004
- Berti V, Mosconi L, Pupi A. Brain: normal variations and benign findings in FDG PET/CT imaging. *PET Clin.* (2014) 9:129–40. doi: 10.1016/j.cpet.2013.10.006
- López-González FJ, Silva-Rodríguez J, Paredes-Pacheco J, Niñerola-Baizán A, Efthimiou N, Martín-Martín C, et al. Intensity normalization

- methods in brain FDG-PET quantification. *Neuroimage*. (2020) 222:117229. doi: 10.1016/j.neuroimage.2020.117229
9. Borghammer P, Jonsdottir KY, Cumming P, Ostergaard K, Vang K, Ashkanian M, et al. Normalization in PET group comparison studies—the importance of a valid reference region. *Neuroimage*. (2008) 40:529–40. doi: 10.1016/j.neuroimage.2007.12.057
 10. Nobili F, Festari C, Altomare D, Agosta F, Orini S, Van Laere K, et al. Automated assessment of FDG-PET for differential diagnosis in patients with neurodegenerative disorders. *Eur J Nucl Med Mol Imaging*. (2018) 45:1557–66. doi: 10.1007/s00259-018-4030-3
 11. Della Rosa PA, Cerami C, Gallivanone F, Prestia A, Caroli A, Castiglioni I, et al. A standardized [18F]-FDG-PET template for spatial normalization in statistical parametric mapping of dementia. *Neuroinformatics*. (2014) 12:575–93. doi: 10.1007/s12021-014-9235-4
 12. Patterson JC, Lilien DL, Takalkar A, Pinkston JB. Early detection of brain pathology suggestive of early AD using objective evaluation of FDG-PET scans. *Int J Alzheimers Dis*. (2011) 2011:1–9. doi: 10.4061/2011/946590
 13. Daniel Slater J, Eduardo Betting L, Meng F, Wang K, Liu T, Zhao X, et al. Comparative study of voxel-based epileptic foci localization accuracy between statistical parametric mapping and three-dimensional stereotactic surface projection. *Neurol*. (2016) 7:164. doi: 10.3389/fneur.2016.00164
 14. Tournier J-D, Smith R, Raffelt D, Tabbara R, Dhollander T, Pietsch M, et al. MRtrix3: A fast, flexible and open software framework for medical image processing and visualisation. *Neuroimage*. (2019) 202:116137. doi: 10.1016/j.neuroimage.2019.116137
 15. Busk M, Munk OL, Jakobsen S, Frøkiær J, Overgaard J, Horsman MR, et al. reproducibility in tumor-bearing mice: comparing a traditional SUV approach with a tumor-to-brain tissue ratio approach. *Acta Oncol*. (2017) 56:706–12. doi: 10.1080/0284186X.2016.1276620
 16. Fahey FH, Kinahan PE, Doot RK, Kocak M, Thurston H, Poussaint TY. Variability in PET quantitation within a multicenter consortium. *Med Phys*. (2010) 37:3660–6. doi: 10.1118/1.3455705
 17. Adams MC, Turkington TG, Wilson JM, Wong TZ. A systematic review of the factors affecting accuracy of SUV measurements. *Am J Roentgenol*. (2010) 195:310–20. doi: 10.2214/AJR.10.4923
 18. Borghammer P. Perfusion and metabolism imaging studies in Parkinson's disease. *Dan Med J*. (2012) 59:B4466.
 19. Yakushev I, Landvogt C, Buchholz H-G, Fellgiebel A, Hammers A, Scheurich A, et al. Choice of reference area in studies of Alzheimer's disease using positron emission tomography with fluorodeoxyglucose-F18. *Psychiatry Res Neuroimaging*. (2008) 164:143–53. doi: 10.1016/j.pscychresns.2007.11.004
 20. Casteels C, Vunckx K, Aelvoet SA, Baekelandt V, Bormans G, van Laere K, et al. Construction and evaluation of quantitative small-animal PET probabilistic atlases for [18F]FDG and [18F]FECT functional mapping of the mouse brain. *PLoS ONE*. (2013) 8:e65286. doi: 10.1371/journal.pone.0065286
 21. Borghammer P, Aanerud J, Gjedde A. Data-driven intensity normalization of PET group comparison studies is superior to global mean normalization. *Neuroimage*. (2009) 46:981–8. doi: 10.1016/j.neuroimage.2009.03.021
 22. Zhang H, Wu P, Ziegler SI, Guan Y, Wang Y, Ge J, et al. Data-driven identification of intensity normalization region based on longitudinal coherency of 18F-FDG metabolism in the healthy brain. *NeuroImage*. (2017) 146:589–99. doi: 10.1016/j.neuroimage.2016.09.031
 23. Nie B, Liang S, Jiang X, Duan S, Huang Q, Zhang T, et al. An automatic method for generating an unbiased intensity normalizing factor in positron emission tomography image analysis after stroke. *Neurosci Bull*. (2018) 34:833–41. doi: 10.1007/s12264-018-0240-8
 24. Sijbesma JWA, Van Waarde A, García DV, Boersma HH, Slart RHJA, Dierckx RAJO, et al. Test-retest stability of cerebral 2-Deoxy-2-[18F]Fluoro-D-Glucose ([18F]FDG) positron emission tomography (PET) in male and female rats. *Mol Imaging Biol*. (2019) 21:240–8. doi: 10.1007/s11307-018-1245-4
 25. Moraga-Amaro R, Van Waarde A, Doorduyn J, De Vries EFJ. Sex steroid hormones and brain function: PET imaging as a tool for research. *J Neuroendocrinol*. (2018);30:e12565. doi: 10.1111/jne.12565

Conflict of Interest: The authors declare that the research was conducted in the absence of any commercial or financial relationships that could be construed as a potential conflict of interest.

Publisher's Note: All claims expressed in this article are solely those of the authors and do not necessarily represent those of their affiliated organizations, or those of the publisher, the editors and the reviewers. Any product that may be evaluated in this article, or claim that may be made by its manufacturer, is not guaranteed or endorsed by the publisher.

Copyright © 2021 Proesmans, Raedt, Germonpré, Christiaen, Descamps, Boon, De Herdt and Vanhove. This is an open-access article distributed under the terms of the Creative Commons Attribution License (CC BY). The use, distribution or reproduction in other forums is permitted, provided the original author(s) and the copyright owner(s) are credited and that the original publication in this journal is cited, in accordance with accepted academic practice. No use, distribution or reproduction is permitted which does not comply with these terms.



Translation of Preclinical PET Imaging Findings: Challenges and Motion Correction to Overcome the Confounding Effect of Anesthetics

Alan Miranda¹, Daniele Bertoglio¹, Sigrid Stroobants^{1,2}, Steven Staelens¹ and Jeroen Verhaeghe^{1*}

¹ Molecular Imaging Center Antwerp, University of Antwerp, Antwerp, Belgium, ² University Hospital Antwerp, Antwerp, Belgium

OPEN ACCESS

Edited by:

Adriana Tavares,
University of Edinburgh,
United Kingdom

Reviewed by:

Takuya Toyonaga,
Yale University, United States
Kritika Subramanian,
Weill Cornell Medicine, United States

*Correspondence:

Jeroen Verhaeghe
jeroen.verhaeghe@uantwerpen.be

Specialty section:

This article was submitted to
Nuclear Medicine,
a section of the journal
Frontiers in Medicine

Received: 05 August 2021

Accepted: 27 September 2021

Published: 22 October 2021

Citation:

Miranda A, Bertoglio D, Stroobants S,
Staelens S and Verhaeghe J (2021)
Translation of Preclinical PET Imaging
Findings: Challenges and Motion
Correction to Overcome the
Confounding Effect of Anesthetics.
Front. Med. 8:753977.
doi: 10.3389/fmed.2021.753977

Preclinical brain positron emission tomography (PET) in animals is performed using anesthesia to avoid movement during the PET scan. In contrast, brain PET scans in humans are typically performed in the awake subject. Anesthesia is therefore one of the principal limitations in the translation of preclinical brain PET to the clinic. This review summarizes the available literature supporting the confounding effect of anesthesia on several PET tracers for neuroscience in preclinical small animal scans. In a second part, we present the state-of-the-art methodologies to circumvent this limitation to increase the translational significance of preclinical research, with an emphasis on motion correction methods. Several motion tracking systems compatible with preclinical scanners have been developed, each one with its advantages and limitations. These systems and the novel experimental setups they can bring to preclinical brain PET research are reviewed here. While technical advances have been made in this field, and practical implementations have been demonstrated, the technique should become more readily available to research centers to allow for a wider adoption of the motion correction technique for brain research.

Keywords: positron emission tomography, preclinical, brain, anesthesia, motion correction

INTRODUCTION

Positron emission tomography (PET) is a molecular imaging technique that allows to quantify the distribution of radiolabeled biomolecules in the living body. In the clinic, PET is commonly used for diagnostic workup and treatment monitoring in fields like oncology, neurology, or cardiology (1–4). In addition, PET is a valuable tool for clinical as well as fundamental research in these fields as it allows to investigate molecular mechanisms of several diseases or drugs and their efficacy.

Preclinical PET, commonly performed in non-human primates and rodents to help development and validation of novel radiotracers, investigate molecular mechanisms of disease in animal models, test drug safety, efficacy, and response to treatments. In contrast to PET in humans, animal scans are usually performed using anesthesia to maintain the animal still during the scan. Propofol, ketamine, and isoflurane are some of the most common anesthetics used for animal immobilization in preclinical PET (5). Unfortunately these compounds can have a pharmacological effect, affecting physiological parameters such as body temperature and cerebral blood flow, which in turn can

affect the pharmacokinetics of a radiotracer (6). In addition, these anesthetics have been proven to work principally by interaction with neurotransmitter systems (7), which, for many neurological studies, are in fact the object of study. Because of these effects, the use of anesthesia in preclinical brain PET studies can be considered a confounding factor, and one of the principal limitations for translation of preclinical results to the clinic (8).

Several studies have investigated the effect of anesthesia on preclinical brain PET for many different anesthetics and tracers in the context of brain PET imaging. In the following sections these studies are summarized. In the second part we discuss motion correction solutions to circumvent the use of anesthesia in preclinical brain PET. Motion correction techniques offer the advantage of being potentially adaptable to common preclinical PET scanners, as well as allowing free animal motion.

ANESTHESIA AS A CONFOUNDING FACTOR IN PRECLINICAL PET STUDIES

The first use of anesthetics dates back to the nineteenth century (7), however, despite being used for more than 100 years, it is only since the last decades that research on their molecular mechanisms of action has been possible thanks to the development of advanced techniques. Nonetheless, fundamental aspects of their mechanisms of action still need to be elucidated (9).

Molecular Effects of General Anesthesia

Several hypotheses on the mechanisms of action of anesthetic agents have been formulated from the observation that the potency of anesthetic agents increased in proportion to its solubility in lipids. These theories stipulated that anesthetic agents changed the properties of the membrane lipid bilayer, such as its permeability, fluidity, and dimensions (10). Many of these theories were proved inconsistent with experimental results and were discarded. Although the focus has been shifted to the interaction of anesthetics with voltage and ligand gated ion-channels (see below), recent research has pointed again to the interaction of anesthetics with the cellular membrane, but instead of acting on the membrane bulk, it has been suggested that the interaction occurs at membrane rafts (11). Rafts are regions of ordered lipids (e.g., cholesterol, sphingolipids, and phospholipids) in the membrane, which in contrast to the more fluid bulk of the bilayer, are more rigid (12). Several ion channels associate with membrane drafts and it is believed that the interaction with these rafts can regulate the channel physiology (12). In a study by Pavel et al. (11), it is shown that anesthesia (e.g., chloroform and isoflurane) induced disruption of membrane rafts associated with the 2-pore domain K^+ channel TREK-1, a mechano-, and thermo-sensitive K^+ channel. This disruption activates this channel, which in turn affects anesthesia potency. This theory was further validated using TREK-1 knock-out mice. These mice displayed more resistance to anesthetics compared to control animals as measured by the onset time of anesthesia action, the loss of righting reflex, and the inspired minimum alveolar anesthetic concentration (11, 13).

As mentioned above, other mechanisms of action involve the direct interaction of anesthetics with voltage-gated and ligand-gated ion channels, the latter being the most frequent case (7, 9). For example, the anesthetic ketamine is an antagonist of the glutamatergic N-methyl-D-aspartate (NMDA) receptor, inhibiting glutamate binding to the receptor. However, it is not clear if blocking of the NMDA receptor is the main mechanism of action of anesthetics targeting this receptor (14). Using dizocilpine (MK 801), a more potent NMDA receptor antagonist than ketamine, no hypnotic effect is observed, suggesting that NMDA receptor antagonism is not the main mechanism of action of ketamine. Other receptors, such as nicotinic acetylcholine (nACh) receptors and cyclic nucleotide-gated potassium channels are other targets of ketamine that may play an important role in its anesthetic effect (14).

Another receptor targeted by anesthetic agents is the γ -aminobutyric acid type A (GABA_A) receptor. Several anesthetics (such as propofol, isoflurane, and halothane) are known to interact with the GABA_A receptor (15) and potentiate its inhibitory effect. GABA_A is composed of several subunits such as α , β , and γ subunits. Using knock-out mouse models lacking one of these subunits, it has been found that some anesthetics act particularly on only some of these subunits. For example, in β_3 knock-out mice the immobilization effect of the anesthetics enflurane and halothane was decreased (15), while the effect of isoflurane remained unchanged (16). The effect on the GABA_A receptor also depends on its location on the neuron. While synaptic GABA_A receptors respond to fast, transient inhibitory currents in response to presynaptic GABA release, extra-synaptic GABA_A receptors, located on the non-synaptic membrane, respond to low, ambient concentrations of GABA, producing a persistent inhibitory current (9). Interaction with extra-synaptic GABA_A receptors is thought to be responsible for the memory-related effects of anesthetic agents, since a low concentration of anesthetics can cause amnesia, but not immobilization. Moreover, anesthetics such as isoflurane and etomidate are attributed to increase cell surface expression of GABA_A receptors by change in extra-synaptic GABA_A receptor trafficking, effect which is associated with long-term cognitive changes (17).

Altogether, evidence suggest that anesthetics act by interacting with several voltage- and ligand-gated ion channels, and the different anesthetic effects (e.g., analgesia, hypnosis, and immobility) might be mediated by different receptors. Moreover, studies of gene expression changes caused by anesthetics (18) might give a better insight on their mechanisms of action. The reader is referred to reviews focusing on the molecular mechanisms of action of anesthetics for a more complete insight on the topic (7, 9, 10, 14, 15, 19).

Effects of Anesthesia in Brain PET

The interaction of anesthetics on neuroreceptors and membrane permeability in the central and peripheral nervous system results in important physiological changes, including respiratory rate, cardiovascular function, and glucose metabolism (8). For instance, pentobarbital induces respiratory depression and reduced blood pressure in rodents (8). Ketamine administration

causes muscle rigidity, and respiratory depression (20), while ketamine/xylazine reduces heart rate (21). Isoflurane depresses respiration without altering cardiac function (22), and increases cerebral blood flow (23). In addition, both ketamine and isoflurane induce hypothermia in small animals (24, 25). Changes in physiological parameters, such as cerebral blood flow and cardiac output, can in turn affect the biodistribution of PET tracers (8). In a review by Alstrup and Smith (6) the effect of several anesthetics on the brain PET reading is summarized.

Given that receptors with which anesthetic agents interact (e.g., dopamine and GABA_A receptors), can also be the target of PET ligands, anesthetics can modify the binding of these PET tracers. In this section we review several experiments that studied the effect of anesthesia on the brain PET reading of different tracers, summarizing the respective authors' hypothesis on the mechanism of interaction.

Methods to Study the Effect of Anesthesia in PET

As a first approach, the effects of anesthesia on the PET reading can be investigated by comparing PET scans performed using different anesthetics. This method allows visualization of the tracer kinetics from the onset of administration but does not reflect the awake state. To compare the state under anesthesia with the awake state, several approaches can be used: (i) Animals can be administered with the PET radiotracer in the awake state and, after some uptake period, sacrificed to perform autoradiography. Unlike dynamic PET, this method only delivers a single time point image of the radiotracer uptake in the sacrificed animal, but animals can be sacrificed at several time points to obtain pseudo-dynamic data. (ii) The animal can be administered with the radiotracer in the awake state, and following an awake uptake period (between 20 and 60 min uptake depending on the study), the animal can be anesthetized and scanned for the remainder of the uptake period. It is assumed that the effect of anesthesia is small and, if this is true, this scan reflects the awake state uptake. This approach does not allow to study the kinetics of the tracer from the onset of radiotracer administration, but pseudo-dynamic data can be obtained. (iii) The animal can be restrained during the scan and the tracer can be administered in the awake state. This method allows to perform the PET scan from the radiotracer administration onset in the awake state, but the stress caused by restraining can also affect the radiotracer uptake (e.g., due to activation/inactivation of stress related brain regions or neurotransmitters release, see section Effect of Physical Restrain in Brain PET Tomography). (iv) Using advanced methods, such as the specialized PET scanners or motion correction (described in section Small Animal Head Motion Tracking), the animal can be scanned in the awake state without physical restraining. These methods might be the optimal solution to visualize the tracer in the awake state, since no anesthesia or restrain stress is present. However, some stress might still be present by the scanning procedure itself and by restricting the animal motion to a reduced enclosure. In addition, administration of the tracer in the awake state might be challenging. **Table 1** shows a summary of the studies presented in the next sections.

Comparison of Different Anesthetics

Using [¹¹C]raclopride, a dopamine D₂ receptor antagonist, striatum binding potential was doubled when using fentanyl-fluanisone-midazolam compared to isoflurane anesthesia in rats scans (34). Authors point out that different baseline binding potential depending on the anesthetic used might cause differing binding potential changes in challenge experiments.

The anesthetics isoflurane and α -chloralose were compared in the uptake of [¹¹C]cocaine (dopamine transporter antagonist) in the rat brain (38). This tracer was used in a cocaine challenge to study the physiological response to cocaine under different anesthetics. Using laser Doppler flowmetry and in parallel with multi-wavelength optical spectroscopy, cerebral blood flow, cerebral blood volume and tissue hemoglobin oxygenation was measured. These parameters were decreased in rats anesthetized with isoflurane compared to rats anesthetized with α -chloralose. Moreover, the clearance of [¹¹C]cocaine from the brain was faster in isoflurane-anesthetized rats than in α -chloralose rats. Different interaction of cocaine with the anesthetics, e.g., due to increase in intracellular calcium caused by cocaine, might have caused these differences (38).

Brain glucose metabolism has been investigated in a caffeine challenge, comparing the [¹⁸F]FDG uptake in isoflurane and α -chloralose anesthetized rats for different caffeine doses (28). While in isoflurane anesthetized rats the highest caffeine dose significantly increased tracer uptake in several brain regions compared to baseline, the opposite effect was observed in α -chloralose anesthetized rats, i.e., lower tracer uptake than baseline at higher caffeine doses. Neurotransmitters release by caffeine administration (e.g., GABA and dopamine) and the different interaction with different anesthetics could have caused the different response (28).

Awake Uptake Followed by Autoradiography

[¹⁸F]FDG uptake was compared in the conscious state and under the anesthetics ketamine + xylazine, ketamine, chloral hydrate, pentobarbital, propofol, and isoflurane (26). Although ketamine did not change the overall brain [¹⁸F]FDG uptake compared to the conscious animals, it did change the brain uptake pattern, with a significant decrease uptake in the frontal cerebral cortex and a significant increase uptake in the posterior cerebral cortex. The other tested anesthetics significantly reduced the tracer uptake compared to the conscious group.

In an amphetamine challenge study, it was found that the change in tracer binding potential (compared to control rats) using the dopamine D_{2/3} receptor agonist [¹¹C]-(+)-PHNO compared to the change in binding potential in the same amphetamine challenge but using [¹¹C]raclopride, was larger using [¹¹C]-(+)-PHNO. This increased difference in BP using [¹¹C]-(+)-PHNO compared to [¹¹C]raclopride was observed in isoflurane-anesthetized rats, but not in conscious rats (37). This study could suggest altered dopamine levels caused by a drug/therapeutic intervention might be present in anesthetized animals but absent in clinical studies performed in conscious subjects. The authors discuss several possible mechanisms that could have caused this difference (e.g., changes in cerebral blood

TABLE 1 | Summary of the studies investigating the effect of anesthetic agents in PET brain radiotracers.

Anesthetic(s)	Method	Outcome
[¹⁸F]FDG (glucose metabolism)		
Ketamine + xylazine, ketamine, chloral hydrate, pentobarbital, propofol, and isoflurane	Autoradiography	Decrease glucose metabolism under anesthesia compared to awake (26).
Isoflurane	Awake uptake	Difference between saline and morphine withdrawal observed in anesthetized but not awake rats (27).
Isoflurane, α -chloralose	Anesthetics comparison	Isoflurane: increased FDG uptake after caffeine challenge, α -chloralose: decreased FDG uptake after caffeine challenge (28).
Isoflurane	Restrained scan	Reduced uptake and faster tracer kinetics in anesthetized compared to awake (29).
MMB, ketamine + xylazine, chloral-hydrate, pentobarbital, propofol, and isoflurane	Restrained scan	Decreased two-tissue K_3 , and regional increased or decreased cerebral blood flow, in anesthetized compared to awake (30).
Isoflurane	Awake unrestrained	Faster tracer kinetics and lower brain SUV in anesthetized compared to awake (31).
Isoflurane	Awake unrestrained	Decaying brain FDG uptake after awake uptake period in anesthetized mice, but not in awake mice (32).
[¹¹C]SCH23390 (dopamine D₁ receptor)		
Chloral hydrate, ketamine, and pentobarbital anesthesia	Restrained scan	Higher binding potential in chloral hydrate and ketamine, lower in pentobarbital, compared to awake (33).
[¹¹C]raclopride (dopamine D₂ receptor)		
Isoflurane, fentanyl-fluanisone-midazolam	Anesthetics comparison	Doubled binding potential in isoflurane compared to fentanyl-fluanisone-midazolam (34).
Isoflurane	Restrained scan	Lower binding potential in whole-body restrained and anesthetized mice compared to free-walking restrained (35).
Ketamine-xylazine	Awake unrestrained	Reduced binding potential in anesthetized rats (36).
[¹¹C]-(+)-PHNO (dopamine D_{2/3} receptor)		
Isoflurane	Autoradiography	Greater increase in binding potential after amphetamine challenge visible in anesthetized rats but not in awake rats (37).
[¹¹C]cocaine (Dopamine transporter blocker)		
Isoflurane, α -chloralose	Anesthetics comparison	Clearance of [¹¹ C]cocaine from the brain was faster in isoflurane-anesthetized rats than in α -chloralose rats (38).
[¹⁸F]FPWAY (Serotonin receptor 5-HT_{1A})		
Isoflurane	Awake uptake	Higher distribution ratio than conscious (39).
[¹⁸F]MK-9470 (Type 1 cannabinoid receptor)		
Isoflurane and pentobarbital	Awake uptake	Higher or lower regional relative SUV compared to conscious (40).
[¹⁸F]flumazenil (GABA_A receptor)		
Isoflurane, ketamine/dexmedetomidine	Awake uptake	Frontal cortex and hippocampus uptake in isoflurane and ket/dex anesthetized mice was 10 and 3-fold higher than in awake mice, respectively (41).
[¹¹C]-(R)-Rolipram (Phosphodiesterase subtype 4)		
Isoflurane	Restrained scan	Tracer B _{max} and K _D significantly higher in conscious compared to anesthetized (42).

MMB, medetomidine, midazolam, and butorphanol; Ket/dex, ketamine/dexmedetomidine.

flow, increase dopamine release under anesthesia) but no clear hypothesis was defined.

Awake Radiotracer Uptake With Scan Under Anesthesia

Using the 5-HT_{1A} receptor antagonist ligand [¹⁸F]FPWAY, the distribution ratio of the tracer was compared in isoflurane anesthetized and conscious rats (39). Isoflurane anesthetized rats showed a significant higher hippocampus (63%) and cerebellum (32%) tracer distribution ratio than conscious rats, which the authors attribute to the decreased serotonin release in isoflurane anesthetized rats.

The influence of isoflurane and pentobarbital anesthesia on the type 1 cannabinoid receptor tracer [¹⁸F]MK-9470 has been investigated (40). Although absolute standardized uptake value

(SUV) was not significantly different between anesthetized and awake rats, relative SUV (to the whole brain) was significantly different between anesthetized and conscious rats in several brain regions (decrease or increase). Difference was not significant when quantified using absolute SUV values, this might have been because of the higher variability in absolute SUV values compared to normalized relative SUV values.

The GABA_A receptor antagonist tracer [¹⁸F]flumazenil has been investigated under isoflurane, and ketamine/dexmedetomidine (ket/dex) anesthesia, and under the dexmedetomidine (dex) anxiolytic alone compared to awake uptake in mice (41). At 25 min post-tracer injection the frontal cortex and hippocampus uptake in isoflurane and ket/dex anesthetized mice was 10 and 3-fold higher than in awake mice. In the *ex-vivo* analysis, the hippocampus and

frontal cortex uptake were significantly higher in all anesthetized conditions compared to the awake state. Either frontal cortex or hippocampus volume of distribution (calculated from pseudo-dynamic data) was significantly different under isoflurane, ket/dex, and dex compared to the awake condition. Several effects are hypothesized to have caused these differences, such as changes in cardiac output (43) and cerebral blood flow due to anesthesia (8).

In a morphine self-administration experiment, the effect of isoflurane anesthesia was investigated in the [^{18}F]FDG uptake of rats that underwent withdrawal from morphine (27). Following a 45 min [^{18}F]FDG uptake either awake or under isoflurane, a 30 min PET scan under isoflurane anesthesia was acquired. A significant increase in striatum glucose metabolism in the morphine withdrawal group compared to the saline group was observed after an anesthetized tracer uptake but not after awake uptake. Authors hypothesize that higher basal glucose levels in awake animals might have hindered visualizing of changes in awake animals.

Awake Scan in Restrained Animals

The uptake of the dopamine D_1 receptor ligand [^{11}C]SCH23390 was compared in restrained conscious rats vs. the uptake in anesthetized rats using the anesthetics chloral hydrate, ketamine, and pentobarbital anesthesia (33). Compared to the conscious state, the authors observed that the striatum binding potential of [^{11}C]SCH23390 was higher using chloral hydrate and ketamine, but lower using pentobarbital. It is suggested that physiological changes (e.g., in cerebral blood flow), or blockade of the NMDA receptor by ketamine and chloral hydrate, but not pentobarbital, could have caused the difference in binding potential (33).

In another study, the binding site density (B_{max}) and tracer affinity ($1/K_D$) of the phosphodiesterase subtype 4 (PDE4) tracer [^{11}C]-(*R*)-Rolipram, was compared in conscious and isoflurane anesthetized rats (42). B_{max} and K_D were determined from a saturation analysis. It was found that both B_{max} and K_D were significantly higher in restrained conscious rats compared to anesthetized rats. Changes in the phosphorylation status of PDE4 caused by anesthesia might have caused the differences (42).

In mice, the brain uptake of [^{18}F]FDG has been investigated in awake animals and compared to isoflurane anesthetized mice (29). Brain SUV and glucose metabolic rate was significantly reduced in anesthetized mice compared to awake mice. The tracer kinetics were also modified by the use of isoflurane, indeed the [^{18}F]FDG uptake plateau in awake mice was reached after about 30 min whereas with anesthetized mice the plateau was reached already after 2 min. The phosphorylation rate constant (k_3) was reduced under anesthesia, but the glucose transport constant remained unchanged (K_1).

Using a special restraining device in which the mouse head was restrained, but the extremities were allowed to move (free-walking state), scans using [^{11}C]raclopride were compared also in whole-body restrained mice, and mice anesthetized with isoflurane (35). Heart rate in free walking mice was significantly lower than whole-body restrained mice. Striatum binding potential (calculated using simplified reference tissue model with cerebellum as reference region) was significantly

lower in whole-body restrained mice and isoflurane-anesthetized mice compared with restrained free-walking mice. Although both isoflurane anesthesia and restraining stress cause increment in extracellular dopamine release, authors indicate that competition is not the main cause in binding potential differences (35).

Using a soft restrainer to scan rats in the awake state, [^{18}F]FDG kinetic modeling has been performed and compared with scans under a mix of medetomidine, midazolam, and butorphanol (MMB) anesthesia, ketamine + xylazine, chloralhydrate, pentobarbital, propofol, and isoflurane anesthesia (30). Two tissue compartment K_1 , k_2 , and k_4 were not significantly different between conditions, but the phosphorylation reaction constant k_3 was significantly lower in all anesthetic conditions compared to the awake state. The cerebral metabolic rate of glucose was significantly higher in the conscious group compared to all anesthesia groups (Figure 1). Moreover, cerebral blood flow, measure using [^{125}I]IMP, was not significantly different from conscious and chloral hydrate rats, but was significantly lower (compared to conscious) for MMB, ketamine + xylazine, pentobarbital, and propofol rats, and significantly higher in isoflurane anesthetized rats.

Awake and Unrestrained PET Scan

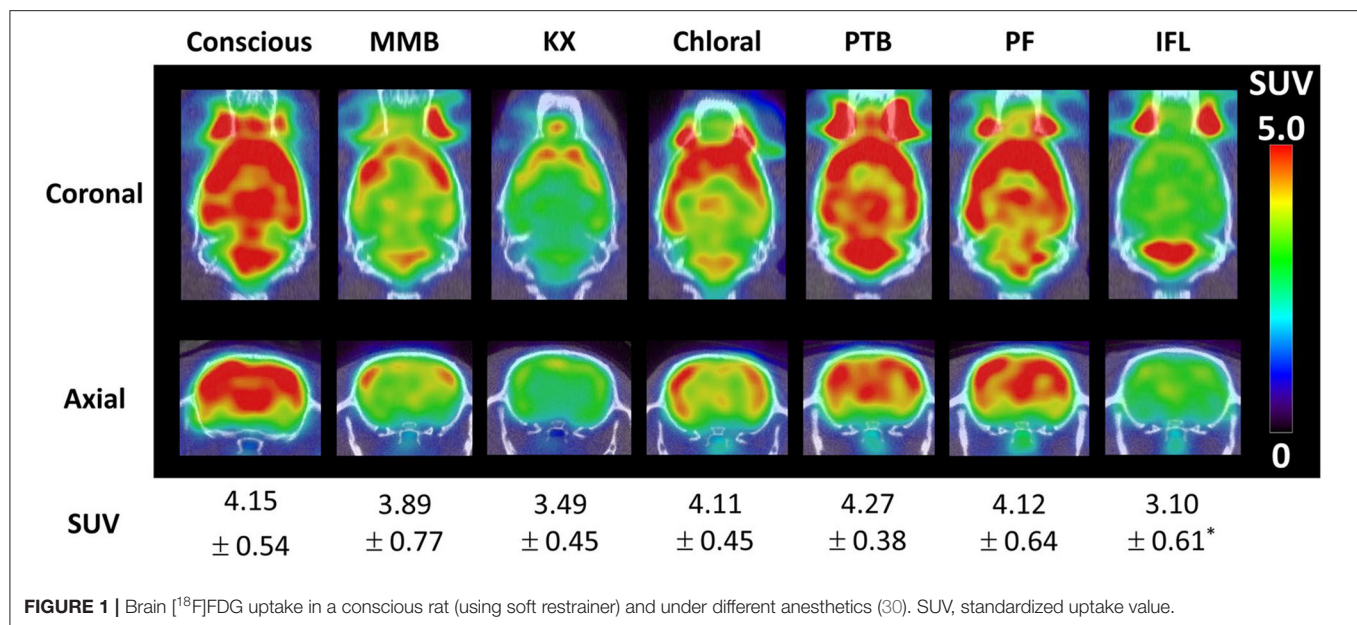
The RatCAP, a miniaturized PET scanner that can be surgically attached on the rat head (36, 44), has been used to compare the [^{11}C]raclopride binding potential in awake and ketamine-xylazine anesthetized rats, finding that anesthesia reduced binding potential, although not significantly.

Using motion tracking and motion correction reconstruction, the effect of isoflurane anesthesia in rat brain [^{18}F]FDG uptake was investigated (31). Time-activity curves showed a faster wash-in in the brain of anesthetized rats compared to awake rats. The regional SUV in the cortex, vestibular nuclei, diencephalon, and inferior colliculi was significantly different (lower or higher) between awake and anesthetized animals.

In another study using motion tracking and motion correction, [^{18}F]FDG uptake was investigated in awake and anesthetized mice (32). Allowing an awake uptake period of 20 min, mice were scanned awake freely moving and under isoflurane anesthesia. Slope of regional time activity curves was significantly different from zero (negative slope) in anesthetized mice, but not in awake mice (i.e., approximately constant uptake). This shows anesthesia can have an effect even after considering some awake uptake period (32).

Effect of Physical Restrain in Brain PET Tomography

As described above, physical restrain is used to avoid the use of anesthesia. However, restraining stress itself represents a confounding factor also altering the uptake of the radiotracer. Sung et al. (45) performed [^{18}F]FDG scans in rats that underwent restrain immobilization and awake uptake. In all conditions with restrain there was a significant [^{18}F]FDG uptake difference compared to unrestrained rats in several brain regions related with stress processing (limbic system). When removing the restraining and allowing 1 h restraint free period, uptake in some of these (e.g., hypothalamus, motor cortex) regions normalized



again and did not show difference compared to unrestrained rats. In some other regions (e.g., hippocampus, thalamus) this was not the case and the differences persisted. Corticosterone levels increased over time in restrained rats, plateauing at about 30 min after immobilization began, and reduced again for rats that were allowed to recover after 1 h of immobilization. These results were similar in the brain [^{18}F]FDG uptake in mice (46). Brain uptake decreased in proportion to the duration of the restrain procedure (10, 20, and 40 min), with 20 and 40 min restrain showing significantly different brain uptake than in unrestrained mice.

Patel et al. (47) investigated the rat brain uptake of [^{11}C]raclopride considering an awake uptake period, a methamphetamine challenge, and immobilization stress. Both restrained and methamphetamine groups showed significantly lower striatal [^{11}C]raclopride binding than unrestrained rats without methamphetamine challenge, but no significant difference was found between methamphetamine and restrained rats. Alteration of neurotransmitter levels due to handling stress might have caused these differences (47).

Using reverse-phase chromatography, levels of dopamine metabolites in the nucleus accumbens septi, caudate putamen, and frontal cortex were investigated in mice undergoing restraining stress for 30 and 120 min (48). Significant increase in metabolites levels were observed in the nucleus accumbens septi after 30 min immobilization, but only after 120 min in caudate putamen and frontal cortex. This effect was likened to the effect high doses of amphetamine can have (48).

The uptake of [^{11}C]-DASB, a serotonin transporter tracer, was investigated in mice exposed to chronic restraining stress (49). Mice were restrained 4h daily for 6 weeks and scanned on the 6th week with [^{11}C]-DASB. Compared to control animals, significantly lower [^{11}C]-DASB levels were found in the cortex of restrained animals. Given that absence of CB₁ cannabinoid receptor activity can impair serotonin negative feedback, sensitivity of the CB₁ cannabinoid receptor to environmental

stress might have caused the effect of stress on the tracer uptake (49).

The effect of cage transport and restraining stress was investigated in the rat brain uptake of the 5-HT_{1A} receptor ligand [^{18}F]MPPF (50). Hippocampal binding potential in rats undergoing cage transport, and transport plus restrain stress, was significantly higher than in control rats. Changes in 5-HT_{1A} receptor expression due to exposure to stressful situations might have caused the change in tracer binding (50).

The expression of acetylcholinesterase has also been observed to change following restrain-related stress (51). Acetylcholinesterase specific enzyme activity was significantly reduced in mice subject to 150 min immobilization.

All these evidence points that the brain response to restraining stress involves the reaction of many neurotransmitter systems (52), such as those in dopaminergic, cholinergic, and serotonergic neurons, as well as causing change of brain glucose consumption (53). Therefore, the brain response to restraining stress can interfere (e.g., by endogenous neurotransmitter competition of binding sites) with the PET reading of tracers targeting these systems, producing results that differ from unrestrained animals. Brain uptake differences comparable to those observed in drug challenges (47) can also be caused by restraining stress. Response of brain receptors to environmental stress (49), or its expression (50), can also modify uptake of tracers targeting these receptors or systems interacting with these receptors.

BRAIN PET SCANS IN NON-ANESTHETIZED UNRESTRAINED ANIMALS TO IMPROVE RESULTS TRANSLATION TO THE CLINIC

From all the methods described in the previous section to study the effect of anesthetics, methods that allow scans of awake

unrestrained animals resemble more closely the conditions in typical clinical PET scans. Although specialized scanners, such as the RatCAP (44), can be used to scan awake unrestrained animals, motion correction methods are more promising since typical preclinical scanners, already installed in research facilities, can potentially be used with these methods. Therefore, in the following sections we further describe the motion correction technique and the new possibilities it can bring to small animal brain PET scanning.

Small Animal Head Motion Tracking

The motion tracking technique allows to scan awake unrestrained rodents by tracking the motion of the animal head, with any compatible tracking technology. Motion correction techniques, considering only rigid motion from the head, can then be applied to obtain motion corrected images. This method has been initially used in motion correction for clinical brain PET scans. However, motion tracking of the rodent head presents more challenges than human head motion tracking. First, the spatial resolution of preclinical scanners is usually better than in clinical scanners, with some modern systems reaching sub-millimetric resolution (54). Therefore, the tracking system should be able to deliver sub-millimetric tracking information. Second, the scanner bore in most preclinical scanners is small and narrow. If the tracking system is located on the exterior of the scanner, its field-of-measurement will be limited due to occlusion caused by the scanner bore. Third, rodent head motion can have a larger range than human head motion, and, if the scanner bore allows it, the animal can move in all directions. This is particularly detrimental for tracking systems that require the animal to be facing the tracking device. Moreover, it is necessary to track continuous motion, as opposed to discrete motion tracking which in some cases is enough for clinical PET head motion tracking (55). To overcome all these challenges, research on this technique is ongoing and several tracking methods have been proposed.

Characteristics of a Tracking System for Small Animal Brain PET

To use a tracking system for head motion correction in small animals, the system needs to meet certain criteria. The accuracy of the tracking system should be better than the spatial resolution of the PET scanner. If the position of a 3D point determined with the tracking system has an uncertainty larger than the spatial resolution of the scanner, the motion correction calculation will have the same uncertainty, therefore producing blurred images with respect to the image spatial resolution.

The tracking system additionally must have a high tracking frame rate in order to capture high-speed motion. For example, if the animal moves at a speed of 2 cm/s and a tracking frame rate of 30 frames per second is used, the animal would have moved about 0.7 mm within one frame, which is comparable with the spatial resolution of a preclinical PET scanner. Thus, an uncertainty of 0.7 mm will be present in the motion tracking data, which could translate into image blurring after motion correction. It is important to note that since most PET system perform reconstruction after data acquisition, it is not necessary to

perform real-time tracking, and therefore tracking processing can be performed off-line.

In order to minimally affect the animal due to the tracking procedure, the tracking method should be minimally invasive and with appropriate dimensions to fit with the PET scanner. This restricts the use of many tracking systems that use bulky systems or markers that cannot be attached to the animal head. Markerless tracking systems are therefore attractive for animal head motion tracking. These systems require no physical markers to track motion and instead can use, for example, either the natural features of the rodent head as reference points (see section Optical Motion Tracking Detecting Natural Head Features) or make use of projected structured light patterns on the animal head that help to calculate the 3D model of the head (see section Optical Motion Tracking Using Structured Light).

Ideally, the tracking system should also be able to track the motion of the animal irrespective of its position in the scanner field of view. However, many tracking systems have a limited field of measurement or the success of the tracking depends on the marker position itself. For example, for many optical tracking systems, the subject has to be facing the camera to be able to track its motion.

Finally, overall practicality is desired in order to be able to perform these types of scans on a regular basis. If the setup of the tracking system requires specialized personnel, laboratories lacking this type of personnel will not be able to perform the procedure. Moreover, if the setup of the tracking system or the time for the animal preparation is long, throughput can be compromised. Therefore, a practical tracking system is necessary to allow a wider spread of motion correction for preclinical brain PET scans. Below several tracking systems proposed for preclinical brain PET, with strengths and weaknesses in some of the requirements, are presented (Table 2).

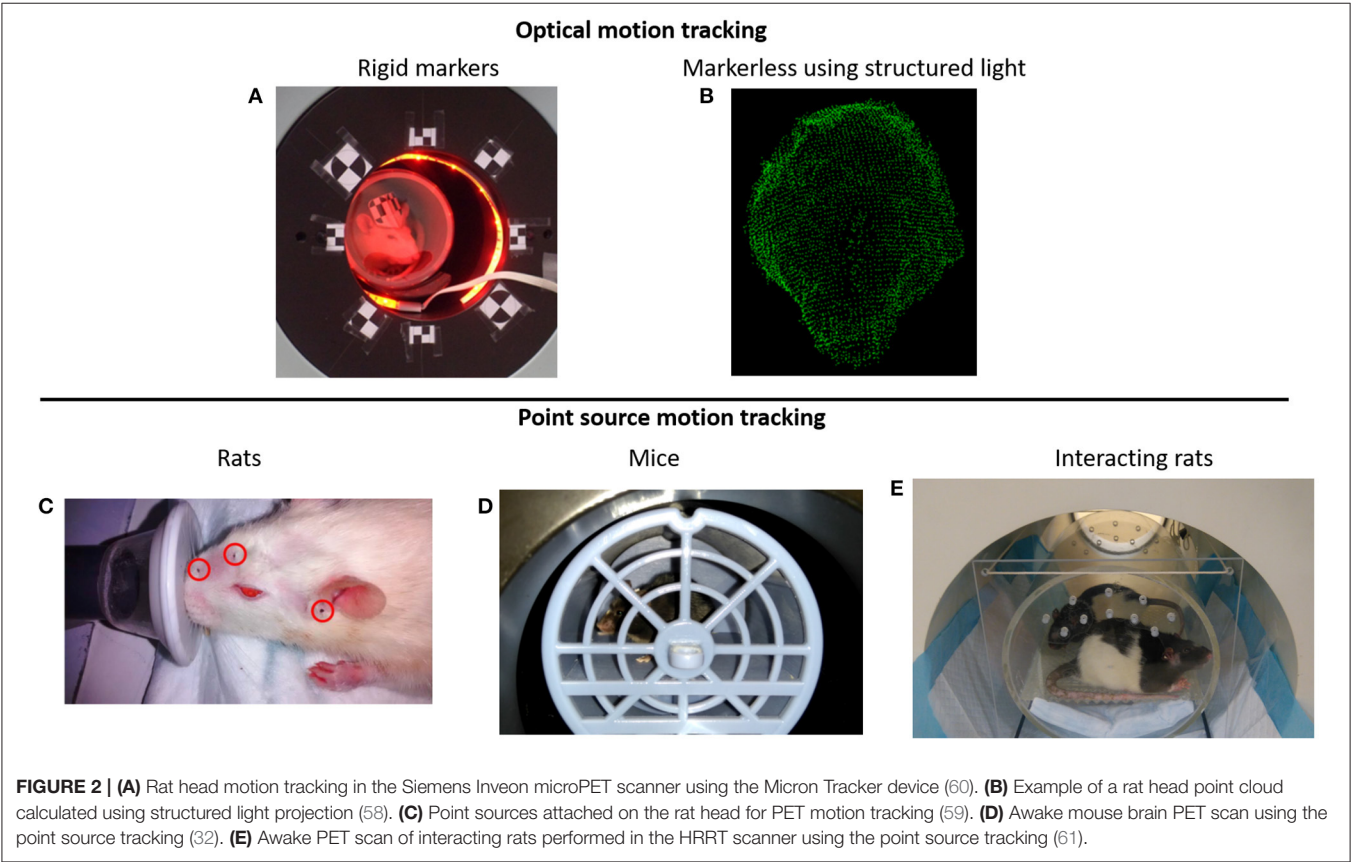
Optical Motion Tracking Using Rigid Markers

One of the first methods proposed to track the rat's head motion makes use of the Micron Tracker camera (Claron Technology Inc., Toronto, Canada). This camera uses stereo-vision to determine the 6 degrees of freedom (3 translation coordinates and 3 rotation angles) motion of checkerboard markers that can be printed on paper and attached to a rigid surface (Figure 2A). This camera offers sub-millimetric tracking accuracy (0.25 mm), and the markers can be made small enough to be attached to the rat head. In order to synchronize the motion tracking data with the PET data, a temporal and spatial synchronization between the tracker and the PET scanner must be performed. This camera has been adapted to the Siemens Focus 220 microPET scanner (31, 62) and the Siemens Inveon microPET (60) for rat head motion tracking.

As with many optical tracking systems, the animal head must be facing the tracking camera. When the animal moves with the head opposite to the tracker, or at positions where the marker is occluded by the scanner bore, no tracking information can be acquired, and therefore the PET data during that period cannot be corrected for motion. Moreover, it might be difficult to use this marker-based camera in scanners with small bores.

TABLE 2 | Characteristics of the different motion tracking techniques for small animal brain PET.

Tracking method	Accuracy (mm)	Species	Frame rate (Hz)	Characteristics
Optical using rigid markers	0.25	Rats	20–40	Makes use of the MicronTracker camera. Markers with a checkerboard pattern are attached on the rat head (56).
Optical using natural features	0.2	Rats	Up to 60	Several cameras obtain different views of the object. Feature detected in different views are matched to calculate their 3D location (57).
Optical using structured light	0.33	Rats	30	Makes use of the Ensenso camera. An infrared pattern projected on the object is used to calculate the object surface point cloud (58).
PET-based point source tracking	0.24	Rats/mice	Up to 60	Tracking based on the PET image. Radioactive fiducial markers are attached on the animal head, and detected in short time frames (59).



This tracking system has been used together with a robotic arm in order to maximize the time the animal is inside the scanner field of view (63, 64). The platform in which the rat can move is positioned on a mechanical arm with 6 degrees of freedom motion and using the head tracking information, every time the animal moves out of the scanner field of view, it is repositioned back into the FOV.

Optical Motion Tracking Detecting Natural Head Features

Another approach to track the animal head motion consists of detecting natural features on the animal head to determine its 6 degrees of freedom pose (57). Therefore, no markers need to be attached to the animal head. Distinctive features that can be

uniquely identified (e.g., around the eyes or nose) are determined using image feature detection algorithms (65) in images acquired from several views of the object. Then, several of these features are matched in two or more images, and the 3D position of the features can be calculated. With more than 3 of these features, the 6 degrees of freedom of the animal head can be determined. In practice, it was necessary to paint a black pattern on the animal head in order to obtain enough distinctive features to match the images in different views (57).

Optical Motion Tracking Using Structured Light

Combining the use of stereo vision with structured light projection the 3D surface of the animal head can be represented with point clouds (**Figure 2B**), which then can be used to determine the 3D pose (position and orientation) of the rat

head (58). With the aid of a speckled dot pattern projected with infrared light on the surface of the object to be tracked, the 3D position of every pixel (within tracking range) in the stereo images can be determined. After acquiring the point cloud of the animal head on short time frames, the head can be registered to a reference frame using the iterative closest point algorithm (66).

PET-Based Motion Tracking Using Radioactive Point Sources

The use of radioactive fiducial markers to track the motion of the animal head has been proposed by our group (59). Radioactive PET point sources are attached to the rat head (**Figure 2C**), and by determining the spatial location of the point sources in the PET data, the pose of the head can be calculated. At least 3 non-collinear point sources are necessary to uniquely determine the pose of the animal head. Unlike the optical tracking methods presented above, this method does not require temporal or spatial calibration with the PET scanner and does not suffer from occlusion of the optical camera field of view. Therefore, it is possible to track the motion of the animal in the entire scanner field of view irrespective of the animal position. Of all the tracking methods presented here, this has been the only method adapted for mice head motion tracking [**Figure 2D**; (32)], or for simultaneous tracking of 2 rats [**Figure 2E**; (61)].

Rigid Motion Correction Reconstruction

Once the animal head motion information has been acquired with any tracking system, the PET data can be corrected for motion. Methods devised for human head motion correction can be used in small animal motion head correction (67). Event-by-event motion correction (68) has been the preferred method for small animal motion correction since methods that consider only sporadic, discrete motion (55) might perform poorly for small animal motion correction due to the erratic nature of the animal motion.

Event-by-event motion correction consists of repositioning every line of response (LOR) of the PET scan back to a reference pose using the motion tracking information. For brain motion correction only rigid motion/transformations are considered (68) with the assumption the brain only undergoes rigid motion, but non-rigid event-by-event motion correction could also be performed for respiratory motion correction (69). In theory, if one knows the pose of every individual LOR, the LOR can be repositioned individually. However, in practice, due to the finite tracking frame rate of the motion tracking system, LORs are repositioned in time bins with the same size as the tracking frame size. Interpolation between poses can be performed to calculate the pose of every individual LOR, but this has been shown to only minimally improve the image quality (56).

Once LORs are repositioned, they can be rebinned into sinograms, or reconstructed with list-mode reconstruction (68), using for example the maximum-likelihood expectation maximization algorithm (ML-EM) (70). In both cases, the LORs need to be corrected for detection efficiency (normalization). For sinogram rebinning, the compression factor of the sinogram must be considered to calculate the sinogram bin normalization factor (71). For list-mode reconstruction, the normalization

correction image of all possible detectable LORs should be calculated for every motion pose. For example, for a scan time of 20 min and a tracking frequency of 30 frames per second, 36,000 normalization correction images should be calculated. This is an impractical calculation, and therefore approximations are performed to calculate normalization correction in list-mode motion correction reconstruction. One of these approximations considers only a random number of the total LORs in every pose (72), while another calculates the normalization correction image by interpolation in the image space (68). The former method has been reported to perform well depending on the number of LORs considered and the randomization algorithm (72), while the latter performs well in terms of quantitative accuracy, comparable with motion-free reconstructions (68).

Due to the free motion of the animal in the scanner field of view, attenuation, and scatter correction need to be adapted for motion correction. Since the position of the animal body can have different orientations with respect to the head, the attenuation factors from the body also can change over time. An approximation to calculate the moving animal attenuation map considers the outline of the body activity as the attenuation map, with a constant attenuation factor of soft tissue (73). Since bone structures are small in rodents, this is a good approximation. Another solution consists on defining a “virtual scanner” fixed to the animal head to determine LORs originating in the head, and not traversing the torso (74), which then are used in the motion correction reconstruction. However, many LORs have to be discarded with this technique, degrading the image quality. Regarding scatter correction no solution has been proposed for freely moving animals motion correction, but since the proportion of scatter events in small animal brain scans is relatively small (<2.5%), this does not represent a considerable source of error (31).

Additional corrections can be performed to improve the image quality of the motion-corrected reconstruction. One of these corrections estimates the blurring caused by the uncertainty in the motion data to calculate a deconvolution correction in the motion-corrected image (60). Another correction calculates the motion-dependent point spread function of the motion scan by attaching a point source to the moving subject (75). The point spread function calculated from the point source image is then used in a deconvolution correction. Correction for the parallax effect in motion scans has also been developed (76). For this method, the motion-dependent and spatially variant point spread function of the motion scan is analytically calculated for every voxel in the image and then used for resolution modeling in the ML-EM reconstruction.

Novel Possibilities for Brain Behavioral Studies in Freely Moving Awake Rodents

Although one of the main motivations to perform motion correction PET scans of awake animals is to circumvent the use of anesthesia, this scanning setup also allows to perform new experimental designs not possible in anesthetized or restrained animals. In particular, quantification of the animal behavior during the PET scan has been explored using motion correction.

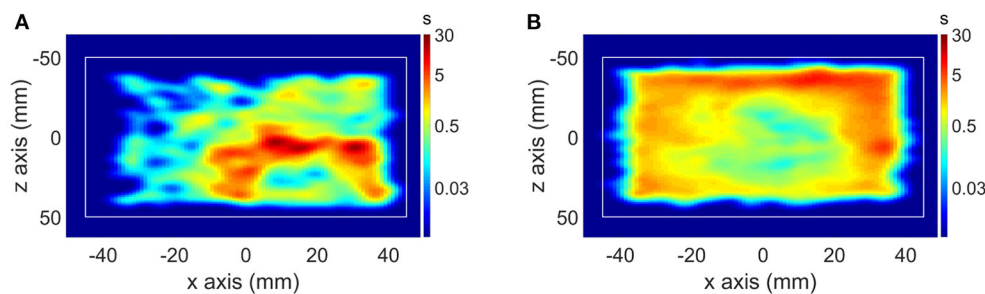


FIGURE 3 | (A) Motion histogram (top view) of a mouse PET study in a control scan and **(B)** motion histogram of the same mouse in a memantine challenge scan.

One of the first studies in which the animal behavior was quantified simultaneously during the PET scan was in mouse memantine challenge scans performed with the point source tracking (32). The mouse behavior was observed during the PET scan in a memantine challenge experiment, showing significantly increased locomotion in memantine challenge mice compared to control mice (**Figure 3**). Another novel experimental setup using the point source tracking is the scan of freely moving and interacting rats (61). The large field of view of the human brain High Resolution Research Tomograph allowed tracking of 2 freely moving rats placed in a cage fitted to the FOV of the scanner.

Using marker-based motion tracking, Kyme et al. (64) investigated the effect of an amphetamine challenge in the binding of [^{11}C]raclopride. Using rats with an implanted catheter, [^{11}C]raclopride was administered in the awake state, followed by administration of amphetamine 20 min later. After amphetamine administration [^{11}C]raclopride binding significantly reduced compared to saline administered rats, while locomotion increased.

DISCUSSION

The effect of anesthesia in small animal brain PET has been demonstrated in studies performed since the early days of microPET. Since studies investigating the mechanisms of action of anesthetics demonstrate that they modify physiological parameters (e.g., respiratory rate, cerebral blood flow, etc.) and interact with neurotransmitter systems, it is expected that anesthetics will also modify the brain response to PET tracers. Tracers targeting receptors such as dopamine, serotonin, and GABA_A, as well as the glucose analog [^{18}F]FDG, have been demonstrated to be influenced by anesthetics during PET tomography.

Among the suggested mechanisms causing the difference in tracer binding due to anesthesia are the changes in physiological parameters. Changes in cerebral blood flow caused by anesthesia has been indicated as one of the possible factors producing differences in the tracer uptake compared to the awake state (34, 47). For dopamine receptor tracers, although competition with the dopamine release caused by the anesthetic (e.g., isoflurane) can be linked to changes in the tracer uptake, this competition

is assumed to be minimal due to the low level of dopamine release caused by the anesthetic (37, 39). Similarly, inhibition of serotonin release due to isoflurane has been suggested as a possible cause on the different uptake of the serotonin receptor 5-HT_{1A} tracer [^{18}F]FPWAY compared to the awake state, although this was not proven (39).

Due to the methodological differences of the studies presented, different additional confounding factors can be present, making a direct comparison of the reported results difficult. For example, studies allowing awake uptake followed by anesthesia scanning might have already an influence of anesthesia, especially for reversible tracers, depending on the pharmacokinetics of the anesthesia. In addition, stress caused by the different handling procedures, even in freely moving animal scans, can have an influence in the PET outcome. However, considering all the studies presented with different possible confounding factors, it is clear that anesthesia can influence the radiotracer uptake and kinetics in small animal brain studies.

Among the different methods used to elucidate the effect of anesthesia on the animal brain PET reading, motion tracking together with motion correction reconstruction most closely resemble the condition in the clinic, i.e., awake and unrestrained. Overall, the tracking systems presented here have good enough tracking accuracy (~ 0.25 mm) relative to the spatial resolution of typical preclinical scanners (1.5–1 mm). In addition, although motion correction reconstruction methods require approximations, images have comparable quality and quantitative accuracy to motion-free reconstructions.

As demonstrated in the mouse memantine (32), and rat amphetamine (64) challenge studies, the behavior of the animals in response to a drug can also be observed and quantified simultaneously with the PET scan using motion correction. Response to other non-pharmacological challenges could also be investigated in freely moving animals using PET, such as response to visual (77), olfactory (78), and auditory stimulus (79). Finally, more elaborated experiments, involving for example interaction of animals (61), or the response of the animal to a training or conditioning/reinforcement experiment, could be explored in freely moving animals with PET.

One of the main reasons motion tracking and motion correction for brain PET scans is not widely adopted is the need for complex software, and sometimes additional hardware,

to perform these procedures. Improving practicality and ease of use would allow the adoption of this technique for regular implementation in PET brain small animal scans. Therefore, additional collaboration between industry and research centers would be needed for the wider adoption and implementation of these types of scans.

CONCLUSIONS

The use of anesthesia in small animal preclinical brain PET studies represents the main confounding factor for proper translational understanding of animal models. Since clinical PET studies are usually performed without the use of anesthesia, translation of results from anesthetized animals to awake patients can also be compromised. Motion tracking with subsequent motion correction reconstruction offers the possibility to perform brain PET scans in freely moving unanesthetized animals. Several research developments have been performed in the last years, improving the accuracy and practicality of this technique, allowing the simultaneous study of animal behavior and molecular brain PET imaging. Further research and

collaboration with the industry would allow wider adaptation of motion tracking and motion correction for brain PET preclinical scans.

AUTHOR CONTRIBUTIONS

AM, DB, SStr, SSta, and JV were involved in drafting and editing the manuscript and figures. All authors approved the final manuscript and they are accountable for the content of the work.

FUNDING

AM was supported by the ERA-NET NEURON project SleepLess supported by BMBF (01EW1808) and FWO under the frame of Neuron Co-fund, and by a Research Project (G0A8517N) from the Research Foundation Flanders (FWO). DB was supported by the Research Foundation Flanders (FWO) through a post-doctoral fellowship (1229721N). The University of Antwerp also founded the work through a partial assistant professor position for JV and a full professor position for SSta.

REFERENCES

- Hess S, Blomberg BA, Zhu HJ, Hoiland-Carlsen PF, Alavi A. The pivotal role of FDG-PET/CT in modern medicine. *Acad Radiol.* (2014) 21:232–49. doi: 10.1016/j.acra.2013.11.002
- Duclos V, Iep A, Gomez L, Goldfarb L, Besson FL. PET molecular imaging: a holistic review of current practice and emerging perspectives for diagnosis, therapeutic evaluation and prognosis in clinical oncology. *Int J Mol Sci.* (2021) 22:4159. doi: 10.3390/ijms22084159
- Slough C, Masters SC, Hurley RA, Taber KH. Clinical positron emission tomography (PET) neuroimaging: advantages and limitations as a diagnostic tool. *J Neuropsych Clin Neurosci.* (2016) 28:66–71. doi: 10.1176/appi.neuropsych.16030044
- Singh V, Malhotra S. Nuclear cardiology in the literature: a selection of recent, original research papers. *J Nucl Cardiol.* (2020) 26:363–5. doi: 10.1007/s12350-020-02065-9
- Lancelot S, Zimmer L. Small-animal positron emission tomography as a tool for neuropharmacology. *Trends Pharmacol Sci.* (2010) 31:411–7. doi: 10.1016/j.tips.2010.06.002
- Alstrup AK, Smith DF. Anaesthesia for positron emission tomography scanning of animal brains. *Lab Anim.* (2013) 47:12–8. doi: 10.1258/la.2012.011173
- Franks NP, Lieb WR. Molecular and cellular mechanisms of general anaesthesia. *Nature.* (1994) 367:607–14. doi: 10.1038/367607a0
- Hildebrandt IJ, Su H, Weber WA. Anesthesia and other considerations for *in vivo* imaging of small animals. *ILAR J.* (2008) 49:17–26. doi: 10.1093/ilar.49.1.17
- Hemmings HC Jr., Riegelhaupt PM, Kelz MB, Solt K, Eckenhoff RG, Orser BA, et al. Towards a comprehensive understanding of anesthetic mechanisms of action: a decade of discovery. *Trends Pharmacol Sci.* (2019) 40:464–81. doi: 10.1016/j.tips.2019.05.001
- Franks NP. Molecular targets underlying general anaesthesia. *Br J Pharmacol.* (2006) 147(Suppl. 1):S72–81. doi: 10.1038/sj.bjp.0706441
- Pavel MA, Petersen EN, Wang H, Lerner RA, Hansen SB. Studies on the mechanism of general anesthesia. *Proc Natl Acad Sci USA.* (2020) 117:13757–66. doi: 10.1073/pnas.2004259117
- Dart C. Lipid microdomains and the regulation of ion channel function. *J Physiol.* (2010) 588(Pt 17):3169–78. doi: 10.1113/jphysiol.2010.191585
- Heurteaux C, Guy N, Laigle C, Blondeau N, Duprat F, Mazzuca M, et al. TREK-1, a K⁺ channel involved in neuroprotection and general anesthesia. *EMBO J.* (2004) 23:2684–95. doi: 10.1038/sj.emboj.7600234
- Petrenko AB, Yamakura T, Sakimura K, Baba H. Defining the role of NMDA receptors in anesthesia: are we there yet? *Eur J Pharmacol.* (2014) 723:29–37. doi: 10.1016/j.ejphar.2013.11.039
- Rudolph U, Mohler H. Analysis of GABAA receptor function and dissection of the pharmacology of benzodiazepines and general anesthetics through mouse genetics. *Annu Rev Pharmacol Toxicol.* (2004) 44:475–98. doi: 10.1146/annurev.pharmtox.44.101802.121429
- Rau V, Oh I, Liao M, Bodarky C, Fanselow MS, Homanics GE, et al. Gamma-aminobutyric acid type A receptor beta3 subunit forebrain-specific knockout mice are resistant to the amnestic effect of isoflurane. *Anesth Analg.* (2011) 113:500–4. doi: 10.1213/ANE.0b013e3182273aff
- Zurek AA, Yu J, Wang DS, Haffey SC, Bridgwater EM, Penna A, et al. Sustained increase in alpha5GABAA receptor function impairs memory after anesthesia. *J Clin Invest.* (2014) 124:5437–41. doi: 10.1172/JCI76669
- Upton DH, Popovic K, Fulton R, Kassiou M. Anaesthetic-dependent changes in gene expression following acute and chronic exposure in the rodent brain. *Sci Rep.* (2020) 10:9366. doi: 10.1038/s41598-020-66122-6
- Weinrich M, Worcester DL. The actions of volatile anesthetics: a new perspective. *Acta Crystallogr D Struct Biol.* (2018) 74(Pt 12):1169–77. doi: 10.1107/S2059798318004771
- Sarton E, Teppema LJ, Olivier C, Nieuwenhuijs D, Matthes HW, Kieffer BL, et al. The involvement of the mu-opioid receptor in ketamine-induced respiratory depression and antinociception. *Anesth Analg.* (2001) 93:1495–500. doi: 10.1097/0000539-200112000-00031
- Hart CY, Burnett JC, Jr., Redfield MM. Effects of avertin versus xylazine-ketamine anesthesia on cardiac function in normal mice. *Am J Physiol Heart Circ Physiol.* (2001) 281:H1938–45. doi: 10.1152/ajpheart.2001.281.5.H1938
- Cesarovic N, Nicholls F, Rettich A, Kronen P, Hassig M, Jirkof P, et al. Isoflurane and sevoflurane provide equally effective anaesthesia in laboratory mice. *Lab Anim.* (2010) 44:329–36. doi: 10.1258/la.2010.009085
- Maekawa T, Tommasino C, Shapiro HM, Keifer-Goodman J, Kohlenberger RW. Local cerebral blood flow and glucose utilization during isoflurane anesthesia in the rat. *Anesthesiology.* (1986) 65:144–51. doi: 10.1097/0000542-198608000-00003

24. Murphy TJ, Murnane KS. The serotonin 2C receptor agonist WAY-163909 attenuates ketamine-induced hypothermia in mice. *Eur J Pharmacol.* (2019) 842:255–61. doi: 10.1016/j.ejphar.2018.11.003
25. Rufiange M, Leung VSY, Simpson K, Pang DSJ. Pre-warming before general anesthesia with isoflurane delays the onset of hypothermia in rats. *PLoS ONE.* (2020) 15:e0219722. doi: 10.1371/journal.pone.0219722
26. Matsumura A, Mizokawa S, Tanaka M, Wada Y, Nozaki S, Nakamura F, et al. Assessment of microPET performance in analyzing the rat brain under different types of anesthesia: comparison between quantitative data obtained with microPET and *ex vivo* autoradiography. *Neuroimage.* (2003) 20:2040–50. doi: 10.1016/j.neuroimage.2003.08.020
27. Park TY, Nishida KS, Wilson CM, Jaiswal S, Scott J, Hoy AR, et al. Effects of isoflurane anesthesia and intravenous morphine self-administration on regional glucose metabolism ([18F]FDG-PET) of male Sprague-Dawley rats. *Eur J Neurosci.* (2017) 45:922–31. doi: 10.1111/ejn.13542
28. Peng SL, Chiu H, Wu CY, Huang CW, Chung YH, Shih CT, et al. The effect of caffeine on cerebral metabolism during alpha-chloralose anesthesia differs from isoflurane anesthesia in the rat brain. *Psychopharmacology.* (2019) 236:1749–57. doi: 10.1007/s00213-018-5157-4
29. Mizuma H, Shukuri M, Hayashi T, Watanabe Y, Onoe H. Establishment of *in vivo* brain imaging method in conscious mice. *J Nucl Med.* (2010) 51:1068–75. doi: 10.2967/jnumed.110.075184
30. Suzuki C, Kosugi M, Magata Y. Conscious rat PET imaging with soft immobilization for quantitation of brain functions: comprehensive assessment of anesthesia effects on cerebral blood flow and metabolism. *EJNMMI Res.* (2021) 11:46. doi: 10.1186/s13550-021-00787-6
31. Spangler-Bickell MG, de Laat B, Fulton R, Bormans G, Nuyts J. The effect of isoflurane on (18F)-FDG uptake in the rat brain: a fully conscious dynamic PET study using motion compensation. *EJNMMI Res.* (2016) 6:86. doi: 10.1186/s13550-016-0242-3
32. Miranda A, Glorie D, Bertoglio D, Vleugels J, De Bruyne G, Stroobants S, et al. Awake (18F)-FDG PET imaging of memantine-induced brain activation and test-retest in freely running mice. *J Nucl Med.* (2019) 60:844–50. doi: 10.2967/jnumed.118.218669
33. Momosaki S, Hatano K, Kawasumi Y, Kato T, Hosoi R, Kobayashi K, et al. Rat-PET study without anesthesia: anesthetics modify the dopamine D-1 receptor binding in rat brain. *Synapse.* (2004) 54:207–13. doi: 10.1002/syn.20083
34. Alstrup AKO, Simonsen M, Landau AM. Type of anesthesia influences positron emission tomography measurements of dopamine D-2/3 receptor binding in the rat brains. *Scand J Lab Anim Sci.* (2011) 38:195–200. doi: 10.23675/sjlas.v38i3.240
35. Takuwa H, Maeda J, Ikoma Y, Tokunaga M, Wakizaka H, Uchida S, et al. [(11C)]Raclopride binding in the striatum of minimally restrained and free-walking awake mice in a positron emission tomography study. *Synapse.* (2015) 69:600–6. doi: 10.1002/syn.21864
36. Schulz D, Southekal S, Junnarkar SS, Pratte JF, Purschke ML, Stoll SP, et al. Simultaneous assessment of rodent behavior and neurochemistry using a miniature positron emission tomograph. *Nat Methods.* (2011) 8:347–52. doi: 10.1038/nmeth.1582
37. McCormick PN, Ginovart N, Wilson AA. Isoflurane anaesthesia differentially affects the amphetamine sensitivity of agonist and antagonist D2/D3 positron emission tomography radiotracers: implications for *in vivo* imaging of dopamine release. *Mol Imaging Biol.* (2011) 13:737–46. doi: 10.1007/s11307-010-0380-3
38. Du CW, Tully M, Volkow ND, Schiffer WK, Yu M, Luo ZC, et al. Differential effects of anesthetics on cocaine's pharmacokinetic and pharmacodynamic effects in brain. *Eur J Neurosci.* (2009) 30:1565–75. doi: 10.1111/j.1460-9568.2009.06931.x
39. Tokugawa J, Ravasi L, Nakayama T, Lang LX, Schmidt KC, Seidel J, et al. Distribution of the 5-HT1A receptor antagonist [F-18]FPWAY in blood and brain of the rat with and without isoflurane anesthesia. *Eur J Nucl Med Mol Imaging.* (2007) 34:259–66. doi: 10.1007/s00259-006-0228-x
40. Casteels C, Bormans G, Van Laere K. The effect of anaesthesia on [(18F)]MK-9470 binding to the type 1 cannabinoid receptor in the rat brain. *Eur J Nucl Med Mol Imaging.* (2010) 37:1164–73. doi: 10.1007/s00259-010-1383-7
41. Palmer M, Beinart C, Banister S, Zanderigo F, Park JH, Shen B, et al. Effects of common anesthetic agents on [(18F)]flumazenil binding to the GABA_A receptor. *EJNMMI Res.* (2016) 6:80. doi: 10.1186/s13550-016-0235-2
42. Itoh T, Abe K, Zoghbi SS, Inoue O, Hong JS, Imaizumi M, et al. PET measurement of the *in vivo* affinity of C-11-(R)-rolipram and the density of its target, phosphodiesterase-4, in the brains of conscious and anesthetized rats. *J Nucl Med.* (2009) 50:749–56. doi: 10.2967/jnumed.108.058305
43. Bentzen BH, Grunnet M. Central and peripheral GABA(A) receptor regulation of the heart rate depends on the conscious state of the animal. *Adv Pharmacol Sci.* (2011) 2011:578273. doi: 10.1155/2011/578273
44. Vaska P, Woody CL, Schlyer DJ, Shokouhi S, Stoll SP, Pratte JF, et al. RatCAP: miniaturized head-mounted PET for conscious rodent brain imaging. *IEEE Trans Nucl Sci.* (2004) 51:2718–22. doi: 10.1109/TNS.2004.835740
45. Sung KK, Jang DP, Lee S, Kim M, Lee SY, Kim YB, et al. Neural responses in rat brain during acute immobilization stress: a [F-18]FDG micro PET imaging study. *Neuroimage.* (2009) 44:1074–80. doi: 10.1016/j.neuroimage.2008.09.032
46. Luft C, Greggio S, Venturin GT, da Costa MS, da Costa JC, Donadio MVF. Sex differences in the effects of acute stress on cerebral glucose metabolism: a microPET study. *Brain Res.* (2019) 1722:146355. doi: 10.1016/j.brainres.2019.146355
47. Patel VD, Lee DE, Alexoff DL, Dewey SL, Schiffer WK. Imaging dopamine release with Positron Emission Tomography (PET) and (11C)-raclopride in freely moving animals. *Neuroimage.* (2008) 41:1051–66. doi: 10.1016/j.neuroimage.2008.02.065
48. Cabib S, Kempf E, Schlee C, Oliverio A, Puglisi-Allegra S. Effects of immobilization stress on dopamine and its metabolites in different brain areas of the mouse: role of genotype and stress duration. *Brain Res.* (1988) 441:153–60. doi: 10.1016/0006-8993(88)91393-5
49. Burokas A, Martin-Garcia E, Gutierrez-Cuesta J, Rojas S, Herance JR, Gispert JD, et al. Relationships between serotonergic and cannabinoid system in depressive-like behavior: a PET study with [11C]-DASB. *J Neurochem.* (2014) 130:126–35. doi: 10.1111/jnc.12716
50. Buchecker V, Waldron AM, van Dijk RM, Koska I, Brendel M, von Ungern-Sternberg B, et al. [(18F)]MPPF and [(18F)]FDG muPET imaging in rats: impact of transport and restraint stress. *EJNMMI Res.* (2020) 10:112. doi: 10.1186/s13550-020-00693-3
51. Das A, Kapoor K, Sayeepriyadarshini AT, Dikshit M, Palit G, Nath C. Immobilization stress-induced changes in brain acetylcholinesterase activity and cognitive function in mice. *Pharmacol Res.* (2000) 42:213–7. doi: 10.1006/phrs.2000.0678
52. Konstandi M, Johnson E, Lang MA, Malamas M, Marselos M. Noradrenaline, dopamine, serotonin: different effects of psychological stress on brain biogenic amines in mice and rats. *Pharmacol Res.* (2000) 41:341–6. doi: 10.1006/phrs.1999.0597
53. Deleye S, Verhaeghe J, Wyffels L, Dedeurwaerdere S, Stroobants S, Staelens S. Towards a reproducible protocol for repetitive and semi-quantitative rat brain imaging with (18) F-FDG: exemplified in a memantine pharmacological challenge. *Neuroimage.* (2014) 96:276–87. doi: 10.1016/j.neuroimage.2014.04.004
54. Amirrashedi M, Zaidi H, Ay MR. Advances in preclinical PET instrumentation. *Pet Clin.* (2020) 15:403–26. doi: 10.1016/j.cpet.2020.06.003
55. Picard Y, Thompson CJ. Motion correction of PET images using multiple acquisition frames. *IEEE Trans Med Imaging.* (1997) 16:137–44. doi: 10.1109/42.563659
56. Spangler-Bickell MG, Zhou L, Kyme AZ, De Laat B, Fulton RR, Nuyts J. Optimising rigid motion compensation for small animal brain PET imaging. *Phys Med Biol.* (2016) 61:7074–91. doi: 10.1088/0031-9155/61/19/7074
57. Kyme A, Se S, Meikle S, Angelis G, Ryder W, Popovic K, et al. Markerless motion tracking of awake animals in positron emission tomography. *IEEE Trans Med Imaging.* (2014) 33:2180–90. doi: 10.1109/TMI.2014.2332821
58. Miranda A, Staelens S, Stroobants S, Verhaeghe J. Markerless rat head motion tracking using structured light for brain PET imaging of unrestrained awake small animals. *Phys Med Biol.* (2017) 62:1744–58. doi: 10.1088/1361-6560/aa5a46
59. Miranda A, Staelens S, Stroobants S, Verhaeghe J. Fast and accurate rat head motion tracking with point sources for awake brain PET. *IEEE Trans Med Imaging.* (2017) 36:1573–82. doi: 10.1109/TMI.2017.2667889
60. Miranda A, Staelens S, Stroobants S, Verhaeghe J. Estimation of and correction for finite motion sampling errors in small animal

- PET rigid motion correction. *Med Biol Eng Comput.* (2019) 57:505–18. doi: 10.1007/s11517-018-1899-8
61. Miranda A, Kang MS, Blinder S, Bouhachi R, Soucy JP, Aliaga-Aliaga A, et al. PET imaging of freely moving interacting rats. *Neuroimage.* (2019) 191:560–7. doi: 10.1016/j.neuroimage.2019.02.064
 62. Kyme AZ, Zhou VW, Meikle SR, Fulton RR. Real-time 3D motion tracking for small animal brain PET. *Phys Med Biol.* (2008) 53:2651–66. doi: 10.1088/0031-9155/53/10/014
 63. Zhou V, Eisenhuth J, Kyme A, Akhtar M, Fulton R, Meikle S. A motion adaptive animal chamber for PET imaging of freely moving animals. *IEEE Trans Nucl Sci.* (2013) 60:3423–31. doi: 10.1109/TNS.2013.2277857
 64. Kyme AZ, Angelis GI, Eisenhuth J, Fulton RR, Zhou V, Hart G, et al. Open-field PET: simultaneous brain functional imaging and behavioural response measurements in freely moving small animals. *Neuroimage.* (2019) 188:92–101. doi: 10.1016/j.neuroimage.2018.11.051
 65. Bay H, Ess A, Tuytelaars T, Van Gool L. Speeded-up robust features (SURF). *Comput Vis Image Und.* (2008) 110:346–59. doi: 10.1016/j.cviu.2007.09.014
 66. Chetverikov D, Stepanov D, Krsek P. Robust Euclidean alignment of 3D point sets: the trimmed iterative closest point algorithm. *Image Vision Comput.* (2005) 23:299–309. doi: 10.1016/j.imavis.2004.05.007
 67. Kyme AZ, Fulton RR. Motion estimation and correction in SPECT, PET and CT. *Phys Med Biol.* (2021) 66. doi: 10.1088/1361-6560/ac093b
 68. Rahmim A, Dinelle K, Cheng JC, Shilov MA, Segars WP, Lidstone SC, et al. Accurate event-driven motion compensation in high-resolution PET incorporating scattered and random events. *IEEE Trans Med Imaging.* (2008) 27:1018–33. doi: 10.1109/TMI.2008.917248
 69. Chan C, Onofrey J, Jian Y, Germino M, Papademetris X, Carson RE, et al. Non-rigid event-by-event continuous respiratory motion compensated list-mode reconstruction for PET. *IEEE Trans Med Imaging.* (2018) 37:504–15. doi: 10.1109/TMI.2017.2761756
 70. Vardi Y, Shepp LA, Kaufman L. A statistical-model for positron emission tomography. *J Am Stat Assoc.* (1985) 80:8–20. doi: 10.1080/01621459.1985.10477119
 71. Zhou VW, Kyme AZ, Meikle SR, Fulton R. A scheme for PET data normalization in event-based motion correction. *Phys Med Biol.* (2009) 54:5321–39. doi: 10.1088/0031-9155/54/17/016
 72. Carson RE, Barker WC, Liow JS, Johnson CA. Design of a motion-compensation OSEM list-mode algorithm for resolution-recovery reconstruction for the HRRT. *IEEE Nucl Sci Conf Rec.* (2004) 5:3281–5. doi: 10.1109/NSSMIC.2003.1352597
 73. Angelis G, Bickell M, Kyme A, Ryder W, Zhou L, Nuyts L, et al. Calculated attenuation correction for awake small animal brain PET studies 2013. In: *IEEE Nuclear Science Symposium and Medical Imaging Conference (NSS/MIC)* Seoul, South Korea (2013).
 74. Angelis GI, Kyme AZ, Ryder WJ, Fulton RR, Meikle SR. Attenuation correction for freely moving small animal brain PET studies based on a virtual scanner geometry. *Phys Med Biol.* (2014) 59:5651–66. doi: 10.1088/0031-9155/59/19/5651
 75. Angelis G, Gillam JE, Kyme AZ, Fulton RR, Meikle SR. Image-based modelling of residual blurring in motion corrected small animal PET imaging using motion dependent point spread functions. *Biomed Phys Eng Expr.* (2018) 4. doi: 10.1088/2057-1976/aab922
 76. Miranda A, Staelens S, Stroobants S, Verhaeghe J. Motion dependent and spatially variant resolution modeling for PET rigid motion correction. *IEEE Trans Med Imaging.* (2020) 39:2518–30. doi: 10.1109/TMI.2019.2962237
 77. Dubois A, Herard AS, Flandin G, Duchesnay E, Besret L, Frouin V, et al. Quantitative validation of voxel-wise statistical analyses of autoradiographic rat brain volumes: application to unilateral visual stimulation. *Neuroimage.* (2008) 40:482–94. doi: 10.1016/j.neuroimage.2007.11.054
 78. Yuan TF, Slotnick BM. Roles of olfactory system dysfunction in depression. *Prog Neuropsychopharmacol Biol Psychiatry.* (2014) 54:26–30. doi: 10.1016/j.pnpbp.2014.05.013
 79. Moraes MM, Rabelo PCR, Pinto VA, Pires W, Wanner SP, Szawka RE, et al. Auditory stimulation by exposure to melodic music increases dopamine and serotonin activities in rat forebrain areas linked to reward and motor control. *Neurosci Lett.* (2018) 673:73–8. doi: 10.1016/j.neulet.2018.02.058

Conflict of Interest: The authors declare that the research was conducted in the absence of any commercial or financial relationships that could be construed as a potential conflict of interest.

Publisher's Note: All claims expressed in this article are solely those of the authors and do not necessarily represent those of their affiliated organizations, or those of the publisher, the editors and the reviewers. Any product that may be evaluated in this article, or claim that may be made by its manufacturer, is not guaranteed or endorsed by the publisher.

Copyright © 2021 Miranda, Bertoglio, Stroobants, Staelens and Verhaeghe. This is an open-access article distributed under the terms of the Creative Commons Attribution License (CC BY). The use, distribution or reproduction in other forums is permitted, provided the original author(s) and the copyright owner(s) are credited and that the original publication in this journal is cited, in accordance with accepted academic practice. No use, distribution or reproduction is permitted which does not comply with these terms.



Multi-Scale Imaging of Vascular Pathologies in Cardiovascular Disease

Ashish Tiwari¹, Betsalel Elgrably¹, Galit Saar² and Katrien Vandoorne^{1*}

¹ Faculty of Biomedical Engineering, Technion-Israel Institute of Technology, Haifa, Israel, ² Biomedical Core Facility, Rappaport Faculty of Medicine, Technion-Israel Institute of Technology, Haifa, Israel

OPEN ACCESS

Edited by:

Terry Jones,
University of California, Davis,
United States

Reviewed by:

Sridhar Goud,
National Institutes of Health (NIH),
United States
Claudia Mani,
National Institute of Allergy and
Infectious Diseases (NIH),
United States

*Correspondence:

Katrien Vandoorne
k.vandoorne@technion.ac.il

Specialty section:

This article was submitted to
Translational Medicine,
a section of the journal
Frontiers in Medicine

Received: 06 August 2021

Accepted: 13 December 2021

Published: 05 January 2022

Citation:

Tiwari A, Elgrably B, Saar G and
Vandoorne K (2022) Multi-Scale
Imaging of Vascular Pathologies in
Cardiovascular Disease.
Front. Med. 8:754369
doi: 10.3389/fmed.2021.754369

Cardiovascular disease entails systemic changes in the vasculature. The endothelial cells lining the blood vessels are crucial in the pathogenesis of cardiovascular disease. Healthy endothelial cells direct the blood flow to tissues as vasodilators and act as the systemic interface between the blood and tissues, supplying nutrients for vital organs, and regulating the smooth traffic of leukocytes into tissues. In cardiovascular diseases, when inflammation is sensed, endothelial cells adjust to the local or systemic inflammatory state. As the inflamed vasculature adjusts, changes in the endothelial cells lead to endothelial dysfunction, altered blood flow and permeability, expression of adhesion molecules, vessel wall inflammation, thrombosis, angiogenic processes, and extracellular matrix production at the endothelial cell level. Preclinical multi-scale imaging of these endothelial changes using optical, acoustic, nuclear, MRI, and multimodal techniques has progressed, due to technical advances and enhanced biological understanding on the interaction between immune and endothelial cells. While this review highlights biological processes that are related to changes in the cardiac vasculature during cardiovascular diseases, it also summarizes state-of-the-art vascular imaging techniques. The advantages and disadvantages of the different imaging techniques are highlighted, as well as their principles, methodologies, and preclinical and clinical applications with potential future directions. These multi-scale approaches of vascular imaging carry great potential to further expand our understanding of basic vascular biology, to enable early diagnosis of vascular changes and to provide sensitive diagnostic imaging techniques in the management of cardiovascular disease.

Keywords: endothelial cells, cardiovascular disease, multimodality imaging, optical imaging, positron emission tomography, magnetic resonance imaging, single photon emission contrast tomography

INTRODUCTION

Cardiovascular disease (CVD) is the leading cause of death worldwide and is associated with several chronic diseases and adverse health outcomes. A multitude of etiologies can jeopardize heart function, and subsequently lead to heart failure. Some well-recognized etiological factors include lack of exercise, diabetes, unhealthy diet, smoking and family history (1). In CVDs, inflammation activates the endothelial cells lining the systemic vasculature (2), involving a complex interplay between molecular mediators, endothelial cells and immune cells. Systemic changes to the endothelium constitute key early events that shape CVDs through their direct impact

on the heart and large vessels and are a hallmark of CVD progression and pathogenesis. For instance, a systemically inflamed endothelium initiates atherosclerotic plaques, which can remain asymptomatic for decades, until a plaque rupture narrows or occludes a vessel (2). Occlusion of vessels impedes blood flow to vital organs, such as the heart, causing myocardial infarction (MI). Identifying the mechanisms leading to atherosclerosis and MI, has the potential to distinctly lower cardiovascular mortality. Therefore, an in-depth understanding, combined with early detection and prognosis of endothelial changes hold the potential to prevent fatal events by enabling early treatment, minimizing the risk and reducing severity of CVD. This review covers imaging techniques used to detect early and late vascular changes in the heart and the large vessels during CVDs.

Vascular Biology

The vascular system transports nutrients and oxygen to all organs and enables the circulation of blood and immune cells throughout the body. The endothelium, first identified by Wilhelm His in 1865, comprises the inner cell layer of blood vessels and lymphatics and is present in all adult mammalian tissues. The introduction of electron microscopy (EM) in the 1960's, supplied new insights into and a better understanding of the tightly connected endothelium comprised of the endothelial cells surrounded by a continuous basement membrane (3). During steady state, the vessel density and perfusion of the heart contribute to the normal function of the heart. A healthy endothelium is considered a regulator of vascular tones; in response to vasoactive agents, the normal-functioning endothelium vasodilates as it produces nitric oxide (NO) (4, 5). Cell junctions between endothelial cells are tight at the endothelium of the heart and large vessels, to prevent leakage of plasma proteins in these vital areas (2, 3). Moreover, under normal circumstances the endothelium is anti-inflammatory, as it resists prolonged contact with circulating leukocytes (2). The steady-state endothelium is anti-thrombotic, inhibiting the formation of blood clots in the vasculature (6). In addition, in healthy adult heart and large vessels, the formation of new vessels from preexisting vessels, called angiogenesis is imperceptible. Finally, during homeostasis, endothelial cells are surrounded by a balanced amount of extracellular matrix (ECM) supporting the vasculature (3, 7, 8). All these features of healthy endothelial cells are important for cardiovascular health (Figure 1A).

In the pathogenesis of CVDs, endothelial cells undergo modifications as the vasculature adjusts to the inflammatory state (2). Systematic vascular changes are crucial for prediction of the early endothelial pathologies that can be imaged during CVD progression. Endothelial cells interact with circulating innate immune cells supplied by hematopoietic organs in the body, and therefore play a crucial role in the development and eventual outcome of CVD. Non-invasive imaging techniques can be used as a translational tool to study and quantify endothelial cell features and changes (9). Endothelial cell imaging and monitoring of vascular changes can provide improved strategies for early detection and risk stratification in CVDs.

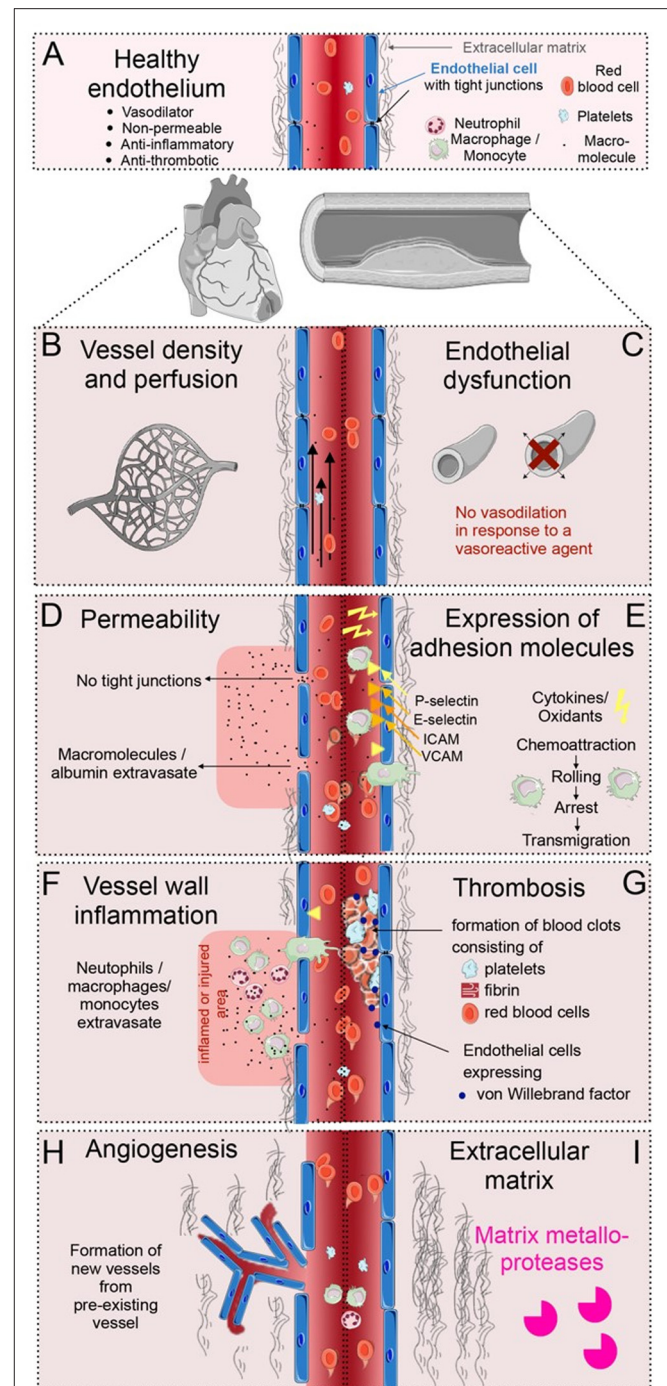


FIGURE 1 | Overview of vascular processes in cardiovascular disease (CVD). **(A)** The healthy endothelium of the heart and the large vessels, is able to dilate, is non-permeable, anti-inflammatory and anti-thrombotic, with tight junction between the endothelial cells, and a balanced amount of extracellular matrix (ECM) surrounding the vessels. **(B)** Alterations in the vessel density and perfusion occur during CVD. **(C)** Endothelial dysfunction is a condition that occurs early in the pathogenesis of CVD, debilitating the local vasodilator response to vasoactive agents. **(D)** Vascular permeability occurs when tight junctions between endothelial cells loosen; molecules and proteins can then extravasate from the circulation. **(E)** Adhesion molecules occurring in specific regions of the vasculature slow down leukocytes at specific regions of

(Continued)

FIGURE 1 | the endothelium. **(F)** Vessel wall inflammation occurs when neutrophils, monocytes and macrophages extravasate into an inflamed or injured area. **(G)** Thrombosis is induced when activated endothelial cells release thrombotic factors, e.g., von Willebrand factor, and form blood clots at the vascular wall together with fibrin, platelets and red blood cells. **(H)** Angiogenesis is the formation of new blood vessels. This happens during infarct healing and in atherosclerotic plaque development. **(I)** Irregular ECM turnover in CVD is a product of imbalanced ECM production and proteolytic activities by matrix metalloproteases.

In cardiomyopathies, reduced perfusion or even occlusion of vessels induces ischemia in the heart (**Figure 1B**) (7). Early in the pathogenesis of CVDs, the endothelial vasomotor function is compromised resulting in an impaired arterial vasoreactivity (i.e., a diminished vasodilator response to vasoactive agents) (**Figure 1C**) (4, 5). In addition, early in CVD development, the endothelial cells can become permeable as tight junctions loosen. Permeable vessels allow for extravasation of serum proteins in cardiac and plaque-associated vasculature (**Figure 1D**) (2, 3). Furthermore, during inflammatory conditions, endothelial cells express adhesion molecules, which slow down circulating leukocytes (**Figure 1E**). When these leukocytes cross the vessel wall, transmigrating neutrophils, macrophages and monocytes cause vessel wall inflammation, breaching the vessel wall, and releasing cytokines (**Figure 1F**) (6). Additionally, activated endothelial cells can release procoagulant and prothrombotic factors, subsequently inducing blood clots in the circulation (**Figure 1G**) (10). Moreover, proangiogenic programs in endothelial cells can be activated during CVDs, inducing the development of new vessels, specifically during infarct healing and in atherosclerotic plaque development (**Figure 1H**) (3, 7). Finally, the unbalanced rearrangement of the ECM and activation of proteolytic activities surrounding the vasculature are crucial biological processes in the progression and outcome of CVDs (**Figure 1I**) (8). Although, there are distinct biological processes that occur at different stages of CVD progression, some, such as endothelial dysfunction, vascular permeability, and perfusion defects can co-occur or overlap. These endothelial changes take place in a complex microenvironment, involving interaction with many other cell types, such as leukocytes, perivascular smooth muscle cells, fibroblasts and the extracellular matrix.

Multi-Scale Imaging Modalities in Vascular Imaging

Current molecular imaging techniques of the heart and the large vessels allow for new biological understanding, early detection and diagnosis of CVDs, as well as targeted treatments and therapy monitoring. Key vascular information can be obtained *via* molecular multi-scale imaging, ranging from optical micro-scale imaging, optoacoustic imaging, and ultrasound, to macro-scale single-photon emission computed tomography (SPECT), positron emission tomography (PET), X-ray computed

tomography (CT), and magnetic resonance imaging (MRI) imaging (**Table 1**).

Optical imaging includes both high-resolution micro-scale intravital microscopy (IVM) as well as whole-body optical fluorescence and bioluminescence imaging. IVM can visualize cellular and subcellular biological processes at early and late stages of CVD, both *ex vivo* and with high sensitivity *in vivo* (11). While it enables visualization at single-cell resolution, it is often time-consuming and necessitates dedicated experts to run the system (11). One of the disadvantages of optical imaging is the limited penetration depth and the lack of anatomical information, with fluorescence imaging in mice performing as deep as 2–3 cm (12), and bioluminescence imaging up to 5 mm deep (13). Both optical fluorescence and bioluminescence imaging are high-throughput and are applied to validate cellular internalization of various imaging agents and for intracellular tracking of small objects. Both optical imaging techniques are highly sensitive (fluorescence: 10^{-9} – 10^{-12} M; bioluminescence: 10^{-15} – 10^{-17} M; **Table 1**), but their spatial resolution is limited. Due to its relatively low cost and high-throughput, optical imaging is widely used for a broad range of imaging applications (12–14). A range of commercially available fluorescence probes, such as organic fluorescent and near-infrared dyes, and bioluminescence imaging probes, like luciferase, are widely used in vascular imaging application (14).

Unlike other imaging modalities like CT, SPECT, PET, and MRI, both optoacoustic and ultrasound imaging have limited penetration depth (**Table 1**). Optoacoustic is an alternative optical-based technique that allows for both microscopic and deeper whole-body imaging. In optoacoustic imaging, the target tissue absorbs light and heats up, which is accompanied by tissue expansion. This expansion results in emission of an acoustic signal, which can be detected with an ultrasound transducer. The use of near-infrared pulses of light, together with the absence of acoustic background signal, provides for increased resolution depth. Contrast is present due to endogenous proteins (hemoglobin, melanin), and near-infrared probes (14, 15). Ultrasound imaging, a real-time anatomical imaging modality, is used to visualize the heart and the vasculature in disease diagnosis. Ultrasonic waves are transduced around the tissue and subsequently a backscattered wave is generated. This wave is then recorded, and an image is generated. In preclinical research, the acoustic response of targeted microbubbles is measured to visualize targeted molecular changes in CVD. These microbubbles allow for high sensitivity (10^{-9} M) and accuracy (16–19).

CT, SPECT, PET and MRI are imaging techniques with unlimited penetration depth. CT is not considered to offer high sensitivity, and thus has limited ability to image cells. Iodine (I) or gold (Au) are used to provide contrast or label cells. CT visualizes differences in tissue attenuation of x-rays, but is hardly used for gaining molecular information. PET and SPECT imaging techniques offer very high sensitivity for radiolabeled probes for targeted molecules in the body, however they fail to provide anatomical information. Therefore, they are most often combined with CT. Both PET and SPECT imaging provide quantitative biomarker information and can achieve high

TABLE 1 | Multi-scale imaging modalities and their technical specifications.

Imaging modality	Spatial resolution	Depth of penetration	Scan time	Sensitivity (mol/L)	Molecular probes
IVM	1–10 μm	<700 μm	Sec-hrs	Single cell	Fluorescent, near-infrared dyes
Optical fluorescence	2–3 mm	<1 mm	Sec-min	10^{-9} – 10^{-12}	Fluorescent, near-infrared dyes
Optical bioluminescence	3–5 mm	1–2 cm	Sec-min	10^{-15} – 10^{-17}	Luciferase
Optoacoustic imaging	10 μm –1 mm	mm-cm	Sec-min	N/A	Endogenous, near-infrared dyes
Ultrasound	30–500 μm	mm-cm	Sec-min	10^{-6} – 10^{-9}	Microbubble
SPECT	0.3–1 mm	No limit	Min	10^{-10} – 10^{-11}	^{111}In , ^{67}Ga , ^{99}Tcm
PET	1–2 mm	No limit	Sec-min	10^{-11} – 10^{-12}	^{18}F , ^{64}Cu , ^{68}Ga , ^{89}Zr
CT	25–250 μm	No limit	Min	N/A	I, Au
MRI	50–250 μm	No limit	Min-hrs	10^{-3} – 10^{-5}	Gd, Fe, Eu, Mn

IVM, Intravital microscopy; SPECT, single-photon emission computed tomography; PET, positron emission tomography; CT, X-ray computed tomography; MRI, magnetic resonance imaging.

sensitivity of 10^{-11} M. SPECT uses radionuclides, such as gamma emitters; emitted gamma rays are detected to create the images. In PET, a radionuclide annihilates an electron and emits two photons that are detected in a coincident fashion. Combined PET/MRI systems is an additional emerging technology that aims to capitalize the advantages of MRI, including increased soft tissue contrast, tissue characterization and molecular imaging, in combination with PET. MRI can image tissue, organ and whole-body anatomy, with unlimited depth of penetration and high sensitivity. gadolinium (Gd), iron (Fe), europium (Eu), and Manganese (Mn) are contrast agents that can produce sufficient contrast in various MRI techniques. While its sensitivity ($\sim 10^{-4}$ M) is lower than modalities such as PET or SPECT (Table 1), its accurate anatomical soft tissue information and versatility (i.e., the availability of multiple imaging strategies like T_1 , T_2 , CEST) render MRI an appreciated molecular imaging technique in CVD. MRI is applied to assess vascular changes, recruitment of immune cells and for dynamic distribution imaging. The main disadvantage of MRI is its temporal resolution, requiring minutes to hours to complete a scan (20). A hurdle in all imaging modalities, that should be noted for cardiovascular imaging, is the motion of the lungs, heart, and large vessels, which is several orders of magnitude larger than the cellular and molecular processes of interest. Therefore, accurate cardiac and respiratory gating, either prospectively or retrospectively, is essential in vascular imaging of CVD (11).

Biomarkers verified on a single-cell level by optical imaging in preclinical CVD animal models can be converted to optoacoustic, ultrasound, SPECT, PET, or MRI markers when bound to specific contrast agents. These molecular targets could be imaged by ultrasound, SPECT, PET, and MRI molecular imaging techniques and advance novel preclinical molecular imaging techniques that eventually could reach the clinics. From a basic science perspective, multi-scale vascular imaging and advances in imaging instrumentation and quantification have enhanced insights into vascular biology and promoted the exploration of novel molecular targets on endothelial cells, which can be applied to verify vascular changes in animal models. Novel vascular imaging techniques can be translated to the clinic for diagnostics, and for monitoring response to treatment.

MULTI-SCALE IMAGING OF HEART AND LARGE VESSELS

Vessel Density and Perfusion

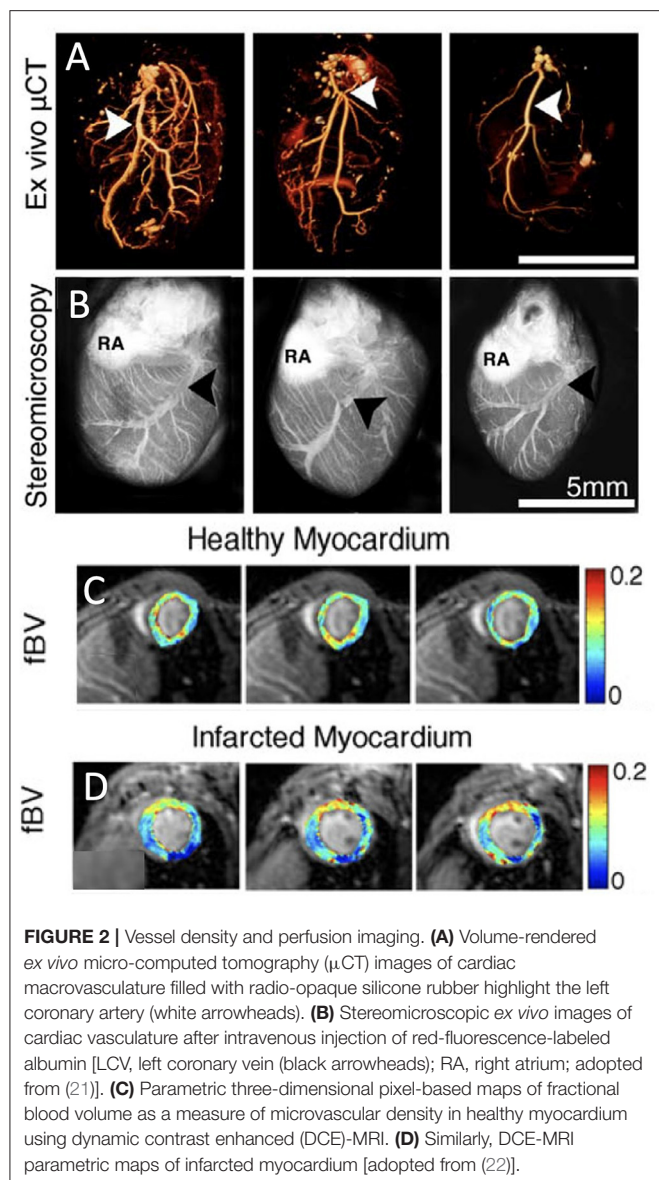
Sufficient blood flow and perfusion are vital for normal functioning of the heart. Therefore, reduced cardiac vessel density and perfusion can indicate cardiomyopathies and vessel occlusion suggest ischemic states. Cardiac imaging techniques measuring cardiac capillary network density, myocardial blood flow, perfused capillary blood volume, and first-pass distribution volume are meaningful for assessment of cardiovascular health (Figure 1B) (7).

Coronary vessel density can be quantified *ex vivo* by injection of fluorescent blood pool agents for optical imaging (Figures 2A,B) (22) or injection of radio-opaque silicone rubber for micro-CT imaging (Figures 2A,B) (21). This could be of particular interest when studying microvascular vessel density in the heart in mouse models. However, these *ex vivo* techniques do not offer any real-time *in vivo* information and cannot be translated to the clinic.

Lee and colleagues introduced a two-photon method for IVM visualization of blood vessels at subcellular resolution, in the normal murine heart (11) and successfully demonstrated real-time *in vivo* imaging of cardiac tissue dynamics under normal conditions. The technique was also applied in a rat ischemia-reperfusion model, and extracted dynamic biological information on vessel density and vessel structure (23).

Myocardial perfusion imaging is a non-invasive method for the evaluation of blood flow through coronary vessels continuously feeding the pumping heart. After blockage of a coronary vessel, the downstream blood supply in the heart is jeopardized. Standard imaging techniques are used for clinically examining vascular perfusion across the entire heart and assessing the extent of damage to the cardiac muscle. PET and MRI have been widely implemented to monitor blood flow and oxygen supply in absolute blood flow quantification. The absolute quantification of perfusion systematically improves prognostics and diagnostic accuracy.

Myocardial perfusion imaging is also widely used for the assessment and quantification of infarct size in heart disease



(20, 24). An *in vivo* mouse study using a clinical SPECT system showed perfect estimation of perfusion defects and non-invasive quantitation of myocardial infarct size (25). Perfusion imaging using either gated blood pool SPECT with ^{99m}Tc -sestamibi or SPECT with labeled erythrocytes using ^{99m}Tc -pertechnetate has low resolution and is mainly used to non-invasively quantify myocardial infarct size (26). Previous studies have used ^{13}N -ammonia for detection of myocardial perfusion, as well as radiolabeled fluorodeoxyglucose (FDG), a glucose tracer, for detection of myocardial glucose metabolism, viability and left ventricular function (26). These methods are also widely used to quantify myocardial perfusion defects in MI patients (27).

In contrast to perfusion SPECT and PET, several MRI techniques have sufficient spatial resolution to quantify the density of blood vessels at the murine myocardium *in vivo*. In both first-pass bolus and macromolecular dynamic contrast enhanced (DCE) MRI, intravenous injection of an MRI contrast

agent, followed by MR monitoring of its dynamics through the vasculature of the heart is used to estimate myocardial perfusion. First-pass perfusion MRI using low-molecular-weight Gd diethylenetriaminepentaacetic acid (Gd-DTPA) can identify perfusion delays in the infarcted heart in mice (28) and rats (29). It can also detect myocardial morphology and function, assess viability of cardiomyocytes and predict future myocardial impairment (29). Bolus tracking with Gd-DTPA is widely used for human cardiac perfusion quantification and infarct size measurements (20). To estimate rodent myocardial fractional blood volume, Gd-DTPA-conjugated albumin has been injected and followed with T_1 mapping. The initial enhancement of DCE MRI at the first time point after injection of macromolecular contrast agent, provides a measure of vessel density, namely the fractional blood volume. In healthy myocardium in C57BL/6 mice cardiac blood volume fraction, evaluating the vessel density, is estimated at around 12%. Three days after MI, a capillary density reduction of ~5% was observed in the infarcted region in a permanent occluded MI model (**Figures 2A–D**) (22). This perfusion deficit at the infarcted region, was similar to the areas of perfusion deficit shown using other cardiac MRI techniques such as first-pass perfusion (28) and arterial spin labeling (30). Although arterial spin labeling also measures myocardial microcirculatory perfusion, it employs arterial water as an endogenous tracer instead of an injectable contrast agent (11, 22). Chemical exchange saturation transfer (CEST) imaging can also visualize myocardial perfusion following intravenous injection of a contrast agent (31). Mn-enhanced MRI, that has been used in the heart mainly to early detect of abnormalities in myocardial calcium handling, can also quantify viable myocardium pointing out areas with microvascular obstruction. It should be noted though that Mn has toxic effects and has therefore limited translational potential (32). Finally, in patients, contrast-enhanced ultrasound imaging has been applied to quantify microvascular blood flow and blood volume (23). It has been shown effective in assessing blood flow, volume, and flow velocity and to bear translational potential for the safe assessment of microvascular blood flow in the clinic (16).

Although, only single-marker imaging studies of vascular density and perfusion imaging in small animals were presented here, we anticipate vessel density and perfusion imaging to soon be performed using multimodal imaging methods, such as PET/MRI, for a better understanding of CVDs and for clinical translation.

Endothelial Dysfunction

When stimulated by physiological or pharmacological stimuli, the normal endothelium responds by vasodilating. Early in the pathogenesis of CVD, the production of nitric oxide (NO) by endothelial cells and subsequent vasodilation are compromised (**Figure 1C**). A malfunctioning endothelium exhibits widespread abnormalities in endothelial integrity, such that permeability changes often coincide with endothelial dysfunction. Endothelial permeability will be discussed in the next section. Although endothelial dysfunction is an early indicator of CVD, it occurs in all stages of vascular disease, such as atherosclerosis, hypertension, diabetes, as well as vascular aging (4). As

endothelial dysfunction is an important signature in CVD, the assessment of NO-dependent vasodilation in large and small vessels throughout the body is often used to predict the adverse outcomes of vascular events (5). Identification of impaired endothelium-dependent vasodilation can assist in cardiovascular risk stratification, as it can predict adverse cardiovascular events and unfavorable long-term outcomes.

Endothelial relaxation has been established by imaging, using ultrasound, PET, and MRI techniques, of vessel dilation following intravenous injection of vasodilators in different mouse models of CVDs. *In vivo* determination of endothelial function in mouse carotid arteries can be achieved by intravenous injection of acetylcholine, followed by ultrasound visualization of vessel relaxation measured by the increased diameter of the arteries. Atherosclerotic mice deficient in apolipoprotein E (*apoE*^{-/-}) on a western diet exhibited impaired relaxation *in vivo*. These results matched gold-standard measurements in isolated carotid arterial rings (Figures 3A–D) (17). ¹¹C-acetate micro-PET imaging performed in mice exposed to hypercapnia stress was applied to evaluate systemic coronary vasodilatation and endothelial function in the heart and appeared instrumental to assess NO-mediated endothelial response (33). Murine MRI has been demonstrated a sensitive and reproducible tool for detection of artery dilation in response to vasodilators (like acetylcholine) or in response to increased flow. Impaired acetylcholine-induced vasodilation was observed at high-resolution by *in vivo* MRI (34–36). Measurement of endothelial dysfunction in patients by acquisition of pulse-wave Doppler velocity or quantitative CT angiography is well-established (37).

Vascular Permeability

Cell junctions between endothelial cells are strictly regulated under physiological conditions. While healthy coronary arteries and large vessels have very limited leakiness, in CVDs, tight junctions can loosen in specific regions of the vasculature. Permeability of vessels in the heart and large vessels is triggered by inflammatory or angiogenic cytokines in CVDs, and is associated with the very first stages of angiogenesis but is also accompanied by inflammatory processes (2, 3). Permeable vessels facilitate the extravasation of circulating proteins or molecules toward tissue (Figure 1D). Elevated vascular permeability in CVDs as observed, for example, in infarct healing or atherosclerotic plaques, results in the extravasation of trackable macromolecular molecules (38). Vessel permeability can be imaged using several *in vivo* methods and can be exploited to estimate the cross-endothelial transport of molecules either between endothelial cells (intercellular pathway) and/or through the endothelial cells (transcytosis).

Molecular imaging of endothelial permeability is performed by the assessment of blood pool agents that are generally confined to the intravascular space. Typically, small molecules, such as low-molecular-weight MR-based Gd-chelates, can swiftly extravasate from injured vessels after MI or in atherosclerotic lesions. Delayed-enhancement imaging with MRI consists of the acquisition of one pre-image and one post-image acquired before and after contrast agent injection, respectively. Very rapid diffusion could hamper the evaluation of delicate differences in

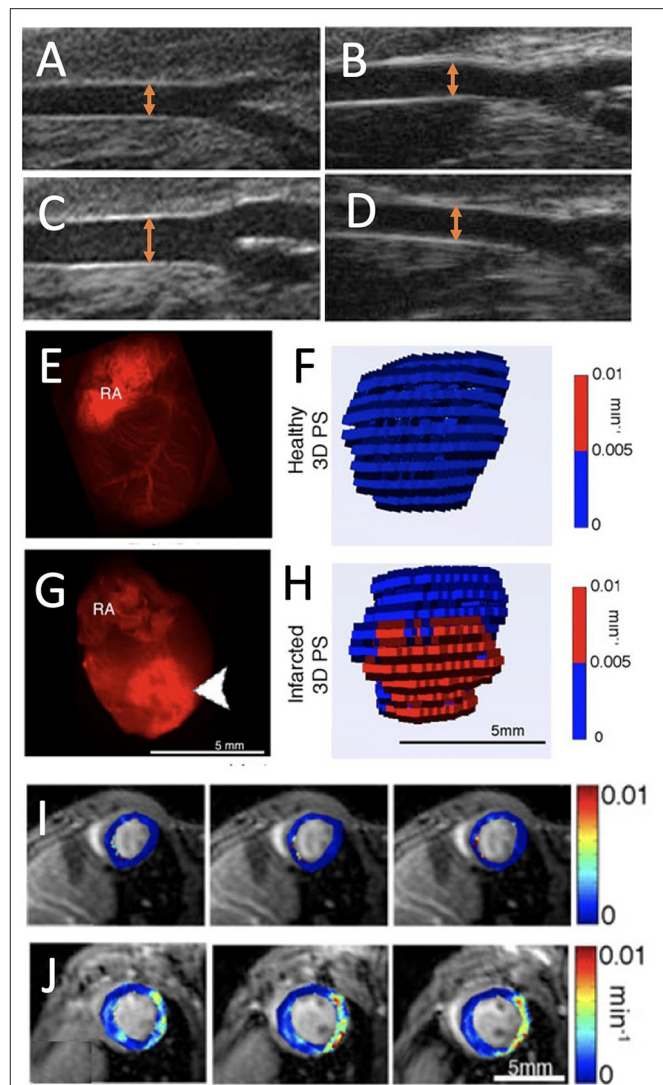


FIGURE 3 | Endothelial dysfunction imaging. (A,B) Ultrasound images of *apoE*^{-/-} mouse carotid arteries at baseline and (C,D) after a dose of acetylcholine (20 μg/kg/min) on a Western diet [orange arrows represent the artery diameter; adopted from (17)]. (E) *Ex vivo* fluorescence images of red fluorescent rhodamine-bovine serum albumin-gadopentetate dimeglumine (rhodamine-BSA-GdDTPA) confined to the blood vessel in healthy myocardium and (F) corresponding three-dimensional (3D) visualization of permeability surface area product (PS) in healthy myocardium. (G) Extravasated rhodamine-BSA-GdDTPA at the infarct (arrowheads) of an infarcted myocardium (RA, right atrium) with (H) 3D representation of PS in infarcted myocardium. (I,J) Parametric maps show the absence of permeability in healthy myocardium and PS in infarcted myocardium [adopted from (22)].

permeability. However, high-molecular-weight contrast agents, such as labeled albumin, improves the sensitivity of detection of mild elevations in vascular permeability. Loosened tight junctions with intercellular pore size of about 20 nm diameter allow the influx of albumin, an ellipsoid-shaped molecule, with a diameter of 3.8 nm and long axis of 15 nm, into the tissue (39). A time-series of scans is acquired after intravenous injection of

either macromolecular agents or agents that bind proteins in the blood.

Epifluorescence whole-heart images, captured 30 min after intravenous injection of labeled albumin, showed albumin's confinement to the blood vessel in healthy myocardium and its influx to the infarcted region (**Figures 3E–H**) (22). Similarly, a permeable endothelium can be imaged *in situ*, after intravenous injection of Evans blue dye (EBD), which binds to serum albumin in the blood and extravasates in a similar way in atherosclerotic lesions (39). For PET imaging, serum albumin can be targeted *in vivo* with isotopically labeled EBD with ^{18}F and ^{64}C . This labeling technique has been employed to non-invasively visualize and quantify vascular leakage and permeability in a mouse model of MI (40).

For MRI, the above-mentioned first-pass imaging post-MI can be used to determine perfusion. At a later time point, in a process called late Gd enhancement, which typically occurs 15–30 min after contrast injection, MRI mapping of Gd-DTPA can also define the infarct size (41). This is mainly considered a measure of cardiac injury but is based on the vascular permeability at the infarcted region of the heart. Non-invasive, three-dimensional MRI has been set up to visualize permeability using high-molecular contrast agent in the murine healthy and infarcted heart (22). While low-molecular Gd-DTPA extravasates in any permeable vessel, high-molecular contrast agent can sensitively quantify all shades of permeability from low till high. After MRI quantification of endogenous myocardial T_1 values, a time series of myocardial scans was performed after intravenous injection of labeled albumin. The vascular permeability in myocardial blood vessels was assessed across the entire heart from the dynamics of injected albumin, and showed increased permeability in infarcted areas. Through the quantification of endogenous myocardial T_1 , the leakage of albumin-conjugated contrast agents, extravasating through permeable myocardial blood vessels, was monitored on short axis cardiac MR images. These permeability measurements identified high vascular permeability in the infarcted region compared to remote regions in the heart 3 days post-infarct (**Figures 3I,J**). The MRI results were validated using *ex vivo* fluorescence imaging (22). This method has been applied to better understand the effect of statins during early and late phases of infarct healing after MI. Early increases in vascular permeability were observed in impaired atherosclerotic infarct healing. The findings in this study revealed that statins lowered permeability and reduced the transit of unfavorable inflammatory leukocytes into the infarcted tissue, consequently improving left ventricular function (42). Similarly, in a recent work, the efficacy of a regenerative hydrogel loaded with insulin growth factor and vascular endothelial growth factor (VEGF) to ameliorate infarct healing, were assessed by albumin-based DCE-MRI. Altered vascular permeability was observed in the treated infarct regions (43). Lipid-based macromolecular contrast agents, such as liposomes containing Gd-DOTA-lipids, have also been applied in mouse infarct models (44). Because of their similar size, such lipid-based agents are comparable to those of albumin-Gd-DTPA and generated contrast enhancement of the remote myocardium 1 day after an acute MI, as the infarct core remained isointense. T_1 mapping performed to quantify liposome accumulation in the infarcted

area, found that the largest post- and pre-contrast longitudinal relaxation rate difference (ΔR_1) was in the infarct region ($0.60 \pm 0.13 \text{ s}^{-1}$). Further, in remote tissue ($0.15 \pm 0.08 \text{ s}^{-1}$) and in healthy cardiac tissue ($0.23 \pm 0.05 \text{ s}^{-1}$), the contrast agent exhibited a similar ΔR_1 (44).

In murine atherosclerotic lesion models, *in vivo* MRI using low-molecular weight Gd, or albumin-binding contrast agents (e.g., Gadofosveset) have been similarly used to detect vascular permeability. In atherosclerotic mice, increased Gadofosveset uptake was observed during plaque progression. Time-dependent changes in relaxation rate of the vessel wall and blood showed high uptake of contrast in the plaque region. Delayed enhancement imaging after Gd-DTPA injection was performed in mice to measure endothelial permeability in the aortic root and to verify reduction in permeability after administration of statin-loaded lipoprotein nanoparticle (45). In parallel, widening of cell-cell junctions and morphological changes of endothelial cells in the region of increased vascular permeability was shown by electron microscopy sections of the plaques (39). Both DCE-MRI and CT imaging are advanced applications for the assessment of vascular perfusion and permeability. DCE-MRI enables two-step pharmacokinetics analysis, comprising intravascular and extravascular component imaging. Initial uptake and first pass of contrast agent in the circulation provide intravascular imaging for perfusion assessment. Subsequent passage of contrast agents to the extravascular space enables delayed imaging and measure of vascular permeability (46). A combined *in vivo* DCE-MRI/CT imaging approach was found beneficial and highly accurate for the assessment of permeability in an acute ischemic stroke study in rats (47). This type of multimodal assessment has not been applied for cardiac or large-vessel imaging, but we believe that, in the future, these types of imaging combinations will provide new avenues for cardiovascular imaging as well.

Expression of Adhesion Molecules

Adhesion molecules are groups of proteins expressed on the endothelial cell surface that are involved in the multi-step adhesion cascade of leukocytes in CVDs. This adhesion includes initial attachment, rolling, arrest and transmigration of leukocytes from the blood to the underlying tissue. Leukocyte rolling is initiated by the interplay between leukocyte carbohydrate-based ligands, endothelial leukocyte adhesion molecule-1 (E-selectin), and endothelial platelets adhesion molecule-1 (P-selectin). Firm adhesion is driven by the interplay between leukocyte integrin, endothelial intercellular adhesion molecule (ICAM)-1 and vascular cell adhesion molecule (VCAM)-1. Expression of these adhesion molecules and their early detection is important in inflammation and cardiac healing as they play an essential role in tissue repair and immune-vasculature interactions in CVDs. Adhesion molecules can also be involved in thrombus formation (6). Adhesion molecules, like E- and P-selectin or VCAM-1 and ICAM-1, mark early signs of an activated endothelium and can be specifically targeted and imaged in CVDs (**Figure 1E**). *In vivo* optical, ultrasound, PET and MRI imaging techniques have been employed to assess these biomarkers in CVDs (19).

Cell-adhesion molecules cooperate in the early advancement of atherosclerotic lesions by assisting in leukocyte recruitment to the vessel wall. A dual optical and MRI imaging approach applied to visualize VCAM-1 targeting using both near-infrared dyes and chelated Gd ions demonstrated its utility in targeting adhesion molecules in a murine atherosclerotic *apoE*^{-/-} model. The team demonstrated delivery of contrast agent to atherosclerotic plaque regions by targeting cell receptors present on endothelial cells. *Ex vivo* fluorescence and *in vivo* MR imaging showed the uptake and targeting ability of the contrast agent in aortas and the abdominal aorta (Figures 4A–C) (12). This imaging method for detection and quantification of VCAM-1 allows for early identification of inflammation in atherosclerosis. Similar real-time detection of VCAM-1 expression was employed to identify activated cells in human plaques. Research aligning with these studies, was performed in *apoE*^{-/-} mice, in which contrast agent uptake in developing plaques was dynamically evaluated for 28 days. High-contrast uptake in the region of VCAM-1 expression by endothelial cells was quantified in atherosclerotic plaques with high affinity and sensitivity. This enabled real-time assessment of VCAM-1 expression in atherosclerosis, which served as a proxy for activated cells in human plaques (48).

Using an ultrasound-based strategy, microbubbles designed to target the adhesion molecule ICAM-1 have been injected and imaged to detect inflammation and consequent signs for transplant rejection of heterotopic hearts in rats (18). Progressive atherosclerotic plaques exhibit active expression of P-selectin during activation of the endothelium overlying active atherosclerotic plaques. Inactive fibrous plaques do not exhibit expression of P-selectin. *In vivo* characterization of P-selectin expression by PET imaging of active plaques was achieved with ⁶⁸Ga-Fucoidan, a highly sensitive polysaccharidic ligand of P-selectin (49). Furthermore, ⁶⁴Cu-labeled anti-P-selectin monoclonal antibodies were used to target endothelial activation at atherosclerotic lesions in low-density lipoprotein receptor-deficient *Ldlr*^{-/-} mice on a high-cholesterol diet. PET/CT fusion imaging revealed selective and prominent accumulation of the probe in the aortic root. *Ex vivo* autoradiography of aortas additionally confirmed probe uptake (50).

Targeting of E-selectin using an appropriate contrast agent, together with visualization of immune cell recruitment and their interaction with endothelial cells, was performed both *in vitro* and *in vivo* models of hepatitis in mice. The targeted contrast agent, particularly iron nanoparticles, recognized E-selectin and bound extracellularly to E-selectin overexpressed on activated endothelial cells, thus facilitating *in vivo* MRI of endothelial cell activation (51). In a mouse model of inflammation, the distribution of E-selectin expression on an activated vascular endothelium and its localization was validated using iron nanoparticles; histological analysis confirmed their distribution (52). Two MRI studies used iron nanoparticles to target VCAM-1 on activated endothelium in atherosclerotic *apoE*^{-/-} mice (53, 54). The VCAM-1-targeted iron nanoparticles accumulated in plaques, which resulted in negative contrast enhancement, highlighting plaques rich in macrophages. VCAM-1 targeting appeared very sensitive, as a low dose of contrast agent was sufficient to identify activated plaque regions

(53). In addition, the accumulation of VCAM-1-targeted iron nanoparticles in atherosclerotic lesions highlighted the applicability of atherosclerosis imaging with MRI (54).

Imaging of adhesion molecules in vascular processes is important because it zooms in to areas in the endothelium that harness the recruitment of immune cells, which is crucial in both cardiac healing and atherosclerotic progression.

Vessel Wall Inflammation

When adhesion molecules are expressed, leukocyte-like neutrophils, monocytes and macrophages can transmigrate through the endothelial lining and cause vessel wall inflammation. After intravenous injection, nanoparticles are internalized by leukocytes, primarily by monocytes, macrophages, and less so by neutrophils. Once in the tissue, the leukocytes with internalized nanoparticles, can be imaged as they transmigrate into the vessel wall. In this way, the progression of vessel wall inflammation can be non-invasively tracked (Figure 1F).

The uptake of fluorescently labeled iron nanoparticles by macrophages has been imaged in infarcted myocardium using both *in vivo* optical imaging and MRI. The fluorescent signal throughout the heart was quantified *via* fluorescence molecular tomography images of mice with MI. Besides fluorescence imaging, non-invasive infiltration of iron nanoparticles at the infarcted areas of the heart was shown as a hypointense signal using MRI. This could be of significant value in both preclinical and clinical settings. The techniques developed can also be used to image other existing fluorescent and magneto-fluorescent probes and can significantly expand the role of fluorescence imaging in the heart (55). Another study in mice quantified the uptake of iron-nanoparticle-based contrast agents in plaque regions in cardiac arteries using *in vivo* MRI. MRI mapping and accumulation of the contrast agent showed that average T₂ values in the plaque region decreased from a baseline value of 34.5 ± 0.6 ms to 24.0 ± 0.4 ms 1 day after injection. The T₂ values were inversely related to the amount of iron nanoparticles in the plaque region assessed by *ex vivo* particle electron paramagnetic resonance. Furthermore, plaque progression and treatment outcomes were assessed and monitored (56). Similarly, visualization of emulsified perfluorocarbon, by *in vivo* fluorine (¹⁹F) MRI in an acute cardiac ischemia murine model showed its significant uptake in lymph nodes and identified that circulating monocytes/macrophages are the main cell fraction contributing to image contrast. This MRI-based approach allows numerous applications of inflammatory disease states (57).

Iron nanoparticles have also been applied to track macrophage-rich atherosclerotic plaques using positive-contrast MRI in small animals. Iron nanoparticle uptake and signal enhancement were found specifically in inflamed atherosclerotic plaques (58). In hyperlipidemic rabbits, iron nanoparticle-based contrast agents were shown to accumulate in plaques with high macrophage content and generated significant contrast and signal changes in infected regions (59). Macrophage recruitment in acute atherosclerosis was also studied, and quantification of macrophages directly correlated with dynamically monitored vascular changes in plaque inflammation. Moreover, *in vitro*

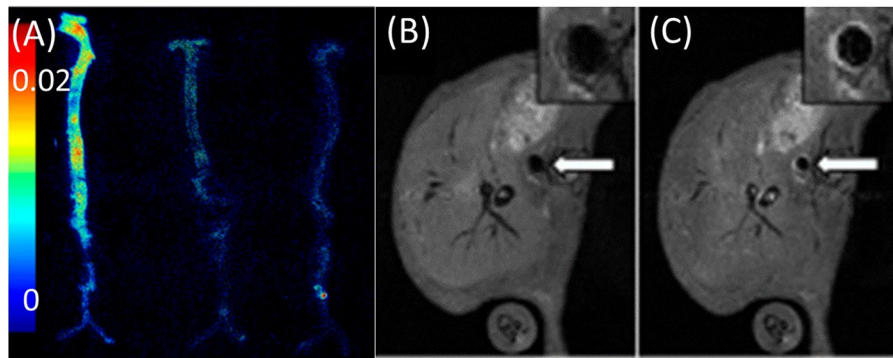


FIGURE 4 | Imaging of adhesion molecules. **(A)** *Ex vivo* fluorescence image of aortas obtained by VCAM imaging of *apoE*^{-/-} mice injected with (from left to right) VCAM-TMV, PEG-TMV, and PBS, respectively. **(B)** Pre-injection and **(C)** post-injection MRI scans of VCAM-TMV in *apoE*^{-/-} mice. Insets show magnified images of abdominal aorta with regions of interest [adopted from (12)]. VCAM, vascular cell adhesion molecule; PEG, Polyethylene glycol; TMV, Tobacco mosaic virus.

validation results displayed concentration-dependent contrast agent uptake by macrophages (60).

In a recent study, nanoparticles were used for macrophage imaging in inflamed cardiovascular tissues using multi-scale imaging. It was shown that ¹⁸F-Macroflor, a modified nanoparticle with high avidity for macrophages, was enriched in cardiac and plaque macrophages. This enabled the sensitive tracking of macrophages in a PET/MRI study of the infarcted heart in both mice and rabbits (61). Another multimodal strategy was recently implemented and applied to quantify ⁸⁹Zr-labeled liposomal nanoparticle uptake in the atherosclerotic vessel wall of rabbits using PET, in conjunction with CT and DCE-MRI with low-molecular Gd-DTPA for vascular permeability. The analysis showed that uptake was significantly higher in atherosclerotic compared to control rabbits (1.8 vs. 0.9 g/mL). Nanoparticle biodistribution and vessel wall targeting in a rabbit atherosclerosis model was also evaluated *ex vivo* using optical imaging and autoradiography. The study provided a multimodal tool to accurately validate nanoparticle targeting of plaques in atherosclerotic vessel walls (62).

Dextranated and DTPA-modified magneto-fluorescent nanoparticles labeled with PET tracer ⁶⁴Cu were used for *in vivo* multimodal imaging to directly detect macrophages in atherosclerotic plaques of *apoE*^{-/-} mice. This new PET-based contrast agent with avidity for macrophages was developed with optimized pharmacokinetics to allow for *in vivo* imaging of macrophage recruitment to injured aortas. The contrast agent facilitated the quantification of an elevated number of macrophages in *apoE*^{-/-} aortas compared to wild type aortas. The study provided an improved imaging probe with enhanced sensitivity and direct correlation to PET signal intensities and localization (63). Of note, intravenous injection of iron nanoparticles may change the course of infarct healing after MI, as these nanoparticles have proven cardioprotective features (64).

Thrombosis

During homeostasis, endothelial cells are key regulators of thrombosis as they produce anticoagulant and antithrombotic

factors, such as prostacyclin, NO and plasminogen activator and its inhibitor. After activation or injury of endothelial cells, they become procoagulant and prothrombotic (10). Thrombosis is the formation of blood clots, which are comprised of platelets and fibrin, inside a vessel. In this process, endothelial cells release von Willebrand Factor, a blood glycoprotein involved in hemostasis that assists with platelet adhesion to exposed matrix, and eventually to blood flow obstruction. Atherosclerotic plaques that exhibit thrombo-modulatory factors have been shown to be less stable (10), thus making thrombosis a key process to that can serve as a marker of unstable plaques (Figure 1G).

The process of cellular thrombosis formation has been assessed using fluorescent probes *in vivo* as well as in an *ex vivo* flow chamber system. Fluorescein isothiocyanate (FITC)-labeled isolectin at the endothelial cells, whereas circulating platelets were fluorescently stained by rhodamine 6G. After *ex vivo* isolation of cremasteric arteries of mice, thrombus formation after functional damage to the endothelium was visualized (65). Complement C3 is a factor that is involved in thrombosis and has been targeted for imaging; non-invasive ultrasound imaging displayed serum complement C3 adherence of albumin-encapsulated microbubbles to the vascular endothelium at atherosclerotic plaques in *apoE*^{-/-} mice. Microbubbles were also fluorescently labeled so that the adherence to activated endothelium of atherosclerotic plaque could be confirmed by fluorescent microscopy (66).

In atherosclerotic rabbits, plaque rupture with subsequent thrombosis was imaged with MRI using fibrin-binding Gd-labeled peptide (EP-1873) (67). A fibrin nanoagent has been targeted and labeled for both MRI and optical imaging using iron nanoparticle and near-infrared fluorescence agent, respectively, to assess and detect microthrombosis in a rat MI model (68). Fibrin is a major constituent of arterial and venous thrombi and has been targeted in several multimodal imaging methods of thrombosis (69–71). A recent ¹⁹F MRI study showed the selective targeting of activated platelets using activated integrin glycoprotein IIb/IIIa labeled with perfluorocarbon, in both mice and humans (72). The fibrin-binding probe FBP7 labeled with

^{64}Cu has been developed for PET, to detect both arterial and venous thrombi in rats with either carotid crush injury (mural thrombosis model) or embolic stroke (occlusive thrombosis model) (69). Multisite thrombus imaging and estimation of fibrin content were also achieved with whole-body PET in similar studies (69, 70, 73). Furthermore, *in vivo* multimodal imaging was performed using MRI/PET/SPECT techniques to detect and visualize vascular injury and thrombogenic plaque in mice using ^{64}Cu -labeled glycoprotein VI-Fc ^{64}Cu -GPVI-Fc contrast agent. *Ex vivo* histology and *in vivo* MRI and PET imaging results were validated and collagen content, plaque burden and vessel wall functioning in the endothelial cell injury and thrombus detection were measured. Uptake of ^{64}Cu -GPVI-Fc was found higher in the injured left carotid artery wall than in the intact right carotid artery. As validated in *apoE*^{-/-} mice, ^{64}Cu -GPVI-Fc uptake in the aortic arch was significantly higher compared to wild type mice (*apoE*^{-/-}: $13.2 \pm 1.5 \text{ Bq/cm}^3$ vs. wild type mice: $5.1 \pm 0.5 \text{ Bq/cm}^3$, $P = 0.028$). Similarly, high relaxation rates were measured in the injured carotid wall in T₁ MR scanning (injured carotid wall: $1.44 \pm 0.08 \text{ s}^{-1}$ vs. intact carotid wall: $0.91 \pm 0.02 \text{ s}^{-1}$; $P = 0.028$) (74). In a more recent study, fluorescently labeled, activatable, cell-penetrating peptides (ACPPs) were designed and used to visualize their *in vivo* uptake, after their cleavage by matrix metalloproteinases (MMPs) or thrombin. ACPP uptake, mapped *ex vivo* in the whole aortas, was higher in disrupted compared to non-disrupted plaques. The combination of optical molecular and Gd-enhanced MRI imaging for detection and assessment of endothelial defects, facilitated the identification of high-risk unstable plaques in atherothrombosis (Figures 5A,B) (75).

Angiogenesis

Angiogenesis is a complex molecular and cellular process that involves the proliferation of endothelial cells after cardiac ischemia and during atherosclerotic plaque development. The process of angiogenesis entails not only endothelial cell activation by pro-angiogenic factors, but also increased permeability, as discussed above, and ECM remodeling (3, 7). Although ECM remodeling is key to the development of new vessels, it will be discussed separately below, as the ECM can also remodel in fibrotic processes with little connection to angiogenic changes. Targets for pro-angiogenic imaging in infarct healing, and in atherosclerotic plaques include VEGF, its receptor (VEGFR) and $\alpha_v\beta_3$ integrin on activated endothelial cells. In response to an ischemic lesion, VEGF is released at the myocardium or in plaques to stimulate the formation of vessels to supply oxygen and nutrients (Figure 1H). Activation of the $\alpha_v\beta_3$ integrins on the ECM side of the endothelial cells, is essential for endothelial cell propagation. Short peptide sequences, like Arg-Gly-Asp (RGD), can recognize and label $\alpha_v\beta_3$ integrin activation for several imaging modalities. Although the main imaging markers for angiogenesis are VEGF and $\alpha_v\beta_3$ integrin, we will also point out some other pro-angiogenic imaging strategies (76, 77).

Angiogenesis in Infarct Healing

After MI, a large area of hypoxic tissue within the heart initiates the expression of various pro-angiogenic genes in endothelial cells. Angiogenesis is an important biological process that occurs during the proliferative phase of myocardial healing after the infarct. Tracking the angiogenic responses is crucial when monitoring the response of healing after infarction, particularly in the assessment of efficacy and safety of novel regenerative treatments after MI. Recent progress in molecular imaging has brought to the development of a platform to visualize the formation of new blood vessels using optical, ultrasound, SPECT, PET, and MRI imaging approaches *in vivo* (78).

Angiogenesis is an integral part of scar formation after MI. Apln is expressed in response to hypoxia and has been employed to visualize sprouting blood vessels at the MI border zone using confocal microscopy (79). In addition, after an ischemic event, the pro-angiogenic factor VEGF and its receptor VEGFR are highly expressed and serve as targets for imaging myocardial angiogenesis. In stroke, bioluminescence imaging with luciferase has been used to image VEGF receptor 2 (VEGFR2). A novel approach for optical quantification of angiogenic sprouts after MI involves study of the apelin (Apln) reporter mice (79). Transgenic mouse expressing firefly luciferase under the control of the VEGFR2 promoter were utilized to non-invasively decipher the temporal profile of VEGFR2 expression after stroke highlighting VEGF/VEGFR2 signaling (13).

Furthermore, *in vivo* ultrasonography imaging of VEGFR2 expression on endothelial cells was used for molecular and functional assessment in a mouse hind limb ischemia model (80). In murine hind-limb ischemia study, ^{64}Cu -VEGF₁₂₁ has been employed to image angiogenesis by PET. In this study, VEGF was upregulated following treadmill exercise training (81). In a rat model of MI, the same ^{64}Cu -VEGF₁₂₁ tracer was tracked by *in vivo* cardiac PET imaging. This dynamic study showed that VEGF levels peaked 3 days after MI and subsequently declined over time, reaching baseline levels 24 days after MI (82). For tumor imaging, both VEGFR-1 and VEGFR-2 receptors were exploited as PET radiotracers and successfully validated the mapping of angiogenesis (83). In the future, we envision that these types of studies, can also be applied in cardiac vascular imaging after MI to reveal dynamic biological processes.

Another approach used to image angiogenic processes targets the transmembrane protein $\alpha_v\beta_3$ integrin that can be imaged with labeled RGD after acute MI (77). For instance, a targeted radiotracer of $\alpha_v\beta_3$ integrin was utilized to dynamically track angiogenesis in a murine limb ischemia model. More specifically, a ^{99}Tc -labeled peptide that binds to $\alpha_v\beta_3$ integrin, was employed to follow the activation of $\alpha_v\beta_3$ integrin over time at the ischemic region (84). In the same hind-limb model, a multimodal approach was used to assess angiogenesis by labeling the $\alpha_v\beta_3$ integrin-binding peptide not only for SPECT imaging (by ^{99}Tc), but also for *in vivo* fluorescence imaging (85). Serial *in vivo* SPECT imaging has been performed in both rat and canine MI models using a ^{111}In -labeled $\alpha_v\beta_3$ -targeting agent. This approach demonstrated increased myocardial radiotracer uptake in the infarcted region, indicating myocardial angiogenesis (86). Its

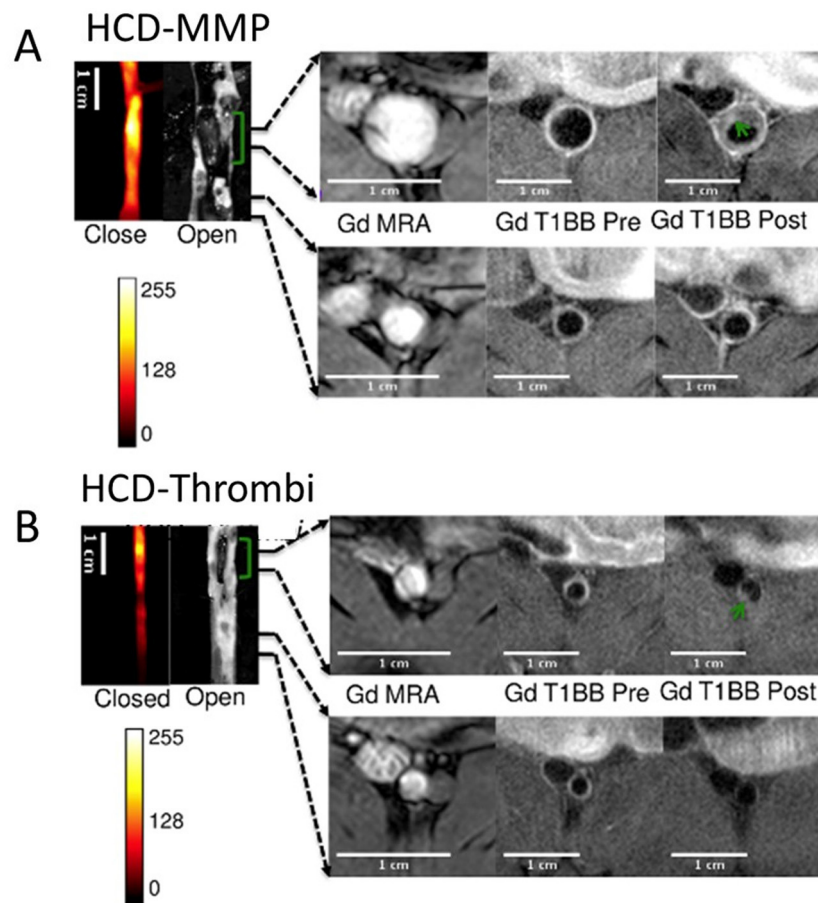


FIGURE 5 | Thrombus imaging. Fluorescence and MRI images of rabbits collected using a **(A)** HCD+MMP-ACPP probe and **(B)** HCD+ Thrombin-ACPP probe, respectively. The closed view of the fluorescence images shows a sub-section of the abdominal aorta and the corresponding open view reflects images showing the location of thrombi (green brackets). The regions within the two black lines represent examples of non-disrupted and disrupted plaques, respectively, and correspond to the MRI images on the right. All MRI images were obtained after injection of Gd-DTPA according to acquisition protocols. Illustrated are the pre-triggering magnetic resonance angiography (MRA) and the fat suppressed T₁BB images obtained before and after pharmacological triggering (from left to right). Thrombi are marked by green arrows in post-triggering Gd-T₁BB (T₁ black blood) images [adopted from (75)]. HCD, high-cholesterol diet; MMPs, matrix metalloproteinases; ACPP, activatable cell-penetrating peptides; Gd, DTPA, gadolinium chelate.

uptake in the infarcted myocardium coincided with regions of hypoxia, as imaged *in vivo* due to elevated levels of the hypoxic marker ¹¹¹In-RP4748 (87). Additionally, ¹⁸F-RGD has been applied in a rat model of MI. One week after permanent left coronary artery (LCA) ligation, rats were injected with ¹⁸F-RGD to evaluate $\alpha_v\beta_3$ integrin expression in the infarcted area using a small-animal PET scanner. In the same rats, changes in LV cavity size, LV function, and infarct size were studied by serial ¹³N-ammonia PET and MRI measurements at 1 and 12 weeks after MI. Uptake of ¹⁸F-RGD was compared with the presence of angiogenesis in histologic samples at 1 week after MI in a subgroup of rats. Increased uptake of ¹⁸F-RGD in the perfusion defect area early after MI correlated with improved cardiac function and eventual outcome (Figure 6) (88). These imaging studies have marked $\alpha_v\beta_3$ integrin as a biomarker of myocardial repair processes after MI. This combination of PET/CT molecular imaging with functional cardiac MRI has

found its way to the clinic. Multimodal imaging of cardiac $\alpha_v\beta_3$ integrin in patients after acute MI has been performed using PET/CT/MRI imaging (83, 84). Finally, multiparametric PET and MRI using $\alpha_v\beta_3$ integrin as a target have been used in infarct patients to predict long-term cardiac function. Imaging of elevated angiogenic markers in infarct healing has been demonstrated an important prognostic approach after MI (89).

Angiogenesis in Atherosclerotic Plaques

Plaque angiogenesis and rapid growth of the vasa vasorum in the vessel wall, have been associated with the development of unstable plaques, particularly in patients with diabetes and unstable coronary syndrome. Neovascularization of the plaque can cause plaque rupture through several mechanisms. Immature vessels increase permeability and protease activation, which, in turn, could lead to hemorrhages from plaque capillaries, induction of inflammation and plaque instability

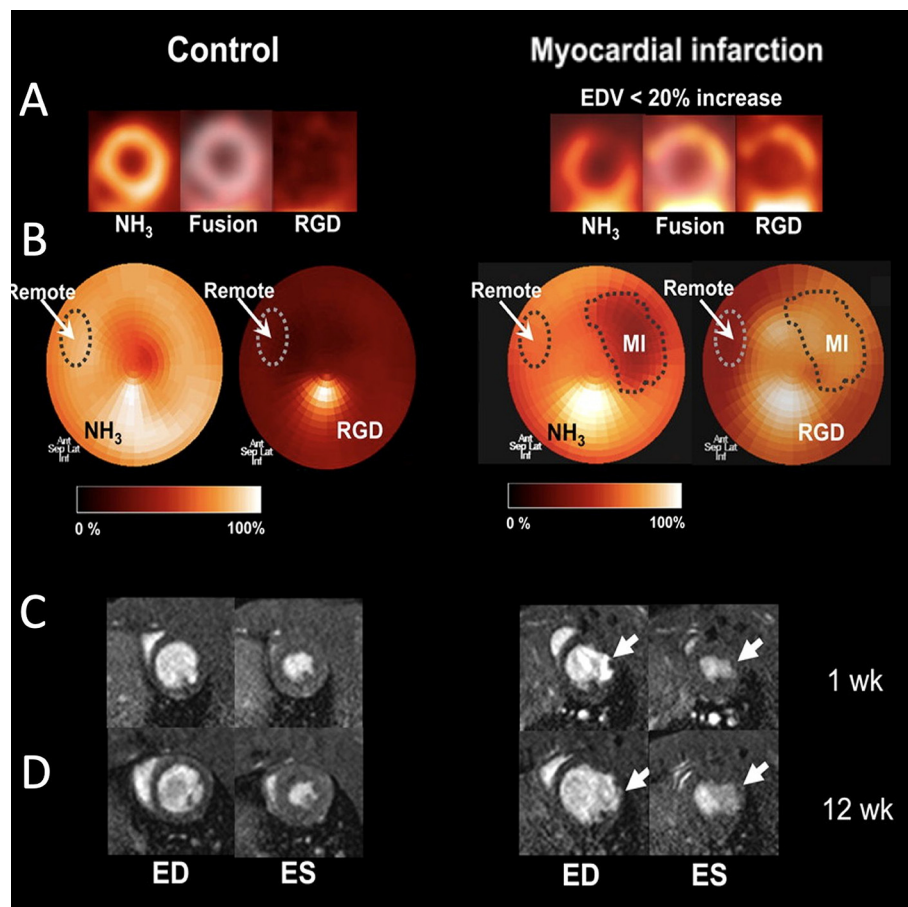


FIGURE 6 | Imaging of angiogenesis in myocardial infarction (MI). **(A)** PET images of control rats and rats after MI (right), which show separate and fused co-registered ^{18}F -RGD and ^{18}F -NH₃ tomograms. **(B)** ^{18}F -NH₃ polar maps and co-registered ^{18}F -RGD polar maps. Each ^{18}F -NH₃ polar map was normalized to its corresponding remote myocardium uptake and defect area region of interest (ROI) was defined using 50% threshold. Subsequently, remote and defect ROIs were co-registered in the ^{18}F -RGD polar map using same axes to evaluate ^{18}F -RGD uptake in infarcted and remote myocardium. **(C)** Representative cross-sectional MR images of the left ventricle (LV) during end-diastole (ED) and end-systole (ES) 1 week after MI. **(D)** Corresponding MR images of same rats 12 week after MI [adopted from (88)]. ^{18}F -RGD, ^{18}F -galacto-RGD.

(85, 86). *In vivo* tracking can be exploited to better understand the involvement of angiogenesis in the pathophysiology of atherosclerosis, by quantifying pro-angiogenic markers along large vessels.

The advancement of unstable plaques is associated with increased VEGF/VEGFR signaling and is enhanced in diabetes (90). *Ex vivo* near-infrared fluorescence imaging with anti-VEGF-800CW, identified VEGF-A overexpression in atherosclerotic plaques (91).

A VEGF-based SPECT tracer labeled with ^{99}Tc was shown to identify accelerated atherosclerosis in diabetic atherosclerotic *apoE*^{-/-} mice (92). The same *apoE*^{-/-} mice were used to test statin therapy, known to stabilize atherosclerotic plaques. These mice were probed by non-invasive SPECT imaging of atherosclerotic neovascularization using a ^{99}Tc -labeled anti-VEGF antibody. This imaging strategy allowed for the non-invasive diagnosis and assessment of plaque neovascularization, showing the antiangiogenic effect of atorvastatin (93).

Plaque angiogenesis has also been non-invasively probed using integrin $\alpha_v\beta_3$ ligands. Following intravenous injection of $\alpha_v\beta_3$ -integrin-targeted paramagnetic nanoparticles into atherosclerotic rabbits, increased MRI signals were recorded at the regions of the neovasculature, specifically throughout the abdominal aortic wall (94). Finally, atherosclerotic plaque angiogenesis in the abdominal aorta was also probed using PET/MR imaging and ^{68}Ga -labeled, GEBP11 peptide-targeted magnetic iron oxide nanoparticles in a rabbit model of atherosclerosis (Figure 7) (95).

Extracellular Matrix Rearrangement

The ECM is critical for all aspects of vascular biology. Together with supporting cells, endothelial cells form a basement membrane matrix contributing to structural and organizational stability of the vasculature. In the progression of CVDs, the basement membrane matrix supporting the endothelium can be degraded by matrix metalloproteinases (MMPs) (Figure 11).

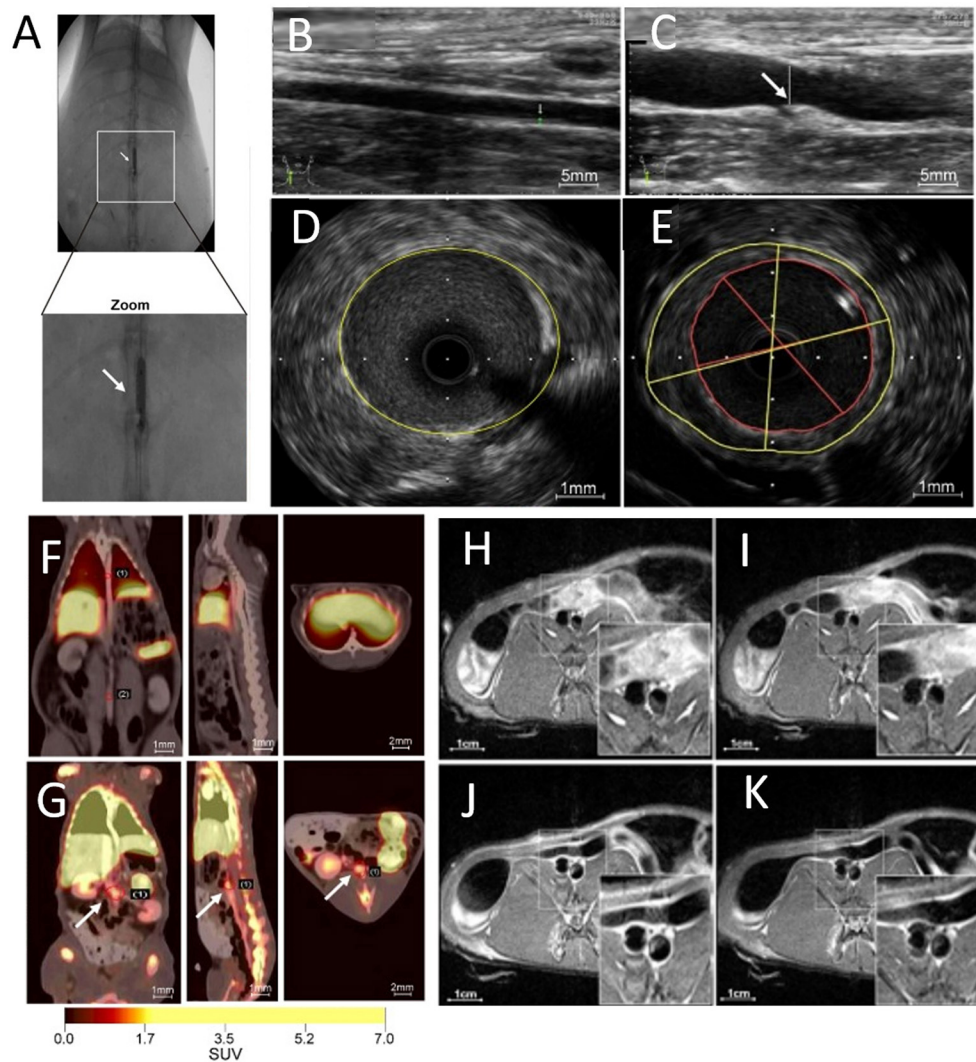


FIGURE 7 | Multimodal imaging of angiogenesis. **(A)** Abdominal aorta balloon denudation model, showing ultrasonic images of **(B)** control vessels and **(C)** vessels after denudation injury displaying vessel enlargement and plaque formation 8 weeks after injury. Representative intravascular ultrasonic images of **(D)** control and **(E)** injured vessels, showing a greater plaque burden and plaque eccentricity in the injured mice. PET images of rabbits 2 h after **(F)** ^{68}Ga -NGD-MNPs or **(G)** ^{68}Ga -NUD-MNPs injection. MR images of abdominal aorta before and 4 h after **(H,I)** control NUD-MNPs injection or **(J,K)** GE11 peptide targeted NGD-MNPs injection [Scale bar (H–K) – 1 cm; adopted from (95) with pending permission]. ^{68}Ga -NUD-MNPs, ^{68}Ga -NOTA-unrelated peptide-DMSA-MNPs; ^{68}Ga -NGD-MNPs, ^{68}Ga -NOTA-GE11-DMSA-MNPs; DMSA-MNPs, 2, 3-dimercaptosuccinic acid-coated paramagnetic nanoparticles; NOTA, 1,4,7-triazacyclononane- N,N',N'' -triacetic acid; GE11, peptide with angiogenic affinity.

The ECM supports essential functions of endothelial cells (8). For example, in angiogenesis, the ECM facilitates migration, invasion, proliferation, and survival of endothelial cells, as it serves as a scaffold protecting and guiding the endothelial cells. Subsequently, integrins are activated, as described in the angiogenesis section (8). Proper balance between proteolytic activities and ECM production is pivotal in cardiovascular health (96).

Matrix Metalloproteinases

MMPs are a family of zinc-dependent endopeptidases that play an essential role CVDs. By degradation of the surrounding

matrix, MMPs facilitate angiogenesis as they clear the way for endothelial cell to grow and migrate. Likewise, they rearrange the ECM in the heart and the vessel wall during CVDs. Therefore, MMPs and their enzymatic activities are important targets for optical, SPECT, PET, and MRI imaging.

A near-infrared fluorescent probe, activated by proteolytic cleavage by MMP2 and MMP9, has been characterized for optical imaging of MMP activity in the heart after MI, and applied to show increased MMPs activity in infarcted region (97). An MMP-sensitive, activatable fluorescent probe (MMPsenseTM 680) has been applied to visualize MMP activity in carotid plaques of symptomatic patients. Deep-tissue multispectral optoacoustic

tomography (MSOT) technology visualized MMP activity in vulnerable plaques with high specificity, allowing staging of plaque vulnerability (**Figures 8A,B**) (15). An *ex vivo* murine MI study used a MMP imaging strategy based on activatable cell-penetrating peptide probes, and displayed high sensitivity to the proteolytic activity of MMP2 and MMP9. *Ex vivo* histology and autoradiography showed MMP activity at the infarct region and the border zone of the heart after MI (**Figures 8C,D**) (98).

In addition, MMP activation in atherosclerotic mouse aorta was assessed using *in vivo* SPECT/CT imaging using an ^{111}In -labeled tracer targeting activated MMP (99). The study revealed the heterogeneity of atherosclerotic plaques and appeared a powerful tool for tracking plaque biology (**Figure 8E**). In a rabbit study, MMP activity in atherosclerotic lesions was also reported using *in vivo* SPECT imaging with a ^{99}Tc -radiolabeled MMP inhibitor molecule. Tracer uptake quantification proved a feasible method for MMP detection and assessment of plaque vulnerability (100). Similarly, [^{123}I]I-HO-CGS 27023A, a broad-spectrum radiolabeled MMP inhibitor, was used to image MMP presence using SPECT, at ligated carotid arteries in *apoE*^{-/-} mice (101). An ^{111}In -labeled small molecule with broad specificity for activated MMPs (RP782) has been used for *in vivo* microSPECT/CT imaging of the remodeling process following mechanical injury in *apoE*^{-/-} mice (102).

Moreover, non-invasive MRI has been used to evaluate MMPs in atherosclerotic rabbits and mice using a Gd-based contrast agent. *In vivo* MRI and *ex vivo* validation demonstrated the accurate visualization and delineation of MMP-rich atherosclerotic plaques (103). Similarly, *in vivo* MR imaging of MMPs and their activity in ECM was performed in atherosclerotic rabbits using a Gd-based contrast agent. This study supported the use of MRI as a clinical tool for *in vivo* detection of vascular remodeling (104). In the thrombosis section above, we discussed a dual imaging approach that targeted not only vulnerable plaques by quantifying MMP activity with a fluorescent probe, but also endothelial injury by imaging the plaques with Gd-enhanced MRI (**Figures 5A,B**) (75).

Extracellular Matrix

The ECM provides structural support and promotes force transmission in the heart and the large vessels. The deposition and degradation of the ECM are well-orchestrated and dynamic. Accordingly, imbalanced ECM rearrangement is part of the pathogenesis of CVDs. As endothelial cells are embedded in the ECM, it is a crucial factor of endothelial biology in CVDs. In the sections above, we have already discussed some components of the ECM, including integrin, thrombotic factors and MMPs. Other targets in the cardiac and vessel wall ECM, discussed below, are collagen and elastin. Fibrosis is a series of actions through which the ECM expands. This process alters organization of collagen networks and increases levels of collagen. Fibrosis occurs either at one spot during MI or more diffusely throughout the cardiac tissue, with certain patterns correlating to different stages of heart failure (105). Thus, imaging of collagen can qualitatively and quantitatively reveal ECM rearrangements, such as fibrosis.

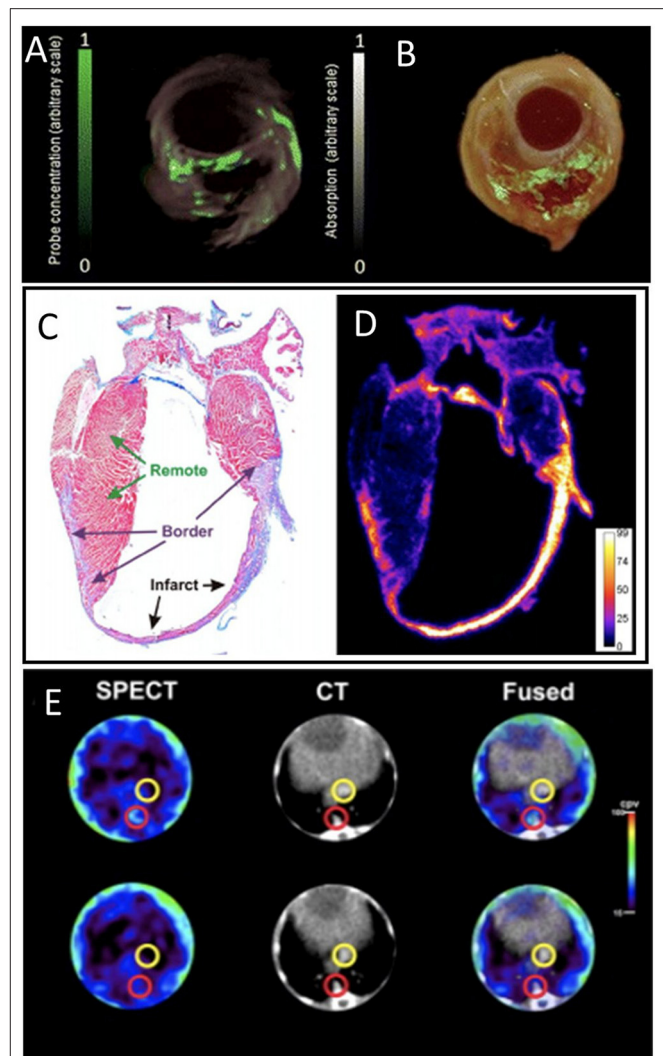
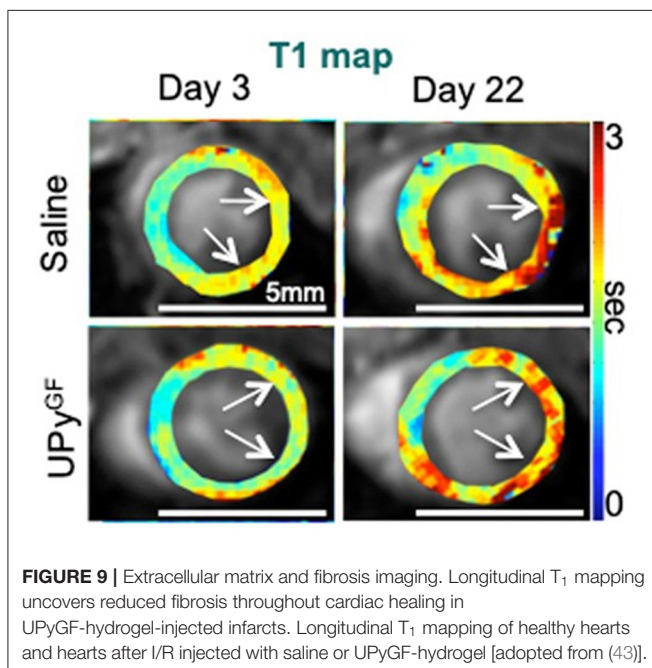


FIGURE 8 | Matrix metalloproteinase (MMP) activity imaging. **(A)** Imaging of intact plaques made using deep-tissue multispectral optoacoustic tomography. Cross-sectional multispectral reconstruction, revealing the location of MMPsense 680 activity in the slice (green) superimposed onto morphological optoacoustic images. **(B)** The corresponding epi-fluorescence images of a dissected plaque (in green) superimposed onto color images of cryosections from the three carotid plaque specimen [adopted from (15)]. Histology and autoradiography of a coronal section of the mouse heart 20 h post-injection of ^{177}Lu -ACPP 10 days after myocardial infarction. **(C)** Representative azan staining showing infarct scar in blue and remote myocardium in red. **(D)** Autoradiography shows enhanced uptake of ^{177}Lu -ACPP in the infarct zone in an adjacent section [adopted from (98)]. **(E)** Transversal SPECT, CT, and fused SPECT and CT images of MMP activation using RP782 in atherosclerotic *apoE*^{-/-} mice, demonstrating areas of high (top) and low (bottom) tracer uptake in aorta (red circles). Slight tracer uptake can be detected in IVC [yellow circles; adopted from (99)]. ACPP, Activatable cell-penetrating peptides; RP782, ^{111}In -labeled tracer specific to MMP activity.

PET and SPECT imaging methods using radioactive probes that bind to target ECM molecules have been developed. These approaches can image ECM with the highest specificity and sensitivity, but due to their low resolution, the images are often

difficult to interpret. To date, some PET and SPECT probes targeting collagen, have been tested on animal models for fibrosis, but have not made their way to the clinics yet (96). Because of its high resolution, MRI has been suggested a promising technique for quantifying ECM at the heart and the large vessels *in vivo*. In our recent work, we used cardiac T_1 -mapping to measure ECM fibrosis after MI. The study measured several aspects of myocardial healing during a hydrogel-based regenerative treatment after MI. Besides the use of cardiac T_1 -mapping (Figure 9), DCE-MRI and strain imaging were performed in a single imaging session. This *in vivo* imaging platform enabled the accurate detection of improved regeneration after MI (43).

A Gd-based MRI study targeted type I collagen for fibrosis imaging, and detected elevated levels of collagen at the infarcted zone after MI (106). *In vivo* MRI-based plaque characterization by quantification of intraplaque elastin content in a murine atherosclerotic study was performed using an elastin-specific Gd-based contrast agent. Such monitoring of changes in elastin content and the high abundance of elastin during plaque development, provide a non-invasive tool for assessing plaque burden in atherosclerosis (107). Another *in vivo* MRI protocol has been established to quantify elastin content using a Gd-based elastin-binding contrast agent in a murine MI model. This $^1\text{H}/^{19}\text{F}$ MRI study simultaneously assessed inflammation, by perfluorocarbon nanoparticle injection that target macrophages and consequently inflammation, alongside with elastin remodeling, and identified the interplay between these two biological processes affects infarct healing (108). Thus, changes in ECM content during infarct healing and plaque development, provide potential targets for non-invasive assessment of plaque burden and cardiac outcome.



DISCUSSION

The development of preclinical vascular imaging techniques has provided insights into vascular biology allowing for clinical translation of these imaging techniques. Despite significant advances in vascular imaging over the past decades, some challenges remain. Nevertheless, exciting multimodal opportunities lie ahead for imaging and quantitation of vascular pathologies, possibly in conjunction with imaging of other cellular processes in CVDs, such as cardiac muscle imaging. The strength of multi-scale imaging lies in the combination of imaging probes, which enables exploitation of the advantages of each imaging modality while compensating for the disadvantages by using an additional imaging modality. Particularly for vascular pathologies, we envision that multi-scale, multimodal imaging studies can provide for early detection of key changes in endothelial cells and, in that way, report on cardiovascular risk at an early stage. Processes such as increased vascular permeability, vessel wall inflammation, expression of adhesion molecules or extracellular matrix remodeling, have the potential to serve as single or combined targets for early diagnosis of endothelial changes during the silent phase of CVDs, with possible value in predicting disease, assessing severity and quantitating the effects of therapeutic interventions.

Basic-Science Perspective

From a basic-science perspective, it is not fully understood how early endothelial changes evolve and if there are biomarkers that can detect early events and predict adverse cardiovascular events. Probing early endothelial biomarkers or changes at the endothelial lining, may provide novel insights into endothelial cell behavior and functioning and into their interactions with immune cells. For example, imaging of interactions and regulation of Delta L4 and Notch1 signaling in CVD is largely unexplored (10).

Past preclinical vascular imaging research in CVDs has focused on vital organs, such as the heart and large vessels. However, the exploration of other vascular beds related to inflammatory processes may be the key to understanding CVDs on a system level. Recently, we used a multi-scale imaging approach to probe the hematopoietic bone marrow vasculature, the gatekeeper of massive release of innate immune cells after acute inflammation (109). *In vivo* multichannel single cell microscopy toward multiplex PET/SPECT/MRI studies are expected to drive discovery of molecular and cellular interactions in different organ systems in CVD.

Of course, developing novel imaging techniques should be accompanied by more comprehensive biological profiling, including flow cytometric analysis of endothelial cells and other biological assays. Another critical need is higher-sensitivity imaging that will enable the visualization of molecular changes in endothelial cells during disease progression. Even though optical methods are certainly capable of following endothelial cell changes, they are difficult to implement in the deep-cardiac and large-vessel arenas. There is still a lack of preclinical imaging methods capable of tracking molecular changes at high resolution in deep tissue and throughout the whole body. More recently

developed imaging methods, such as photoacoustic imaging, might reach such sensitivity levels.

Clinical Considerations

Multi-scale imaging of vascular pathologies can potentially advance cardiovascular medicine in multiple ways. Because molecular-imaging-based strategies can provide insights into biological processes in vascular phenotypes, they can improve risk assessment and early detection of disease. Such developments can eventually lead to improved personalized medicine and better monitoring of therapeutic efficacy and outcome. Moreover, experimental multi-scale imaging will improve our basic biological understanding of vascular pathologies, and subsequently set the stage for new routes for diagnostic and therapeutic developments.

Clinically established imaging of vascular pathologies includes structural imaging, such as echocardiography and cardiac MRI (27), contrast-enhanced ultrasound imaging to measure microvascular blood flow and blood volume (23), as well as targeted dual-isotope PET viability studies with ^{13}N -ammonia and ^{18}F -FDG, to measure myocardial perfusion and viability (20, 24, 26, 27). Other examples of clinically targeted vascular imaging include imaging of vascular permeability of carotid arteries (38, 110), imaging of vessel inflammation by iron oxide nanoparticles (59), PET/MRI to detect $\alpha_v\beta_3$ integrin activation and predict outcome in infarct patients (89) and magnetization transfer MRI for fibrosis evaluation (111).

With the development of gene or stem cell therapy for CVD, costs, and complexity of clinical development are continuing to rise. Multi-scale molecular imaging could help identify promising therapies at an early stage of development of a potentially new therapy, reducing these escalating costs. For example, we recently described a multiparametric MRI approach, that gave insights into various biological aspects of a novel treatment for ischemic heart disease (i.e., vascular permeability, myocardial strain, and extracellular matrix remodeling) (43). The classical structural evaluation of anatomical changes to assess clinical outcomes in CVD tends to ignore delicate key biological changes. Therefore, complex new therapeutic strategies will necessitate advanced multi-scale vascular imaging for a more sensitive and

multi-marker assessment of their therapeutic efficacy and safety, expected to shorten the therapy development process.

Summary

This review attempted to clarify, illustrate, and expound on multi-scale imaging technologies applied to visualize endothelial cell alterations appearing during the pathogenesis of CVDs. Spatially and temporally resolved molecular imaging of endothelial changes is expanding our understanding of how endothelial cells change and interact during the progression of CVDs. The non-invasive assessment of these processes and the integration of multi-scale technologies, represent an extraordinary opportunity to decode the cellular and molecular activities of endothelial cells at unparalleled resolution. These developments in preclinical vascular imaging science are expected to help drive a new era of precision medicine in the treatment of CVDs. Although, CVDs are highly complex involving multiple cell types, systemic changes and biological mechanisms driving disease progression, we believe that multifaceted vascular imaging approaches could pave the way toward a better understanding of endothelial involvement in CVDs health in the future.

AUTHOR CONTRIBUTIONS

AT and KV reviewed and synthesized the relevant information and were the primary authors of this review article. GS and BE made substantial contributions to the drafting and revision of the article. All authors contributed to the article and approved the submitted version.

FUNDING

AT was supported in part by a grant from the Zeff Fellowship. KV was supported by the Israeli Science Foundation 446/21 and 660/21.

ACKNOWLEDGMENTS

We thank Yehudit Posen for editing the manuscript.

REFERENCES

- Lim GB. Public health: global burden of cardiovascular disease. *Nat Rev Cardiol.* (2013) 10:59. doi: 10.1038/nrcardio.2012.194
- Packard RRS, Libby P. Inflammation in atherosclerosis: from vascular biology to biomarker discovery and risk prediction. *Clin Chem.* (2008) 54:24–38. doi: 10.1373/clinchem.2007.097360
- Aird WC. Phenotypic heterogeneity of the endothelium: I. Structure, function, and mechanisms. *Circ Res.* (2007) 100:158–73. doi: 10.1161/01.RES.0000255691.76142.4a
- Davignon J, Ganz P. Role of endothelial dysfunction in atherosclerosis. *Circulation.* (2004) 109:f8. doi: 10.1161/01.CIR.0000131515.03336.f8
- Flammer AJ, Lüscher TF. Human endothelial dysfunction: EDRFs. *Pflugers Arch Eur J Physiol.* (2010) 459:1005–13. doi: 10.1007/s00424-010-0822-4
- Haverslag R, Pasterkamp G, Hoefer I. Targeting adhesion molecules in cardiovascular disorders. *Cardiovasc Hematol Disord Targets.* (2008) 8:252–60. doi: 10.2174/187152908786786188
- Bhagat K. Endothelial function and myocardial infarction. *Cardiovasc Res.* (1998) 39:312–7. doi: 10.1016/S0008-6363(98)00138-2
- Lu P, Takai K, Weaver VM, Werb Z. Extracellular matrix degradation and remodeling in development and disease. *Cold Spring Harb Perspect Biol.* (2011) 3:a005058. doi: 10.1101/cshperspect.a005058
- Nahrendorf M. Myeloid cell contributions to cardiovascular health and disease. *Nat Med.* (2018) 24:711–20. doi: 10.1038/s41591-018-0064-0
- Krüger-Genge A, Blocki A, Franke R-P, Jung F. Vascular endothelial cell biology: an update. *Int J Mol Sci.* (2019) 20:4411. doi: 10.3390/ijms20184411
- Lee S, Vinegoni C, Feruglio PF, Fexon L, Gorbato R, Pivoravov M, et al. Real-time *in vivo* imaging of the beating mouse heart at microscopic resolution. *Nat Commun.* (2012) 3:1–8. doi: 10.1038/ncomms2060
- Bruckman MA, Jiang K, Simpson EJ, Randolph LN, Luyt LG Yu X, Steinmetz NF. Dual-modal magnetic resonance and fluorescence imaging of atherosclerotic plaques *in vivo* using VCAM-1 targeted tobacco mosaic virus. *Nano Lett.* (2014) 14:1551–8. doi: 10.1021/nl404816m

13. Adamczak JM, Schneider G, Nelles M, Que I, Suidgeest E, van der Weerd L, et al. *In vivo* bioluminescence imaging of vascular remodeling after stroke. *Front Cell Neurosci.* (2014) 8:274. doi: 10.3389/fncel.2014.00274
14. Willadsen M, Chaise M, Yarovsky I, Zhang AQ, Parashurama N. Engineering molecular imaging strategies for regenerative medicine. *Bioeng Transl Med.* (2018) 3:232–55. doi: 10.1002/btm.2.10114
15. Razansky D, Harlaar NJ, Hillebrands JL, Taruttis A, Herzog E, Zeebregts CJ, et al. Multispectral optoacoustic tomography of matrix metalloproteinase activity in vulnerable human carotid plaques. *Mol Imaging Biol.* (2012) 14:277. doi: 10.1007/s11307-011-0502-6
16. Lindner JR, Belcik T, Widlansky M, Harmann LM, Karafin MS, Wandersee NJ, et al. Contrast-enhanced ultrasound detects changes in microvascular blood flow in adults with sickle cell disease. *PLoS ONE.* (2019) 14:218783. doi: 10.1371/journal.pone.0218783
17. Wang H, Shan Z, Li W, Chu M, Yang J, Yi D, et al. Guidelines for assessing mouse endothelial function via ultrasound imaging: a report from the International Society of Cardiovascular Translational Research. *J Cardiovasc Transl Res.* (2015) 8:89. doi: 10.1007/s12265-015-9614-8
18. Weller GER, Lu E, Csikari MM, Klibanov AL, Fischer D, Wagner WR, et al. Ultrasound imaging of acute cardiac transplant rejection with microbubbles targeted to intercellular adhesion molecule-1. *Circulation.* (2003) 108:218–24. doi: 10.1161/01.CIR.0000080287.74762.60
19. Hwang SJ, Ballantyne CM, Sharrett AR, Smith LC, Davis CE, Gotto AM, et al. Circulating adhesion molecules VCAM-1, ICAM-1, and E-selectin in carotid atherosclerosis and incident coronary heart disease cases: the Atherosclerosis Risk In Communities (ARIC) study. *Circulation.* (1997) 96:4219–25. doi: 10.1161/01.CIR.96.12.4219
20. Bakermans AJ, Abdurrahim D, Moonen RPM, Motaal AG, Prompers JJ, Strijkers GJ, et al. Small animal cardiovascular MR imaging and spectroscopy. *Prog Nucl Magn Reson Spectrosc.* (2015) 88–9:1–47. doi: 10.1016/j.pnmrs.2015.03.001
21. Vandoorne K, Vandsburger MH, Raz T, Shalev M, Weisinger K, Biton I, et al. Chronic Akt1 deficiency attenuates adverse remodeling and enhances angiogenesis after myocardial infarction. *Circ Cardiovasc Imaging.* (2013) 6:992–1000. doi: 10.1161/CIRCIMAGING.113.000828
22. Vandoorne K, Vandsburger MH, Jacobs I, Han Y, Dafni H, Nicolay K, et al. Non-invasive mapping of endothelial dysfunction in myocardial ischemia by magnetic resonance imaging using an albumin-based contrast agent. *NMR Biomed.* (2016) 29:1500–10. doi: 10.1002/nbm.3599
23. Matsuura R, Miyagawa S, Fukushima S, Goto T, Harada A, Shimozaki Y, et al. Intravital imaging with two-photon microscopy reveals cellular dynamics in the ischemia-reperfused rat heart. *Sci Rep.* (2018) 8:1–9. doi: 10.1038/s41598-018-34295-w
24. Thomas D, Bal H, Arkles J, Horowitz J, Araujo L, Acton PD, et al. Noninvasive assessment of myocardial viability in a small animal model: comparison of MRI, SPECT, and PET. *Magn Reson Med.* (2008) 59:252–9. doi: 10.1002/mrm.21445
25. Wollenweber T, Zach C, Rischpler C, Fischer R, Nowak S, Nekolla SG, et al. Myocardial perfusion imaging is feasible for infarct size quantification in mice using a clinical single-photon emission computed tomography system equipped with pinhole collimators. *Mol Imaging Biol.* (2010) 12:427–34. doi: 10.1007/s11307-009-0281-5
26. Cicone F, Viertl D, Quintela Pousa AM, Denoël T, Gnesin S, Scopinaro F, et al. Cardiac radionuclide imaging in rodents: a review of methods, results, and factors at play. *Front Med.* (2017) 4:35. doi: 10.3389/fmed.2017.00035
27. Garcia MJ, Kwong RY, Scherrer-Crosbie M, Taub CC, Blankstein R, Lima J, et al. State of the art: imaging for myocardial viability: a scientific statement from the American Heart Association. *Circ Cardiovasc Imaging.* (2020) 13:53. doi: 10.1161/HCI.0000000000000053
28. Coolen BF, Moonen RPM, Paulis LEM, Geelen T, Nicolay K, Strijkers GJ. Mouse myocardial first-pass perfusion MR imaging. *Magn Reson Med.* (2010) 64:1658–63. doi: 10.1002/mrm.22588
29. Stuckey DJ, Carr CA, Meader SJ, Tyler DJ, Cole MA, Clarke K. First-pass perfusion CMR two days after infarction predicts severity of functional impairment six weeks later in the rat heart. *J Cardiovasc Magn Reson.* (2011) 13:1–10. doi: 10.1186/1532-429X-13-38
30. Vandsburger MH, Janiczek RL, Xu Y, French BA, Meyer CH, Kramer CM, et al. Improved arterial spin labeling after myocardial infarction in mice using cardiac and respiratory gated look-locker imaging with fuzzy C-means clustering. *Magn Reson Med.* (2010) 63:648–57. doi: 10.1002/mrm.22280
31. Vandsburger M, Vandoorne K, Oren R, Leftin A, Mpofu S, Castelli DD, et al. Cardio-chemical exchange saturation transfer magnetic resonance imaging reveals molecular signatures of endogenous fibrosis and exogenous contrast media. *Circ Cardiovasc Imaging.* (2015) 8:2180. doi: 10.1161/CIRCIMAGING.114.002180
32. Spath NB, Thompson G, Baker AH, Dweck MR, Newby DE, Semple SIK. Manganese-enhanced MRI of the myocardium. *Heart.* (2019) 105:1695–700. doi: 10.1136/heartjnl-2019-315227
33. Croteau E, Renaud JM, Archer C, Klein R, DaSilva JN, Ruddy TD, et al. β_2 -adrenergic stress evaluation of coronary endothelial-dependent vasodilator function in mice using ^{11}C -acetate micro-PET imaging of myocardial blood flow and oxidative metabolism. *EJNMMI Res.* (2014) 4. doi: 10.1186/s13550-014-0068-9
34. Bar A, Targosz-Korecka M, Suraj J, Proniewski B, Jasztal A, Marczyk B, et al. Degradation of glycocalyx and multiple manifestations of endothelial dysfunction coincide in the early phase of endothelial dysfunction before atherosclerotic plaque development in apolipoprotein E/low-density lipoprotein receptor-deficient mice. *J Am Heart Assoc.* (2019) 8:11171. doi: 10.1161/JAHA.118.011171
35. Bar A, Skórka T, Jasiński K, Sternak M, Bartel Z, Tyrankiewicz U, et al. Retrospectively gated MRI for *in vivo* assessment of endothelium-dependent vasodilation and endothelial permeability in murine models of endothelial dysfunction. *NMR Biomed.* (2016) 29:1088–97. doi: 10.1002/nbm.3567
36. Bar A, Olkowicz M, Tyrankiewicz U, Kus E, Jasinski K, Smolenski RT, et al. Functional and biochemical endothelial profiling *in vivo* in a murine model of endothelial dysfunction; comparison of effects of 1-methylnicotinamide and angiotensin-converting enzyme inhibitor. *Front Pharmacol.* (2017) 8:183. doi: 10.3389/fphar.2017.00183
37. Flammar AJ, Anderson T, Celermajer DS, Creager MA, Deanfield J, Ganz P, et al. The assessment of endothelial function – from research into clinical practice. *Circulation.* (2012) 126:753. doi: 10.1161/CIRCULATIONAHA.112.093245
38. Nahrendorf M, Vandoorne K. Albumin-binding MR probe detects high-risk coronary plaques in patients. *JACC Cardiovasc Imaging.* (2019) 12:307–9. doi: 10.1016/j.jcmg.2017.11.026
39. Phinikaridou A, Andia ME, Protti A, Indermuehle A, Shah A, Smith A, et al. Noninvasive magnetic resonance imaging evaluation of endothelial permeability in murine atherosclerosis using an albumin-binding contrast agent. *Circulation.* (2012) 126:707–19. doi: 10.1161/CIRCULATIONAHA.112.092098
40. Niu G, Lang L, Kiesewetter DO, Ma Y, Sun Z, Guo N, et al. *In vivo* labeling of serum albumin for PET. *J Nucl Med.* (2014) 55:1150–6. doi: 10.2967/jnumed.114.139642
41. Young A, French B, Yang Z, Cowan B, Gilson W, Berr S, et al. Reperfused myocardial infarction in mice: 3D mapping of late gadolinium enhancement and strain. *J Cardiovasc Magn Reson.* (2006) 8:685–92. doi: 10.1080/10976640600721767
42. Leenders GJ, Smeets MB, Van Den Boomen M, Berben M, Nabben M, Van Strijp D, et al. Statins promote cardiac infarct healing by modulating endothelial barrier function revealed by contrast-enhanced magnetic resonance imaging. *Arterioscler Thromb Vasc Biol.* (2018) 38:186–94. doi: 10.1161/ATVBAHA.117.310339
43. Boomen M, Kause HB, Assen HC, Dankers PYW, Bouten CVC, Vandoorne K. Triple-marker cardiac MRI detects sequential tissue changes of healing myocardium after a hydrogel-based therapy. *Sci Rep.* (2019) 9:19366. doi: 10.1038/s41598-020-59864-w
44. Coolen BF, Geelen T, Paulis LEM, Nicolay K, Strijkers GJ. Regional contrast agent quantification in a mouse model of myocardial infarction using 3D cardiac T1 mapping. *J Cardiovasc Magn Reson.* (2011) 13:56. doi: 10.1186/1532-429X-13-56
45. Duivenvoorden R, Tang J, Cormode DP, Mieszawska AJ, Izquierdo-Garcia D, Ozcan C, et al. A statin-loaded reconstituted high-density lipoprotein nanoparticle inhibits atherosclerotic plaque inflammation. *Nat Commun.* (2014) 5:4065. doi: 10.1038/ncomms4065
46. O'Connor JPB, Tofts PS, Miles KA, Parkes LM, Thompson G, Jackson A. Dynamic contrast-enhanced imaging techniques:

- CT and MRI. *Br J Radiol.* (2011) 84:S112. doi: 10.1259/bjr/55166688
47. Merali Z, Wong T, Leung J, Gao MMY, Mikulis D, Kassner A. Dynamic contrast-enhanced MRI and CT provide comparable measurement of blood-brain barrier permeability in a rodent stroke model. *Magn Reson Imaging.* (2015). doi: 10.1016/j.mri.2015.06.021
48. Nahrendorf M, Jaffer FA, Kelly KA, Sosnovik DE, Aikawa E, Libby P, et al. Noninvasive vascular cell adhesion molecule-1 imaging identifies inflammatory activation of cells in atherosclerosis. *Circulation.* (2006) 114:1504–11. doi: 10.1161/CIRCULATIONAHA.106.646380
49. Li X, Bauer W, Israel I, Kreissl MC, Weirather J, Richter D, et al. Targeting p-selectin by gallium-68-labeled fucoidan positron emission tomography for noninvasive characterization of vulnerable plaques: correlation with *in vivo* 176Tl MRI. *Arterioscler Thromb Vasc Biol.* (2014) 34:1661–7. doi: 10.1161/ATVBAHA.114.303485
50. Nakamura I, Hasegawa K, Wada Y, Hirase T, Node K, Watanabe Y. Detection of early stage atherosclerotic plaques using PET and CT fusion imaging targeting P-selectin in low density lipoprotein receptor-deficient mice. *Biochem Biophys Res Commun.* (2013) 433:47–51. doi: 10.1016/j.bbrc.2013.02.069
51. Boutry S, Laurent S, Elst LV, Muller RN. Specific E-selectin targeting with a superparamagnetic MRI contrast agent. *Contrast Media Mol Imaging.* (2006) 1:15–22. doi: 10.1002/cmmi.87
52. Reynolds PR, Larkman DJ, Haskard DO, Hajnal JV, Kennea NL, George AJT, et al. Detection of vascular expression of E-selectin *in vivo* with MR imaging. *Radiology.* (2006) 241:469–76. doi: 10.1148/radiol.2412050490
53. Burtea C, Ballet S, Laurent S, Rousseaux O, Dencausse A, Gonzalez W, et al. Development of a magnetic resonance imaging protocol for the characterization of atherosclerotic plaque by using vascular cell adhesion molecule-1 and apoptosis-targeted ultrasmall superparamagnetic iron oxide derivatives. *Arterioscler Thromb Vasc Biol.* (2012) 32:2454–5. doi: 10.1161/ATVBAHA.112.245415
54. Michalska M, MacHtoub L, Manthey HD, Bauer E, Herold V, Krohne G, et al. Visualization of vascular inflammation in the atherosclerotic mouse by ultrasmall superparamagnetic iron oxide vascular cell adhesion molecule-1-specific nanoparticles. *Arterioscler Thromb Vasc Biol.* (2012) 32:2350–7. doi: 10.1161/ATVBAHA.112.255224
55. Sosnovik DE, Nahrendorf M, Deliolanis N, Novikov M, Aikawa E, Josephson L, et al. Fluorescence tomography and magnetic resonance imaging of myocardial macrophage infiltration in infarcted myocardium *in vivo*. *Circulation.* (2007) 115:1384–91. doi: 10.1161/CIRCULATIONAHA.106.663351
56. Moonen RPM, Coolen BF, Sluimer JC, Daemen MJAP, Strijkers GJ. Iron oxide nanoparticle uptake in mouse brachiocephalic artery atherosclerotic plaque quantified by T2-mapping MRI. *Pharmaceutics.* (2021) 13:1–12. doi: 10.3390/pharmaceutics13020279
57. Fogel U, Ding Z, Harding H, Jander S, Reichmann G, Jacoby C, et al. *In vivo* monitoring of inflammation after cardiac and cerebral ischemia by fluorine magnetic resonance imaging. *Circulation.* (2008) 118:140–8. doi: 10.1161/CIRCULATIONAHA.107.737890
58. Korosoglou G, Weiss RG, Kedziorek DA, Walczak P, Gilson WD, Schär M, et al. Noninvasive detection of macrophage-rich atherosclerotic plaque in hyperlipidemic rabbits using “positive contrast” magnetic resonance imaging. *J Am Coll Cardiol.* (2008) 52:483–91. doi: 10.1016/j.jacc.2008.03.063
59. Kool ME, Cappendijk VC, Cleutjens KBJM, Kessels AGH, Kitslaar PJEHM, Borgers M, et al. Accumulation of ultrasmall superparamagnetic particles of iron oxide in human atherosclerotic plaques can be detected by *in vivo* magnetic resonance imaging. *Circulation.* (2003) 107:2453–8. doi: 10.1161/01.CIR.0000068315.98705.CC
60. Morishige K, Kacher DF, Libby P, Josephson L, Ganz P, Weissleder R, et al. High-resolution magnetic resonance imaging enhanced with superparamagnetic nanoparticles measures macrophage burden in atherosclerosis. *Circulation.* (2010) 122:1707–15. doi: 10.1161/CIRCULATIONAHA.109.891804
61. Keliher EJ, Ye YX, Wojtkiewicz GR, Aguirre AD, Tricot B, Senders ML, et al. Polyglucose nanoparticles with renal elimination and macrophage avidity facilitate PET imaging in ischemic heart disease. *Nat Commun.* (2017) 8:1–12. doi: 10.1038/ncomms14064
62. Lobatto ME, Binderup T, Robson PM, Giesen LFP, Calcagno C, Witjes J, et al. Multimodal positron emission tomography imaging to quantify uptake of 89Zr-labeled liposomes in the atherosclerotic vessel wall. *Bioconjug Chem.* (2020) 31:360–8. doi: 10.1021/acs.bioconjchem.9b00256
63. Nahrendorf M, Zhang H, Hembard S, Panizzi P, Sosnovik DE, Aikawa E, et al. Nanoparticle PET-CT imaging of macrophages in inflammatory atherosclerosis. *Circulation.* (2008) 117:379–87. doi: 10.1161/CIRCULATIONAHA.107.741181
64. Xiong F, Wang H, Feng Y, Li Y, Hua X, Pang X, et al. Cardioprotective activity of iron oxide nanoparticles. *Sci Rep.* (2015) 5:1–8. doi: 10.1038/srep08579
65. Kawamura Y, Takahara Y, Tamura N, Eguchi Y, Urano T, Ishida H, et al. Imaging of structural changes in endothelial cells and thrombus formation at the site of FeCl(3)-induced injuries in mice cremasteric arteries. *J Atheroscler Thromb.* (2009) 16:807–14. doi: 10.5551/jat.2030
66. Anderson DR, Tsutsui JM, Xie F, Radio SJ, Porter TR. The role of complement in the adherence of microbubbles to dysfunctional arterial endothelium and atherosclerotic plaque. *Cardiovasc Res.* (2007) 73:597–606. doi: 10.1016/j.cardiores.2006.11.029
67. Botnar RM, Perez AS, Witte S, Wiethoff AJ, Laredo J, Hamilton J, et al. *In vivo* molecular imaging of acute and subacute thrombosis using a fibrin-binding magnetic resonance imaging contrast agent. *Circulation.* (2004) 109:2023–9. doi: 10.1161/01.CIR.0000127034.50006.C0
68. Song Y, Huang Z, Xu J, Ren D, Wang Y, Zheng X, et al. Multimodal SPION-CREKA peptide based agents for molecular imaging of microthrombus in a rat myocardial ischemia-reperfusion model. *Biomaterials.* (2014) 35:2961–70. doi: 10.1016/j.biomaterials.2013.12.038
69. Ay I, Blasi F, Rietz TA, Rotile NJ, Kura S, Brownell AL, et al. *In vivo* molecular imaging of thrombosis and thrombolysis using a fibrin-binding positron emission tomographic probe. *Circ Cardiovasc Imaging.* (2014) 7:697–705. doi: 10.1161/CIRCIMAGING.113.001806
70. Ciesinski KL, Yang Y, Ay I, Chonde DB, Loving GS, Rietz TA, et al. Fibrin-targeted PET probes for the detection of thrombi. *Mol Pharm.* (2013) 10:1100–10. doi: 10.1021/mp300610s
71. Oliveira BL, Blasi F, Rietz TA, Rotile NJ, Day H, Caravan P. Multimodal molecular imaging reveals high target uptake and specificity of 111In- and 68Ga-labeled fibrin-binding probes for thrombus detection in rats. *J Nucl Med.* (2015) 56:1587–92. doi: 10.2967/jnumed.115.160754
72. Wang X, Temme S, Grapentin C, Palasubramaniam J, Walsh A, Krämer W, et al. Fluorine-19 magnetic resonance imaging of activated platelets. *J Am Hear Assoc Cardiovasc Cerebrovasc Dis.* (2020) 9:16971. doi: 10.1161/JAHA.120.016971
73. Blasi F, Oliveira BL, Rietz TA, Rotile NJ, Naha PC, Cormode DP, et al. Multisite thrombus imaging and fibrin content estimation with a single whole-body PET scan in rats. *Arterioscler Thromb Vasc Biol.* (2015) 35:2114–21. doi: 10.1161/ATVBAHA.115.306055
74. Bigalke B, Phinikaridou A, Andia ME, Cooper MS, Schuster A, Schönberger T, et al. Positron emission tomography/computed tomographic and magnetic resonance imaging in a murine model of progressive atherosclerosis using 64Cu-labeled glycoprotein VI-Fc. *Circ Cardiovasc Imaging.* (2013) 6:957–64. doi: 10.1161/CIRCIMAGING.113.000488
75. Hua N, Baik F, Pham T, Phinikaridou A, Giordano N, Friedman B, et al. Identification of high-risk plaques by MRI and fluorescence imaging in a rabbit model of atherothrombosis. *PLoS ONE.* (2015) 10:e0139833. doi: 10.1371/journal.pone.0139833
76. Kargozar S, Bano F, Hamzehlou S, Hamblin MR, Mozafari M. Nanotechnology for angiogenesis: opportunities and challenges. *Chem Soc Rev.* (2020) 49:5008–57. doi: 10.1039/C8CS01021H
77. Cui J, Yue JB. Current status and advances in arginine-glycine-aspartic acid peptide-based molecular imaging to evaluate the effects of anti-angiogenic therapies. *Precis Radiat Oncol.* (2019) 3:29–34. doi: 10.1002/pro.660
78. Mandic L, Traxler D, Gugerell A, Zlabinger K, Lukovic D, Pavo N, et al. Molecular imaging of angiogenesis in cardiac regeneration. *Curr Cardiovasc Imaging Rep.* (2016) 9:27. doi: 10.1007/s12410-016-9389-6
79. Liu Q, Hu T, He L, Huang X, Tian X, Zhang H, et al. Genetic targeting of sprouting angiogenesis using Aplyn-CreER. *Nat Commun.* (2015) 6:1–12. doi: 10.1038/ncomms7020
80. Liu R, Trindade A, Sun Z, Kumar R, Weaver FA, Krasnoperov V, et al. Inhibition of Notch signaling by DLL4-Fc promotes reperfusion of

- acutely ischemic tissues. *Biochem Biophys Res Commun.* (2012) 418:173–9. doi: 10.1016/j.bbrc.2012.01.002
81. Willmann JK, Chen K, Wang H, Paulmurugan R, Rollins M, Cai W, et al. Monitoring of the biological response to murine hindlimb ischemia with ⁶⁴Cu-labeled vascular endothelial growth factor-121 positron emission tomography. *Circulation.* (2008) 117:915–22. doi: 10.1161/CIRCULATIONAHA.107.733220
82. Rodriguez-Porcel M, Cai W, Gheysens O, Willmann JK, Chen K, Wang H, et al. Imaging of VEGF receptor in a rat myocardial infarction model using PET. *J Nucl Med.* (2008) 49:667. doi: 10.2967/jnumed.107.040576
83. Meyer JP, Edwards KJ, Kozlowski P, Backer MV, Backer JM, Lewis JS. Selective imaging of VEGFR-1 and VEGFR-2 using ⁸⁹Zr-labeled single-chain VEGF mutants. *J Nucl Med.* (2016) 57:1811–6. doi: 10.2967/jnumed.116.173237
84. Hua J, Dobrucki LW, Sadeghi MM, Zhang J, Bourke BN, Cavaliere P, et al. Noninvasive imaging of angiogenesis with a ^{99m}Tc-labeled peptide targeted at $\alpha v \beta 3$ integrin after murine hindlimb ischemia. *Circulation.* (2005) 111:3255–60. doi: 10.1161/CIRCULATIONAHA.104.485029
85. Kim MH, Kim SG, Kim CG, Kim DW. A novel Tc-99m and fluorescence labeled peptide as a multimodal imaging agent for targeting angiogenesis in a murine hindlimb ischemia model. *Appl Radiat Isot.* (2017) 121:22–7. doi: 10.1016/j.apradiso.2016.12.026
86. Meoli DF, Sadeghi MM, Krassilnikova S, Bourke BN, Giordano FJ, Dione DP, et al. Non-invasive imaging of myocardial angiogenesis following experimental myocardial infarction. *J Clin Invest.* (2004) 113:1684–91. doi: 10.1172/JCI200420352
87. Kalinowski L, Dobrucki LW, Meoli DF, Dione DP, Sadeghi MM, Madri JA, et al. Targeted imaging of hypoxia-induced integrin activation in myocardium early after infarction. *J Appl Physiol.* (2008) 104:1504–12. doi: 10.1152/jappphysiol.00861.2007
88. Sherif HM, Saraste A, Nekolla SG, Weidl E, Reder S, Tapfer A, et al. Molecular imaging of early $\alpha v \beta 3$ integrin expression predicts long-term left-ventricle remodeling after myocardial infarction in rats. *J Nucl Med.* (2012) 53:318–23. doi: 10.2967/jnumed.111.091652
89. Makowski MR, Rischpler C, Ebersberger U, Keithahn A, Kasel M, Hoffmann E, et al. Multiparametric PET and MRI of myocardial damage after myocardial infarction: correlation of integrin $\alpha v \beta 3$ expression and myocardial blood flow. *Eur J Nucl Med Mol Imaging.* (2021) 48:1070–80. doi: 10.1007/s00259-020-05034-z
90. Virmani R, Kolodgie FD, Burke AP, Finn AV, Gold HK, Tulenko TN, et al. Atherosclerotic plaque progression and vulnerability to rupture: angiogenesis as a source of intraplatelet hemorrhage. *Arterioscler Thromb Vasc Biol.* (2005) 25:2054–61. doi: 10.1161/01.ATV.0000178991.71605.18
91. Huisman LA, Steinkamp PJ, Hillebrands J-L, Zeebregts CJ, Linssen MD, Jorritsma-Smit A, et al. Feasibility of *ex vivo* fluorescence imaging of angiogenesis in (non-) culprit human carotid atherosclerotic plaques using bevacizumab-800CW. *Sci Rep.* (2021) 11:1–11. doi: 10.1038/s41598-021-82568-8
92. Tekabe Y, Kollaros M, Zerihoun A, Zhang G, Backer MV, Backer JM, et al. Imaging VEGF receptor expression to identify accelerated atherosclerosis. *EJNMMI Res.* (2014) 4:1–9. doi: 10.1186/s13550-014-0041-7
93. Tan H, Zhou J, Yang X, Abudupataer M, Li X, Hu Y, et al. ^{99m}Tc-labeled bevacizumab for detecting atherosclerotic plaque linked to plaque neovascularization and monitoring antiangiogenic effects of atorvastatin treatment in ApoE $-/-$ mice. *Sci Rep.* (2017) 7:1–12. doi: 10.1038/s41598-017-03276-w
94. Winter PM, Morawski AM, Caruthers SD, Fuhrhop RW, Zhang H, Williams TA, et al. Molecular imaging of angiogenesis in early-stage atherosclerosis with $\alpha v \beta 3$ -integrin-targeted nanoparticles. *Circulation.* (2003) 108:2270–4. doi: 10.1161/01.CIR.0000093185.16083.95
95. Su T, Wang YB, Han D, Wang J, Qi S, Gao L, et al. Multimodality imaging of angiogenesis in a rabbit atherosclerotic model by GEBP11 peptide targeted nanoparticles. *Theranostics.* (2017) 7:7491–804. doi: 10.7150/thno.20767
96. Pinkert MA, Hortensius RA, Ogle BM, Eliceiri KW. Imaging the cardiac extracellular matrix. *Adv Exp Med Biol.* 1098:21–44. doi: 10.1007/978-3-319-97421-7_2
97. Chen J, Tung CH, Allport JR, Chen S, Weissleder R, Huang PL. Near-infrared fluorescent imaging of matrix metalloproteinase activity after myocardial infarction. *Circulation.* (2005) 111:1800–5. doi: 10.1161/01.CIR.0000160936.91849.9F
98. Van Duijnhoven SMJ, Robillard MS, Hermann S, Kuhlmann MT, Schäfers M, Nicolay K, et al. Imaging of MMP activity in postischemic cardiac remodeling using radiolabeled MMP-2/9 activatable peptide probes. *Mol Pharm.* (2014) 11:1415–23. doi: 10.1021/mp400569k
99. Razavian M, Tavakoli S, Zhang J, Nie L, Dobrucki LW, Sinusas AJ, et al. Atherosclerosis plaque heterogeneity and response to therapy detected by *in vivo* molecular imaging of matrix metalloproteinase activation. *J Nucl Med.* (2011) 52:1795–802. doi: 10.2967/jnumed.111.092379
100. Fujimoto S, Hartung D, Ohshima S, Edwards DS, Zhou J, Yalamanchili P, et al. Molecular imaging of matrix metalloproteinase in atherosclerotic lesions. Resolution with dietary modification and statin therapy. *J Am Coll Cardiol.* (2008) 52:1847–57. doi: 10.1016/j.jacc.2008.08.048
101. Schäfers M, Riemann B, Kopka K, Breyholz HJ, Wagner S, Schäfers KP, et al. Scintigraphic imaging of matrix metalloproteinase activity in the arterial wall *in vivo*. *Circulation.* (2004) 109:2554–9. doi: 10.1161/01.CIR.0000129088.49276.83
102. Zhang J, Nie L, Razavian M, Ahmed M, Dobrucki LW, Asadi A, et al. Molecular imaging of activated matrix metalloproteinases in vascular remodeling. *Circulation.* (2008) 118:1953–60. doi: 10.1161/CIRCULATIONAHA.108.789743
103. Lancelot E, Amirbekian V, Brigger I, Raynaud JS, Ballet S, David C, et al. Evaluation of matrix metalloproteinases in atherosclerosis using a novel noninvasive imaging approach. *Arterioscler Thromb Vasc Biol.* (2008) 28:425–32. doi: 10.1161/ATVBAHA.107.149666
104. Hyafil F, Vucic E, Cornily JC, Sharma R, Amirbekian V, Blackwell F, et al. Monitoring of arterial wall remodelling in atherosclerotic rabbits with a magnetic resonance imaging contrast agent binding to matrix metalloproteinases. *Eur Heart J.* (2011) 32:1561–71. doi: 10.1093/eurheartj/ehq413
105. de Graaf WL, Vandoorne K, Arslan F, Nicolay K, Strijkers GJ. Contrast-enhanced T1-mapping MRI for the assessment of myocardial fibrosis. *Curr Cardiovasc Imaging Rep.* (2014) 7:9260. doi: 10.1007/s12410-014-9260-6
106. Caravan P, Das B, Dumas S, Epstein FH, Helm PA, Jacques V, et al. Collagen-targeted MRI contrast agent for molecular imaging of fibrosis. *Angew Chemie - Int Ed.* (2007) 46:8171–3. doi: 10.1002/anie.200700700
107. Makowski MR, Wiethoff AJ, Blume U, Cuello F, Warley A, Jansen CHP, et al. Assessment of atherosclerotic plaque burden with an elastin-specific magnetic resonance contrast agent. *Nat Med.* (2011) 17:383–9. doi: 10.1038/nm.2310
108. Ramos IT, Henningson M, Nezafat M, Lavin B, Lorrio S, Gebhardt P, et al. Simultaneous assessment of cardiac inflammation and extracellular matrix remodeling after myocardial infarction. *Circ Cardiovasc Imaging.* (2018) 11:7453. doi: 10.1161/CIRCIMAGING.117.007453
109. Vandoorne K, Rohde D, Kim HY, Courties G, Wojtkiewicz G, Honold L, et al. Imaging the vascular bone marrow niche during inflammatory stress. *Circ Res.* (2018) 123:415–27. doi: 10.1161/CIRCRESAHA.118.313302
110. Engel LC, Landmesser U, Abdelwahed YS, Gigengack K, Wurster T, Manes C, et al. *In vivo* assessment of endothelial permeability of coronary lesions with variable degree of stenosis using an albumin-binding MR probe. *Int J Cardiovasc Imaging.* (2021) 37:3049–55. doi: 10.1007/s10554-021-02293-1
111. Ali Z, Stropm TA, Vandsburger MH. Fractal analysis of cardiac fibrosis patterns derived from magnetization transfer contrast MRI in patients with end-stage renal disease. *Am J Roentgenol.* (2020) 214:506–13. doi: 10.2214/AJR.19.21745

Conflict of Interest: The authors declare that the research was conducted in the absence of any commercial or financial relationships that could be construed as a potential conflict of interest.

Publisher's Note: All claims expressed in this article are solely those of the authors and do not necessarily represent those of their affiliated organizations, or those of the publisher, the editors and the reviewers. Any product that may be evaluated in

this article, or claim that may be made by its manufacturer, is not guaranteed or endorsed by the publisher.

Copyright © 2022 Tiwari, Elgrably, Saar and Vandoorne. This is an open-access article distributed under the terms of the Creative Commons Attribution License (CC

BY). The use, distribution or reproduction in other forums is permitted, provided the original author(s) and the copyright owner(s) are credited and that the original publication in this journal is cited, in accordance with accepted academic practice. No use, distribution or reproduction is permitted which does not comply with these terms.



[¹⁸F] Sodium Fluoride Dose Reduction Enabled by Digital Photon Counting PET/CT for Evaluation of Osteoblastic Activity

Maria I. Menendez^{1*}, Richard R. Moore¹, Mahmoud Abdel-Rasoul², Chadwick L. Wright¹, Soledad Fernandez², Rebecca D. Jackson³ and Michael V. Knopp¹

¹ Department of Radiology, The Wright Center of Innovation in Biomedical Imaging, The Ohio State University Wexner Medical Center, Columbus, OH, United States, ² Center for Biostatistics, College of Medicine, The Ohio State University, Columbus, OH, United States, ³ Department of Internal Medicine, Endocrinology, Diabetes and Metabolism, The Ohio State University Wexner Medical Center, Columbus, OH, United States

OPEN ACCESS

Edited by:

Monique Bernsen,
Erasmus Medical Center, Netherlands

Reviewed by:

Alberto Miceli,
Università di Genova, Italy
Christian Vanhove,
Ghent University, Belgium

*Correspondence:

Maria I. Menendez
menendez.59@buckeyemail.osu.edu

Specialty section:

This article was submitted to
Nuclear Medicine,
a section of the journal
Frontiers in Medicine

Received: 14 June 2021

Accepted: 17 December 2021

Published: 12 January 2022

Citation:

Menendez MI, Moore RR, Abdel-Rasoul M, Wright CL, Fernandez S, Jackson RD and Knopp MV (2022) [¹⁸F] Sodium Fluoride Dose Reduction Enabled by Digital Photon Counting PET/CT for Evaluation of Osteoblastic Activity. *Front. Med.* 8:725118. doi: 10.3389/fmed.2021.725118

The aim of the study was to assess the quality and reproducibility of reducing the injected [¹⁸F] sodium fluoride ([¹⁸F]NaF) dose while maintaining diagnostic imaging quality in bone imaging in a preclinical skeletal model using digital photon counting PET (dPET) detector technology. Beagles ($n = 9$) were administered three different [¹⁸F]NaF doses: 111 MBq ($n = 5$), 20 MBq ($n = 5$), and 1.9 MBq ($n = 9$). Imaging started ≈ 45 min post-injection for ≈ 30 min total acquisition time. Images were reconstructed using Time-of-Flight, ultra-high definition (voxel size of $1 \times 1 \times 1$ mm³), with 3 iterations and 3 subsets. Point spread function was modeled and Gaussian filtering was applied. Skeleton qualitative and quantitative molecular image assessment was performed. The overall diagnostic quality of all images scored excellent (61%) and acceptable (39%) by all the reviewers. [¹⁸F]NaF SUV_{mean} showed no statistically significant differences among the three doses in any of the region of interest assessed. This study demonstrated that a 60-fold [¹⁸F]NaF dose reduction was not significantly different from the highest dose, and it had not significant effect on overall image quality and quantitative accuracy. In the future, ultra-low dose [¹⁸F]NaF dPET/CT imaging may significantly decrease PET radiation exposure to preclinical subjects and personnel.

Keywords: [¹⁸F] sodium fluoride, PET/CT, digital photon counting, bone imaging, bone metabolism, sodium fluoride dose reduction, preclinical molecular imaging, canine PET

INTRODUCTION

Sodium Fluoride ([¹⁸F]NaF) Positron Emission Tomography—Computed Tomography (PET/CT) is used clinically in oncology patients to detect and characterize osteoblastic metastatic lesions (1–4), as well as to aid visualization of atherosclerotic calcifications and plaques in patients with cardiovascular disease (5–7). Recently, [¹⁸F]NaF has also been used as a bone imaging biomarker to assess and quantify bone metabolic processes (i.e., osteoblastic activity) in non-oncologic musculoskeletal disorders such as osteoarthritis and osteoporosis (8–20). The radiolabeled fluoride ion exchanges with the hydroxyl groups in hydroxyapatite crystals on the surface of the bone matrix to form fluoroapatite. Therefore, uptake of [¹⁸F]NaF uptake can be used a marker of osteoblastic

bone metabolism. [^{18}F]NaF PET/CT imaging is a sensitive, noninvasive, imaging approach to assess bone metabolism (21–23). Due to its [^{18}F]NaF favorable pharmacokinetics, such as high bone uptake, minimal binding to serum proteins, rapid single-pass extraction, and fast clearance from the soft tissues, [^{18}F]NaF PET is more sensitive for detecting abnormal osteoblastic activity and lesions than the current clinical gold standard, $^{99\text{m}}\text{Tc}$ -MDP gamma scintigraphy. When compared with $^{99\text{m}}\text{Tc}$ -MDP gamma scintigraphy, [^{18}F]NaF PET has higher sensitivity, superior image resolution, and improved target-to-background ratio (24). Hybrid imaging modalities such as PET/CT and PET/Magnetic Resonance Imaging (MRI) are currently used for assessing bone metabolism (22–25). PET/MRI presents operational challenges including attenuation correction for PET, longer than desired MRI image acquisition times when compared with CT, and reduced field of view when using dedicated MRI coils (e.g., knee coils) which fail to aid in whole body skeletal assessment (25–27). Radiation exposure can be a concern due to ionizing radiation from PET radiotracers (28). Minimizing radiation exposure is important not only for research subjects and patients, but also for imaging technologists, nursing personnel and subject/patient caregivers. It is believed that significant reductions in PET radiotracer doses will benefit pediatric subjects/patients and those subjects/patients participating in longitudinal studies with multiple serial PET studies by reducing cumulative radiation exposure (29, 30). Many imaging studies have focused on CT radiation dose reduction without addressing the potential dose reduction strategies associated with the administered PET radiotracers (31, 32). Most PET radiotracer dose reduction has been focused on the widely clinically utilized radiotracer: 2-deoxy-2-[^{18}F]-fluorodeoxyglucose (^{18}F -FDG) (33–36). The current recommended guidelines for human [^{18}F]NaF injected doses from the European Association of Nuclear Medicine (EANM) are weight based. For Adults: 1.5–3.7 MBq/kg (megabecquerel (MBq) per kilogram (kg) of body weight (BW), and Pediatrics: 2.2 MBq/kg (37). The Society of Nuclear Medicine and Molecular Imaging (SNMMI) guidelines recommend a fixed dose for adults: 185–370 MBq, and weight-based for Pediatrics (2.22 MBq/kg) (38). Some clinical studies have examined [^{18}F]NaF dose reduction and reported no effect on image quality (30, 39–41). However, comprehensive preclinical [^{18}F]NaF dose reduction studies in translational large animal models and its impact on overall PET image quality are missing.

The recent introduction of clinically approved PET/CT systems equipped with digital photon counting PET (dPET) detector technology enables new PET imaging approaches for addressing PET radiotracer dose reduction, faster PET image acquisition times, and higher definition in PET image reconstruction (42, 43). Digital photon counting PET detector technology enables ultra-high definition reconstruction with voxel volume of $1 \times 1 \times 1 \text{ mm}^3$ and more precisely localizes PET annihilation events (i.e., reduces partial volume effects) which improve quantitative PET accuracy for imaging biomarker assessment (44–46). Additionally, lower PET doses can be implemented in dPET imaging in accordance with ALARA (As Low as Reasonably Achievable) while maintaining diagnostic

imaging quality (47–49). With the recent advances in dPET detector technology, there is an immediate opportunity to minimize PET radiotracer doses in preclinical research subjects imaged on these clinical dPET/CT systems and likewise reduce radiation exposures to PET staff and handling personnel. This study is an important step to develop and standardize low-dose hybrid PET-CT imaging methodologies in preclinical imaging, and to provide guidance for future clinical studies, and clinical trials applying [^{18}F]NaF PET dose reduction.

The aim of the study was to assess the quality and reproducibility of reducing the injected [^{18}F]NaF dose while maintaining diagnostic imaging quality in bone imaging in a preclinical skeletal model using digital photon counting PET (dPET) detector technology.

We hypothesized that 5- to 60-fold reductions in administered [^{18}F]NaF activity would provide equivalent image quality on dPET/CT when compared with the standard [^{18}F]NaF doses.

MATERIALS AND METHODS

Animals

This study was conducted according to NIH guidelines, and according to protocols approved by the Institutional Animal Care and Use Committee (IACUC) of The Ohio State University. Nine healthy skeletally mature male beagles [weight (kg) mean \pm SEM; 15 ± 4.7] were used.

Positron Emission Tomography/Computed Tomography Acquisition

Subjects underwent general anesthesia induced by acepromazine [Aceproject; Henry Schein Animal Health, Dublin OH; intravenously (IV), 0.1 mg/kg], ketamine (Ketasthesia; Henry Schein Animal Health, Dublin OH; IV, 10 mg/kg), and diazepam (Hospira; Lake Forest, IL; IV, 0.25 mg/kg) and maintained by isoflurane (Isothesia; Henry Schein Animal Health, Dublin, OH; 1–4%). The subjects were placed in supine position with the front and distal extremities extended and supported in a custom-made multimodal imaging positioning device to mimic human scans and to improve the precision and positional consistency among scans (13, 50). Subjects were intravenously administered 3 different [^{18}F]NaF target doses: 111 MBq (standard dose/SD; $n = 5$), $20 \pm 7.8 \text{ MBq}$ [mean \pm standard error of the mean (SEM); low dose/LD; $n = 5$], and 1.9 MBq (ultra-low dose/ULD; $n = 9$) (see **Table 1**).

All imaging was performed using the Vereos dPET/CT system (Philips, Cleveland, Ohio). A low-dose computed tomography (CT) scan was performed for attenuation correction and coregistration. For the low dose (LD) and ultra-low dose (ULD), whole-body PET imaging began at $\sim 45 \text{ min}$ post-injection using acquisition times of 180 s/bed position in list-mode for 10 bed positions (total dPET image acquisition time $\sim 30 \text{ min}$). The standard dose (SD) ($n = 5$) began at $\sim 30 \text{ min}$ and was acquired with 120 sec/bed. All SD dPET acquisitions were retrospectively list-mode clipped from 120 s/bed to 4 s/bed to simulate the same count density as ULD. In addition, all LD dPET acquisitions were retrospectively list-mode clipped from 180 s/bed to 18 s/bed to simulate the same count density

TABLE 1 | Dogs and corresponding standard (SD), low (LD) [mean ± standard error of the mean (SEM)], and ultra-Low (ULD) [^{18}F]NaF doses.

Dog	Standard dose (111 MBq)	Low dose (20 ± 7.8 MBq)			Ultra-low dose (1.9 MBq)
		37 MBq	18.5 MBq	3.7 MBq	
111		X			X
112			X		X
113		X		X	X
114	X			X	X
115					X
116	X				X
117	X				X
118	X				XX
107	X				

as ULD. All list-mode clipped SD, list-mode clipped LD, and ULD acquisitions were reconstructed using Time-of-Flight and ultra-high-definition (voxel volume = $1 \times 1 \times 1 \text{ mm}^3$), three iterations, and three subsets. Point spread function (PSF) was modeled and Gaussian filtering was applied (Figures 1, 2) (Supplementary Material).

Qualitative Image Analysis

Philips Intellispace Portal was used to generate the images for subsequent review by a blinded reader panel using REDCap survey platform. Each dPET scan was presented with three non-rotating maximum intensity projection (MIP) images, with 0° (ventral projection), 108° (right posterior oblique projection) and -90° (left lateral projection) angles, with a PET SUV window level of 0–10. REDCap surveys recorded the reader assessment of [^{18}F]NaF dPET image quality (Figure 1). The images were reviewed by three authors (CW, MVK, MIM) working independently and blinded to radiotracer dose administered. Reviewers performed imaging assessment of the entire imaging dataset twice with at least 1 week between reader assessments to control for visual memory. The image datasets were randomly ordered between surveys.

Qualitative reader assessment outcome parameters included: overall diagnostic quality of the images, and regional bone [^{18}F]NaF uptake of the following regions of interest (ROI): cervical, thoracic, and lumbar, spine, skull, proximal long bones (scapula, humerus, and radius and ulna), distal long bones (femur, tibia, and pelvis), short bones (carpal joint bones, metacarpal bones, tarsal joint bones, metatarsal bones, proximal, middle, and distal phalanges) (Table 2).

The qualitative [^{18}F]NaF uptake was scored 1–4 (1 = not acceptable; 2 = insufficient; 3 = acceptable; 4 = excellent).

Semi-Quantitative Image Analysis

Maximum and mean standardized uptake values (SUV_{max} and SUV_{mean}) for [^{18}F]NaF activity were assessed using two-dimensional (2D) ROI, manually traced over representative

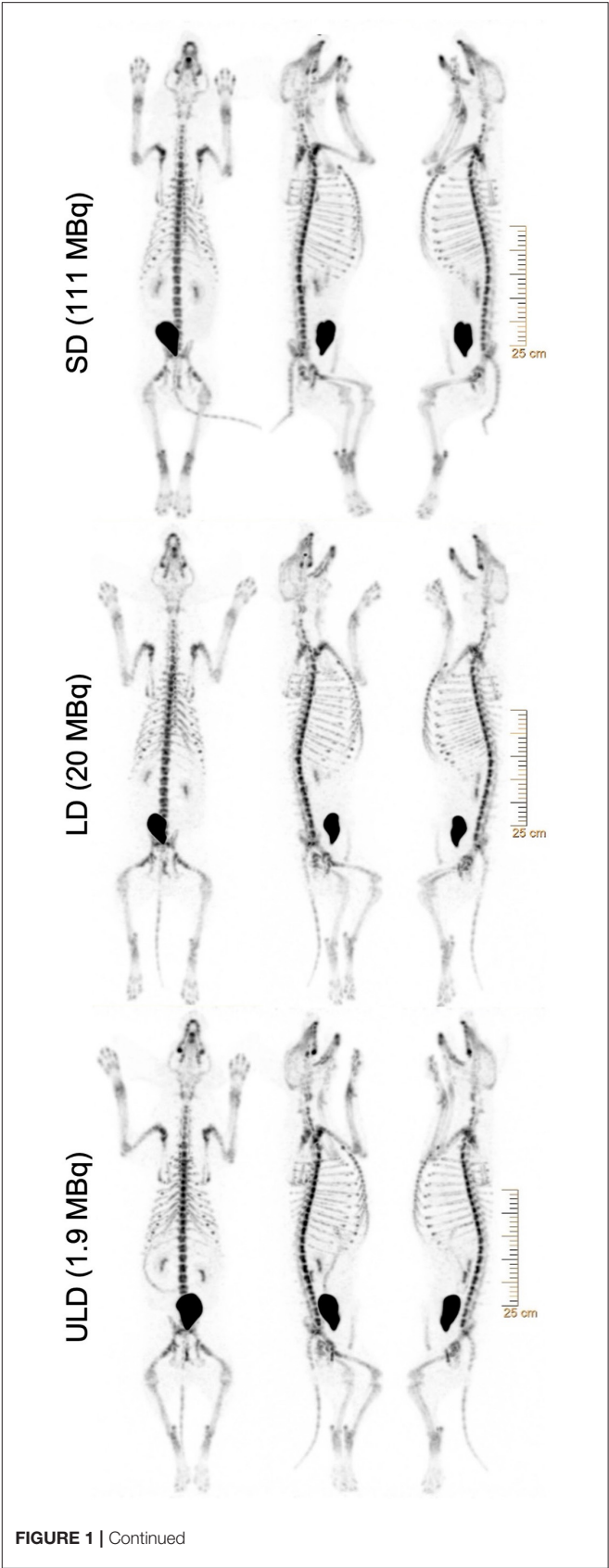


FIGURE 1 | Representative whole-body [^{18}F]NaF PET maximum intensity projections (MIPs) REDCap surveys showing the same subject with standard (SD), low (LD), and ultra-low dose (ULD) from top to bottom. Subject scans were presented with three maximum intensity projections (MIPs), with 0° , 108° , and -90° angles (from left to right), with a gray level of 10.00. All images were reconstructed using ultra-high-definition (voxel volume = $1 \times 1 \times 1 \text{ mm}^3$), 3 iterations, and 3 subsets. Point spread function (PSF) was modeled and Gaussian filtering was applied. SD and LD were retrospectively list-mode clipped accordingly to simulate the same count density as ULD.

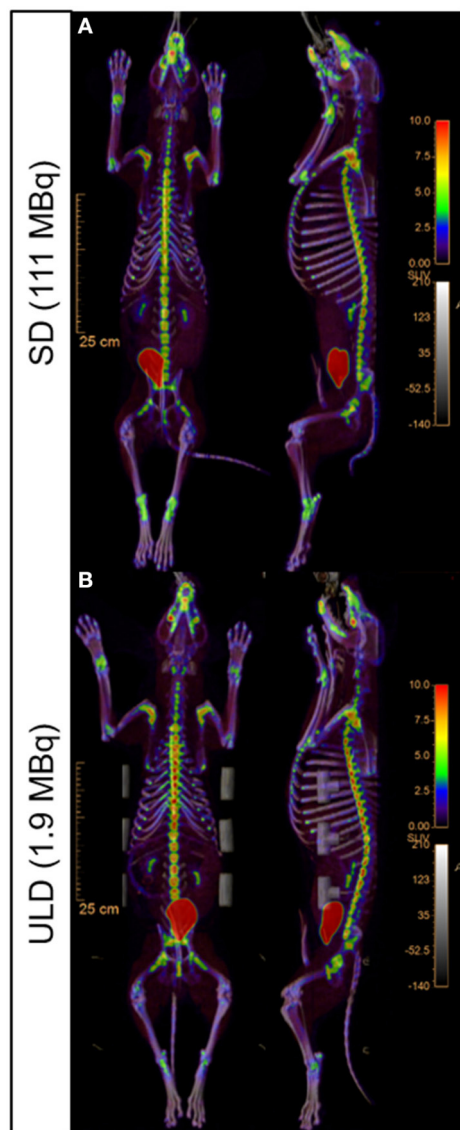


FIGURE 2 | Representative whole-body [^{18}F]NaF PET/CT uptake fusion showing the metabolic bone activity. Standard dose [SD; (A)] and ultra-low dose [ULD; (B)] dorsal (left) and sagittal (right) images.

osseous structures including mandible, carpus, first lumbar vertebral body, distal femur, tarsus, caudal vertebrae, and a region of the liver (Tables 3, 4).

Statistical Analysis

Reviewer ratings of images are reported as rating frequencies and percentages for each ROI are represented in Table 2. Continuous outcome variables for dPET: SUV_{max} , and SUV_{mean} were modeled using linear mixed models with random intercepts and categorical fixed effects representing dose (Tables 3, 4). The random intercepts account for correlation between repeated measures on each canine. Results are reported as model based estimated means and 95% confidence intervals. Overall p -values for groups effects are also reported. All hypothesis tests were conducted at a 5% type I error level. All statistical analyses were conducted using SAS version 9.4 (SAS Institute, Cary, NC).

RESULTS

All dPET/CT imaging studies were completed and all dPET image datasets ($n = 19$) were deemed evaluable.

Qualitative Image Analysis

The overall diagnostic quality of all images was scored as excellent (61%) and acceptable (39%) by the three reviewers (Table 2). The skull images scored excellent (66%) and acceptable (34%). Both thoracic and lumbar spine images were scored excellent (98%) and acceptable (2%). The proximal long bones images were scored excellent (61%) and acceptable (39%). Cervical spine images were scored excellent (43%), acceptable (54%), and insufficient (4%). Distal long bones images were scored excellent (41%), acceptable (58%), and insufficient (1%). Short bones images were scored excellent (46%), acceptable (52%), and insufficient (2%). Only between 1 and 4% of the cervical spine, distal long bones, and short bones images were scored as insufficient [^{18}F]NaF uptake compared to 96–99% acceptable and excellent uptake scores. None of the ROI images were scored as not acceptable. Table 2 summarizes the reviewer's score frequency for each skeletal ROI.

Semi-Quantitative Image Analysis

Sodium fluoride ([^{18}F]NaF) SUV_{mean} showed no statistically significant differences among the three doses (SD, LD, and ULD) in any of the osseous structures assessed (i.e., mandible, carpus, first lumbar vertebra, distal femur, tarsus, caudal vertebrae, and a region of the liver) (Table 3). For the [^{18}F]NaF SUV_{max} (Table 4), only the first lumbar vertebra showed statistically significant differences among the three doses with the SUV_{max} at SD significantly lower than the SUV_{max} values at LD ($p < 0.03$) and ULD ($p < 0.02$). The mandible, carpus, distal femur, tarsus, caudal vertebrae, and a region of the liver showed no statistically significant differences among the three doses.

DISCUSSION

This study demonstrates that a 60-fold sodium fluoride ([^{18}F]NaF) dose (ULD) reduction did not significantly differ in image quality and quantification compared to the standard dose (SD) in a healthy canine model. Our findings present a feasible option to markedly reduce [^{18}F]NaF radiotracer doses

TABLE 2 | Qualitative image analysis as score frequencies and percentages (%) for the overall image quality and the skeletal regions of interest using standard (SD), low (LD), and ultra-low (ULD) [^{18}F]NaF doses.

Region of interest	Score	Standard dose (111 MBq)	Low dose (20 MBq)	Ultra-low dose (1.9 MBq)
Overall image quality				
	Excellent	25 (62.5%)	24 (60.0%)	39 (54.2%)
	Acceptable	15 (37.5%)	16 (40.0%)	33 (45.8%)
	Insufficient	0 (0.0%)	0 (0.0%)	0 (0.0%)
	Not acceptable	0 (0.0%)	0 (0.0%)	0 (0.0%)
Cervical spine				
	Excellent	16 (40.0%)	20 (50.0%)	34 (47.2%)
	Acceptable	22 (55.0%)	18 (45.0%)	38 (52.8%)
	Insufficient	2 (5.0%)	2 (5.0%)	0 (0.0%)
	Not acceptable	0 (0.0%)	0 (0.0%)	0 (0.0%)
Thoracic spine				
	Excellent	40 (100.0%)	39 (97.5%)	69 (97.2%)
	Acceptable	0 (0.0%)	1 (2.5%)	2 (2.8%)
	Insufficient	0 (0.0%)	0 (0.0%)	0 (0.0%)
	Not acceptable	0 (0.0%)	0 (0.0%)	0 (0.0%)
Lumbar spine				
	Excellent	40 (100.0%)	39 (97.5%)	70 (97.2%)
	Acceptable	0 (0.0%)	1 (2.5%)	2 (2.8%)
	Insufficient	0 (0.0%)	0 (0.0%)	0 (0.0%)
	Not acceptable	0 (0.0%)	0 (0.0%)	0 (0.0%)
Skull				
	Excellent	15 (37.5%)	15 (38.5%)	27 (37.5%)
	Acceptable	25 (62.5%)	24 (61.5%)	45 (62.5%)
	Insufficient	0 (0.0%)	0 (0.0%)	0 (0.0%)
	Not acceptable	0 (0.0%)	0 (0.0%)	0 (0.0%)
Proximal long bones				
	Excellent	18 (45.0%)	17 (42.5%)	28 (38.9%)
	Acceptable	22 (55.0%)	23 (57.5%)	44 (61.1%)
	Insufficient	0 (0.0%)	0 (0.0%)	0 (0.0%)
	Not acceptable	0 (0.0%)	0 (0.0%)	0 (0.0%)
Distal long bones				
	Excellent	19 (47.5%)	19 (48.7%)	27 (37.5%)
	Acceptable	21 (52.5%)	20 (51.3%)	42 (58.3%)
	Insufficient	0 (0.0%)	0 (0.0%)	3 (4.2%)
	Not acceptable	0 (0.0%)	0 (0.0%)	0 (0.0%)
Short bones				
	Excellent	20 (50.0%)	20 (50.0%)	32 (44.4%)
	Acceptable	20 (50.0%)	16 (40.0%)	40 (55.6%)
	Insufficient	0 (0.0%)	4 (10.0%)	0 (0.0%)
	Not acceptable	0 (0.0%)	0 (0.0%)	0 (0.0%)

Reviewer's scores are combined.

in a translational preclinical system of bone imaging using a dPET/CT system without loss of overall imaging quality.

Regardless of the [^{18}F]NaF dose, the overall dPET image quality assessment demonstrated diagnostic image quality in

TABLE 3 | [^{18}F]NaF mean standardized uptake values (SUV_{mean}) of regions of interest (ROIs).

	Standard dose (111 MBq)	Low dose (20 MBq)	Ultra-low dose (1.9 MBq)	Overall p-value
ROI	Mean (95%CI)	Mean (95%CI)	Mean (95%CI)	
First lumbar	8.6 (7.0, 10.1)	8.8 (7.3, 10.4)	9.2 (8.0, 10.3)	0.7723
Distal femur	3.1 (2.6, 3.6)	3.1 (2.6, 3.6)	2.5 (2.1, 2.9)	0.0528
Carpus	3.2 (2.2, 4.1)	2.8 (1.8, 3.9)	2.9 (2.2, 3.6)	0.8394
Mandible	2.5 (2.1, 3.0)	2.3 (1.9, 2.8)	2.5 (2.1, 2.9)	0.6241
Tarsus	2.9 (2.2, 3.6)	2.6 (1.9, 3.3)	2.1 (1.6, 2.7)	0.2124
Caudal vertebrae	0.7 (0.2, 1.2)	1.2 (0.7, 1.7)	1.2 (0.9, 1.6)	0.1776
Liver	0.6 (0.4, 0.9)	0.5 (0.2, 0.8)	0.7 (0.5, 0.9)	0.4803

[^{18}F]NaF, sodium fluoride; CI, confidence intervals. * $p < 0.05$ considered significant.

TABLE 4 | [^{18}F]NaF maximum standardized uptake values (SUV_{max}) of regions of interest (ROIs).

	Standard dose (111 MBq)	Low dose (20 MBq)	Ultra-low dose (1.9 MBq)	Overall p-value
ROI	Mean (95%CI)	Mean (95%CI)	Mean (95%CI)	
First lumbar	14.8 (11.7, 17.9)*	19.6 (16.5, 22.7)	19.7 (17.3, 22.0)	0.0380
Distal femur	4.6 (3.8, 5.3)	4.1 (3.1, 5.0)	3.6 (3.0, 4.3)	0.1025
Carpus	7.2 (5.4, 9.1)	7.7 (5.7, 9.8)	7.2 (5.8, 8.6)	0.8861
Mandible	6.9 (5.6, 8.2)	7.4 (5.8, 8.9)	8.6 (7.6, 9.6)	0.0821
Tarsus	6.3 (4.9, 7.7)	7.4 (6.0, 8.8)	6.1 (5.1, 7.2)	0.3149
Caudal vertebrae	6.3 (4.2, 8.5)	6.2 (3.5, 8.9)	6.2 (4.6, 7.9)	0.9951
Liver max	0.7 (0.4, 1.0)	0.6 (0.3, 1.0)	1.0 (0.8, 1.2)	0.1428

[^{18}F]NaF, sodium fluoride; CI, confidence intervals. * $p < 0.05$ considered significant.

all [^{18}F]NaF dPET image data sets with 61% of the scans scored as excellent and 39% scored as acceptable. No dPET imaging study received an insufficient or not acceptable score. These results indicate that ULD [^{18}F]NaF dPET image quality was comparable to SD and even LD [^{18}F]NaF dPET images (Table 2). ULD imaging is readily achieved with the new dPET detector capabilities enabled by improved spatial and temporal resolutions, reduced dead time, and higher dynamic count rate range when compared with conventional, analog photomultiplier tube based PET (cPET) detectors which has been previously described (43, 45, 46, 51, 52). In existing cPET systems, multiple scintillation crystals are coupled to multiple photomultiplier tube-based detectors whereas each scintillation crystal is coupled 1:1 with a single digital photon counting dPET detector. Hence, the combination of the direct coupling (1:1), with the enhanced time of flight (TOF) improves the timing and volumetric resolutions of the digital over the analog PET (44–46). The advantages of the dPET compared to cPET, leveraged with the reconstruction capabilities that allow for a 64-fold matrix reduction (from $4 \times 4 \times 4$ to $1 \times 1 \times 1 \text{ mm}^3$) favor radiation exposure reduction without sacrificing image quality.

It allows us to move preclinical nuclear medicine imaging forward with substantial reduced exposure levels while preserving image quality.

This study showed that using a clinical dPET/CT system in a large animal model might provide guidance to perform translational studies that currently are only feasible in small laboratory animals using specialized micro PET/CT systems.

In the regional image quality assessment, the skull, thoracic and lumbar spine, and proximal long bones were scored excellent and acceptable, with the thoracic and lumbar spine scoring the highest on image quality. This finding is consistent with a study in skeletally immature healthy canines (53), and a human study of the spine with [^{18}F]NaF in healthy individuals where thoracic and lumbar spine had significant higher uptake compared to the cervical spine (54). An intriguing finding of the current study was that the cervical spine images were scored excellent and acceptable for most of the samples (96%) and 4% were scored insufficient. The atlas (C1) and the axis (C2) showed an uptake similar to the skull and lower than the rest of the cervical vertebrae (C3–C7) (**Table 2**). This may be due to anatomical differences and blood perfusion in those vertebrae, and the fact that C1–C2 lack vertebral bodies and marrow cavities, which provide capacity for higher blood perfusion (and hence bone radiotracer uptake), in addition to have anatomically different spinous and transverse processes. The short bones images were scored excellent and acceptable (98%) with a 2% that were scored insufficient, this small percentage may be due to the lower uptake of the distal phalanges due to a relatively decreased peripheral blood flow which leads to less radiotracer availability regionally in these areas when compared with the axial skeletal structures. Additionally, if the distal extremities were relatively colder to the axial skeleton, peripheral vasoconstriction would have decreased the relative blood flow to these regions and therefore, the [^{18}F]NaF radiotracer uptake.

Overall, ULD [^{18}F]NaF dPET imaging demonstrated the feasibility of marked radiotracer dose reduction without impairing diagnostic image quality. Additionally, the dPET image data sets were quantitatively assessed and ULD [^{18}F]NaF dPET did not significantly underrepresent SUV_{mean} and SUV_{max} values when compared with LD and SD. As expected in a healthy canine, the average skeletal osteoblastic activity (i.e., SUV_{mean}) showed no statistically significant differences among the 3 doses (**Table 3**). This further suggests that ULD [^{18}F]NaF dPET is feasible. In addition, quantitative assessment in terms of SUV_{max} showed no statistically significant differences among SD, LD and ULD doses except in the first lumbar vertebra (**Table 4**). The first lumbar vertebra demonstrated SUV_{max} values significantly lower on SD when compared with LD or ULD but no significant differences in SUV_{mean} value were noted for these 3 doses. This may be due to an increase heterogeneity of [^{18}F]NaF uptake in the lumbar vertebrae among subjects which the SUV_{max} will highlight and the SUV_{mean} will not. The caudal vertebrae (tail), which contains several small bones more distally located, showed no differences among doses in our qualitative and quantitative assessments. This further supports that ULD [^{18}F]NaF dPET is sufficient for assessing

normal osteoblastic activity even in small distal bones which are biomechanically active.

This study showed that using a clinical dPET system in a large animal model might provide guidance to perform translational studies that currently are only feasible in small laboratory animals using specialized micro PET/CT systems. A limitation of the study was that not all dogs received the three doses (ULD, LD, and SD); however, eight of the nine dogs received the ULD in addition to either the SD or LD. The use of a translational large animal model is expensive, requires extensive preparation and coordination, and presents more challenges when compared to smaller laboratory animals. Future studies will be needed to further assess this ULD [^{18}F]NaF dPET/CT imaging approach for oncologic and non-oncologic osteoblastic diseases in preclinical large animal models.

Ultra-low dose [^{18}F]NaF dPET/CT demonstrated a comparable diagnostic image quality and quantitative accuracy when compared with SD. This ULD dPET approach is consistent with the goals of ALARA in terms of minimizing radiation exposure not only to research subjects but also PET technologists, veterinary personnel, and caretakers.

DATA AVAILABILITY STATEMENT

The original contributions presented in the study are included in the article/**Supplementary Material**, further inquiries can be directed to the corresponding author/s.

ETHICS STATEMENT

The animal study was reviewed and approved by the Institutional Animal Care and Use Committee (IACUC) of The Ohio State University.

AUTHOR CONTRIBUTIONS

MM and MK: study design and take responsibility for the integrity of the data analysis. MM, RM, and MK: study conduct. MM and RM: data collection. MM, RM, MA-R, SF, CW, and MK: data analysis. MM, MA-R, SF, RJ, and MK: data interpretation. MM: drafting manuscript. MM, RM, MA-R, SF, CW, RJ, and MK: revising manuscript content and approving final version of manuscript. All authors contributed to the article and approved the submitted version.

FUNDING

This study was supported by Award Number Grant KL2TR002734 from the National Center for Advancing Translational Sciences, Ohio Third Frontier grants TECH 10-012, TECH 11-044, and TECH 13-060 and the Wright Center of Innovation in Biomedical Imaging Development Fund. REDCap electronic data capture tools hosted at The Ohio State University and supported by CTSA grant UL1TR002733.

Funding bodies had no role in the design, data analysis, or writing of the manuscript.

ACKNOWLEDGMENTS

The authors thank George Aliulis, Jim Ellis, Dr. Katherine Binzel, and Michael Friel for operating the dPET/CT system and their assistance with radiation safety protocols, and Dr. Jun Zhang for technical support. Heather Lansky for REDCap assistance. Corinne Uskali and the Center for Design and

Manufacturing Excellence at The Ohio State University for the help and assistance designing and manufacturing the Preclinical Multimodal Imaging Positioning Device. ULAR staff for animal technical assistance.

SUPPLEMENTARY MATERIAL

The Supplementary Material for this article can be found online at: <https://www.frontiersin.org/articles/10.3389/fmed.2021.725118/full#supplementary-material>

REFERENCES

- Minamimoto R, Loening A, Jamali M, Barkhodari A, Mosci C, Jackson T, et al. Prospective comparison of ^{99m}Tc -MDP scintigraphy, combined ^{18}F -NaF and ^{18}F -FDG PET/CT, and whole-body MRI in patients with breast and prostate cancer. *J Nucl Med*. (2015) 56:1862–8. doi: 10.2967/jnumed.115.162610
- Kulshrestha RK, Vinjamuri S, England A, Nightingale J, Hogg P. The role of ^{18}F -sodium fluoride PET/CT bone scans in the diagnosis of metastatic bone disease from breast and prostate cancer. *J Nucl Med Technol*. (2016) 44:217–22. doi: 10.2967/jnmt.116.176859
- Langsteger W, Rezaee A, Pirich C, Beheshti M. (^{18}F -NaF-PET/CT and (^{99m}Tc -MDP bone scintigraphy in the detection of bone metastases in prostate cancer. *Semin Nucl Med*. (2016) 46:491–501. doi: 10.1053/j.semnuclmed.2016.07.003
- Lim I, Lindenberg ML, Mena E, Verdini N, Shih JH, Mayfield C, et al. (^{18}F -Sodium fluoride PET/CT predicts overall survival in patients with advanced genitourinary malignancies treated with cabozantinib and nivolumab with or without ipilimumab. *Eur J Nucl Med Mol Imaging*. (2019) 47:178–184. doi: 10.1007/s00259-019-04483-5
- Silva Mendes BI, Oliveira-Santos M, Vidigal Ferreira MJ. Sodium fluoride in cardiovascular disorders: a systematic review. *J Nucl Cardiol*. (2019) 28:1461–1473. doi: 10.1007/s12350-019-01832-7
- Vancheri F, Longo G, Vancheri S, Danial JSH and Henein MY. Coronary artery microcalcification: imaging and clinical implications. *Diagnostics*. 2019 9:125. doi: 10.3390/diagnostics9040125
- Creager MD, Hohl T, Hutcheson JD, Moss AJ, Schlottter F, Blaser MC, et al. (^{18}F -Fluoride signal amplification identifies microcalcifications associated with atherosclerotic plaque instability in positron emission tomography/computed tomography images. *Circ Cardiovasc Imag*. (2019) 12:e007835. doi: 10.1161/CIRCIMAGING.118.007835
- Watkins L, MacKay J, Haddock B, Mazzoli V, Uhlrich S, Gold G, et al. Assessment of quantitative [^{18}F] Sodium fluoride PET measures of knee subchondral bone perfusion and mineralization in osteoarthritic and healthy subjects. *Osteoarthritis Cartilage*. (2021) 29:849–58. doi: 10.1016/j.joca.2021.02.563
- MacKay J, Watkins L, Gold G, and Kogan F. [^{18}F]NaF PET-MRI provides direct in-vivo evidence of the association between bone metabolic activity and adjacent synovitis in knee osteoarthritis: a cross-sectional study. *Osteoarthritis Cartilage*. (2021) 8:S1063-4584(21)00727-5. doi: 10.1016/j.joca.2021.04.014
- Raynor WY, Borja AJ, Hancin EC, Werner TJ, Alavi A, Revheim ME. Novel musculoskeletal and orthopedic applications of ^{18}F -sodium fluoride PET. *PET Clin*. (2021) 16:295–311. doi: 10.1016/j.cpet.2020.12.006
- Khaw TH, Raynor WY, Borja AJ, Al-Zaghal A, Jonnakuti VS, Cheng N, et al. Assessing the effects of body weight on subchondral bone formation with quantitative ^{18}F -sodium fluoride PET. *Ann Nucl Med*. (2020) 34:559–64. doi: 10.1007/s12149-020-01482-7
- Tibrewala R, Podoia V, Bucknor M, Majumdar S. Principal component analysis of simultaneous PET-MRI reveals patterns of bone-cartilage interactions in osteoarthritis. *J Magn Reson Imag*. (2020) 52:1462–74. doi: 10.1002/jmri.27146
- Menendez MI, Hettlich B, Wei L, Knopp MV. Feasibility of Na(^{18}F) PET/CT and MRI for noninvasive *in vivo* quantification of knee pathophysiological bone metabolism in a canine model of post-traumatic osteoarthritis. *Mol Imaging*. (2017) 16:1536012117714575. doi: 10.1177/1536012117714575
- Savic D, Podoia V, Seo Y, Yang J, Bucknor M, Franc BL, et al. Imaging bone-cartilage interactions in osteoarthritis using [^{18}F]-NaF PET-MRI. *Mol Imaging*. (2016) 15:1–12. doi: 10.1177/1536012116683597
- Haddock B, Fan AP, Jorgensen NR, Suetta C, Gold GE, Kogan F. Kinetic [^{18}F]-fluoride of the knee in normal volunteers. *Clin Nucl Med*. (2019) 44:377–85. doi: 10.1097/RLU.0000000000002533
- Tibrewala R, Bahroos E, Mehrabian H, Foreman SC, Link TM, Podoia V, et al. [(^{18}F)-Sodium fluoride PET/MR imaging for bone-cartilage interactions in hip osteoarthritis: a feasibility study. *J Orthopaedic Res*. (2019). doi: 10.1016/j.joca.2019.02.213
- Reilly CC, Raynor WY, Hong AL, Kargilis DC, Lee JS, Alecxih AG, et al. Diagnosis and monitoring of osteoporosis with (^{18}F)-sodium fluoride PET: an unavoidable path for the foreseeable future. *Semin Nucl Med*. (2018) 48:535–40. doi: 10.1053/j.semnuclmed.2018.07.007
- Austin AG, Raynor WY, Reilly CC, Zadeh MZ, Werner TJ, Zhuang H, et al. Evolving Role of MR Imaging and PET in Assessing Osteoporosis. *PET Clin*. (2019) 14:31–41. doi: 10.1016/j.cpet.2018.08.007
- Raynor W, Houshmand S, Gholami S, Emamzadehfard S, Rajapakse CS, Blomberg BA, et al. Evolving Role of Molecular Imaging with (^{18}F)-Sodium Fluoride PET as a Biomarker for Calcium Metabolism. *Curr Osteoporos Rep*. (2016) 14:115–25. doi: 10.1007/s11914-016-0312-5
- Kogan F, Fan AP, Monu U, Iagaru A, Hargreaves BA, Gold GE. Quantitative imaging of bone-cartilage interactions in ACL-injured patients with PET-MRI Osteoarthritis and cartilage / OARS, Osteoarthritis Research Society. (2018) 26:790–6. doi: 10.1016/j.joca.2018.04.001
- Beheshti M. (^{18}F -Sodium Fluoride PET/CT and PET/MR Imaging of Bone and Joint Disorders. *PET Clin*. (2018) 13:477–90. doi: 10.1016/j.cpet.2018.05.004
- Blau M, Nagler W, Bender MA. Fluorine-18: a new isotope for bone scanning *Journal of nuclear medicine: official publication, Society of Nuclear Medicine*. (1962) 3:332–4.
- Blau M, Ganatra R, Bender MA. *^{18}F -fluoride for bone imaging Seminars in nuclear medicine*. (1972) 2:31–7. doi: 10.1016/S0001-2998(72)80005-9
- Wondergem M, van der Zant FM, Knol RJ, Burgers AM, Bos SD, Jong IJ, et al. (^{99m}Tc -HDP bone scintigraphy and (^{18}F)-sodiumfluoride PET/CT in primary staging of patients with prostate cancer. *World J Urol*. (2018) 36:27–34. doi: 10.1007/s00345-017-2096-3
- Boellaard R, Quick HH. Current image acquisition options in PET/MR Seminars in nuclear medicine. (2015) 45:192–200. doi: 10.1053/j.semnuclmed.2014.12.001
- Oehmigen M, Lindemann ME, Gratz M, Kirchner J, Ruhlmann V, Umutlu L, et al. Impact of improved attenuation correction featuring a bone atlas and truncation correction on PET quantification in whole-body PET/MR. *Eur J Nucl Med Mol Imag*. (2018) 45:642–53. doi: 10.1007/s00259-017-3864-4
- Aasheim LB, Karlberg A, Goa PE, Håberg A, Sørhaug S, Fagerli UM, et al. PET/MR brain imaging: evaluation of clinical UTE-based attenuation correction. *Eur J Nucl Med Mol Imag*. (2015) 42:1439–46. doi: 10.1007/s00259-015-3060-3

28. Salvatori M, Rizzo A, Rovera G, Indovina L, Schillaci O. Radiation dose in nuclear medicine: the hybrid imaging. *La Radiologia medica*. (2019) 124:768–76. doi: 10.1007/s11547-019-00989-y
29. Chawla SC, Federman N, Zhang D, Nagata K, Nuthakki S, McNitt-Gray M, et al. Estimated cumulative radiation dose from PET/CT in children with malignancies: a 5-year retrospective review. *Pediatr Radiol*. (2010) 40:681–6. doi: 10.1007/s00247-009-1434-z
30. Usmani S, Van den Wyngaert T, Ahmed N, Marafi F, Esmail A, Al Kandari F, et al. Technical feasibility, radiation dosimetry and clinical use of (18)F-sodium fluoride (NaF) in evaluation of metastatic bone disease in pediatric population. *Ann Nucl Med*. (2018) 32:594–601. doi: 10.1007/s12149-018-1279-3
31. Yang CC, Yang BH, Tu CY, Wu TH, Liu SH. Low-dose computed tomography scans with automatic exposure control for patients of different ages undergoing cardiac PET/CT and SPECT/CT. *Nucl Med Commun*. (2017) 38:546–55. doi: 10.1097/MNM.0000000000000679
32. Jang J, Jung SE, Jeong WK, Lim YS, Choi JJ, Park MY, et al. Radiation doses of various CT protocols: a multicenter longitudinal observation study. *J Korean Med Sci*. (2016) 31:S24–31. doi: 10.3346/jkms.2016.31.S1.S24
33. Sekine T, Delso G, Zeimpekis KG, Galiza Barbosa F, Ter Voert EE, Huellner M, et al. Reduction of (18)F-FDG dose in clinical PET/MR imaging by using silicon photomultiplier detectors. *Radiology*. (2018) 286:249–59. doi: 10.1148/radiol.2017162305
34. Prieto E, Garcia-Velloso MJ, Rodriguez-Fraile M, Moran V, Garcia-Garcia B, Guillen F, et al. Significant dose reduction is feasible in FDG PET/CT protocols without compromising diagnostic quality. *Phys Med*. (2018) 46:134–9. doi: 10.1016/j.ejmp.2018.01.021
35. Seith F, Schmidt H, Kunz J, Kustner T, Gatidis S, Nikolaou K, et al. Simulation of tracer dose reduction in (18)F-FDG PET/MRI: effects on oncologic reading, image quality, and artifacts. *J Nucl Med*. (2017) 58:1699–705. doi: 10.2967/jnumed.116.184440
36. Zucchetta P, Branchini M, Zorz A, Bodanza V, Cecchin D, Pauso M, et al. Quantitative analysis of image metrics for reduced and standard dose pediatric (18)F-FDG PET/MRI examinations. *Br J Radiol*. (2019) 92:20180438. doi: 10.1259/bjr.20180438
37. Beheshti M, Mottaghy FM, Paycha F, Behrendt FF, Van den Wyngaert, Folgeman I, et al. 18F-NaF PET/CT: EANM procedure guidelines for bone imaging. *Eur J Nucl Med Mol Imag*. (2015) 42:1767–77. doi: 10.1007/s00259-015-3138-y
38. Segall G, Delbeke D, Stabin MG, et al. SNM practice guideline for sodium 18F-fluoride PET/CT bone scans 1.0. *J Nucl Med*. (2010) 51:1813–20. doi: 10.2967/jnumed.110.082263
39. Ohnona J, Michaud L, Balogova S, Paycha F, Nataf V, Chauchat P, et al. Can we achieve a radionuclide radiation dose equal to or less than that of 99mTc-hydroxymethane diphosphonate bone scintigraphy with a low-dose 18F-sodium fluoride time-of-flight PET of diagnostic quality? *Nucl Med Commun*. (2013) 34:417–25. doi: 10.1097/MNM.0b013e32835fcd9d
40. Lim R, Fahey FH, Drubach LA, Connolly LP, Treves ST. Early experience with fluorine-18 sodium fluoride bone PET in young patients with back pain. *J Pediatric Orthopedics*. (2007) 27:277–82. doi: 10.1097/BPO.0b013e31803409ba
41. Marafi F, Esmail A, Rasheed R, Alkandari F, Usmani S. *Novel weight-based dose threshold for 18F-NaF PET-CT imaging using advanced PET-CT systems: a potential tool for reducing radiation burden Nuclear medicine communications*. (2017) 38:764–70. doi: 10.1097/MNM.0000000000000706
42. Oddstig J, Leide Svegborn S, Almquist H, Bitzen U, Garperd S, Hedeer F, et al. Comparison of conventional and Si-photomultiplier-based PET systems for image quality and diagnostic performance. *BMC Med Imag*. (2019) 19:81. doi: 10.1186/s12880-019-0377-6
43. Zhang J, Maniawski P, Knopp MV. Performance evaluation of the next generation solid-state digital photon counting PET/CT system. *EJNMMI Res*. (2018) 8:97. doi: 10.1186/s13550-018-0448-7
44. Lopez-Mora DA, Estorch M, Fuentes-Ocampo F, Perez Garcia JJ, Moral A, Carrio I. Digital PET/CT vs analogue PET/CT in a parathyroid gland study with (18)F-Fluorocholine. *Revista española de medicina nuclear e imagen molecular*. (2019) 38:121–2. doi: 10.1016/j.remnie.2018.10.012
45. Lopez-Mora DA, Flotats A, Fuentes-Ocampo F, Camcho V, Fernandez A, Ruiz A, et al. Comparison of image quality and lesion detection between digital and analog PET/CT. *Eur J Nucl Med Mol Imaging*. (2019) 46:1383–90. doi: 10.1007/s00259-019-4260-z
46. Fuentes-Ocampo F, Lopez-Mora DA, Flotats A, Paillahueque G, Camacho V, Duch J, et al. Digital vs. analog PET/CT: intra-subject comparison of the SUVmax in target lesions and reference regions. *European journal of nuclear medicine and molecular imaging*. (2019) 46:1745–1750. doi: 10.1007/s00259-019-04280-0
47. Wright CL, Binzel K, Zhang J, Knopp MV. Advanced functional tumor imaging and precision nuclear medicine enabled by digital PET technologies. *Contrast Media Mol Imag*. (2017) 2017:5260305. doi: 10.1155/2017/5260305
48. Wright CL, Binzel K, Zhang J, Wuthrick EJ, Knopp MV. Clinical feasibility of (90)Y digital PET/CT for imaging microsphere biodistribution following radioembolization. *Eur J Nucl Med Mol Imag*. (2017) 44:1194–7. doi: 10.1007/s00259-017-3694-4
49. Wright CL, Maly JJ, Zhang J, Knopp MV. Advancing Precision Nuclear Medicine and Molecular Imaging for Lymphoma. *PET Clin*. (2017) 12:63–82. doi: 10.1016/j.cpet.2016.08.005
50. Menendez MI, Hettlich B, Wei L, Knopp MV. *Preclinical Multimodal Molecular Imaging Using 18F-FDG PET/CT and MRI in a Phase I Study of a Knee Osteoarthritis in In Vivo Canine Model Mol Imaging*. (2017) 16:1536012117697443. doi: 10.1177/1536012117697443
51. Nguyen NC, Vercher-Conejero JL, Sattar A, Miller MA, Maniawski PJ, Jordan DW, et al. Image quality and diagnostic performance of a digital pet prototype in patients with oncologic diseases: initial experience and comparison with analog PET. *J Nucl Med*. (2015) 56:1378–85. doi: 10.2967/jnumed.114.148338
52. Wright CL, Washington IR, Bhatt AD, Knopp MV. Emerging opportunities for digital PET/CT to advance locoregional therapy in head and neck cancer seminars in radiation. *Oncology*. (2019) 29:93–101. doi: 10.1016/j.semradonc.2018.11.005
53. Valdes-Martinez A, Kraft SL, Brundage CM, Arceneaux BK, Stewart JA, Gibbons DS. Assessment of blood pool, soft tissue, and skeletal uptake of sodium fluoride F 18 with positron emission tomography-computed tomography in four clinically normal dogs. *Am J Vet Res*. (2012) 73:1589–95. doi: 10.2460/ajvr.73.10.1589
54. Ayubcha C, Zirkachian Zadeh M, Stockendahl MJ, Al-Zaghal A, Hartvigsen J, Rajapakse CS, et al. Quantitative evaluation of normal spinal osseous metabolism with 18F-NaF PET/CT. *Nucl Med Commun*. (2018) 39:945–50. doi: 10.1097/MNM.0000000000000891

Conflict of Interest: The authors declare that the research was conducted in the absence of any commercial or financial relationships that could be construed as a potential conflict of interest.

Publisher's Note: All claims expressed in this article are solely those of the authors and do not necessarily represent those of their affiliated organizations, or those of the publisher, the editors and the reviewers. Any product that may be evaluated in this article, or claim that may be made by its manufacturer, is not guaranteed or endorsed by the publisher.

Copyright © 2022 Menendez, Moore, Abdel-Rasoul, Wright, Fernandez, Jackson and Knopp. This is an open-access article distributed under the terms of the Creative Commons Attribution License (CC BY). The use, distribution or reproduction in other forums is permitted, provided the original author(s) and the copyright owner(s) are credited and that the original publication in this journal is cited, in accordance with accepted academic practice. No use, distribution or reproduction is permitted which does not comply with these terms.



Multimodal *in vivo* Imaging of the Integrated Postnatal Development of Brain and Skull and Its Co-modulation With Neurodevelopment in a Down Syndrome Mouse Model

OPEN ACCESS

Edited by:

Monique Bernsen,
Erasmus Medical Center, Netherlands

Reviewed by:

Maria Raposo,
New University of Lisbon, Portugal
Yann Hérault,
Centre national de la recherche
scientifique (CNRS), France

*Correspondence:

Neus Martínez-Abadías
neusmartinez@ub.edu
Greetje Vande Velde
greetje.vandavelde@kuleuven.be

†These authors have contributed
equally to this work and share last
authorship

Specialty section:

This article was submitted to
Translational Medicine,
a section of the journal
Frontiers in Medicine

Received: 15 November 2021

Accepted: 14 January 2022

Published: 11 February 2022

Citation:

Llambich S, González R, Albaigès J,
Wouters J, Marain F, Himmelreich U,
Sharpe J, Dierssen M, Gsell W,
Martínez-Abadías N and Vande
Velde G (2022) Multimodal *in vivo*
Imaging of the Integrated Postnatal
Development of Brain and Skull and
Its Co-modulation With
Neurodevelopment in a Down
Syndrome Mouse Model.
Front. Med. 9:815739.
doi: 10.3389/fmed.2022.815739

Sergi Llambich¹, Rubèn González^{2,3,4}, Julia Albaigès^{3,4,5}, Jens Wouters¹, Fopke Marain¹,
Uwe Himmelreich¹, James Sharpe^{3,4,6,7}, Mara Dierssen^{3,4,5}, Willy Gsell¹,
Neus Martínez-Abadías^{2,3,4,7*} and Greetje Vande Velde^{1*}

¹ Biomedical MRI, Department of Imaging and Pathology, KU Leuven, Flanders, Belgium, ² Grup de Recerca en Antropologia
Biològica (GREAB), Department of Biologia Evolutiva, Ecologia i Ciències Ambientals (BEECA), Universitat de Barcelona,
Barcelona, Spain, ³ Center for Genomic Regulation, The Barcelona Institute of Science and Technology, Barcelona, Spain,
⁴ Universitat Pompeu Fabra, Barcelona, Spain, ⁵ Centro de Investigación Biomédica en Red Enfermedades Raras (CIBERER),
Barcelona, Spain, ⁶ Institució Catalana de Recerca i Estudis Avançats, Barcelona, Spain, ⁷ European Molecular Biology
Laboratory (EMBL) Barcelona, European Molecular Biology Laboratory, Barcelona, Spain

The brain and skeletal systems are intimately integrated during development through common molecular pathways. This is evidenced by genetic disorders where brain and skull dysmorphologies are associated. However, the mechanisms underlying neural and skeletal interactions are poorly understood. Using the Ts65Dn mouse model of Down syndrome (DS) as a case example, we performed the first longitudinal assessment of brain, skull and neurobehavioral development to determine alterations in the coordinated morphogenesis of brain and skull. We optimized a multimodal protocol combining *in vivo* micro-computed tomography (μ CT) and magnetic resonance imaging (μ MRI) with morphometric analyses and neurodevelopmental tests to longitudinally monitor the different systems' development trajectories during the first postnatal weeks. We also explored the impact of a perinatal treatment with green tea extracts enriched in epigallocatechin-3-gallate (GTE-EGCG), which can modulate cognition, brain and craniofacial development in DS. Our analyses quantified alterations associated with DS, with skull dysmorphologies appearing before brain anomalies, reduced integration and delayed acquisition of neurodevelopmental traits. Perinatal GTE-EGCG induced disparate effects and disrupted the magnitude of integration and covariation patterns between brain and skull. Our results exemplify how a longitudinal research approach evaluating the development of multiple systems can reveal the effect of morphological integration modulating the response of pathological phenotypes to treatment, furthering our understanding of complex genetic disorders.

Keywords: development, brain and skull integration, down syndrome, GTE-EGCG, μ CT imaging, μ MRI

INTRODUCTION

It has long been recognized that neural and skeletal development are intimately integrated throughout development (1–3). Although the specific mechanisms are unknown, the interactions between common signaling pathways such as Hedgehog, Wnt, Notch, TGF β and FGF may underlie the tight link between the brain, the face and the skull (2). In pathological conditions affecting brain and craniofacial structures, the most accepted hypothesis is that craniofacial malformations arise because of altered signals emanating from the brain leading to instructional misinformation to the skull (2, 3). However, it could also be possible that defects in craniofacial morphogenesis affect brain development, or that brain and craniofacial dysmorphologies do not induce one another but are produced simultaneously by inappropriate gene expression occurring within each tissue.

The tendency of different traits or systems to vary in a coordinated manner, known as morphological integration, can be assessed by statistical analysis of covariance patterns between phenotypic traits (4). Patterns of morphological integration can reflect genetic, developmental, or functional interactions between anatomical structures (5). In a complex system such as the head, with high interdependence among the brain, cranium and face (1, 2, 6), integration patterns of the head and skull are largely conserved across mammals (7). This shared pattern of skull covariation is usually preserved even under genetic and developmental alterations (8–10).

Morphological integration can influence how the system responds to changes induced by genetic and environmental factors, facilitating or preventing morphological evolution in certain directions of shape change (11). Integration patterns can also modulate the phenotypic output resulting from disease and genetic alterations as those causing rare disorders associated with craniofacial dysmorphologies (12). However, no studies to date have tested how treatments can alter the proper coordination among the different regions of the growing head (8, 10, 12), modulating the dysmorphologies of genetic disorders that present simultaneous brain and craniofacial alterations, such as holoprosencephaly, micro- and macrocephaly, Apert, Pfeiffer and Crouzon craniosynostosis or Down syndrome (DS), the case example in this study.

In DS, a genetic disorder caused by trisomy of chromosome 21, the overexpression of hundreds of genes alters multiple systems and results in intellectual disability, brain malformations and skeletal and craniofacial dysmorphologies (13). Intellectual disability is present in all cases of DS, with varying degrees of severity and including impaired executive function, short-term and working memory and explicit long-term memory (14). The most common gross brain dysmorphologies in DS include a decrease in brain and cerebellar volumes along with an increase in the lateral ventricles' volume (14–17). Simultaneously, craniofacial shape is also altered in DS, showing a brachycephalic shape (with shorter, wider and rounder skulls) and a flattened face with a shorter mandibular ramus (18–20). In this study, we interrogated whether DS is not only affecting multiple systems independently but also their integration and whether there is a co-modulation between dysmorphology and behavioral neurodevelopment impairment.

Interestingly, previous studies have shown that epigallocatechin-3-gallate (EGCG) pure or in enriched green tea extracts (GTE-EGCG) can modulate cognitive performance as well as brain and skeletal development, partly due to its ability to inhibit the kinase activity of the Dual Specificity Tyrosine-(Y)-Phosphorylation Regulated Kinase 1A (DYRK1A), a kinase involved in neural and skeletal development overexpressed in DS (21–27). Accumulating evidence shows that GTE-EGCG can modulate skull morphogenesis in Ts65Dn mouse models (28). In a previous study, we evaluated the effect of high (100 mg/kg/day) or low doses (30 mg/kg/day) of GTE-EGCG, administered from embryonic day 9 to post-natal day 29, on the facial skeletal development in the Ts65Dn DS mouse model (20). Our results identified both negative and positive effects of GTE-EGCG on the craniofacial structure, depending on the dosage, with low doses normalizing craniofacial phenotypes and high doses inducing disparate effects on facial morphology in both trisomic and euploid mice (20). Here we interrogated whether the disruption of normal development produced by high doses of GTE-EGCG alters morphological integration patterns of the brain and the head and how these related to neurobehavioral development, as the treatment may modulate multiple systems simultaneously.

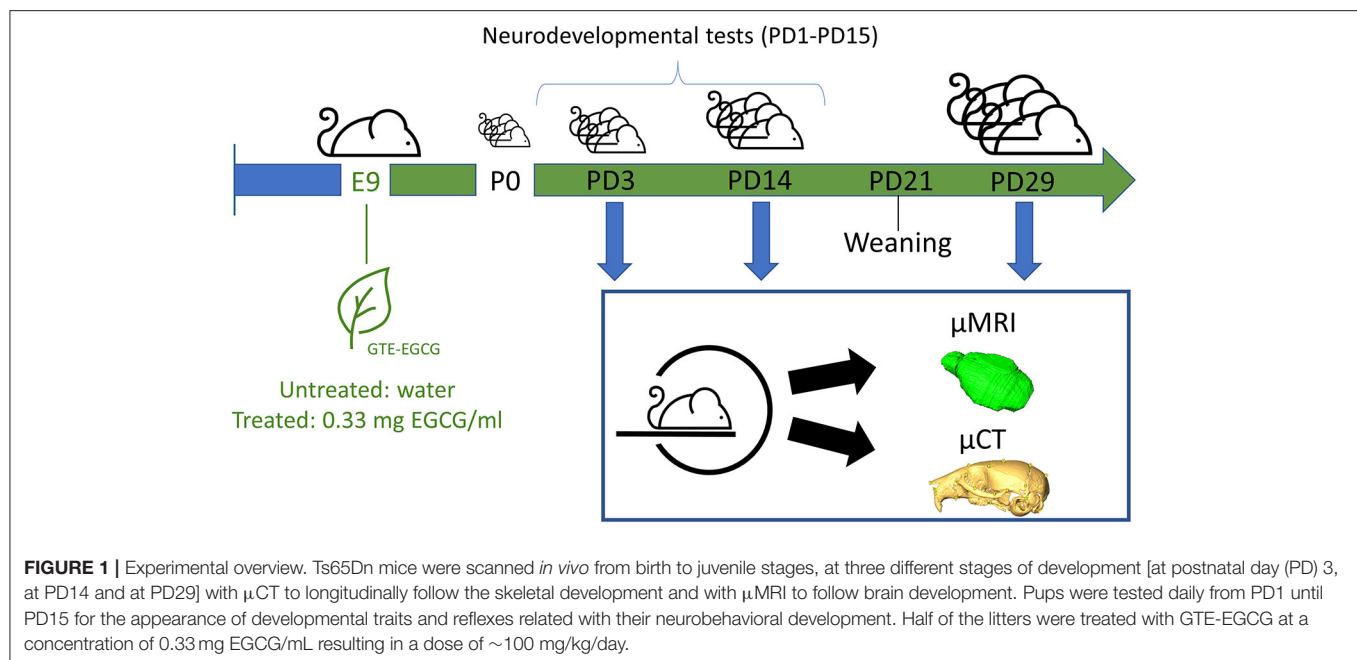
To evaluate the effects of morphological integration patterns on these tightly developing systems, we put forward a novel, multimodal methodological approach. Where most previous studies have focused on either one system or one time point in a cross-sectional design (24, 25, 28–31), we here developed and demonstrated the feasibility of a multimodal imaging-based approach combined with morphometric analyses and parallel neurodevelopmental tests to longitudinally monitor multiple systems' postnatal developmental trajectories simultaneously in live, individual animals from soon after birth into adulthood.

We hypothesize that treatments such as EGCG, affecting both brain and craniofacial development could have an impact on morphological integration patterns. We also propose that alterations to integration may affect early development in DS mouse models. To test this hypothesis, we followed brain and skull postnatal development in parallel in the Ts65Dn mouse model. This holistic approach can help disentangle the direct and indirect effects of potential treatments that regulate altered development in syndromic disorders.

MATERIALS AND METHODS

Animals, Experimental Setup, Treatment and Ethical Statement

Trisomic Ts65Dn (B6EiC3Sn-a/A-Ts (1716)65Dn) mice and euploid littermates were obtained from our in-house breeding colony, established and maintained by crossing Ts65Dn trisomic females to B6EiC3SnF1/J males (refs. 001924 and 001875, the Jackson Laboratory Bar Harbor, ME, USA). Date of conception (E0) was determined as the day in which a vaginal plug was present. Mice were housed at the animal facility of KU Leuven in standard individually ventilated cages (40 cm long \times 25 cm wide \times 20 cm high) under a 12 h light/dark schedule in controlled environmental conditions of humidity (50–70%) and temperature ($22 \pm 2^\circ\text{C}$) with food and water supplied



ad libitum. All pups were labeled with a non-toxic tattoo ink (Ketchum Animal Tattoo Ink, Green Paste) for identification over longitudinal experiments.

We bred a total of 7 litters, three of which were administered a treatment with GTE-EGCG [Mega Green Tea Extract, Life Extension, USA; with estimated composition of 53.6% EGCG, 4.5% epicatechin (EC), 9% epicatechin gallate (ECG) and 12.5% epigallocatechin (EGC)] via the drinking water at a concentration of 0.33 mg EGCG/mL. As EGCG crosses the placenta and reaches the embryo (32), GTE-EGCG treatment started prenatally at embryonic day 9 (E9) via the drinking water of the pregnant dams and continued until the end of the experiment. After weaning, from P21 to P29, GTE-EGCG dissolved in water at the same concentrations was made available to the young mice *ad libitum* (Figure 1). The dosage of EGCG received for an adult mouse was ~ 100 mg/kg/day, considering that, on average, early adult mice weigh 20 g and drink 6 mL of water per day, according to our measurements. In developing embryos and pups before weaning, the received dosage was lower since previous studies indicate that maternal plasma concentrations of catechins were about 10 times higher than in placenta and 50–100 times higher than in the fetal brain (32, 33) and EGCG in milk and plasma of postnatal day 1 (PD1) to PD7 pups was detected at low concentrations (30). Three litters of mice were treated following this protocol and four litters were left untreated for comparison. To minimize potential batch effects, the treatment for all mice was prepared freshly every 3 days from the same batch of GTE-EGCG and water intake was monitored in each cage.

Mice were genotyped at PD14 by PCR from ear snips adapting the protocol in Shaw et al. (34). Trisomic primers, Chr17fwd-5'-GTGGCAAGAGACTCAAATTC AAC-3' and Chr16rev-5'-TGGCTTATTATTATCAGGGCATTT-3'; and positive control primers, IMR8545-5'-AAAGTCGCTCTGAGTTGTTAT-3' and IMG8546-5'-GGAGCGGGAGAAATGGATATG-3' were used.

The following PCR cycle conditions were used: step 1: 94°C for 2 min; step 2: 94°C for 30 s; step 3: 55°C for 45 s; step 4: 72°C for 1 min (steps 2–4 repeated for 40 cycles); step 5: 72°C for 7 min, and a 4°C hold. PCR products were separated on a 1% agarose gel. Randomization for genotype was performed by testing all the pups in each litter, which contain both WT and TS mice. Treatment was randomized by treating half of the litters.

Mice were allocated to groups according to their genotype and pharmacological intervention: wild-type (WT) and trisomic Ts65Dn (TS) mice untreated or treated with GTE-EGCG. During experimentation the investigators were blinded to genotype but not to treatment since they administered the treatment. During data analysis, all investigators were blinded to both genotype and treatment. The sample size for each experiment is described in **Supplementary Table S1**. Differences in sample size are due to technical reasons such as missing scan because the micro-CT or MR scanner was not operating on the scanning day, movement scanning artifacts that impaired image quality, or mouse death during the experiment. Moreover, during the data analyses, few individual mice were excluded when identified as outliers by the ROUT test (35) using GraphPad Prism (v8.02, GraphPad Software, San Diego, California USA) with a Q (maximum desired False Discovery Rate) of 1%. The number of outliers per group is specified in **Supplementary Table S1**.

All procedures complied with all local, national and European regulations and ARRIVE guidelines and were authorized by the Animal Ethics Committee of KU Leuven (ECD approval number P004/2016).

In vivo Micro-Magnetic Resonance Imaging

Mice were anesthetized by inhalation of 1.5–2% of isoflurane (Piramal Healthcare, Morpeth, Northumberland, United Kingdom) in pure oxygen. *In vivo* anatomical μ MR

images were acquired through a 3D T2 weighted RARE sequence (TR/TE: 1,000/ 60 ms; RARE factor: 16; FOV: $24 \times 15 \times 8.3$ mm³; matrix $256 \times 160 \times 88$; acquisition time 15 min) on a 9.4 T Bruker Biospec small animal μ MR scanner (Bruker Biospin, Ettlingen, Germany; 20 cm horizontal bore) equipped with actively shielded gradients (600 mT m⁻¹). A dedicated 3D printed holder was used to accommodate the pups at PD3 and PD14 and to minimize movement artifacts. A quadrature radio-frequency resonator (inner diameter 7.2 cm, Bruker Biospin) was used for transmission of radiofrequency pulses and decoupled to a brain surface coil (quadrature shaped surface coil optimized for mouse brain scanning, Bruker Biospin).

In vivo Micro-Computed Tomography

After μ MRI, mice were anesthetized and scanned *in vivo* with the SkyScan 1278 (Bruker Micro-CT, Kontich, Belgium) for 3 min using the optimized parameters specified in **Supplementary Table S2**.

Image Data Processing

To segment the whole brain and the ventricles from the μ MR images, data were first converted to Analyze file format using ImageJ (1.52 d, National Institute of Health) and then loaded into Amira 2019.3 (Visualization Sciences Group, FEI). Brain and ventricles were manually segmented by drawing a region of interest (ROI) covering those structures on each image slice. Segmentations were used to generate 3D models and to estimate the associated volume.

To segment the craniofacial complex, μ CT data was first reconstructed (NRecon software, Bruker Micro-CT, Kontich, Belgium) and then loaded into Amira 2019.3 (Visualization Sciences Group, FEI). 3D models of craniofacial structures were automatically generated by creating an isosurface based on specific threshold for bone.

Size Analysis

To evaluate if growth trajectories of brain and ventricular structures were significantly different between groups, we analyzed the data by fitting a mixed model as implemented in GraphPad Prism 8.0, with the Geisser-Greenhouse correction. This mixed model uses a compound symmetry covariance matrix and is fit using Restricted Maximum Likelihood (REML). In the presence of randomly missing values, the results can be interpreted like a repeated measures ANOVA. In these analyses, three factors were analyzed, time (reflecting growth across different stages), group (reflecting either genotype or treatment differences at baseline, depending on the groups analyzed) and the interaction between time and group (reflecting differences in the growth patterns). Since time resulted always significant as all groups of mice grew and increased their volume over the different stages analyzed, we focused on differences in the growth patterns as reflected by the interaction effect. Then, since the data were not normally distributed according to Shapiro-Wilk tests, Mann Whitney tests were performed between each pair of experimental groups (WT vs. TS, WT vs. WT Treated, WT vs. TS Treated, TS vs. WT Treated, TS vs. TS Treated, TS Treated vs. WT Treated) at each timepoint to assess if the volumes of the brain and the

ventricles were significantly different between groups within each stage using GraphPad Prism (v8.02, GraphPad Software, San Diego, California USA). Only the *P*-values that were classified as discoveries according to the Benjamini–Hochberg correction for multiple comparisons ($Q = 5\%$) are reported.

Shape Analysis

We compared the morphology of brain and craniofacial structures in WT and TS mice with and without GTE-EGCG treatment using quantitative shape analyses (36). Geometric Morphometrics (GM) is a sophisticated body of statistical tools developed for measuring and comparing shapes with increased precision and efficiency (11, 37). The analysis was based on the 3D coordinates of anatomical homologous landmarks recorded over the structures of interest at each developmental stage, as defined in **Supplementary Figure S1** and **Supplementary Tables S3–S5**. Landmarks were acquired using Amira 2019.3 (Visualization Sciences Group, FEI) and all the GM analyses were performed using MorphoJ v1.06d (38).

To extract shape information from the 3D coordinates of the landmark configurations we performed a Generalized Procrustes Analysis (GPA), which minimizes the influence of size and adopts a single orientation for all specimens. After landmark superimposition, we performed a Principal Component Analysis (PCA), a data exploration technique that performs an orthogonal decomposition of the data and transforms variance covariance matrices into a smaller number of uncorrelated variables called Principal Components (PCs), which successively account for the largest amount of variation in the data (39). Shape variation was represented by creating a morphospace based on the two first PCs, which explain the largest percentages of morphological variation within the sample. If there are no dysmorphologies associated with DS or the treatment, WT and TS mice, treated or not, will overlap in the PCA scatterplot, showing similar phenotypes. If there are differences due to genotype or treatment, groups of mice will be separated from each other, showing a distinct phenotype. PCA results were plotted with the ggpubr package in R (40, 41).

From the 3D coordinates of the brain landmarks we estimated additional brain measures. The cephalic index was calculated as the ratio of the Euclidean distance between landmarks number 4 and 5 and landmarks number 1 and 3 (1 and 11 at PD3) of the brain. The length of the olfactory bulbs and the length of the cerebellum were determined as the Euclidean distance between landmarks number 1 and 2 and 10 and 3, respectively (see **Supplementary Table S3** for landmark definitions).

To statistically quantify overall differences between WT, TS, WT treated and TS treated mice, we estimated the Procrustes distances between the average shapes of pairs of groups at each stage of development. Procrustes distances are used in GM to quantify group shape differences after the process of superimposition and are calculated as the square root of the sum of squared differences in the positions of the landmarks in the two average shapes. Permutation tests based on the Procrustes distances were used to estimate the associated *P*-values and to assess the statistical significance of shape differences between groups.

To further evaluate whether more severe brain malformations were associated with more severe skull malformations, we estimated brain and skull deviance as the Procrustes distance between the brain and skull of each mouse and the average shape of the WT untreated group. Then, we calculated the Pearson's coefficients per group and plotted the results using the *ggpubr* package in R (40, 41).

Finally, brain and skull integration was evaluated analyzing the covariation patterns of the brain and skull shape during development by performing a two-block partial least square (PLS) analysis (42). This method performs a singular value decomposition of the covariance matrix between the two blocks of shape data (i.e., the brain and the skull data). Uncorrelated pairs of new axes are derived as linear combinations of the original variables, with the first pair accounting for the largest amount of inter-block covariation, the second pair for the next largest amount and so on. The degree of covariation is measured by the RV coefficient, a multivariate analogue of the squared correlation (43). Statistical significance was tested using permutation tests under the null hypothesis of complete independence between the two blocks of variables. The results were plotted and the Pearson's coefficients for correlation between the two blocks were calculated for each group using the *ggpubr* package in R (40, 41).

Developmental Tests

Testing for neurobehavioral development was carried out daily from PD1 to PD15 as previously described (44). Pups were kept in their home cage and were taken out of the cage one at a time for testing whereas the mother was separated before testing. Once all pups were evaluated, mothers were put back in the cage. The day of appearance of developmental landmarks was recorded and used as the unit of analysis. Neurobehavioral analysis included a battery of tests evaluating pre-weaning sensorial responses that reflect the maturation of the central nervous system. During the experiment, tactile startle response (blast response; a strong blow causes an immediate startle response, a sudden extension of the head and fore and hindlimbs, which are then withdrawn and a crouching position assumed), vibrissae placing (when the mouse is suspended by the tail and lowered so that the vibrissae contact a solid object, the head is raised and the fore limbs are extended to grasp the object), tactile orientation, opening of the eyes, detachment of the pinna and incisor eruption were evaluated. The first day in which the reflexes or landmarks appeared was recorded.

Since sex differences were not significant, we pooled data from male and female mice for analysis.

Developmental tests were analyzed with a logrank test (Mantel-Haenszel approach), where the day of appearance of the landmark or reflex was introduced as an event using GraphPad Prism.

RESULTS

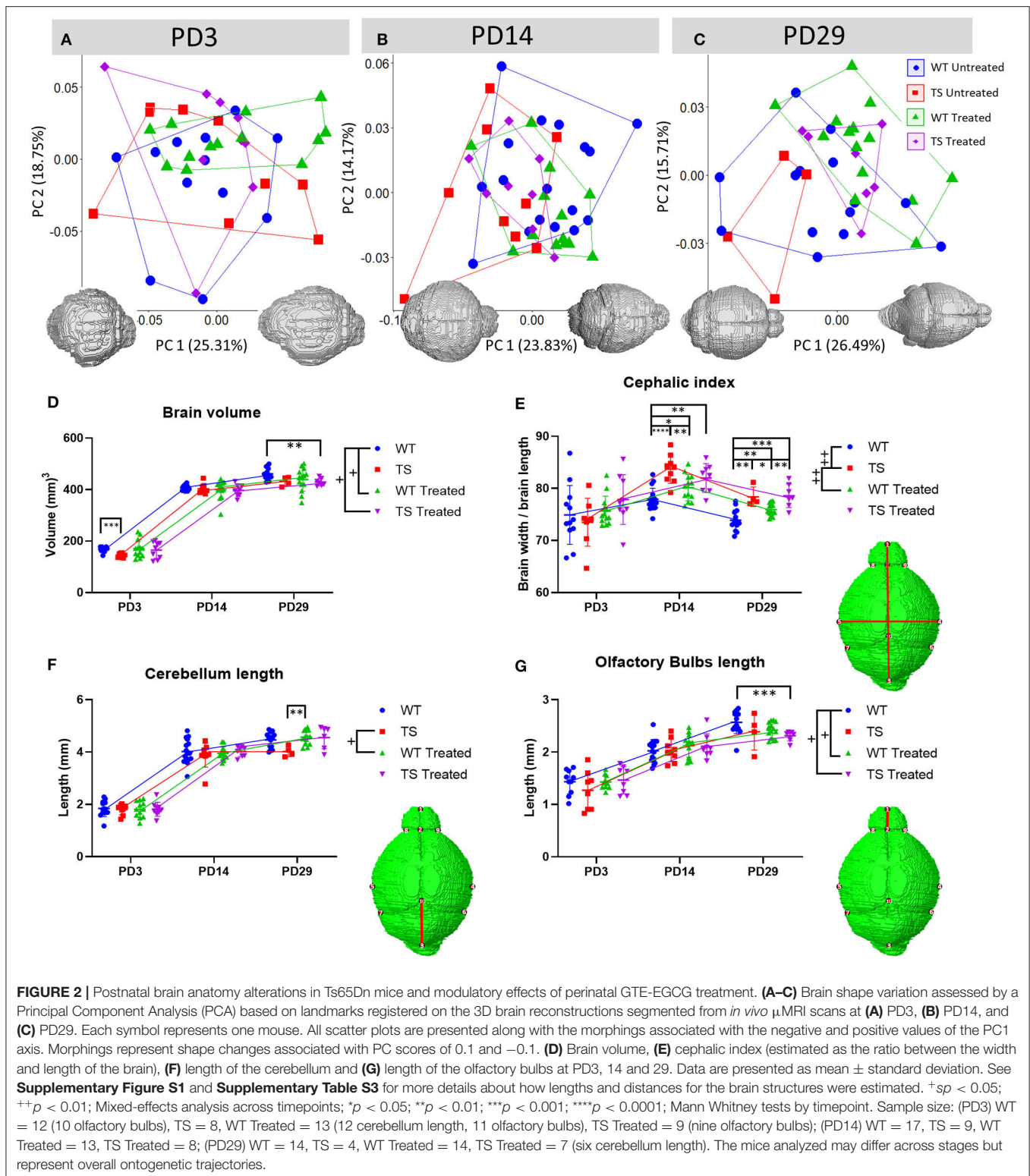
We developed a combination of *in vivo* micro computed tomography (μ CT) and magnetic resonance imaging (μ MRI) to investigate the skeletal and brain development over postnatal

developmental through quantitative morphometric analysis in parallel with a battery of developmental tests to evaluate the neurobehavioral development (**Figure 1**). For our case study, we used the Ts65Dn (TS) Down syndrome mouse model, which is a widely studied DS mouse model (45, 46) that carries a segment with \sim 120 genes homologous to Hsa21 (starting upstream of *Mrpl39* to the telomeric end of *Mmu16*), translocated to a small centromeric part of *Mmu17* (47–49). These mice are trisomic for about two-thirds of the genes orthologous to Hsa21, but also carry genes originating from the *Mmu17* that are not related to DS disease, including about 46 protein-coding genes, 35 nonprotein-coding genes and 35 pseudogenes (50). These genetic alterations do not fully represent Down syndrome's aneuploidy, but recapitulate the main craniofacial, brain and neurodevelopmental alterations associated with DS (20, 21, 51–53). We experimentally evaluated the effect of a green tea extract (GTE-EGCG; Mega Green Tea Extract, Life Extension, USA) on these systems during pre- and postnatal development of mice. The GTE-EGCG solution was prepared freshly using the same batch of the Mega Green Tea Extract in all the experiments, with an estimated composition of 53.6% EGCG, 4.5% epicatechin (EC), 9% epicatechin gallate (ECG) and 12.5% epigallocatechin (EGC).

Postnatal Brain Anatomy Alterations in Ts65Dn Mice and Modulatory Effects of Perinatal GTE-EGCG Treatment

In the first series of experiments, we defined the postnatal trajectories of brain development and the effects of a perinatal 100 mg/kg/day GTE-EGCG treatment. At PD3, the shape analysis based on brain MRI indicated that overall brain morphology, defined by a set of 10 brain landmarks, was similar between WT and TS mice, as the two groups overlapped on the morphospace created by the first two Principal Components, which explained 44.06% of total morphological variance (**Figure 2A**). Permutation tests based on the Procrustes distance between WT and TS mice, confirmed that their brain shape was not significantly different at this early stage (P -value = 0.5553) (**Supplementary Table S6**). The brain shape differences between WT and TS mice developed over time and became significant by PD14 (P -value = 0.0095; **Figure 2B**). In comparison to WT mice, TS mice presented shorter and wider brains at PD14. However, by PD29 interindividual morphological variation increased and shape differences were no longer significant at this last stage (P -value = 0.0519) (**Figure 2C**; **Supplementary Table S6**).

Regarding GTE-EGCG treatment effects, perinatal 100 mg/kg/day GTE-EGCG supplementation negatively affected the control group at the earliest and latest stages, as even though there was some overlap between WT treated and WT untreated mice in the PCA (**Figures 2A,C**), the two groups were significantly different at PD3 (P -value = 0.026) and PD29 (P -value = 0.009). TS treated mice did not show any significant effect of GTE-EGCG treatment at PD3 and PD14, but by PD29, they no longer overlapped with TS untreated mice and presented a significantly different brain shape than TS untreated (P -value



= 0.011) and WT untreated mice (P -value = 0.016) (**Figure 2C**; **Supplementary Table S6**).

Regarding brain volume, a mixed-effects analysis revealed no significant differences in the growth trajectories of TS untreated mice as compared to WT untreated mice (P -value

= 0.0597) (**Figure 2D**). The Mann Whitney tests indicated that TS mice presented smaller brains at PD3 (P -value = 0.0003). However, there was a period of intense growth from PD3 to PD14, in which both WT and TS mice increased their brain size and TS mice caught up in their growth, so that no

genotype-dependent differences were detected at PD14 and PD29 (**Figure 2D**).

GTE-EGCG treatment altered the brain growth trajectory of WT treated mice (P -value 0.0393) (**Figure 2D**). At PD3, perinatal 100 mg/kg/day GTE-EGCG increased the brain size of several WT and TS treated mice, resulting in TS treated mice not being significantly different than WT untreated mice (P -value = 0.917). However, since this rescuing effect was not achieved in all treated mice, TS treated mice were not significantly different than TS untreated mice (P -value = 0.3088). This effect of the treatment was not detected at later stages. In fact, at PD29, TS treated mice presented smaller brains than WT untreated mice (P -value = 0.0023) (**Figure 2D**).

Besides overall brain shape, we also assessed specific head and brain traits that are typically associated with DS. We estimated the ratio of brain width and length (cephalic index), as a proxy of head brachycephaly, a common dysmorphology in DS associated with a shorter and wider head (18, 54) (**Figure 2E**). The comparison of cephalic indexes over development reflects how the brain proportions of length and width change, until reaching adult final size and shape (**Figure 2E**). The mixed-effects analysis indicated that, as compared to WT untreated mice, TS untreated mice presented a significantly different brain growth pattern (P -value = 0.0049). The Mann Whitney tests revealed disproportionately higher cephalic indexes in TS untreated mice than WT untreated mice by PD14 (P -value < 0.0001), and PD29 (P -value = 0.0026) (**Figure 2E**). GTE-EGCG treatment did not have any effect in TS mice, as they maintained high cephalic indexes, but increased the cephalic index in WT treated mice as compared with WT untreated mice at PD14 (P -value = 0.0154) and PD29 (P -value = 0.0058) (**Figure 2E**).

We also assessed alterations in the cerebellum, as this is one of the most affected brain regions in DS (55, 56). The mixed-effects analysis revealed significant differences in the growth trajectories only between WT treated and TS untreated mice (P -value = 0.0271), specifically at PD29 (P -value = 0.0026, Mann Whitney tests) (**Figure 2F**).

No genotype differences were found in the olfactory bulbs, but GTE-EGCG modified the growth trajectory in WT treated mice (P -value = 0.0403). No significant effects were detected in TS treated mice as compared to TS untreated mice, but TS treated mice showed a significantly different growth pattern (P -value = 0.0392) and a reduced length at PD29 (P -value = 0.0008) as compared to WT untreated mice (**Figure 2G**).

Postnatal Ventricular Alterations in Ts65Dn Mice and Modulatory Effects of Perinatal GTE-EGCG Treatment

Next, since ventricular anomalies are usually associated with DS (15–17, 57, 58), we evaluated the volume and shape of the ventricles, as defined by a set of nine landmarks located on the ventricles. At PD3, the shape of the ventricular system was similar between all groups of mice, as indicated by the overlap between groups at the PCA (**Figure 3A**). However, WT treated mice showed a disparate range of morphological variation, with most mice falling outside the range of variation

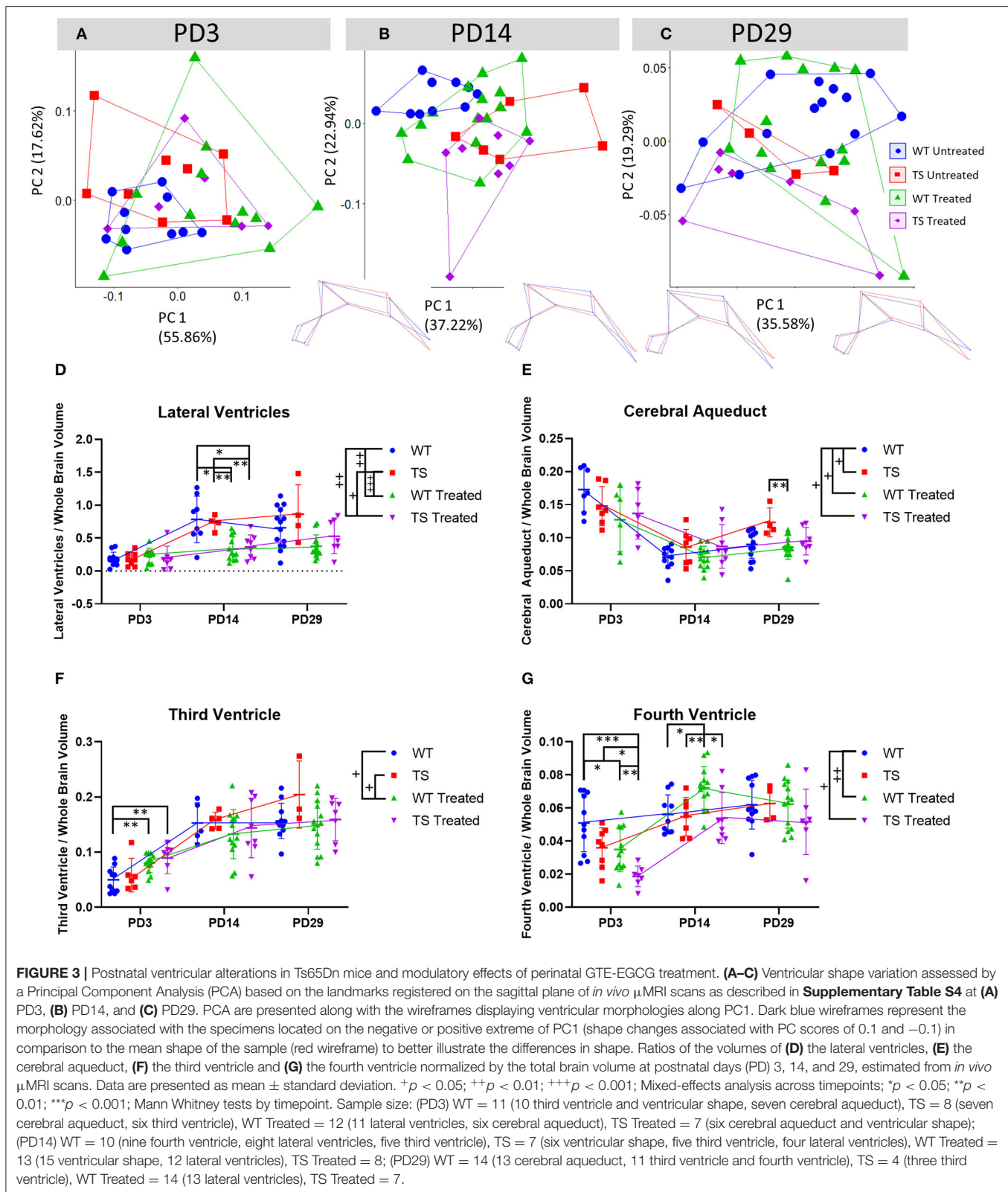
of WT untreated mice (**Figure 3A**). Permutation tests revealed significant differences between untreated and treated WT mice (P -value = 0.017), indicating that 100 mg/kg/day perinatal GTE-EGCG treatment significantly altered WT treated mice at this early stage. At PD14, all groups were significantly different from each other (**Supplementary Table S7**), indicating both genotype and treatment effects (**Figure 3B**). At PD29, however, the morphological differences were reduced, and all groups overlapped except for TS treated mice (**Figure 3C**), which showed a significantly different ventricular shape compared to WT untreated mice (P -value = 0.026) but were not different from TS untreated mice (P -value = 0.387).

Although ventriculomegaly has often been associated with DS (15–17, 57, 58), we did not find larger lateral ventricles over postnatal development in TS untreated mice (**Figure 3D**). Only at PD29, TS untreated mice tended to present larger lateral ventricles, but this difference did not reach significance (P -value = 0.5052). TS untreated mice showed a significantly different growth pattern in the cerebral aqueduct (P -value = 0.0203) (**Figure 3E**), but no significant differences in the volume of the third (**Figure 3F**) and fourth ventricle (**Figure 3G**).

Our analysis suggested that GTE-EGCG had diverse effects on the volume of the ventricles depending on the ventricular structure and developmental time. The mixed-effects analysis revealed that GTE-EGCG treatment significantly modulated the growth trajectories of the lateral ventricles of WT treated (P -value = 0.0015) and TS treated mice (P -value = 0.0260) (**Figure 3D**). Specifically, the Mann Whitney tests showed that GTE-EGCG decreased the volume of the lateral ventricles in both WT treated (P -value = 0.0302) and TS treated (P -value = 0.0031) mice at PD14 (**Figure 3D**). The mixed-effects analysis detected significant differences between WT treated and WT untreated mice in the growth trajectories of the cerebral aqueduct (P -value = 0.0223), third (P -value = 0.0259) and fourth ventricle (P -value = 0.0018) (**Figures 3E–G**). Perinatal 100 mg/kg/day GTE-EGCG significantly increased the volume of the third ventricle in WT treated mice at PD3 (P -value = 0.0071) (**Figure 3F**), reduced the volume of the fourth ventricle in WT treated (P -value = 0.0317) and TS treated (P -value = 0.014) mice at PD3, increased the volume of the fourth ventricle in WT treated mice (P -value = 0.0111) at PD14 and had no effect at PD29 (**Figure 3G**).

Craniofacial Alterations in Ts65Dn Mice Are Not Rescued by Perinatal GTE-EGCG

To evaluate the development of craniofacial morphology over time we used the μ CT images acquired in parallel to the *in vivo* μ MR images with which we assessed brain development. Our quantitative shape analyses indicated that the morphological differences between the skull of WT and TS untreated mice were already significant at PD3 (P -value = 0.0042) and that these shape differences were maintained at PD14 (P -value < 0.0001) and PD29 (P -value = 0.0003) (**Figures 4A–C**). TS untreated mice showed shorter, wider and more globular skulls, as compared to elongated and flat skulls typically associated with WT untreated mice (**Figures 4A–C**).



Craniofacial malformations were not rescued by perinatal 100 mg/kg/day GTE-EGCG treatment at any stage, as TS treated

mice never overlapped with WT untreated mice (**Figures 4A–C**). On the contrary, GTE-EGCG supplementation altered skull

development as WT and TS treated mice were displaced away from their untreated counterparts in the PCA, with TS treated mice occupying the most extreme position in the morphospace in comparison to WT untreated mice at PD29 and showing the most dysmorphic shapes (**Figure 4C**). Results from the permutation tests indicated that these differences were not significant in TS treated mice but confirmed the shape changes in WT treated mice at PD14 and PD29 (**Supplementary Table S8**).

Correlation Between Brain and Skull Dysmorphology Altered by Genotype and Perinatal GTE-EGCG Treatment

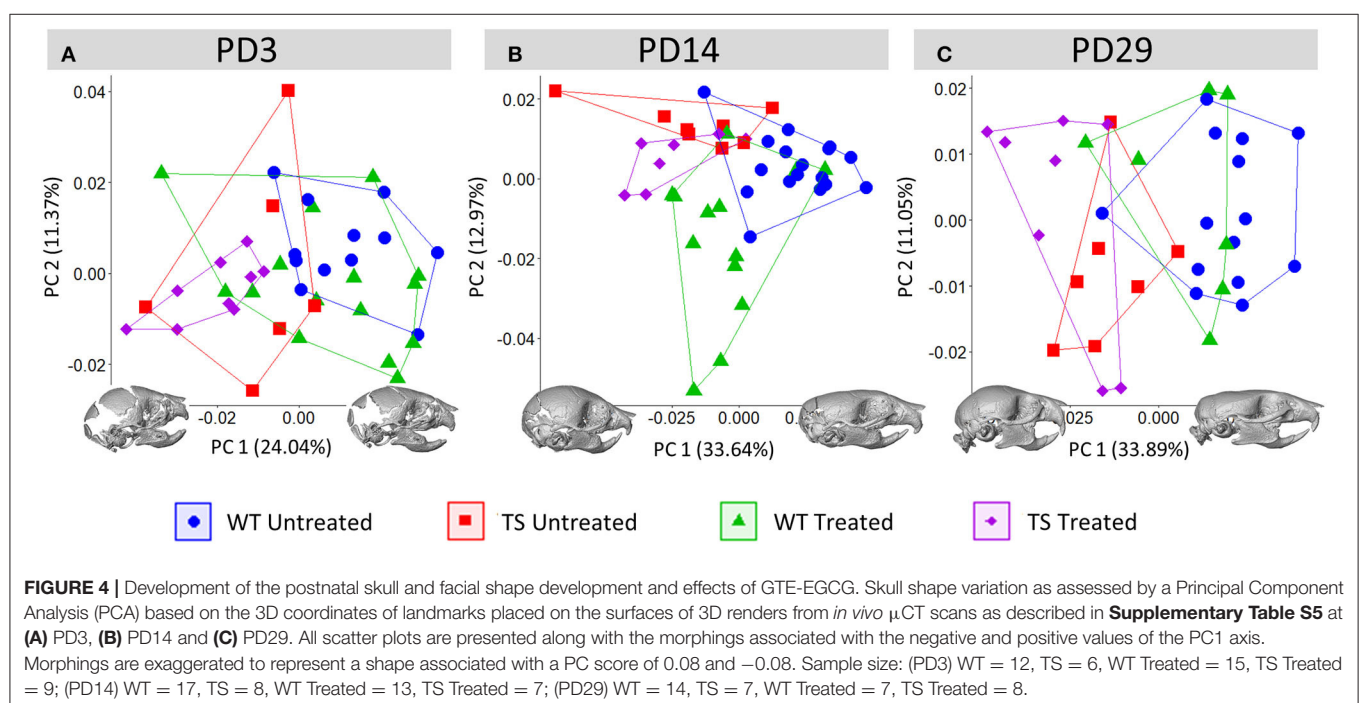
Next, we assessed brain and skull patterns of variation and tested whether deviations from the normal co-variation, induced by genotype and treatment in brain and skull shape were correlated over development. To this aim, for those mice for which both μ CT and μ MR scans were available, we estimated the deviation from WT-like in brain and skull morphology as the Procrustes distance of each mouse to the average shape of the WT untreated group. Then, we performed a correlation between the Procrustes distances based on brain and skull shape. In this analysis, we included mice from the WT untreated group as this correlation assessed intra-group variation and thus served as an indicator of variance of normal development. In the WT treated, TS untreated and TS treated groups, low Procrustes distances indicated WT morphology or slight dysmorphologies, whereas high Procrustes distances indicated strong deviations, that could be related to increased dysmorphologies (**Figures 5A–C**).

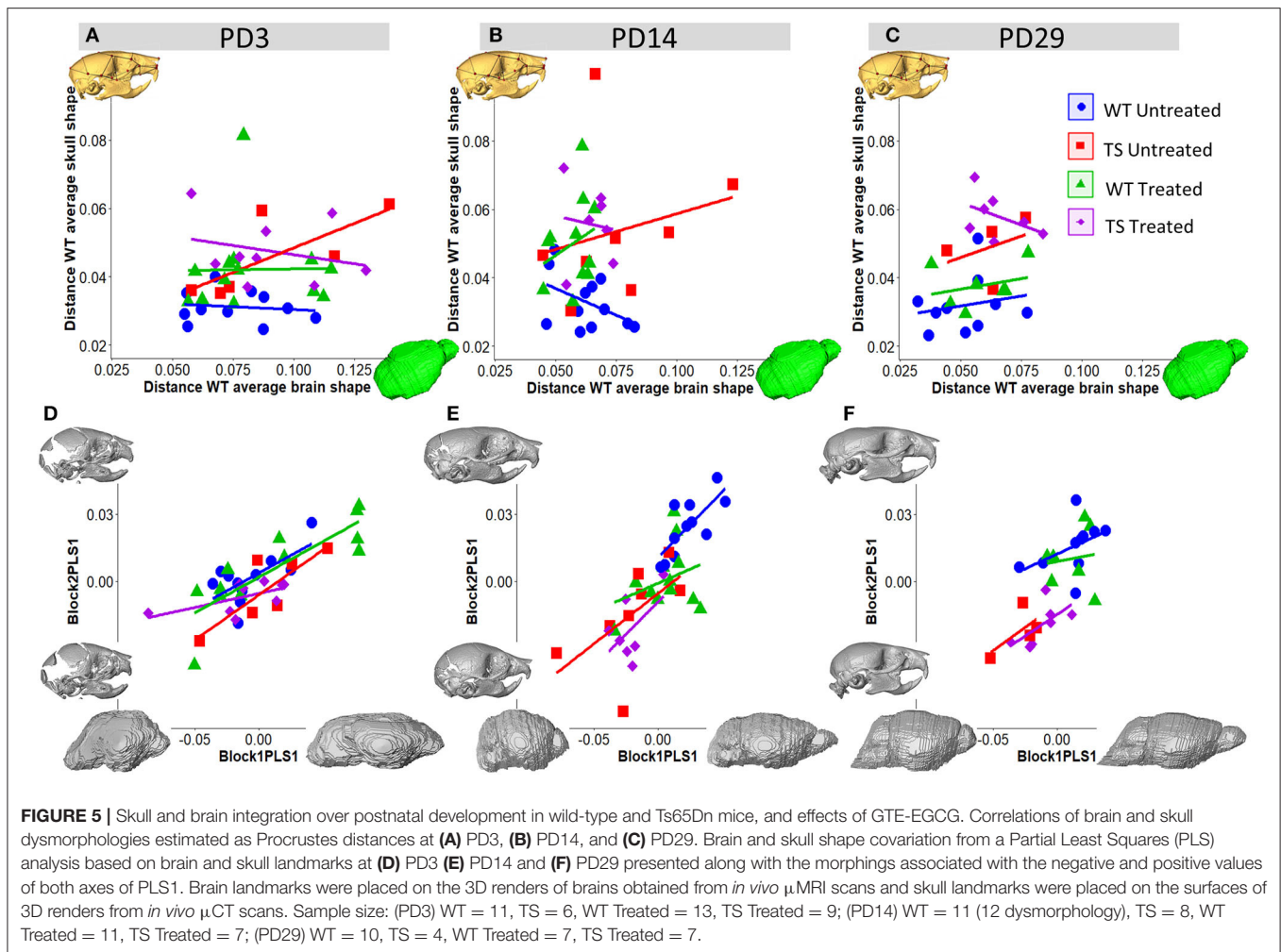
Regarding the normal developmental trajectory, at PD3, WT untreated mice showed high variation in brain shape (large scattering along the x -axis) and low variation in skull

shape (restricted scattering along the y -axis), indicating that in normal conditions early brain development is more variable and probably under a more active process than skull development (**Figure 5A**). By PD14, the variation ranges in WT untreated mice switched from the x -axis to the y -axis, suggesting an adjustment in development at the juvenile stage at which craniofacial development was more variable and predominant after brain development was likely almost completed (**Figure 5B**). By PD29, the ranges of variation were reduced in both axes, suggesting that both brain and skull development were likely almost completed (**Figure 5C**).

The regression between brain and skull Procrustes distances was almost flat and not significant in WT untreated mice at PD3 ($R = -0.13$, P -value = 0.70) and PD29 ($R = 0.19$, P -value = 0.59). On the contrary, the regression in TS untreated mice showed a positive although not significant correlation at PD3 ($R = 0.75$, P -value = 0.08), PD14 ($R = 0.24$, P -value = 0.57), and PD29 ($R = 0.37$, P -value = 0.63), suggesting that TS mice with the most severe brain dysmorphologies also tended to show the most severe skull dysmorphologies (**Figure 5A**). Moreover, at PD14, TS untreated mice presented an abnormally wide range of variation in the brain as compared to WT untreated mice (**Figure 5B**), suggesting that between PD3 and PD14, TS mice may lag behind in development. At PD29, normal ranges of variation were reestablished in TS untreated mice (**Figure 5C**).

GTE-EGCG treated TS mice showed a completely different pattern across development, showing non-significant low and negative correlation between brain and skull deviances from WT average at PD3 ($R = -0.27$, P -value = 0.49), PD14 ($R = -0.12$, P -value = 0.80), and PD29 ($R = -0.45$, P -value = 0.32). Contrary to the rest of groups, TS treated mice with more distinct brain morphologies at PD29 presented less distinct skull morphologies





(Figures 5A–C). Overall, the observed changes may suggest that perinatal 100 mg/kg/day GTE-EGCG affected brain more than skull morphology in treated TS mice.

Early Brain and Skull Integration Are Altered by Genotype and Perinatal GTE-EGCG Treatment

Finally, we further investigated the integrated development of brain and skull over postnatal stages and how the two systems interact by analyzing their covariation patterns, evaluating how morphological changes in one structure were associated with morphological changes in the other structure.

First, we selected the mice for which we had simultaneous brain and skull images and performed a partial least square (PLS) analysis using the skull and brain 3D landmarks registered in the μ CT and μ MR scans. The magnitude of the integration between the skull and brain and their covariation pattern in WT untreated mice defined normal integrated development, whereas deviations from this pattern indicated genetic- and/or treatment-dependent alterations. The PLS across stages indicated that morphological integration changed over time in WT untreated mice. WT mice

presented a significant brain and skull integration, with moderate to high correlation at PD3 (Figure 5D) ($R = 0.67$, P -value = 0.025) and PD14 (Figure 5E) ($R = 0.75$, P -value = 0.007). However, at the latest stage of development, covariation was reduced, and brain and skull were no longer tightly integrated, being the correlation coefficient low and non-significant in WT untreated mice at PD29 (Figure 5F) ($R = 0.44$, P -value = 0.2). The morphings representing the correlated skull and brain shape changes associated with the negative and positive extremes of PLS1 axes indicated that mice presenting with more brachycephalic skulls also presented with wider and shorter brains. This covariation pattern was present at PD3 and maintained until PD29 (Figures 5D–F).

In TS untreated mice, PLS analyses showed that brain and skull were also highly correlated at PD3 ($R = 0.83$, P -value = 0.041), but the magnitude of integration was weaker and not significant by PD14 (Figure 5E) ($R = 0.60$, P -value = 0.12) and PD29 (Figure 5F) ($R = 0.64$, P -value = 0.36). Despite the large genetic imbalance associated with DS, and the brain and skull morphological dysmorphologies induced by these genotype differences in TS mice (Figures 2C, 4C), WT and TS untreated mice presented similar patterns of covariation, as the correlated

shape changes were consistent with those in WT mice and the slopes indicating how the brain and skull covary were parallel (**Figures 5D–F**), even when they gradually separated over development. These results indicated that trisomy did not alter the normal covariation patterns in TS mice (**Figure 5F**).

GTE-EGCG induced alterations in both the magnitude of the integration and the covariation pattern between the brain and skull. At PD3, the strength of the integration in TS treated mice was lower and not significant ($R = 0.61$, P -value = 0.081) as compared to TS untreated mice ($R = 0.83$, P -value = 0.041). Indeed, the pattern of covariation was deviated, as the slope of TS treated mice was not parallel to the other groups and mice with more elongated skulls presented with slightly shorter and wider brains instead (**Figure 5D**). However, this deviation in the brain and skull covariation pattern was reestablished in TS treated mice at PD14 and PD29, as the slopes of TS treated and untreated mice were parallel at these stages (**Figures 5E,F**). In WT untreated mice, the integration was significant at PD14 ($R = 0.75$, P -value = 0.007), however, in WT treated mice the integration was weak and not significant ($R = 0.32$, P -value = 0.32) and GTE-EGCG slightly deviated the slope at PD14 and PD29 (**Figures 5E,F**). Overall, these results showed that GTE-EGCG treatment slightly modulated the morphological integration patterns between the brain and skull.

Delayed Acquisition of Developmental Traits in Ts65Dn Mice With Mixed Effects of Perinatal GTE-EGCG Treatment

To investigate whether treatment effects were limited to anatomical structures or may also modulate functional developmental traits, we performed a battery of developmental tests from PD1 to PD15 to evaluate the appearance of developmental landmarks and neurobehavioral reflexes in TS and WT mice with and without treatment (**Figures 6A–F**).

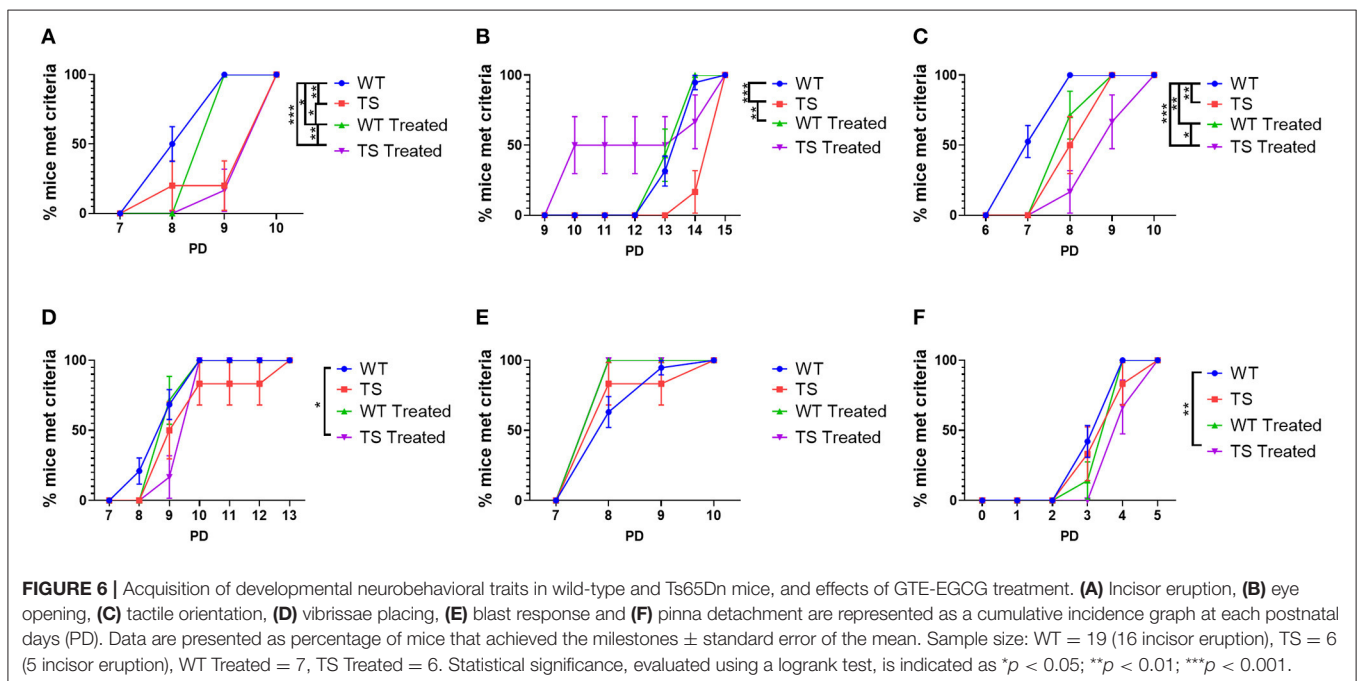
TS untreated mice presented a significant delay in day of appearance of the incisors (P -value = 0.0028, logrank tests) and opening of the eyes (P -value = 0.0007), as well as in the acquisition of tactile orientation reflex (P -value = 0.0015) (**Figures 6A–C**). Treatment with GTE-EGCG accelerated the opening of the eyes that occurred earlier in TS treated mice than in WT untreated mice and the acquisition of the blast response in both WT and TS treated mice, even though these results did not reach significance (**Figures 6B,E**). However, GTE-EGCG significantly delayed incisor eruption (P -value = 0.0235) and tactile orientation (P -value = 0.0036) in WT treated mice as compared to WT untreated mice (**Figures 6A,C**).

DISCUSSION

Complex genetic disorders such as Down syndrome (DS) affect multiple body systems and produce a constellation of integrated congenital abnormalities, including skeletal and brain alterations leading to delayed neurodevelopment (13, 54). Research of such complex disorders has typically focused on cross-sectional studies at a certain stage of development, commonly using qualitative univariate measurements to investigate each system as an isolated and independent entity, without considering their integrated nature (24, 25, 28–31). This approach has impeded to assess how the genetic and developmental interactions between the affected systems modulate phenotypic outcomes and treatment responses.

Getting the Full Picture in DS: Integrated Analysis and Treatment of Brain, Skull and Neurobehavioral Development

We here have developed a novel protocol to characterize the simultaneous development of brain, skeleton, and the acquisition of neurodevelopmental traits in the same mice



from birth to juvenile stages. This approach combines (1) a state-of-the-art imaging pipeline using *in vivo* brain MRI and whole-body μ CT to visualize the brain and skeletal systems over development, with (2) geometric morphometric methods to quantify shape variation across multiple systems and timepoints; and (3) a battery of developmental tests to evaluate neurobehavioral development. We have optimized imaging protocols and data analysis to statistically compare normal and altered morphological and neurodevelopmental traits of newborn up to juvenile mice, identifying how growth trajectories are altered by genetic disorders and whether these trajectories are reestablished simultaneously in different systems by potential treatments. A summary of the main results can be found in **Figure 7**.

Our method revealed simultaneous brain and craniofacial abnormalities along with delayed appearance of some neurodevelopmental traits in Ts65Dn (TS) mice. Consistent with previous studies (16, 54, 59, 60) we detected global brain shape alterations in DS, including brachycephaly and reduced brain size. Those alterations were not found at all developmental stages, but interestingly, the most significant dysmorphologies were found at the later stages, supporting the hypothesis that DS is a developmental disorder (61–63). Ventriculomegaly, a trait often associated with DS, has been detected in DS models with the same triplicated genomic region as the Ts65Dn, such

as Ts2Cje (15–17, 57, 58), but not in adult Ts65Dn mice (64). Our analyses did not detect ventriculomegaly at early postnatal stages, although a trend toward larger ventricles was observed at PD29. These differences between studies could be explained by (1) technical differences, since we used *in vivo* 3D MR images while previous articles used either ultrasound images, histological tissue sections, *ex vivo* MR or 2D MR images, and (2) differences associated with the developmental stage analyzed, as ours is the first study to evaluate the ventricular volume at early postnatal stages in mice. Moreover, we also evaluated ventricular morphology in a detail never assessed before, detecting an anterior-posterior ventricular bending in TS mice at PD14 and PD29 (**Figures 3B,C**) consistent with the brachycephaly and craniofacial dysmorphologies reported in our study and typically found in DS (18–20).

Skull malformations were present in TS mice since the earliest stage of postnatal development studied, PD3, whereas brain dysmorphologies generally appeared later, at PD14 and PD29. This is different from the human condition, where brain and craniofacial malformations are simultaneously present prenatally (59) and are maintained at birth (16, 65). Contrary to the most common idea that the brain induces changes in the skull (2, 3), our results indicate that malformations arose first in the skull, and through correlated changes may have indirectly impacted the brain.

		Genotype			Treatment			
		PD3	PD14	PD29	PD3	PD14	PD29	
Brain	Shape	Altered			Altered in WT	Altered in WT & TS		
	Volume	Reduced size				Increased size WT & TS	Significantly different growth trajectory in WT	
	Cephalic index	Significantly different growth trajectory			Increased cephalic index in WT			
	Cerebellum length	No effect			No effect			
	OB length	No effect			Significantly different growth trajectory in WT			
Ventricles	Shape	Altered			Altered in WT	Altered in WT & TS		
	Lateral ventricles	No effect			Significantly different growth trajectories in WT and TS, reduced size at PD14			
	C. Aqueduct	Significantly different growth trajectory			Significantly different growth trajectory in WT			
	Third ventricle	No effect			Significantly different growth trajectory in WT, increased size at PD3			
	Fourth ventricle	No effect			Significantly different growth trajectory in WT			
					Reduced size WT & TS	Increased size in WT		
Skull	Shape	Shorter, wider, more globular skulls			Altered in WT			
Integration	Dysmorphology	Distinct brain morphologies also tended to distinct skull morphologies			Distinct brain morphologies tended to less distinct skull morphologies in TS			
	Shape	Reduced magnitude but unaltered pattern			Altered magnitude and pattern in TS	Altered magnitude and pattern in WT	Altered pattern in WT	
Dev. traits	Day of appearance	Delayed appearance of incisors, opening of eyes and acquisition of tactile orientation reflex			Delayed appearance of incisors and acquisition of tactile orientation reflex in WT			

FIGURE 7 | Summary of the main findings of the current article. Each system and parameter analyzed is presented in rows. Genotype and treatment effects are presented in columns at each postnatal day (PD), presented in sub columns. OB length, olfactory bulbs length; C. aqueduct, cerebral aqueduct; Dev. Traits, developmental traits.

The combined use of μ MRI and μ CT also enabled us to directly investigate the integration pattern of brain and skeletal systems throughout development. Covariation patterns precisely define interdependence among systems and reflect genetic, developmental or functional interaction (11, 12). Our results demonstrated that brain and skull shape covary at PD3 and PD14 in WT untreated mice, indicating that the integration between brain and skull is strong during early stages of postnatal development, when both systems are still growing to achieve their adult size and shape. Our longitudinal analysis showed that the integration of brain and skull lasted until PD29, where the correlation between the two systems faded and became non-significant. This is in line with a previous study showing low brain and skull integration in adult humans (66) and suggests that integration becomes less relevant when the two systems have almost completed their growth.

In trisomic mice, the magnitude of integration was reduced earlier in development, but we did not observe a disrupted brain and skull covariation pattern, indicating that the integration pattern was preserved despite the genetic dosage imbalance associated with DS. This is in line with previous studies in mouse models for Apert and Crouzon syndromes (67), in which despite severe dysmorphologies, the correlation pattern between brain and skull is not altered, thus confirming the high stability of integration in the vertebrate head (7, 9, 12, 68).

Interestingly, perinatal GTE-EGCG supplementation (100 mg/kg/day) modified both the magnitude and the covariation pattern of brain and skull. In WT treated mice, GTE-EGCG altered the integration patterns at PD14 and PD29, and in TS treated mice, it reduced the magnitude of integration between the brain and skull at PD3, a crucial period for head development in which these organs are integrated and grow together to properly accommodate their development. GTE-EGCG treatment no longer showed an effect on the integration patterns at PD14 and PD29, even though the altered correlation between brain and skull dysmorphologies was maintained, suggesting that altering early integration patterns may have downstream effects over development. In summary, our results suggest that the modulatory effects of GTE-EGCG on brain and skull may not be just the direct effect of altering associated signaling pathways in the brain and skeletal cranial tissues, but also to indirect effects induced by alterations in the normal magnitude and pattern of integration, which may explain further secondary dysmorphogenesis in DS. This highlights the important role of early integration of the brain and skull and suggests that altering this integration may lead to further dysregulating effects.

In this study, we assessed the overall effect of GTE-EGCG on development, and confirmed that it can significantly alter brain, skull and neurobehavioral development, as well as the integrated development of the head. Future experiments specifically designed to assess the mechanisms of action should now further elucidate the mechanisms underlying these effects. Reduction of DYRK1A kinase activity is one of the reigning hypotheses behind the mechanism of action of EGCG (24, 69). However, as there are other compounds present in the GTE formulation administered to the mice, more research is required to investigate whether other mechanisms not related

to modulation of DYRK1A could be also contributing to the observed effects.

Our results showed that treatment response was variable across treated mice. To ensure that the variation observed in this experiment was representative of biological variation and the natural response to GTE-EGCG treatment, we minimized confounding experimental factors as much as possible. All F1 littermates were bred from the same colony of progenitors, acquired on the same date, and all mice were treated with the same batch of GTE-EGCG. Although it was not possible to ensure that all pups consumed the exact amount of water because we did not administer the treatment via oral gavage to reduce the stress of the pups, we monitored the amount of water consumed by each cage and estimated the average intake per pup, assuming that all pups were drinking similar amounts of water and taking the same dose of treatment. Other factors such as litter effects could also potentially induce some variability in our sample. Since these factors are inevitable in experimental designs and biological samples are inherently variable, our longitudinal approach largely overcomes statistical issues with inter-litter and inter-individual variability as compared to cross-sectional studies, allowing to statistically analyze the growth trajectories of groups of individuals across development.

Future Perspectives: Further Integrated Research of Developmental Disorders and Modulation

Studies focusing on just one single system and timepoint ignore the effects on other systems at different stages of development. Our results highlight the added value of a longitudinal research approach evaluating the integrated development of multiple systems and their interactions from early to late postnatal stages, as well as the simultaneous modulatory effects of a pharmacological intervention, to reveal the complex etiology of congenital malformations.

In the context of DS, comparing the results from different cross-sectional studies poses a challenge given the high subject-to-subject and across generation variability of the TS65Dn mouse model (34). The advantage of a longitudinal approach is that the same mice are evaluated throughout development, assessing multiple systems simultaneously and increasing the statistical power. Our multimodal approach to investigate the integrated development of brain and skeletal systems in the Ts65Dn model of DS can be further expanded to structural and functional evaluation of other systems, such as lungs and heart, which are also altered in DS and present common signaling pathways (70), but also to other multisystemic disorders such as holoprosencephaly, micro- and macrocephaly, Apert, Pfeiffer and Crouzon craniosynostosis syndromes, investigating each syndrome not only as a compendium of diseases and alterations, but as an integrated system with interrelated development.

DATA AVAILABILITY STATEMENT

The raw data supporting the conclusions of this article will be made available by the authors, without undue reservation.

ETHICS STATEMENT

The animal study was reviewed and approved by Animal Ethics Committee of KU Leuven.

AUTHOR CONTRIBUTIONS

NM-A and GV: conceptualization, supervision, and funding acquisition. WG, NM-A, and GV: methodology. SL, RG, and FM: formal analysis. SL, JA, and JW: investigation. NM-A, GV, MD, UH, and JS: resources. SL, NM-A, and GV: data curation, writing—original draft preparation, and visualization. SL, NM-A, MD, and GV: writing—review and editing. GV: project administration. All authors have read and agreed to the published version of the manuscript.

FUNDING

This research was funded by research grants from CRG Awards BrainFace, the Jerome Lejeune Foundation

(3M180477), KU Leuven BOF (C24/17/061 and STG/15/024), Grup de Recerca Consolidat en Antropologia Biològica, GREAB (2017 SGR 1630) and a 2-year doctoral fellowship from the Marie-Marguerite Delacroix Foundation to SL.

ACKNOWLEDGMENTS

Imaging data was acquired in the Molecular Small Animal Imaging Center (MoSAIC), a core facility of Department of Imaging and Pathology, Group Biomedical Sciences, KU Leuven. The authors acknowledge the Laboratory Animal Centre core facility of KU Leuven for support with animal care.

SUPPLEMENTARY MATERIAL

The Supplementary Material for this article can be found online at: <https://www.frontiersin.org/articles/10.3389/fmed.2022.815739/full#supplementary-material>

REFERENCES

- Marcucio RS, Young NM, Hu D, Hallgrímsson B. Mechanisms that underlie co-variation of the brain and face. *Genesis*. (2011) 49:177–89. doi: 10.1002/dvg.20710
- Richtsmeier JT, Flaherty K. Hand in glove: brain and skull in development and dysmorphogenesis. *Acta Neuropathol.* (2013) 125:469–89. doi: 10.1007/s00401-013-1104-y
- Gondré-Lewis MC, Gboluaje T, Reid SN, Lin S, Wang P, Green W, et al. The human brain and face: mechanisms of cranial, neurological and facial development revealed through malformations of holoprosencephaly, cyclopia and aberrations in chromosome 18. *J Anat.* (2015) 227:255–67. doi: 10.1111/joa.12343
- Klingenberg CP. Studying morphological integration and modularity at multiple levels: concepts and analysis. *Philos Transact R Soc B Biol Sci.* (2014) 369:20130249. doi: 10.1098/rstb.2013.0249
- Mitteroecker P, Bookstein F. The conceptual and statistical relationship between modularity and morphological integration. *Syst Biol.* (2007) 56:818–36. doi: 10.1080/10635150701648029
- Hallgrímsson B, Lieberman DE, Young NM, Parsons T, Wat S. Evolution of covariance in the mammalian skull. *Tinkering.* (2006) 284:164–90. doi: 10.1002/9780470319390.ch12
- Anjali G. Cranial modularity shifts during mammalian evolution. *Am Nat.* (2006) 168:270–80. doi: 10.1086/505758
- Hallgrímsson B, Brown JY, Ford-Hutchinson AF, Sheets HD, Zelditch ML, Jirik FR. The brachymorph mouse and the developmental-genetic basis for canalization and morphological integration. *Evol Dev.* (2006) 8:61–73. doi: 10.1111/j.1525-142X.2006.05075.x
- Hallgrímsson B, Lieberman DE, Liu W, Ford-Hutchinson AF, Jirik FR. Epigenetic interactions and the structure of phenotypic variation in the cranium. *Evol Dev.* (2007) 9:76–91. doi: 10.1111/j.1525-142X.2006.00139.x
- Richtsmeier J, DeLeon V. Morphological integration of the skull in craniofacial anomalies. *Orthodont Craniofac Res.* (2009) 12:149–58. doi: 10.1111/j.1601-6343.2009.01448.x
- Klingenberg CP. Evolution and development of shape: integrating quantitative approaches. *Nat Rev Genet.* (2010) 11:623–35. doi: 10.1038/nrg2829
- Martínez-Abadías N, Heuzé Y, Wang Y, Jabs EW, Aldridge K, Richtsmeier JT. FGF/FGFR signaling coordinates skull development by modulating magnitude of morphological integration: evidence from Apert Syndrome mouse models. *PLoS ONE.* (2011) 6:e26425. doi: 10.1371/journal.pone.0026425
- Wiseman FK, Alford KA, Tybulewicz VLJ, Fisher EMC. Down syndrome—recent progress and future prospects. *Human Mol Genet.* (2009) 18:R75–83. doi: 10.1093/hmg/ddp010
- Lott IT, Dierssen M. Cognitive deficits and associated neurological complications in individuals with Down's syndrome. *Lancet Neurol.* (2010) 9:623–33. doi: 10.1016/S1474-4422(10)70112-5
- Pearlson GD, Breiter SN, Aylward EH, Warren AC, Grygorciewicz M, Frangou S, et al. MRI brain changes in subjects with Down syndrome with and without dementia. *Dev Med Child Neurol.* (1998) 40:326–34. doi: 10.1111/j.1469-8749.1998.tb15384.x
- Patkee PA, Baburamani AA, Kyriakopoulou V, Davidson A, Avini E, Dimitrova R, et al. Early alterations in cortical and cerebellar regional brain growth in Down Syndrome: an *in vivo* fetal and neonatal MRI assessment. *NeuroImage Clin.* (2020) 25:102139. doi: 10.1016/j.nicl.2019.102139
- Movsas TZ, Spitzer AR, Gewolb IH. Ventriculomegaly in very-low-birthweight infants with Down syndrome. *Dev Med Child Neurol.* (2016) 58:1167–71. doi: 10.1111/dmcn.13191
- Richtsmeier JT, Baxter LL, Reeves RH. Parallels of craniofacial maldevelopment in down syndrome and Ts65Dn mice. *Dev Dyn.* (2000) 217:137–45. doi: 10.1002/(SICI)1097-0177(200002)217:2<137::AID-DVDY1>3.0.CO;2-N
- Suri S, Tompson BD, Cornfoot L. Cranial base, maxillary and mandibular morphology in Down syndrome. *Angle Orthodont.* (2010) 80:861–9. doi: 10.2319/111709-650.1
- Starbuck JM, Llambrich S, González R, Albaigès J, Sarlé A, Wouters J, et al. Green tea extracts containing epigallocatechin-3-gallate modulate facial development in Down syndrome. *Sci Rep.* (2021) 11:4715. doi: 10.1038/s41598-021-83757-1
- Blazek JD, Abeysekera I, Li J, Roper RJ. Rescue of the abnormal skeletal phenotype in Ts65Dn Down syndrome mice using genetic and therapeutic modulation of trisomic Dyrk1a. *Hum Mol Genet.* (2015) 24:5687–96. doi: 10.1093/hmg/ddv284
- de la Torre R, de Sola S, Hernandez G, Farré M, Pujol J, Rodriguez J, et al. Safety and efficacy of cognitive training plus epigallocatechin-3-gallate in young adults with Down's syndrome (TESDAD): a double-blind, randomised, placebo-controlled, phase 2 trial. *Lancet Neurol.* (2016) 15:801–10. doi: 10.1016/S1474-4422(16)30034-5

23. Abeysekera I, Thomas J, Georgiadis TM, Berman AG, Hammond MA, Dria KJ, et al. Differential effects of Epigallocatechin-3-gallate containing supplements on correcting skeletal defects in a Down syndrome mouse model. *Mol Nutr Food Res.* (2016) 60:717–26. doi: 10.1002/mnfr.201500781
24. De la Torre R, De Sola S, Pons M, Duchon A, de Lagran MM, Farré M, et al. Epigallocatechin-3-gallate, a DYRK1A inhibitor, rescues cognitive deficits in Down syndrome mouse models and in humans. *Mol Nutr Food Res.* (2014) 58:278–88. doi: 10.1002/mnfr.201300325
25. Guedj F, Sébrié C, Rivals I, Ledru A, Paly E, Bizot JC, et al. Green tea polyphenols rescue of brain defects induced by overexpression of DYRK1A. *PLoS ONE.* (2009) 4:e4606. doi: 10.1371/journal.pone.0004606
26. Goodlett CR, Stringer M, LaCombe J, Patel R, Wallace JM, Roper RJ. Evaluation of the therapeutic potential of Epigallocatechin-3-gallate (EGCG) via oral gavage in young adult Down syndrome mice. *Sci Rep.* (2020) 10:10426. doi: 10.1038/s41598-020-61733-z
27. Gu Y, Moroy G, Paul JL, Rebillat AS, Dierssen M, de la Torre R, et al. Molecular rescue of Dyrk1A overexpression alterations in mice with Fontup(®) dietary supplement: role of green tea catechins. *Int J Mol Sci.* (2020) 1404:1–19. doi: 10.3390/ijms21041404
28. McElyea SD, Starbuck JM, Tumbleson-Brink DM, Harrington E, Blazek JD, Ghoneima A, et al. Influence of prenatal EGCG treatment and Dyrk1a dosage reduction on craniofacial features associated with Down syndrome. *Hum Mol Genet.* (2016) 25:4856–69. doi: 10.1093/hmg/ddw309
29. Stringer M, Abeysekera I, Dria KJ, Roper RJ, Goodlett CR. Low dose EGCG treatment beginning in adolescence does not improve cognitive impairment in a Down syndrome mouse model. *Pharmacol Biochem Behav.* (2015) 138:70–9. doi: 10.1016/j.pbb.2015.09.002
30. Souchet B, Duchon A, Gu Y, Dairou J, Chevalier C, Daubigney F, et al. Prenatal treatment with EGCG enriched green tea extract rescues GAD67 related developmental and cognitive defects in Down syndrome mouse models. *Sci Rep.* (2019) 9:3914. doi: 10.1038/s41598-019-40328-9
31. Stagni F, Giacomini A, Emili M, Guidi S, Ciani E, Bartesaghi R. Epigallocatechin gallate: a useful therapy for cognitive disability in Down syndrome? *Neurogenesis.* (2017) 4:e1270383. doi: 10.1080/23262133.2016.1270383
32. Chu KO, Wang CC, Chu CY, Choy KW, Pang CP, Rogers MS. Uptake and distribution of catechins in fetal organs following *in utero* exposure in rats. *Hum Reprod.* (2006) 22:280–7. doi: 10.1093/humrep/del353
33. Chu KO, Wang CC, Chu CY, Chan KP, Rogers MS, Choy KW, et al. Pharmacokinetic studies of green tea catechins in maternal plasma and fetuses in rats. *J Pharm Sci.* (2006) 95:1372–81. doi: 10.1002/jps.20594
34. Shaw PR, Klein JA, Aziz NM, Haydar TF. Longitudinal neuroanatomical and behavioral analyses show phenotypic drift and variability in the Ts65Dn mouse model of Down syndrome. *Dis Models Mech.* (2020) 13:1–16. doi: 10.1242/dmm.046243
35. Motulsky HJ, Brown RE. Detecting outliers when fitting data with nonlinear regression - a new method based on robust nonlinear regression and the false discovery rate. *BMC Bioinform.* (2006) 7:123. doi: 10.1186/1471-2105-7-123
36. Dryden IL, Mardia KV. *Statistical Shape Analysis*. Chichester: Wiley (1998).
37. James Rohlf F, Marcus LF. A revolution morphometrics. *Trends Ecol Evol.* (1993) 8:129–32. doi: 10.1016/0169-5347(93)90024-J
38. Klingenberg CP. MorphoJ: an integrated software package for geometric morphometrics. *Mol Ecol Resour.* (2011) 11:353–7. doi: 10.1111/j.1755-0998.2010.02924.x
39. Hallgrímsson B, Percival CJ, Green R, Young NM, Mio W, Marcucio R. Morphometrics, 3D imaging, and craniofacial development. *Curr Top Dev Biol.* (2015) 115:561–97. doi: 10.1016/bs.ctdb.2015.09.003
40. R Core Team. *R: A Language and Environment for Statistical Computing*. 3.6.2 ed. Vienna: R Foundation for Statistical Computing (2019).
41. Kassambara A. *ggpubr: 'ggplot2' Based Publication Ready Plots: R Package Version 0.4.0*. (2020). Available online at: <https://CRAN.R-project.org/package=ggpubr>
42. Rohlf FJ, Corti M. Use of two-block partial least-squares to study covariation in shape. *Syst Biol.* (2000) 49:740–53. doi: 10.1080/106351500750049806
43. Klingenberg CP. Morphometric integration and modularity in configurations of landmarks: tools for evaluating a priori hypotheses. *Evol Dev.* (2009) 11:405–21. doi: 10.1111/j.1525-142X.2009.00347.x
44. Dierssen M, Fotaki V, Martínez de Lagrán M, Gratacós M, Arbonés M, Fillat C, et al. Neurobehavioral development of two mouse lines commonly used in transgenic studies. *Pharmacol Biochem Behav.* (2002) 73:19–25. doi: 10.1016/S0091-3057(02)00792-X
45. Reeves RH, Irving NG, Moran TH, Wohn A, Kitt C, Sisodia SS, et al. A mouse model for Down syndrome exhibits learning and behaviour deficits. *Nat Genet.* (1995) 11:177–84. doi: 10.1038/ng1095-177
46. Davisson MT, Schmidt C, Akeson EC. Segmental trisomy of murine chromosome 16: a new model system for studying Down syndrome. *Progr Clin Biol Res.* (1990) 360:263–80.
47. Herault Y, Delabar JM, Fisher EMC, Tybulewicz VLJ, Yu E, Brault V. Rodent models in Down syndrome research: impact and future opportunities. *Dis Model Mech.* (2017) 10:1165–86. doi: 10.1242/dmm.029728
48. Duchon A, Raveau M, Chevalier C, Nalesso V, Sharp AJ, Herault Y. Identification of the translocation breakpoints in the Ts65Dn and Ts1Cje mouse lines: relevance for modeling Down syndrome. *Mamm Genome.* (2011) 22:674–84. doi: 10.1007/s00335-011-9356-0
49. Reinholdt LG, Ding Y, Gilbert GJ, Czechanski A, Solzak JP, Roper RJ, et al. Molecular characterization of the translocation breakpoints in the Down syndrome mouse model Ts65Dn. *Mamm Genome.* (2011) 22:685–91. doi: 10.1007/s00335-011-9357-z
50. MuñozMoreno MdM, Brault V, Birling M-C, Pavlovic G, Herault Y. Modeling down syndrome in animals from the early stage to the 4.0 models and next. In: Dierssen M, editor. *Progress in Brain Research*. Amsterdam: Elsevier (2020). p. 91–143.
51. Aziz NM, Guedj F, Pennings JLA, Olmos-Serrano JL, Siegel A, Haydar TF, et al. Lifespan analysis of brain development, gene expression and behavioral phenotypes in the Ts1Cje, Ts65Dn and Dp(16)1/Yey mouse models of Down syndrome. *Dis Models Mech.* (2018) 11:dmm031013. doi: 10.1242/dmm.031013
52. Blazek JD, Gaddy A, Meyer R, Roper RJ, Li J. Disruption of bone development and homeostasis by trisomy in Ts65Dn Down syndrome mice. *Bone.* (2011) 48:275–80. doi: 10.1016/j.bone.2010.09.028
53. Gupta M, Dhanasekaran AR, Gardiner KJ. Mouse models of Down syndrome: gene content and consequences. *Mammalian Genome.* (2016) 27:538–55. doi: 10.1007/s00335-016-9661-8
54. Rodrigues M, Nunes J, Figueiredo S, Martins de Campos A, Geraldo AF. Neuroimaging assessment in Down syndrome: a pictorial review. *Insights Imaging.* (2019) 10:52. doi: 10.1186/s13244-019-0729-3
55. Shapiro BL. Developmental instability of the cerebellum and its relevance to Down syndrome. In: Lubec G, editor. *Protein Expression in Down Syndrome Brain*. Vienna: Springer Vienna (2001). p. 11–34.
56. Baxter LL, Moran TH, Richtsmeier JT, Troncoso J, Reeves RH. Discovery and genetic localization of Down syndrome cerebellar phenotypes using the Ts65Dn mouse. *Hum Mol Genet.* (2000) 9:195–202. doi: 10.1093/hmg/9.2.195
57. Raveau M, Nakahari T, Asada S, Ishihara K, Amano K, Shimohata A, et al. Brain ventriculomegaly in Down syndrome mice is caused by Pcp4 dose-dependent cilia dysfunction. *Hum Mol Genet.* (2017) 26:923–31. doi: 10.1093/hmg/ddx007
58. Ishihara K, Amano K, Takaki E, Shimohata A, Sago HJ, Epstein C, et al. Enlarged brain ventricles and impaired neurogenesis in the Ts1Cje and Ts2Cje mouse models of Down Syndrome. *Cerebr Cortex.* (2009) 20:1131–43. doi: 10.1093/cercor/bhp176
59. Guihard-Costa A-M, Khung S, Delbecq K, Ménez F, Delezoide A-L. Biometry of face and brain in fetuses with trisomy 21. *Pediatr Res.* (2006) 59:33–8. doi: 10.1203/01.pdr.0000190580.88391.9a
60. Aldridge K, Reeves RH, Olson LE, Richtsmeier JT. Differential effects of trisomy on brain shape and volume in related aneuploid mouse models. *Am J Med Genet Part A.* (2007) 143A:1060–70. doi: 10.1002/ajmg.a.31721
61. Holtzman DM, Santucci D, Kilbridge J, Chua-Couzens J, Fontana DJ, Daniels SE, et al. Developmental abnormalities and age-related neurodegeneration in a mouse model of Down syndrome. *Proc Natl Acad Sci USA.* (1996) 93:13333–8. doi: 10.1073/pnas.93.23.13333
62. Lockrow JP, Fortress AM, Granholm A-CE. Age-related neurodegeneration and memory loss in Down Syndrome. *Curr Gerontol Geriatr Res.* (2012) 2012:463909. doi: 10.1155/2012/463909

63. Perluigi M, Di Domenico F, Butterfield DA. Unraveling the complexity of neurodegeneration in brains of subjects with Down syndrome: insights from proteomics. *Proteom Clin Appl*. (2014) 8:73–85. doi: 10.1002/prca.201300066
64. Duchon A, del Mar Muniz Moreno M, Martin Lorenzo S, Silva de Souza MP, Chevalier C, Nalesso V, et al. Multi-influential genetic interactions alter behaviour and cognition through six main biological cascades in Down syndrome mouse models. *Hum Mol Genet*. (2021) 30:771–88. doi: 10.1093/hmg/ddab012
65. Fischer-Brandies H, Schmid RG, Fischer-Brandies E. Craniofacial development in patients with Down's syndrome from birth to 14 years of age. *Eur J Orthodont*. (1986) 8:35–42. doi: 10.1093/ejo/8.1.35
66. Bruner E, Amano H, de la Cuétara JM, Ogihara N. The brain and the braincase: a spatial analysis on the midsagittal profile in adult humans. *J Anat*. (2015) 227:268–76. doi: 10.1111/joa.12355
67. Motch Perrine SM, Stecko T, Neuberger T, Jabs EW, Ryan TM, Richtsmeier JT. Integration of brain and skull in prenatal mouse models of Apert and Crouzon Syndromes. *Front Hum Neurosci*. (2017) 11:369. doi: 10.3389/fnhum.2017.00369
68. Porto A, de Oliveira FB, Shirai LT, De Conto V, Marroig G. The evolution of modularity in the mammalian skull I: morphological integration patterns and magnitudes. *Evol Biol*. (2009) 36:118–35. doi: 10.1007/s11692-008-9038-3
69. Duchon A, Herault Y. DYRK1A, a dosage-sensitive gene involved in neurodevelopmental disorders, is a target for drug development in Down Syndrome. *Front Behav Neurosci*. (2016) 10:104. doi: 10.3389/fnbeh.2016.00104
70. Arron JR, Winslow MM, Polleri A, Chang C-P, Wu H, Gao X, et al. NFAT dysregulation by increased dosage of DSCR1 and DYRK1A on chromosome 21. *Nature*. (2006) 441:595–600. doi: 10.1038/nature04678

Conflict of Interest: The authors declare that the research was conducted in the absence of any commercial or financial relationships that could be construed as a potential conflict of interest.

Publisher's Note: All claims expressed in this article are solely those of the authors and do not necessarily represent those of their affiliated organizations, or those of the publisher, the editors and the reviewers. Any product that may be evaluated in this article, or claim that may be made by its manufacturer, is not guaranteed or endorsed by the publisher.

Copyright © 2022 Llambrich, González, Albaigès, Wouters, Marain, Himmelreich, Sharpe, Dierssen, Gsell, Martínez-Abadías and Vande Velde. This is an open-access article distributed under the terms of the Creative Commons Attribution License (CC BY). The use, distribution or reproduction in other forums is permitted, provided the original author(s) and the copyright owner(s) are credited and that the original publication in this journal is cited, in accordance with accepted academic practice. No use, distribution or reproduction is permitted which does not comply with these terms.



Recent Technical Advances in Accelerating the Clinical Translation of Small Animal Brain Imaging: Hybrid Imaging, Deep Learning, and Transcriptomics

Wuwei Ren^{1,2*}, Bin Ji³, Yihui Guan⁴, Lei Cao⁵ and Ruiqing Ni^{6,7*}

OPEN ACCESS

Edited by:

Adriana Tavares,
University of Edinburgh,
United Kingdom

Reviewed by:

Sridhar Goud,
National Institutes of Health (NIH),
United States
Sonia Waiczies,
Max Delbrück Center for Molecular
Medicine in the Helmholtz
Association, Germany
Kuangyu Shi,
University of Bern, Switzerland

*Correspondence:

Wuwei Ren
renww@shanghaitech.edu.cn
Ruiqing Ni
ruiqing.ni@uzh.ch

Specialty section:

This article was submitted to
Translational Medicine,
a section of the journal
Frontiers in Medicine

Received: 07 September 2021

Accepted: 16 February 2022

Published: 24 March 2022

Citation:

Ren W, Ji B, Guan Y, Cao L and
Ni R (2022) Recent Technical
Advances in Accelerating the Clinical
Translation of Small Animal Brain
Imaging: Hybrid Imaging, Deep
Learning, and Transcriptomics.
Front. Med. 9:771982.
doi: 10.3389/fmed.2022.771982

¹ School of Information Science and Technology, ShanghaiTech University, Shanghai, China, ² Shanghai Engineering Research Center of Energy Efficient and Custom AI IC, Shanghai, China, ³ Department of Radiopharmacy and Molecular Imaging, School of Pharmacy, Fudan University, Shanghai, China, ⁴ PET Center, Huashan Hospital, Fudan University, Shanghai, China, ⁵ Shanghai Changsheng Tech, Ltd., Shanghai, China, ⁶ Institute for Regenerative Medicine, University of Zurich, Zurich, Switzerland, ⁷ Institute for Biomedical Engineering, ETH Zürich and University of Zurich, Zurich, Switzerland

Small animal models play a fundamental role in brain research by deepening the understanding of the physiological functions and mechanisms underlying brain disorders and are thus essential in the development of therapeutic and diagnostic imaging tracers targeting the central nervous system. Advances in structural, functional, and molecular imaging using MRI, PET, fluorescence imaging, and optoacoustic imaging have enabled the interrogation of the rodent brain across a large temporal and spatial resolution scale in a non-invasively manner. However, there are still several major gaps in translating from preclinical brain imaging to the clinical setting. The hindering factors include the following: (1) intrinsic differences between biological species regarding brain size, cell type, protein expression level, and metabolism level and (2) imaging technical barriers regarding the interpretation of image contrast and limited spatiotemporal resolution. To mitigate these factors, single-cell transcriptomics and measures to identify the cellular source of PET tracers have been developed. Meanwhile, hybrid imaging techniques that provide highly complementary anatomical and molecular information are emerging. Furthermore, deep learning-based image analysis has been developed to enhance the quantification and optimization of the imaging protocol. In this mini-review, we summarize the recent developments in small animal neuroimaging toward improved translational power, with a focus on technical improvement including hybrid imaging, data processing, transcriptomics, awake animal imaging, and on-chip pharmacokinetics. We also discuss outstanding challenges in standardization and considerations toward increasing translational power and propose future outlooks.

Keywords: deep learning, magnetic resonance imaging, multimodal imaging, neuroimaging, positron emission tomography, optoacoustic imaging, image registration, fluorescence imaging

INTRODUCTION

Clinically deployed imaging modalities, including MRI, PET, and single-photon emission CT (SPECT), have vastly facilitated the understanding of human brain function (1–3) and the development of disease biomarkers for brain disorders such as brain tumors, Alzheimer's disease, ischemic stroke, and multiple sclerosis toward personalized medicine (4). MRI sequences for brain imaging, such as diffusion-weighted imaging (DWI), diffusion tensor imaging (DTI) for white matter integrity (5), structural T₁ and T₂ for regional brain atrophy, arterial spin labeling (ASL) for cerebral perfusion, and susceptibility-weighted imaging for microbleed assessment, are routinely performed both in animal models in the laboratory and in human patients in the clinical setting (6). The development of 7 T human MRI allows imaging of the living human brain at the mesoscopic level with a high spatial and temporal signal-to-noise ratio (SNR) (7, 8). There are currently seven Food and Drug Administration approved commercially available MR contrast agents with indications for central nervous system lesions (9). This gadolinium (III)-based contrast agents are widely used in the clinical setting. In addition, targeted agents, activatable agents, high-relaxivity agents, and gadolinium-free MR contrast agents are being developed (9). Gadolinium(III)-based contrast agents have been successful as they provide essential diagnostic information that often cannot be obtained with other non-invasive techniques. PET has been widely used as a highly quantitative non-invasive tool to detect neurotransmitter receptors and protein/enzyme levels, e.g., cerebral glucose metabolism ([¹⁸F]fluorodeoxyglucose, FDG), dopamine receptor ([¹¹C]raclopride), glial activation, and amyloid- β plaques, in the living human brain (10). It is also noted that optical imaging accounts for a large segment of clinical imaging and has been used in image-guided surgery, although far fewer contrast agents have been approved for optical imaging than PET (11, 12). Emerging optical imaging methods, including fluorescence and optoacoustic imaging (OAT) (13, 14), have shown increasing value for assisting diagnosis and surgical navigation. Observation of molecular, structural, and functional changes in the brains of small animal models that recapitulate human diseases is highly valuable for understanding physiological function (15) and the mechanisms underlying brain disorders (16). Small animal brain imaging has been indispensable for the development of novel therapeutic drugs and diagnostic imaging probes. A previous study showed that preclinical dosimetry studies and models facilitate the prediction of clinical doses of new PET tracers (17). Here, we summarize the gaps in the translation of preclinical neuroimaging and focus on the recent technical developments in improving its clinical relevance, especially regarding data acquisition (hybrid imaging and awake animal imaging), data analysis using deep learning (DL), and transcriptomics. We also outline the current outstanding challenges in closing the translational gap and propose outlooks for the future.

HYBRID IMAGING

The most commonly used hybrid systems in small animal imaging are the integration of molecular imaging using PET, SPECT, fluorescence molecular tomography (FMT), and OAT with structural imaging using MRI and CT. Both PET/SPECT-CT and PET/SPECT-MRI provide research tools for probing molecular and structural information and have demonstrated significant value in brain research (18, 19). Molecular imaging modalities generally lack high-spatial resolution and soft tissue contrast to accurately allocate the distribution of specified molecular signals. Thus, it is essential to provide accurate anatomical information along with the molecular imaging modalities to better interpret the acquired molecular signals (20–22). There are two approaches to address this: sequential-mode using different standalone modalities and follow-up image processing/image registration (23) or hybridized multimodal imaging (24). Sequential-mode multimodal imaging allows convenient data acquisition and minimal interference from each modality, while hybridization of the multimodal method enables dynamic imaging data from multiple channel signal sources, enhanced image reconstruction with prior structural information, and improved quantitative information (25).

Positron Emission Tomography/SPECT-CT and PET/SPECT-MRI

Positron emission tomography/SPECT provides quantitative *in vivo* detection of picomolar concentrations of the target within a large field-of-view (26–28). The resolution of commercially available microPET is approximately 0.5–2 mm (29–32), which is sufficient for rat brain imaging but suboptimal for mouse brain imaging considering the spillover and size of the mouse brain (10 mm × 10 mm × 15 mm) (33). The concept of combining PET/SPECT with CT was first introduced to clinical trials in the early 2000s (34). An early prototype PET/SPECT-CT scanner used a coaxial configuration and minimal axial translation of a movable couch to facilitate the sequential acquisition of PET/SPECT and CT during a single imaging session (35). The CT image serves as (1) an anatomical reference to map the molecular information given by PET and (2) an attenuation map for PET reconstruction to achieve more quantitative data (36). For hybridization of PET/SPECT and MRI, MRI provides better soft-tissue contrast without radiation and contains multiparametric (structural, molecular, and functional) readouts (25, 27, 37–39). Various MRI contrast agents, such as superparamagnetic iron oxide, can be applied to identify microglial activation/macrophage infiltration along with simultaneous PET using [¹⁸F]DPA-714 for glial activation in mouse models of relapsing-remitting experimental autoimmune encephalomyelitis (40) (**Figures 1a,e**). As a high magnetic field exists in preclinical MRI scanners, the space inside the scanner bore is significantly limited. Several PET inserts in 7T or 9.4T MRI have been reported, such as Hyperion II and MADPET4 with digital silicon photomultiplier technology (41–47). Recently,

Liu et al. reported a multimodal intravital imaging system that provided a coregistered *in vivo trans-scale* and transparent platform (PET, MRI, microscopy) and quantitative evaluation of tumor anatomy, vasculature, and the microenvironment, including glucose, oxygen, and acidity metabolism (48).

Fluorescence Molecular Tomography-CT and FMT-MRI

In addition to PET/SPECT, fluorescence imaging provides an alternative molecular imaging method with the features of high sensitivity, low cost, and non-ironizing radiation. FMT utilizes near-infrared light to penetrate living tissue up to several centimeters deep and applies a model-based reconstruction algorithm to recover the three-dimensional distribution of fluorescence probes (49). FMT-CT was first introduced by combining FMT in transmission mode with a commercial CT scanner (50) (**Figure 1b**); a point-shaped collimated laser source and a charge-coupled device (CCD) camera were placed on the opposite sides of the imaging object and mounted onto the CT gantry perpendicular to the X-ray instrumentation axis (51). The irregularly shaped boundary and heterogeneous inner structure can be rendered by CT and used for more accurate FMT image reconstruction (52). The FMT image quality is significantly improved with prior information from CT (53, 54). The FMT-CT hybrid system has been used for the detection of amyloid- β deposition in mouse models of Alzheimer's disease and lung cancer (50, 55–59). FMT has been combined with MRI, such as detecting overexpressed epidermal growth factor receptors in a mouse model with gliomas (60) (**Figure 1c**). Similarly, an MR-compatible optical imager was inserted into a preclinical MRI scanner (61) using optical fibers or a silicon-based single-photon avalanche diode array to collect the emitted photons (61, 62). The anatomical reference obtained by MRI can be used as a prior information in a finite-element-method-based reconstruction algorithm to achieve a more accurate allocation of any fluorescent probe. In addition, dynamic image acquisition using FMT-MRI was performed to evaluate vascular perfusion and permeability in a breast tumor mouse model (63) and to quantify the target availability during therapy (64) (**Figure 1f**).

Optoacoustic Tomography-CT and OAT-MRI

Optoacoustic imaging combines the rich optical image contrast and exquisite spatiotemporal resolution given by ultrasound; consequently, it has developed rapidly into a common research tool for the preclinical studies (65, 66). OAT imaging has been applied to detect molecular and functional alterations in ischemic stroke, brain tumors, and Alzheimer's disease rodent models (22, 67–70). However, the identification of different tissues or organs is difficult due to the limited soft-tissue contrast given in OAT. Several studies have utilized hybrid imaging systems combining OAT and ultrasound that offer moderate anatomical information in small animal imaging (71–73). Although the image formation mechanisms are different in these two modalities, it is relatively straightforward to combine

OAT and ultrasound, as they utilize the same transducer array and coupling medium during measurement. The development of OAT-CT and OAT-MRI is still at an early stage. Sequential-mode multimodal imaging with OAT-CT and OAT-MRI has also been reported (74–79). Coregistration of images sequentially acquired with OA and other methods is performed for volume-of-interest analysis using dedicated algorithms (80, 81), either software-based (82–85) or a hardware-assisted protocol based on stable bimodal imaging support and a rigorous data acquisition procedure (81, 86). Similar to FMT-MRI and PET-MRI hybrid systems, the combination of OAT and MRI is highly restricted by the limited space inside the MRI bore and electromagnetic interference mainly caused by radiofrequency (RF) coils. To address these challenges, the optoacoustic signal readout can be properly shielded by copper and synchronized according to different MRI sequences. More recently, a proof-of-concept hybrid OAT-MRI system that allows simultaneous recording kinetics of two contrast agents in a phantom was reported (87), for which an MR-compatible OAT insert was developed with a specifically distributed transducer array and copper-made shielding (**Figure 1d**). For data acquisition, the excitation laser pulse signal and MRI pulse sequence were synchronized to avoid interference between the two modalities. Hybridization with MRI greatly enhances the performance of OAT by enabling the simultaneous readings of multichannel dynamic information, including resting-state functional MRI (rs-fMRI) for blood-oxygen-level-dependent (BOLD) signals, oxygen saturation, or contrast agent biodistribution (88). Applications of OA imaging in clinical research have shown promising results and are still limited to the peripheral system (89–91). *In vivo* OA imaging in non-human primates has been demonstrated (92) and in the neonatal brain (93). A recent OA/functional MRI study of the living adult human brain demonstrated the potential of its application in the clinical neuroimaging (94, 95). However, significant challenges in skull aberrations and acoustic distortions still need to be addressed for potential clinical application and to further close the translational gap. Excitation lasers with longer wavelengths, such as in the near-infrared II window, and ultrasound transducers with lower central frequencies reduce both optical attenuation and acoustic aberration (96). The anatomical information containing both the skull and brain obtained by CT or MRI in those hybrid systems can be used for accurate modeling for light and ultrasound propagation, which can potentially improve OAT reconstruction (87).

TRANSLATIONAL GAPS

Translational gaps exist in developing imaging biomarkers, including those (1) between *in vitro* and *in vivo* animal studies, (2) between animal and patient translation as a robust medical research tool, and (3) between research tools and integrated clinical applications (97, 98). For clinical imaging, rapid and safe processes, reliable readouts and the added value to patients (in comparison to the existing option) are important. Imaging biomarker generates added value by facilitating drug development, monitoring of treatment response

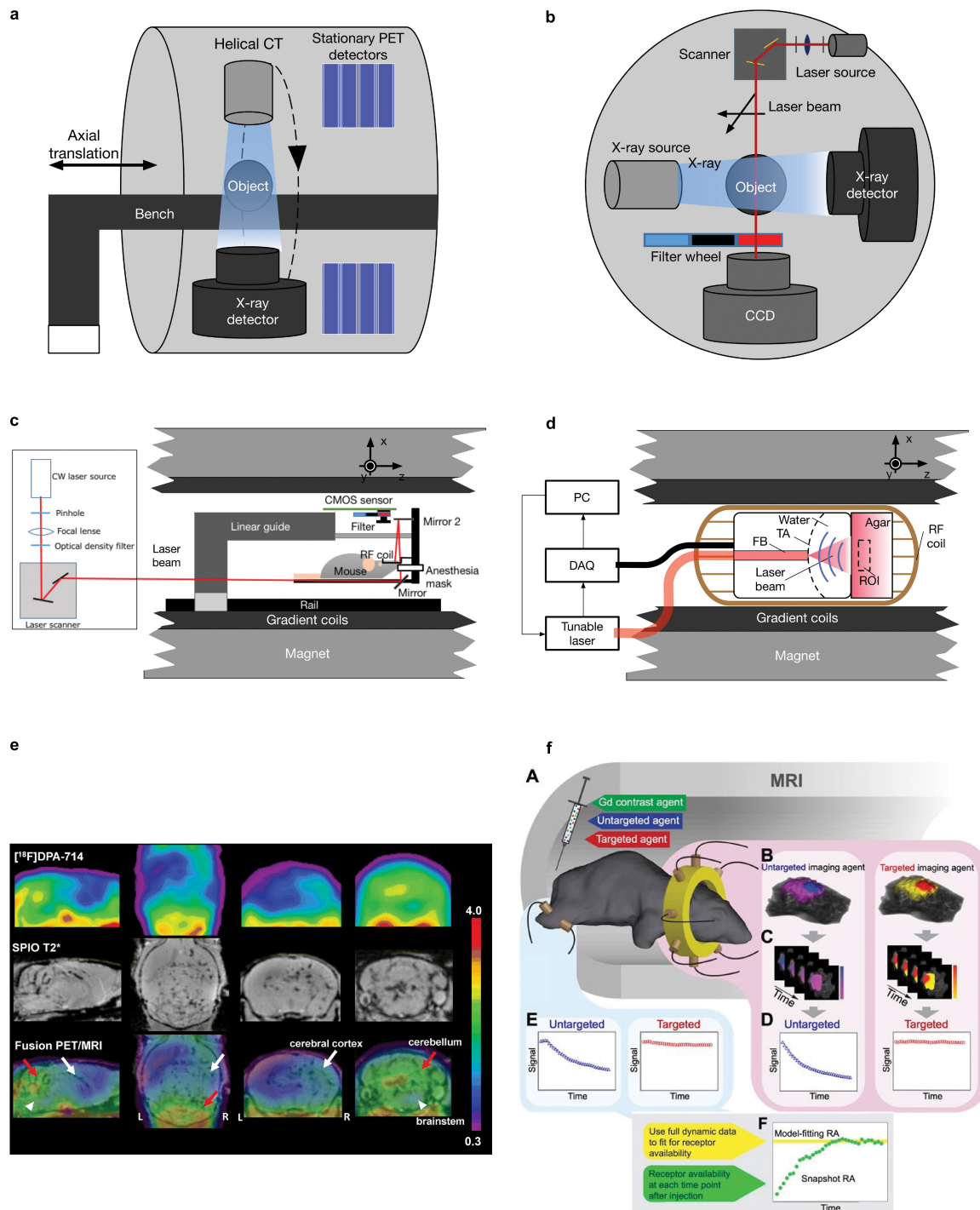


FIGURE 1 | Schematics and example of different small animal hybrid imaging systems. **(a)** PET-CT uses a coaxial configuration with a helical CT scanner and stationary PET detectors aligned in parallel in one imaging chamber. A movable bench carrying the measured object allows minimal axial translation, facilitating dual-modal imaging. **(b)** A cross-sectional view of the FMT-CT configuration. In a transmission-mode FMT, the charge-coupled device detector and the illumination module, including a laser source and a scanning device, are placed on the opposite sides of the imaging object. Perpendicular to the optical path of FMT measurement, an X-ray source/detector pair is aligned in the same CT gantry. **(c)** FMT-MRI can be implemented by using an MR-compatible optical imager inserted into a preclinical MRI scanner. The major component of the insert includes a CMOS array and a customized RF coil [adapted from Ren et al. (63) with permission from Springer Nature]. **(d)** Similar to FMT-MRI, in OAT-MRI, an MR-compatible ultrasound transducer array together with the coupling medium was used as an OAT insert inside an MRI scanner. A pulsed light source and a data acquisition module (DAQ) are placed outside the MRI bore (adapted from Ren et al. (87) with permission from John Wiley & Sons, Inc.). **(e)** Sagittal, coronal, and transaxial $[^{18}\text{F}]\text{DPA-714}$ PET, SPIO T_2^* MRI, and PET/MRI fusion images of a representative (Continued)

FIGURE 1 | experimental autoimmune encephalomyelitis mouse. PET images represent summed scans (20–50 min postinjection) normalized to the left cerebral neocortex SUV values. Increased radiotracer uptake and loss of T_2^* signal can be observed in the cerebellum (red arrow), brainstem (white arrowheads), and, to a lesser extent, right cerebral cortex (white arrow) in the experimental autoimmune encephalomyelitis mouse but not in the control. R, right; L, left. Reproduced from Coda et al. (40) with permission from Springer Nature. **(f)** MRI-FMT animal interface. (A) Illustration inside the magnet bore showing the tomographic fiber array encircling the head and a pair of optical fibers on the leg to acquire normal tissue kinetics. (B) Representative volumetric images of fluorescence activity (one frame) in the brain and tumor for both targeted and untargeted agents. Volumes such as these were acquired at approximately 0.5 Hz over the course of over 60 min, resulting in dynamic image stacks of each agent (C). Fluorescence activity was then extracted from the tumor and normal tissue to produce dynamic uptake curves, as shown in (D) and (E), respectively. Data from these curves were then used to determine RA using the model-fitting and snapshot approaches, as illustrated in (F). Reproduced from (64) with permission from Ivyspring International Publisher.

(99), and reducing cost per quality-adjusted life year gained by enabling early diagnosis (100). Closing the translational gaps requires enormous technical, biological, and clinical validation and also cost effectiveness assessment (101). The lack of a satisfactory animal model is a shared problem for research on brain diseases, including stroke, neurodegenerative diseases, psychiatric diseases, and multiple sclerosis (102). Many reviews have outlined the challenges in animal models and the need for models better mimicking human diseases to improve translational power (103, 104). Using the genome engineering technology CRISPR/Cas9, humanized knock-in animal models are under rapid development. However, species differences exist in the size of the brain, anatomical structure, cerebral cortical folding, parcellation, and connectivity neuron size in humans, non-human primates, and mice (105, 106). Microglia and astrocyte in humans and mice exhibit different vulnerabilities and responses to external stressors (107, 108). The differences in gene expression and protein level between small animals and humans increase the difficulty of translation of targeting ligands (109). Moreover, there are pharmacological and behavioral differences between mice and rats, which need to be considered when interpreting the results. In addition, strain- and substrain-dependent vulnerability to pathological interventions such as permanent focal cerebral ischemia in a mouse model has been documented (110, 111). Bailey et al. showed that the C57BL/6 strain background has an influence on tauopathy progression in the rTg4510 transgenic mouse model originally of the FVB/129 background (112). Moreover, the recent findings highlighted the unique vulnerability of humans to Alzheimer's disease or primary tauopathy, and the amyloid- β and tau deposits formed in the brains from transgenic mouse models over 1–2 years are structurally different compared with those found in aged patients (113). A similar difference has been reported for α -synuclein aggregates in patients with Parkinson's disease (114). These differences are reflected in the divergent binding properties observed in tau/amyloid- β / α -synuclein imaging probes binding to the brains of rodent models, non-human primates, and patients (115–117). In addition to the aforementioned developments, recent single-cell tracking PET, a cellular global positioning system, was able to detect a single cell over time in a living mouse and directly related the *in vivo* imaging pattern to a single cell with its molecular profiles (118). Moreover, Tournier et al. and Nutma et al. developed fluorescence-activated cell sorting to radioligand-treated tissues (FACS-RTT) to reveal the cell origin of the radioligand translocator protein binding (119, 120) (**Figure 2F**).

AWAKE ANIMAL IMAGING

Anesthesia leads to alterations in the brain state, cardiovascular physiology, and hemodynamic properties. Functional readouts derived from rs-fMRI (BOLD signal) and ASL-MRI (cerebral blood flow) are especially affected by awake or anesthesia status (121). In addition, PET imaging in rodents, such as [^{18}F]FDG for cerebral glucose metabolism (122) and [^{18}F]MPPF for serotonin 1A receptor (123), is also largely influenced by anesthesia, restraint stress, and physiological stability of the animal. A key difference between rodent and human functional imaging is the use of anesthesia to reduce motion during scanning. To overcome this gap, imaging in awake behaving rodents has been increasingly reported in the two-photon optical imaging, functional ultrasound imaging, electrophysiology, PET, and MRI in the recent years (124–127). These imaging platforms enable the integration of molecular-, behavioral-level, and circuit-level understanding of the brain. However, the duration, setup, and imaging type suitable for use in awake rodents are still limited and require extensive habituation and further development.

DEEP LEARNING IN MULTIMODAL IMAGING POSTPROCESSING

Deep learning-based methods have recently gained great momentum in both image reconstruction (128) and postprocessing (129, 130). Here, we focus on the DL application in image postprocessing with emphasis on image segmentation in a mono-modality and registration between different modalities. For a standalone modality such as MRI, DL has successfully been used in assisting the diagnosis of brain disease and analyzing the whole brain vasculature (131). Several pipelines for registration and segmentation of high-resolution mouse brain data onto brain atlases have been developed, such as aMAP (132, 133) and AMaSiNe (134). In addition to conventional manual feature extraction, the emerging applications of DL entail an enormous advancement in discovering new characteristic features in data (135–137). Given sufficient training, it can learn complex non-linear functions from high-dimensional and unstructured data (138). The potential of artificial intelligence has already been revealed in medical applications such as computerized diagnosis and prognosis (139). Regardless of sequential-mode multimodal imaging or truly hybrid systems, developing software-based algorithms for accurate and automatic registering molecular information with structural information is of high interest. For small animal PET, SPECT, CT, and MRI data,

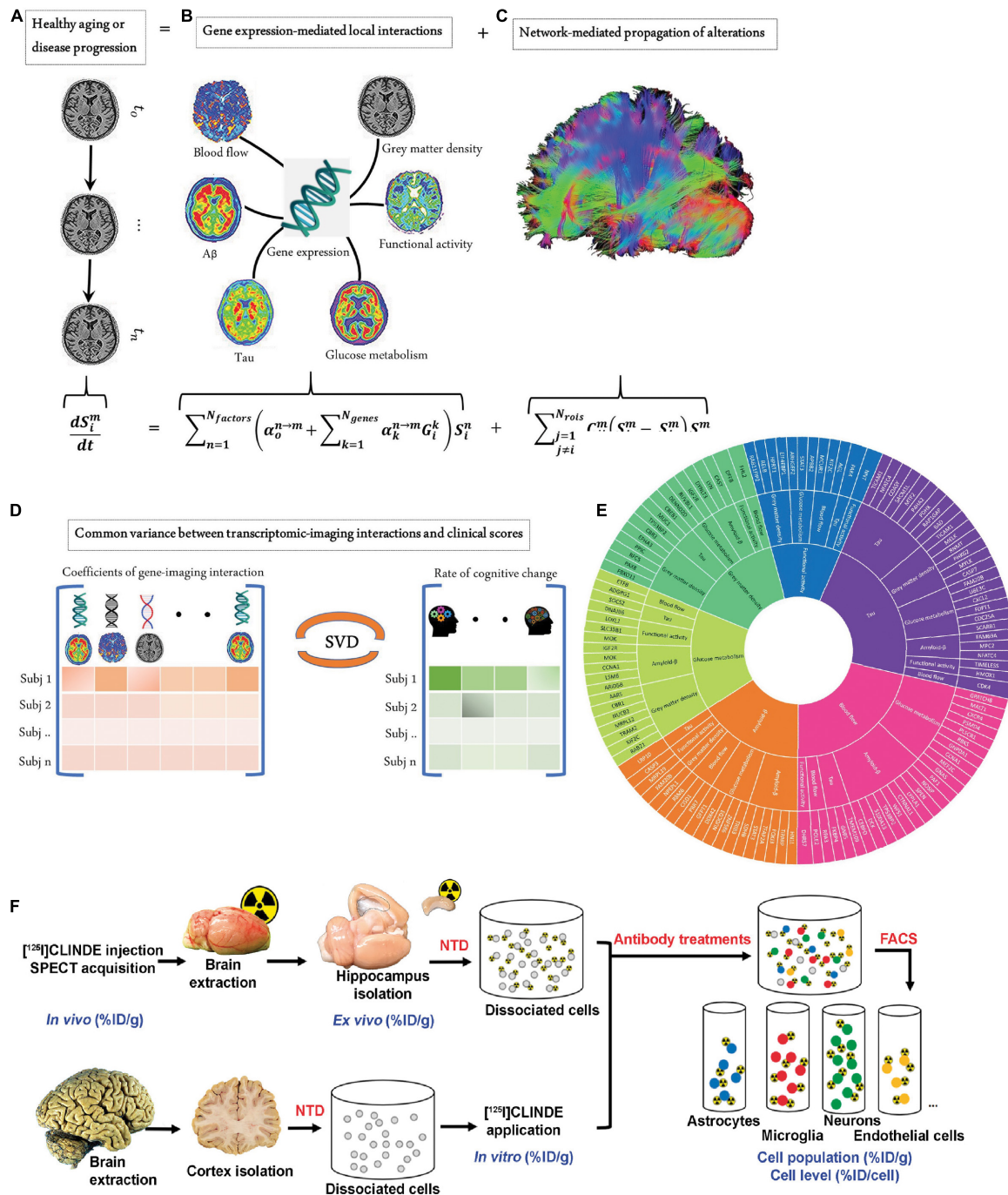


FIGURE 2 | Measures to close biological gaps. **(A–E)** Integrated transcriptomic and neuroimaging data to understand biological mechanisms in aging and Alzheimer's disease. **(A)** The longitudinal alteration of macroscopic biological factors in healthy and diseased brains due to gene-imaging interactions and the propagation of the ensuing alterations across brain networks. **(B)** Regional multifactorial interactions between six macroscopic biological factors/imaging modalities are modulated by local gene expression. **(C)** Causal multifactorial propagation network capturing the interregional spread of biological factor alterations through physical connections. **(D)** By applying a multivariate analysis through singular value decomposition (SVD), the maximum cross-correlation between age-related changes in cognitive/clinical evaluation and the magnitude of genetic modulation of imaging modalities was determined in a cohort of stable healthy subjects (for healthy aging), mild cognitive impairment (MCI) converters, and Alzheimer's disease (AD) subjects (for AD progression). **(E)** The key causal genes driving healthy aging and AD progression are identified through their absolute contributions to the explained common variance between the gene-imaging interactions and cognitive scores. Reproduced from (148) with permission from eLife Sciences Publications, Ltd. **(F)** Overview of the fluorescence-activated cell sorting to radioligand-treated tissues (FACS-RTT) protocol. Schematic overview of the methodology used for the *in vivo*, *ex vivo*, *in vitro* and cellular measurement of the radioligand. % ID/cell: percentage of the injected dose/cell; % ID/g: percentage of the injected dose/g tissue weight; NTD: neural tissue dissociation. Reproduced from (120) with permission from Sage Publication.

several established pipelines and commercial software such as ANTs, statistical parametric mapping (SPM), AFNI, PMOD, etc., have been established and routinely used (140–142). For OAT data, challenges remain in reconstruction processing, including segmentation and registration. Different detection configurations generate OAT images with different features. As OAT images have limited soft-tissue contrast, segmentation, and registration are thus difficult and highly dependent on the user experience. Human inputs were involved in the previously reported OAT-MRI registration methods to a certain extent, such as piecewise linear mapping algorithms (82). Gehrung et al. developed an integrated protocol for OAT-MRI registration by using a customized animal holder and landmark-based registration software (86). Ren et al. reported semiautomated OAT-MRI brain imaging data registration software that used active contour segmentation as the first step and an adaptive mutual information-based registration algorithm (84). Hu et al. developed a fully automated registration method for OAT-MRI brain imaging data registration empowered by DL, which consists of (1) two U-net-like neural networks to segment OAT and MRI images (71) and (2) an adaptive neural network to transform these generated OAT/MRI masks (reference). The accuracy and robustness of such DL-based registration have been shown to be comparable with classic methods but at a much higher speed without manual efforts on either landmark selection or boundary drawing (143).

TRANSCRIPTOMICS

With the affordability of single-cell sequencing, metabolomics, and transcriptomics (144–146), deep phenotyping techniques allow us to elucidate the similarities and differences in the genetics (147) and protein expression in animal models and humans (109, 148–151). Single-cell transcriptomic profiling of aging and Alzheimer's disease combined with data from amyloid and tau PET, [^{18}F]FDG PET, and rs-Fmri, and structural MRI to unveil the gene and macroscopic factor interactions and the biological mechanisms underlying Alzheimer's disease (148) (**Figures 2A–E**). Spatially resolved transcriptomics in particular, such as fluorescence *in situ* hybridization, showed promising application in convergent cellular, transcriptomic, and molecular neuroimaging data (149, 152, 153). Allen brain transcriptomics mouse and human datasets provide an excellent platform for exploring the link between mice and humans, integrated with connectivity and histology data (154). Other gene expression databases, such as “Brain RNA-Seq”¹ (109) and machine-learning models to improve mouse-to-human inference “Found In Translation,”² non-human primate platforms (155) are available to facilitate the interpretation of experimental observations. In addition, the uptake of several tracers, such as [^{18}F]GE-180 (for glial activation) and [^{18}F]FDG (for cerebral glucose metabolism), is influenced by sex (156–158). Further transcriptomic analysis

may reveal sex-specific molecular differences associated with the uptake of different tracers.

ORGAN-ON-CHIP PHARMACOKINETICS

There is a continued need for small animals as a powerful model system to advance neuroimaging and translational brain research (159). The biodistribution and pharmacokinetic information of pharmaceuticals in rodents and *ex vivo* target validation are prerequisites for phase 1 studies. Recent developments in organoids from induced pluripotent stem cells have introduced a paradigm shift for drug development (160). Cerebral organoids and blood–brain barrier organoids that mimic mouse or human physiology for investigating the permeability of compounds have been developed (161). With the goal of implementing the 3R principle (replacement, refinement, and reduction), recent efforts have been made to assess the behavior of imaging ligands using organ-on-chip systems employing organoids (162, 163). In addition, several recent studies reported systems for the characterization of cellular pharmacokinetics based on microfluidic systems, including a continuously infused microfluidic radioassay (164), microfluidics-coupled radioluminescence microscopy (165), and droplet-based single-cell radiometric assay (166). Further research on *in vitro in vivo* extrapolation will facilitate the translation and development of imaging ligands toward clinical application.

DISCUSSION

Imaging methods that non-invasively record rapidly changing functional and molecular imaging data have been crucial for our understanding of human and small animal brains. Recent developments in optogenetics, chemogenomics, two-photon microscopy, and all optical interrogation have improved the understanding of physiological and pathological processes in the rodent brains (167–175). However, these imaging methods are limited to preclinical applications. To further improve the translational power of PET, MRI, and CT and optical imaging, we suggest the following considerations:

Standardization, Quality Assurance, and Quality Control

Standardization of imaging protocols and data analysis: The standardization of PET, CT, and MRI procedures in humans is more advanced than that in preclinical imaging and is a prerequisite for clinical trials. Even for structural MRI, scan session, head tilt, interscan interval, acquisition sequence, and processing stream have been found to influence the imaging results (176). The standardization of preclinical PET-CT/PET-MRI protocols, including CT, absorbed dose guidelines, has not been fully established. The updated ARRIVE guideline 2.0 provides a general checklist of *in vivo* experiments to facilitate the reproducibility of the results and methodological rigor (177, 178). Previous systematic reviews have systematically evaluated the choice of anesthetic/sedative regimen and the variation

¹<https://www.brainrnaseq.org/>

²<http://www.mouse2man.org>

in fMRI rodent imaging (179–181). In a recent multicenter study in the United States and Europe, standardization of the preclinical PET/CT acquisition and reconstruction protocols have been shown to increase the quantitative accuracy as well as the reproducibility of imaging results (182). Similar multicenter, cross-scanner validation studies are needed for PET, SPECT, MRI, ultrasound, CT, optical imaging, hybrid imaging, and less established imaging tools, e.g., OAT or FMT. Osborne et al. proposed useful guidance for QC and scanner calibration procedures for the preclinical imaging laboratories with a balanced cost consideration (183). In the terms of data postprocessing, recent comparisons of different fMRI processing pipelines outline the importance of consensus and move beyond processing and analysis-associated variation to increase the reproducibility in human neuroimaging data (184, 185). For mouse brain imaging, recent multicenter rs-fMRI analyses have reported common functional networks in the mouse brain (186). Further comprehensive QA/QC consensus and multicenter studies are needed for the scanner as well as for the entire pipeline, including data acquisition, reconstruction, and postprocessing to improve reproductivity and reduce variation across different studies.

Open Data Sharing

The open sharing of neuroimaging research data is critical to promote the reproducibility of scientific findings (187, 188). Large international initiatives in human brain imaging data sharing, such as ADNI (189), OpenNeuro (190), the human connectome project (191), and OASIS (192), have greatly facilitated the advancement of the research field. In contrast, less

small animal neuroimaging data sharing has been achieved thus far. There is thus a need for promoting the sharing of mouse and rat neuroimaging data that are compliant with brain imaging data structure (BIDS) following the FAIR principles (193). Increasing the sample size of animal studies and cross-study comparisons add to the reliability of the findings (194).

CONCLUSION

In conclusion, developments in hybrid imaging, deep learning in data processing, awake animal imaging, and transcriptomics have greatly improved the translation of preclinical brain imaging. Further efforts on standardization, quality assurance/quality control, data sharing, and on-chip modeling for the translation of preclinical small animal brain imaging from bench to bedside need to be undertaken.

AUTHOR CONTRIBUTIONS

WR and RN wrote the draft. All authors contributed to the manuscript.

FUNDING

WR received a start-up grant from ShanghaiTech University. RN received funding from Helmut Horten Stiftung, Vontobel Stiftung, and University of Zurich [MEDEF-20-021].

REFERENCES

- Finnema SJ, Nabulsi NB, Eid T, Detyniecki K, Lin SF, Chen MK, et al. Imaging synaptic density in the living human brain. *Sci Transl Med.* (2016) 8:348ra396. doi: 10.1126/scitranslmed.aaf6667
- Glasser MF, Coalson TS, Robinson EC, Hacker CD, Harwell J, Yacoub E, et al. A multi-modal parcellation of human cerebral cortex. *Nature.* (2016) 536:171–8. doi: 10.1038/nature18933
- Poldrack RA, Farah MJ. Progress and challenges in probing the human brain. *Nature.* (2015) 526:371–9. doi: 10.1038/nature15692
- Weiskopf N, Edwards LJ, Helms G, Mohammadi S, Kirilina E. Quantitative magnetic resonance imaging of brain anatomy and *in vivo* histology. *Nat Rev Phys.* (2021) 3:570–88.
- Shah D, Jonckers E, Praet J, Vanhoutte G, Delgado y Palacios R, Bigot C, et al. Resting state fMRI reveals diminished functional connectivity in a mouse model of amyloidosis. *PLoS One.* (2013) 8:e84241. doi: 10.1371/journal.pone.0084241
- Debette S, Schilling S, Duperron M-G, Larsson SC, Markus HS. Clinical significance of magnetic resonance imaging markers of vascular brain injury: a systematic review and meta-analysis. *JAMA Neurol.* (2019) 76:81–94. doi: 10.1001/jamaneurol.2018.3122
- Dumoulin SO, Fracasso A, van der Zwaag W, Siero JCW, Petridou N. Ultra-high field MRI: advancing systems neuroscience towards mesoscopic human brain function. *Neuroimage.* (2018) 168:345–57. doi: 10.1016/j.neuroimage.2017.01.028
- Triantafyllou C, Hoge RD, Krueger G, Wiggins CJ, Potthast A, Wiggins GC, et al. Comparison of physiological noise at 1.5 T, 3 T and 7 T and optimization of fMRI acquisition parameters. *Neuroimage.* (2005) 26:243–50. doi: 10.1016/j.neuroimage.2005.01.007
- Wahsner J, Gale EM, Rodríguez-Rodríguez A, Caravan P. Chemistry of MRI contrast agents: current challenges and new Frontiers. *Chem Rev.* (2019) 119:957–1057. doi: 10.1021/acs.chemrev.8b00363
- Lammertsma AA. Forward to the past: the case for quantitative PET imaging. *J Nucl Med.* (2017) 58:1019–24. doi: 10.2967/jnumed.116.188029
- de Boer E, Harlaar NJ, Taruttis A, Nagengast WB, Rosenthal EL, Ntziachristos V, et al. Optical innovations in surgery. *Br J Surg.* (2015) 102:e56–72. doi: 10.1002/bjs.9713
- Weber J, Beard PC, Bohndiek SE. Contrast agents for molecular photoacoustic imaging. *Nat Methods.* (2016) 13:639–50.
- Deán-Ben XL, Robin J, Ni R, Razansky D. Noninvasive three-dimensional optoacoustic localization microangiography of deep tissues. *arXiv.* (2020) [Preprint]. arXiv:2007.00372
- Razansky D, Buehler A, Ntziachristos V. Volumetric real-time multispectral optoacoustic tomography of biomarkers. *Nat Protoc.* (2011) 6:1121–9. doi: 10.1038/nprot.2011.351
- Hagihara KM, Bukalo O, Zeller M, Aksoy-Aksel A, Karalis N, Limoges A, et al. Intercalated amygdala clusters orchestrate a switch in fear state. *Nature.* (2021) 594:403–7. doi: 10.1038/s41586-021-03593-1
- Zimmer ER, Parent MJ, Cuello AC, Gauthier S, Rosa-Neto P. MicroPET imaging and transgenic models: a blueprint for Alzheimer's disease clinical research. *Trends Neurosci.* (2014) 37:629–41. doi: 10.1016/j.tins.2014.07.002
- Garrow AA, Andrews JPM, Gonzalez ZN, Corral CA, Portal C, Morgan TEF, et al. Preclinical dosimetry models and the prediction of clinical doses of novel positron emission tomography radiotracers. *Sci Rep.* (2020) 10:15985. doi: 10.1038/s41598-020-72830-w
- Cheng SH, Yu D, Tsai HM, Morshed RA, Kanojia D, Lo LW, et al. Dynamic *In vivo* SPECT imaging of neural stem cells functionalized with radiolabeled nanoparticles for tracking of glioblastoma. *J Nucl Med.* (2016) 57:279–84. doi: 10.2967/jnumed.115.163006

19. Ho KC, Toh CH, Li SH, Liu CY, Yang CT, Lu YJ, et al. Prognostic impact of combining whole-body PET/CT and brain PET/MR in patients with lung adenocarcinoma and brain metastases. *Eur J Nucl Med Mol Imaging*. (2019) 46:467–77. doi: 10.1007/s00259-018-4210-1
20. Kadir A, Almkvist O, Forsberg A, Wall A, Engler H, Langstrom B, et al. Dynamic changes in PET amyloid and FDG imaging at different stages of Alzheimer's disease. *Neurobiol Aging*. (2012) 33:e191–114. doi: 10.1016/j.neurobiolaging.2010.06.015
21. Osmanski B, Pezet S, Ricobaraza A, Lenkei Z, Tanter M. Functional ultrasound imaging of intrinsic connectivity in the living rat brain with high spatiotemporal resolution. *J Cerebr Blood F Met*. (2016) 36:566–8. doi: 10.1038/ncomms6023
22. Razansky D, Klohs J, Ni R. Multi-scale optoacoustic molecular imaging of brain diseases. *Eur J Nucl Med Mol Imaging*. (2021) 48:4152–70. doi: 10.1007/s00259-021-05207-4
23. Promteangtrong C, Kolber M, Ramchandra P, Moghbel M, Houshmand S, Scholl M, et al. Multimodality imaging approaches in Alzheimer's disease. Part II: 1H MR spectroscopy, FDG PET and amyloid PET. *Dement Neuropsychol*. (2015) 9:330–42. doi: 10.1590/1980-57642015DN94000330
24. Lammertsma AA. On the origin of hybrid imaging. *J Nucl Med*. (2020) 61:166s–7s.
25. Rudin M. *Molecular Imaging: Basic Principles and Applications in Biomedical Research*. London: Imperial College Press (2012).
26. Herfert K, Mannheim JG, Kuebler L, Marciano S, Amend M, Parl C, et al. Quantitative rodent brain receptor imaging. *Mol Imaging Biol*. (2020) 22:223–44. doi: 10.1007/s11307-019-01368-9
27. Judenhofer MS, Wehrl HF, Newport DF, Catana C, Siegel SB, Becker M, et al. Simultaneous PET-MRI: a new approach for functional and morphological imaging. *Nat Med*. (2008) 14:459–65. doi: 10.1038/nm1700
28. Miyaoka RS, Lehnert AL. Small animal PET: a review of what we have done and where we are going. *Phys Med Biol*. (2020) 65:24TR04. doi: 10.1088/1361-6560/ab8f71
29. Amirrashedi M, Zaidi H, Ay MR. Advances in preclinical PET instrumentation. *PET Clin*. (2020) 15:403–26. doi: 10.1016/j.cpet.2020.06.003
30. Lai Y, Wang Q, Zhou S, Xie Z, Qi J, Cherry SR, et al. H(2)RSPET: a 0.5 mm resolution high-sensitivity small-animal PET scanner, a simulation study. *Phys Med Biol*. (2021) 66:065016. doi: 10.1088/1361-6560/abe558
31. Nagy K, Tóth M, Major P, Patay G, Egri G, Häggkvist J, et al. Performance evaluation of the small-animal nanoScan PET/MRI system. *J Nucl Med*. (2013) 54:1825–32. doi: 10.2967/jnumed.112.119065
32. Yang Y, Bec J, Zhou J, Zhang M, Judenhofer MS, Bai X, et al. A prototype high-resolution small-animal pet scanner dedicated to mouse brain imaging. *J Nucl Med*. (2016) 57:1130–5. doi: 10.2967/jnumed.115.165886
33. Fang YH, Muzic RF Jr. Spillover and partial-volume correction for image-derived input functions for small-animal 18F-FDG PET studies. *J Nucl Med*. (2008) 49:606–14. doi: 10.2967/jnumed.107.047613
34. Townsend DW, Carney JP, Yap JT, Hall NC. PET/CT today and tomorrow. *J Nucl Med*. (2004) 45 (Suppl. 1):4S–14S.
35. Lawrence J, Rohren E, Provenzale J. PET/CT today and tomorrow in veterinary cancer diagnosis and monitoring: fundamentals, early results and future perspectives. *Vet Comp Oncol*. (2010) 8:163–87. doi: 10.1111/j.1476-5829.2010.00218.x
36. Dogdas B, Stout D, Chatziioannou AF, Leahy RM. Digimouse: a 3D whole body mouse atlas from CT and cryosection data. *Phys Med Biol*. (2007) 52:577–87. doi: 10.1088/0031-9155/52/3/003
37. Lake EMR, Ge X, Shen X, Herman P, Hyder F, Cardin JA, et al. Simultaneous cortex-wide fluorescence Ca²⁺ imaging and whole-brain fMRI. *Nat Methods*. (2020) 17:1262–71.
38. Yu X, He Y, Wang M, Merkle H, Dodd SJ, Silva AC, et al. Sensory and optogenetically driven single-vessel fMRI. *Nat Methods*. (2016) 13:337–40. doi: 10.1038/nmeth.3765
39. Zürcher NR, Walsh EC, Phillips RD, Cernasov PM, Tseng C-EJ, Dharanikota A, et al. A simultaneous [11C]raclopride positron emission tomography and functional magnetic resonance imaging investigation of striatal dopamine binding in autism. *Transl Psychiatry*. (2021) 11:33. doi: 10.1038/s41398-020-01170-0
40. Coda AR, Anzilotti S, Boscia F, Greco A, Panico M, Gargiulo S, et al. *In vivo* imaging of CNS microglial activation/macrophage infiltration with combined [(18)F]DPA-714-PET and SPIO-MRI in a mouse model of relapsing remitting experimental autoimmune encephalomyelitis. *Eur J Nucl Med Mol Imaging*. (2021) 48:40–52. doi: 10.1007/s00259-020-04842-7
41. Grant AM, Deller TW, Khalighi MM, Maramraju SH, Delso G, Levin CS. NEMA NU 2-2012 performance studies for the SiPM-based ToF-PET component of the GE SIGNA PET/MR system. *Med Phys*. (2016) 43:2334. doi: 10.1118/1.4945416
42. Gsell W, Molinos C, Correcher C, Belderbos S, Wouters J, Junge S, et al. Characterization of a preclinical PET insert in a 7 tesla MRI scanner: beyond NEMA testing. *Phys Med Biol*. (2020) 65:245016. doi: 10.1088/1361-6560/aba08c
43. Hallen P, Schug D, Weissler B, Gebhardt P, Salomon A, Kiessling F, et al. PET performance evaluation of the small-animal Hyperion II(D) PET/MRI insert based on the NEMA NU-4 standard. *Biomed Phys Eng Express*. (2018) 4:065027. doi: 10.1088/2057-1976/aae6c2
44. Omidvari N, Cabello J, Topping G, Schneider FR, Paul S, Schwaiger M, et al. PET performance evaluation of MADPET4: a small animal PET insert for a 7 T MRI scanner. *Phys Med Biol*. (2017) 62:8671–92. doi: 10.1088/1361-6560/aa910d
45. Omidvari N, Topping G, Cabello J, Paul S, Schwaiger M, Ziegler SI. MR-compatibility assessment of MADPET4: a study of interferences between an SiPM-based PET insert and a 7 T MRI system. *Phys Med Biol*. (2018) 63:095002. doi: 10.1088/1361-6560/aab9d1
46. Schug D, Lerche C, Weissler B, Gebhardt P, Goldschmidt B, Wehner J, et al. Initial PET performance evaluation of a preclinical insert for PET/MRI with digital SiPM technology. *Phys Med Biol*. (2016) 61:2851–78. doi: 10.1088/0031-9155/61/7/2851
47. Stortz G, Thiessen JD, Bishop D, Khan MS, Kozlowski P, Retière F, et al. Performance of a PET insert for high-resolution small-animal PET/MRI at 7 tesla. *J Nucl Med*. (2018) 59:536–42. doi: 10.2967/jnumed.116.187666
48. Liu Z, Cheng T, Düwel S, Jian Z, Topping GJ, Steiger K, et al. Proof of concept of a multimodal intravital molecular imaging system for tumour transpathology investigation. *Eur J Nucl Med Mol Imaging*. (2021). doi: 10.1007/s00259-021-05574-y [Epub ahead of print].
49. Ntziachristos V, Tung CH, Bremer C, Weissleder R. Fluorescence molecular tomography resolves protease activity *in vivo*. *Nat Med*. (2002) 8:757–60. doi: 10.1038/nm729
50. Hyde D, de Kleine R, MacLaurin SA, Miller E, Brooks DH, Krucker T, et al. Hybrid FMT-CT imaging of amyloid-beta plaques in a murine Alzheimer's disease model. *Neuroimage*. (2009) 44:1304–11. doi: 10.1016/j.neuroimage.2008.10.038
51. Ale A, Ermolayev V, Herzog E, Cohrs C, de Angelis MH, Ntziachristos V. FMT-XCT: *in vivo* animal studies with hybrid fluorescence molecular tomography-X-ray computed tomography. *Nat Methods*. (2012) 9:615–20. doi: 10.1038/nmeth.2014
52. Li BQ, Maafi F, Berti R, Pouliot P, Rheume E, Tardif JC, et al. Hybrid FMT-MRI applied to *in vivo* atherosclerosis imaging. *Biomed Opt Express*. (2014) 5:1664–76. doi: 10.1364/BOE.5.001664
53. Ren W, Isler H, Wolf M, Ripoll J, Rudin M. Smart toolkit for fluorescence tomography: simulation, reconstruction, and validation. *IEEE Trans Biomed Eng*. (2020) 67:16–26. doi: 10.1109/TBME.2019.2907460
54. Ren W, Jiang J, Costanzo Mata AD, Kalyanov A, Ripoll J, Lindner S, et al. Multimodal imaging combining time-domain near-infrared optical tomography and continuous-wave fluorescence molecular tomography. *Opt Express*. (2020) 28:9860–74. doi: 10.1364/OE.385392
55. Ale A, Ermolayev V, Deliolanis NC, Ntziachristos V. Fluorescence background subtraction technique for hybrid fluorescence molecular tomography/x-ray computed tomography imaging of a mouse model of early stage lung cancer. *J Biomed Opt*. (2013) 18:56006. doi: 10.1117/1.JBO.18.5.056006
56. Mohajerani P, Hipp A, Willner M, Marschner M, Trajkovic-Arsic M, Ma X, et al. FMT-PCCT: hybrid fluorescence molecular tomography-x-ray phase-contrast CT imaging of mouse models. *IEEE Trans Med Imaging*. (2014) 33:1434–46. doi: 10.1109/TMI.2014.2313405

57. Niedre M, Ntziachristos V. Elucidating structure and function *in vivo* with hybrid fluorescence and magnetic resonance imaging. *Proc IEEE*. (2008) 96:382–96. doi: 10.1109/jproc.2007.913498
58. Ren W, Ni R, Vaas M, Klohs J, Ripoll J, Wolf M, et al. Non-invasive visualization of amyloid-beta deposits in Alzheimer amyloidosis mice using magnetic resonance imaging and fluorescence molecular tomography. *bioRxiv*. (2021) [Preprint]. doi: 10.1101/2021.11.20.466221
59. Schulz RB, Ale A, Sarantopoulos A, Freyer M, Soehngen E, Zientkowska M, et al. Hybrid system for simultaneous fluorescence and x-ray computed tomography. *IEEE Trans Med Imaging*. (2010) 29:465–73. doi: 10.1109/TMI.2009.2035310
60. Davis SC, Samkoe KS, Tichauer KM, Sexton KJ, Gunn JR, Deharvengt SJ, et al. Dynamic dual-tracer MRI-guided fluorescence tomography to quantify receptor density *in vivo*. *Proc Natl Acad Sci USA*. (2013) 110:9025–30. doi: 10.1073/pnas.1213490110
61. Stuker F, Baltes C, Dikaïou K, Vats D, Carrara L, Charbon E, et al. Hybrid small animal imaging system combining magnetic resonance imaging with fluorescence tomography using single photon avalanche diode detectors. *IEEE Trans Med Imaging*. (2011) 30:1265–73. doi: 10.1109/TMI.2011.2112669
62. Davis SC, Samkoe KS, O'Hara JA, Gibbs-Strauss SL, Paulsen KD, Pogue BW. Comparing implementations of magnetic-resonance-guided fluorescence molecular tomography for diagnostic classification of brain tumors. *J Biomed Opt*. (2010) 15:051602. doi: 10.1117/1.3483902
63. Ren W, Elmer A, Buehlmann D, Augath M-A, Vats D, Ripoll J, et al. Dynamic measurement of tumor vascular permeability and perfusion using a hybrid system for simultaneous magnetic resonance and fluorescence imaging. *Mol Imaging Biol*. (2016) 18:191–200. doi: 10.1007/s11307-015-0884-y
64. Meng B, Folaron MR, Strawbridge RR, Sadeghipour N, Samkoe KS, Tichauer K, et al. Noninvasive quantification of target availability during therapy using paired-agent fluorescence tomography. *Theranostics*. (2020) 10:11230–43. doi: 10.7150/thno.45273
65. Kneipp M, Turner J, Estrada H, Rebling J, Shoham S, Razansky D. Effects of the murine skull in optoacoustic brain microscopy. *J Biophotonics*. (2016) 9:117–23. doi: 10.1002/jbio.201400152
66. Wang LV, Hu S. Photoacoustic tomography: *in vivo* imaging from organelles to organs. *Science*. (2012) 335:1458. doi: 10.1126/science.1216210
67. Gottschalk S, Degtyaruk O, Mc Larney B, Rebling J, Hutter MA, Deán-Ben XL, et al. Rapid volumetric optoacoustic imaging of neural dynamics across the mouse brain. *Nat Biomed Eng*. (2019) 3:392–401.
68. Lv J, Li S, Zhang J, Duan F, Wu Z, Chen R, et al. *In vivo* photoacoustic imaging dynamically monitors the structural and functional changes of ischemic stroke at a very early stage. *Theranostics*. (2020) 10:816–28. doi: 10.7150/thno.38554
69. Ni R, Rudin M, Klohs J. Cortical hypoperfusion and reduced cerebral metabolic rate of oxygen in the arcA β mouse model of Alzheimer's disease. *Photoacoustics*. (2018) 10:38–47. doi: 10.1016/j.pacs.2018.04.001
70. Ni R, Villosio A, Dean-Ben XL, Chen Z, Vaas M, Stavakis S, et al. In-vitro and in-vivo characterization of CRANAD-2 for multi-spectral optoacoustic tomography and fluorescence imaging of amyloid-beta deposits in Alzheimer mice. *Photoacoustics*. (2021) 23:100285. doi: 10.1016/j.pacs.2021.100285
71. Lafci B, Mercep E, Morscher S, Dean-Ben XL, Razansky D. Deep learning for automatic segmentation of hybrid optoacoustic ultrasound (OPUS) images. *IEEE Trans Ultrason Ferroelectr Freq Control PP*. (2020) 68:688–96. doi: 10.1109/TUFFC.2020.3022324
72. McNally LR, Mezera M, Morgan DE, Frederick PJ, Yang ES, Eltoum IE, et al. Current and emerging clinical applications of multispectral optoacoustic tomography (MSOT) in oncology. *Clin Cancer Res*. (2016) 22:3432–9. doi: 10.1158/1078-0432.CCR-16-0573
73. Mercep E, Dean-Ben XL, Razansky D. Combined pulse-echo ultrasound and multispectral optoacoustic tomography with a multi-segment detector array. *IEEE Trans Med Imaging*. (2017) 36:2129–37. doi: 10.1109/TMI.2017.2706200
74. Cheng Y, Lu T, Wang YD, Song YL, Wang SY, Lu QL, et al. Glutathione-mediated clearable nanoparticles based on ultrasmall Gd₂O₃ for MSOT/CT/MR imaging guided photothermal/radio combination cancer therapy. *Mol Pharmaceut*. (2019) 16:3489–501. doi: 10.1021/acs.molpharmaceut.9b00332
75. Ke KM, Yang W, Xie XL, Liu R, Wang LL, Lin WW, et al. Copper manganese sulfide nanoplates: a new two-dimensional theranostic nanoplateform for MRI/MSOT dual-modal imaging-guided photothermal therapy in the second near-infrared window. *Theranostics*. (2017) 7:4763–76. doi: 10.7150/thno.21694
76. Song YL, Wang YL, Zhu Y, Cheng Y, Wang YD, Wang SY, et al. Biomodal tumor-targeted and redox-responsive Bi₂Se₃ hollow nanocubes for MSOT/CT imaging guided synergistic low-temperature photothermal radiotherapy. *Adv Healthc Mater*. (2019) 8:e1900250. doi: 10.1002/adhm.201900250
77. Vaas M, Ni R, Rudin M, Kipar A, Klohs J. Extracerebral tissue damage in the intraluminal filament mouse model of middle cerebral artery occlusion. *Front Neurol*. (2017) 8:85. doi: 10.3389/fneur.2017.00085
78. Wang SY, You Q, Wang JP, Song YL, Cheng Y, Wang YD, et al. MSOT/CT/MR imaging-guided and hypoxia-maneuvered oxygen self-supply radiotherapy based on one-pot MnO₂-mSiO₂(2)/Au nanoparticles. *Nanoscale*. (2019) 11:6270–84. doi: 10.1039/c9nr00918c
79. Yang S, You Q, Yang LF, Li PS, Lu QL, Wang SY, et al. Rodlike MSN@Au nanohybrid-modified supermolecular photosensitizer for NIRF/MSOT/CT/MR quadmodal imaging-guided photothermal/photodynamic cancer therapy. *Acs Appl Mater Inter*. (2019) 11:6777–88. doi: 10.1021/acsami.8b19565
80. Ni R, Dean-Ben XL, Kirschenbaum D, Rudin M, Chen Z, Crimi A, et al. Whole brain optoacoustic tomography reveals strain-specific regional beta-amyloid densities in Alzheimer's disease amyloidosis models. *bioRxiv*. (2020) [Preprint]. doi: 10.1101/2020.02.25.964064
81. Zhang S, Qi L, Li X, Liang Z, Wu J, Huang S, et al. *In vivo* co-registered hybrid-contrast imaging by successive photoacoustic tomography and magnetic resonance imaging. *bioRxiv* (2021) [Preprint]. doi: 10.1101/2021.03.06.434031
82. Attia ABE, Ho CJH, Chandrasekharan P, Balasundaram G, Tay HC, Burton NC, et al. Multispectral optoacoustic and MRI coregistration for molecular imaging of orthotopic model of human glioblastoma. *J Biophotonics*. (2016) 9:701–8. doi: 10.1002/jbio.201500321
83. Ni R, Vaas M, Ren W, Klohs J. Noninvasive detection of acute cerebral hypoxia and subsequent matrix-metalloproteinase activity in a mouse model of cerebral ischemia using multispectral-optoacoustic-tomography. *Neurophotonics*. (2018) 5:015005. doi: 10.1117/1.NPh.5.1.015005
84. Ren W, Skulason H, Schlegel F, Rudin M, Klohs J, Ni R. Automated registration of magnetic resonance imaging and optoacoustic tomography data for experimental studies. *Neurophotonics*. (2019) 6:025001. doi: 10.1117/1.NPh.6.2.025001
85. Vagenknecht P, Luzgin A, Ono M, Ji B, Higuchi M, Noain D, et al. Non-invasive imaging of tau-targeted probe uptake by whole brain multi-spectral optoacoustic tomography. *Eur J Nucl Med Mol Imaging*. (2022). doi: 10.1007/s00259-022-05708-w [Epub ahead of print].
86. Gehrung M, Tomaszewski M, McIntyre D, Disselhorst J, Bohnndiek S. Co-registration of optoacoustic tomography and magnetic resonance imaging data from murine tumour models. *Photoacoustics*. (2020) 18:100147. doi: 10.1016/j.pacs.2019.100147
87. Ren W, Dean-Ben XL, Augath MA, Razansky D. Development of concurrent magnetic resonance imaging and volumetric optoacoustic tomography: a phantom feasibility study. *J Biophotonics*. (2021) 14:e202000293. doi: 10.1002/jbio.202000293
88. Blockley NP, Griffith VEM, Simon AB, Buxton RB. A review of calibrated blood oxygenation level-dependent (BOLD) methods for the measurement of task-induced changes in brain oxygen metabolism. *Nmr Biomed*. (2013) 26:987–1003. doi: 10.1002/nbm.2847
89. Garcia-Urbe A, Erpelding TN, Krumholz A, Ke H, Maslov K, Appleton C, et al. Dual-modality photoacoustic and ultrasound imaging system for noninvasive sentinel lymph node detection in patients with breast cancer. *Sci Rep*. (2015) 5:15748. doi: 10.1038/srep15748
90. Knieling F, Neufert C, Hartmann A, Claussen J, Urlich A, Egger C, et al. Multispectral optoacoustic tomography for assessment of crohn's disease activity. *N Engl J Med*. (2017) 376:1292–4. doi: 10.1056/NEJMc1612455
91. Masthoff M, Helfen A, Claussen J, Karlas A, Markwardt NA, Ntziachristos V, et al. Use of multispectral optoacoustic tomography to diagnose

- vascular malformations. *JAMA Dermatol.* (2018) 154:1457–62. doi: 10.1001/jamadermatol.2018.3269
92. Chang K-W, Zhu Y, Hudson HM, Barbay S, Guggenmos DJ, Nudo RJ, et al. Photoacoustic imaging of squirrel monkey cortical and subcortical brain regions during peripheral electrical stimulation. *Photoacoustics.* (2022) 25:100326. doi: 10.1016/j.pacs.2021.100326
 93. Mahmoodkalayeh S, Kratkiewicz K, Manwar R, Shahbazi M, Ansari MA, Natarajan G, et al. Wavelength and pulse energy optimization for detecting hypoxia in photoacoustic imaging of the neonatal brain: a simulation study. *Biomed Opt Express.* (2021) 12:7458–77. doi: 10.1364/BOE.439147
 94. Na S, Russin JJ, Lin L, Yuan X, Hu P, Jann KB, et al. Massively parallel functional photoacoustic computed tomography of the human brain. *Nat Biomed Eng.* (2021). doi: 10.1038/s41551-021-00735-8 [Epub ahead of print].
 95. Na S, Wang LV. Photoacoustic computed tomography for functional human brain imaging [Invited]. *Biomed Opt Express.* (2021) 12:4056–83. doi: 10.1364/BOE.423707
 96. Nie L, Cai X, Maslov K, Garcia-Urbe A, Anastasio MA, Wang LV. Photoacoustic tomography through a whole adult human skull with a photon recycler. *J Biomed Opt.* (2012) 17:110506. doi: 10.1117/1.JBO.17.11.110506
 97. Blocker SJ, Mowery YM, Holbrook MD, Qi Y, Kirsch DG, Johnson GA, et al. Bridging the translational gap: implementation of multimodal small animal imaging strategies for tumor burden assessment in a co-clinical trial. *PLoS One.* (2019) 14:e0207555. doi: 10.1371/journal.pone.0207555
 98. O'Connor JPB, Aboagye EO, Adams JE, Aerts HJWL, Barrington SF, Beer AJ, et al. Imaging biomarker roadmap for cancer studies. *Nat Rev Clin Oncol.* (2017) 14:169–86. doi: 10.1038/nrclinonc.2016.162
 99. Kaufmann TJ, Smits M, Boxerman J, Huang R, Barboriak DP, Weller M, et al. Consensus recommendations for a standardized brain tumor imaging protocol for clinical trials in brain metastases. *Neuro Oncol.* (2020) 22:757–72. doi: 10.1093/neuonc/noaa030
 100. Waterhouse DJ, Fitzpatrick CRM, Pogue BW, O'Connor JPB, Bohndiek SE. A roadmap for the clinical implementation of optical-imaging biomarkers. *Nat Biomed Eng.* (2019) 3:339–53. doi: 10.1038/s41551-019-0392-5
 101. Shaw RC, Tamagnan GD, Tavares AAS. Rapidly (and Successfully) translating novel brain radiotracers from animal research into clinical use. *Front Neurosci.* (2020) 14:871. doi: 10.3389/fnins.2020.00871
 102. Rothstein JD. Of mice and men: reconciling preclinical ALS mouse studies and human clinical trials. *Ann Neurol.* (2003) 53:423–6. doi: 10.1002/ana.10561
 103. de Jong M, Essers J, van Weerden WM. Imaging preclinical tumour models: improving translational power. *Nat Rev Cancer.* (2014) 14:481–93. doi: 10.1038/nrc3751
 104. Zahs KR, Ashe KH. 'Too much good news' – are Alzheimer mouse models trying to tell us how to prevent, not cure, Alzheimer's disease? *Trends Neurosci.* (2010) 33:381–9. doi: 10.1016/j.tins.2010.05.004
 105. Beaulieu-Laroche L, Brown NJ, Hansen M, Toloza EHS, Sharma J, Williams ZM, et al. Allometric rules for mammalian cortical layer 5 neuron biophysics. *Nature.* (2021) 600:274–8. doi: 10.1038/s41586-021-04072-3
 106. Van Essen DC, Donahue CJ, Coalson TS, Kennedy H, Hayashi T, Glasser MF. Cerebral cortical folding, parcellation, and connectivity in humans, nonhuman primates, and mice. *Proc Natl Acad Sci USA.* (2019) 116:26173–80. doi: 10.1073/pnas.1902299116
 107. Li J, Pan L, Pembroke WG, Rexach JE, Godoy MI, Condro MC, et al. Conservation and divergence of vulnerability and responses to stressors between human and mouse astrocytes. *Nat Commun.* (2021) 12:3958. doi: 10.1038/s41467-021-24232-3
 108. Zhou Y, Song WM, Andhey PS, Swain A, Levy T, Miller KR, et al. Human and mouse single-nucleus transcriptomics reveal TREM2-dependent and TREM2-independent cellular responses in Alzheimer's disease. *Nat Med.* (2020) 26:131–42. doi: 10.1038/s41591-019-0695-9
 109. Zhang Y, Sloan SA, Clarke LE, Caneda C, Plaza CA, Blumenthal PD, et al. Purification and characterization of progenitor and mature human astrocytes reveals transcriptional and functional differences with mouse. *Neuron.* (2016) 89:37–53. doi: 10.1016/j.neuron.2015.11.013
 110. Majid A, He YY, Gidday JM, Kaplan SS, Gonzales ER, Park TS, et al. Differences in vulnerability to permanent focal cerebral ischemia among 3 common mouse strains. *Stroke.* (2000) 31:2707–14. doi: 10.1161/01.str.31.11.2707
 111. Zhao L, Mulligan MK, Nowak TS Jr. Substrain- and sex-dependent differences in stroke vulnerability in C57BL/6 mice. *J Cereb Blood Flow Metab.* (2019) 39:426–38. doi: 10.1177/0271678X17746174
 112. Bailey RM, Howard J, Knight J, Sahara N, Dickson DW, Lewis J. Effects of the C57BL/6 strain background on tauopathy progression in the rTg4510 mouse model. *Mol Neurodegener.* (2014) 9:8. doi: 10.1186/1750-1326-9-8
 113. Walker LC, Jucker M. The exceptional vulnerability of humans to Alzheimer's disease. *Trends Mol Med.* (2017) 23:534–45. doi: 10.1016/j.molmed.2017.04.001
 114. Denny P, Justice MJ. Mouse as the measure of man? *Trends Genet.* (2000) 16:283–7. doi: 10.1016/s0168-9525(00)02039-4
 115. Holec SAM, Woerman AL. Evidence of distinct α -synuclein strains underlying disease heterogeneity. *Acta Neuropathol.* (2021) 142:73–86. doi: 10.1007/s00401-020-02163-5
 116. Ni R, Ji B, Ono M, Sahara N, Zhang MR, Aoki I, et al. Comparative *in vitro* and *in vivo* quantifications of pathologic tau deposits and their association with neurodegeneration in tauopathy mouse models. *J Nucl Med.* (2018) 59:960–6. doi: 10.2967/jnumed.117.201632
 117. Rosen RF, Walker LC, Levine H III. PIB binding in aged primate brain: enrichment of high-affinity sites in humans with Alzheimer's disease. *Neurobiol Aging.* (2011) 32:223–34. doi: 10.1016/j.neurobiolaging.2009.02.011
 118. Jung KO, Kim TJ, Yu JH, Rhee S, Zhao W, Ha B, et al. Whole-body tracking of single cells via positron emission tomography. *Nat Biomed Eng.* (2020) 4:835–44. doi: 10.1038/s41551-020-0570-5
 119. Nutma E, Ceyzeriat K, Amor S, Tsartsalis S, Millet P, Owen DR, et al. Cellular sources of TSPO expression in healthy and diseased brain. *Eur J Nucl Med Mol Imaging.* (2021) 49:146–63. doi: 10.1007/s00259-020-05166-2
 120. Tournier BB, Tsartsalis S, Ceyzeriat K, Medina Z, Fraser BH, Grégoire MC, et al. Fluorescence-activated cell sorting to reveal the cell origin of radioligand binding. *J Cereb Blood Flow Metab.* (2020) 40:1242–55. doi: 10.1177/0271678X19860408
 121. Tremoleda JL, Kerton A, Gsell W. Anaesthesia and physiological monitoring during *in vivo* imaging of laboratory rodents: considerations on experimental outcomes and animal welfare. *EJNMMI Res.* (2012) 2:44. doi: 10.1186/2191-219X-2-44
 122. Deleye S, Waldron AM, Richardson JC, Schmidt M, Langlois X, Stroobants S, et al. The effects of physiological and methodological determinants on 18F-FDG mouse brain imaging exemplified in a double transgenic Alzheimer model. *Mol Imaging.* (2016) 15:1536012115624919. doi: 10.1177/1536012115624919
 123. Buchecker V, Waldron AM, van Dijk RM, Koska I, Brendel M, von Ungern-Sternberg B, et al. [(18)F]MPPF and [(18)F]FDG μ PET imaging in rats: impact of transport and restraint stress. *EJNMMI Res.* (2020) 10:112.
 124. Chen X, Tong C, Han Z, Zhang K, Bo B, Feng Y, et al. Sensory evoked fMRI paradigms in awake mice. *Neuroimage.* (2020) 204:116242. doi: 10.1016/j.neuroimage.2019.116242
 125. Kenkel WM, Yee JR, Moore K, Madularu D, Kulkarni P, Gamber K, et al. Functional magnetic resonance imaging in awake transgenic fragile X rats: evidence of dysregulation in reward processing in the mesolimbic/habenular neural circuit. *Transl Psychiatry.* (2016) 6:e763–763. doi: 10.1038/tp.2016.15
 126. Miranda A, Glorie D, Bertoglio D, Vleugels J, De Bruyne G, Stroobants S, et al. Awake (18)F-FDG PET Imaging of memantine-induced brain activation and test-retest in freely running mice. *J Nucl Med.* (2019) 60:844–50. doi: 10.2967/jnumed.118.218669
 127. Tsurugizawa T, Tamada K, Ono N, Karakawa S, Kodama Y, Debacker C, et al. Awake functional MRI detects neural circuit dysfunction in a mouse model of autism. *Sci Adv.* (2020) 6:eav4520. doi: 10.1126/sciadv.aav4520
 128. Wang G, Ye JC, Mueller K, Fessler JA. Image reconstruction is a new Frontier of machine learning. *IEEE Trans Med Imaging.* (2018) 37:1289–96. doi: 10.1109/TMI.2018.2833635
 129. Hakim A, Christensen S, Winzeck S, Lansberg MG, Parsons MW, Lucas C, et al. Predicting infarct core from computed tomography perfusion in acute ischemia with machine learning: lessons from the ISLES challenge. *Stroke.* (2021) 52:2328–37. doi: 10.1161/STROKEAHA.120.030696

130. Katabathula S, Wang Q, Xu R. Predict Alzheimer's disease using hippocampus MRI data: a lightweight 3D deep convolutional network model with visual and global shape representations. *Alzheimers Res Ther.* (2021) 13:104. doi: 10.1186/s13195-021-00837-0
131. Todorov MI, Paetzold JC, Schoppe O, Tetteh G, Shit S, Efremov V, et al. Machine learning analysis of whole mouse brain vasculature. *Nat Methods.* (2020) 17:442–9. doi: 10.1038/s41592-020-0792-1
132. Lein ES, Hawrylycz MJ, Ao N, Ayres M, Bensinger A, Bernard A, et al. Genome-wide atlas of gene expression in the adult mouse brain. *Nature.* (2007) 445:168–76.
133. Niedworok CJ, Brown APY, Jorge Cardoso M, Osten P, Ourselin S, Modat M, et al. aMAP is a validated pipeline for registration and segmentation of high-resolution mouse brain data. *Nat Commun.* (2016) 7:11879. doi: 10.1038/ncomms11879
134. Song JH, Choi W, Song Y-H, Kim J-H, Jeong D, Lee S-H, et al. Precise mapping of single neurons by calibrated 3D reconstruction of brain slices reveals topographic projection in mouse visual cortex. *Cell Rep.* (2020) 31:107682. doi: 10.1016/j.celrep.2020.107682
135. Esser SK, Merolla PA, Arthur JV, Cassidy AS, Appuswamy R, Andreopoulos A, et al. Convolutional networks for fast, energy-efficient neuromorphic computing. *Proc Natl Acad Sci USA.* (2016) 113:11441–6. doi: 10.1073/pnas.1604850113
136. Ithapu VK, Singh V, Okonkwo OC, Chappell RJ, Dowling NM, Johnson SC. Imaging-based enrichment criteria using deep learning algorithms for efficient clinical trials in mild cognitive impairment. *Alzheimers Dement.* (2015) 11:1489–99. doi: 10.1016/j.jalz.2015.01.010
137. LeCun Y, Bengio Y, Hinton G. Deep learning. *Nature.* (2015) 521:436–44.
138. Sengupta S, Basak S, Saikia P, Paul S, Tsalavoutis V, Atiah F, et al. A review of deep learning with special emphasis on architectures, applications and recent trends. *Knowl Based Syst.* (2020) 194:105596. doi: 10.3892/ijo.2020.5063
139. Suk HI, Lee SW, Shen D. Latent feature representation with stacked auto-encoder for AD/MCI diagnosis. *Brain Struct Funct.* (2015) 220:841–59. doi: 10.1007/s00429-013-0687-3
140. Avants BB, Tustison N, Song G. Advanced normalization tools (ANTS). *Insight J.* (2009) 2:1–35. doi: 10.1007/s11682-020-00319-1
141. Cox RW. AFNI: software for analysis and visualization of functional magnetic resonance neuroimages. *Comput Biomed Res.* (1996) 29:162–73.
142. Penny WD, Friston KJ, Ashburner JT, Kiebel SJ, Nichols TE. *Statistical Parametric Mapping: The Analysis of Functional Brain Images.* Amsterdam: Elsevier (2011).
143. Hu Y, Lafci B, Luzgin A, Wang H, Klohs J, Dean-Ben XL, et al. Deep learning facilitates fully automated brain image registration of optoacoustic tomography and magnetic resonance imaging. *arXiv.* (2021) [Preprint]. arXiv:2109.01880.
144. Argelaguet R, Cuomo ASE, Stegle O, Marioni JC. Computational principles and challenges in single-cell data integration. *Nat Biotechnol.* (2021) 39:1202–15. doi: 10.1038/s41587-021-00895-7
145. Dhar R, Falcone GJ, Chen Y, Hamzehloo A, Kirsch EP, Noche RB, et al. Deep learning for automated measurement of hemorrhage and perihematomal edema in supratentorial intracerebral hemorrhage. *Stroke.* (2020) 51:648–51. doi: 10.1161/STROKEAHA.119.027657
146. Yu Y, Xie Y, Thammi T, Gong E, Ouyang J, Huang C, et al. Use of deep learning to predict final ischemic stroke lesions from initial magnetic resonance imaging. *JAMA Netw Open.* (2020) 3:e200772. doi: 10.1001/jamanetworkopen.2020.0772
147. Tecott LH. The genes and brains of mice and men. *Am J Psychiatry.* (2003) 160:646–56. doi: 10.1176/appi.ajp.160.4.646
148. Adewale Q, Khan AF, Carbonell F, Iturria-Medina Y. Integrated transcriptomic and neuroimaging brain model decodes biological mechanisms in aging and Alzheimer's disease. *Elife.* (2021) 10:e62589. doi: 10.7554/eLife.62589
149. Martins D, Giacometti A, Williams S, Turkheimer F, Dipasquale O, Veronese M. Imaging transcriptomics: Convergent cellular, transcriptomic, and molecular neuroimaging signatures in the healthy adult human brain. *Cell Rep.* (2021) 37:110173. doi: 10.1016/j.celrep.2021.110173
150. Ximerakis M, Lipnick SL, Innes BT, Simmons SK, Adiconis X, Dionne D, et al. Single-cell transcriptomic profiling of the aging mouse brain. *Nat Neurosci.* (2019) 22:1696–708. doi: 10.1038/s41593-019-0491-3
151. Zhang Y, Chen K, Sloan SA, Bennett ML, Scholze AR, Keefe S, et al. An RNA-sequencing transcriptome and splicing database of glia, neurons, and vascular cells of the cerebral cortex. *J Neurosci.* (2014) 34:11929. doi: 10.1523/JNEUROSCI.1860-14.2014
152. Girgenti MJ, Wang J, Ji D, Cruz DA, Alvarez VE, Benedek D. Transcriptomic organization of the human brain in post-traumatic stress disorder. *Nat Neurosci.* (2021) 24:24–33. doi: 10.1038/s41593-020-00748-7
153. Su JH, Zheng P, Kinrot SS, Bintu B, Zhuang X. Genome-scale imaging of the 3D organization and transcriptional activity of chromatin. *Cell.* (2020) 182:1641.e–59.e. doi: 10.1016/j.cell.2020.07.032
154. Tasic B, Yao Z, Graybiuck LT, Smith KA, Nguyen TN, Bertagnolli D, et al. Shared and distinct transcriptomic cell types across neocortical areas. *Nature.* (2018) 563:72–8. doi: 10.1038/s41586-018-0654-5
155. Messinger A, Sirmipilatz N, Heuer K, Loh KK, Mars RB, Sein J, et al. A collaborative resource platform for non-human primate neuroimaging. *NeuroImage.* (2021) 226:117519. doi: 10.1016/j.neuroimage.2020.117519
156. Biechele G, Franzmeier N, Blume T, Ewers M, Luque JM, Eckenweber F, et al. Glial activation is moderated by sex in response to amyloidosis but not to tau pathology in mouse models of neurodegenerative diseases. *J Neuroinflammation.* (2020) 17:374. doi: 10.1186/s12974-020-02046-2
157. Chan SR, Salem K, Jeffery J, Powers GL, Yan Y, Shoghi KI, et al. Sex as a biologic variable in preclinical imaging research: initial observations with (18)F-FLT. *J Nucl Med.* (2018) 59:833–8. doi: 10.2967/jnumed.117.199406
158. Hu Y, Xu Q, Li K, Zhu H, Qi R, Zhang Z, et al. Gender differences of brain glucose metabolic networks revealed by FDG-PET: evidence from a large cohort of 400 young adults. *PLoS One* (2013) 8:e83821. doi: 10.1371/journal.pone.0083821
159. Homberg JR, Adan RAH, Alenina N, Asiminas A, Bader M, Beckers T, et al. The continued need for animals to advance brain research. *Neuron.* (2021) 109:2374–9. doi: 10.1016/j.neuron.2021.07.015
160. Ma C, Peng Y, Li H, Chen W. Organ-on-a-chip: a new paradigm for drug development. *Trends Pharmacol Sci.* (2021) 42:119–33. doi: 10.1016/j.tips.2020.11.009
161. Bergmann S, Lawler SE, Qu Y, Fadzen CM, Wolfe JM, Regan MS, et al. Blood-brain-barrier organoids for investigating the permeability of CNS therapeutics. *Nat Protoc.* (2018) 13:2827–43. doi: 10.1038/s41596-018-0066-x
162. Bhatia SN, Ingber DE. Microfluidic organs-on-chips. *Nat Biotechnol.* (2014) 32:760–72.
163. Herland A, Maoz BM, Das D, Somayaji MR, Prantil-Baun R, Novak R, et al. Quantitative prediction of human pharmacokinetic responses to drugs via fluidically coupled vascularized organ chips. *Nat Biomed Eng.* (2020) 4:421–36.
164. Liu Z, Jian Z, Wang Q, Cheng T, Feueracker B, Schwaiger M, et al. A continuously infused microfluidic radioassay system for the characterization of cellular pharmacokinetics. *J Nucl Med.* (2016) 57:1548–55. doi: 10.2967/jnumed.115.169151
165. Kim TJ, Ha B, Bick AD, Kim M, Tang SKY, Pratz G. Microfluidics-coupled radioluminescence microscopy for *in vitro* radiotracer kinetic studies. *Anal Chem.* (2021) 93:4425–33. doi: 10.1021/acs.analchem.0c04321
166. Gallina ME, Kim TJ, Shelor M, Vasquez J, Mongersun A, Kim M, et al. Toward a droplet-based single-cell radiometric assay. *Anal Chem.* (2017) 89:6472–81. doi: 10.1021/acs.analchem.7b00414
167. Banerjee A, Parente G, Teutsch J, Lewis C, Voigt FF, Helmchen F. Value-guided remapping of sensory cortex by lateral orbitofrontal cortex. *Nature.* (2020) 585:245–50. doi: 10.1038/s41586-020-2704-z
168. Barson D, Hamodi AS, Shen X, Lur G, Constable RT, Cardin JA, et al. Simultaneous mesoscopic and two-photon imaging of neuronal activity in cortical circuits. *Nat Methods.* (2020) 17:107–13. doi: 10.1038/s41592-019-0625-2
169. Bottes S, Jaeger BN, Pilz GA, Jörg DJ, Cole JD, Kruse M, et al. Long-term self-renewing stem cells in the adult mouse hippocampus identified by intravital imaging. *Nat Neurosci.* (2021) 24:225–33. doi: 10.1038/s41593-020-00759-4
170. Jun JJ, Steinmetz NA, Siegle JH, Denman DJ, Bauza M, Barbarits B, et al. Fully integrated silicon probes for high-density recording of neural activity. *Nature.* (2017) 551:232–6. doi: 10.1038/nature24636

171. Pilz GA, Bottes S, Betizeau M, Jörg DJ, Carta S, Simons BD, et al. Live imaging of neurogenesis in the adult mouse hippocampus. *Science*. (2018) 359:658–62. doi: 10.1126/science.aao5056
172. Seiriki K, Kasai A, Hashimoto T, Schulze W, Niu M, Yamaguchi S, et al. High-speed and scalable whole-brain imaging in rodents and primates. *Neuron*. (2017) 94:1085.e–100.e. doi: 10.1016/j.neuron.2017.05.017
173. Sun Q, Li X, Ren M, Zhao M, Zhong Q, Ren Y, et al. A whole-brain map of long-range inputs to GABAergic interneurons in the mouse medial prefrontal cortex. *Nat Neurosci*. (2019) 22:1357–70. doi: 10.1038/s41593-019-0429-9
174. Wang T, Ouzounov DG, Wu C, Horton NG, Zhang B, Wu CH, et al. Three-photon imaging of mouse brain structure and function through the intact skull. *Nat Methods*. (2018) 15:789–92. doi: 10.1038/s41592-018-0115-y
175. Zong W, Wu R, Chen S, Wu J, Wang H, Zhao Z, et al. Miniature two-photon microscopy for enlarged field-of-view, multi-plane and long-term brain imaging. *Nat Methods*. (2021) 18:46–9.
176. Hedges EP, Dimitrov M, Zahid U, Vega BB, Si S, Dickson H, et al. Reliability of structural MRI measurements: the effects of scan session, head tilt, inter-scan interval, acquisition sequence, FreeSurfer version and processing stream. *Neuroimage*. (2021) 246:118751. doi: 10.1016/j.neuroimage.2021.118751
177. Percie du Sert N, Ahluwalia A, Alam S, Avey MT, Baker M, Browne WJ, et al. Reporting animal research: Explanation and elaboration for the ARRIVE guidelines 2.0. *PLoS Biol*. (2020) 18:e3000411. doi: 10.1371/journal.pbio.3000411
178. Percie du Sert N, Hurst V, Ahluwalia A, Alam S, Avey MT, Baker M, et al. The ARRIVE guidelines 2.0: updated guidelines for reporting animal research. *PLoS Biol*. (2020) 18:e3000410.
179. Reimann HM, Niendorf T. The (Un)conscious mouse as a model for human brain functions: key principles of anesthesia and their impact on translational neuroimaging. *Front Syst Neurosci*. (2020) 14:8. doi: 10.3389/fnsys.2020.00008
180. Steiner AR, Rousseau-Blass F, Schroeter A, Hartnack S, Bettschart-Wolfensberger R. Systematic review: anaesthetic protocols and management as confounders in rodent blood oxygen level dependent functional magnetic resonance imaging (BOLD fMRI)—part A: effects of changes in physiological parameters. *Front Neurosci*. (2020) 14:577119.
181. Steiner AR, Rousseau-Blass F, Schroeter A, Hartnack S, Bettschart-Wolfensberger R. Systematic review: anesthetic protocols and management as confounders in rodent blood oxygen level dependent functional magnetic resonance imaging (BOLD fMRI)—part B: effects of anesthetic agents, doses and timing. *Animals*. (2021) 11:199. doi: 10.3390/ani11010199
182. McDougald W, Vanhove C, Lehnert A, Lewellen B, Wright J, Mingarelli M, et al. Standardization of preclinical PET/CT imaging to improve quantitative accuracy, precision, and reproducibility: a multicenter study. *J Nucl Med*. (2020) 61:461–8. doi: 10.2967/jnumed.119.231308
183. Osborne DR, Kuntner C, Berr S, Stout D. Guidance for efficient small animal imaging quality control. *Mol Imaging Biol*. (2017) 19:485–98.
184. Botvinik-Nezer R, Holzmeister F, Camerer CF, Dreber A, Huber J, Johannesson M, et al. Variability in the analysis of a single neuroimaging dataset by many teams. *Nature*. (2020) 582:84–8.
185. Li X, Ai L, Giavasis S, Jin H, Feczko E, Xu T, et al. Moving beyond processing and analysis-related variation in neuroscience. *bioRxiv*. (2021) [Preprint]. doi: 10.1101/2021.12.01.470790
186. Grandjean J, Canella C, Anckaerts C, Ayranci G, Bougacha S, Bienert T, et al. Common functional networks in the mouse brain revealed by multi-centre resting-state fMRI analysis. *Neuroimage*. (2020) 205:116278.
187. Gau R, Noble S, Heuer K, Bottenhorn KL, Bilgin IP, Yang YF, et al. Brainhack: Developing a culture of open, inclusive, community-driven neuroscience. *Neuron*. (2021) 109:1769–75.
188. Poldrack RA, Gorgolewski KJ. Making big data open: data sharing in neuroimaging. *Nat Neurosci*. (2014) 17:1510–7.
189. Petersen RC, Aisen PS, Beckett LA, Donohue MC, Gamst AC, Harvey DJ, et al. Alzheimer's disease neuroimaging initiative (ADNI): clinical characterization. *Neurology*. (2010) 74:201–9.
190. Markiewicz CJ, Gorgolewski KJ, Feingold F, Blair R, Halchenko YO, Miller E, et al. The OpenNeuro resource for sharing of neuroscience data. *Elife*. (2021) 10:e71774.
191. Van Essen DC, Smith SM, Barch DM, Behrens TE, Yacoub E, Ugurbil K. The WU-minn human connectome project: an overview. *Neuroimage*. (2013) 80:62–79.
192. LaMontagne PJ, Benzinger TLS, Morris JC, Keefe S, Hornbeck R, Xiong C, et al. OASIS-3: longitudinal neuroimaging, clinical, and cognitive dataset for normal aging and alzheimer disease. *medRxiv*. (2019) [Preprint]. doi: 10.1101/2019.12.13.19014902
193. Gorgolewski KJ, Auer T, Calhoun VD, Craddock RC, Das S, Duff EP, et al. The brain imaging data structure, a format for organizing and describing outputs of neuroimaging experiments. *Sci Data*. (2016) 3:160044.
194. Button KS, Ioannidis JPA, Mokrysz C, Nosek BA, Flint J, Robinson ESJ, et al. Power failure: why small sample size undermines the reliability of neuroscience. *Nat Rev Neurosci*. (2013) 14:365–76.

Conflict of Interest: LC is employed in Shanghai Changes Tech, Ltd.

The remaining authors declare that the research was conducted in the absence of any commercial or financial relationships that could be construed as a potential conflict of interest.

Publisher's Note: All claims expressed in this article are solely those of the authors and do not necessarily represent those of their affiliated organizations, or those of the publisher, the editors and the reviewers. Any product that may be evaluated in this article, or claim that may be made by its manufacturer, is not guaranteed or endorsed by the publisher.

Copyright © 2022 Ren, Ji, Guan, Cao and Ni. This is an open-access article distributed under the terms of the Creative Commons Attribution License (CC BY). The use, distribution or reproduction in other forums is permitted, provided the original author(s) and the copyright owner(s) are credited and that the original publication in this journal is cited, in accordance with accepted academic practice. No use, distribution or reproduction is permitted which does not comply with these terms.



Molecular Imaging of Aortic Aneurysm and Its Translational Power for Clinical Risk Assessment

Vinamr Rastogi^{1†}, Sanne J. M. Stefens^{2†}, Judith Houwaart², Hence J. M. Verhagen¹, Jorg L. de Bruin¹, Ingrid van der Pluijm^{1,2} and Jeroen Essers^{1,2,3*}

¹ Department of Vascular Surgery, Erasmus University Medical Center, Rotterdam, Netherlands, ² Department of Molecular Genetics, Erasmus University Medical Center, Rotterdam, Netherlands, ³ Department of Radiation Oncology, Erasmus University Medical Center, Rotterdam, Netherlands

OPEN ACCESS

Edited by:

Carmel Mary Moran,
University of Edinburgh,
United Kingdom

Reviewed by:

Karlheinz Peter,
Baker Heart and Diabetes
Institute, Australia
Marie-José Goumans,
Leiden University Medical
Center, Netherlands

*Correspondence:

Jeroen Essers
j.essers@erasmusmc.nl

[†]These authors have contributed
equally to this work

Specialty section:

This article was submitted to
Translational Medicine,
a section of the journal
Frontiers in Medicine

Received: 12 November 2021

Accepted: 21 March 2022

Published: 15 April 2022

Citation:

Rastogi V, Stefens SJM, Houwaart J, Verhagen HJM, de Bruin JL, van der Pluijm I and Essers J (2022) Molecular Imaging of Aortic Aneurysm and Its Translational Power for Clinical Risk Assessment. *Front. Med.* 9:814123. doi: 10.3389/fmed.2022.814123

Aortic aneurysms (AAs) are dilations of the aorta, that are often fatal upon rupture. Diagnostic radiological techniques such as ultrasound (US), magnetic resonance imaging (MRI), and computed tomography (CT) are currently used in clinical practice for early diagnosis as well as clinical follow-up for preemptive surgery of AA and prevention of rupture. However, the contemporary imaging-based risk prediction of aneurysm enlargement or life-threatening aneurysm-rupture remains limited as these are restricted to visual parameters which fail to provide a personalized risk assessment. Therefore, new insights into early diagnostic approaches to detect AA and therefore to prevent aneurysm-rupture are crucial. Multiple new techniques are developed to obtain a more accurate understanding of the biological processes and pathological alterations at a (micro)structural and molecular level of aortic degeneration. Advanced anatomical imaging combined with molecular imaging, such as molecular MRI, or positron emission tomography (PET)/CT provides novel diagnostic approaches for *in vivo* visualization of targeted biomarkers. This will aid in the understanding of aortic aneurysm disease pathogenesis and insight into the pathways involved, and will thus facilitate early diagnostic analysis of aneurysmal disease. In this study, we reviewed these molecular imaging modalities and their association with aneurysm growth and/or rupture risk and their limitations. Furthermore, we outline recent pre-clinical and clinical developments in molecular imaging of AA and provide future perspectives based on the advancements made within the field. Within the vastness of pre-clinical markers that have been studied in mice, molecular imaging targets such as elastin/collagen, albumin, matrix metalloproteinases and immune cells demonstrate promising results regarding rupture risk assessment within the pre-clinical setting. Subsequently, these markers hold potential as a future diagnosticum of clinical AA assessment. However currently, clinical translation of molecular imaging is still at the onset. Future human trials are required to assess the effectivity of potentially viable molecular markers with various imaging modalities for clinical rupture risk assessment.

Keywords: aortic aneurysm, aortic rupture, molecular imaging, biomarkers, disease models, animal, translational medical research

INTRODUCTION

Aortic Aneurysms (AA) are pathological dilations of the aorta, in which the diameter is enlarged to over 50% of its original size or over 30 mm (1, 2). Depending on their location, 'AAs' can be classified into either thoracic (TAA), thoracoabdominal (ThAAA), and abdominal aortic aneurysms (AAA). 'TAAs' are located within the chest cavity and are subclassified into aneurysms involving the aortic root, ascending aorta, aortic arch and/or the descending thoracic aorta. 'AAAs' are naturally located below the diaphragm within the abdomen, usually presenting at an infrarenal level (3). As such, ThAAA are extensive aortic dilations covering the aortic portion within both the chest and abdomen.

Whilst TAA has an estimated prevalence of 5.3 per 100,000 (0.0053%) within the Western world (4), AAA is more prevalent, affecting an estimate of 1.3–8.9% of males and 1.0–2.2% of females (5–8). Interestingly, for the development of TAAs, aortic dilatation of the root and ascending aorta are often attributed to single genetic defects, such as in Marfan syndrome (9) and Loeys-Dietz syndrome (10). This is in contrast to AAAs, in which lifestyle seems to have a major contribution to disease progression (11). Predominantly men above the age of 65 are at risk of developing AAA (11), and additional risk factors besides a genetic predisposition include those similar to other cardiovascular diseases such as smoking (12), age, hypertension and obesity (13).

Aortic aneurysms are fatal upon rupture and therefore life-threatening, elucidating the necessity of timely intervention. This has resulted in screening of moderate risk populations (males aged above 65 years with cardiovascular risk profile) in countries including England and Sweden, leading to a reduction in all-cause mortality (14), whilst cost-effectiveness is questioned (15). Nevertheless, AA diagnosis in most countries remains a concomitant incidental finding, as only a small fraction of AAs leads to symptoms. After detection of aortic aneurysmal disease, clinical risk assessment of rupture is only done by measuring maximum diameter resulting in a one-size-fits-all threshold for repair set at 5.0–5.5 cm in various clinical guidelines, as no better method is currently available (1, 2, 16, 17). However, a recent study by Tan et al. reported that though these clinical practice guidelines were considered of adequate methodological quality to recommend their use in clinical practice, these still showed areas for improvement, potentially through performing economic analysis and trial application of recommendations (18). Furthermore, although aortic diameter is correlated with rupture risk, the expansion rate of AA differs greatly per individual (19), is discontinuous (20), and therefore is no exclusive parameter to deliver a highly accurate risk of rupture. Furthermore, studies on ruptured AAAs demonstrated that large variations in diameters were found with a considerable number of patients rupturing their AAAs at diameters >7–8 cm (21, 22). Therefore, a more patient tailored approach seems to be desirable.

Currently, AA patients are increasingly treated with minimally invasive, endovascular aneurysm repair (EVAR) which has become the standard of care for patients with

suitable anatomy, as EVAR has substantially improved early survival compared with open repair (23, 24). However, prophylactic treatment of asymptomatic AA does not come without risks. Despite a perioperative survival advantage of EVAR (1.1%) compared with open repair (4.4%) in infrarenal AAA, this advantage dissipates over time alongside high rates of reinterventions, concisely revealing some of the current challenges in aortic repair (25–27). These risks highlight the challenges for clinicians regarding a timely provision of elective surgical indication, to prevent the high mortality rate of 85% following rupture (28, 29).

These limitations emphasize the need for additional and novel imaging techniques with increased accuracy for rupture risk assessment, that will allow for a more patient centered approach for elective repair. This review article will highlight the development of novel clinical imaging techniques based on molecular pathophysiological insights of AA development, within the pre-clinical and clinical settings, targeting aneurysm-specific biomarkers for better risk stratification and disease monitoring.

THE STATE OF THE ART IN AA IMAGING

Commonly used imaging techniques for monitoring AAs include ultrasound scanning (US), computed tomography (CT) and magnetic resonance imaging (MRI), all mainly aimed at determining the aortic diameter or volume. Although the diameter is a quick and relatively easy parameter to determine, its use is limited as it can give inaccurate measure in asymmetric aneurysms. For this reason, new imaging parameters such as aneurysm volume and aortic size index (ratio of aortic diameter and body surface area) are being explored within these existing techniques (30–33). US uses high-frequency sound waves and is an effective technique as it is time- and cost-efficient and allows for real-time imaging of the aorta without the use of radiation. Additional novel techniques such as contrast-enhancement using microbubbles makes US even useful for assessment of the microvascular anatomy of the aorta, providing valuable physiological information due to the physical and safety profiles of these administered microbubbles (34). Nevertheless, the interpretation of US images is user-dependent and provides relatively less detail compared to other imaging techniques in routine imaging procedures.

Computed Tomography Angiography (CTA) can provide full 3D reconstructions of the aorta (35). While non-contrast images allow for detection of calcification and previously applied surgical graft material (35), iodinated contrast agents are used to enhance bloodpool density and visualize arterial lumen. In addition, electrocardiogram (ECG)-gating of the CTA has the ability to correct for cardiac motion, providing increased image quality. Despite its wide applicability, it should be noted that CTA has an intrinsic relative disadvantage of using ionizing radiation, making it a less attractive solution alongside a growing awareness regarding the possible health risks (36). Nevertheless, this radiation dose has vastly decreased over the years, only producing a dosage of 10 milli-Gray in adults (37).

Moreover, magnetic resonance imaging (MRI) has also been used for 3D visualization of the aorta. This technique essentially does not require a contrast agent. However, contrast enhanced magnetic resonance angiography (MRA; with gadolinium) allows for additional imaging features and can provide useful information for the development of an AA such as 4D phase contrast (38, 39). This is relevant as the flow pattern and amount of flow in the false lumen is related to aortic expansion, and leading to secondary aneurysmal disease following the dissection (40). Nevertheless, MRI is a time-consuming and expensive diagnostic technique, which makes its current use limited in the contribution of routine preoperative and postoperative risk assessment of aneurysmal disease.

With our growing understanding of the pathophysiology and molecular mechanisms underlying aneurysmal disease, novel targets for molecular imaging have become available.

BIOLOGY OF AORTIC ANEURYSM DEVELOPMENT

The aorta distributes oxygenated blood from the lungs to the systemic circulation. In order to facilitate the propulsion of blood from the heart to peripheral organs, the aorta possesses a high level of elasticity (41). Like other arteries, the vessel wall of the aorta is composed of three layers; the inner tunica intima, consisting of a basement membrane lined with endothelial cells (ECs), the middle tunica media, consisting of smooth muscle cells (SMCs) producing extracellular matrix (ECM) proteins, and the outer tunica adventitia, a connective tissue layer containing small vessels (vasa vasorum) and nerves (**Figure 1**) (42, 43). The ECM, present in all layers of the vessel wall, is a highly structured network containing elastin, collagen and proteoglycans and is essential for tensile strength and flexibility of the vessel wall. In pathological conditions such as AA formation, the structural and functional integrity of the vessel wall is compromised due to degeneration of the aortic media, characterized by loss of SMCs and aberrant synthesis, deposition or degradation of ECM proteins (42, 44).

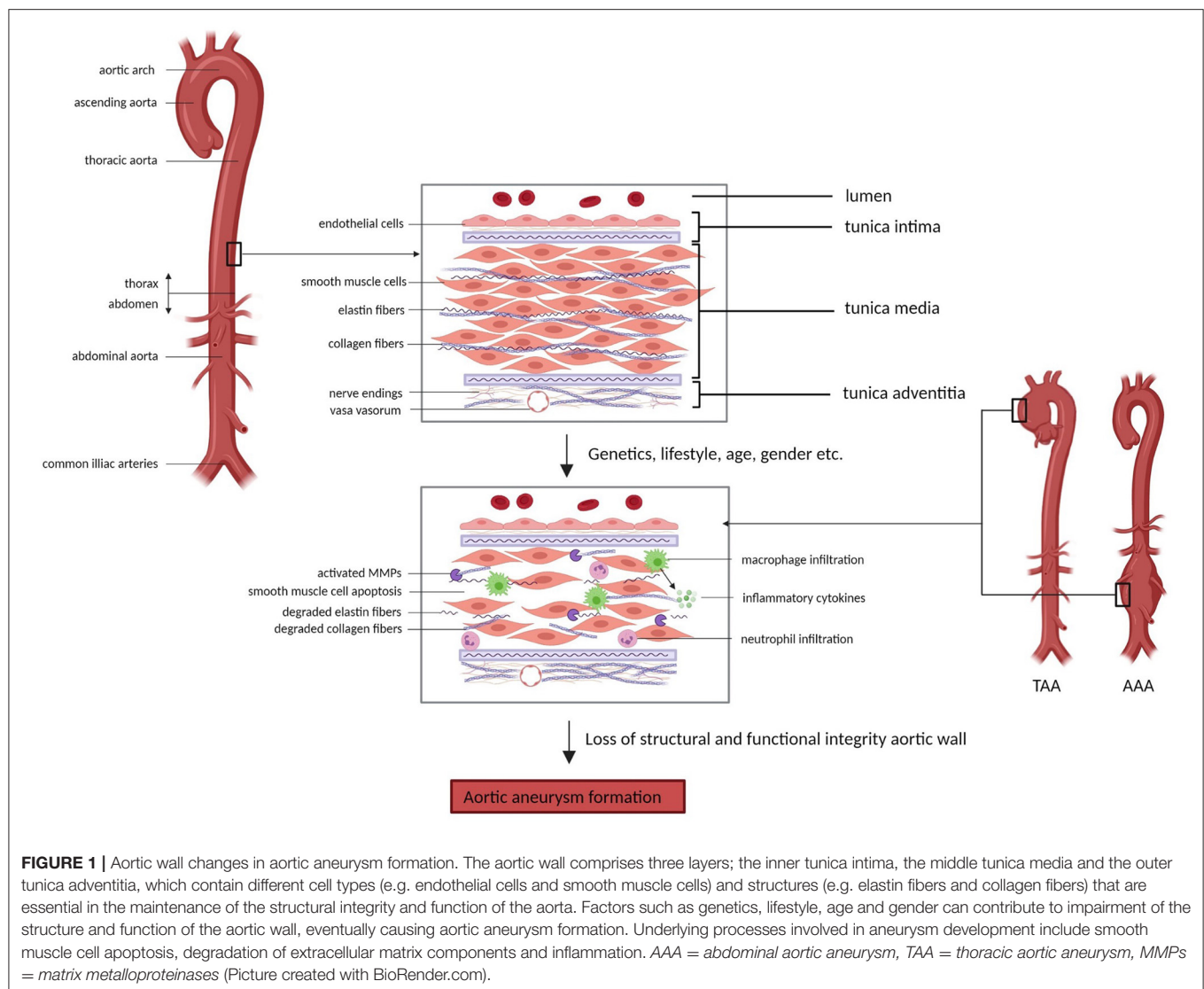
Elastin and collagen are the main ECM proteins involved in pathological remodeling of the aortic wall upon aneurysm formation. Elastin is the main component of elastic fibers, which are organized into fenestrated sheets, or elastic laminae (43). Elastic laminae are situated between SMCs in the aortic media and provide elasticity to the aortic wall, allowing the aorta to expand and relax with each cardiac cycle (45, 46). Fibrillar collagens (predominantly type I and III) surround the SMCs and elastic laminae and provide structure and tensile strength to the aorta (47). Additionally, elastin and collagen fibers regulate SMC adhesion, proliferation and migration by interaction through integrins and other proteins (48, 49). Degradation or disorganization of elastin and collagen fibers therefore compromises arterial structure and function and has been shown to play an important role in aneurysm formation (50, 51). The degradation of elastin and collagen is regulated by matrix metalloproteinases (MMPs) and tissue inhibitors of matrix metalloproteinases (TIMPs) (52). Imbalance between the

activity and presence of these MMPs and their inhibitors results in maladaptive remodeling of the ECM in the aortic wall. Normally, MMPs are produced by ECs, SMCs and fibroblasts and contribute to physiological remodeling of the aorta (53). Especially in AAAs, aneurysm formation involves a pronounced inflammatory component, with local infiltration of immune cells (mainly macrophages, T-cells and B-cells) into the aneurysmal aortic wall (54). Inflammatory cytokines (i.e., TGF- β , IL-1 β , IL-6) trigger increased MMP production by SMCs and additionally, MMPs are produced by immune cells present in the aorta (55). Furthermore, circulating elastin fragments resulting from elastin degradation are able to trigger an inflammatory response, presumably through binding to macrophage surface receptors, which then causes further elastin degradation through MMP activation (43, 56). A large set of MMPs has been shown to be upregulated in the aneurysmal aorta, including MMP-1, MMP-2, MMP-3, MMP-9, MMP-12, MMP-13 and MMP-14 (57, 58). MMP-2, predominantly produced by SMCs, and MMP-9, predominantly produced by macrophages, were found to be the main MMPs involved in AAA development, causing ECM remodeling, apoptosis of SMCs and further inflammation (59, 60). These events compromise aortic wall integrity and consequently, prolong cyclic strain and increase wall tension resulting in aortic dilation.

Despite similarities in macroscopic appearance, TAAs and AAAs hold distinctly different underlying pathophysiological mechanisms. This can partly be attributed to the different embryological origin of cells from the thoracic and abdominal aorta (61). Additionally, there are structural differences, with the abdominal aorta containing less fibromuscular layers and vasa vasorum compared to the thoracic aorta (62). Lastly, the underlying causes of aneurysm formation differ between the thoracic and the abdominal aorta, where genetic deficiencies play a large role in TAA development and a more multifactorial process underlies AAA development with lifestyle as a large contributor. Accordingly, different targets for diagnostics and therapy might be of interest between TAAs and AAAs. Therefore, it is important to discriminate between molecular mechanisms of AA development in the thoracic vs. the abdominal part of the aorta.

Genetics and Molecular Mechanism of TAA Development

TAAs are often syndromic and are generally caused by variants in genes involved in ECM integrity and structure (e.g. *FBN1* and *EFEMP2*), transforming growth factor β (TGF- β) signaling (e.g. *SMAD3* and *TGFBR1/2*) and cytoskeleton maintenance and motility (e.g. *ACTA2* and *MYH11*) (13). Heterozygous mutations in the gene for ECM protein Fibrillin-1, *FBN1*, cause Marfan syndrome (MFS1; MIM 154700) in patients, an autosomal dominant disorder with wide clinical variability affecting the cardiovascular, ocular and skeletal systems (63). Homozygous or compound heterozygous mutations in the gene for ECM protein Fibulin-4, *EFEMP2*, cause cutis laxa syndrome (ARCL1B; MIM 614437) in patients, characterized by systemic connective tissue abnormalities, including loose skin, lung emphysema, bone



fragility, vascular tortuosity and aneurysms (64). Mutations in the *ELN* gene, encoding for elastin, can also cause cutis laxa syndrome (ADCL1; MIM 123700) (65). These ECM proteins are involved in vascular maturation and maintenance of structural integrity and elasticity of the aortic wall. Fibrillin-1 and Fibulin-4 proteins form microfibrils in the ECM, where they associate with other ECM proteins such as elastin and are therefore essential for the structural integrity of the aortic wall. Both Fibrillin-1 and Fibulin-4 associate with latent TGF- β binding protein (LTBP) and are thereby involved in the regulated release of TGF- β from large latent complexes (LLCs) in which free TGF- β is bound to the ECM (66–68). Consequently, deficiency in these proteins results in increased release of active TGF- β and dysregulated TGF- β signaling (69, 70). Downstream effects are increased activity of MMPs, elastin degradation, deposition of ECM proteins and aberrant cytoskeleton fibers. This causes increased stiffness of the aortic wall, making it less resilient to mechanical stress which promotes aneurysm formation.

TGFBR1/2 and *SMAD2/3* encode proteins involved in TGF- β signaling and mutations in these genes cause Loeys-Dietz syndrome (LDS) in patients (*TGFBR1*; LDS1; MIM 609192, *TGFBR2*; LDS2; MIM 61068, *SMAD2*; LDS6; MIM 619656, *SMAD3*; LDS3 (AOS); MIM 613795). LDS is characterized by arterial aneurysms, dissections and cardiac abnormalities (71, 72). As *TGFBR1/2* and *SMAD2/3* are important regulators of the TGF- β pathway, deficiency of these proteins causes dysregulated downstream signaling of this pathway in LDS patients (72–74). Paradoxically, increased *pSMAD2* signal is detected in the aortic wall of *TGFBR1/2* and *SMAD3* patients, suggesting TGF- β pathway activation whereas pathway inhibition is expected (75, 76). This can be explained by the fact that upstream TGF- β signaling is activated, but downstream the signal is not transduced resulting in a discordance between up- and downstream TGF- β pathway activation (77). Aneurysm development in LDS patients is characterized by a pronounced inflammatory response, which is thought to be initiated by

changes in aortic wall structure and subsequently triggers rapid progression of aneurysmal growth.

Mutations in *ACTA2*, *MYH11*, *MYLK* and *PRKG1* lead to non-syndromic familial aortic aneurysms (AAT1; MIM 607086) (76). The proteins encoded by these genes are involved in SMC contractility, therefore deficiency of these proteins functionally impairs contraction of the aortic wall. Additionally, increased TGF- β signaling was found in the aorta of patients, again emphasizing the role of this signaling pathway in aneurysm formation (78). Dysfunctional actin and myosin filament assembly impairs proper formation of fibronectin fibrils in the ECM. This further causes aberrant fibrillin-1 microfibril assembly, causing increased release of free TGF- β and promoting TGF- β signaling.

Molecular Mechanism of AAA Development

As previously mentioned, AAA development is generally caused by a multifactorial process and cannot be attributed to a single cause. Risk factors for AAA development are smoking, advanced age, male gender, hypertension, and family history (79). Despite the important role of lifestyle in AAA development, a prior systematic review identified 33 single nucleotide polymorphisms (SNPs) associated with AAA diagnosis at genome-wide significance that were previously validated in multiple cohorts. However, the functional consequences of these SNPs on AAA growth still have to be established. Furthermore, since AAA primarily affects elderly men, the role of sex hormones are becoming of increased interest. Villard et al. have recently reported an association between increased progesterone levels and early AAA development within males, as well as higher circulating levels of estradiol and lower levels of testosterone in men with AAA (80). Similarly, in comparison to females before their menopause, the higher prevalence of cardiovascular disease in postmenopausal females has been found to be related to the diminishing levels of female sex hormones during menopause.

At the cellular level, hallmarks of AAA pathology include apoptosis of SMCs, ECM degeneration, inflammatory cell infiltration and oxidative stress (44). As described previously, these cellular processes cause a loss of structural integrity of the aortic wall, consequently leading to aortic dilation and eventually rupture. An imbalance in MMP activity causes ECM degeneration, triggering reduced levels of elastin, collagen and glycosaminoglycans in the aortic wall. AAA formation is characterized by a pronounced inflammatory response and therefore macrophages and neutrophils, as well as inflammatory factors such as TNF- α , TGF- β and interleukins, are often present in the aneurysmal aorta (81).

Thus, several of these previously described processes are characteristic for TAA and AAA development and progression, respectively, and therefore are interesting targets for diagnosis and monitoring of disease in patients. As AAAs are often attributed to a convergence of multifactorial genetic causes combined with external factors, it is a lot more challenging to identify molecular mechanisms at play in each individual patient compared to TAA patients for which the single

genetic cause and thus the associated molecular mechanism can be used as a target for molecular imaging. However, the majority of AA cases are abdominal (82), so there is an even bigger need to find suitable imaging techniques for this type of AA. Not every imaging technique might be applicable to monitor both TAAs and AAAs, and effectiveness may vary dependent on the different mechanisms underlying AA formation and development. This emphasizes the importance of understanding the molecular mechanisms governing AA, which potentially can be elucidated with pre-clinical research in animal models.

MOUSE MODELS FOR AORTIC ANEURYSM

Aneurysmal mouse models are used to test the effectivity of imaging techniques as disease development and progression are predictable and can be closely monitored. Mice have a fast reproduction rate, a short lifespan and are genetically similar to humans, and are therefore considered to be of value in medical research (83). Moreover, mice can be bred in an isogenic background, by which the gene or process of interest can be studied, not affected by genetic heterogeneity. Many different murine models for AA have been created in which we can distinguish between TAA and AAA models, either genetically or chemically induced, or a combination of both. As the pathophysiology is unique for TAA and AAA and as AA development is a multigenetic and multifactorial process, these models subsequently elucidate individual mechanisms involved in aneurysm formation.

TAA Mouse Models

Aneurysms in the thoracic part of the aorta typically result from degeneration of the aortic media with apoptosis of SMCs and elastic fiber degradation. Several genetic deficiencies resulting in TAA formation in patients, as described previously, have been mimicked in mouse models to study the underlying pathophysiological pathways (84) (Figure 2).

Several mouse models were created to mimic Marfan syndrome, in which patients develop TAAs due to Fibrillin-1 deficiency. Marfan syndrome was first mimicked in *Fbn1*^{mg Δ /mg Δ} mice, with an in-frame deletion of exons 19–24 in the *Fbn1* gene causing severe (ten-fold) reduction of *Fbn1* expression (85). These mice die at an early postnatal age of 3 weeks due to cardiovascular complications, which complicates the study of disease progression. Additional murine models for Marfan syndrome include the *Fbn1*^{C1039G/C1039G} model, in which mice have a missense mutation causing normal *Fbn1* expression but aberrant fiber formation (86), and the *Fbn1*^{GT-8/GT-8} model, where Fibrillin-1 is truncated and has four-fold reduced expression (87). However, these mice also die at a postnatal age when harboring the homozygous mutation. To overcome this, mice with a hypomorphic *Fbn1* mutation (mgR), causing a four-fold reduction in normal Fibrillin-1 expression, were generated (88). These *Fbn1*^{mgR/mgR} mice develop aneurysms similarly to human


<div> <div>Thoracic Aortic Aneurysm</div>  <div>Mutated genes</div> </div>	Disease	Gene (protein function)	Mouse model	Effect on expression	Advantages	Limitations	Literature
	Marfan syndrome	<i>Fbn1</i> (ECM protein)	<i>Fbn1^{mgA/mgA}</i>	Tenfold reduction	• Characteristics relevant to human condition	• Death at early postnatal age	(85)
			<i>Fbn1^{C1039G/C1039G}</i>	Normal (missense mutation)	• Characteristics comparable to human condition	• Death at early postnatal age	(86)
			<i>Fbn1^{GT-8/GT-8}</i>	Fourfold reduction (truncated protein)	• Characteristics comparable to human condition	• Death at early postnatal age	(87)
			<i>Fbn1^{mgR/mgR}</i>	Fourfold reduction	• Aneurysm development similar to patients	• Death at around 4 months	(88)
	Cutis laxa syndrome	<i>Fibulin-4</i> (ECM protein)	<i>Fibulin-4^{-/-}</i>	No expression	• Useful for research on Fibulin-4 function in cardiovascular system	• Embryonic lethality	(89)
			<i>Fibulin-4^{f/-}/SM22Cre⁺</i>	No expression in VSMCs	• Enables specific study on effect of defects in VSMCs on aneurysm development • Aneurysm development similar to patients	• Phenotype might be partially masked by Fibulin-4 secreted by adjacent tissues	(90)
			<i>Fibulin-4^{R/R}</i>	Fourfold reduction	• Aneurysm development similar to patients	• Death at around 3 months	(91,92)
			<i>Fibulin-4^{E57K/E57K}</i>	Normal (missense mutation)	• Aneurysm development similar to patients • Induced by human disease-causing mutation	• Only 50% of homozygous animals develop aneurysms	(93)
	Loeys-Dietz syndrome	<i>Smad3</i> (TGF- β signaling)	<i>Smad3^{-/-}</i>	No expression	• Aneurysm development similar to patients	• Heterogeneous disease progression and sudden death	(98, 77)
		<i>Tgfb1/2</i> (TGF- β signaling)	<i>Tgfb1/2</i> knockout	No expression	• Useful for research on TGFBR1/2 function in cardiovascular system	• Embryonic lethality	(94,95)
			<i>Tgfb1/2</i> conditional knockout	No expression in specific cell types (ECs, VSMCs)	• Enables study on effect of defects in specific cell types on aneurysm development	• Fail to completely represent all characteristics of LDS	(96,97)
	Non-syndromic familial aortic aneurysms	<i>Acta2</i> (muscle contraction)	<i>Acta2</i> null	No expression	• Useful for research on α -SMA function in cardiovascular system	• Do not develop aneurysms	(100)
		<i>Myh11</i> (muscle contraction)	<i>Myh11</i> null	No expression	• Useful for research on MYH11 function in cardiovascular system	• Do not develop aneurysms	(99)

FIGURE 2 | Contemporary murine models for TAA. Thoracic aortic aneurysm can be modeled in mice through genetic modification of specific genes (*Fbn1*, *Efemp2* (*Fibulin-4*), *Smad3*, *Tgbr1/2*, *Acta2* and *Myh11*) involved in aneurysm formation. (Picture created with BioRender.com).

Marfan patients, showing vascular inflammation and elastin degradation in the aortic wall, and die at around 4 months as a result of aortic dissection. This makes this model not only useful for investigating underlying molecular mechanisms of disease, but also suitable for testing imaging techniques targeting major processes involved in aneurysm development in Marfan patients.

Additionally, to study the underlying mechanism of aneurysm formation in cutis laxa syndrome caused by Fibulin-4 deficiency, several mouse models have been developed. Complete knockout of the *Efemp2* gene, the gene encoding Fibulin-4, appeared to cause perinatal lethality in mice (89). Therefore, an SMC specific knockout of *Fibulin-4* (*Fibulin-4^{f/-}/SM22Cre⁺*) was generated, causing AA formation in the ascending aorta (90). Additionally, mutant mice were developed with a four-fold decreased expression of *Fibulin-4* (*Fibulin-4^{R/R}*) (91). *Fibulin-4^{R/R}* mice show dilation and tortuosity of the ascending aorta and die of aortic dissection at an early age of 3 months. Aneurysm formation in *Fibulin-4^{R/R}* mice is highly similar to that in patients at a macroscopic and molecular level. *Fibulin-4^{R/R}* aneurysmal aortas show elastin fragmentation and increased deposition of ECM, as well as increased TGF- β signaling and mitochondrial dysfunction (91, 92). This model has proven to be very valuable for studying underlying molecular mechanisms of aneurysm formation, but also for pre-clinical testing of imaging techniques targeting these molecular processes. Lastly, a knock-in mouse model was created carrying the human disease-causing E57K mutation in the *Fibulin-4* gene, causing normal protein expression but reduced ECM assembly (93). *Fibulin-4^{E57K/E57K}* mice

show characteristics similar to human patients and develop ascending aortic aneurysms, which makes this model useful for studying underlying molecular mechanisms of disease and potentially also pre-clinical testing of imaging techniques targeting these processes.

Furthermore, several mouse models were created to mimic LDS, which is caused by mutations in *TGFBR1/2* and *SMAD3* genes in patients. Both *Tgfb1* and *Tgfb2* deletion cause embryonic lethality in mice due to severe defects in vascular development (94, 95). Conditional knockouts of *Tgfb1* and *Tgfb2* in ECs and SMCs show several symptoms of LDS but fail to completely represent all characteristics (96, 97). *Smad3* knockout mice, although in isogenic background, show similar heterogeneity in disease development to patients and die suddenly from TAA formation (98). The aortic wall of these mice shows elastin disruption and a pronounced infiltration of inflammatory cells with MMP activity, which promotes further deterioration of the aortic wall and could therefore explain the rapid disease progression (77).

Lastly, mouse models were developed to represent disease development as seen in familial TAA in patients with *ACTA2* and *MYH11* mutations. However, despite causing cardiovascular abnormalities, complete loss of *ACTA2* and *MYH11* protein expression does not cause aneurysm formation in mice which makes these models unsuitable for studying *ACTA2* and *MYH11* induced aneurysmal disease development (99, 100). However, Angiotensin II infusion of *Acta2^{-/-}* mice did result in enhanced dilation of the thoracic aorta, demonstrating that deficiency of *ACTA2* promotes aneurysm formation in combination with chemical induction (101).

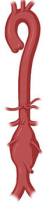

Abdominal Aortic Aneurysm   Chemical induction	Method of chemical induction	Outcome	Advantages	Limitations	Literature
	Angiotensin II infusion (in <i>ApoE</i> ^{-/-} or <i>Ldlr</i> ^{-/-} background)	Vascular inflammation, remodeling of the ECM and luminal aortic enlargement	<ul style="list-style-type: none"> Displays important characteristics of human AAA 	<ul style="list-style-type: none"> Aneurysms are typically formed in suprarenal aorta 	(103-110)
	Intraluminal perfusion or periadventitial application of elastase	Elastin degradation, infiltration of inflammatory cells and luminal aortic enlargement	<ul style="list-style-type: none"> Induction of AAA formation Displays important characteristics of human AAA 	<ul style="list-style-type: none"> Aneurysms do not dissect No long-term progressive expansion of aneurysms Technically challenging 	(111-113)
	Periadventitial application of CaCl ₂	Elastin degradation, infiltration of inflammatory cells, angiogenesis and calcification of the aorta	<ul style="list-style-type: none"> Induction of aneurysm formation Site-specific (can induce both TAA and AAA) 	<ul style="list-style-type: none"> Aneurysms do not dissect or rupture 	(114)
	Periadventitial application of PBS + CaCl ₂	Addition of phosphate increases calcification of the aorta			(115)
	Oral administration of β -aminopropionitrile (BAPN)	Medial degradation	<ul style="list-style-type: none"> Induces severe TAA or AAA in combination with elastase or AngII infusion Induces thoracic aortic dissection 	<ul style="list-style-type: none"> Exact dosage is unreliable when using administration via drinking water 	(116-118)

FIGURE 3 | Contemporary murine models for AAA. Abdominal aortic aneurysm can be modeled through chemical induction using Angiotensin II (in *ApoE*^{-/-} and *Ldlr*^{-/-} mice), elastase, calcium chloride [CaCl₂, with/without phosphate (PBS)] and β -aminopropionitrile (BAPN). (Picture created with BioRender.com).

AAA Mouse Models

Several mouse models of AAAs have been developed that use a combination of genetic manipulation and chemical induction for reproducing aneurysmal disease development (Figure 3). Hyperlipidemic apolipoprotein E deficient (*ApoE*^{-/-}) or low-density lipoprotein receptor deficient (*Ldlr*^{-/-}) mice were initially used in research on atherosclerosis but were found to develop AAAs when being fed a high-fat diet (102). This model represents similar characteristics of vascular inflammation, atherosclerosis and AA formation caused by obesity in humans.

The most common method to induce AAA in *ApoE*^{-/-} or *Ldlr*^{-/-} mice is infusion of Angiotensin II (AngII), a hormone which increases blood pressure by promoting vasoconstriction and aldosterone secretion (103, 104). However, not the increase in blood pressure, but rather the induction of inflammation in the aorta is what causes aneurysm formation in the AngII model (105). While the AngII-infused *ApoE*-deficient mouse is one of the most widely used murine models for human AAA due to vascular inflammation, remodeling of the ECM, and activation of SMCs, its limitations are well recognized (106). These mice typically form aneurysms in the suprarenal aorta, whereas human AAAs are most commonly infrarenal (107). Differences in elastin and collagen composition between locations might impact mechanical properties of the aortic wall (108). In addition, the animals tend to form aneurysms as a consequence of hypertension-induced aortic dissection and intramural hematoma, whereas the vast majority of AAA disease in humans is not secondary to these diseases, but a consequence of smoking and atherosclerosis (109). AngII induction has also been shown to cause AAA formation in wildtype C57BL/6 mice, but the incidence is much lower than in hyperlipidemic models (110).

Another commonly used method to chemically induce AAA formation uses elastase. In this model, the aorta is exposed to porcine pancreatic elastase by either intraluminal perfusion or periadventitial application (102, 111). Elastase penetrates into the aortic medial layer, where it causes elastin degradation and

subsequent infiltration of inflammatory cells and luminal aortic enlargement (112). Despite the fact that this technique is able to properly induce AAA formation in mice, these aneurysms do not dissect. Additionally, these aneurysms show no long-term progressive expansion as they usually stabilize after 2 to 3 weeks (111, 113). Furthermore, the technique is technically challenging making it a less preferable model for AAA induction.

Application of calcium chloride (CaCl₂) or calcium phosphate (CaCl₂ and PBS) to the adventitia of the aorta is another method to chemically induce AAA formation. This model induces elastin degradation, infiltration of inflammatory cells, angiogenesis and calcification of the aorta, subsequently resulting in AAA formation (114). The addition of phosphate increases calcification of the aorta (115). This model is site-specific and can therefore be used to induce both AAAs and TAAs, which is advantageous compared to the other methods. However, this model does not result in dissection or rupture of the aorta, making it less representative for human AA formation.

Lastly, oral administration of the lysyl oxidase (LOX) inhibitor β -aminopropionitrile (BAPN) is a method to chemically induce both AAA and TAA formation in mice. BAPN causes medial disruption by blocking crosslinking of elastin and collagen, resulting in reduced stability of the ECM (116). It has been used in combination with elastase or AngII infusion to induce severe AAA or TAA, promoting aortic rupture and dissection respectively (117). When administered individually, BAPN has been shown to induce thoracic aortic dissection (118). The fact that BAPN promotes dissection and rupture of the aorta, thereby representing important features of human AA formation, makes this a clinically relevant model (102).

These mouse models represent several important characteristics of human AAA development and therefore form interesting models for testing diagnostic and therapeutic markers. However, these methods are considered to be quite invasive to induce AAA formation and none of these models fully represent the natural progression of AAA growth in human patients. A complicating factor of pre-clinical testing in mice

is that molecular pathways that are changed in these mice could be different, or not at all affected in patients, therefore impairing translatability. The fact that aneurysm development and progression is much faster in mice compared to the chronic AAA development seen in patients contributes to this concern. Difficulties in establishing a representative mouse model that mimics human AAA are attributed to the fact that in AAAs there is not one single cause of disease. Many risk factors such as smoking, age, weight and genetic variances are encountered during a long period of time and are hard to replicate in a model organism. Moreover, even a combination of all risk factors does not guarantee growth of an AAA. On the contrary, since TAAs are mostly caused by a single genetic defect, mouse models have been successfully created that represent important characteristics of TAA development in human patients. This makes these models more suitable for pre-clinical testing of imaging techniques targeting underlying molecular mechanisms of TAA development, since these are similar in mice compared to human patients.

Despite the development of several murine models that quite accurately mimic human AA disease at a macroscopic and molecular level, the use of murine models *per se* presents with limitations concerning translatability. The human and murine genome are largely similar, but not all physiological and pathological processes can be identically reproduced in mice. For example, distinct differences were found in response to inflammatory trauma in terms of gene expression (119). Considering the important role of inflammation in AA disease, these findings imply that we should be mindful with the extrapolation of pre-clinical findings to the clinical setting. Despite these facts, murine models have been largely applied and proven useful for pre-clinical testing of imaging techniques to diagnose and monitor AA development and progression.

PRE-CLINICAL AORTIC ANEURYSM IMAGING

At present, several non-invasive high-resolution imaging techniques, including US, micro computed tomography (μ CT), MRI and photo-acoustic imaging (PAI), are commonly applied to monitor AA development and progression in mice (116). The approach of US is similar in pre-clinical and clinical applications, besides the use of a higher frequency when imaging mice, producing images with higher spatial resolution (120–122). US has different modalities which can be applied to obtain more detailed information on the vasculature such as Doppler US examination to measure blood flow velocity, M-mode US examination for quantifying circumferential strain, and volumetric US examination to visualize complex lesions. Another pre-clinical imaging technique is small animal μ CT, which produces high-resolution three-dimensional images of the aorta by using a vascular contrast agent that allows for accurate measurement of aortic volume (123, 124). Furthermore, high-field MRI using small bore systems, especially in combination with contrast agents targeting specific markers, has been proven valuable in pre-clinical imaging of AA disease

in murine models (125, 126). Lastly, PAI is a novel method, which relies on the detection of ultrasound waves generated by the interaction of light pulses with tissue and molecules and their subsequent thermo-elastic expansion. In other words, light pulses are converted to ultrasound waves, enabling deeper tissue penetration compared with light detection. Endogenous contrast can be generated by the presence of light absorbers like hemoglobin or melanin while exogenous contrast can be generated by probes which absorb light in the NIR (near infrared region) such as fluorescent proteins, dyes and nanoparticles. PAI, for example, allows the simultaneous visualization of changes in the oxygenation of the blood (e.g., due to local hypoxia) and precise localization of specific targeted probes, thereby providing anatomical, functional and molecular information. Studies already successfully applied PAI to image atherosclerotic tissue, since this technique allows the detection of lipid distribution, and is also suggested to be suitable for imaging aneurysms (127).

Currently, novel imaging techniques are being explored that apply molecular targeting of specific underlying pathways involved in AA formation and progression. Several of the previously mentioned mouse models have been used in pre-clinical trials to test these novel imaging techniques. Molecular targets that are under investigation for imaging applications with respect to AA formation include ECM proteins, MMPs, immune cells and SMC phenotype (Figure 4).

Detection of Extracellular Matrix Proteins in TAA and AAA

As previously described, degradation of ECM proteins, like collagen, is an important process involved in AA development and therefore forms an interesting target for diagnostic imaging to monitor disease progression. A method to image collagen degradation in mouse aorta is through paramagnetic/fluorescent nanoparticles containing a collagen-I-binding protein (CNA-35) (128). Following intravenous injection of the nanoparticles, the primary fibrotic response in the aortic wall can be visualized with high-resolution, multisequence MRI. The CNA-35 probe significantly improved MR signal in AngII-induced aneurysmal mice, but its predictability of AAA development and progression remains to be proven. In a different study, a collagen-IV-targeted MRI/fluorescence dual probe (CDR) was developed, which enabled early detection of collagen type IV exposure in the aortic wall and was shown to form a suitable marker for early prediction of rupture risk in a BAPN-induced TAA model (129). The percentage normalized signal enhancement (NSE) was significantly higher in animals with ruptured TAAs compared to animals with stable, unruptured TAAs and NSE was negatively correlated with the time until rupture after BAPN administration. Additionally, a gadolinium-based probe that specifically binds to type I collagen (EP-3533) was created to enhance MR images. Use of this probe enabled differentiation between collagen-rich and collagen-poor aneurysms, of which the latter is more prone to rupture, in AngII-infused *ApoE*^{-/-} mice (130). Since these probes have been tested in chemically induced models of AAA, future clinical trials will have to prove

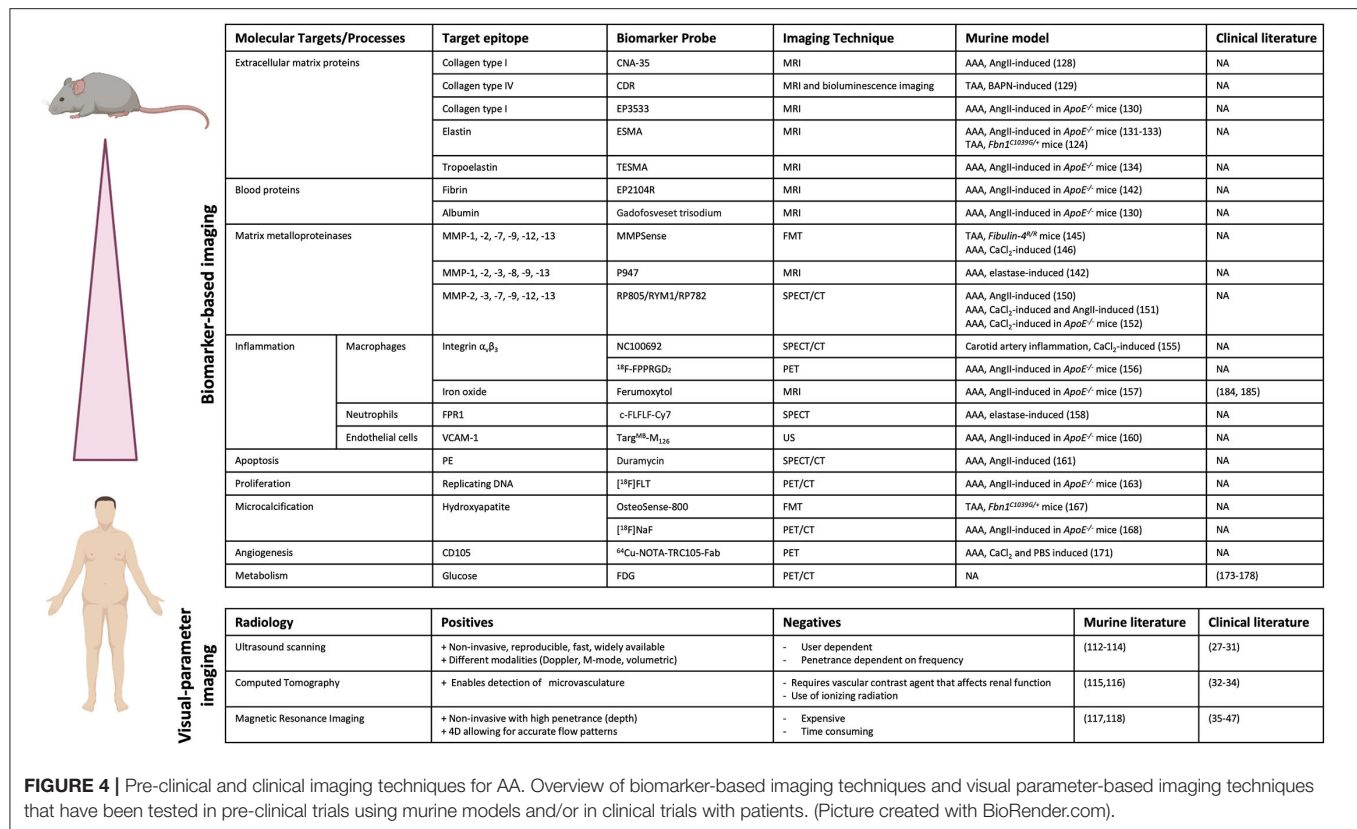


FIGURE 4 | Pre-clinical and clinical imaging techniques for AA. Overview of biomarker-based imaging techniques and visual parameter-based imaging techniques that have been tested in pre-clinical trials using murine models and/or in clinical trials with patients. (Picture created with BioRender.com).

viability of this concept in human disease progression and will have to subsequently demonstrate its added value to prediction of rupture risk.

Similar to collagen, elastin is a key structural protein for integrity of the aortic wall and distinctive for AA development. Therefore, targeting elastin in MRI imaging could be useful for AA risk analysis. A gadolinium-based, elastin-specific magnetic resonance molecular imaging agent (Gd-ESMA) was used to image AAA in *ApoE*^{-/-} mice infused with AngII (131). ESMA exhibits preferential binding to elastin molecules and is labeled with gadolinium as a contrast agent. Gd-ESMA-enhanced MR images were compared to *ex vivo* area measurements, which confirmed the correlation between enhanced MRI signal and presence of elastin in the aortic wall. Additionally, Gd-ESMA was able to accurately detect a decrease in elastin content in the aortic wall of Marfan mice (*Fbn1*^{C1039G/+}) compared to wild-type controls (132). When comparing Gd-ESMA to a non-specific contrast reagent (Gd-DTPA), which shows no selectivity toward elastin, it was apparent that Gd-DTPA did not result in an enhanced image of the aneurysmal wall, whilst Gd-ESMA clearly improved imaging by specifically targeting elastin (131). Gd-ESMA was also used to study the therapeutic effect of IL-1β neutralization on AAA progression in AngII-infused *ApoE*^{-/-} mice by monitoring elastin degradation in the aortic wall (133). Besides early *in vivo* evaluation and quantification of AAAs, the probe enabled monitoring of the response to anti-inflammatory treatment. Gd-ESMA enables the

prediction of AAA rupture with a sensitivity of 80% and a specificity of 78%, further suggesting that elastin is a useful marker for the prediction of rupture risk (134). Additionally, tropoelastin, a monomeric precursor of cross-linked elastin, was also shown to be increased upon AAA formation and to correlate with disease progression. Use of a gadolinium-based tropoelastin-specific MRI contrast agent (Gd-TESMA) to enhance MRI images, based on a peptide that selectively binds to tropoelastin, enabled identification of dysfunctional ECM remodeling in aneurysmal tissue of AngII-infused *ApoE*^{-/-} mice (135). However, the predictive value of Gd-TESMA enhanced imaging concerning AAA progression and rupture still has to be proven. Thus, monitoring elastin degradation or tropoelastin accumulation using MRI in combination with probes that specifically target these molecules could provide a useful tool to monitor aneurysm formation and potentially assess the risk of rupture.

Additional ECM proteins that have been shown to be upregulated in AAA tissue, and that might serve as suitable targets for molecular imaging, are thrombospondin, fibronectin and periostin (136, 137). Thrombospondin-1 is a secreted adhesive glycoprotein that mediates cell-to-matrix interactions by binding to ECM proteins such as collagen, fibrinogen and fibronectin. Periostin is an ECM protein that binds to integrin molecules on cell surfaces and its upregulation has been shown to correlate to AAA progression and inflammation, possibly making it an interesting target for monitoring disease progression (138).

Detection of Blood Proteins in AAA

Fibrin is a fibrous protein involved in blood clotting and is associated with formation of focal hematoma in aortic wall dissection and the development of larger thrombi during AAA progression (139, 140). Increased turnover of the fibrin protein was recently linked to stimulation of inflammatory pathways (139–141). This marker is especially important as thrombus growth is increasingly seen as a predictor of rupture in AA (142). Molecular MRI with a fibrin-specific molecular probe (EP2104R) was tested in AngII-infused *ApoE*^{−/−} mice (143). This method allowed for detection of aortic dissection even before visible aortic dilation, by visualizing hematoma formation. Moreover, no relevant expression of collagen or elastin was measured on histological sections at this early time point in disease development, meaning no structural changes in the ECM had taken place yet (143). Early phase thrombus also resulted in an enhanced MR signal with the fibrin-specific probe. In later stages the signal decreased, but at this time expression of collagen and elastin in the thrombus increased, allowing for early- and late phase thrombus distinction. Therefore, this probe could contribute to more accurate AAA rupture risk prediction in patients and is especially interesting since it has already been successfully clinically tested (144).

A different study used detection of albumin, one of the major plasma proteins in the blood, to visualize changes in vascular permeability that are observed in AAA formation. Gadofosveset trisodium, a gadolinium-containing MRI probe that binds to albumin, enhanced *in vivo* MR signal in AngII-infused *ApoE*^{−/−} mice and was able to predict AAA rupture with 100% sensitivity and 86% specificity in these mice (130). Therefore, this albumin-targeting probe shows great potential for AAA risk prediction in a clinical setting, especially since it has already been clinically approved.

An additional blood protein that is upregulated in AAA and that might serve as a suitable target for molecular imaging is Factor XII (FXII). FXII is involved in thrombus formation and its expression and activity correlate with AAA size. Furthermore, inhibition of FXIIa (the active form of FXII) activity as well as FXII depletion inhibit dilation of the suprarenal aorta in AngII-infused *ApoE*^{−/−} mice. However, while FXII is found in increased amounts in the serum of patients with expanding AAA, the combination of FXII with aneurysm diameter had limited predictive effect on aneurysm progression vs. diameter alone.

Detection of Matrix Metalloproteinases in TAA and AAA

As previously mentioned, activity and presence of MMPs is increased in AAs, resulting in degradation of the ECM in the aortic wall. Therefore, MMPs form a useful target for diagnostic imaging to visualize AA development and progression. The protease-activatable near-infrared fluorescence (NIRF) probe MMPsense 680 targets MMP-1, MMP-2, MMP-7, MMP-9, MMP-12 and MMP-13 activity, enabling *in vivo* visualization of MMP activation using fluorescence mediated tomography (FMT)-CT imaging. This probe was able to detect increased MMP activity even before aneurysms had formed in aortas of

Fibulin-4^{R/R} mice, proving its value as a predictive biomarker for TAA formation (145). The MMPsense probe also showed promising results in a CaCl₂-induced AAA mouse model, where fluorescent signal correlated to AAA growth inhibition by doxycycline treatment (146). In a different study, a contrast agent named P947 was developed that targets a wide range of MMPs (147, 148). In elastase-infused rats, the P947 contrast agent resulted in a significantly enhanced MR signal (149). The predictive value of this marker targeted by this contrast agent still has to be assessed. A limitation is the possibility that elastase-induction itself may affect the activity of MMPs and thus enhance the image in this model. Hence, exploring this molecular probe in other mouse models, such as the previously mentioned genetic TAA mouse models that do not require chemical induction for aneurysm formation, could be useful to exclude false-positive image enhancement due to elastase administration. Another technique to target MMPs is Single Photon Emission Computed Tomography (SPECT). SPECT uses a radioactive tracer in combination with CT. In AngII-infused mice, MMPs were targeted using RP805, a technetium-99m-labeled (^{99m}Tc) MMP-specific tracer (150). This study showed a significant increase in uptake of RP805 in mice that later developed rupture or AAA, showing its predictive value (150). The ^{99m}Tc-RYM1 tracer, based on the MMP inhibitor RYM, showed favorable pharmacokinetics compared to RP805 and was able to specifically detect MMP activity in both CaCl₂ and AngII-infused mice (151). ^{99m}Tc-RYM1 signal was significantly higher in the AAA group. Similarly, RP782, a indium-111m-labeled (¹¹¹In) MMP tracer, was used in CaCl₂-induced *ApoE*^{−/−} mice to enhance the SPECT image (152). Increased RP782 uptake correlated with later aneurysm expansion, suggesting that RP872 enhanced imaging can predict future aneurysmal growth. Thus, several studies suggest that MMP targeted molecular imaging is a useful tool for more accurate prediction of aneurysm growth and rupture. These results are particularly relevant due to the wide availability of CT equipment in hospitals and considering the speed and cost-effectiveness of SPECT imaging.

Detection of Immune Cells in AAA

Besides ECM proteins, immune cells and inflammatory cytokines are also known to play a key role in aneurysm progression. Immune cells accumulate in the aortic wall at the site of aneurysm formation and produce (pro-inflammatory) cytokines and proteases, which stimulate breakdown of the SMC layer (153). Macrophages are one of the primary immune cells infiltrating into the aortic wall upon aneurysm formation, making them a relevant target for diagnostic imaging. Additionally, the number of macrophages is increased in dissected areas, suggesting that the amount of macrophages is a predicting factor for aneurysm progression and rupture (154). Specific targeting of integrin $\alpha_v\beta_3$, expressed on the cell-surface of monocytes and macrophages, using a ^{99m}Tc-cyclic arginine-glycine-aspartate (RGD) peptide tracer (NC100692) for μ SPECT/CT has been proven successful in detecting vascular inflammation in a CaCl₂-infused murine model of carotid artery inflammation (155). This study did not yet investigate the predictability of aneurysm growth or rupture of this marker. The radiolabeled RGD positron

emission tomography (PET) tracer ^{18}F -FPPRGD₂, which also targets integrin $\alpha_v\beta_3$, was able to detect vascular inflammation in AngII-infused *ApoE*^{-/-} mice but did not correlate with aneurysm size (156). This suggests that integrin $\alpha_v\beta_3$ might be less suitable as a target for predicting aneurysm growth and rupture. A different method to specifically target activated pro-inflammatory macrophages is by exploiting their uptake and retention of iron particles (157). MRI analysis targeting macrophages with an iron-oxide reagent (ferumoxytol) was performed in AngII-infused *ApoE*^{-/-} mice (134). The iron-oxide reagent could predict aneurysm rupture with a sensitivity of 80% and a specificity of 89%, in comparison to Gd-ESMA which showed a sensitivity of 80% and a specificity of 78%. The best result was obtained with a combination of the iron-oxide and elastin probes which could predict rupture with selectivity and specificity of 100% and 89%, respectively (134). Additionally, a different study combined the type I collagen-targeted gadolinium-based probe (EP-3533) and the iron oxide-based probe (ferumoxytol) to simultaneously image ECM remodeling and inflammation in aortas of AngII-infused *ApoE*^{-/-} mice (130). Combined use of these probes yielded a sensitivity of 80% and a specificity of 100% for AAA rupture prediction, which again was superior compared to the predictive abilities of the individual probes alone. These probes do not interfere with each other's visualization and quantification and their combined use greatly enhances the amount of information obtained from one single MRI scan. Thus, this dual-probe molecular MRI approach looks very promising and could have a lot of potential in clinical settings, especially since the iron-oxide agent is already being used in the clinic and the gadolinium-based agents are very similar to currently clinically applied contrast agents.

Infiltration and activation of neutrophils has also been shown to be involved in the inflammatory response in AAAs. Activated neutrophils can be targeted for *in vivo* imaging via the formyl peptide receptor 1 (FPR1), using the FPR1 ligand c-FLFLF labeled with either Cy7 to enable fluorescence imaging or $^{99\text{m}}\text{Tc}$ to enable SPECT imaging (158). This probe enabled the detection of AAA development and progression in elastase-infused mice with both imaging techniques and shows potential for the prediction of aortic rupture.

Theranostics, the combination of therapeutics and diagnostics, is a novel technique that applies agents that can simultaneously be used for diagnostic imaging as well as therapeutic drug delivery. A molecule that has been targeted for theranostics is vascular cell adhesion molecule-1 (VCAM-1) which is present on inflamed ECs and mediates accumulation and adhesion of leukocytes. VCAM-1 is upregulated in AAA and has been shown to play a role in the inflammatory response in aneurysms (159). Microbubbles coated with an antibody directed toward VCAM-1 (Targ^{MB}-M₁₂₆) were applied for simultaneous ultrasound imaging and drug delivery of a microRNA (miR-126), which downregulates VCAM-1 expression, in AngII-infused *ApoE*^{-/-} mice (160). This novel theranostic application provides a functional contrast agent to assess the inflammatory state of the endothelium as well as targeted delivery of therapeutic drugs.

Detection of Apoptosis and Proliferation in AAA

Apoptosis of SMCs in the aortic wall is one of the main cellular hallmarks of AA formation, making this process an interesting target for diagnostic imaging to visualize AA development. The SPECT/CT imaging probe $^{99\text{m}}\text{Tc}$ -duramycin was developed to specifically target phosphatidylethanolamine (PE), which translocates from the inner to the outer cell membrane upon apoptosis (161). $^{99\text{m}}\text{Tc}$ -duramycin enabled successful detection of SMC apoptosis at the site of aneurysm formation in AngII-infused mice. Considering the important role of SMC apoptosis in AA development, this imaging probe could be very useful for early detection of AA formation, but its predictive value should be further assessed.

In response to vascular injury, SMCs can undergo phenotypic switching to a synthetic, proliferative phenotype to promote remodeling of the vessel wall (162). Proliferation of SMCs is an early event in AAA and could therefore form a useful early marker for AAA detection. Proliferating cells can be targeted *in vivo* using the PET/CT radiotracer fluorine-18 fluorothymidine (^{18}F FLT), which accumulates in proliferating cells (163). ^{18}F FLT signal increased during the active growth phase of AAA formation in AngII-infused *ApoE*^{-/-} mice and shows potential for early detection of AAA. Less probe uptake was observed in later phase AAA, where the growth phase plateaus, therefore this marker might be less useful for the prediction of aneurysm rupture.

Detection of Microcalcification and Angiogenesis in TAA and AAA

Vascular calcification is a risk factor for developing cardiovascular disease and microcalcification of the aortic wall has been shown to be associated with AAA progression (164). Microcalcification is the deposition of calcium hydroxyapatite at the (sub)micrometer scale in the aortic wall and is associated with instability and rupture of plaques in atherosclerosis (165, 166). The bis-phosphonate NIRF probe OsteoSense-800 targets hydroxyapatite and enables *in vivo* visualization of microcalcification using FMT imaging. This probe was able to visualize microcalcifications in the ascending aorta of *Fbn1*^{C1039G/+} mice, a model for Marfan syndrome (167). Additionally, microcalcification can be visualized using fluorine-18-sodium fluoride (^{18}F -NaF) PET/CT. ^{18}F -NaF binds to calcium hydroxyapatite structures and correlates with AAA development and progression in AngII-infused *ApoE*^{-/-} mice (168). Exclusively abdominal aortas that showed early signals of microcalcification subsequently developed aneurysms, which shows the predictive potential of this marker for aneurysm development.

Angiogenesis, the formation of new blood vessels, is a process that is observed in both AAA and TAA tissue and is thought to contribute to inflammation as well as remodeling and weakening of the aortic wall (169, 170). CD105 is an important marker for angiogenesis and the ^{64}Cu -labeled TRC105 Fab fragment specifically binds to CD105 (171). ^{64}Cu -NOTA-TRC105-Fab enhanced PET imaging showed increased angiogenesis in a

calcium phosphate-induced AAA mouse model and shows potential in the detection of AAA progression (171). Further research is necessary to confirm whether this probe can be used for prediction of aneurysm development and rupture.

Finally, several studies show the involvement of stem cells in AA pathogenesis, and stem cells were shown to be significantly elevated in AAA tissue from patients compared to control tissue. Interestingly, it has been shown in Ang-II infused *ApoE*^{-/-} mice that intravenous administration of mesenchymal stem cells can prevent aortic dilation (172). Stem cells possess several markers that could be exploited for specific targeting. Targeting stem cells for molecular imaging, therapy or even theranostics (combined diagnostics and therapeutics) would therefore be an interesting topic for future investigation.

CLINICAL TRIALS IN MOLECULAR AORTIC ANEURYSM IMAGING

Several imaging techniques that specifically target underlying molecular mechanisms of AA development are successfully being explored in mice. However, the clinical translation of molecular imaging for AA is relatively new and this process requires much time and is costly. Besides the necessity of human trials, testing for efficacy and accuracy outcomes, proper understanding of toxicology, bio-distribution, and circulation time analysis are of utmost importance to ensure patients safety. These difficulties secondarily clarify why only few of the markers that have been tested in mice, have presently been tested clinically.

Despite these challenges in clinical translation, some molecular markers have already been translated toward the clinical phase (Figure 4). However, due to the aforementioned challenges in clinical translation, it is crucial to select viable individuals/populations who are prospectively to benefit the most. Consequently, current clinical studies on molecular imaging for AA ultimately aim to improve rupture risk assessment, trying to improve the main prevailing challenge in aortic repair today. And, as such, current research on these techniques are mainly being performed in context of AAA rather than TAA, due to the higher prevalence of AAA.

18-fluorodeoxyglucose (FDG) positron emission tomography (PET) based on an *in vivo* introduction of radioactively labeled glucose, of which cellular uptake can be detected with PET, is increasingly utilized in the last years (173). FDG-PET is used to detect sites of inflammation based on an increased glucose metabolic rate. A combination of wall inflammation and increased mechanical stress increases the risk of rupture, visualizing the grade of inflammation of the aortic wall, which could potentially translate to a higher pathogenicity and rupture risk. Various studies have explored the effectivity of FDG-PET for clinical AA risk-prediction, and found a correlation between wall degradation and the visualized inflammation (174, 175). Interestingly, this relationship was even more profound in patients with intraluminal thrombus (plaque deposition on aortic wall) (176), a finding which is associated with increased rupture risk (176, 177). Nevertheless, accurate AA risk prediction with FDG-PET remains uncertain, as few studies provide data

demonstrating conflicting evidence regarding the associations of visualized inflammation with aneurysm dilatation (178, 179), and eventual rupture risk (180). Jalalzadeh et al. provided a systematic review of six studies of which 2 studies reported a significant correlation with FDG uptake and aortic inflammation, whereas 4 studies demonstrated no clear association (178).

Besides FDG, ¹⁸F-NaF (fluorine-18-sodium fluoride) that binds to calcium hydroxyapatite structures, has been studied in the clinic, demonstrating that high uptake is associated with aneurysmal disease and rupture/repair risk in humans too (181). Within *ex vivo* human aortic tissue, a couple of studies reported promising outcomes with regard to the radiotracer for $\alpha_v\beta_3$ integrin and chemokine receptor 2 (CCR2) in *ex vivo* human aortic tissue, as autoradiography demonstrated specific binding of ¹⁸F-Fluciclatide and ⁶⁴Cu-DOTA-ECL1i to $\alpha_v\beta_3$ integrin and CCR2, respectively (182, 183). Furthermore, histopathological analysis demonstrated increased expression of CCR2 was co-localized with CD68+ macrophages. Although the prior study also found that, within rats, CCR2 tracer uptake in AAAs that subsequently ruptured ($SUV = 1.31 \pm 0.14$, $p < 0.005$) demonstrated uptake nearly twice that of non-ruptured AAAs ($SUV = 0.73 \pm 0.11$). However, how effective these new tracer molecules will be in assessing a more accurate rupture risk prediction in human AAA remains an important factor for future investigation.

As proven in mouse models, ultrasmall paramagnetic particles of iron oxide, or ferumoxytol, was effective in detection of inflammation with PET/MR, and to help predict AA rupture (134). For a clinical study in 2011, aortic wall inflammation was imaged with ferumoxytol in a small group of AAA patients (184), and in 2017 a similar study was performed on a larger patient group, demonstrating a higher predictability of disease progression (185). In the latter study by Forsythe et al. in 2017, ferumoxytol enhancement was associated with reduced event-free survival for aneurysm rupture or repair ($P = 0.0275$), all-cause mortality ($P = 0.0635$), and aneurysm-related mortality ($P = 0.0590$) (185). However, after correcting for known risk factors such as maximum preoperative AAA diameter and smoking status, the addition of ferumoxytol enhancement to the multivariate model did not improve event prediction (c-statistic, 0.7935–0.7936).

Besides markers that have been tested in human AAA, other potentially viable markers that have been clinically tested in other diseases might hold potential in AAA too. Earlier it was shown that hypoxia positron emission tomography (PET) imaging agent ⁶⁴Cu-diacetyl-bis (N4-methylthiosemicarbazone) (⁶⁴Cu-ATSM) could be used for visualizing hypoxic cells in atherosclerosis in animal models (186), and recently this has been proven to be viable in human atheroma too (187). Although this study focused on carotid atherosclerotic plaques, the biological processes of atherosclerotic AA are similar, thus possibly holding potential in risk prediction too. As the aortic wall's primary source of oxygen is luminal blood flow, that gets disrupted in aortic tissue with intraluminal thrombus, it has been suggested that this is in part the source for aortic expansion and rupture (142). Secondarily highlighting the potential of this molecular marker.

Although MMPs have clearly shown to be convincing molecular markers for AAA degeneration in murine models (146), no clinical studies performing *in vivo* MMP imaging have yet been performed. Nevertheless, besides the fact that plasma levels of MMPs were demonstrated to be elevated in humans with AAA (188), Ducas et al. recently confirmed a correlation between *in vitro* human aortic tissue with intraluminal thrombus deposition and MMPs (142). Furthermore, in the last two decades, several fluorescent-labeled or radio-labeled MMP inhibitors have been developed as imaging agents for diseases, such as in myocardial infarction, intracranial aneurysms and multiple sclerosis (MS) (189), and should be clinically tested for AA in the future as well.

Besides the abovementioned biomarkers, molecular markers that have proven to be effective for rupture risk in the pre-clinical phase, targeting ECM proteins (type I/IV collagen and elastin), albumin, and immune cells, have yet to be tested clinically for practical use. Emphasizing that a great leap remains to be made toward the transition of human trials to test for clinical validity.

PERSPECTIVES AND CONCLUSIONS

Contemporary imaging techniques for AA risk prediction rely on visual parameters such as the maximum aortic diameter. Although radiological methods have improved over the years, risk prediction for AA ruptures through imaging remains suboptimal, resulting in a one-size-fits-all policy for intervention while a more tailored patient specific approach is desirable. Murine models for TAA and AAA continue to provide us with an in-depth understanding of the pathophysiological pathways at a cellular and molecular level that are consequential to aortic degeneration and AA formation. With the advancement of technology, newer imaging techniques are capable of targeting these molecular pathways involved in disease progression, potentially allowing the determination of disease progression not only in mice, but also in patients. Interestingly, these clinical applications might in return also lead to more detailed understanding of pathophysiological processes.

Within the pre-clinical setting, new potentially promising biomarkers such as collagen hybridizing peptide (190), targeting processes that are foundational in the pathophysiology of AA formation and rupture, will be subject to future study. However, forthcoming pre-clinical studies should be more attuned to the potential viability in clinical translation by focusing effectivity of biomarkers on rupture risk assessment. Notwithstanding, the current delay in clinical translation is in part due to the inability of creating an appropriate mouse model that replicates AA formation in humans. One of the biggest limitations is the difference in locations of AAs in murine models and humans, which may reflect regional differences in molecular composition, secondarily resulting in different mechanical properties. Furthermore, AAA murine models are induced chemically, and are consequentially unable to reproduce the complex nature of human AAA development. Improvement of the pre-clinical replica will lead to an enhanced anticipation whether successful pre-clinical markers will mirror its findings

in humans as well. Additionally, to get a better view on the clinical applicability of molecular imaging markers, pre-clinical studies can be improved by assessing the predictability of markers in mouse models for AAA as well as TAA. Currently, most markers are being tested in mouse models for AAA, and especially considering the differences in underlying molecular mechanisms, it is useful to know whether imaging techniques can be applied for both AAA and TAA. Therefore, additionally, to get a better view on the clinical applicability of molecular imaging markers, pre-clinical studies can be improved by assessing the predictability of markers in mouse models for AAA as well as TAA.

Besides the assessment of the predictive value of biomarkers, novel molecular imaging techniques mentioned in this review can be particularly valuable for pre-clinical testing of the efficacy of potential interventional therapeutics. Molecular imaging of elastin in mice treated with IL-1 β neutralizing antibodies allowed the monitoring of the response to the inflammatory treatment, which reduced aneurysm expansion, besides the prediction of AAA growth and rupture (133). This shows the potential of molecular imaging techniques to improve monitoring of the efficacy of interventional therapeutics, possibly also in a clinical setting. Additionally, a novel theranostic application using ultrasound imaging of VCAM-1-targeted microbubbles allowed simultaneous diagnostic imaging and targeted delivery of therapeutic drugs. This study demonstrates the potential of simultaneous targeting of molecules underlying AA development for molecular imaging as well as for therapy.

Future studies will have to evaluate whether novel radiological techniques utilizing molecular biomarkers could be of routine use in clinical practice and provide us with a more accurate and personalized risk prediction for AA disease. At present, the clinical literature does not yet report a feasible molecular marker that is independently associated with AA risk rupture. Accumulation or degradation of specific ECM proteins, increased MMP activity and immune cell infiltration have been shown to be highly correlated with AA development, progression, and even rupture risk in the pre-clinical phase, and, therefore potentially hold a predictive value for more accurate risk assessment for surgical intervention in the clinic as well. In order to achieve clinical applicability, prospective human trials need to be initiated. Although few biomarkers have already proven their association with disease progression in a few initial studies, it remains of importance to assess the clinical viability by providing a significantly more accurate risk prediction of AA rupture.

At first it will be essential to study which probes lead to highest sensitivity and specificity of rupture prediction within a given time frame. Pre-clinical studies already give insight into which markers could be most suitable. Specifically, probes targeting ECM proteins collagen and elastin as well as blood protein albumin were shown to successfully predict rupture risk in a mouse model of induced AAA. Furthermore, combined molecular imaging targeting elastin or collagen as well as immune cells showed superior results concerning AAA rupture prediction compared to molecular imaging of these targets individually. Markers such as MMPs and microcalcification hold predictive value concerning aneurysm growth, but whether

they are also able to predict aneurysm rupture still has to be assessed. Thus, prioritizing translation of these markers is of utmost importance. Besides evaluation of independent molecular markers, future studies should assess the additional value of molecular imaging in which quantitative imaging analysis might play an important role. As AA development and progression is a multifactorial process, combined imaging of involved target molecules as well as visual parameters could provide us with a more comprehensive and complete view of the disease process and potentially allow for a more accurate risk assessment for AA development, progression, and even rupture risk. Leveraging computational methods and artificial intelligence that combine visual parameters with molecular imaging and the clinical presentation of the patient, shall potentially help lead toward even higher accuracy risk prediction of AA rupture. Furthermore, molecular markers that can be imaged with readily available imaging techniques in hospitals shall have a priority. Markers that need to be imaged with MRI, rather than by SPECT or CT, will be less practical due to the inherent time and cost of this imaging technique. As mentioned previously, ultrasound has been tested as theranostic molecular imaging modality within the pre-clinical setting, by utilizing microbubbles (160, 191). Furthermore, the use of ultrasound as a molecular imaging modality as clinical AA-risk assessment tool holds great potential, given its wide use and practicality. Currently, there have not been any clinical trials utilizing molecular imaging with ultrasound in context of AA. Thus, new promising molecular markers regarding clinical AA-risk assessment, shall require future investigation with ultrasound as the imaging modality.

Furthermore, other technologies surrounding molecular imaging should be assessed. As previously mentioned, recent studies have demonstrated that the use of a dual probe in AAA murine models that concurrently target markers both in the processes of ECM degradation alongside inflammatory activity, leads to higher sensitivity (80%) and specificity (90–100%) of risk prediction (130, 134). As aneurysmal disease (especially AAA) is a multifactorial environment of pathobiological activity within a degraded aortic wall, simultaneous insights in molecular pathways from different biological processes could provide us with a better understanding of the ongoing disease process and therefore allow us to provide more accurate risk prediction analyses. Combinations of probes with different pathophysiological processes should be assessed, to evaluate the most effective combinations for potential clinical use.

AUTHOR CONTRIBUTIONS

VR, SS, JB, IP, and JE contributed to conception and design of the study. VR, SS, and JH wrote the first draft of the manuscript. HV, JB, IP, and JE wrote sections of the manuscript. All authors contributed to manuscript revision, read, and approved the submitted version.

FUNDING

This work was supported by NWO-FAPESP project 457002001 (IvdP, SS).

REFERENCES

- Chaikof EL, Dalman RL, Eskandari MK, Jackson BM, Lee WA, Mansour MA, et al. The society for vascular surgery practice guidelines on the care of patients with an abdominal aortic aneurysm. *J Vasc Surg.* (2018) 67:2–77.e2. doi: 10.1016/j.jvs.2017.10.044
- Wanhainen A, Verzini F, Van Herzele I, Allaire E, Bown M, Cohnert T, et al. Editor's choice – European Society for Vascular Surgery (ESVS) 2019 clinical practice guidelines on the management of abdominal aorto-iliac artery aneurysms. *Eur J Vasc Endovasc Surg.* (2019) 57:8–93. doi: 10.1016/j.ejvs.2018.09.020
- Johnston KW, Rutherford RB, Tilson MD, Shah DM, Hollier L, Stanley JC. Suggested standards for reporting on arterial aneurysms. subcommittee on reporting standards for arterial aneurysms, ad hoc committee on reporting standards, society for vascular surgery and north american chapter, international society for cardiovascular surgery. *J Vasc Surg.* (1991) 13:452–8. doi: 10.1067/mva.1991.26737
- Gouveia e Melo R, Silva Duarte G, Lopes A, Alves M, Caldeira D, Fernandes e Fernandes R, et al. Incidence and prevalence of thoracic aortic aneurysms: a systematic review and meta-analysis of population-based studies. *Semin Thorac Cardiovasc Surg.* (2021) 34:1–16. doi: 10.1053/j.semtcv.2021.02.029
- Scott RAP, Ashton HA, Buxton MJ, Day NE, Kim LG, Marteau TM, et al. The Multicentre Aneurysm Screening Study (MASS) into the effect of abdominal aortic aneurysm screening on mortality in men: a randomised controlled trial. *Lancet.* (2002) 360:1531–9. doi: 10.1016/S0140-6736(02)11522-4
- Norman PE, Jamrozik K, Lawrence-Brown MM, Le MTQ, Spencer CA, Tuohy RJ, et al. Population based randomised controlled trial on impact of screening on mortality from abdominal aortic aneurysm. *Br Med J.* (2004) 329:1259–62. doi: 10.1136/bmj.329.7477.1259
- Lindholt JS, Juul S, Fasting H, Henneberg EW. Screening for abdominal aortic aneurysms: single centre randomised controlled trial. *Br Med J.* (2005) 330:750–2. doi: 10.1136/bmj.38369.620162.82
- Ashton HA, Gao L, Kim LG, Druce PS, Thompson SG, Scott RAP. Fifteen-year follow-up of a randomized clinical trial of ultrasonographic screening for abdominal aortic aneurysms. *Br J Surg.* (2007) 94:696–701. doi: 10.1002/bjs.5780
- McKusick VA. Heritable disorders of connective tissue. III The marfan syndrome. *J Chronic Dis.* (1955) 2:609–44. doi: 10.1016/0021-9681(55)90192-2
- Van Hemelrijck C, Renard M, Loeys B. The loeys-dietz syndrome: an update for the clinician. *Curr Opin Cardiol.* (2010) 25:546–51. doi: 10.1097/HCO.0b013e32833f0220
- Kent KC, Zwolak RM, Egorova NN, Riles TS, Manganaro A, Moskowitz AJ, et al. Analysis of risk factors for abdominal aortic aneurysm in a cohort of more than 3 million individuals. *J Vasc Surg.* (2010) 52:539–48. doi: 10.1016/j.jvs.2010.05.090
- Lederle FA, Nelson DB, Joseph AM. Smokers' relative risk for aortic aneurysm compared with other smoking-related diseases: a systematic review. *J Vasc Surg.* (2003) 38:329–34. doi: 10.1016/S0741-5214(03)00136-8
- Pinard A, Jones GT, Milewicz DM. Genetics of thoracic and abdominal aortic diseases: aneurysms, dissections, and ruptures. *Circ Res.* (2019) 124:588–606. doi: 10.1161/CIRCRESAHA.118.312436
- Thompson SG, Ashton HA, Gao L, Buxton MJ, Scott RAP. Final follow-up of the Multicentre Aneurysm Screening Study (MASS) randomized trial of abdominal aortic aneurysm screening. *Br J Surg.* (2012) 99:1649–56. doi: 10.1002/bjs.8897
- Wanhainen A, Hultgren R, Linné A, Holst J, Gottsäter A, Langenskiöld M, et al. Outcome of the swedish nationwide

- abdominal aortic aneurysm screening program. *Circulation*. (2016) 134:1141–8. doi: 10.1161/CIRCULATIONAHA.116.022305
16. Hirsch AT, Haskal ZJ, Hertzner NR, Bakal CW, Creager MA, Halperin JL, et al. ACC/AHA 2005 practice guidelines for the management of patients with peripheral arterial disease (lower extremity, renal, mesenteric, and abdominal aortic). *Circulation*. (2006) 113:e463–654. doi: 10.1161/CIRCULATIONAHA.106.174526
 17. Erbel R, Aboyans V, Boileau C, Bossone E, Di Bartolomeo R, Eggebrecht H, et al. 2014 ESC guidelines on the diagnosis and treatment of aortic diseases. *Eur Heart J*. (2014) 35:2873–926. doi: 10.5603/KP.2014.0225
 18. Tan KHM, Salim S, Machin M, Geroult A, Onida S, Lane T, et al. Abdominal aortic aneurysm clinical practice guidelines: a methodological assessment using the AGREE II instrument. *BMJ Open*. (2022) 12:e056750. doi: 10.1136/bmjopen-2021-056750
 19. Brady AR, Thompson SG, Fowkes FGR, Greenhalgh RM, Powell JT. Abdominal aortic aneurysm expansion: risk factors and time intervals for surveillance. *Circulation*. (2004) 110:16–21. doi: 10.1161/01.CIR.0000133279.07468.9F
 20. Kurvers H, Veith FJ, Lipsitz EC, Ohki T, Gargiulo NJ, Cayne NS, et al. Discontinuous, staccato growth of abdominal aortic aneurysms. *J Am Coll Surg*. (2004) 199:709–15. doi: 10.1016/j.jamcollsurg.2004.07.031
 21. Laine MT, Vanttinen T, Kantonen I, Halmesmaki K, Weselius EM, Laukontaus S, et al. Rupture of abdominal aortic aneurysms in patients under screening age and elective repair threshold. *Eur J Vasc Endovasc Surg*. (2016) 51:511–6. doi: 10.1016/j.ejvs.2015.12.011
 22. Nicholls SC, Gardner JB, Meissner MH, Johansen KH. Rupture in small abdominal aortic aneurysms. *J Vasc Surg*. (1998) 28:884–8. doi: 10.1016/S0741-5214(98)70065-5
 23. Chiu P, Goldstone AB, Schaffer JM, Lingala B, Miller DC, Mitchell RS, et al. Endovascular versus open repair of intact descending thoracic aortic aneurysms. *J Am Coll Cardiol*. (2019) 73:643–51. doi: 10.1016/j.jacc.2018.10.086
 24. Schermerhorn ML, O'Malley JA, Jhaveri A, Philip C, Pomposelli F, Landon B. Endovascular versus open repair of abdominal aortic aneurysms in the medicare population. *N Engl J Med*. (2008) 52:222–3. doi: 10.1097/01.SA.0000307957.69920.56
 25. Budtz-Lilly J, Venermo M, Debus S, Behrendt CA, Altreuther M, Beiles B, et al. Editor's choice – assessment of international outcomes of intact abdominal aortic aneurysm repair over 9 years. *Eur J Vasc Endovasc Surg*. (2017) 54:13–20. doi: 10.1016/j.ejvs.2017.03.003
 26. Schermerhorn ML, Buck DB, O'Malley AJ, Curran T, McCallum JC, Darling J, et al. Long-Term outcomes of abdominal aortic aneurysm in the medicare population. *N Engl J Med*. (2015) 373:328–38. doi: 10.1056/NEJMoa1405778
 27. Patel R, Sweeting MJ, Powell JT, Greenhalgh RM. Endovascular versus open repair of abdominal aortic aneurysm in 15-years' follow-up of the UK endovascular aneurysm repair trial 1 (EVAR trial 1): a randomised controlled trial. *Lancet*. (2016) 388:2366–74. doi: 10.1016/S0140-6736(16)31135-7
 28. Briggs CS, Sibille JA, Yammine H, Ballast JK, Anderson W, Nussbaum T, et al. Short-Term and midterm survival of ruptured abdominal aortic aneurysms in the contemporary endovascular era. *J Vasc Surg*. (2018) 68:408–14.e1. doi: 10.1016/j.jvs.2017.12.037
 29. Van Beek SC, Conijn AP, Koelemay MJ, Balm R. Editor's choice – endovascular aneurysm repair versus open repair for patients with a ruptured abdominal aortic aneurysm: a systematic review and meta-analysis of short-term survival. *Eur J Vasc Endovasc Surg*. (2014) 47:593–602. doi: 10.1016/j.ejvs.2014.03.003
 30. Lindquist Liljeqvist M, Hultgren R, Gasser TC, Roy J. Volume growth of abdominal aortic aneurysms correlates with baseline volume and increasing finite element analysis-derived rupture risk. *J Vasc Surg*. (2016) 63:1434e3–42.e3. doi: 10.1016/j.jvs.2015.11.051
 31. Oliveira-Pinto J, Oliveira NFG, Bastos-Gonçalves FM, Hoeks S, Rijn MJ, Van, Raa S Ten, et al. Long-term results after standard endovascular aneurysm repair with the endurant and excluder stent grafts. *J Vasc Surg*. (2020) 71:64–74. doi: 10.1016/j.jvs.2019.03.039
 32. Adriaans BP, Wildberger JE, Westenberg JJM, Lamb HJ, Schalla S. Predictive imaging for thoracic aortic dissection and rupture: moving beyond diameters. *Eur Radiol*. (2019) 29:6396–404. doi: 10.1007/s00330-019-06320-7
 33. Canchi T, Kumar SD, Ng EYK, Narayanan S. A review of computational methods to predict the risk of rupture of abdominal aortic aneurysms. *Biomed Res Int*. (2015) 2015:1–12. doi: 10.1155/2015/861627
 34. Li X, Staub D, Rafailidis V, Al-Natour M, Kalva S, Partovi S. Contrast-enhanced ultrasound of the abdominal aorta – current status and future perspectives. *Vasa - Eur J Vasc Med*. (2019) 48:115–25. doi: 10.1024/0301-1526/a000749
 35. Baliyan V, Verdini D, Meyersohn NM. Noninvasive aortic imaging. *Cardiovasc Diagn Ther*. (2018) 8:S3–18. doi: 10.21037/cdt.2018.02.01
 36. Wang L, Li Q, Wang X-M, Hao G-Y, Jie-Bao, Hu S, Hu C-H. Enhanced radiation damage caused by iodinated contrast agents during CT examination. *Eur J Radiol*. (2017) 92:72–7. doi: 10.1016/j.ejrad.2017.04.005
 37. Gottukmala R V, Mannudeep KK, Tabari A, Otrakji A, Gee MS. Advanced CT techniques for de-creasing radiation dose, reducing sedation requirements, and opti-mizing image quality in children. *Radiographics*. (2019) 39:709–26. doi: 10.1148/rg.2019180082
 38. Clough RE, Waltham M, Giese D, Taylor PR, Schaeffter T. A new imaging method for assessment of aortic dissection using four-dimensional phase contrast magnetic resonance imaging. *J Vasc Surg*. (2012) 55:914–23. doi: 10.1016/j.jvs.2011.11.005
 39. Szafer J, Ho-Shon K. A comparison of 4D flow MRI-derived wall shear stress with computational fluid dynamics methods for intracranial aneurysms and carotid bifurcations – a review. *Magn Reson Imaging*. (2018) 48:62–9. doi: 10.1016/j.mri.2017.12.005
 40. Rudenick PA, Segers P, Pineda V, Cuellar H, Garcia-Dorado D, Evangelista A, et al. False lumen flow patterns and their relation with morphological and biomechanical characteristics of chronic aortic dissections. Computational model compared with magnetic resonance imaging measurements. *PLoS ONE*. (2017) 12:1–20. doi: 10.1371/journal.pone.0170888
 41. Poduri A. “Cellular mechanisms of ascending aortic aneurysms,” In *New Approaches to Aortic Diseases from Valve to Abdominal Bifurcation*. Academic Press (2018). p. 79–84.
 42. Jana S, Hu M, Shen M, Kassiri Z. Extracellular matrix, regional heterogeneity of the aorta, and aortic aneurysm. *Exp Mol Med*. (2019) 51:1–15. doi: 10.1038/s12276-019-0286-3
 43. Coccione AJ, Hawes JZ, Staiculescu MC, Johnson EO, Murshed M, Wagenseil JE. Elastin, arterial mechanics, and cardiovascular disease. *Am J Physiol Circ Physiol*. (2018) 315:H189–205. doi: 10.1152/ajpheart.00087.2018
 44. Quintana RA, Taylor WR. %J C research. cellular mechanisms of aortic aneurysm formation. *Circ Res*. (2019) 124:607–18. doi: 10.1161/CIRCRESAHA.118.313187
 45. O'Connell MK, Murthy S, Phan S, Xu C, Buchanan J, Spilker R, et al. The three-dimensional micro- and nanostructure of the aortic medial lamellar unit measured using 3D confocal and electron microscopy imaging. *Matrix Biol*. (2008) 27:171–81. doi: 10.1016/j.matbio.2007.10.008
 46. Yanagisawa H, Wagenseil J. Elastic fibers and biomechanics of the aorta: insights from mouse studies. *Matrix Biol*. (2020) 85–86:160–172. doi: 10.1016/j.matbio.2019.03.001
 47. Robert L, Birembaut P. “Extracellular Matrix of the Arterial Vessel Wall.” In: *Diseases of the Arterial Wall*, editors. J-P Camilleri, CL Berry, J-N Fiessinger, J Bériaty. London: Springer p. 43–54.
 48. Karnik SK, Brooke BS, Bayes-Genis A, Sorensen L, Wythe JD, Schwartz RS, et al. critical role for elastin signaling in vascular morphogenesis and disease. *Development*. (2003) 130:411–23. doi: 10.1242/dev.00223
 49. Pozzi A, Wary KK, Giancotti FG, Gardner HA. Integrin alpha1beta1 mediates a unique collagen-dependent proliferation pathway *in vivo*. *J Cell Biol*. (1998) 142:587–94. doi: 10.1083/jcb.142.2.587
 50. Carmo M, Colombo L, Bruno A, Corsi FR, Roncoroni L, Cuttin MS, et al. Alteration of elastin, collagen and their cross-links in abdominal aortic aneurysms. *Eur J Vasc Endovasc Surg*. (2002) 23:543–9. doi: 10.1053/ejvs.2002.1620
 51. Tsamis A, Krawiec JT, Vorp DA. Elastin and collagen fibre microstructure of the human aorta in ageing and disease: a review. *J R Soc Interface*. (2013) 10:20121004. doi: 10.1098/rsif.2012.1004
 52. Nagase H, Visse R, Murphy G. Structure and function of matrix metalloproteinases and TIMPs. *Cardiovasc Res*. (2006) 69:562–73. doi: 10.1016/j.cardiores.2005.12.002

53. Wang X, Khalil RA. Matrix metalloproteinases, vascular remodeling, and vascular disease. *Adv Pharmacol.* (2018) 81:241–330. doi: 10.1016/bs.apha.2017.08.002
54. Shimizu K, Mitchell RN, Libby P. Inflammation and cellular immune responses in abdominal aortic aneurysms. *Arterioscler Thromb Vasc Biol.* (2006) 26:987–94. doi: 10.1161/01.ATV.0000214999.12921.4f
55. van Dorst DCH, de Wagenaar NP, van der Pluijm I, Roos-Hesselink JW, Essers J, Danser AHJ. Transforming growth factor- β and the renin-angiotensin system in syndromic thoracic aortic aneurysms: implications for treatment. *Cardiovasc drugs Ther.* (2020) 35:1233–52. doi: 10.1007/s10557-020-07116-4
56. Guo G, Muñoz-García B, Ott CE, Grünhagen J, Mousa SA, Pletschacher A, et al. Antagonism of GxxPG fragments ameliorates manifestations of aortic disease in marfan syndrome mice. *Hum Mol Genet.* (2013) 22:433–43. doi: 10.1093/hmg/ddt439
57. Kadoglou NP, Liapis CD. Matrix metalloproteinases: contribution to pathogenesis, diagnosis, surveillance and treatment of abdominal aortic aneurysms. *Curr Med Res Opin.* (2004) 20:419–32. doi: 10.1185/030079904125003143
58. Rabkin SW. The role matrix metalloproteinases in the production of aortic aneurysm. *Prog Mol Biol Transl Sci.* (2017) 147:239–65. doi: 10.1016/bs.pmbts.2017.02.002
59. Tamarina NA, McMillan WD, Shively VP, Pearce WH. Expression of matrix metalloproteinases and their inhibitors in aneurysms and normal aorta. *Surgery.* (1997) 122:262–4. doi: 10.1016/S0039-6060(97)90017-9
60. Thompson RW, Holmes DR, Mertens RA, Liao S, Botney MD, Mecham RP, et al. Production and localization of 92-kilodalton gelatinase in abdominal aortic aneurysms. An elastolytic metalloproteinase expressed by aneurysm-infiltrating macrophages. *J Clin Invest.* (1995) 96:318–26. doi: 10.1172/JCI118037
61. Kuivaniemi H, Ryer EJ, Elmore JR, Tromp G. Understanding the pathogenesis of abdominal aortic aneurysms. *Expert Rev Cardiovasc Ther.* (2015) 13:975–87. doi: 10.1586/14779072.2015.1074861
62. Wolinsky H, Glagov S. Comparison of abdominal and thoracic aortic medial structure in mammals. deviation of man from the usual pattern. *Circ Res.* (1969) 25:677–86. doi: 10.1161/01.RES.25.6.677
63. Pyeritz RE. The marfan syndrome. *Annu Rev Med.* (2000) 51:481–510. doi: 10.1146/annurev.med.51.1.481
64. Hoyer J, Kraus C, Hammersen G, Geppert JB, Rauch A. Lethal cutis laxa with contractural arachnodactyly, overgrowth and soft tissue bleeding due to a novel homozygous fibulin-4 gene mutation. *Clin Genet.* (2009) 76:276–81. doi: 10.1111/j.1399-0004.2009.01204.x
65. Graul-Neumann L, Hausser I, Essayie M, Rauch A, Kraus C. Highly variable cutis laxa resulting from a dominant splicing mutation of the elastin gene. *Am J Med Genet A.* (2008) 146A:977–83. doi: 10.1002/ajmg.a.32242
66. Ono RN, Sengle G, Charbonneau NL, Carlberg V, Bächinger HP, Sasaki T, et al. Latent transforming growth factor β -binding proteins and fibulins compete for fibrillin-1 and exhibit exquisite specificities in binding sites *. *J Biol Chem.* (2009) 284:16872–81. doi: 10.1074/jbc.M809348200
67. Robertson IB, Horiguchi M, Zilberberg L, Dabovic B, Hadjiolova K, Rifkin DB. Latent TGF- β -binding proteins. *Matrix Biol.* (2015) 47:44–53. doi: 10.1016/j.matbio.2015.05.005
68. Tsuda T. Extracellular interactions between fibulins and transforming growth factor (TGF)- β in physiological and pathological conditions. *Int J Mol Sci.* (2018) 19:2787. doi: 10.3390/ijms19092787
69. Burger J, van Vliet N, van Heijningen P, Kumra H, Kremers GJ, Alves M, et al. Fibulin-4 deficiency differentially affects cytoskeleton structure and dynamics as well as TGF β signaling. *Cell Signal.* (2019) 58:65–78. doi: 10.1016/j.cellsig.2019.02.008
70. Ramnath NW, Hawinkels LJ, van Heijningen PM, te Riet L, Paauwe M, Vermeij M, et al. Fibulin-4 deficiency increases TGF- β 2 signalling in aortic smooth muscle cells due to elevated TGF- β 2 levels. *Sci Rep.* (2015) 5:16872. doi: 10.1038/srep16872
71. Loeys BL, Dietz HC. Loeys-Dietz Syndrome. In: Adam MP, Ardinger HH, Pagon RA, Wallace SE, Bean LJH, Mirzaa G, Amemiya A, editors. *GeneReviews*. R. Seattle (WA) (1993–2022).
72. van de Laar IM, Oldenburg RA, Pals G, Roos-Hesselink JW, de Graaf BM, Verhagen JM, et al. Mutations in SMAD3 cause a syndromic form of aortic aneurysms and dissections with early-onset osteoarthritis. *Nat Genet.* (2011) 43:121–6. doi: 10.1038/ng.744
73. Loeys BL, Chen J, Neptune ER, Judge DP, Podowski M, Holm T, et al. A syndrome of altered cardiovascular, craniofacial, neurocognitive and skeletal development caused by mutations in TGFBR1 or TGFBR2. *Nat Genet.* (2005) 37:275–81. doi: 10.1038/ng1511
74. Micha D, Guo DC, Hilhorst-Hofstee Y, van Kooten F, Atmaja D, Overwater E, et al. SMAD2 mutations are associated with arterial aneurysms and dissections. *Hum Mutat.* (2015) 36:1145–9. doi: 10.1002/humu.22854
75. Akhurst RJ, Hata A. Targeting the TGF β signalling pathway in disease. *Nat Rev Drug Discov.* (2012) 11:790–811. doi: 10.1038/nrd3810
76. Takeda N, Hara H, Fujiwara T, Kanaya T, Maemura S, Komuro I. TGF- β Signaling-Related genes and thoracic aortic aneurysms and dissections. *Int J Mol Sci.* (2018) 19:2125. doi: 10.3390/ijms19072125
77. van der Pluijm I, van Vliet N, von der Thüsen JH, Robertus JL, Ridwan Y, van Heijningen PM, et al. Defective connective tissue remodeling in smad3 mice leads to accelerated aneurysmal growth through disturbed downstream TGF- β signaling. *EBioMedicine.* (2016) 12:280–94. doi: 10.1016/j.ebiom.2016.09.006
78. Renard M, Callewaert B, Baetens M, Campens L, MacDermot K, Fryns J-P, et al. Novel MYH11 and ACTA2 mutations reveal a role for enhanced TGF β signaling in FTAAD. *Int J Cardiol.* (2013) 165:314–21. doi: 10.1016/j.ijcard.2011.08.079
79. Altobelli E, Rapacchietta L, Profeta VF, Fagnano R. Risk factors for abdominal aortic aneurysm in population-based studies: a systematic review and meta-analysis. *Int J Environ Res Public Health.* (2018) 15:2805. doi: 10.3390/ijerph15122805
80. Villard C, Roy J, Bogdanovic M, Eriksson P, Hultgren R. Sex hormones in men with abdominal aortic aneurysm. *J Vasc Surg.* (2021) 74:2023–9. doi: 10.1016/j.jvs.2021.06.020
81. Davis FM, Rateri DL, Daugherty A. Mechanisms of aortic aneurysm formation: translating preclinical studies into clinical therapies. *Heart.* (2014) 100:1498–505. doi: 10.1136/heartjnl-2014-305648
82. Abbas AK, Lichtman AH, Pillai S. *Cellular and Molecular Immunology*. 9th edition. Elsevier (2018).
83. Bryda EC. The mighty mouse: the impact of rodents on advances in biomedical research. *Mo Med.* (2013) 110:207–11.
84. Bellini C, Bersi MR, Caulk AW, Ferruzzi J, Milewicz DM, Ramirez F, et al. Comparison of 10 murine models reveals a distinct biomechanical phenotype in thoracic aortic aneurysms. *J R Soc Interface.* (2017) 14:1–8. doi: 10.1098/rsif.2016.1036
85. Pereira L, Andrikopoulos K, Tian J, Lee SY, Keene DR, Ono R, et al. Targeting of the gene encoding fibrillin-1 recapitulates the vascular aspect of marfan syndrome. *Nat Genet.* (1997) 17:218–22. doi: 10.1038/ng1097-218
86. Judge DP, Biery NJ, Keene DR, Geubtner J, Myers L, Huso DL, et al. Evidence for a critical contribution of haploinsufficiency in the complex pathogenesis of marfan syndrome. *J Clin Invest.* (2004) 114:172–81. doi: 10.1172/JCI200420641
87. Charbonneau NL, Carlson EJ, Tufa S, Sengle G, Manalo EC, Carlberg VM, et al. *In vivo* studies of mutant fibrillin-1 microfibrils. *J Biol Chem.* (2010) 285:24943–55. doi: 10.1074/jbc.M110.130021
88. Schwill S, Seppelt P, Grünhagen J, Ott C-E, Jugold M, Ruhparwar A, et al. The fibrillin-1 hypomorphic mgR/mgR murine model of marfan syndrome shows severe elastolysis in all segments of the aorta. *J Vasc Surg.* (2013) 57:1628–36.e3. doi: 10.1016/j.jvs.2012.10.007
89. McLaughlin PJ, Chen Q, Horiguchi M, Starcher BC, Stanton JB, Broekelmann TJ, et al. Targeted disruption of fibulin-4 abolishes elastogenesis and causes perinatal lethality in mice. *Mol Cell Biol.* (2006) 26:1700–9. doi: 10.1128/MCB.26.5.1700-1709.2006
90. Huang J, Davis EC, Chapman SL, Budatha M, Marmorstein LY, Word RA, et al. Fibulin-4 deficiency results in ascending aortic aneurysms: a potential link between abnormal smooth muscle cell phenotype and aneurysm progression. *Circ Res.* (2010) 106:583–92. doi: 10.1161/CIRCRESAHA.109.207852
91. Hanada K, Vermeij M, Garinis GA, de Waard MC, Kunen MG, Myers L, et al. Perturbations of vascular homeostasis and aortic valve

- abnormalities in fibulin-4 deficient mice. *Circ Res.* (2007) 100:738–46. doi: 10.1161/01.RES.0000260181.19449.95
92. van der Pluijm I, Burger J, van Heijningen PM, Ijpma A, van Vliet N, Milanese C, et al. %J C research. decreased mitochondrial respiration in aneurysmal aortas of Fibulin-4 mutant mice is linked to PGC1A regulation. *Cardiovasc Res.* (2018) 114:1776–93. doi: 10.1093/cvr/cvy150
 93. Halabi CM, Broekelmann TJ, Lin M, Lee VS, Chu ML, Mecham RP. Fibulin-4 is essential for maintaining arterial wall integrity in conduit but not muscular arteries. *Sci Adv.* (2017) 3:1776–1793. doi: 10.1126/sciadv.1602532
 94. Larsson J, Goumans MJ, Sjöstrand LJ, van Rooijen MA, Ward D, Levéen P, et al. Abnormal angiogenesis but intact hematopoietic potential in TGF-beta type I receptor-deficient mice. *EMBO J.* (2001) 20:1663–73. doi: 10.1093/emboj/20.7.1663
 95. Oshima M, Oshima H, Taketo MM. TGF- β receptor type II deficiency results in defects of yolk sac hematopoiesis and vasculogenesis. *Dev Biol.* (1996) 179:297–302. doi: 10.1006/dbio.1996.0259
 96. Carvalho RL, Itoh F, Goumans MJ, Lebrin F, Kato M, Takahashi S, et al. Compensatory signalling induced in the yolk sac vasculature by deletion of TGFbeta receptors in mice. *J Cell Sci.* (2007) 120:4269–77. doi: 10.1242/jcs.013169
 97. Choudhary B, Zhou J, Li P, Thomas S, Kaartinen V, Sucov HM. Absence of TGFbeta signaling in embryonic vascular smooth muscle leads to reduced lysyl oxidase expression, impaired elastogenesis, and aneurysm. *Genesis.* (2009) 47:115–21. doi: 10.1002/dvg.20466
 98. Ye P, Chen W, Wu J, Huang X, Li J, Wang S, et al. GM-CSF contributes to aortic aneurysms resulting from SMAD3 deficiency. *J Clin Invest.* (2013) 123:2317–31. doi: 10.1172/JCI67356
 99. Kuang SQ, Kwartler CS, Byanova KL, Pham J, Gong L, Prakash SK, et al. Rare, nonsynonymous variant in the smooth muscle-specific isoform of myosin heavy chain, MYH11, R247C, alters force generation in the aorta and phenotype of smooth muscle cells. *Circ Res.* (2012) 110:1411–22. doi: 10.1161/CIRCRESAHA.111.261743
 100. Schildmeyer LA, Braun R, Taffet G, DeBiasi M, Burns AE, Bradley A, et al. Impaired vascular contractility and blood pressure homeostasis in the smooth muscle alpha-actin null mouse. *FASEB J.* (2000) 14:2213–20. doi: 10.1096/fj.99-0927com
 101. Cheng J, Zhou X, Jiang X, Sun T. Deletion of ACTA2 in mice promotes angiotensin II induced pathogenesis of thoracic aortic aneurysms and dissections. *J Thorac Dis.* (2018) 10:4733–40. doi: 10.21037/jtd.2018.07.75
 102. Golledge J, Krishna SM, Wang Y. Mouse models for abdominal aortic aneurysm. *Br J Pharmacol.* (2020) 179:792–810. doi: 10.1111/bph.15260
 103. Daugherty A, Cassis LA. Mouse models of abdominal aortic aneurysms. *Arter Thromb Vasc Biol.* (2004) 24:429–34. doi: 10.1161/01.ATV.0000118013.72016.ea
 104. Patelis N, Moris D, Schizas D, Damaskos C, Perrea D, Bakoyiannis C, et al. Animal models in the research of abdominal aortic aneurysms development. *Physiol Res.* (2017) 66:899–915. doi: 10.33549/physiolres.933579
 105. Cassis LA, Gupte M, Thayer S, Zhang X, Charnigo R, Howatt DA, et al. Infusion promotes abdominal aortic aneurysms independent of increased blood pressure in hypercholesterolemic mice. *Am J Physiol Hear Circ Physiol.* (2009) 296:H1660–5. doi: 10.1152/ajpheart.00028.2009
 106. Daugherty A, Manning MW, Cassis LA. Angiotensin II promotes atherosclerotic lesions and aneurysms in apolipoprotein E-deficient mice. *J Clin Invest.* (2000) 105:1605–12. doi: 10.1172/JCI7818
 107. Saraff K, Babamusta F, Cassis LA, Daugherty A. Aortic dissection precedes formation of aneurysms and atherosclerosis in angiotensin II-infused, apolipoprotein E-deficient mice. *Arter Thromb Vasc Biol.* (2003) 23:1621–6. doi: 10.1161/01.ATV.0000085631.76095.64
 108. Halloran BG, Davis VA, McManus BM, Lynch TG, Baxter BT. Localization of aortic disease is associated with intrinsic differences in aortic structure. *J Surg Res.* (1995) 59:17–22. doi: 10.1006/jsre.1995.1126
 109. Rateri DL, Davis FM, Balakrishnan A, Howatt DA, Moorleghen JJ, O'Connor WN, et al. Angiotensin II induces region-specific medial disruption during evolution of ascending aortic aneurysms. *Am J Pathol.* (2014) 184:2586–95. doi: 10.1016/j.ajpath.2014.05.014
 110. Haskett D, Speicher E, Fouts M, Larson D, Azhar M, Utzinger U, et al. The effects of angiotensin II on the coupled microstructural and biomechanical response of C57BL/6 mouse aorta. *J Biomech.* (2012) 45:772–9. doi: 10.1016/j.jbiomech.2011.11.017
 111. Busch A, Holm A, Wagner N, Ergün S, Rosenfeld M, Otto C, et al. Extra- and intraluminal elastase induce morphologically distinct abdominal aortic aneurysms in mice and thus represent specific subtypes of human disease. *J Vasc Res.* (2016) 53:49–57. doi: 10.1159/000447263
 112. Pyo R, Lee JK, Shipley JM, Curci JA, Mao D, Ziporin SJ, et al. Targeted gene disruption of matrix metalloproteinase-9 (gelatinase B) suppresses development of experimental abdominal aortic aneurysms. *J Clin Invest.* (2000) 105:1641–9. doi: 10.1172/JCI8931
 113. Sénémaud J, Caligiuri G, Etienne H, Delbosc S, Michel JB, Coscas R. Translational relevance and recent advances of animal models of abdominal aortic aneurysm. *Arterioscler Thromb Vasc Biol.* (2017) 37:401–10. doi: 10.1161/ATVBAHA.116.308534
 114. Wang Y, Krishna S, Golledge J. The calcium chloride-induced rodent model of abdominal aortic aneurysm. *Atherosclerosis.* (2013) 226:29–39. doi: 10.1016/j.atherosclerosis.2012.09.010
 115. Yamanouchi D, Morgan S, Stair C, Seedial S, Lengfeld J, Kent KC, et al. Accelerated aneurysmal dilation associated with apoptosis and inflammation in a newly developed calcium phosphate rodent abdominal aortic aneurysm model. *J Vasc Surg.* (2012) 56:455–61. doi: 10.1016/j.jvs.2012.01.038
 116. Busch A, Bleichert S, Ibrahim N, Wortmann M, Eckstein H-H, Brostjan C, et al. Translating mouse models of abdominal aortic aneurysm to the translational needs of vascular surgery. *JVS-Vascular Sci.* (2021) 2:219–23. doi: 10.1016/j.jvssci.2021.01.002
 117. Zheng H, qiong, Rong J, bing, Ye F, ming, Xu Y, chuan, Lu HS, Wang J, An. Induction of thoracic aortic dissection: a mini-review of β -aminopropionitrile-related mouse models. *J Zhejiang Univ Sci B.* (2020) 21:603–10. doi: 10.1631/jzus.B2000022
 118. Ren W, Liu Y, Wang X, Jia L, Piao C, Lan F, et al. β -Aminopropionitrile monofumarate induces thoracic aortic dissection in C57BL/6 mice. *Sci Rep.* (2016) 6:1–7. doi: 10.1038/srep28149
 119. Burkhardt AM, Zlotnik A. Translating translational research: mouse models of human disease. *Cell Mol Immunol.* (2013) 10:373–4. doi: 10.1038/cmi.2013.19
 120. Soepriatna AH, Damen FW, Vlachos PP, Goergen CJ. Cardiac and respiratory-gated volumetric murine ultrasound. *Int J Cardiovasc Imaging.* (2018) 34:713–24. doi: 10.1007/s10554-017-1283-z
 121. Favreau J, Nguyen BT, Goa I, Yu P, Tao M, Schneiderman J, et al. Murine ultrasound imaging for circumferential strain analyses in the angiotensin II abdominal aortic aneurysm model. *J Vasc Surg.* (2012) 56:462–9. doi: 10.1016/j.jvs.2012.01.056
 122. Azuma J, Maegdefessel L, Kitagawa T, Dalman RL, McConnell M V., Tsao PS. Assessment of elastase-induced murine abdominal aortic aneurysms: comparison of ultrasound imaging with in situ video microscopy. *J Biomed Biotechnol.* (2011) 2011:1–10. doi: 10.1155/2011/252141
 123. Vandeghinste B, Trachet B, Renard M, Casteleyn C, Staelens S, Loeys B, et al. Replacing vascular corrosion casting by in vivo micro-ct imaging for building 3D cardiovascular models in mice. *Mol Imaging Biol.* (2011) 13:78–86. doi: 10.1007/s11307-010-0335-8
 124. Trachet B, Fraga-Silva RA, Piersigilli A, Tedgui A, Sordet-Dessimoz J, Astolfo A, et al. Dissecting abdominal aortic aneurysm in ang II-infused mice: suprarenal branch ruptures and apparent luminal dilatation. *Cardiovasc Res.* (2015) 105:213–22. doi: 10.1093/cvr/cvu257
 125. Turner GH, Olzinski AR, Bernard RE, Aravindhan K, Karr HW, Mirabile RC, et al. In vivo serial assessment of aortic aneurysm formation in apolipoprotein E-deficient mice via MRI. *Eur Cardiovasc Imaging.* (2008) 9:220–6. doi: 10.1161/CIRCIMAGING.108.787358
 126. Goergen CJ, Barr KN, Huynh DT, Eastham-Anderson JR, Choi G, Hedehus M, et al. In vivo quantification of murine aortic cyclic strain, motion, and curvature: implications for abdominal aortic aneurysm growth. *J Magn Reson Imaging.* (2010) 32:847–58. doi: 10.1002/jmri.22331
 127. Sangha GS, Phillips EH, Li R, Cheng J-X, Goergen CJ. Abstract 253: vibrational photoacoustic imaging of lipid in murine abdominal aortic aneurysms and atherosclerosis. *Arterioscler Thromb Vasc Biol.* (2015) 35:A253. doi: 10.1161/atvb.35.suppl_1.253

128. Klink A, Heynens J, Herranz B, Lobatto ME, Arias T, Sanders HMHE, et al. *In Vivo* characterization of a new abdominal aortic aneurysm mouse model with conventional and molecular magnetic resonance imaging. *J Am Coll Cardiol*. (2011) 58:2522–30. doi: 10.1016/j.jacc.2011.09.017
129. Xu K, Xu C, Zhang Y, Qi F, Yu B, Li P, et al. Identification of type IV collagen exposure as a molecular imaging target for early detection of thoracic aortic dissection. *Theranostics*. (2018) 8:437–49. doi: 10.7150/thno.22467
130. Adams LC, Brangsch J, Reimann C, Kaufmann JO, Buchholz R, Karst U, et al. Simultaneous molecular MRI of extracellular matrix collagen and inflammatory activity to predict abdominal aortic aneurysm rupture. *Sci Rep*. (2020) 10:15206. doi: 10.1038/s41598-020-71817-x
131. Botnar RM, Wiethoff AJ, Ebersberger U, Lacerda S, Blume U, Warley A, et al. In vivo assessment of aortic aneurysm wall integrity using elastin-specific molecular magnetic resonance imaging. *Circ Cardiovasc Imaging*. (2014) 7:679–89. doi: 10.1161/CIRCIMAGING.113.001131
132. Okamura H, Pisani LJ, Dalal AR, Emrich F, Dake BA, Arakawa M, et al. Assessment of elastin deficit in a marfan mouse aneurysm model using an elastin-specific magnetic resonance imaging contrast agent. *Circ Cardiovasc Imaging*. (2014) 7:690–6. doi: 10.1161/CIRCIMAGING.114.001658
133. Brangsch J, Reimann C, Kaufmann JO, Adams LC, Onthank D, Thöne-Reineke C, et al. Molecular MR-Imaging for noninvasive quantification of the anti-inflammatory effect of targeting interleukin-1 β in a mouse model of aortic aneurysm. *Mol Imaging*. (2020) 19:1–13. doi: 10.1177/1536012120961875
134. Brangsch J, Reimann C, Kaufmann JO, Adams LC, Onthank DC, Thöne-Reineke C, et al. Concurrent molecular magnetic resonance imaging of inflammatory activity and extracellular matrix degradation for the prediction of aneurysm rupture. *Circ Cardiovasc Imaging*. (2019) 12:1–11. doi: 10.1161/CIRCIMAGING.118.008707
135. Lavin B, Lacerda S, Andia ME, Lorrio S, Bakewell R, Smith A, et al. Tropoelastin: an *in vivo* imaging marker of dysfunctional matrix turnover during abdominal aortic dilation. *Cardiovasc Res*. (2020) 116:995–1005. doi: 10.1093/cvr/cvz178
136. Didangelos A, Yin X, Mandal K, Saje A, Smith A, Xu Q, et al. Extracellular matrix composition and remodeling in human abdominal aortic aneurysms: a proteomics approach. *Mol Cell Proteomics*. (2011) 10:M111.008128 1–15. doi: 10.1074/mcp.M111.008128
137. Yagi H, Nishigori M, Murakami Y, Osaki T, Muto S, Iba Y, et al. Discovery of novel biomarkers for atherosclerotic aortic aneurysm through proteomics-based assessment of disease progression. *Sci Rep*. (2020) 10:6429. doi: 10.1038/s41598-020-67561-x
138. Yamashita O, Yoshimura K, Nagasawa A, Ueda K, Morikage N, Ikeda Y, et al. Periostin links mechanical strain to inflammation in abdominal aortic aneurysm. *PLoS ONE*. (2013) 8:e79753. doi: 10.1371/journal.pone.0079753
139. Parry DJ, Al-Barjas HS, Chappell L, Rashid ST, Ariëns RAS, Scott DJA. Markers of inflammation in men with small abdominal aortic aneurysm. *J Vasc Surg*. (2010) 52:145–51. doi: 10.1016/j.jvs.2010.02.279
140. Parry DJ, Al-Barjas HS, Chappell L, Rashid T, Ariëns RAS, Scott DJA. Haemostatic and fibrinolytic factors in men with a small abdominal aortic aneurysm. *Br J Surg*. (2009) 96:870–7. doi: 10.1002/bjs.6632
141. Robson SC, Shephard EG, Kirsch RE. Fibrin degradation product D-dimer induces the synthesis and release of biologically active IL-1 β , IL-6 and plasminogen activator inhibitors from monocytes *in vitro*. *Br J Haematol*. (1994) 86:322–6. doi: 10.1111/j.1365-2141.1994.tb04733.x
142. Ducas AA, Kuhn DCS, Bath LC, Lozowy RJ, Boyd AJ. Increased matrix metalloproteinase 9 activity correlates with flow-mediated intraluminal thrombus deposition and wall degeneration in human abdominal aortic aneurysm. *JVS Vasc Sci*. (2020) 1:190–9. doi: 10.1016/j.jvssci.2020.09.004
143. Botnar RM, Brangsch J, Reimann C, Janssen CHP, Razavi R, Hamm B, et al. *In vivo* molecular characterization of abdominal aortic aneurysms using fibrin-specific magnetic resonance imaging. *J Am Heart Assoc*. (2018) 7:1–11. doi: 10.1161/JAHA.117.007909
144. Spuentrup E, Botnar RM, Wiethoff AJ, Ibrahim T, Kelle S, Katoh M, et al. MR imaging of thrombi using EP-2104R, a fibrin-specific contrast agent: initial results in patients. *Eur Radiol*. (2008) 18:1995–2005. doi: 10.1007/s00330-008-0965-2
145. Kaijzel EL, van Heijningen PM, Wielopolski PA, Vermeij M, Koning GA, van Cappellen WA, et al. Multimodality imaging reveals a gradual increase in matrix metalloproteinase activity at aneurysmal lesions in live fibulin-4 mice. *Circ Cardiovasc Imaging*. (2010) 3:567–77. doi: 10.1161/CIRCIMAGING.109.933093
146. Sheth RA, Maricevich M, Mahmood U. *In vivo* optical molecular imaging of matrix metalloproteinase activity in abdominal aortic aneurysms correlates with treatment effects on growth rate. *Atherosclerosis*. (2010) 212:181–7. doi: 10.1016/j.atherosclerosis.2010.05.012
147. Amirbekian V, Aguinaldo JGS, Amirbekian S, Hyafil F, Vucic E, Sirol M, et al. Atherosclerosis and matrix metalloproteinases: experimental molecular MR imaging *in vivo*. *Radiology*. (2009) 251:429–38. doi: 10.1148/radiol.2511080539
148. Lancelot E, Amirbekian V, Brigger I, Raynaud JS, Ballet S, David C, et al. Evaluation of matrix metalloproteinases in atherosclerosis using a novel noninvasive imaging approach. *Arterioscler Thromb Vasc Biol*. (2008) 28:425–32. doi: 10.1161/ATVBAHA.107.149666
149. Bazeli R, Coutard M, Dupont BD, Lancelot E, Corot C, Laissy JP, et al. *In vivo* evaluation of a new magnetic resonance imaging contrast agent (P947) to target matrix metalloproteinases in expanding experimental abdominal aortic aneurysms. *Invest Radiol*. (2010) 45:662–8. doi: 10.1097/RLI.0b013e3181ee5bbf
150. Golestani R, Razavian M, Nie L, Zhang J, Jung JJ, Ye Y, et al. Imaging vessel wall biology to predict outcome in abdominal aortic aneurysm. *Circ Cardiovasc Imaging*. (2014) 8:1–9. doi: 10.1161/CIRCIMAGING.114.002471
151. Toczek J, Ye Y, Gona K, Kim H-Y, Han J, Razavian M, et al. Preclinical evaluation of RYM1, a matrix metalloproteinase-targeted tracer for imaging aneurysm. *J Nucl Med*. (2017) 58:1318–23. doi: 10.2967/jnumed.116.188656
152. Razavian M, Zhang J, Nie L, Tavakoli S, Razavian N, Dobrucki LW, et al. Molecular imaging of matrix metalloproteinase activation to predict murine aneurysm expansion *in vivo*. *J Nucl Med*. (2010) 51:1107–15. doi: 10.2967/jnumed.110.075259
153. Raffort J, Lareyre F, Clément M, Hassen-Khodja R, Chinetti G, Mallat Z. Monocytes and macrophages in abdominal aortic aneurysm. *Nat Rev Cardiol*. (2017) 14:457–71. doi: 10.1038/nrcardio.2017.52
154. Ikeda H, Ishii A, Sano K, Chihara H, Arai D, Abekura Y, et al. Activatable fluorescence imaging of macrophages in cerebral aneurysms using iron oxide nanoparticles conjugated with indocyanine green. *Front Neurosci*. (2020) 14:370. doi: 10.3389/fnins.2020.00370
155. Razavian M, Marfatia R, Mongue-Din H, Tavakoli S, Sinusas AJ, Zhang J, et al. Integrin-Targeted imaging of inflammation in vascular remodeling. *Arterioscler Thromb Vasc Biol*. (2011) 31:2820–6. doi: 10.1161/ATVBAHA.111.231654
156. Kitagawa T, Kosuge H, Chang E, James ML, Yamamoto T, Shen B, et al. Integrin-targeted molecular imaging of experimental abdominal aortic aneurysms by (18)F-labeled Arg-Gly-Asp positron-emission tomography. *Circ Cardiovasc Imaging*. (2013) 6:950–6. doi: 10.1161/CIRCIMAGING.113.000234
157. Costa da Silva M, Breckwoldt MO, Vinchi F, Correia MP, Stojanovic A, Thielmann CM, Meister M, Muley T, Warth A, Platten M, et al. Iron induces anti-tumor activity in tumor-associated macrophages. *Front Immunol*. (2017) 8:1479. doi: 10.3389/fimmu.2017.01479
158. Shannon AH, Chordia MD, Spinosa MD, Su G, Ladd Z, Pan D, et al. Single-Photon emission computed tomography imaging using formyl peptide receptor 1 ligand can diagnose aortic aneurysms in a mouse model. *J Surg Res*. (2020) 251:239–47. doi: 10.1016/j.jss.2020.01.028
159. Fan J, Li X, Zhong L, Hao-Tong, Di J, Liu F, Zhao HH, Bai SL. MCP-1, ICAM-1 and VCAM-1 are present in early aneurysmal dilatation in experimental rats. *Folia Histochem Cytobiol*. (2010) 48:455–61. doi: 10.2478/v10042-010-0042-y
160. Wang X, Searle AK, Hohmann JD, Liu AL, Abraham MK, Palasubramaniam J, et al. Dual-Targeted theranostic delivery of miRs arrests abdominal aortic aneurysm development. *Mol Ther*. (2018) 26:1056–65. doi: 10.1016/j.jymthe.2018.02.010
161. Hu C, Tan H, Lin Q, Abudupataer M, Zhao Y, Li J, et al. SPECT/CT imaging of apoptosis in aortic aneurysm with radiolabeled duramycin. *Apoptosis*. (2019) 24:745–55. doi: 10.1007/s10495-019-01554-8

162. Ailawadi G, Moehle CW, Pei H, Walton SP, Yang Z, Kron IL, et al. Smooth muscle phenotypic modulation is an early event in aortic aneurysms. *J Thorac Cardiovasc Surg.* (2009) 138:1392–9. doi: 10.1016/j.jtcvs.2009.07.075
163. Gandhi R, Cawthorne C, Craggs LJL, Wright JD, Domarkas J, He P, et al. Cell proliferation detected using [18F]FLT PET/CT as an early marker of abdominal aortic aneurysm. *J Nucl Cardiol.* (2019) 28:1961–1971. doi: 10.1007/s12350-019-01946-y
164. Buijs RVC, Willems TP, Tio RA, Boersma HH, Tiellu IFJ, Slart RHJA, et al. Calcification as a risk factor for rupture of abdominal aortic aneurysm. *Eur J Vasc Endovasc Surg.* (2013) 46:542–8. doi: 10.1016/j.ejvs.2013.09.006
165. Roijers RB, Debernardi N, Cleutjens JPM, Schurgers LJ, Mutsaers PHA, Van Der Vusse GJ. Microcalcifications in early intimal lesions of atherosclerotic human coronary arteries. *Am J Pathol.* (2011) 178:2879–87. doi: 10.1016/j.ajpath.2011.02.004
166. Shioi A, Ikari Y. Plaque calcification during atherosclerosis progression and regression. *J Atheroscler Thromb.* (2018) 25:294–303. doi: 10.5551/jat.RV17020
167. Wanga S, Hibender S, Ridwan Y, van Roomen C, Vos M, van der Made I, et al. Aortic microcalcification is associated with elastin fragmentation in marfan syndrome. *J Pathol.* (2017) 243:294–306. doi: 10.1002/path.4949
168. Li Z, Zhao Z, Cai Z, Sun Y, Li L, Yao F, et al. Runx2 (Runt-Related Transcription Factor 2)-Mediated Microcalcification is a novel pathological characteristic and potential mediator of abdominal aortic aneurysm. *Arterioscler Thromb Vasc Biol.* (2020) 2:1352–69. doi: 10.1161/ATVBAHA.119.314113
169. Kessler K, Borges LF, Ho-Tin-Noé B, Jondeau G, Michel JB, Vranckx R. Angiogenesis and remodelling in human thoracic aortic aneurysms. *Cardiovasc Res.* (2014) 104:147–59. doi: 10.1093/cvr/cvu196
170. Thompson MM, Jones L, Nasim A, Sayers RD, Bell PRF. Angiogenesis in abdominal aortic aneurysms. *Eur J Vasc Endovasc Surg.* (1996) 11:464–9. doi: 10.1016/S1078-5884(96)80183-3
171. Shi S, Orbay H, Yunan Y, Graves S, Nayak TP, Hong H, et al. PET imaging of abdominal aortic aneurysm with 64Cu-labeled anti-CD105 antibody fab fragment. *J Nucl Med.* (2015) 56:927–32. doi: 10.2967/jnumed.114.153098
172. Fu X. ming, Yamawaki-Ogata A, Oshima H, Ueda Y, Usui A, Narita Y. Intravenous administration of mesenchymal stem cells prevents angiotensin II-induced aortic aneurysm formation in apolipoprotein E-deficient mouse. *J Transl Med.* (2013) 11:1–11. doi: 10.1186/1479-5876-11-175
173. Li Y, Behr S. Acute Findings on FDG PET/CT: Key imaging features and how to differentiate them from malignancy. *Curr Radiol Rep.* (2020) 8:1–14. doi: 10.1007/s40134-020-00367-x
174. Tegler G, Ericson K, Srensen J, Björck M, Wanhainen A. Inflammation in the walls of asymptomatic abdominal aortic aneurysms is not associated with increased metabolic activity detectable by 18-fluorodeoxyglucose positron-emission tomography. *J Vasc Surg.* (2012) 56:802–7. doi: 10.1016/j.jvs.2012.02.024
175. Courtois A, Nussgens BV, Hustinx R, Namur G, Gomez P, Somja J, et al. 18F-FDG uptake assessed by PET/CT in abdominal aortic aneurysms is associated with cellular and molecular alterations prefacing wall deterioration and rupture. *J Nucl Med.* (2013) 54:1740–7. doi: 10.2967/jnumed.112.115873
176. Huang Y, Teng Z, Elkhawad M, Tarkin JM, Joshi N, Boyle JR, et al. High structural stress and presence of intraluminal thrombus predict abdominal aortic aneurysm 18F-FDG uptake: insights from biomechanics. *Circ Cardiovasc Imaging.* (2016) 9:1–9. doi: 10.1161/CIRCIMAGING.116.004656
177. Haller SJ, Crawford JD, Courchaine KM, Bohannon CJ, Landry GJ, Moneta GL, et al. Intraluminal thrombus is associated with early rupture of abdominal aortic aneurysm. *J Vasc Surg.* (2018) 67:1051–58.e1. doi: 10.1016/j.jvs.2017.08.069
178. Jalalzadeh H, Indrakusuma R, Planken RN, Legemate DA, Koelemay MJW, Balm R. Inflammation as a predictor of abdominal aortic aneurysm growth and rupture: a systematic review of imaging biomarkers. *Eur J Vasc Endovasc Surg Off J Eur Soc Vasc Surg.* (2016) 52:333–42. doi: 10.1016/j.ejvs.2016.05.002
179. Timur UT, van Herwaarden JA, Mihajlovic D, De Jong P, Mali W, Moll FL. (18F)-FDG PET scanning of abdominal aortic aneurysms and correlation with molecular characteristics: a systematic review. *EJNMMI Res.* (2015) 5:76. doi: 10.1186/s13550-015-0153-8
180. Curci JA, Beckman JA. Positron emission tomography fluorine-18-labeled 2-deoxy-2-fluoro-d-glucose tells a complicated story in the aortic aneurysm wall. *Circ Cardiovasc Imaging.* (2016) 9:1–3. doi: 10.1161/CIRCIMAGING.116.005689
181. Forsythe RO, Dweck MR, McBride OMB, Vesey AT, Semple SI, Shah ASV, et al. 18F-Sodium fluoride uptake in abdominal aortic aneurysms: the SoFIA3 study. *J Am Coll Cardiol.* (2018) 71:513–23. doi: 10.1016/j.jacc.2017.11.053
182. Tegler G, Estrada S, Hall H, Wanhainen A, Björck M, Sörensen J, et al. Autoradiography screening of potential positron emission tomography tracers for asymptomatic abdominal aortic aneurysms. *Ups J Med Sci.* (2014) 119:229–35. doi: 10.3109/03009734.2014.894157
183. English SJ, Sastriques SE, Detering L, Sultan D, Luehmann H, Arif B, et al. CCR2 positron emission tomography for the assessment of abdominal aortic aneurysm inflammation and rupture prediction. *Circ Cardiovasc Imaging.* (2020) 13:1–11. doi: 10.1161/CIRCIMAGING.119.009889
184. Richards MJ, Semple SI, MacGillivray TJ, Gray C, Langrish JP, Williams M, et al. Abdominal aortic aneurysm growth predicted by uptake of ultrasmall superparamagnetic particles of iron oxide: a pilot study. *Circ Cardiovasc Imaging.* (2011) 4:274–81. doi: 10.1161/CIRCIMAGING.110.959866
185. Forsythe R, McBride O, Robson J, Vesey A, Chalmers R, Burns P, et al. Aortic wall inflammation predicts abdominal aortic aneurysm expansion, rupture, and need for surgical repair. *Circulation.* (2017) 136:787–97. doi: 10.1161/CIRCULATIONAHA.117.028433
186. Nie X, Laforest R, Elvington A, Randolph GJ, Zheng J, Voller T, et al. PET/MRI of hypoxic atherosclerosis using 64Cu-ATSM in a rabbit model. *J Nucl Med.* (2016) 57:2006–11. doi: 10.2967/jnumed.116.172544
187. Nie X, Elvington A, Laforest R, Zheng J, Voller T, Zayed M, et al. 64Cu-ATSM PET/MR imaging of hypoxia in human atherosclerosis. *Circ Cardiovasc Imaging.* (2020) 13:2006–2011. doi: 10.1161/CIRCIMAGING.119.009791
188. Wilson WRW, Anderton M, Choke EC, Dawson J, Loftus IM, Thompson MM. Elevated plasma MMP1 and MMP9 are associated with abdominal aortic aneurysm rupture. *Eur J Vasc Endovasc Surg.* (2008) 35:580–4. doi: 10.1016/j.ejvs.2007.12.004
189. Rangasamy L, Di Geronimo B, Ortín I, Coderch C, Zapico JM, Ramos A, et al. Molecular imaging probes based on matrix metalloproteinase inhibitors (MMPis). *Molecules.* (2019) 24:580–584. doi: 10.3390/molecules24162982
190. Hwang J, Huang Y, Burwell TJ, Peterson NC, Connor J, Weiss SJ, et al. In Situ imaging of tissue remodeling with collagen hybridizing peptides. *ACS Nano.* (2017) 11:9825–35. doi: 10.1021/acsnano.7b03150
191. Jones JA, Ruddy JM, Bouges S, Zavadzka JA, Brinsa TA, Stroud RE, et al. Alterations in membrane type-1 matrix metalloproteinase abundance after the induction of thoracic aortic aneurysm in a murine model. *Am J Physiol - Hear Circ Physiol.* (2010) 299:114–24. doi: 10.1152/ajpheart.00028.2010

Conflict of Interest: The authors declare that the research was conducted in the absence of any commercial or financial relationships that could be construed as a potential conflict of interest.

Publisher's Note: All claims expressed in this article are solely those of the authors and do not necessarily represent those of their affiliated organizations, or those of the publisher, the editors and the reviewers. Any product that may be evaluated in this article, or claim that may be made by its manufacturer, is not guaranteed or endorsed by the publisher.

Copyright © 2022 Rastogi, Stefens, Houwaart, Verhagen, de Bruin, van der Pluijm and Essers. This is an open-access article distributed under the terms of the Creative Commons Attribution License (CC BY). The use, distribution or reproduction in other forums is permitted, provided the original author(s) and the copyright owner(s) are credited and that the original publication in this journal is cited, in accordance with accepted academic practice. No use, distribution or reproduction is permitted which does not comply with these terms.

Frontiers in Medicine

Translating medical research and innovation into
improved patient care

A multidisciplinary journal which advances our
medical knowledge. It supports the translation
of scientific advances into new therapies and
diagnostic tools that will improve patient care.

Discover the latest Research Topics

[See more →](#)

Frontiers

Avenue du Tribunal-Fédéral 34
1005 Lausanne, Switzerland
frontiersin.org

Contact us

+41 (0)21 510 17 00
frontiersin.org/about/contact



Frontiers in Medicine

